AGARD-CP-469

AGARD

ADVISORY GROUP FOR AEROSPACE RESEARCH & DEVELOPMENT

7 RUE ANCELLE 92200 NEUILLY SUR SEINE FRANCE

AD-A220 901

DISTRIBUTION STATEMENT A
Approved for public release;
Distribution Unlimited

AGARD CONFERENCE PROCEEDINGS No.469

Secondary Flows in Turbomachines

DTIC
ELECTE
APR 24 1990
S D

NORTH ATLANTIC TREATY ORGANIZATION



DISTRIBUTION AND AVAILABILITY
ON BACK COVER

90 04 23 159

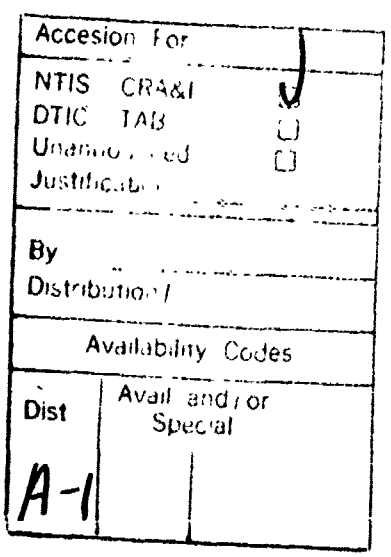
NORTH ATLANTIC TREATY ORGANIZATION

ADVISORY GROUP FOR AEROSPACE RESEARCH AND DEVELOPMENT

(ORGANISATION DU TRAITE DE L'ATLANTIQUE NORD)

AGARD Conference Proceedings No.469

SECONDARY FLOWS IN TURBOMACHINES



Papers presented at the Propulsion and Energetics Panel 74th (B) Specialists' Meeting,
held in Luxembourg, 30 August — 1 September 1989.

THE MISSION OF AGARD

According to its Charter, the mission of AGARD is to bring together the leading personalities of the NATO nations in the fields of science and technology relating to aerospace for the following purposes:

- Recommending effective ways for the member nations to use their research and development capabilities for the common benefit of the NATO community;
- Providing scientific and technical advice and assistance to the Military Committee in the field of aerospace research and development (with particular regard to its military application);
- Continuously stimulating advances in the aerospace sciences relevant to strengthening the common defence posture;
- Improving the co-operation among member nations in aerospace research and development;
- Exchange of scientific and technical information;
- Providing assistance to member nations for the purpose of increasing their scientific and technical potential;
- Rendering scientific and technical assistance, as requested, to other NATO bodies and to member nations in connection with research and development problems in the aerospace field.

The highest authority within AGARD is the National Delegates Board consisting of officially appointed senior representatives from each member nation. The mission of AGARD is carried out through the Panels which are composed of experts appointed by the National Delegates, the Consultant and Exchange Programme and the Aerospace Applications Studies Programme. The results of AGARD work are reported to the member nations and the NATO Authorities through the AGARD series of publications of which this is one.

Participation in AGARD activities is by invitation only and is normally limited to citizens of the NATO nations.

The content of this publication has been reproduced
directly from material supplied by AGARD or the authors.

Published February 1990

Copyright © AGARD 1990
All Rights Reserved

ISBN 92-835-0544-1

Printed by Specialised Printing Services Limited
40 Chigwell Lane, Loughton, Essex IG10 3TZ

RECENT PUBLICATIONS OF THE PROPULSION AND ENERGETICS PANEL

Conference Proceedings

Helicopter Propulsion Systems
AGARD Conference Proceedings No.302, 57th Meeting, May 1981

Ramjets and Ramrockets for Military Applications
AGARD Conference Proceedings No.307, 58th Meeting, October 1981

Problems in Bearings and Lubrication
AGARD Conference Proceedings No.323, 59th Meeting, May/June 1982

Engine Handling
AGARD Conference Proceedings No.324, 60th Meeting, October 1982

Viscous Effects in Turbomachines
AGARD Conference Proceedings No.351, 61st *A* Meeting, June 1983

Auxiliary Power Systems
AGARD Conference Proceedings 352, 61st *B* Meeting, May 1983

Combustion Problems in Turbine Engines
AGARD Conference Proceedings 353, 62nd Meeting, October 1983

Hazard Studies for Solid Propellant Rocket Motors
AGARD Conference Proceedings 367, 63rd *A* Meeting, May/June 1984

Engine Cyclic Durability by Analysis and Testing
AGARD Conference Proceedings No.368, 63rd *B* Meeting, May/June 1984

Gears and Power Transmission Systems for Helicopters and Turboprops
AGARD Conference Proceedings No.369, 64th Meeting October 1984

Heat Transfer and Cooling in Gas Turbines
AGARD Conference Proceedings No.390, 65th Meeting, May 1985

Smokeless Propellants
AGARD Conference Proceedings No.391, 66th *A* Meeting, September 1985

Interior Ballistics of Guns
AGARD Conference Proceedings No.392, 66th *B* Meeting, September 1985

Advanced Instrumentation for Aero Engine Components
AGARD Conference Proceedings No.399, 67th Meeting, May 1986

Engine Response to Distorted Inflow Conditions
AGARD Conference Proceedings No.400, 68th *A* Meeting, September 1986

Transonic and Supersonic Phenomena in Turbomachines
AGARD Conference Proceedings No.401, 68th *B* Meeting, September 1986

Advanced Technology for Aero Engine Components
AGARD Conference Proceedings No.421, 69th Meeting, September 1987

Combustion and Fuels in Gas Turbine Engine
AGARD Conference Proceedings No.422, 70th Meeting, October 1987

Engine Condition Monitoring — Technology and Experience
AGARD Conference Proceedings No.448, 71st Meeting, May/June 1988

Application of Advanced Material for Turbomachinery and Rocket Propulsion
AGARD Conference Proceedings No.449, 72nd *A* Meeting, October 1988

Combustion Instabilities in Liquid-Fuelled Propulsion Systems
AGARD Conference Proceedings No.450, 72nd *B* Meeting, October 1988

Aircraft Fire Safety
AGARD Conference Proceedings No.467, 73rd Meeting, May 1989

Working Group Reports

Through Flow Calculations in Axial Turbomachines
AGARD Advisory Report 175. Results of WG 12 (October 1981)

Alternative Jet Engine Fuels
AGARD Advisory Report 181. Vol.1 and Vol.2. Results of WG 13 (July 1982)

Suitable Averaging Techniques in Non-Uniform Internal Flows
AGARD Advisory Report 182 (in English and French). Results of WG 14 (June/August 1983)

Producibility and Cost Studies of Aviation Kerosines
AGARD Advisory Report 227. Results of WG 16 (June 1985)

Performance of Rocket Motors with Metallized Propellants
AGARD Advisory Report 230. Results of WG 17 (September 1986)

Recommended Practices for Measurement of Gas Path Pressures and Temperatures for Performance Assessment of Aircraft Engines and Components
AGARD Advisory Report 245. Results of WG 19 (In production, 1990)

The Uniform Engine Test Programme
AGARD Advisory Report 248. Results of WG 15 (In production, 1990)

Test Cases for Computation of Internal Flows in Aero Engine Components
AGARD Advisory Report 275. Results of WG 18 (In production, 1990)

Lecture Series

Aircraft Fire Safety
AGARD LS 123 (June 1982)

Operation and Performance Measurement of Engines in Sea Level Test Facilities
AGARD LS 132 (April 1984)

Ramjet and Ramrocket Propulsion Systems for Missiles
AGARD LS 136 (September 1984)

3-D Computation Techniques Applied to Internal Flows in Propulsion Systems
AGARD LS 140 (June 1985)

Engine Airframe Integration for Rotorcraft
AGARD LS 146 (June 1986)

Design Methods Used in Solid Rocket Motors
AGARD LS 150 (April 1987)
AGARD LS 150 (Revised) (April 1988)

Blading Design for Axial Turbomachines
AGARD LS 167 (June 1989)

Other Publications

Rocket Altitude Test Facility Register
AGARD AG 297 (March 1987)

Manual for Aeroelasticity in Turbomachines
AGARD AG 298/1 (March 1987)
AGARD AG 298/2 (June 1988)

Application of Modified Loss and Deviation Correlations to Transonic Axial Compressors
AGARD Report 745 (November 1987)

Measurement Uncertainty within the Uniform Engine Test Programme
AGARD AG 307 (May 1989)

Rotorcraft Drivetrain Life Safety and Reliability
AGARD R 775 (In production 1990)

THEME

The problems arising from secondary flows remain unresolved and continue to be a major source of reduced performance in advanced turbomachinery. Optimization of blade design with regard to secondary flows is still done on an empirical basis. The meeting was intended to assemble specialists on computational and experimental methods for dealing with questions associated with these flows. The meeting was concerned with secondary effects in both compressors and turbines and considered the flows in blade passages and in clearances.

* * *

Les problèmes créés par les écoulements secondaires restent sans solution et sont l'une des causes principales de la diminution des performances dans les turbomachines avancées. L'optimisation de la conception des aubes par rapport aux écoulements secondaires se fait encore de façon empirique. L'objet de la réunion fut de rassembler les spécialistes dans le domaine des méthodes expérimentales et de calcul qui permettent de résoudre les différentes questions soulevées par ces écoulements. La réunion a examiné les effets secondaires créés dans les compresseurs et les turbines, ainsi que les effets des écoulements dans les canaux des aubes et les dégagements.

PROPULSION AND ENERGETICS PANEL

Chairman: M. l'Ing. Princ. de l'Armement Ph. Ramette
Société Européenne de Propulsion
Attaché au Directeur Technique pour les Activités Spatiales
Boîte Postale 303
92156 Suresnes Cedex, France

Deputy Chairman: Professor Dr A.Üçer
Middle East Technical University
O D T Ü
Makina Muh. Bölümü
Ankara, Turkey

PROGRAMME COMMITTEE

Prof. G.K.Serovy (Chairman)
Anson Marston Distinguished Prof.
Dept. of Mechanical Engineering
3038 ME/ESM
Iowa State University
Ames, Iowa 50011, US

Prof. J.Chauvin
LEMFI-Bâtiment 502
Campus Universitaire
91405 Orsay Cedex, France

Prof. D.Dini
Dipartimento di Macchine
Universita di Pisa
Via Diotisalvi 3
56100 Pisa, Italy

Prof. Dr-Ing. L.Fottner
Universität der Bundeswehr München
Institut für Strahlantriebe
Werner Heisenbergweg 39
8014 Neubiberg, Germany

Mr R.K.Garwood
Rolls Royce Ltd
Whittle House
PO Box 3
Filton, Bristol BS12 7QE, UK

Prof. Ch.Hirsch
Vrije Universiteit Brussel
Dienst Stromingsmechanica
Pleinlaan 2
1050 Brussel, Belgium

Prof. K.Papailiou
Thermal Turbomachinery Laboratory
National Technical University
PO Box 64069
15710 Athens, Greece

Prof. H.I.H.Saravanamuttoo
Chairman, Mechanical and Aerospace Engineering
Carleton University
Ottawa, Ontario K1S 5B6, Canada

HOST NATION COORDINATOR

Mr F.Kirch
Ministère de la Force Publique
Plateau du St. Esprit
2915 Luxembourg

PANEL EXECUTIVE

Dr E.Riester
AGARD-NATO-PEP
7 rue Ancelle
92200 Neuilly sur Seine
France

ACKNOWLEDGEMENT

The Propulsion and Energetics Panel wishes to express its thanks to the National Authorities from Luxembourg for the invitation to hold this meeting in Luxembourg, and for the facilities and personnel which made the meeting possible.

CONTENTS

	Page
RECENT PUBLICATIONS OF PEP	iii
THEME	v
PROPULSION AND ENERGETICS PANEL	vi
TECHNICAL EVALUATION REPORT by A.Wennerstrom	ix
	Reference
SESSION I – BASIC FLOW PHENOMENA	
SECONDARY FLOWS AND RADIAL MIXING PREDICTIONS IN AXIAL COMPRESSORS by J.De Ruyck, Ch.Hirsch and P.Segaert	1
THE EFFECTS OF COMPRESSOR ENDWALL FLOW ON AIRFOIL INCIDENCE AND DEVIATION by R.P.Dring and H.D.Joslyn	2
A STUDY ON SECONDARY FLOW AND SPANWISE MIXING IN AXIAL FLOW COMPRESSORS by M.Erkilet and A.Ş.Üçer	3
PARABOLIZED CALCULATIONS OF TURBULENT THREE DIMENSIONAL FLOWS IN A TURBINE DUCT by P.Ferrand, F.Leboeuf, F.Pommel and E.Parkinson	4
EXPERIMENTAL AND NUMERICAL STUDY ON BASIC PHENOMENA OF SECONDARY FLOWS IN TURBINES by R.Niehuis, P.Lücking and B.Stubert	5
SECONDARY FLOWS AND REYNOLDS STRESS DISTRIBUTIONS DOWNSTREAM OF A TURBINE CASCADE AT DIFFERENT EXPANSION RATIOS by A.Perdichizzi, M.Ubaldi and P.Zunino	6
SESSION II – EXPERIMENTAL RESULTS	
AN INVESTIGATION OF SECONDARY FLOWS IN NOZZLE GUIDE VANES by R.G.Dominy and S.C.Harding	7
SECONDARY FLOW PREDICTIONS FOR A TRANSONIC NOZZLE GUIDE VANE by G.C.Horton	8
SECONDARY FLOW IN A TURBINE GUIDE VANE WITH LOW ASPECT-RATIO by D.Wegener, J.Quest and W.Hoffmann	9
MEASUREMENT OF THE FLOW FIELD IN THE BLADE PASSAGE AND SIDE-WALL REGION OF A PLANE TURBINE CASCADE by E.Detemple-Laake	10
Paper is cancelled	
CENTRIFUGAL IMPELLER GEOMETRY AND ITS INFLUENCE ON SECONDARY FLOWS by H.Krain and W.Hoffmann	12
SESSION III – THREE-DIMENSIONAL COMPUTATION AND COMPARISON WITH EXPERIMENTS	
CALCUL DE L'ECOULEMENT TRIDIMENSIONNEL TURBULENT DANS UN AUBAGE RECTILIGNE DE TURBINE par L.Cambier et B.Escande	13
Paper cancelled	

Reference

CALCUL DES ECOULEMENTS SECONDAIRES DANS UNE TURBINE AXIALE
par J.Bernard et F.Falchetti 15

GENERATION AND DECAY OF SECONDARY FLOWS AND THEIR IMPACT ON AERODYNAMIC PERFORMANCE OF MODERN TURBOMACHINERY COMPONENTS
by C.Hah 16

SECONDARY FLOW CALCULATIONS FOR AXIAL AND RADIAL COMPRESSORS
by D.Douvikas, J.Kaldellis and K.D.Papailiou 17

THE NUMERICAL SIMULATION OF MULTISTAGE TURBOMACHINERY FLOWS
by J.J.Adamczyk, T.A.Beach, M.L.Celestina, R.A.Mulac and W.M.To 18

SESSION IV – TIP CLEARANCE FLOWS

RESEARCH ON CASCADE SECONDARY AND TIP-LEAKAGE FLOWS – PERIODICITY AND SURFACE FLOW VISUALIZATION
by L.S.Langston 19

LOSSES IN THE TIP-LEAKAGE FLOW OF A PLANAR CASCADE OF TURBINE BLADES
by M.I.Yaras and S.A.Sjolander 20

COMPUTATIONAL PREDICTION AND MEASUREMENTS OF THE FLOW IN AXIAL TURBINE CASCADES AND STAGES
by H.E.Gallus, K.Weskamp and J.Zeschky 21

Paper is cancelled

ANALYSIS OF THE ROTOR TIP LEAKAGE FLOW WITH TIP COOLING AIR EJECTION
by W.Koschel, H.Schmidt and A.Vornberger 23

SESSION V – SECONDARY FLOW EFFECTS ON HEAT TRANSFER

DETAILED HEAT TRANSFER MEASUREMENTS IN NOZZLE GUIDE VANE PASSAGES IN LINEAR AND ANNULAR CASCADES IN THE PRESENCE OF SECONDARY FLOWS
by N.W.Harvey, Z.Wang, P.T.Ireland and T.V.Jones 24

EFFECTS OF SECONDARY FLOW ON HEAT TRANSFER IN ROTATING PASSAGES
by J.G. Moore and J.Moore 25

ETUDE THEORIQUE DE L'ECOULEMENT DANS UN CANAL EN ROTATION. APPROCHE EXPERIMENTALE PAR LA VISUALISATION DE L'ECOULEMENT DANS UN CANAL COURBE
par J.Guidez, P.J.Michard, D.Dutoya et J.Perucchini 26

THE EFFECT OF SECONDARY FLOW ON THE REDISTRIBUTION OF THE TOTAL TEMPERATURE FIELD DOWNSTREAM OF A STATIONARY TURBINE CASCADE
by W.E.Carscallen and P.H.Oosthuizen 27

TECHNICAL EVALUATION REPORT
on PEP 74th-B Specialists' Meeting
on SECONDARY FLOWS IN TURBOMACHINES

by

Dr A.J.Wennerstrom
Air Force Wright Aeronautical Laboratories/POTX
Wright Patterson Air Force Base
Ohio 45433
United States

1. SUMMARY

The main objective of this meeting was to assemble specialists on computational and experimental methods who are concerned with secondary flows in advanced turbomachinery to establish the state-of-the-art and to see in which direction present and future research is and should be heading. The meeting accomplished this objective.

It was concluded that computational fluid dynamics (CFD) was now providing useful design guidance, gave a very good qualitative picture of secondary flows, but still had some quantitative deficiencies. Hybrid methods, now regularly applied to multi-stage compressor design, are still undergoing useful refinement and appear applicable also to the design of multi-stage turbines. Current experimental work is often characterized by great detail and will aid in evaluating existing secondary flow models as well as in the conception of new models.

Recommendations made included more emphasis on those aspects of CFD which will improve quantitative predictions, more use of CFD for heat transfer computations, application of what is described as the third level of CFD computation to heat transfer in cooled rotors, and continued refinement of hybrid methods including greater emphasis on their application to multi-stage turbines. Another meeting on this or a closely allied topic was recommended five or six years hence.

2. INTRODUCTION

AGARD's first meeting devoted exclusively to the topic of secondary flows in turbomachines was held in March 1977. A closely related topic was addressed six years later when AGARD sponsored a meeting on viscous flow in turbomachines in June 1983. Now, returning once again to the subject of secondary flows, several pronounced new developments can be observed. First, computational fluid dynamics, conspicuous by its absence in the first two meetings, now played a role in over half of the papers comprising the present meeting. On the other hand, applications of classical secondary flow theory and boundary layer analyses were far fewer. Second, hybrid flow models such as introduced by Adkins and Smith (1982) and Gallimore and Cumpsty (1986) now appeared in four papers. By a hybrid model, I am referring to semi-empirical models of secondary flow features superimposed on an axisymmetric solution to obtain a practical design approach suitable for multi-stage turbomachines. Third, secondary flow effects on heat tranfer, a subject not addressed at all in the first two meetings, was discussed in three papers of the present meeting.

3. CONTENT OF THE MEETING

Of the twenty-seven numbered papers in the meeting, twenty-four were presented. Paper Nos. 11, 14 and 22, were withdrawn. No manuscript was available for Paper No. 4 at the time of the meeting.

A total of thirteen papers dealt with computational fluid dynamics (CFD). These were comprised of Paper Nos. 4, 5, 7, 8, 9, 12, 13, 16, 18, 21, 23, 25 and 26. Of these, Paper Nos. 5, 7, 8, 9, 12, 16, 18, 21 and 26 showed comparisons with experiments. Paper Nos. 4, 13, 23 and 25 were computational only. The authors of Paper Nos. 4, 5 and 21 used parabolized methods. The authors of Paper Nos. 8, 16 and 18 showed comparisons with previously established experimental results; the other six authors showing comparisons with data included new experimental results.

Four papers dealt with hybrid through-flow calculations for multi-stage turbomachinery. Paper Nos. 1, 3 and 17 were compressor oriented. Paper No. 15 was focused on turbines. Six papers dealt with experiments only. These papers, all concerning turbines, were Nos. 6, 10, 19, 20, 24 and 27. Eleven papers presented new experimental results. These were comprised of Paper Nos. 5, 6, 7, 9, 10, 12, 20, 21, 24, 26 and 27.

Three papers dealt with heat transfer. Paper No. 24 was experimental only. Paper No. 25 was computational only. Paper No. 26 included both computational and experimental results.

Seven papers dealt with compressors. These were Paper Nos. 1, 2, 3, 12, 16, 17, and 18.

Eighteen papers dealt with turbines. Of these, Paper Nos. 25 and 26 dealt with flow internal to the blades within cooling passages. All the rest dealt with external flow around the blades; these were comprised of Paper Nos. 4, 5, 6, 7, 8, 9, 10, 13, 15, 16, 19, 20, 21, 23, 24 and 27.

The reader will observe from the above that the papers could be grouped in many different ways. Because no particular grouping seemed clearly superior to any other, I have chosen to present a short synopsis of each paper in numerical order according to Paper No. as they are arranged in this Conference Proceedings.

* * *

Session I – Basic Flow Phenomena

1. Secondary Flows and Radial Mixing Predictions in Axial Compressors
by J.De Ruyck, Ch.Hirsch, P.Segaert

De Ruyck et al. present a hybrid axisymmetric through flow computation which uses a modified Gallimore and Cumpsty turbulent mixing concept plus convective transport mechanisms incorporated into an S3-surface computation. The convective model is treated explicitly while the diffusive mixing is modelled empirically. Three test cases are evaluated; a cascade and two compressor rotors. It is concluded that reasonable agreement is generally obtained but some radial velocities on the suction side are under-estimated. Turbulent diffusion appears important in all cases while convective mixing only becomes significant under certain conditions.

2. The Effects of Compressor Endwall Flow on Airflow Incidence and Deviation
by R.P.Dring and H.D.Joslyn

Dring and Joslyn discussed different ways of defining the average flow angle in the blade-to-blade plane downstream of a blade row. They made the point that only one definition is consistent with the formulation of through flow theory. The end-wall regions are particularly sensitive to this and they showed that different averaging methods could lead to discrepancies in incidence and deviation angle of as much as 13 degrees.

3. A Study on Secondary Flow and Spanwise Mixing in Axial Flow Compressors
by M.Eriklet and A.S.Üçer

Eriklet and Üçer present a hybrid axisymmetric through flow computation using the finite element method which combines the Gallimore and Cumpsty spanwise mixing model, two-dimensional loss and deviation correlations and a three-dimensional secondary flow loss correlation. Comparisons are made with both low and high speed compressor data. They conclude that the mixing model appears to behave correctly when given the right data, but that the empirical two and three-dimensional loss, deviation, and end-wall blockage calculations do not yet lead to reliable predictions of radial distributions for multi-stage compressors.

4. Calculs Paraboliśés d'Ecoulements Turbulents Tridimensionnels dans une Turbine
par P.Ferrand, F.Leboeuf, F.Paumel, E.Parkinson, J.Bernard et A.Ribert

Ferrand et al. presented results of some preliminary calculations using a parabolized three-dimensional Navier-Stokes computation to calculate the flow through two curved ducts. One example was a rectangular 90 degree bend, and the second was a two-dimensional turbine-shaped passage lacking periodicity. Results presented were tentative and qualitative; no written manuscript was available. Results with the 90 degree bend illustrate the correct trends. Those with the turbine-shaped passage had some problems. The usual difficulty of parabolized methods treating separation, i.e. reverse flows, was acknowledged.

3. Numerical Study on Basic Phenomena of Secondary Flows in Turbines
by R.Niehuis, P.Lücking and B.Stubert

Niehuis et al. examined an annular cascade of turbine nozzle guide vanes of medium aspect ratio both experimentally and computationally. The computations were done with an Eule code and also a partially-parabolized Navier-Stokes code. Two other model configurations were examined computationally with and without finite blade thickness. Neither type of code used could directly treat reverse flow and separation. These, and also other authors at this meeting, concluded that proper simulation of the inlet conditions, particularly the boundary layer profiles, have a strong influence on computed solutions and must be well modelled if good agreement with experiments is to be obtained. The Euler code provided surprisingly good solutions in spite of its inability to simulate the horseshoe vortices. The partially-parabolized Navier-Stokes code could only partially simulate the horseshoe vortices but also compared well with experiment. The authors concluded that the passage vortex was the dominant secondary flow near the endwalls and the horseshoe vortices appeared to be of minor importance. The additional model configuration calculations also supported this conclusion. Although inlet boundary layers are caused by viscous effects, it was observed that the rolling up process to form secondary vortices is primarily an inviscid effect thus explaining the success of the Euler computations.

6. Secondary Flows and Reynolds Stress Distributions Downstream of a Turbine Cascade at Different Expansion Ratios
by A.Perdichizzi, M.Ubaldi and P.Zunino

Perdichizzi et al. presented results of an experimental investigation using hot wire measurements of secondary flows and turbulence behind a turbine nozzle cascade. Turbulence kinetic energy distributions were determined among other things.

Session II – Experimental Results

7. An Investigation of Secondary Flows in Nozzle Guide Vanes
by R.G.Dominy and S.C.Harding

Dominy and Harding made an experimental and computational investigation of low aspect ratio turbine nozzle guide vanes having three different spanwise stacking philosophies. They showed that three-dimensional considerations allow considerable design control over spanwise loss distributions and can be used to advantage. They conclude that three-dimensional viscous flow calculations are indispensible for reliable analysis of such configurations. Codes used were by Moore, Dawes, and Denton.

8. Secondary Flow Predictions for a Transonic Nozzle Guide Vane
by G.C.Horton

Horton analyzed a similar turbine nozzle guide vane with the Dawes three-dimensional viscous code, and compared his results with experimental data. He also obtained relatively good agreement between computation and experiment, and suggested that the code might be used to predict loss as an integral part of the turbine design process.

9. Secondary Flow in a Turbine Guide Vane with Low Aspect Ratio
by D.Wegener, J.Quest and W.Hoffmann

Wegener et la. also used the Dawes codes to model another similar turbine nozzle guide vane and compared the calculation with extensive experimental results. They also achieved good correspondence between measured and calculated velocities but described the loss prediction as not yet satisfying. They suggested that optimizing the mesh geometry at the trailing edge and in the downstream region might lead to further improvement.

10. Measurement of the Flow Field in the Blade Passage and Side-Wall Region of a Plane Turbine Cascade
by E.Detemple-Laake

Detemple-Laake presented an experimental study of several features of a linear cascade of highly loaded turbine rotor blades. The secondary flow characteristics observed were described. However, the results presented were part of a much more comprehensive program and no conclusions were drawn.

11. Paper is cancelled.

12. Centrifugal Impeller Geometry and its Influence on Secondary Flows
bu H.Krain and W.Hoffmann

Krain and Hoffmann provided one of only two papers dealing with centrifugal compressors. Experimental data for two backswept impellers was presented along with results of supporting three-dimensional viscous computations using the Dawes code. Experimental and computational results both showed significant differences in the secondary flow between the two rotors and were qualitatively in good agreement. The authors suggest that a three-dimensional viscous code can be used for secondary flow control in the design of future impellers.

Session III – Three-Dimensional Computation and Comparison with Experiments

13. Calcul de l'Ecoulement Tridimensionnel Turbulent dans un Aubage Rectiligne de Turbine
par L.Cambier et B.Escande

Cambier and Escande discuss a three-dimensional Navier-Stokes computation of turbulent flow through a linear turbine cascade. A unique feature of this work was a multi-grid scheme employing on O-type subdomain around the blades and H-type subdomains up and downstream in order to model accurately the rounded leading and trailing edges while maintaining up and downstream boundaries sufficiently far from the blades. Results are shown to be qualitatively similar to experimental results obtained at a lower flow velocity.

14. Paper is cancelled.

15. Calcul des Ecoulements Secondaires dans une Turbine Axiale
par J.Bernard et F.Falchetti

Bernard and Falchetti have introduced probably the first published hybrid axisymmetric through flow computation aimed at multi-stage turbines. It employs boundary-layer concepts and is aimed at incorporating secondary-flow effects in this type of calculation. Examples were shown for a low pressure turbine nozzle and a low pressure turbine stage. Results were promising; angle predictions looked good, losses and blockage need further refinement.

16. Generation and Decay of Secondary Flows and their Impact on Aerodynamics Performance of Modern Turbomachinery Components
by C.Hah

Hah used a three-dimensional Navier-Stokes code to study two turbine nozzle designs and two centrifugal compressor impeller designs. In both cases, one design performed significantly better than its counterpart. Hah's objective was to see if such a code could predict the observed differences which are often not evident from axisymmetric design methods supported by correlations. He concluded that such a code can make valid comparisons between candidate designs and thus can be used as a practical design aid to shorten the component development process.

17. Secondary Flow Calculations for Axial and Radial Compressors
by D.Douvikas, J.Kaldellis and K.D.Papailiou

Douvikas et al. have presented a new formulation of secondary flow features incorporated into a hybrid axisymmetric through-flow computation. The notion of a peripheral blockage is introduced. A total kinetic energy equation is substituted for an entrainment equation. Sample results are shown for application to a compressor cascade, a radial impeller, and two single-stage axial compressors. Results appear good. It is suggested that the methodology might be extended to turbines.

18. The Numerical Simulation of Multistage Turbomachinery Flows
by J.J.Adamczyk, T.A.Beach, M.L.Celestina, R.A.Mulac and W.M.To

Adamczyk et al. presented an approach applicable to computational fluid dynamic modelling which raises the level of sophistication to a third level. Early three-dimensional models examined only a single blade row, rotating or stationary. A second level of sophistication was introduced by Denton and subsequently others which took into account the effects of adjacent blade rows by circumferentially averaging the spanwise parameter distributions of adjacent, primarily upstream, blade rows in order to provide better steady flow boundary conditions for the blade row analyzed in three dimensions. Adamczyk et al. have now illustrated an approach to incorporate non-steady terms heretofore neglected. Examples are presented to indicate the importance of these terms.

Session IV — Tip Clearance Flows

19. Research on Cascade Secondary and Tip-Leakage Flows — Periodicity and Surface Flow Visualization
by L.S.Langston

Langston has focused on the achievement of periodicity in testing large linear cascades having few airfoils and also on surface flow visualization techniques and their interpretation. He indicates how certain experimental techniques combined with a potential flow solution can help to achieve periodicity in a cascade of as little as four blades. He describes three surface flow visualization techniques all employing oil and describes their features as well as some precautions concerning their use.

20. Losses in the Tip-Leakage Flow of a Planar Cascade of Turbine Blades
by M.I.Yaras and S.A.Sjolander

Yaras and Sjolander present experimental results associated with tip leakage flow in a linear cascade of turbine rotor blades with stationary end walls. They conclude that the largest part of the loss is associated with the kinetic energy of the flow discharging from the gap, but that much of this loss did not appear in exit plane measurements until about one chord length downstream.

21. Computational Prediction and Measurements of the Flow in Axial Turbine Cascades and Stages
by H.E.Gallus, K.Weskamp and J.Zeschky

Gallus et al. present a comparison between results obtained experimentally with a turbine nozzle cascade and a full turbine stage with computations made using a three-dimensional, partially-parabolized Navier-Stokes code. The paraboiized code limits the computation to cases involving no flow separation and the H-grid employed required a sharp trailing edge. Rotor clearance was not yet included. In spite of these limitations, the computation could describe the principal three-dimensional effects and achieved good agreement with the pitch-averaged stator exit flow.

22. Paper is cancelled.

23. Analysis of the Rotor Tip Leakage Flow with Tip Cooling Air Ejection
by W.Koschel, H.Schmidt and A.Vornberger

Koschel et al. present a numerical simulation of turbine rotor tip leakage flow occurring with three similar configurations. One has a plain square-cut tip; the other two have a trenched tip and are analyzed with and without coolant ejection. Results show that the coolant flow injection had a minor effect on the discharge mass flow in the presence of wall motion but that a pronounced influence of wall motion is observed for the blade with coolant flow injection.

Session V — Secondary Flow Effects on Heat Transfer

24. Detailed Heat Transfer Measurements in Nozzle Guide Vane Passages in Linear and Annular Cascades in the Presence of Secondary Flows
by N.W.Harvey, Z.Wang, P.T.Ireland and T.V.Jones

Harvey et al. present the results of heat transfer measurements in turbine nozzle guide vanes using liquid crystals in a linear cascade and using thin-film gauges in an annular cascade. Both experiments used transient techniques; however, the annular cascade test was accomplished at engine representative Reynolds numbers and Mach numbers. The liquid crystals demonstrated the capability of providing great detail in contours of heat transfer coefficient. A fluorescent dye flow visualization technique was used in the annular cascade test to aid in interpretation. Detailed measurements also proved possible with the thin film gauge technique and could be interpreted in terms of the secondary flow features. A computational technique introduced achieved a reasonable prediction of the streamline pattern.

25. Effects of Secondary Flow on Heat Transfer in Rotating Passages
by J.G.Moore and J.Moore

Moore and Moore have addressed the question of heat transfer through a rotating 180 degree bend using the Moore elliptic three-dimensional Navier-Stokes code. This problem is important for predicting cooling flows in the interior of a cooled turbine blade. The analysis was compared with data from a rotating square channel. Predicted and measured heat transfer rates for rotating channels were substantially higher than for stationary channels. However, some disagreement among different investigations was noted.

26. Etude Théorique de l'Ecoulement dans un Canal en Rotation. Approche Expérimentale par la Visualisation de l'Ecoulement dans un Canal Courbe
par J.Guidez, P.-J.Michard, D.Dutoya et J.Perucchini

Guidez et al. have also evaluated flow through a rotating channel simulating the interior cooling passage of a cooled turbine blade. Their results concur with the Moores' in that rotation increases the heat transfer coefficient. Experimental evidence is provided and is supported by three-dimensional Navier-Stokes computations. The secondary flow features are described.

27. The Effect of Secondary Flow on the Redistribution of the Total Temperature Field Downstream of a Stationary Turbine Cascade
by W.E.Carscallen and P.H.Oosthuizen

Carscallen and Oosthuizen presented results of a cold turbine linear cascade test which, for a uniform inlet total temperature, produced a non-uniform total temperature at the cascade exit. They speculated on possible reasons for this.

* * *

4. CONCLUSIONS

(1) With respect to computational fluid dynamics (CFD), opinions varied concerning how much one could rely on it at the present time. The views expressed can be summarized roughly as follows:

- There was unanimous agreement that CFD can provide useful design guidance.
- All authors felt that CFD could represent qualitative secondary flow features well.
- All authors concerned with turbine blades felt that it was vital to model inlet boundary layers adequately.
- Pressures or velocities seemed reasonably well predicted by all CFD codes discussed.
- There is generally much more disagreement or skepticism concerning how accurately they now predict losses and exit flow angles.
- Three authors used partially-parabolized methods. Recognizing that these codes cannot directly treat separated flows, the authors still felt that the codes modelled the most important secondary flow features to a useful degree.
- CFD appears ready to make significant contributions to heat transfer.
- The paper presented by Adamczyk introduced a third level of three-dimensional CFD modelling. I define the first level of modelling as the study of an isolated blade row in three dimensions and steady flow. The second level of modelling was introduced by Denton and subsequently others wherein the effect of adjacent blade rows is taken into account by circumferentially averaging, particularly the inlet flow, and again treating the problem as a steady flow. The third level of modelling now included some non-steady terms formerly neglected as input data to a succeeding blade row. The fourth level would be the complete three-dimensional non-steady multi-blade row problem.

(2) With respect to hybrid through-flow analyses for multi-stage turbomachines, three authors introduced refinements aimed at improving these methods for compressor design. However, the most notable event which occurred in this area was the SNECMA work presented by Bernard applying this concept to multi-stage turbine design This is the first attempt of this type which I have become aware of. The importance of this is the following. The state-of-the-art for multi-stage turbine design is a purely axisymmetric through-flow computation, just as it was for compressors until recently. Many of the papers presented at this meeting have illustrated how important secondary flows are in turbines. Yet, it is totally impractical to make extensive use of CFD in the design of a multi-stage turbine because of the time and expense required. What is needed for routine design is a hybrid computation conceptually similar to those we now use for compressor design. The models used for turbine secondary flows may be different and they may take some time to develop, but any reasonable model or models will be better than none at all. The paper presented by Papailiou also commented on the applicability of the hybrid approach to turbines as well as compressors.

(3) Many papers dealt either partially or exclusively with experimental work. These experiments which in many cases included exceptional detail, are obviously essential for evaluating the quality of existing secondary flow models as well as for aiding in the conception of new models.

(4) This meeting covered a good cross-section of secondary flow topics and was well attended. Several new ideas were presented which should stimulate future research. I believe the meeting served a useful purpose.

5. RECOMMENDATIONS

(1) Research on improved CFD models should concentrate on those weaknesses which cause inaccurate or questionable predictions of losses and exit flow angle. This deficiency may be closely coupled with the state-of-the-art of turbulence modelling.

(2) More future work should focus on the application of CFD to heat transfer prediction. Efforts consistent with recommendation (1) above will also contribute to this area.

(3) The third level of CFD computation presented by Adamczyk may also have significant impact on the prediction of heat transfer in cooled high pressure turbine rotors. An effort should be made to explore the influence of the non-steady terms on this heat transfer problem.

(4) The refinement of hybrid computation schemes for through-flow computations in multi-stage compressors should continue.

(5) Efforts should be increased for the development of hybrid computation schemes applicable to through-flow computations in multi-stage turbines.

(6) Another AGARD meeting on this or a closely allied topic would be appropriate in five or six years.

SECONDARY FLOWS AND RADIAL MIXING PREDICTIONS IN AXIAL COMPRESSORS

De Ruyck J. — Associate Professor
Hirsch Ch. — Professor
Segaert P. — Research Assistant IWONL

Department of Fluid Mechanics
Vrije Universiteit Brussel
Pleinlaan 2, 1050 Brussels
Belgium

SUMMARY

A radial mixing computation method is presented in the framework of an integrated Quasi-3D approximation method for turbomachinery flow computations. The radial mixing computation is performed on a transverse surface S3, the only type of streamsurface hitherto not considered in the Quasi-3D computation. Both convective and diffusive mixing mechanisms are taken into account : the convective mixing due to secondary flows is computed explicitly, while the diffusive mixing due to the random effects of turbulence is modeled by empirical coefficients. The flow field on the S3-surface is reconstructed from the knowledge of axial vorticity contributions for different flow regions, which are added to constitute the right-hand side of a quasi-harmonic Poisson-type streamfunction equation. These axial vorticity components are obtained through vorticity equations for the inviscid flow region, combined with integral methods for the 3D end-wall boundary layers, 3D profile boundary layers and 3D asymmetric wakes. The validity of the secondary flow computation is assessed through comparisons between computational results and experimental data. The method is applied to predict the redistribution of radial temperature profiles for three axial turbomachines : a linear cascade and two single-stage compressor rotors.

SYMBOLS

b	blockage factor, boundary layer velocity defect parameter
c	chord
f	wake profile model (Pohlhausen polynomial)
g	wake profile model (bridging function)
h	static enthalpy
H	total enthalpy
H_r	relative total enthalpy
I	rothalpy
L	axial stage length
n	boundary layer power law exponent
N	number of blades
q	heat flux
r	radius
s	pitch, streamwise coordinate
T	static temperature
T_t	total temperature
T_t^*	relative total temperature
T_t^*	rotary total temperature
U	wheel speed
V	absolute velocity
W	relative velocity (blade row reference system)
y	normal or circumferential distance from wall
α_r	radial flow angle
β	tangential flow angle
β'	blade angle
γ	stagger angle
δ	physical boundary layer thickness
ε	skewing angle
ε_t	turbulent diffusion mixing coefficient
ε_w	wall skewing angle
ζ	vorticity
η	lean angle, non-dimensional distance u/δ
μ	dynamic viscosity
ν	kinematic viscosity
ρ	density
σ	angle between meridional and axial directions

Subscripts

abs	absolute
p	pressure side
s	suction side, streamwise direction
Q3D	component from Quasi-3D computation
S3	component from S3 computation
m,n,u	meridional coordinates (meridional, normal, circumferential)
z,r,θ	cylindrical coordinates (axial, radial, circumferential)
inv	inviscid region
visc	viscous region
ewbl	end-wall boundary layer region
pbl	profile boundary layer region
wake	wake region

Supersripts

$\bar{}$	geometrical pitch-average
$\tilde{}$	density-weighted pitch-average
'	deviation from geometrical pitch-average
"	deviation from density-weighted pitch-average
^	inviscid or 'freestream' value (density-weighted pitch-average)

Notations

$[\ ]_p^s$	difference between suction and pressure side

I. INTRODUCTION

As the design requirements for turbomachines (in particular axial compressors) have increased considerably during the last twenty years, aerodynamic designers are continuously compelled to analyse the complex flow patterns inside these machines in greater detail. This necessity, together with the advent of powerful digital computers, has led to an enormous progress in the development of computational methods for such internal flows.

Although fully three-dimensional inviscid or Navier-Stokes codes for turbomachinery flow computations are emerging, such computations are, even for steady flow, at the present time too time-consuming to enable them to be used currently in the industrial design process. Therefore, the most widely used methods today are the so-called 'Quasi-3D' methods, which allow efficient and fast computation of turbomachinery flows including the threedimensional aspects of the flow.

These methods all have a common basis, namely the streamsurface theory of Wu [1]. In this theory, a general three-dimensional turbomachinery flow is decomposed into two families of interacting two-dimensional flows on intersecting streamsurfaces : flows on hub-to-shroud surfaces or S2-surfaces and flows on blade-to-blade streamsurfaces or S1-surfaces. The reduction of the flow to an assembly of 2D-flows represents a large simplification with respect to computational procedures, while the three-dimensional character of the flow is conserved through the interaction process between the two families of 2D-flows.

Nearly all the current operational Quasi-3D computation codes contain the simplifying assumption that the blade-to-blade S1-streamsurfaces are surfaces of revolution, i.e. the flow remains on geometrically axisymmetric surfaces as it passes through the machine. However, in a real turbomachinery flow this assumption is not valid. Several physical effects generate a secondary flow pattern in a transverse surface, roughly perpendicular to the main flow direction, thereby destroying the geometrical axisymmetry of the S1-streamsurfaces. In addition, the S1-surfaces are also distorted by the random motions associated to turbulence.

These different interactions result in a transfer of flow properties (in particular energy and losses) between the S1-streamsurfaces, i.e. a process of radial redistribution of flow properties. This phenomenon is called radial mixing.

The present paper proposes a computational method to integrate the effects of radial mixing into a Quasi-3D method for the computation of turbomachinery flows, in order to obtain more accurate predictions of the distribution of flow properties inside a turbomachine.

II. RADIAL MIXING : PHYSICAL MECHANISMS AND COMPUTATIONAL METHODS

As indicated in the introduction, the radial redistribution of flow properties in turbomachines can be attributed to two different physical mechanisms :

a) Convective mixing : the macroscopic transport due to the radial components of the deterministic flows in a transverse surface

b) Diffusive mixing : the microscopic transport due to the radial components of the random motions associated to turbulence

A convective mixing computation method was proposed by Adkins and Smith [2], who were the first to recognize the importance of incorporating the effects of radial mixing into computational methods for multistage axial compressors. They put forward the concept that radial mixing is caused exclusively by secondary flows and model the mixing as a diffusion process, determining the local values of the mixing coefficient from computed secondary radial velocities. The secondary flow computations are based on Smith's inviscid secondary flow theory and include the effects of mainstream non-free vortex flow, end-wall boundary layers, tip clearances, blade end shrouding, and profile boundary layer and wake centrifugation.

A diffusive mixing model was introduced by Gallimore and Cumpsty [3,4], who concluded from experimental research that turbulence is the dominating mixing mechanism. They compute the radial mixing effects by introducing transport terms of diffusive nature into a streamline curvature computation method, the intensity of these terms being determined through semi-empirical turbulence-dependent coefficients.

Despite the fundamental difference between their basic mixing mechanisms, both methods give results that compare favorably with experimental data. This is perhaps due to the use of empirical coefficients in both methods, the fine-tuning of which can obscure possible shortcomings of the theoretical mixing model with respect to the physical reality.

Recently, Wisler et al. [5] conducted a comprehensive measurement program to determine experimentally the nature of the mixing mechanism. They concluded that both secondary flows and turbulent diffusion play an important role in the mixing process, their relative importance depending on the location in the blade row : diffusive mixing is important everywhere and dominates in the so-called 'freestream' or 'core' flow region, while convective mixing is equally important in low-momentum flow regions like end-wall boundary layers, profile boundary layers and wakes.

De Ruyck and Hirsch [6,7,8] proposed a radial mixing computation method which presents a synthesis between the aforementioned mixing models, since both convective and diffusive mixing are accounted for. The results from the computations confirmed the experimental results of Wisler et al. [5] : turbulent diffusion was found to be an important mixing mechanism everywhere, while convective mixing takes place in the low-momentum flow regions, especially at high blade loadings. However, as argued by Gallimore and Cumpsty in their discussion of the results of Wisler et al. [5], this apparent convective mixing can also be attributed to non-isotropic diffusion due to gradients in turbulence intensity, as computations of diffusive mixing with non-uniform turbulent mixing coefficients (a high turbulence level in the viscous regions and a lower turbulence level in the inviscid mainflow region) indicated, De Ruyck and Hirsch [6]. Finally, the computations showed that the mixing process inside a blade row is weak compared to the mixing effects occurring in the wake region.

III. RADIAL MIXING IN THE FRAMEWORK OF A QUASI-3D COMPUTATIONAL METHOD

The present radial mixing computation method is a reformulation and extension of the model of De Ruyck and Hirsch [6,7,8], in order to obtain a method that is adapted to the framework of an operational integrated Quasi-3D computation code for turbomachinery flows, which is based on a density-weighted pitch-averaging procedure, Hirsch and Warzee [9]. The main purpose of the method is therefore the computation of the radial redistribution of flow properties for the axisymmetric throughflow on the meridional S2-plane, through detailed computation of the flow effects occurring on a transverse S3-plane.

III.1 Quasi-3D turbomachinery flow computation

The current approach is a variant of the original Wu method : it consists in splitting the turbomachine flow into two families of interacting two-dimensional flows, using a density-weighted pitch-averaging procedure, Hirsch and Warzee [9]. The first flow is the circumferentially averaged flow on a meridional plane (S2) or 'throughflow', the axisymmetric component of the flowfield. The second flow is the blade-to-blade flow considered on a streamsurface of revolution (S1), obtained by rotation of a meridional streamline, which contains the circumferential distribution of the non-axisymmetric components. The flows on the S1- and S2-surfaces are not independent, but influence each other in an iterative way, the knowledge of the flow on one type of surface being required to solve the flow on the other type of surface.

Although it is theoretically possible to represent a threedimensional flow through two families of twodimensional flows on intersecting streamsurfaces, Yih [10], the current Quasi-3D approach does not give the complete structure of the flowfield. Indeed, the method uses only one throughflow computation (S2-surface) and a small number of blade-to-blade computations (S1-surfaces) in the iterative procedure. Consequently, flow effects occurring in a third kind of surface - a transverse surface S3, roughly perpendicular to the main flow direction - are neglected, which means that radial mixing mechanisms are not considered and radial redistributions are not accounted for in the flow computation.

III.2 Turbomachinery streamsurfaces

As axisymmetric geometry is a general feature of turbomachinery, an orthogonal meridional coordinate system (m,n,u) is especially suited to represent turbomachinery geometry (Figure 1).

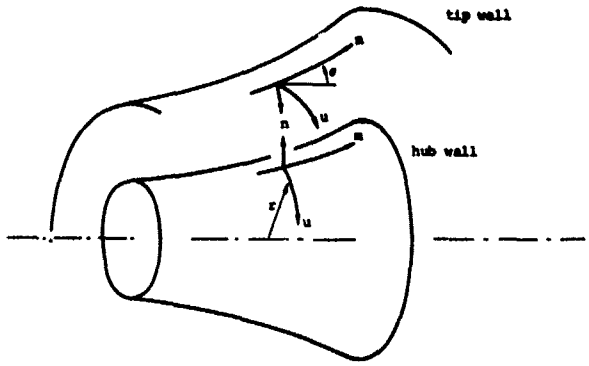


Figure 1 : Meridional coordinate system

In the context of a Quasi-3D method based on a pitch-averaging procedure, it is logical to define the streamlines of the averaged axisymmetric flow on the S2-plane as meridional coordinate lines. Consequently, using the curvilinear (m,n,u)-coordinates as intrinsic coordinates, the following three families of orthogonal surfaces can be distinguished :

(i) Meridional throughflow planes (S2-surfaces) : (m,n)-surfaces containing the machine axis

(ii) Blade-to-blade streamsurfaces (S1-surfaces) : (m,u)-surfaces of revolution

(iii) Transverse surfaces (S3-surfaces) : (n,u)-surfaces of revolution

This clearly shows that the transverse S3-surface, orthogonal to the meridional direction, appears naturally as a third kind of computational surface for the present Quasi-3D computation method.

The present Quasi-3D computation code has been developed in a cylindrical coordinate system (z,r,θ), with the z-axis directed along the machine axis. The meridional S2-plane thus becomes an (r,z)-plane, but the cylindrical coordinates form no intrinsic coordinate system for the S1- and S3-surfaces. However, although the S3-surface appears naturally in a mathematical way, this surface is not suitable from a physical and computational point of view. Indeed, most of the experimental data on secondary flows and associated phenomena in axial compressors is obtained in measurement planes perpendicular to the machine axis, while the computation stations for throughflow computations are very often defined as stations with a constant axial coordinate. Therefore, the information from a mixing computation should really be obtained on an (r,θ)-plane, perpendicular to the machine axis, whose intersection with the meridional S2-plane is a throughflow computation station. Hence, the computation will be directly performed on an (r,θ)-plane and the resulting flow field is considered as the projection of the flow field on the original S3-surface onto this plane.

III.3 Convective mixing

The convective mixing is defined as the mixing caused by the flow pattern on the S3-surface. It is important to note that the S3 flow field is considered as a correction with respect to the Quasi-3D flow

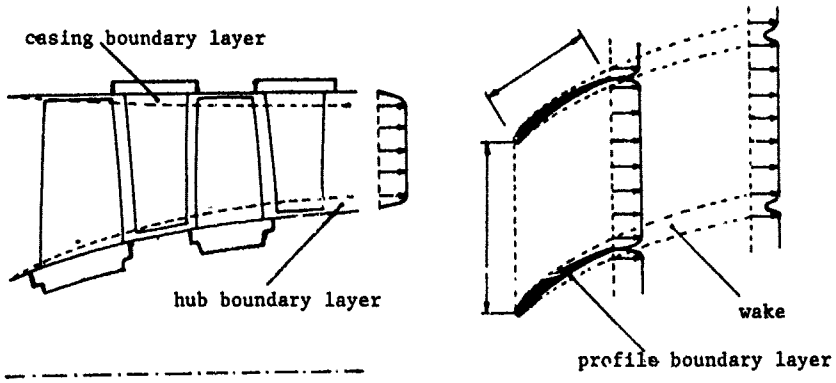


Figure 2 : Orthogonal surfaces in a turbomachine

field and is not the classical secondary flowfield, associated to the development of streamwise vorticity. Accordingly, the total velocity $\vec{W}$ is considered to consist of two components : a Quasi-3D component $\vec{W}_{Q3D}$ and a transverse component $\vec{W}_{S3}$:

$$\vec{W} = \vec{W}_{Q3D} + \vec{W}_{S3} \tag{1}$$

It is important to observe that the Quasi-3D component does not only contain the traditional contributions from the throughflow computation and the blade-to-blade computations , but also includes the 2D-effects of viscous layers (end-wall boundary layers, profile boundary layers and wakes) in these surfaces. In other words, the blockage effect of the viscous layers on the axial velocity profiles and the subsequent influence on the continuity equation is taken into account in the Quasi-3D approximation.

By definition, the transverse component $\vec{W}_{S3}$ represents any deviation between the real flow and the Quasi-3D flow. Following the discussion above, this means that the transverse flow field essentially contains the crossflow components of the viscous layers (circumferential velocity profile for the end-wall boundary layers, radial velocity profile for the profile boundary layers and wakes), i.e. the three-dimensional effects of the viscous layers, occurring in a direction perpendicular to the computation surface considered.

Through the use of a density-weighted, geometrical pitch-average, each of these components can be further subdivided into an averaged, axisymmetric component and a 'fluctuation' component, representing the deviations from axisymmetry, Hirsch and Warzee [9] :

$$\vec{W}_{Q3D} = \tilde{\vec{W}}_{Q3D} + \vec{W}''_{Q3D} \qquad \vec{W}_{S3} = \tilde{\vec{W}}_{S3} + \vec{W}''_{S3} \tag{2}$$

with the geometrical pitch-average or 'passage average' defined by

$$\overline{A} = \frac{1}{\theta_s - \theta_p} \int_p^s A \, d\theta \qquad \overline{A}' = 0 \tag{3}$$

and the density-weighted pitch-average defined by

$$\tilde{A} = \overline{\rho A} / \overline{\rho} \qquad \overline{\rho A''} = 0 \tag{4}$$

Through this approach, one can distinguish two types of non-axisymmetric contributions to the velocity field :

a) Non-axisymmetries due to the flow deflection induced by the blades: $\vec{W}''_{Q3D}$.

The deflection of a flow by a blade row immediately implies the existence of a circumferential pressure gradient, i.e. a turbomachinery flow is intrinsically non-axisymmetric. These non-axisymmetric components are determined in the blade-to-blade computation on the S1-streamsurfaces and influence the throughflow computation of the axisymmetric flow components through interaction terms.

b) Non-axisymmetries due to flow patterns occurring in the transverse S3-surface: $\vec{W}''_{S3}$.

These non-axisymmetries are hitherto not taken into account in the Quasi-3D computation. This paper presents a method to compute explicitly those non-axisymmetric components and their influence on the axisymmetric throughflow computation.

For a detailed discussion of the averaging process and averaging rules, the reader is referred to Hirsch [11].

III.4 Diffusive mixing

The diffusive mixing due to the high levels of turbulence in a turbomachinery flow contributes to the radial redistribution of flow properties in a kind of uniformisation process. The influence of the turbulence level of the flow on the mixing process is modeled through the use of a 'turbulent mixing coefficient' ε_t, the values of which were found to correspond to the wake decay diffusion coefficient, De Ruyck and Hirsch [6].

IV. CONVECTIVE MIXING COMPUTATION : GENERAL PRINCIPLES

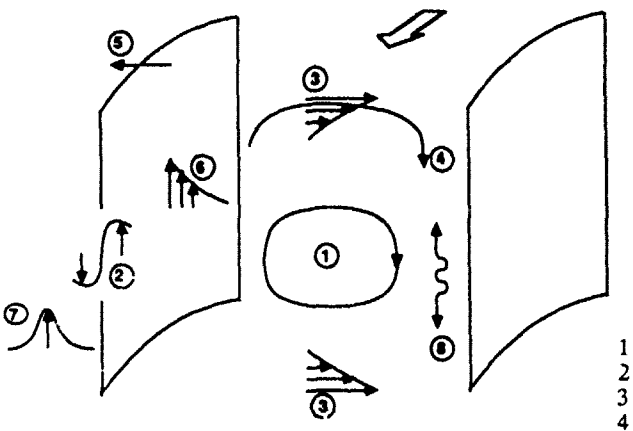
The flow field on the transverse S3-plane is computed explicitly by assuming that the flow effects in this surface do not give rise to velocity components perpendicular to the surface, i.e. the S3 flow field is assumed to be two-dimensional and the S3-surface forms a streamsurface for this flow. In other words, the flow effects only cause additional radial and circumferential velocities, which are associated to an axial vorticity. Furthermore, the S3 flow field is assumed to be steady relative to the blade row reference system, in accordance with the Quasi-3D framework.

IV.1 Turbomachinery flow regions

A turbomachinery flow is always highly turbulent and viscous, but for fluids with very small viscosity, Prandtl's boundary layer theory shows that viscous effects are only important in the vicinity of material walls. On this basis, the turbomachinery flow can be considered to be composed of four different flow regions :

(i) Inviscid flow region ('core' region between viscous layers)
(ii) End-wall boundary layers region (viscous region near hub/tip wall)
(iii) Profile boundary layers region (viscous region near blades)
(iv) Wake region (viscous region, continuation of profile boundary layer)

Each of these regions is a potential source of flow components on the S3-surface, but the underlying physical mechanisms are different in each case (Figure 3).



Flow :	Origin :
1 Main passage vortex	Flow non-uniformities
2 Trailing shed and filament vortex	Spanwise changes in circulation
3 End wall boundary cross flow	Boundary layer overturning
4 End wall b. l. passage vortex	Boundary layer overturning
5 Tip clearance flow	Tip clearance pressure difference
6 Profile boundary layer radial flow	Centrifugation
7 Wake radial flow	Centrifugation
8 Radial diffusion	Turbulence

Figure 3 : Sources of flow effects on the S3-surface

These physical mechanisms will be detailed in subsequent paragraphs, where the computation of the separate contributions for each region will be described.

IV.2 Fundamental equations

Streamfunction ψ

Assuming the turbomachinery flow compressible and steady relative to a blade row, the continuity equation (conservation of mass) for this flow is

$$\vec{\nabla}.(\rho\vec{W}) = 0 \tag{5}$$

Substitution of the decomposition (1), taking into account that continuity is already satisfied by the Quasi-3D flow field (including boundary layer axial blockage effects), leads to :

$$\vec{\nabla}.(\rho\vec{W}_{S3}) = 0 \tag{6}$$

Since the flow on the S3-plane is assumed to be two-dimensional, a streamfunction $\psi(r,\theta)$ can be introduced to satisfy the continuity equation (6). In cylindrical coordinates, ψ is thus defined by :

$$W_{r,S3} = -\frac{1}{\rho}\frac{1}{r}\frac{\partial\psi}{\partial\theta}$$
$$W_{\theta,S3} = \frac{1}{\rho}\frac{\partial\psi}{\partial r} \qquad (7)$$

This reduces the problem of determining a two-dimensional flowfield to the determination of the distribution of a scalar function.

Poisson-equation

Taking into account that the streamfunction ψ is independent of z and substituting the definitions of equation (7), one can write in cylindrical coordinates :

$$\vec{\nabla}.(\frac{1}{\rho}\vec{\nabla}\psi) = \frac{1}{r}\frac{\partial}{\partial r}(rW_{\theta,S3}) - \frac{1}{r}\frac{\partial}{\partial\theta}(W_{r,S3}) \qquad (8)$$

The axial relative vorticity due to the Quasi-3D flow field is given by

$$\zeta_{z,Q3D} = \frac{1}{r}\frac{\partial}{\partial r}(rW_{\theta,Q3D}) - \frac{1}{r}\frac{\partial}{\partial\theta}(W_{r,Q3D}) \qquad (9)$$

and is a priori known from the Quasi-3D computations. Substituting equation (9) into equation (8), taking into account decomposition (1), yields the following final equation

$$\vec{\nabla}.(\frac{1}{\rho}\vec{\nabla}\psi) = \zeta_z - \zeta_{z,Q3D} = \zeta_{z,S3} \qquad (10)$$

where ζ_z represents the axial vorticity component of the total flow field.

The quasi-harmonic Poisson-type equation (10) determines the streamfunction distribution in the S3-plane from the knowledge of the axial vorticity components and is the basic equation to be solved.

IV.3 General computation strategy

For the computation of the S3 flow field, the following superposition principle is introduced : The axial vorticity component $\zeta_{z,S3}$ can be decomposed as follows :

$$\zeta_{z,S3} = \zeta_{z,S3,inv} + \zeta_{z,S3,visc} \qquad (11)$$

$\zeta_{z,S3,inv}$ is the axial vorticity component associated to the S3 flows induced by the inviscid 'core' flow region and is defined over the entire computational domain. $\zeta_{z,S3,visc}$ is the axial vorticity component associated to the viscous regions and consists of separate contributions for each type of viscous region. All the axial vorticity components relevant to the flow on a certain S3-plane are superposed, and this yields the axial vorticity $\zeta_{z,S3}$, the unknown right-hand side of the basic Poisson-equation, from which the S3 flow field can be reconstructed.

This leads to the following sequence of computations :

(i) Through flow computation

(ii) Computation of end-wall boundary layers and the corresponding pitch-averaged axial vorticity contribution $\bar{\zeta}_{z,ewbl}$

(iii) Computation of the pitch-averaged axial vorticity contribution $\bar{\zeta}_{z,inv}$ of the inviscid flow region

(iv) Computation of the secondary flow field induced by the superposition of vorticity contributions (ii) and (iii), through the solution of the basic equation (10)

(v) Superposition of the secondary flow field on the Quasi-3D flow field

(vi) Computation of the profile boundary layers or the wake and the associated axial vorticity contribution $\zeta_{z,pbl}$ or $\zeta_{z,wake}$, depending whether the S3-plane (whose intersection with the meridional plane forms a throughflow computation station) is located inside the blade row or the wake region

(vii) Computation of the secondary flow field induced by the vorticity contribution (vi) through the solution of the basic equation (10)

(viii) Superposition of the secondary flow field on the flow field obtained in (v)

(ix) Computation of the radial mixing effects, including the effects of turbulent diffusion, through a stationary transport equation

The computational domain on which the basic equation (10) has to be solved is delimited by the intersection of the S3-plane considered with the hub and tip end-walls and the surfaces of two adjacent blades or their imaginary extensions into the wake region (periodicity of turbomachinery flow). For numerical computations, a regular radial-tangential mesh allowing non-uniform spacings (i.e. clustering) is generated.

V. CONVECTIVE MIXING : INVISCID FLOW REGION

V.1 Physical mechanism

The inviscid flow region contributes to the S3-flowfield through the well-known classical secondary flow mechanism : deflection (through the presence of material walls) of a sheared flow generates flows in a surface perpendicular to the main flow direction.

V.2 Analytical equations

The governing equation of motion for the inviscid part of the flow is the Helmholtz vorticity equation, written relative to the blade row (absolute frame of reference for a stator ; steadily rotating frame of reference for a rotor) [12] :

$$\frac{\partial \vec{\zeta}}{\partial t} + (\vec{W}.\vec{\nabla})\vec{\zeta} = [(\vec{\zeta}.\vec{\nabla})\vec{W} - \vec{\zeta}.(\vec{\nabla}.\vec{W})] + \vec{\nabla}p\times\vec{\nabla}(\frac{1}{\rho}) + \vec{\nabla}\times\vec{f}_e + 2[(\vec{\Omega}.\vec{\nabla})\vec{W} - \vec{\Omega}.(\vec{\nabla}.\vec{W})] \tag{12}$$

with

$$\begin{aligned} \vec{\zeta} &= \vec{\nabla} \times \vec{W} && \text{relative vorticity} \\ \vec{\Omega} &= \Omega.\vec{1}_z && \text{rotation vector} \end{aligned} \tag{13}$$

If one neglects the presence of volume forces and assumes the fluid to be a perfect gas with polytropic behaviour, the Helmholtz equation can be written in a condensed conservative form, using the tensorial product ⊗ :

$$\frac{\partial}{\partial t}[\vec{\zeta}_{abs}] + \vec{\nabla}.[\vec{W} \otimes \vec{\zeta}_{abs} - \vec{\zeta}_{abs} \otimes \vec{W}] = 0 \tag{14}$$

Note that the vorticity appearing in the equation is the absolute vorticity ($\vec{\zeta}_{abs} = \vec{\zeta} + 2\vec{\Omega}$) . Furthermore, although the equation takes compressibility effects into account, the density does not appear in the equation !

Since the method is developed in the framework of a Quasi-3D method based on an averaging procedure, it is assumed that the axial vorticity contribution $\zeta_{z,S3,inv}$ can be adequately approximated by its passage-averaged value $\bar{\zeta}_{z,S3,inv}$. Indeed, only spanwise passage-averaged profiles of all the Quasi-3D flow properties are available, and in fact, the passage-averaged axial vorticity represents the 'trace' of the unknown circumferential non-axisymmetric velocity distribution. It is precisely from this trace that the velocity field on the S3-plane will be reconstructed.
Therefore, the axial projection of equation (14) is passage-averaged, yielding :

$$\begin{aligned} \bar{W}_m \frac{\partial}{\partial m}\bar{\zeta}_{abs,z} = {} & \bar{\zeta}_{abs,r}\frac{1}{\bar{b}}\frac{\partial(b\bar{W}_z)}{\partial r} - \bar{\zeta}_{abs,z}\frac{1}{br}\frac{\partial}{\partial r}(rb\bar{W}_r) + \frac{1}{2\pi b/N}[(\vec{\zeta}_{abs}.\vec{n})W_z]_p^s \\ & + \frac{1}{br}\frac{\partial}{\partial r}[rb(\overline{W'_z\zeta'}_{abs,r} - \overline{W'_r\zeta'}_{abs,z})] \end{aligned} \tag{15}$$

where b is the tangential blockage factor defined by $\theta_s - \theta_p = 2\pi b/N$ and $\vec{n}$, the vector perpendicular to the blade surface S, is defined as

$$\vec{n} = \vec{\nabla}S = (-\frac{1}{r}\,tg\eta).\vec{1}_r + (\frac{1}{r}).\vec{1}_\theta + (-\frac{1}{r}\,tg\beta').\vec{1}_z \tag{16}$$

with the blade surface angles defined as

$$tg\eta = r\frac{\partial\theta}{\partial r} \quad \text{lean angle} \qquad\qquad tg\beta' = r\frac{\partial\theta}{\partial z} \quad \text{blade angle} \tag{17}$$

Simplifying equation (15) by neglecting the fluctuation terms and assuming constant blockage (which amounts to an error of second order) yields

$$\begin{aligned} \bar{W}_m \frac{\partial}{\partial m}\bar{\zeta}_{abs,z} = {} & \bar{\zeta}_{abs,r}\frac{\partial\bar{W}_z}{\partial r} - \bar{\zeta}_{abs,z}\frac{1}{r}\frac{\partial}{\partial r}(r\bar{W}_r) \\ & - \frac{1}{bs}(\bar{\zeta}_{abs,r}tg\eta - \bar{\zeta}_{abs,\theta} + \bar{\zeta}_{abs,z}tg\beta')[W_z]_p^s \end{aligned} \tag{18}$$

Furthermore, the flow on the S1-surfaces is considered to be a potential flow. Hence, the absolute vorticity component normal to any S1 surface is zero and this yields the following relation between radial and axial vorticity components :

$$\zeta_{n,abs} = \zeta_{r,abs}\cos\sigma - \zeta_{z,abs}\sin\sigma = 0 \quad \Rightarrow \quad \bar{\zeta}_{r,abs} = tg\sigma\,\bar{\zeta}_{z,abs} \tag{19}$$

where σ is the angle between the meridional and axial directions. Equation (18) thus becomes :

$$\bar{W}_m \frac{\partial}{\partial m} \bar{\zeta}_{abs,z} = \bar{\zeta}_{abs,z} \left(tg\sigma \frac{\partial}{\partial r} \bar{W}_z - \frac{1}{r} \frac{\partial}{\partial r}(r\bar{W}_r) \right) - \frac{1}{bs} \left(\bar{\zeta}_{abs,z}(tg\sigma tgn + tg\beta') - \bar{\zeta}_{abs,\theta} \right) [W_z]_p^s \tag{20}$$

This equation describes the evolution in the meridional direction of the axial component of the absolute total vorticity associated to the inviscid flow region.

The last term describes the generation of axial vorticity through the presence of a deflection $[W_z]_p^s$. This deflection can either be obtained directly from a blade-to-blade computation or has to be estimated from throughflow properties by expressing that the normal component of vorticity is zero (eq. 19), and pitch-averaging this condition yields

$$[W_z]_p^s = bs \cos\sigma \frac{1}{r} \overline{\frac{\partial}{\partial m}(rV_{\theta,Q3D})} \tag{21}$$

Of course, this deflection is considered in the inviscid approximation, since it would otherwise be zero because of the no-slip condition.

The first term describes the generation of axial vorticity through radial velocity gradients and corresponds to the physical mechanism of vortex stretching. It is important to note that these velocity components are <u>total</u> velocities, i.e. :

$$\bar{W}_r = \bar{W}_{r,Q3D} + \bar{W}_{r,S3} \qquad \text{and} \qquad \bar{W}_z = \bar{W}_{z,Q3D} \tag{22}$$

The passage-averaged tangential vorticity $\bar{\zeta}_{\theta,abs}$ is computed directly from the definition

$$\bar{\zeta}_{abs,\theta} = \overline{\frac{\partial W_r}{\partial z} - \frac{\partial W_z}{\partial r}} = \frac{\partial \bar{W}_r}{\partial z} - \frac{\partial \bar{W}_z}{\partial r} - \frac{1}{bs} \left(tg\beta' [W_r]_p^s - tgn [W_z]_p^s \right) \tag{23}$$

in which the velocity components are again total velocities.

<u>V.3 Numerical solution</u>

The basic equation to be solved is the pitch-averaged axial component of the Helmholtz vorticity equation, equation (20), whereby the following parameters are considered to be known :

1) Blade and blade row geometrical data
2) Pitch-averaged velocities : $\bar{W}_r$, $\bar{W}_z$
3) Velocity jump $[W_z]_p^s$: either known directly from a blade-to-blade computation or from eq. (21)
4) Averaged tangential vorticity component $\bar{\zeta}_{abs,\theta}$ is estimated through eq. (23)

The only remaining unknowns are the averaged total vorticity $\bar{\zeta}_{abs,z}$, which is the main unknown variable and the jump in radial velocity $[W_r]_p^s$. The latter unknown can be computed through an additional equation obtained by pitch-averaging the mass conservation law over a half pitch and assuming a parabolic distribution for W_θ and a linear distribution for W_r, which yields, neglecting density variations in the circumferential direction :

$$\frac{\pi}{6bN} \frac{d^2}{dr^2}(br[W_r]_p^s) + \left(\frac{tgn}{3br} + \frac{\pi}{6brN}\right) \frac{d}{dr}(br[W_r]_p^s) - \frac{1}{brs}(br[W_r]_p^s) = \bar{\zeta}_{abs,z} - \frac{1}{br} \frac{\partial}{\partial r}(rb\bar{W}_{\theta,Q3D}) \tag{24}$$

This second-order linear ordinary differential equation is discretized using second-order accurate central finite differences for a regular mesh with non-uniform mesh spacings on the S3(r,θ)-plane. This results in a linear tridiagonal system, that can easily be solved using the Thomas-algorithm [12].

Remark however, that this computation of the velocity jump $[W_r]_p^s$ is not necessary if its order of magnitude is much smaller than the other terms in eq.(23).

The basic equation can now be written in the form :

$$\bar{W}_m \frac{\partial}{\partial m} \bar{\zeta}_{abs,z} = f(m, \bar{\zeta}_{abs,z}) \tag{25}$$

and will be numerically solved using a fourth-order Runge-Kutta integration method. The equation is thereby integrated in the m-direction from the blade row inlet to the blade row outlet in several intermediate steps, and at each step the right-hand side of eq. (20) is recomputed. Each time, this recomputation involves solving the additional equation (24) to estimate $[W_r]_p^s$ and using linear interpolation to estimate Quasi-3D quantities between throughflow computation stations. The radial

derivatives occurring in the rhs of eq. (20) are again estimated using second-order accurate central finite difference formulaes for a regular mesh with non-uniform spacing.

VI. CONVECTIVE MIXING : END-WALL BOUNDARY LAYER REGION

VI.1 Physical mechanism

In an end-wall boundary layer (EWBL), crossflows are generated as a consequence of the higher curvature of streamlines inside the EWBL, necessary to maintain equilibrium with the pressure gradient between the pressure side and suction side of the blade passage while the mainflow velocity decreases from its freestream value at the boundary layer edge to zero at the wall. These crossflows then generate radial flows through the presence of the blade walls.
Also included in this region is the influence from tip clearances, causing leakage flows from the pressure side to the suction side of the blade.
The overall result is thus a 2D flow pattern in the S3-surface, which has not been taken into account in the Quasi-3D computation, although the blockage effect of the EWBLs on the axial velocity profile has been introduced in the Quasi-3D computation.

VI.2 Analytical equations

End-wall boundary layers (EWBL) are predicted through a 3D integral method where end-wall secondary flows and clearance effects are introduced, De Ruyck and Hirsch [13,14,15]. The EWBL procedure essentially solves 3D integral equations, i.e. the entrainment equation and the m- and n-projections of the momentum equation, taking into account extra relations like Ludwieg-Tillman's skin friction relation and correlations for the defect force, De Ruyck and Hirsch [7]. Closure is obtained by the use of passage-averaged velocity profile models. For the Quasi-3D computation, the axial velocity distribution inside the EWBL and the corresponding circumferential velocity distribution are given by :

$$\frac{\bar{W}_{z,ewbl}}{W_{z,Q3D}} = 1 - b\left(1 - \frac{y}{\delta}\right)^n \qquad \bar{W}_{\theta,ewbl} = \bar{W}_{z,ewbl}\, tg\beta \tag{26}$$

The circumferential crossflow velocity profile, associated with the 3D effects of the EWBL and inducing flows on the S3 surface, is modeled as :

$$\frac{\bar{W}_{\theta,S3,ewbl}}{W_{z,Q3D}} = \frac{\bar{W}_{\theta} - \bar{W}_{\theta,ewbl}}{W_{z,Q3D}} = (1-b)tg\varepsilon'_w\left(1 - \frac{y}{\delta}\right)^n \tag{27}$$

where y is the normal distance from the end-wall. Observe that the EWBL crossflow is thus defined as the non-collateral part of the boundary layer flow.

For a detailed description of the EWBL computation procedure, the reader is referred to De Ruyck [14].

VI.3 Vorticity contribution

The axial vorticity component associated to this EWBL-contribution to the S3 flow pattern is estimated through the following equation, which has been derived by averaging the axial component of the definition of vorticity :

$$\bar{\zeta}_{z,ewbl} = \frac{1}{r}\frac{\partial}{\partial r}(r\bar{W}_{\theta,S3,ewbl}) - \frac{1}{bs}tgn\,[W_{\theta,S3,ewbl}]_p^s - \frac{1}{bs}[W_{r,S3,ewbl}]_p^s \tag{28}$$

The second term can be neglected with respect to the first in most cases (tgn small), but this is not the case for the last term. For the numerical computation of the radial derivatives second-order accurate central finite differences for a mesh with non-uniform spacing are again used.

VII. CONVECTIVE MIXING : PROFILE BOUNDARY LAYERS

VII.1 Physical mechanism

Boundary layers along turbomachine blades are three dimensional and contribute to both the radial convection and turbulent diffusion. Physically, the low-momentum profile boundary layer fluid is centrifugated by the rotary movement in a rotor and moves inward through pressure gradients in a stator.

VII.2 Analytical equations

In the present approach, the boundary layer equations are developed in the cylindrical coordinate system, and not in a coordinate system associated to the profile walls, which is a rather unusual way to proceed. It presents however some practical advantages such as an easier theoretical development and an easier computation. The 3D integral boundary layer equations used can be found in De Ruyck and Hirsch [7,8]. In order to obtain closure, models for the velocity distribution inside the profile boundary layer are introduced. In analogy with the EWBL profile models, the following model equation is used for the radial velocity profile associated with the 3D-effects of the profile boundary layer :

$$\frac{W_{r,S3,pbl}}{W_{s,Q3D}} = \frac{W_r - W_{s,pbl}\,tg\alpha_r}{W_{s,Q3D}} = (1-b)tg\varepsilon'_w\left(1 - \frac{y}{\delta}\right)^n \tag{29}$$

where α_r is the radial flow angle (induced by throughflow, and inviscid and EWBL region S3 flows), and y/δ is the non-dimensional circumferential distance from the profile wall. $W_{s,pbl}$ denotes the streamwise velocity profile inside the profile boundary layer (s lines are the projection of streamlines on an axisymmetric streamsurface), and is modeled by

$$\frac{W_{s,pbl}}{W_{s,Q3D}} = 1 - b\left(1 - \frac{y}{\delta}\right)^n \tag{30}$$

Observe that the profile boundary layer contribution to the S3 flowfield is modeled in such a way, that the radial velocities induced by the inviscid and EWBL flow regions are already taken into account for the PBL computation (through the radial flow angle), i.e. the PBL contribution is an extra radial velocity component, to be superposed on the previous components.

VII.3 Numerical solution

Analogous to the EWBL procedure, the fundamental integral equations can be written in the following form :

$$\frac{\partial}{\partial m}\{b,\ tg\varepsilon'_w,\ n\} = F\{m,\ b,\ tg\varepsilon'_w,\ n\} \tag{31}$$

where b, $tg\varepsilon'_w$ and n are the unknown variables for which the system must be solved. However, in the profile boundary layer computation there is a set of unknowns {b, $tg\varepsilon'_w$, n} for each radial position and each blade side, while the EWBL computation contains only two sets of unknowns, for the hub and tip boundary layer respectively. Therefore, the system of equations (31) is actually integrated in the m-direction for every radial position. Again, a fourth order Runge-Kutta integration from blade row inlet to blade row outlet is used, while the discretization techniques for radial derivatives are identical to the previous ones.

The following parameters are again considered as being known :

1) Blade row and blade geometrical data

2) Pitch-averaged velocities : $\bar{W}_r$, $\bar{W}_z$, $\bar{W}_\theta$

3) Secondary flowfield induced by the inviscid flow region and the end-wall boundary layers

Initialisation

The profile boundary layer computation is initialised by assuming the following default values for the momentum thickness and shape factor : θ=0.001, H=1.3, which are typical values for a 'well-behaving' thin boundary layer.

VII.4 Vorticity contribution

The axial vorticity component associated to the contribution of the profile boundary layer flows to the S3 flow pattern is approximated by :

$$\zeta_{z,pbl} = -\frac{1}{r}\frac{\partial}{\partial\theta} W_{r,S3,pbl} \tag{32}$$

whereby it is assumed that for profile boundary layer flows, radial variations may be neglected with respect to circumferential variations. Observe that a local value for the vorticity is determined, in contradiction with the inviscid and EWBL vorticities which are pitch-averaged quantities.

VIII. CONVECTIVE MIXING : WAKE REGION

VIII.1 Physical mechanism

Since the wake is the continuation of the profile boundary layer region, the convective mixing is caused by the same mechanism, namely by centrifugation of the low-momentum fluid. In addition, the wake can be considered as a very important element in the overall mixing, since peak radial velocities are observed in the near wake, where very low velocities may induce a very strong centrifugation effect.

VIII.2 Analytical equations

Adkins and Smith [2] treated the wake by writing the mainstream and radial momentum conservation laws along the wake center. They characterise the radial flows by 'peak' radial velocities at the wake center whereas the total amount of radial flow is found by modeling the wake profiles. Since symmetric wake models are used, they are not able to simulate asymmetric radial wake profiles.
In the present wake approach, pressure and suction side of the wake are treated separately and the concept of 'peak velocities' is not used, De Ruyck and Hirsch [7]. The reason for this is that wake profiles may be very asymmetric, and pressure and suction side radial flows may even have opposite signs as appears in the experiments of Dring et al.[16].

Wake profiles

A model is introduced determined by a function f and the skewing angle ε. It is valid at one of the wake sides, the two wake sides being coupled by a 'bridging function' g. The streamwise velocity profile inside the wake layer is modeled as

$$\frac{W_{s,wake}}{W_{s,Q3D}} = 1 - bf(\eta) - (\bar{b}-b)g(\eta) \tag{33}$$

while the radial velocity profile associated to the 3D effects of the wake and inducing flows on the S3-surface is modeled by

$$\frac{W_{r,S3,wake}}{W_{s,Q3D}} = \frac{W_r - W_{s,wake}\,tg\alpha_r}{W_{s,Q3D}} \tag{34}$$
$$= (1-b)(tg\varepsilon)f(\eta) + \left[(1-\bar{b})t\bar{g}\varepsilon - (1-b)tg\varepsilon\right]g(\eta) + (1-\bar{b})(t\bar{g}\alpha - tg\alpha)g(\eta)$$

where η is the non-dimensional circumferential distance from the wake centerline and

$$f(\eta) = 1 - 6\eta^2 + 8\eta^3 - 3\eta^4 \qquad g(\eta) = e^{-\eta/\eta_o} \tag{35}$$

The overbars in equation (35) indicate arithmetic mean values between pressure and suction side. Notice that radial velocities induced by the troughflow and the S3 flow regions in the blade row have been taken into account through the radial flow angle α_r. The function g corrects the profile in the neighbourhood of the centerwake to fit with the opposite wake side. It affects the profile over a distance determined by η_o. For small values of η_o, pressure and suction side of the wake conserve their identity, at higher values both sides are mixed and the wake shape becomes more symmetric. Large second derivatives are present around the centerline and the asymmetry gives rise to a diffuse mixing between pressure and succion side of the wake. Hence η_o can be approached by the following formula, based on diffusion theory :

$$\eta_o = \frac{1}{\delta}\sqrt{\varepsilon_t \Delta z / W_z} \tag{36}$$

where Δz is the distance from the trailing edge and ε_t is the turbulent mixing coefficient which will be discussed below.

Wake momentum equations

Three-dimensional integral wake momentum equations are used. Since pressure and suction side of the wake are considered separately,the following set of integral equations is solved :

1) Axial momentum equation, integrated over the wake thickness, at both the pressure side and the suction side
2) Radial momentum equation, intgrated over the full wake width
3) Axial momentum equation, expressed locally at the wake center
4) Difference between the local axial momentum equations at pressure and suction sides
5) Difference between the local radial momentum equations at pressure and suction sides

The reader is referred to De Ruyck and Hirsch [7,8] for a detailed derivation and discussion of these equations.

VIII.3 Numerical solution

Wake initialisation

The wake computation is initialised by carrying over two parameters from the PBL computation : the shape factor H and the physical boundary layer thickness. Using the velocity profile models, all other variables needed to start the wake computation can be calculated from these two variables.

Wake computation

The system of wake equations also assumes the form of eq. (31). They are also integrated in the m-direction using a Runge-Kutta method, starting at the trailing edge and proceeding to a specified distance downstream of the trailing edge. The equations are again discretized using second-order accurate central differences for a mesh with non-uniform spacing.
The following parameters are again considered as being known :

1) Geometrical parameters
2) Pitch-averaged velocities : $\bar{W}_r$, $\bar{W}_z$, $\bar{W}_\theta$
3) Secondary flowfield induced inside the preceding blade row by the inviscid flow region, the end-wall boundary layers and the profile boundary layers

VIII.4 Axial vorticity contribution

The axial vorticity component associated to the contribution of the wake flow to the S3 flow pattern is approximated by :

$$\zeta_{z,wake} = -\frac{1}{r}\frac{\partial}{\partial\theta} W_{r,S3,wake} \tag{37}$$

As for the profile boundary layer flows, it is assumed that radial variations may be neglected with respect to circumferential variations. Again observe that a local value for the vorticity is determined.

IX. TURBULENT MIXING

The high turbulence levels in a turbomachinery flow also contribute substantially to the radial mixing process, as shown experimentally by Gallimore and Cumpsty [3]. No attempt is made here to make an explicit computation of the turbulence field, since the mechanism of turbulence and its numerical simulation is still largely an unresolved problem. Rather, the effects of turbulence are introduced through the use of an empirical 'turbulent mixing coefficient' ε_t . Since it has been mentioned that the wake has a large impact on the radial mixing process, DeRuyck and Hirsch [6], it seems logical to correlate this overall turbulent mixing coefficient to a parameter describing the magnitude of turbulent diffusion in the wake. According to Schlichting [17], the following expression can be used for the wake decay diffusion coefficient :

$$\varepsilon_t = K\delta b\hat{W}_z \tag{38}$$

where δ denotes the physical wake thickness and K depends on the turbulence intensity. Following values were observed when applying the wake theory on some test cases, De Ruyck and Hirsch [7] :

K = 0.005 for an airfoil wake with thin trailing edge
K = 0.010 for a compressor blade wake at design point
K = 0.045 for a compressor blade wake near stall
K = 0.047 for a cylinder wake (Schlichting, 1968)

leading to the following general non-dimensional values :

$\frac{\varepsilon_t}{W_z L} \approx 0.001$ for a compressor blade wake at design point

$\frac{\varepsilon_t}{W_z L} \approx 0.006$ for a compressor blade wake near stall

Interestingly, these values are of the same order as the global mixing coefficients observed by Gallimore and Cumpsty [3], see De Ruyck and Hirsch [6].

X. GENERAL MIXING EQUATION

The governing equation for the radial mixing process is derived from a basic law, i.e. the first law of thermodynamics formulated for a compressible flow. Neglecting volume forces and external heat sources, assuming steady flow, taking into account only the contribution of the work of the shear stresses related to the viscous diffusion of kinetic energy and assuming the Prandtl number $Pr = \mu C_p/k$ equal to one, the energy equation for the blade row reference system reduces to, see Hirsch [12] :

$$\vec{\nabla}.(\rho\vec{W}I) = \vec{\nabla}.(\mu\vec{\nabla}H_r) \tag{39}$$

with the rothalpy I defined as

$$I = h + \frac{W^2}{2} - \frac{U^2}{2} = H - UV_\theta \tag{40}$$

where $H = h + V^2/2$ is the total enthalpy and $H_r = h + W^2/2$ is the relative total enthalpy. Comparing equation (39) with the energy equation $\vec{\nabla}.(\rho\vec{W}I) = 0$ (rothalpy constant along a streamline) for the Quasi-3D formulation incorporating the distributed loss model, one sees immediately that the non-zero right-hand side describes a diffusion of energy between the streamlines, thereby destroying the constancy of the rothalpy.
In a turbomachine, the energy is most often described by the total temperature, so the mixing should be performed on this flow property, Hirsch and Dring [18]. Defining the relative total temperature as $T_t^r = H_r/C_p$ and the rotary total temperature $T_t^* = I/C_p$ and taking into account the continuity equation, equation (39) is further reduced to :

$$(\vec{W}.\vec{\nabla})T_t^* = \frac{\mu}{\rho}\Delta T_t^r = \nu\Delta T_t^r \tag{41}$$

with the kinematic viscosity ν appearing as a diffusion coefficient. Since a turbomachinery flow is highly turbulent, this coefficient will of course be the eddy viscosity and not the much smaller molecular viscosity. Thus, we may define this coefficient as the turbulent diffusion mixing coefficient ε_t, which yields the following mixing equation :

$$(\vec{W}.\vec{\nabla})T_t^* = \varepsilon_t \Delta T_t^r \tag{42}$$

For a stator blade row $T_t^* = T_t^r = T_t$, and a convection-diffusion equation for the total temperature T_t is obtained.

Inserting decomposition (1), taking into account that one seeks to compute the radial redistributions on the meridional plane, due to hitherto neglected flow effects on the transverse S3-plane, and thus reducing the convective velocity in the S3-plane to the S3 velocity, gives :

$$W_{z,Q3D}\frac{\partial T_t^*}{\partial z} = -W_{r,S3}\frac{\partial T_t^*}{\partial r} - W_{\theta,S3}\frac{1}{r}\frac{\partial T_t^*}{\partial \theta} + \varepsilon_t\left(\frac{1}{r}\frac{\partial}{\partial r}\left[r\frac{\partial T_t^r}{\partial r}\right] + \frac{1}{r^2}\frac{\partial^2 T_t^r}{\partial \theta^2}\right) \qquad (43)$$

whereby $\partial^2 T_t^r/\partial z^2$ was assumed to be very small.

This transport equation controls the energy redistribution in the machine. In the right-hand side, two different sources of energy redistribution can be distinguished :

1) The first two terms of the transport equation are determined by the velocity components $W_{r,S3}$ and $W_{\theta,S3}$ and hence describe the convective mixing of the rotary total temperature by the S3 flow field.

2) The last term is of a diffusive nature totally determined by ε_t, the turbulent mixing coefficient and hence describes the diffusive mixing of the relative total temperature by turbulence.

It is important to note that the transport equation (43) describes a two- dimensional mixing process in the S3-plane. Notice that, if the kinetic energies are small compared to the static enthalpy, equation (43) may be reduced to a 2D convection-diffusion equation for the static temperature.
The boundary condition for the mixing equation expresses that the machine operates adiabatically.
The mixing equation (43) is solved numerically by a two-dimensional upwind discretisation, again using second-order accurate finite differences for a non-uniform mesh.

XI. RESULTS

The present method is applied to three test cases :

i) VUB linear cascade, tested at the Department of Fluid Mechanics of the Vrije Universiteit Brussel

ii) UTRC single compressor rotor, investigated by Dring et al. [16]

iii) ONERA single compressor rotor, investigated by Larguier [19]

These three cases have different secondary flow patterns, and consequently a different radial mixing behaviour. The cascade has no centrifugation effects and a weak non-free vortex behaviour, so the end-wall boundary layer convection effects will be dominant. The blades of the ONERA rotor have a radially constant solidity and no twist, which causes a substantial non-free vortex behaviour, so the secondary flows induced by the inviscid flow region will be dominant. The UTRC rotor is more representative for commercial machines, where the different flow regions that contribute to the secondary flow pattern are more or less of equal importance.

The main geometrical and flow parameters for these machines are summarised in table 1.

	VUB cascade	ONERA rotor	UTRC rotor
Aspect ratio	1.0	0.89	1.0
Solidity	1.11	1.34	1.0
hub/tip radius	-	0.68	0.8
Blade inlet angle	33°	50°	59.5°
Blade outlet angle	-13°	30°	17.5°
Flow coefficient	-	0.74	0.75
Absolute deflection	34°	30°	33°

Table 1 : Blade geometries and flow data at mid-span

XI.1 Secondary flow computation : comparison with experimental data

In order to obtain a preliminary idea of the validity of the presented method, results from the secondary flow computations are compared with experimental data. In particular, it is important to assess the accuracy of the radial secondary flows, since these influence directly the radial transfer of flow properties.
One of the test cases, the VUB linear cascade, was specially built for the experimental investigation of secondary flows and detailed measurements using the hot-wire technique were obtained [20]. A global comparison between the computed secondary flow field and the experimental secondary flow field can be obtained through the use of velocity vector plots. Figure 4a shows the experimental secondary flowfield on the S3-plane just aft of the trailing edge of the VUB cascade, while Figure 4b shows the computed secondary flowfield at the same location. A good qualitative agreement is observed, except in the wake at mid-span, where the experiment indicates a flow from the suction side of the wake towards the pressure side of the wake. This gives rise to vortices in the wake, turning in opposite sense to the passage vortices. This discrepancy is probably due to the trailing edge separation effects, which are not yet implemented. However, in general a reasonable quantitative agreement between computation and experiment

is observed .

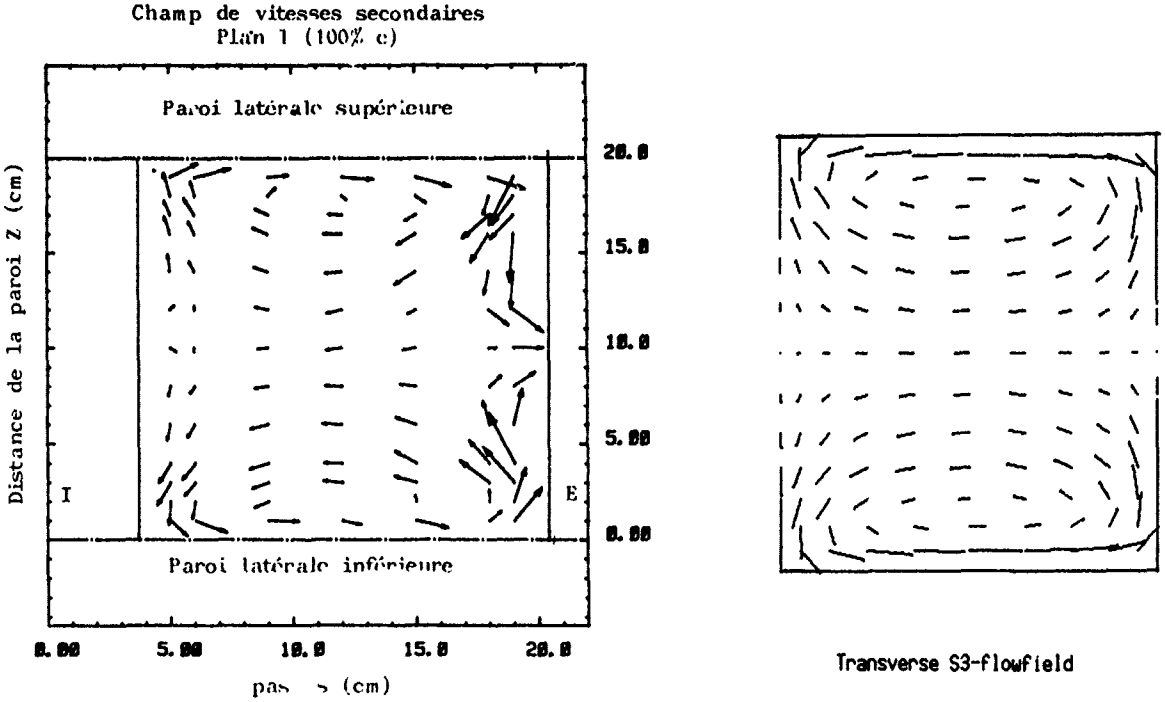


Figure 4a, 4b : Velocity vector plots of secondary flowfield (VUB cascade)

The theoretical secondary flow patterns for the UTRC and ONERA rotor are shown on Figures 7a and 8a. Comparison with experimental data for these cases were already shown, De Ruyck and Hirsch [6]. Although the approach in this paper is different, the overall quantitative results do not differ in a significant way.
The improvement with respect to [6] lies mainly in the details of the wake, where continuity was not satisfied in [6], due to an a posteriori superposition of velocities. In the present method, vorticities are superposed and the continuity is automatically satisfied through the introduction of the streamfunction.

XI.2 Radial mixing computations

Figures 5 to 8 show for each test case the secondary flow field on the S3-plane, contour plots of the temperature distribution on this plane and the corresponding pitch-averaged radial temperature profiles. Since earlier computations indicated that the amount of radial mixing inside a blade row is small compared to the mixing effects in the wake region [6], the present results are obtained on S3-planes located at a certain distance downstream of the trailing edge of the blades.

The mixing is performed on the static temperature, meaning that the kinetic energies are neglected with respect to the static temperature.
Four different lines are drawn on the pitch-averaged temperature plots. The dashed line is an arbitrary axisymmetrical input temperature profile which is chosen to be quadratic (since a linear profile has a zero second derivative, turbulent diffusion would not be accounted for). The solid line with circles is obtained from a one dimensional diffusion process through

$$\bar{W}_z \frac{\partial \bar{T}}{\partial z} = \varepsilon_t \frac{\partial^2 \bar{T}}{\partial r^2} \qquad (44)$$

This equation is one dimensional and solved with as boundary conditions $\frac{\partial T}{\partial r} = 0$ at the end-walls (adiabatic machine). The solid line with triangles is obtained from the same equation, but with ε_t replaced by

$$\varepsilon = (z-z_0)\, \tilde{W}_z \int_{pitch} \left(\frac{W_r^2}{W_z^2}\right) r d\theta + \varepsilon_t \qquad (45)$$

This is the coefficient of Adkins and Smith [2] (without the additional corrections) plus turbulent diffusion. The value z_0 was taken at leading edge, the radial velocities being local values. The solid line with squares is obtained from the computation of equation (43), whereby the kinetic energies are neglected with respect to the static temperature. In this case, the results on the figures are passage averaged values of the computed 2D temperature fields.

VUB cascade

The results for the linear cascade are shown on Figures 5a to 5c.
Although the length of the wake region in a multistage turbomachine is equal to the axial spacing between

successive blade rows, i.e. of the order of magnitude of the blade chord, the S3-plane is located 2 chords downstream of the trailing edge because the radial mixing effects are quite small in this case.
Figure 5a, the secondary flow field, clearly shows that the end-wall boundary layer convection dominates the secondary flow pattern, as is illustrated by the double-vortex structure. The maximum radial flow velocities reach about 5% of the axial velocity but are zero at mid-span, while the turbulent mixing coefficient has been taken as $\varepsilon_t/W_z L = 0.002$

As is shown from Figure 5c, the radial temperature profile tends to become more uniform. Hence, energy is transported from the end-wall boundary layer regions to the mid-span region, either through convection of high-energy fluid from the end-walls towards mid-span and of low-energy fluid from mid-span towards the endwalls, either through the uniformisation due to turbulence. In this context, it is very important to compare Figure 5b with Figure 5c. Indeed, Figure 5c seems to indicate that turbulent diffusion is the dominant mixing mechanism, because all the temperature profiles are identical. Figure 5b however, shows that the secondary flow pattern distorts the temperature field considerably, but the details of this 2D mixing process are lost through the pitch-averaging procedure, leading to an identical radial temperature redistribution as for a pure turbulent diffusion. This may offer an explanation for the fact that the convective Adkins-Smith model with its diffusive mixing equation and the purely diffusive Gallimore-Cumpsty model yield the same results.
Finally, observe that the symmetry, imposed by the machine geometry, is reflected in the temperature distribution.

In order to enhance the convective mixing effects, the deflection has been arbitrarily increased to 54°. The results are shown on Figures 6a to 6c. As can be seen from the velocity vector plot of the secondary flow field, the secondary velocities have increased. The maximum radial velocities now reach about 8% of the axial velocity. The temperature distribution, Figure 6b, is more severely distorted , i.e. the increased secondary flow leads to increased convective mixing. This can be seen most clearly from Figure 6c, where the radial redistribution computed with the present method has become more uniform compared to Figure 5c, and can now be distinguished from the Adkins-Smith method and the pure turbulent diffusion case, the latter two methods both underestimating the amount of mixing.

UTRC rotor
The mixing results are obtained for an S3-plane, located 1 chord downstream of the trailing edge, a distance which is considered to be representative for the axial spacing between successive blade rows.
The UTRC rotor is representative for commercial machines, where all the different flow regions that contribute to the secondary flowfield have a more or less equal importance. Its main difference with the cascade testcase is the presence of centrifugation effects through the rotary movement. The secondary velocity field, Figure 7a, possesses the familiar double-vortex structure. The maximum radial velocities attain about 6% of the axial flow velocity in the wakes but are zero at mid-span. The turbulent mixing coefficient is again set to the typical value of 0.002.
The temperature contour plot, Figure 7b, shows that the convective mixing by the secondary flowfield is almost negligible, although the radial velocities are of the same order of magnitude as in the VUB cascade. This indicates that, although local radial velocities can be high, the amount of convected fluid is not large enough to induce significant convective mixing. This should not come as a total surprise, since the blading geometry of industrial machines is designed to avoid secondary flows as much as possible, leaving turbulent diffusion as the dominant mixing mechanism. Figure 7c reflects this behaviour, since all the radial temperature profiles coincide.

ONERA rotor
The ONERA rotor has been especially designed to exhibit large secondary flows, through a strong non-free vortex behaviour of the inviscid flow region. This is clear from Figure 8a, showing a large single vortex. Radial velocities may reach up to 20% of the axial velocity.
The temperature distribution, Figure 8b, is strongly distorted by the secondary flowfield, i.e. convective mixing is very important in this case. This is obvious from the radial temperature profiles, Figure 8c, which show that the computation based on pure turbulent diffusion underestimates the mixing with respect to the present method, especially near the hub. This can also be seen from the fact that the profile from the computation with Adkins-Smith coefficient (eq.46), which takes into account convection effects, has become more uniform than the profile obtained by the pure turbulent diffusion computation. Notice also that the profile computed with the present method has become nearly uniform.
Although this testcase exhibits an extreme secondary flow behaviour, one should remark that the continuing trend towards lower aspect ratios and higher blade loadings for axial turbomachinery will lead to increased secondary flows. Thus, in these machines the temperature distribution on the S3-plane can be severely distorted, causing convective mixing effects to become very important.

CONCLUSIONS

A computational method for the prediction of radial mixing in axial compressors has been presented. The method takes into account convective mixing by secondary flows and diffusive mixing due to turbulence. The secondary flow field is reconstructed from the knowledge of axial vorticity contributions for different flow regions, which are added to constitute the right-hand side of a quasi-harmonic Poisson-type streamfunction equation. These axial vorticity components are obtained through vorticity equations for the inviscid flow region, combined with integral methods for the 3D end-wall boundary layers, 3D profile boundary layers and 3D asymmetric wakes. The turbulent diffusion is modeled through an empirical mixing coefficient.

Preliminary comparisons between computed and experimental flow fields indicate reasonable agreement in general, but the computation does have a tendency to underestimate radial velocities near the suction side, where separation effects are likely to occur.

The radial redistributions of the static temperature are computed from a twodimensional transport equation of convection-diffusion type.
This computation has been applied to three different test cases : a linear cascade where the

secondary flows are mainly due to end-wall boundary layer effects, a single compressor rotor with untwisted blading that yields an important non-free vortex, and a single compressor rotor representative for commercial turbomachines. Qualitative results indicate that turbulent diffusion is important in all the cases, while convective mixing only becomes significant when the radial flow velocities exceed about 6% of the main flow velocities. The convective mixing increases rapidly for larger secondary flows (VUB 54° and ONERA testcases) and then has a very considerable impact on the radial temperature profile (ONERA testcase).

ACKNOWLEDGEMENTS

The present research project is supported by the Air Force Office for Scientific Research, Bolling AFB, USA. One of the authors (PS) was able to participate in this research through a grant of the IWONL, Brussels, Belgium.

REFERENCES

[1] WU C.H., "A General Theory of Three-dimensional Flow in Subsonic and Supersonic Turbomachines of Axial-, Radial-, and Mixed-Flow Types", NACA TN 2604, 1952.

[2] ADKINS G.G., SMITH L.H., "Spanwise Mixing in Axial-Flow Turbomachines", ASME Journal of Engineering for Power, Vol.104, January 1982, pp 97-110.

[3] GALLIMORE S.J., CUMPSTY N.A., "Spanwise Mixing in Multistage Axial Flow Compressors : Part I - Experimental Investigation", ASME Journal of Turbomachinery, Vol.108, July 1986, pp 2-9.

[4] GALLIMORE S.J., CUMPSTY N.A., "Spanwise Mixing in Multistage Axial Flow Compressors : Part II - Throughflow Calculations Including Mixing", ASME Journal of Turbomachinery, Vol.108, July 1986, pp 10-16.

[5] WISLER D.C., BAUER R.C., OKIISHI T.H., "Secondary Flow, Turbulent Diffusion and Mixing in Axial-Flow Compressors", ASME Journal of Turbomachinery, Vol.109, October 1987, pp 455-482.

[6] DE RUYCK J., HIRSCH C., "A Radial Mixing Computation Method", ASME Paper 88-GT-68.

[7] DE RUYCK J., HIRSCH C., "Radial Mixing in Turbomachines", Report VUB-TN-39, Dept. of Fluid Mechanics, Vrije Universiteit Brussel, 1987.

[8] DE RUYCK J., HIRSCH C., "Radial Mixing in Turbomachines", Report VUB-TN-40, Dept. of Fluid Mechanics, Vrije Universiteit Brussel, 1987.

[9] HIRSCH C., WARZEE G., "An Integrated Quasi-3D Finite Element Calculation Program for Turbomachinery Flows", ASME Journal of Engineering for Power, Vol.101, January 1979, pp 141-148.

[10] YIH C.S., Fluid Mechanics (2nd Ed.), West River Press, Ann Arbor, 1979.

[11] HIRSCH C., "Computational Models for Turbomachinery Flows", Technical Report NPS67-84-022, Naval Postgraduate School, Monterey, 1984.

[12] HIRSCH C., Numerical Computation of Internal and External Flows, Vol.1 : Fundamentals of Numerical Numerical Discretization, John Wiley, Chichester, 1988.

[13] DE RUYCK J., HIRSCH C., "Investigations of an Axial Compressor End-Wall Boundary Layer Prediction Method", ASME Journall of Eng. for Power, Vol.103, January 1981, pp 20-33.

[14] DE RUYCK J., "Computation of End-Wall Boundary Layers in Axial Compressors", PhD Thesis, Dept. of Fluid Mechanics, Vrije Universiteit Brussel, 1982.

[15] DE RUYCK J., HIRSCH C., "End-Wall Boundary Layers in Multistage Axial Compressors", AGARD 61th Specialist Meeting, Viscous Effects in Turbomachines, AGARD CP 351, 1983.

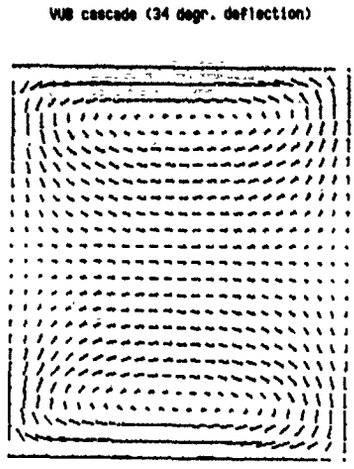
[16] DRING R.P., JOSLYN H.D., HARDIN L.W., "An Investigation of Axial Compressor Rotor Aerodynamics', ASME Journal of Engineering for Power, Vol.104, January 1982, pp 84-96.

[17] SCHLICHTING H., Boundary Layer Theory (6th Ed.), McGraw-Hill, New York, 1968.

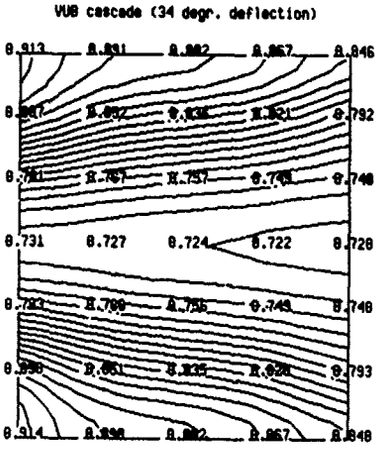
[18] HIRSCH C., DRING R.P., "Through Flow Models for Mass and Momentum Averaged Variables", ASME Journal ASME Journal of Turbomachinery, Vol.109, July 1987, pp 362-370.

[19] LARGUIER R., "Experimental Analysis Methods for Unsteady Flows in Turbomachines", Measurement Methods in Rotating Components of Turbomachinery, p 71, ASME, 1980.

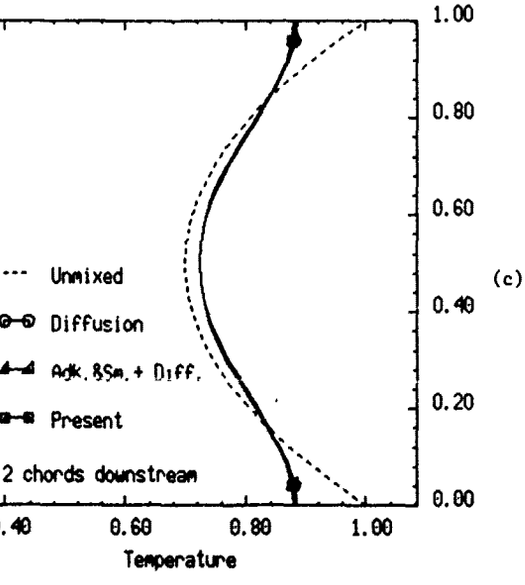
[20] BELKAID A., "Etude de l'ecoulement secondaire dans une grille d'aubes de compresseur", Master's Thesis, Centre d'Etudes Nucleaires et Solaires, Algerie, 1987.



(a)

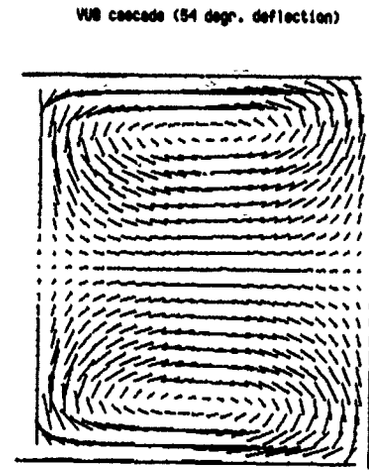


(b)

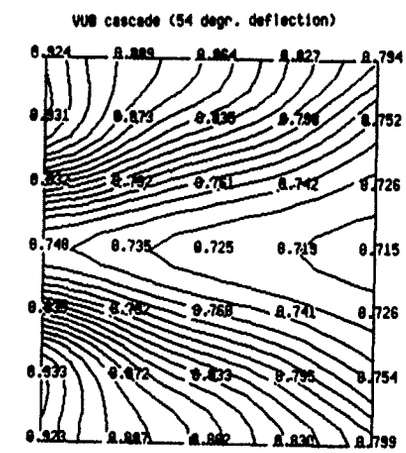


(c)

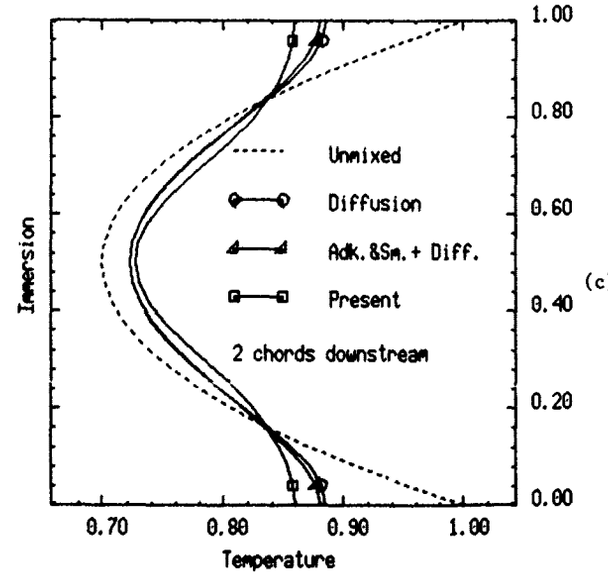
Figure 5 : Secondary velocity field, 2D temperature field and radial temperature profiles for the VUB cascade (34° defl.)



(a)

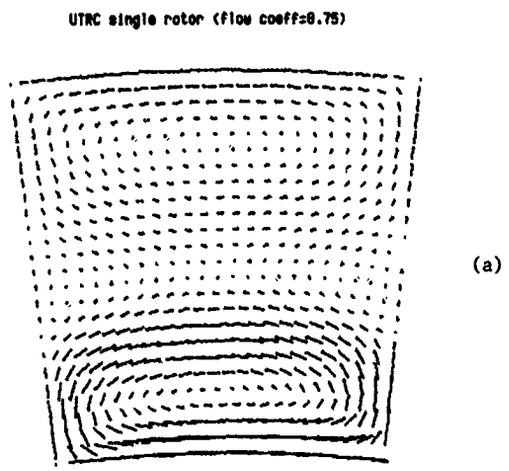


(b)

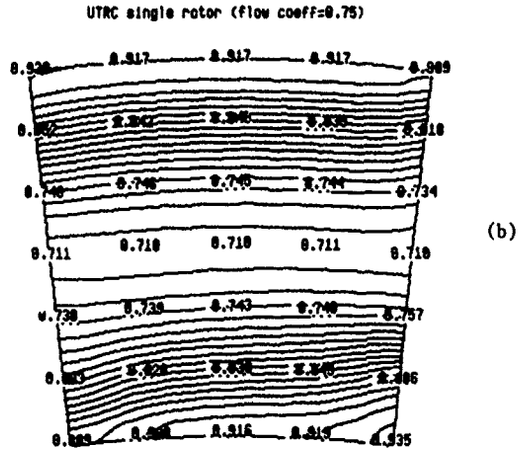


(c)

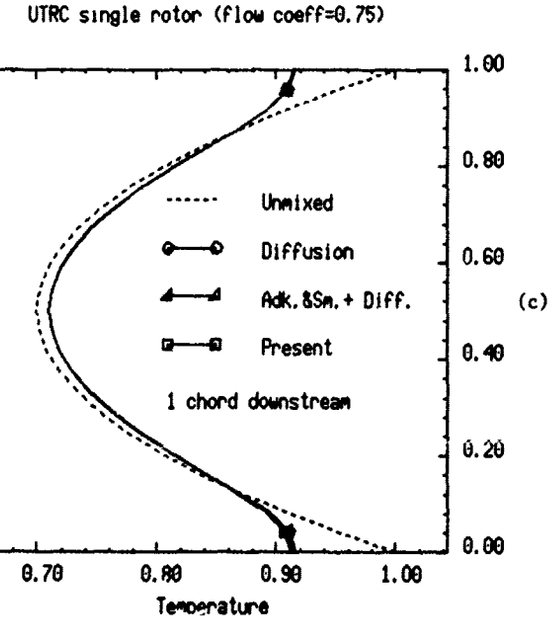
Figure 6 : Secondary velocity field, 2D temperature field and radial temperature profiles for the VUB cascade (54° defl.)



(a)

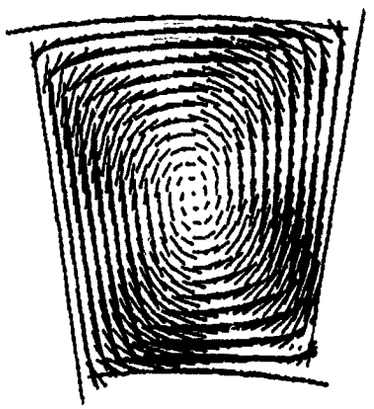


(b)

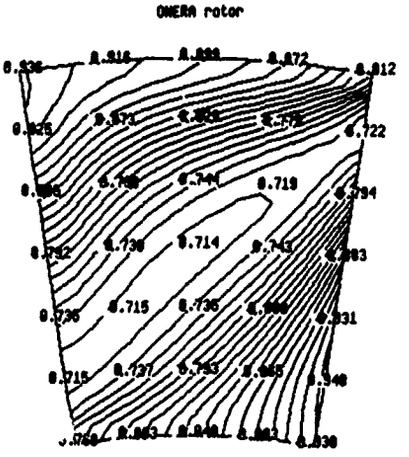


(c)

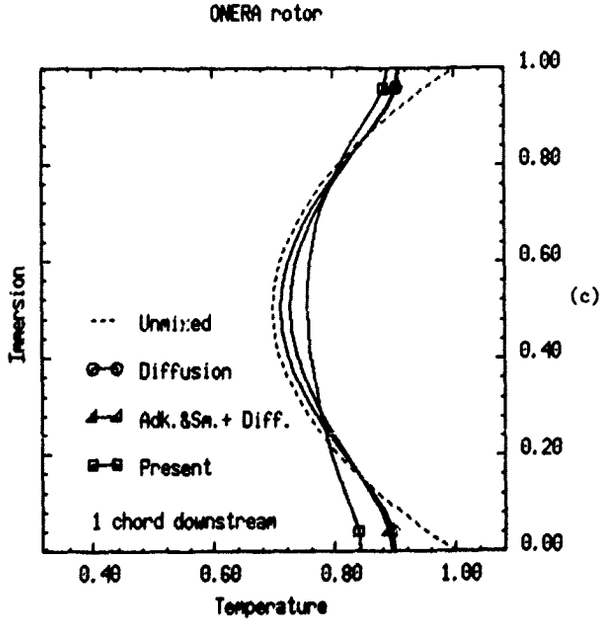
Figure 7 : Secondary velocity field, 2D temperature field and radial temperature profiles for UTRC compressor rotor



(a)



(b)



(c)

Figure 8 : Secondary velocity field, 2D temperature field and radial temperature profiles for ONERA compressor rotor

DISCUSSION

Adamczyk, USA

1. What was the rational for neglecting the velocity vorticity correlations in Eqn (15)?

2. Did you consider the tip leakage Vortex in your model of the secondary flow velocity field?

Author's Reply

1. Since we are concerned with axial machines, it can be expected that the pitchwise fluctuations of radial velocity components, w', and of radial vorticity components, $\zeta'_{abs,r}$, are small with respect to the passage-averaged quantities. Hence, the velocity correlations are assumed to be of second order compared to the passage averaged terms.

   Furthermore, it is assumed that the secondary flow field associated to the inviscid flow region is adequately described by the passage-averaged velocity, $\bar{c}_{abs,z}$. Accordingly, velocity fluctuations $c'_{abs,z}$ are neglected.

2. The effect of the tip leakage vortex is included in the endwall boundary layer computation in a <u>global</u> sense. The defect force thicknesses, which largely condition the development of the endwall boundary layer crossflow and skewing, are directly proportional to the tip clearance. In this way, tip leakage effects influence the passage-averaged endwall boundary layer velocity contribution $\bar{c}_{z,s3,wall}$ and thus are taken into account on an <u>averaged</u> axis.

   This is also justified by the available experimental information on mixed-out profiles, which show no discontinuity in slope or other structures that indicate a dominating local effect from the tip leakage vortex. We consider therefore, that although the tip vortex is not fully represented in all its details, its main effects on the pitch-averaged profiles are taken into account.

Howard, UK

I would like to clarify what variations of loss with span have been used when comparing Gallimore, Adkins/Smith and your methods. It has been found important to specify extra loss near the endwall in the Gallimore model in order to generate an axial velocity profile which in turn increases the mixing near the endwalls.

Author's Reply:

The main objective of the figures shown was to compare the relative importance of mixing by secondary flows (Adkins/Smith), mixing by turbulent diffusion (Gallimore/Cumpsty) and mixing by both mechanisms combined (present method). Therefore, in these examples, the three methods were applied using exactly the same data, i.e., identical spanwise loss profiles and axial velocity profiles.

THE EFFECTS OF COMPRESSOR ENDWALL FLOW ON AIRFOIL INCIDENCE AND DEVIATION

by

Robert P.Dring and H.David Joslyn
United Technologies Research Center
Silver Lane
East Hartford, Connecticut 06108, USA

ABSTRACT

A previous examination of through flow theory in compressors has demonstrated that while there are many ways to define the "average flow angle" at a particular span location downstream of an airfoil, only one definition is consistent with the formulation of through flow theory. It was also demonstrated that the flow in the endwall regions is especially sensitive to this question due to the strong secondary flows and the hub corner separations that commonly occur. The present work deals with the question of how these observations may be extended to the airfoil-to-airfoil flow analysis. It is demonstrated that the question of the correct average can have a strong impact on both airfoil incidence and deviation. Differences of up to 13° are demonstrated. It is also suggested that one specific angle definition results in better predictions of airfoil pressure distributions.

INTRODUCTION

There is a long list of secondary flow mechanisms in axial compressors that can have a powerful impact on the flow field. In addition to generating total pressure losses and altering flow angles from two dimensional values, secondary flows can also cause strong non-axisymmetries to occur in the flow. It is the effect that these non-axisymmetries have on airfoil design, and specifically the effect that they have on incidence and deviation, that is addressed here. These secondary flow mechanisms include (but are not limited to) the following.

- Inviscid secondary flow
- Skewing due to the relative motion of rotors and stators
- Three-dimensional boundary layers
- Rotor tip clearance leakage
- Stator hub clearance leakage
- Corner separation

It is fortunate that the first two mechanisms (inviscid secondary flow and skewing) tend to cancel each other. This in turn causes the three dimensionality of the endwall boundary layers to be relatively weak (Moore and Richardson, 1957). This lack of three dimensionality can be seen in the flow visualization results of Dring and Joslyn (1982 and 1983), and Joslyn and Dring (1985). In both cases the endwall surface streamlines follow the airfoil mean camber line with little evidence of the over-turning normally associated with secondary flows in cascades (without inlet skewing).

Corner separation, especially at the hub of both rotors and stators, appears to be an important endwall flow mechanism. A number of works have been cited in the REFERENCES section that either discuss, or show evidence of, corner separation in both cascade and rotating rig experiments. The strong non-axisymmetries that are generated by corner separation can have a powerful impact on deviation and on the incidence of a downstream airfoil.

The non-axisymmetries generated by corner separation and the other endwall flows can cause a strong circumferential variation in the exit flow angle (deviation). Since both through flow analysis and airfoil-to-airfoil flow analysis require the specification of single value (or average) flow angle, different results would be produced depending on how one defines the "average" flow angle.

As an basis for this discussion, area averaging and mass averaging are defined as follows, for a function "F":

$$F^{-a} = \int_0^\tau F \cdot dt \Big/ \int_0^\tau dt \tag{1}$$

$$F^{-m} = \int_0^\tau F \cdot \varrho \cdot C_x \, dt \Big/ \int_0^\tau \varrho \cdot C_x \, dt \tag{2}$$

where τ is the airfoil pitch, ϱ if the fluid density, and "C_x" is the axial component of velocity. Possible definitions for the averages of the absolute angles (α) and relative angles (β) might include the following.

(1) The mass averaged angles, α^{-m} and β^{-m}.

(2) The angle based on the area averaged velocity components,

$$\hat{\alpha} = \mathrm{Tan}^{-1}(C_t^{-a}/C_x^{-a}) \tag{3}$$

$$\hat{\beta} = \mathrm{Tan}^{-1}(W_t^{-a}/C_x^{-a}) \tag{4}$$

where C_t and W_t are the absolute and relative tangential or "swirl" components of velocity.

(3) The angle based on the mass averaged tangential velocity component and the area averaged axial velocity component,

$$\tilde{\alpha} = \mathrm{Tan}^{-1}(C_t^{-m}/C_x^{-a}) \tag{5}$$

$$\tilde{\beta} = \mathrm{Tan}^{-1}(W_t^{-m}/C_x^{-a}) \tag{6}$$

The significance, or lack thereof, of each of these "average" angles will now be examined.

ANALYSIS

The mass averaged flow angle might, at first glance, be thought to be a reasonable definition to use. However, the arguments offered by Hirsch and Warzee (1979) and by Dring and Oates (1989a and 1989b) show that it is not the correct angle to use in through flow analysis. Furthermore, the arguments offered below will show that it is also not the correct angle to use in calculating the tangential force on an airfoil. It will be shown that averaged angles have no physical significance and the only angles having physical significance are those based on averaged velocity components. Suffice it to say at this point that the differences in these angles can be substantial.

Angles based on the area averaged velocity components ($\hat{\alpha}$ and $\hat{\beta}$) are required by the formulation of through flow analysis. This can be seen in the work by Hirsch and Warzee (1979) where angles are used to relate the averaged velocity components. Their analysis was based on "density" averaged velocity components. In most cases, however, the density averages would be very close to area averages. It has been shown by Dring and Oates (1989a and 1989b) that an extension of this formulation can result in a very accurate prediction of the flow, even when strong non-axisymmetries are present.

Angles based on the mass averaged tangential velocity component and the area averaged axial velocity component ($\tilde{\alpha}$ and $\tilde{\beta}$) result from considering what flow angle is needed to describe the tangential force on a cascade airfoil with non-axisymmetric flow at the inlet and exit. For a cascade with incompressible and non-axisymmetric inlet and exit flow the tangential force per unit span (F_t) on the airfoil is given by the following (for a rotor).

$$(F_t/\varrho \cdot \tau) = (C_x^{-a})^2[\mathrm{Tan}(\tilde{\beta}_1) - \mathrm{Tan}(\tilde{\beta}_2)] \tag{7}$$

The angles needed for through flow analysis ($\hat{\alpha}$ and $\hat{\beta}$) and the angles needed to describe the tangential force on a cascade airfoil ($\tilde{\alpha}$ and $\tilde{\beta}$) are related to each other as follows.

$$\mathrm{Tan}(\tilde{\alpha}) = \mathrm{Tan}(\hat{\alpha}) + [(C_t' \cdot C_x')^{-a}/(C_x^{-a})^2] \tag{8}$$

$$\mathrm{Tan}(\tilde{\beta}) = \mathrm{Tan}(\hat{\beta}) + [(W_t' \cdot C_x')^{-a}/(C_x^{-a})^2] \tag{9}$$

where the primed quantities are the variations from the area average,

$$C_x' = (C_x - C_x^{-a}) \tag{10}$$

$$C_t' = (C_t - C_t^{-a}) \tag{11}$$

$$W_t' = (W_t - W_t^{-a}) \tag{12}$$

and since,

$$W_t = (C_t - U) \tag{13}$$

where "U" is wheel speed, then,

$$W_t' = C_t' \tag{14}$$

It is fortunate that both of these angles ($\hat{\alpha}$ and $\hat{\beta}$ as well as $\bar{\alpha}$ and $\bar{\beta}$ can be calculated in the through flow analysis. Specifically, the through flow analysis for non-axisymmetric flow by Dring and Oates (1989a and 1989b) contains a parameter which accounts for the difference between the area and mass averages of the tangential velocity. This parameter is defined as follows (assuming that area and density weighted averages are equal).

$$DCT = (C_t^{-a} - C_t^{-m})/U_m \tag{15}$$

where "U_m" is the wheel speed at midspan.

This parameter is not directly input to the through flow analysis. Rather, it is calculated from other input data. From the through flow calculation the following information is available (either has as input data, or as a computed result); $\hat{\alpha}$, $\hat{\beta}$, DCT, and (C_x^{-a}/U_m). With this information the following relationships (which are essentially the same as Eqs. (8) and (9)) can be evaluated.

$$\mathrm{Tan}(\bar{\alpha}) = \mathrm{Tan}(\hat{\alpha}) - [DCT/(C_x^{-a}/U_m)] \tag{16}$$

$$\mathrm{Tan}(\bar{\beta}) = \mathrm{Tan}(\hat{\beta}) - [DCT/(C_x^{-a}/U_m)] \tag{17}$$

Thus it is possible, with no additional information, for the through flow analysis of Dring and Oates (1989a and 1989b) to also compute the angles that are needed for the airfoil-to-airfoil flow analysis, $\bar{\alpha}$ and $\bar{\beta}$. In fact, there is no need for $\hat{\alpha}$ and $\hat{\beta}$. The through flow analysis could be carried out using $\bar{\alpha}$ and $\bar{\beta}$ and by using Eqs. (8) and (9) to calculate the angles needed to relate the density averaged velocity components ($\hat{\alpha}$ and $\hat{\beta}$).

In the results that are be presented below, these relationships (Eqs. (8) and (9), or (16) and (17)) cause the deviations based on $\bar{\alpha}$ and $\bar{\beta}$ to be substantially larger than those based on $\hat{\alpha}$ and $\hat{\beta}$. In one case this difference in deviations exceeds 13°. These relationships also cause the incidences based on $\bar{\alpha}$ and $\bar{\beta}$ to be slightly less than those based on $\hat{\alpha}$ and $\hat{\beta}$. This difference, however, is generally small relative to the differences between these inlet angles and the mass averaged inlet angles (α^{-m} and β^{-m}).

It is interesting to note that the angle based on the mass averaged tangential velocity component (W_t^{-m}) and the area averaged axial velocity component (C_x^{-a}), $\bar{\alpha}$ and $\bar{\beta}$, has another convenient property. In a two dimensional wake mixing process (e.g. Stewart, 1959) both of these averaged velocity components are constant for incompressible flow. This is because the mass flow is constant and because there is no change in tangential momentum. Hence, unlike all of the other flow angle definitions, this angle is constant from the unmixed condition close to the airfoil trailing edge to the fully mixed condition far downstream.

EXPERIMENTAL RESULTS

In the following discussion each of these three angle definitions will be examined (β^{-m}, $\hat{\beta}$ and $\bar{\beta}$). The discussion will be based on the body of experimental results acquired in the United Technologies Research Center Large Scale Rotating Rig. This data has been discussed previously in the following references; Dring, Joslyn and Wagner (1983), Joslyn and Dring (1985), Joslyn and Dring (1988), and Dring and Oates(1989a and 1989b). In brief, the compressor consists of an inlet guide vane followed by two stages. The airfoil aspect ratios (span/chord) are 1.5. All of the data in the present discussion were acquired at a second stage rotor tip clearance-to-chord ratio of 0.041. Data will be presented that was acquired both at the compressor's nominal design flow coefficient [$\phi = (C_x/U_m) = 0.51$] and at a near-stall flow coefficient [$\phi = 0.45$].

Spanwise distributions of the absolute and relative flow angles calculated from radial/circumferential traverse data acquired in the stationary frame of reference downstream of the second stage stator are presented in Figure 1 with the compressor operating at its nominal design condition ($\phi = 0.51$). The figure shows a comparison of the circumferentially mass averaged angles with the angles based on circumferentially area and mass averaged velocity components.

Whereas the absolute angles α^{-m} and $\hat{\alpha}$ differ by less than 0.6° the relative angles β^{-m} and $\hat{\beta}$ differ by over 10°. The difference is greatest near the hub where corner separation is strongest (Joslyn and Dring, 1985). As far as deviation is

concerned, $\hat{\alpha}$ and α^{-m} are relatively close to each other. $\bar{\alpha}$ is much larger from the hub out to 25% span. The reason for this can be seen in Eq. (8) where $\hat{\alpha}$ and $\bar{\alpha}$ are positive and where $[(C_t' \cdot C_x')^{-a}/(C_x^{-a})^2]$is a positive number. As far as incidence is concerned, $\hat{\beta}$ is somewhat larger than $\bar{\beta}$ near the hub. The reason for this can be seen in Eq. (9) where $\hat{\beta}$ and $\bar{\beta}$ are negative and where $[(W_t \cdot C_x)^{-a}/(C_x^{-a})^2]$ is a positive number. Both $\hat{\beta}$ and $\bar{\beta}$ are significantly larger than β^{-m} in the region out to 25% span.

Similar comparisons at nominal design conditions ($\phi = 0.51$) for the flow downstream of the first stator and the second rotor showed exit angle (deviation) differences of typically 0.1° and inlet angle (incidence) differences of less than 1°. Both of these airfoils have hub corner separations which are much weaker that that of the second stator. It can safely be anticipated that the differences between the various angle definitions will grow substantially with airfoil loading, i.e., in going from nominal design conditions (Figure 1) to the near-stall condition.

Spanwise distributions of the absolute and relative flow angles calculated from radial/circumferential traverse data acquired in the stationary frame of reference downstream of the first stage stator are presented in Figure 2 with the compressor operating at its near-stall condition ($\phi = 0.45$). The figure shows profiles of the same three angle definitions. All the trends are very similar to those in Figure 1 in that $\hat{\beta}$ and $\bar{\beta}$ are close to each other and significantly larger (by $\approx 5°$) than β^{-m}, and in that $\hat{\alpha}$ and α^{-m} are close to each other and significantly smaller (by $\approx 5°$) than $\bar{\alpha}$.

Spanwise distributions of the absolute and relative flow angles calculated from radial/circumferential traverse data acquired in the rotating frame of reference downstream of the second stage rotor are presented in Figure 3 with the compressor operating at its near-stall condition ($\phi = 0.45$). The figure shows profiles of the same three angle definitions. The figure shows a comparison of the circumferentially mass averaged angles with the angles based on circumferentially area and mass averaged velocity components. The trends downstream of the second stage rotor are very similar to those in Figures 1 and 2. Although the differences are much smaller, it can be seen that $\bar{\alpha}$ and $\hat{\alpha}$ are close to each other and that $\bar{\beta}$ is relatively large. All of these differences, however, are small compared to those in Figures 1 and 2.

Spanwise distributions of the absolute and relative flow angles calculated from radial/circumferential traverse data acquired in the stationary frame of reference downstream of the second stage stator are presented in Figure 4 with the compressor operating at its near-stall condition ($\phi = 0.45$). The figure shows profiles of the same three angle definitions. The trends downstream of the second stage stator at this condition are similar to those in Figures 1, 2 and 3 but the differences are much larger. The powerful effect of airfoil loading can be seen by comparing Figures 1 and 4 (the second stage stator at design and near-stall conditions).

As far as deviation is concerned, the absolute angles α^{-m} and $\dot{\alpha}$ differ by less than 0.6° while $\bar{\alpha}$ exceeds both $\dot{\alpha}$ and α^{-m} by over 13°. The reason for this can again be seen in Eq. (8) where $\hat{\alpha}$ and $\hat{\alpha}$ are positive and where $[(C_t' \cdot C_x')^{-a}/(C_x^{-a})^2]$ is a positive number. As far as incidence is concerned, the relative angles β^{-m} and $\dot{\beta}$ differ by over 12° near the hub where corner separation is strongest (Joslyn and Dring, 1985). The reason for this can be seen in Eq. (9) where $\hat{\beta}$ and $\bar{\beta}$ are negative and where $[(W_t' \cdot C_x')^{-a}(C_x^{-a})]$ is a positive number.

The differences between $\hat{\alpha}$ and $\bar{\alpha}$ and between $\hat{\beta}$ and $\bar{\beta}$ are due to the strong correlation between the deviations of the tangential and axial velocity components from their area averages (Eqs. (8) and (9)). From the single- and multi-stage data base available to the authors [Dring and Joslyn (1982), Dring, Joslyn and Wagner (1983), Joslyn and Dring (1985), and Wagner, Dring and Joslyn (1985)], the following observation can be made. Where there are significant non-axisymmetries in the flow, deviations based on $\bar{\alpha}$ and $\bar{\beta}$ are larger than those based on $\dot{\alpha}$ and $\dot{\beta}$ and incidences based on $\bar{\alpha}$ and $\bar{\beta}$ are smaller than those based on $\dot{\alpha}$ and $\dot{\beta}$.

Summarizing regarding the flow angle definitions, the strong non-axisymmetry generated by the deep and wide wakes, primarily due to the hub corner separation, produces widely different deviations and incidences depending on the particular angle definition used. The improvement in the agreement between measured and computed results that can be obtained using the angle definition based on the area averaged velocity components ($\dot{\alpha}$ and $\dot{\beta}$) and a consistent formulation of through flow theory has been demonstrated by Dring and Oates (1988a and 1988b). Airfoil-to-airfoil flow analysis (airfoil tangential loading) requires angles based on the mass averaged tangential and the area averaged axial velocity components $\bar{\alpha}$ and $\bar{\beta}$. The improvements in the agreement between measured and computed results that can be obtained using this angle definition are demonstrated below in Figures 5, 6 and 7. In these figures the airfoil pressure coefficient (CP) is based on the inlet static pressure (P_1) and the inlet dynamic pressure (Q_1). It is plotted against the normalized axial distance (X/B_x), where B_x is the airfoil axial chord.

Comparisons of the measured and computed pressure distributions for the second stage rotor from the hub out to midspan at near-stall conditions ($\phi = 0.45$) are presented in Figure 5. The symbols represent the measured surface static pressures. The computed results (curves) are based on the potential flow method of Caspar, Hobbs, and Davis (1980) which accounts for total pressure loss and stream tube contraction. The rotor inlet angle used in the calculation was based

both on β_1^m (dashed) and on $\bar{\beta}_1$ (solid). The differences between these two angles decreases from 4.8° near the hub to near zero at midspan (Figure 2). Since all three angle definitions yielded rotor exit flow angles which were close to each other (Figure 3) their effect on the computed results was very small and is not shown in Figure 5.

In general, the inlet angle based on averaged velocity components ($\bar{\beta}_1$) gave much better agreement on the pressure surface. The agreement on the suction surface was improved but was still far from perfect due to the corner separation near the hub (Dring, Joslyn, and Wagner, 1983, Figure 3). The chordwise location of this separation is indicated by the "S" on the CP = 0 axes in Figure 5. This location was determined from surface flow visualization (Dring, Joslyn and Wagner (1983) Figure 3, and Joslyn and Dring (1988) Figure 5).

The inlet angle based on averaged velocity components ($\hat{\beta}_1$) produced a more accurate prediction of the pressure distribution, especially in the leading edge region. Similar comparisons were not done for this rotor at the design flow coefficient (ϕ = 0.51) because the difference between the various inlet angles was very small (≈1°) at that condition.

Even at the near-stall condition the impact of the endwall non-axisymmetries on the various flow angle definitions on the second stator inlet angle was relatively weak ($\Delta a_1 \approx 2°$, Figure 3) Their effect on the exit angle, however, was very strong ($\Delta a_2 \approx 13°$, Figure 4) The effect of this range of exit flow angle is shown in Figure 6 for the 12.5% span location. The results at the other span locations near the hub were similar.

This comparison shows the insensitivity of the computed pressure distribution to the large difference in exit angle (≈13°) between $\bar{a}_2$ and a_2^m. The poor agreement between the measured and computed results is due to the massive hub corner separation on this stator. At this 12.5% span location the separation occurs at the 30% chord location, as indicated by the "S" on the CP = 0 axis.

Figure 6 compares the results of airfoil potential flow calculations at several span locations on a hypothetical third stage rotor operating at near-stall conditions (ϕ = 0.45). The compressor did not have a third stage so the hypothetical third stage rotor geometry was taken to be identical to the second stage rotor. The rotor exit flow angles were taken to be the same as those for the second stage rotor (Figure 3) and the rotor inlet angles, β_1^m and $\bar{\beta}_1$, were those measured downstream of the second stage stator (Figure 4). Note that $\bar{\beta}$ and β^m differ by as much as 10°.

The difference between the two pressure distributions at each span location is large. It seems safe to assume that significantly different airfoils would result depending on which of the two inlet angle distributions a designer was using.

CONCLUSIONS

It has been demonstrated that the non-axisymmetries generated by the endwall flow mechanisms in axial compressors can have a powerful impact on the incidence and deviation angles that are used in both the through flow and airfoil-to-airfoil design analyses. Specific observations and conclusions are as follows.

- Differences of up to 13° between the various definitions have been demonstrated for both inlet angles (incidence) and exit angles (deviation).
- Airfoil-to-airfoil flow calculations are more accurate when they are based on inlet and exit flow angles computed from the mass averaged tangential velocity and the area averaged axial velocity components.
- Through flow analysis must be based on flow angles computed from the area (or density) averaged velocity components ($\hat{a}$ and $\hat{\beta}$).
- There is sufficient information in the through flow analysis of Dring and Oates (1989a and 1989b) to relate $\hat{a}$ and $\bar{a}$ and to relate $\hat{\beta}$ and $\bar{\beta}$.
- The present data suggests that the inlet flow angles $\hat{a}$ and $\bar{a}$ (or $\hat{\beta}$ and $\bar{\beta}$) are relatively close to each other.
- The present data also suggests that while the exit flow angles $\hat{a}$ and $\bar{a}$ (or $\hat{\beta}$ and $\bar{\beta}$) can be very different, the airfoil-to-airfoil flow analysis is much less sensitive to the difference.
- The concepts that have been presented here should be of value in analyzing the growing body of LDV and hot-film data that is becoming available for compressors. This will be particularly true in relating this flow field information to measured airfoil pressure distributions.

ACKNOWLEDGEMENTS

The authors would like to express their gratitude to a number of people who influenced the content of this paper through their thoughtful questions, comments, and suggestions. Specifically, we would like to thank Dr. Leroy Smith of the General Electric Company, Prof. Edward Greitzer of M.I.T., and Mr. David Spear of Pratt and Whitney Aircraft.

REFERENCES

(* = References that discuss or show evidence of corner separation)

Caspar, J. R., Hobbs, D. E., and Davis, R. L., 1980, *Calculation of Two-Dimensional Potential Cascade Flow Using Finite Area Methods*, AIAA Journal, Vol. 18, No. 1, pp. 103-109.

* Cyrus, V., 1986, *Experimental Study of the Flow in an Axial Compressor Stage*, ASME paper no. 86-GT-118.

* Cyrus, V., 1988, *The Effect of the Inlet Velocity Profile in the Three-Dimensional Flow in a Rear Axial Compressor Stage*, ASME paper no. 88-GT-46.

* Dong, Y., Gallimore, S. J., and Hodson, H. P., 1987, *Three-Dimensional Flows and Loss Reduction in Axial Compressors*, ASME paper no. 86-GT-193, Trans. ASME, Journal Turbomachinery, Vol. 109, No. 3, pp. 354-361.

* Dring, R. P., Joslyn, H. D., and Hardin, L. W., 1982, *An Investigation of Compressor Rotor Aerodynamics*, ASME paper no. 81-GT-56, Trans. ASME, Journal of Engineering for Power, Vol. 104, No. 1, pp. 84-96.

* Dring, R. P., Joslyn, H. D., and Wagner, J. H., 1983, *Compressor Rotor Aerodynamics*, AGARD-CP-351, Viscous Flow Effects in Turbomachines, Copenhagen, Denmark.

Dring, R. P., and Oates, G. C., 1989a, *Through Flow Theory for Nonaxisymmetric Turbomachinery Flow. Part 1 - Formulation*, accepted for presentation at the 1989 ASME Gas Turbine Conference and for publication in Trans. ASME, Journal of Turbomachinery.

Dring, R. P., and Oates, G. C., 1989b, *Through Flow Theory for Nonaxisymmetric Turbomachinery Flow, Part 2 - Assessment*, accepted for presentation at the 1989 ASME Gas Turbine Conference and for publication in Trans. ASME, Journal of Turbomachinery.

* Gallus, H. E., and Hoenen, H., 1986, *Experimental Investigations of Airfoil and Endwall Boundary Layers in a Subsonic Compressor Stage*, ASME paper no. 86-GT-143.

* Hirsch, C., and Warzee, G., 1979, *An Integrated Quasi-3D Finite Element Calculation Program for Turbomachinery Flows*, ASME paper no. 78-GT-56, Trans. ASME, Journal of Engineering for Power, Vol. 101, No. 1, pp. 141-148.

* Horlock, J. H., 1966, *Wall Stall in Compressor Stages*, Trans. ASME, Journal of Basic Engineering, Vol. 88, No. 3, pp. 637-648.

* Joslyn, H. D., and Dring, R. P., 1985, *Axial Compressor Stator Aerodynamics*, ASME paper no. 84-GT-90, Trans. ASME, Journal of Engineering for Gas Turbines and Power, Vol. 107, No. 2, pp. 485-493.

Joslyn, H. D., and Dring, R. P., 1988, *Multi-Stage Compressor Airfoil Aerodynamics: Part II - Airfoil Boundary Layer Analysis*, AIAA paper no. AIAA-86-1744, AIAA Journal of Propulsion and Power, (to be published).

* Lakshminarayana, B., and Horlock, J. H., 1967, *Leakage and Secondary Flows in Compressor Cascades*, ARC R&M 3483

Moore, R. W. and Richardson, D. L., 1957, *Skewed Boundary Layer Flow Near the Endwalls of a Compressor Cascade*, Trans. ASME, Vol. 79, pp. 1789-1800.

* Schultz, H. D., and Gallus, H. E., 1988, *Experimental Investigation of the Three-Dimensional Flow in an Annular Compressor Cascade*, ASME paper no. 88-GT-201.

Stewart, W. L., 1959, *Analysis of Two-Dimensional Flow Loss Characteristics Downstream of Turbomachine Blade Rows in Terms of Basic Boundary Layer Characteristics*, NACA TN-3515.

* Tao, D., and Wang, C., 1988, *Experimental Study of End-Wall Flow in a Compressor Stage*, AIAA Journal of Propulsion and Power, Vol. 4, No. 2, pp. 157-163.

* Wagner, J. H., Dring, R. P., and Joslyn, H. D , 1985, *Inlet Boundary Layer Effects in an Axial Compressor Rotor: Part 1 - Blade-to-Blade Effects*, ASME paper no. 84-GT-84, Trans. ASME Journal of Engineering for Gas Turbines and Power, Vol. 107, No. 2, pp. 374-380.

* Wisler, D. C., 1985, *Loss Reduction in Axial Flow Compressors through Low Speed Model Testing*, ASME paper no. 84-GT-184, Trans. ASME, Journal of Engineering for Gas Turbines and Power, Vol. 107, No. 2, pp. 354-363.

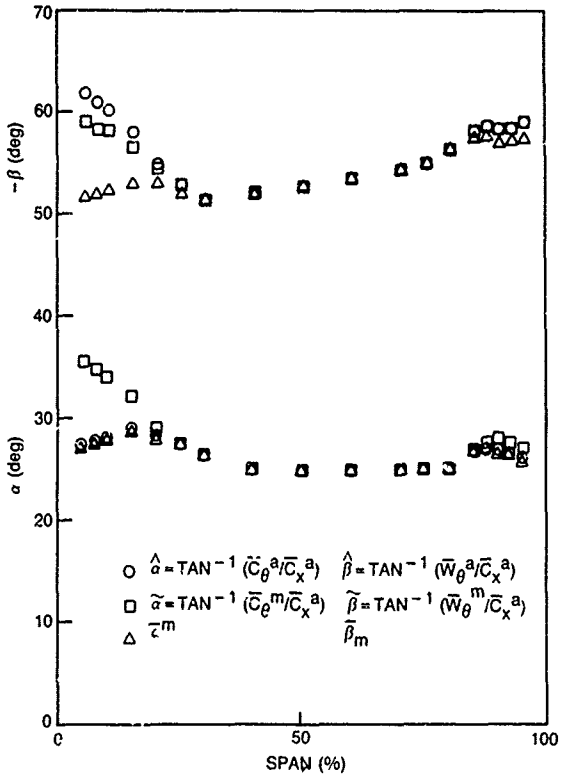


Figure 1 Second Stage Stator Exit Flow Angles Design Flow, $\phi = 0.51$

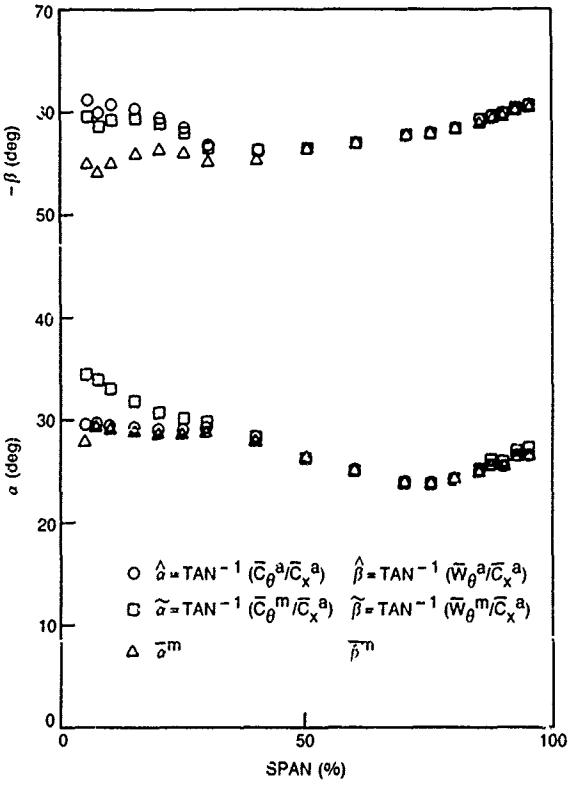


Figure 2 First Stage Stator Exit Flow Angles Near Stall, $\phi = 0.45$

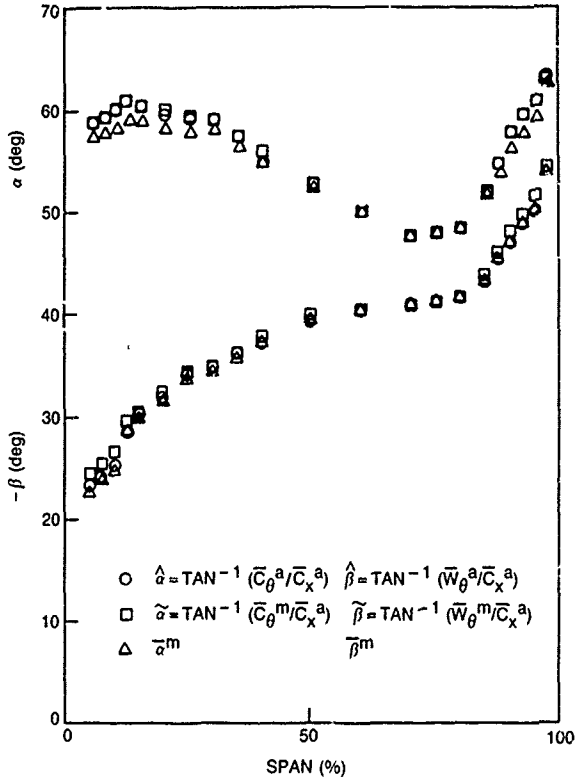


Figure 3 Second Stage Rotor Exit Flow Angles Near Stall, $\phi = 0.45$

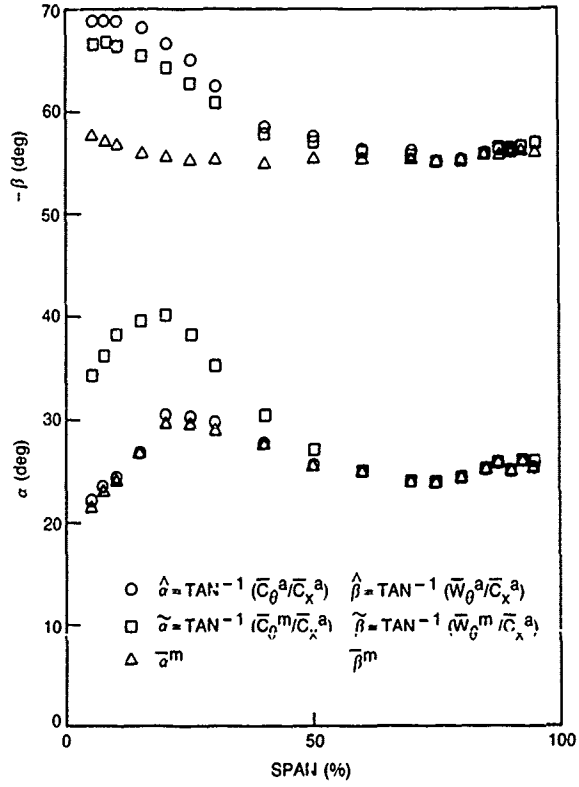


Figure 4 Second Stage Stator Exit Flow Angles Near Stall, $\phi = 0.45$

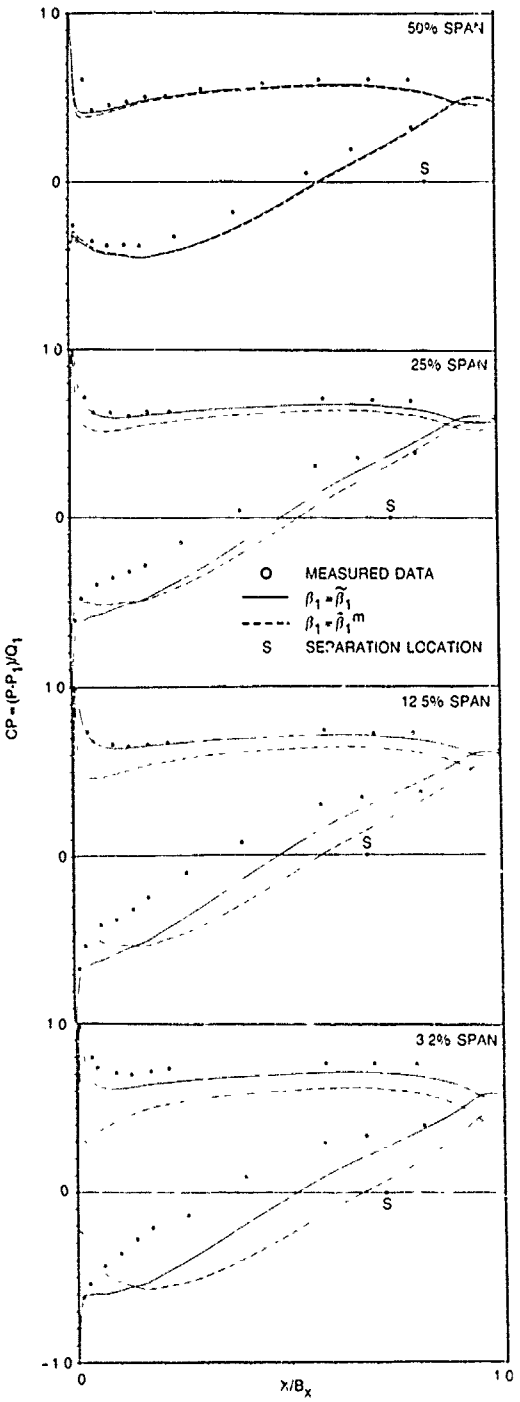


Figure 5 Second Stage Rotor Pressure Distribution, Near Stall, $\phi = 0.45$

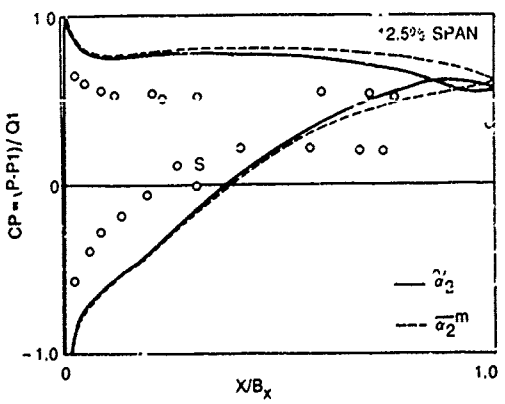


Figure 6 Second Stage Stator Pressure Distribution, Near Stall, $\phi = 0.45$

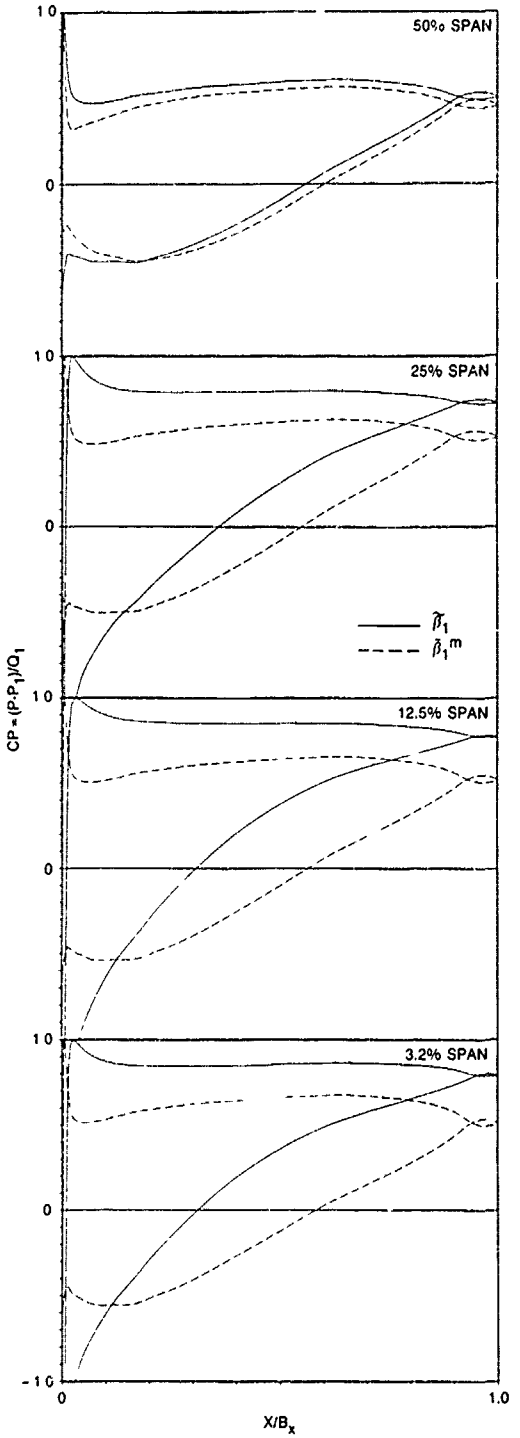


Figure 7 Hypothetical Third Stage Rotor Pressure Distributions, Near Stall, $\phi = 0.45$

DISCUSSION

Adamcyzk, USA

1. If you write a set of equations which are self consistent, then both of your angles will give you the same pressure distribution.

2. Can you write an explicitly or implicitly mathematical relationship for DCT in terms of the axisymmetric flow variables or their derivatives for any given blade row?

Author's Reply:

1. The objective here was to establish a method for calculating the inlet and exit flow angles to be used in a steady airfoil-to-airfoil potential flow analysis. The non-axisymmetry of the flow exiting the upstream row can be very strong near the hub and can result in a very unsteady inflow for the downstream row. The point of the paper was that this method of calculating incidence and deviation caused a significant improvement to the potential flow prediction. It should be of similar value in analyzing the NASA stage 67 LDV data.

2. The term "DCT" is a measure of the non-axisymmetry of the flow. Its value is in relating various types of measured and computed information in both through-flow and airfoil-to-airfoil flow analysis. Any relationship to "axisymmetric flow variables" would probably be based on a data correlation (as is current common practice for loss and deviation in compressor design).

Bullock, USA

One can argue that 4 quantities must be preserved: continuity, energy, tangential momentum, and axial momentum. This determines another angle. The mixing process yielding uniform flow is incomplete, so the question is: How is the rotor going to react? At this time, we have to appeal to experiment, analyze the results, and improve our aerodynamic comprehension of the relevant processes! I think this is an excellent presentation of a real problem and a realistic study of it.

Author's Reply:

You make an excellent point here. The flow is indeed not mixed to uniform flow. The observation here, however, is that the downstream airfoil pressure distribution is acting as if it were fully mixed.

Chen, Switzerland

Cumpsty showed in his paper at the Toronto ASME Meeting this year that the rotor with tip clearance of 3%C produces wall stall and that with 1%C produces hub stall. Could you explain this difference in the stall inception using your model?

Author's Reply:

The results presented were intended to show the impact of endwall wake nonuniformities on airfoil pressures distributions. No attempt was made to examine or explain stall inception. However, all of the cases cited in the references showed corner separation without a clearance of the hub.

A STUDY ON SECONDARY FLOW AND SPANWISE MIXING IN AXIAL FLOW COMPRESSORS

by

Murat Erkilet and Ahmet Ş.Üçer
Mechanical Engineering Department
Middle East Technical University
Makina Muh. Bölümü
06531 Ankara
Turkey

ABSTRACT

Axisymmetric throughflow equations are reformulated in order to introduce the effect of spanwise mixing in axial flow compressors. The spanwise mixing model used in this investigation assumes that turbulent diffusion is the dominant physical mechanism for the onset of spanwise mixing rather than the deterministic nature of secondary flow model. 2-D loss and deviation correlations available in the open literature are used together with the 3-D, secondary flow loss models for middle stages. End-wall boundary layer blockage is either introduced from experimental data if available or calculated using simple models. Finite element method is used for the solution of the equation of motion.

NOTATION

B	Blade force
b	Blade blockage
c_p	Specific heat at constant pressure
f	Dissipative force vector
H	Total enthalpy
I	Rothalpy
i	Unit vector
k_t	Turbulent (eddy) conductivity
L_s	Stage length
m	Streamwise direction
$\dot{m}$	Mass flow rate
Pr_t	Turbulent Prandtl number
q	Heat flux
r	Radial, radius
Re	Reynolds number
s	Entropy
Sc_t	Turbulent Schmidt number
T	Temperature
V	Absolute velocity
W	Relative velocity
z	Axial
ψ	Stream function
ε	Mixing coefficient
ϕ	Dissipation function
λ	Lean angle
τ	Shear stress tensor
θ	Tangential
ρ	Density
μ	Fluid angle
μ_t	Turbulent (eddy) viscosity

Subscripts:

e	Empirical
mix	Mixing

INTRODUCTION

Turbomachinery flow fields are highly complicated in that they contain inviscid, viscous, compressible, unsteady, three dimensional, and rotational effects. Therefore a complete theoretical solution of the flow is still a difficult problem in spite of the advances in computers and numerical techniques. Therefore axisymmetric throughflow solutions incorporating the empirical 2-D loss and deviations of cascade flow and

3-D loss and deviations of secondary flow are of interest. Recently the importance of incorporating the effects of mixing into flow-field calculations of multistage compressors has become apparent. The trend toward higher stage loadings and lower aspect ratios tend to have more of their end wall flows affecting the larger portion of the total flow. As a consequence, secondary flow, turbulence, and mixing require more careful evaluation. Important work has been carried out on the secondary flow effects in axial flow compressors over the years [1-9]. More recently two spanwise mixing models have received great deal of attention. Adkins and Smith [1] used inviscid; small perturbation, secondary flow theory as the basic of their model. This model includes the effects of mainstream non-free vortex flow, end wall boundary layers, blade end clearances, blade end shrouding, and blade boundary layer and wake centrifugation. Gallimore and Cumpsty [2] model of radial mixing, assumes random turbulent type of diffusion process as the dominant mechanism of spanwise mixing. They developed a simple, approximate method for estimating the value of the spanwise mixing coefficient in terms of stage geometry loss and flow coefficient.

In this paper Gallimore and Cumpsty spanwise mixing model is formulated for axisymmetric finite element throughflow code of Üçer et al. [10]. In order to introduce more realistic loss distributions through the blade rows, 3-D secondary flow loss distribution models of Roberts, Serovy, Sandercock [11] were used with Koch and Smith [12] 2-D loss distributions. End wall boundary layer displacement thickness calculation method of Stratford [13] is adopted for determining the growth of boundary layer on the end-walls. The mixing model was tested using benchmark test cases of single duct, stator, and rotor. The method was then used to calculate the flow through 2 stage high speed compressor and 4 stage low speed compressor to demonstrate the radial variation of flow properties due to spanwise mixing.

FORMULATION

The throughflow analysis of flow-field in compressors assumes axisymmetric inviscid steady flow. Cascade information is introduced to such models through empirically determined loss and deviations. The stream surface formulation of the flow field first proposed by Wu [14] is used as basis of the flow modelling inside an axial compressor. Bosman and Marsh [15] developed an improved consistent loss model and a formulation which can be used for any shape of hub and casing walls.

Momentum equation in Crocco form for steady flow in rotating coordinates is

$$\mathbf{W} \times (\nabla \times \mathbf{V}) = \nabla I - T \nabla s - \mathbf{f} \tag{1}$$

where $\mathbf{f}$ is the dissipative force vector and can be represented in terms of shear stress tensor as $\frac{1}{\rho} \nabla \cdot \tau$.

In the distributed loss model this force is obtained from losses and act in the opposite direction of the velocity vector. Momentum equation on the Wu [14] prescribed S2 surface becomes

$$\frac{W_\theta}{r}\left[\frac{\partial (rV_\theta)}{\partial r}\right] - W_z\left[\frac{\partial W_r}{\partial z} - \frac{\partial W_z}{\partial r}\right] = \frac{\partial I}{\partial r} - T\frac{\partial s}{\partial r} - B_r - f_r \tag{2.a}$$

$$-\frac{W_z}{r}\left[\frac{\partial (rV_\theta)}{\partial z}\right] - \frac{W_r}{r}\left[\frac{\partial (rV_\theta)}{\partial r}\right] = -B_\theta - f_\theta \tag{2.b}$$

$$W_r\left[\frac{\partial W_r}{\partial z} - \frac{\partial W_z}{\partial r}\right] + \frac{W_\theta}{r}\left[\frac{\partial (rV_\theta)}{\partial z}\right] = \frac{\partial I}{\partial z} - T\frac{\partial s}{\partial z} - B_z - f_z \tag{2.c}$$

Here, B represents the force field which makes the flow to occur on the prescribed S2 stream surface. f is the dissipative force field which lies inside the S2 stream surface. The geometrical condition of the stream surface is given by the equation

$$W_\theta = -W_r \tan\lambda - W_z \tan\mu \tag{3}$$

utilizing the orthogonality condition of B and W and surface normal vector n and W. μ is the fluid angle and λ is the lean angle of S2 surface.

For a non-rotating S2 surface in the stator blade rows, equations (2) are obtained with W replaced by V and rothalpy I replaced by total enthalpy H.

For flow in ducts with no specified flow surface equations of motion become

$$\frac{V_\theta}{r}\left[\frac{\partial (rV_\theta)}{\partial r}\right] - V_z\left[\frac{\partial V_r}{\partial z} - \frac{\partial V_z}{\partial r}\right] = \frac{\partial I}{\partial r} - T\frac{\partial s}{\partial r} - f_r \tag{4.a}$$

$$-\frac{V_z}{r}\left[\frac{\partial (rV_\theta)}{\partial z}\right] - \frac{V_r}{r}\left[\frac{\partial (rV_\theta)}{\partial r}\right] = -f_\theta \tag{4.b}$$

$$V_r\left[\frac{\partial V_r}{\partial z} - \frac{\partial V_z}{\partial r}\right] + \frac{V_\theta}{r}\left[\frac{\partial (rV_\theta)}{\partial z}\right] = \frac{\partial I}{\partial z} - T\frac{\partial s}{\partial z} - f_z \tag{4.c}$$

For bladed sections of the compressor, equations (2) can be written in 3 new directions as depicted in Fig.1. These directions as Bosman and Marsh [15] had proposed are "m" direction being in the surface and tangent to the streamline (streamwise direction), "N" perpendicular to the streamline and lies in the surface and "n" being perpendicular to the surface. Momentum equation in the N direction therefore contains neither the blade force **B** nor the dissipative force **f**.

For an adiabatic flow on a prescribed S2 surface; 5 equations to be satisfied are; continuity equation, momentum equation in N, m, n directions and energy equation. Equation of state is used to find the other thermodynamic properties . Momentum equation in "N" direction is used as the principal equation. Momentum equation in streamwise direction "m" is replaced by entropy equation, and geometrical condition is specified replacing the momentum equation in "n" direction normal to the surface. Momentum equations in "n" and "m" directions may be used to calculate blade force **B** and dissipative force **f**. Stream function is defined by satisfying the continuity equation along S2 stream surface. Since the dissipative term in the steady flow energy equation,

$$\mathbf{W} \cdot (\nabla I) = \nabla \cdot (\tau \cdot \mathbf{W}) - \nabla \cdot \mathbf{q} \qquad (5)$$

is equal to zero for distributed loss model and **q** is neglected for non-conducting fluids, I stays constant along relative streamlines through rotating blade rows. Similarly total enthalpy H is constant along streamlines through stator blades. Entropy equation which replaces "m" component of momentum equation gives the change of entropy along the streamline in terms of dissipative force and temperature. This change of entropy can be related to the increase of stagnation pressure along streamlines due to losses in blade passages.

Inside ducts, where there is no prescribed stream surface, momentum equations are more conveniently written in $(i_\theta \times \mathbf{V})$ and $\mathbf{V} \times (i_\theta \times \mathbf{V})$ directions. The principal equation is obtained from $(i_\theta \times \mathbf{V})$ direction in which no dissipative force exist because of the orthogonality condition. Instead of the streamwise component of momentum equation, entropy equation is used. $\mathbf{V} \times (i_\theta \times \mathbf{V})$ component gives the tangential momentum change as,

$$\frac{V^2}{r}\frac{\partial(rV_\theta)}{\partial m} = V_\theta\left[\frac{\partial H}{\partial m} - T\frac{\partial s}{\partial m}\right] \qquad (6)$$

which shows that for duct flows with no change of total enthalpy and entropy, tangential momentum is constant along a streamline. In addition to the momentum equations, continuity equation and energy equation must be satisfied. Energy equation reduces to H = const. along a streamline because of the distributed loss model whereas continuity equation is satisfied by introducing an appropriate stream function. The two thermodynamic properties and three velocity components are determined by the above set of five equations. Other thermodynamic variables are obtained using the equation of state.

The distributed loss model described above handles axisymmetric flow fields in bladed and unbladed sections of a compressor. The model makes it possible to solve viscous flows by specifying empirically determined total pressure decrease. Flow in bladed sections is forced on to axisymmetric stream surfaces which are prescribed using the known blade data and deviation correlations.

MIXING MODEL

The important influence of spanwise mixing is the radial distribution of flow properties. Turbulent diffusion type of process modelled by Gallimore[3] is used in this investigation. The model requires the use of the axial radial, and tangential momentum equations and the energy equation to calculate the streamwise changes of stagnation enthalpy, entropy and tangential momentum caused by the radial diffusion of heat and momentum. The model assumes that the radial mixing of momentum and heat occurs by turbulent mixing. Mixing process can be represented by an eddy viscosity μ_t and an eddy conductivity k_t which are related by turbulent Prandtl number $Pr_t = \mu c_p/k_t$. The eddy viscosity is related to mixing coefficient ε through turbulent Schmidt number $Sc_t = \mu_t/(\rho\varepsilon)$. Reynolds number $V_z L_s/\varepsilon$ is a function of blade and stage geometries, loss coefficient and flow coefficient. Prandtl and Schmidt numbers are taken as unity in this investigation.

Turbulent mixing model introduces modifications to the main flow equations. This is because the dissipative force term of equation (1) is split into two parts.

$$\frac{1}{\rho}\nabla \cdot \tau = f_e + \left(\frac{1}{\rho}\nabla \cdot \tau\right)_{mix}$$

The first part represents the distributed dissipative force and it is introduced to the solution through correlations, whereas the second part represents the forces due to viscous dissipation. Mixing model of Gallimore [3] assumes that the flow is axisymmetric, that changes in V_r and their derivatives with position are small, and that changes in the axial direction are negligible. These approximations lead to simplifications in the terms of the stress tensor in cylindrical coordinates. The projection of mixing viscous force term on to the prescribed stream surface modifies the blade force term B and includes the surface normal component of turbulent viscous stress. The principal equation in "N" direction with shear stresses due to radial mixing takes the form,

$$\frac{\partial}{\partial z}\left[\frac{1}{\rho r b}\frac{\partial \psi}{\partial z}\right]+\frac{\partial}{\partial r}\left[\frac{1}{\rho r b}\frac{\partial \psi}{\partial r}\right]=\frac{1}{r}\left[\tan\mu\frac{\partial(rV_\theta)}{\partial r}-\tan\lambda\frac{\partial(rV_\theta)}{\partial z}\right]+\frac{W_\theta T}{W^2}\left[\tan\mu\frac{\partial s}{\partial r}-\tan\lambda\frac{\partial s}{\partial z}\right]+\frac{T}{W^2}\left[W_r\frac{\partial s}{\partial z}-W_z\frac{\partial s}{\partial r}\right]$$

$$-\frac{W_\theta}{W^2}\left[\tan\mu\frac{\partial I}{\partial r}-\tan\lambda\frac{\partial I}{\partial z}\right]-\frac{1}{W^2}\left[W_r\frac{\partial I}{\partial z}-W_z\frac{\partial I}{\partial r}\right]-\frac{1}{\rho W^2}\left\{\left[W_\theta\tan\lambda-W_r\right]\left[\frac{1}{r}\frac{\partial}{\partial r}\left(\mu_t r\frac{\partial V_z}{\partial r}\right)\right]\right.$$

$$\left.+\left[W_r\tan\mu-W_z\tan\lambda\right]\left[\frac{\partial}{\partial r}\left(\mu_t\frac{\partial}{\partial r}\left(\frac{V_\theta}{r}\right)\right)+2\mu_t\frac{\partial}{\partial r}\left(\frac{V_\theta}{r}\right)\right]\right\} \tag{7}$$

in which it is assumed that the lean angle is constant in the radial direction. The above equation is written on prescribed steam surfaces within rotating passages . For stator blade rows the principal equation is obtained by replacing rothalpy by total enthalpy and relative velocity by absolute velocity. The stream function is defined in the form

$$\frac{\partial \psi}{\partial r}=\frac{2\pi}{\dot{m}}\rho r b V_z \qquad \frac{\partial \psi}{\partial z}=-\frac{2\pi}{\dot{m}}\rho r b V_r \tag{8}$$

where b is the tangential blockage due to blades. In ducts tangential blockage does not exist and no tangential momentum is imposed by prescribing stream surfaces. Therefore b is unity and the principal equation is obtained by projecting the mixing shear stress term onto ($i_\theta \times V$) direction which gives

$$\frac{\partial}{\partial z}\left[\frac{1}{\rho r}\frac{\partial \psi}{\partial z}\right]+\frac{\partial}{\partial r}\left[\frac{1}{\rho r}\frac{\partial \psi}{\partial r}\right]=\frac{1}{V_m^2}\left\{\frac{V_\theta}{r}\left[V_r\frac{\partial(rV_\theta)}{\partial z}-V_z\frac{\partial(rV_\theta)}{\partial r}\right]-T\left[V_z\frac{\partial s}{\partial r}+V_r\frac{\partial s}{\partial z}\right]-\left[V_z\frac{\partial H}{\partial r}-V_r\frac{\partial H}{\partial z}\right]\right\}$$

$$+\frac{V_r}{\rho r}\frac{\partial}{\partial r}\left[\mu_t r\frac{\partial V_z}{\partial r}\right] \tag{9}$$

Momentum equation in $V \times (i_\theta \times V)$ direction gives the tangential momentum change in the streamwise direction in the form,

$$\frac{d(rV_\theta)}{dm}=\frac{r}{\rho V_m}rV_\theta\left[\frac{\partial}{\partial r}\left[\mu_t r\frac{\partial}{\partial r}\left(\frac{V_\theta}{r}\right)\right]+2\mu_t\frac{\partial}{\partial r}\left(\frac{V_\theta}{r}\right)\right] \tag{10}$$

relating tangential momentum change to dissipative force due to turbulent diffusion.

In the bladed sections although angular momentum change is prescribed by specifying the stream surface shape, a radial transfer of momentum is expected due to the presence of shear stresses. The relative proportion of rV_θ change in the streamwise direction due to turbulent diffusion must depend on the aspect ratio and solidity of the blade row.

Entropy equation in the streamwise direction becomes

$$\frac{ds}{dm}=\frac{1}{\rho T V}\left[\,\phi+\nabla.q\,\right]+\left[\frac{ds}{dm}\right]_e \tag{11}$$

where the dissipation function is given as

$$\phi=2\mu_t\left\{\left[r\frac{\partial}{\partial r}\left(\frac{V_\theta}{r}\right)\right]^2+\left[\frac{\partial V_z}{\partial z}\right]^2\right\} \tag{12}$$

and heat transfer due to turbulent diffusion by

$$\nabla.q=-\frac{1}{r}\frac{\partial}{\partial r}\left[r k_t\frac{\partial T}{\partial r}\right] \tag{13}$$

The last term in equation (11) represents the change of entropy along streamlines due to the losses in the cascade flow. Total enthalpy of the flow is now affected by the shear stresses and conduction. Therefore a change in H along absolute streamlines is calculated from energy equation.

$$\frac{dH}{dm}=\frac{1}{\rho V}\left\{\phi+V_\theta\frac{\partial}{\partial r}\left[\mu_t r\frac{\partial}{\partial r}\left(\frac{V_\theta}{r}\right)\right]+2V_\theta\mu_t\frac{\partial}{\partial r}\left(\frac{V_\theta}{r}\right)+\frac{V_z}{r}\frac{\partial}{\partial r}\left[\mu_t r\frac{\partial V_z}{\partial r}\right]-\nabla.q\right\} \tag{14}$$

Along relative streamlines rothalpy change is calculated using the energy equation in steadily rotating relative coordinate system.

At the hub and tip walls of the compressor the shear stresses and heat flux are set to zero, in accordance with the adiabatic walls and inviscid distributed loss model of the main flow.

CALCULATION PROCEDURE

Equations (7) and (9) are the principal equations that are used to obtain the stream function distribution in the solution domain and they are discretized using finite element method. Since hub and tip walls of the compressor are streamlines, stream function values are specified on them. At the entry to the solution domain stream function values, total temperature and pressure are specified at the nodes. For the exit of the compressor $\partial\psi/\partial z = 0$. From the stream function distribution, velocities in the radial and axial directions can be calculated from equations (8). From equation (3) the tangential component of the velocity vector is determined. Equations (10), (11), (12) allow the change of entropy, tangential momentum, and stagnation enthalpy along streamlines to be calculated. Since stream function values are known at the nodes of the 8 noded finite elements, a radial layer by layer procedure is adopted. An inverse space marching technique is utilized. The properties of the nodal points at the layer of calculation I is determined using the constancy of stream function along streamlines and the equation below.

$$q_I = q_{I-1} + \left.\frac{\partial q}{\partial m}\right|_{I-1} .dm$$

Property evaluations on streamlines are made using linear interpolation between the stream function and property values of the nodes at the I-1 layer (see Fig.2).

The radial derivatives of velocities and temperature which are required to evaluate shear stresses, dissipation function and the heat transfer terms are calculated using natural cubic spline technique. In the calculation of entropy along a streamline in bladed sections, the increase of entropy due to empirical loss coefficients is included and the total entropy change is evaluated. The variation of tangential momentum in bladed sections is likewise calculated from the summation of two effects. This change is the result of specified blade geometry with empirically determined deviation and an additional force caused by the tangential shear stresses. As a result of shear stresses, the calculated fluid angle at the exit of blade rows will differ from the specified angles. The change of total enthalpy through stator blade rows or rothalpy through rotor blade rows are computed using equation (14) in a straightforward way in the present method, because no blade force appears in the energy equation. It is then possible to set up the enthalpy-entropy diagram along the streamline section of Figure 2 between two layers, and density at the calculation node is evaluated. At this stage of the calculation all variables necessary to set up the right hand side of the principal equations (7) and (9) are evaluated. Fluid density which appears on the left hand side is also known therefore principal equations are recomputed and new stream function values are found. Maximum relative change in stream function values between two consecutive overall iterations are checked for convergence. Maximum relative change is kept under 0.001 and an underrelaxation factor around 0.2 was used in the calculations.

EMPIRICAL CONSIDERATIONS

The present model uses several empirical correlations and data which serve to calculate 2-D cascade losses at design and off design, secondary flow losses, and end-wall boundary layer displacement thickness distributions.

The cascade losses when not specified are calculated using Koch and Smith [12] correlation. Carter's rule is used for design deviation. For off-design deviation and loss Creveling [16] and Çetin et al. [17] are used respectively. The radial distribution of secondary losses are calculated using reference [11]. These losses are added to the Koch and Smith 2-D loss distribution. The calculation of 3-D losses require end wall boundary layer thickness distribution along the compressor. End-wall boundary layer calculation method suggested by Stratford [13] is used for predicting the development of end-wall boundary layer. In the case when displacement thickness prediction method is used the hub and casing boundary conditions (stream function values) are changed, introducing a fictive mass flux compensating for the loss due to shear layers.

RESULTS AND DISCUSSION

Some of the early results obtained from the new version of the computer code will be given here. The modified program is verified for mixing analysis using straight annular duct, isolated stator and isolated stator of Gallimore [18].

Figure 3 shows the capability of the code in conserving the angular momentum. A nearly free vortex tangential velocity distribution was traced along a constant area annular duct as it changes into a forced vortex profile. In this calculation Reynolds number, based on axial velocity annulus height and mixing coefficient was 290. The mixing coefficient ε was set to 0.0035 m^2/s. Prandtl and Schmidt numbers were set to 1.0 . An analysis of the mixing model showed that shear stresses can not be generated in the case when exact free vortex distribution of rV_θ = const. is imposed. Therefore calculation was started from a nearly free vortex distribution. Solid body rotation of forced vortex flow is also free of shear stresses for inviscid boundaries. Therefore, as expected, the forced vortex tangential velocity distribution did not show any change along the annular duct after it is established. Figure 3 shows V_θ variation in the radial direction at 0, 20, 40, 100 span downstream locations along the annular duct. The forced vortex profile is accurately predicted with no inaccuracies at the end walls and no change of tangential momentum during the development from free to forced vortex. This indicates that the model is implemented satisfactorily to the finite element program.

In order to assess the ability of the code to predict the flow through bladed sections, isolated stator and rotor test cases of Gallimore [18] were used. Reynolds number based on axial velocity, span and mixing coefficient was taken as 290 for both test cases Prandtl number was set to unity. The mixing coefficient was 0.0035 m^2 /s. Spanwise loss and deviation distributions suggested by Gallimore were used. Exit flow angle was set to zero at mid-height and 30° at each end-wall with a non-linear variation in between. The spanwise variation of specified loss coefficient was varied from zero at mid-span to 0.5 of both ends. A second order distribution between mid-span and end-walls was used.

Figure 4 shows axial velocity distribution at the exit of the blade row (0 span), 4 span and 8 span downstream of the blade row. The axial velocity distribution flattens out as the flow proceeds down-stream due to the viscous stresses set-up in the flow. Figure 5 shows a similar trend in the yaw angle. The specified 30° end wall yaw angle can not be reached at the exit of the blade row because of mixing in the bladed section, as expected. For a uniform inlet distribution of total enthalpy and Prandtl number of unity, there should be no change of total enthalpy along the streamline passing through the stator blade row even if mixing is present [19]. This is because; the contributions of the shear stresses, heat transfer and dissipation function should cancel each other and not contribute in any way to total enthalpy. It was found that the program algorithm accurately establishes this requirement with negligible changes in the total enthalpy across the downstream stations of the stator blade row.

The isolated rotor test is performed using the geometry of stator. Blades are now rotated at 3000 rpm. In this test case the specified exit relative flow angles varied from 10° at mid-span to 40° at both hub and tip. The loss distribution was the same of the stator. Calculated spanwise variation of axial velocity is shown in Fig. 6. Results are given at the exit of the blade row and two downstream stations. The mixing again tends to flatten the axial velocity profile as they pass downstream. Figure 7 shows the total enthalpy variation at the trailing edge and two downstream locations. The increase of total enthalpy at the tip and hub with mixing is predicted. The redistribution of flow properties tend to reduce the total enthalpy at the mid-span region. For a rotating blade row there should be no change of rothalpy along a streamline for uniform inlet rothalpy and $Pr_t = 1$. The change of rothalpy across the blade row was found to be less than 0.5 % therefore it is concluded that the program algorithm is accurate in predicting flow properties in the rotor section.

Two compressor test cases are used until this time. The first test case was the Cambridge 4 Stage low speed compressor. A substantial amount of data on this compressor can be extracted from references [18-20]. This compressor has untwisted C5 airfoils with hub to tip ratio of 0.8. It was used in mixing analysis by Gallimore [18]. The complete machine with IGV and four stages were analyzed on the computer. Because of the lack of relative flow angle distribution data at the exit of the blade rows, only partial success was achieved in predicting the axial velocity profiles at the exit of rotor blades. Test runs were performed at a flow coefficient of approximately 0.55 which gives a mean axial velocity of approximately 27.0 m/s. The calculated velocity profiles had the same trend as the measured ones with peak axial velocity near to the mid-span position rather than to the tip region. In these calculations spanwise loss distribution data of Gallimore was used with identical loss coefficient distributions for all four rotors; the stator loss distributions were assumed to be the same for each blade row and equal to the radially inverted rotor distributions. In the analysis runs with mixing, Reynolds number based on axial velocity axial stage length and mixing coefficient was set to 340. All axial velocity profiles showed an increase of 3 - 4 % of axial velocity at the hub and a decrease of same amount at tip of blade rows. Figure 8 shows the total pressure distribution at the exit of the compressor. The influence of mixing on the total pressure distribution shows that the losses are convected to the mid span in the case of mixing, producing less total pressure rise at the upper half of the span. Convergence difficulties were experienced in the end wall boundary layer calculations. Empirical assessment of secondary flow loss using the model of reference[11] showed negligible differences in flow properties. 3-D losses were only introduced to the middle stages.

So far the second test case used with the new code, is the NASA 2 stage low aspect ratio transonic fan. This machine is well documented in [21-22]. Mixing coefficient for this machine is estimated using the method of Gallimore and Cumpsty [2] as $\varepsilon = 0.0018$ m^2/s. Second stage exit total pressure distribution predicted by using cascade loss and deviation correlations for design and off design is shown by curve A of figure 9. Correlation set recommended in Çetin et al. [17] is used in this calculation. When end-wall boundary layer calculation of Stratford [13] and secondary losses of [11] are introduced with mixing calculations simultaneously, marked difference in the distribution is experienced. This is because of the combined effect of two-dimensional cascade losses, three-dimensional secondary losses, end wall boundary layer blockage and mixing. A comparison with the measured values of total pressure shows that the complete model improves the prediction only at the tip of the blade row, with less success at the hub region. This is because of the errors in the calculated loss distribution at the hub and consequently its unrealistic spanwise redistribution due to mixing. During the computations for obtaining curve B of figure 9, empirical loss and deviation for design and off-design, three-dimensional loss and end wall boundary layer calculations were included inside the global iteration of stream function. All comparison are made, near peak efficiency test case of NASA 2-Stage fan at 100 % design speed.

Figure 10 shows the measured total pressure distribution at the exit of second stage stator together with the calculated spanwise distributions. The figure clearly shows that when calculated loss and deviations from measured total pressure, total temperature and yaw angle are used, satisfactory total pressure spanwise variation can be computed only when spanwise mixing is included. Computation without mixing using calculated loss and deviation of the experimental data gave larger variation of total pressure from hub to tip with abrupt fluctuations due to supersonic relative flow at the tip region. Mixing, by redistributing the flow properties smooths out the fluctuations at the tip region and predicts the experimental pressure distribution satisfactorily with a slight error near to the tip of blade.

In a number of numerical experiments, 3-D loss model was used simultaneously with 2-D losses and end wall boundary layer calculations. In these test runs calculations without mixing showed about 5 m/s reduction of axial velocity at both hub and tip with very small changes at the mid-span region. Calculation

with mixing on the other hand, gave an increase of axial velocity at the tip region and a reduction at the hub and mid-span regions. This is attributed to the redistribution of losses along the compressor. The calculated axial velocity profiles at rotor and stator exit stations has the same shape as depicted in figure 11 which are far from predicting the details of the flow. When calculated loss and deviations from measured values are specified with mixing, better axial velocity predictions are obtained as shown in figure 11. Axial velocity predictions are better at mid-span and tip regions with less success at the hub. A comparison of predicted and specified loss distributions showed trend differences at the hub of the second stage rotor. However loss distributions had the same trend at the tip. Figure 12 shows the second stage stator exit axial velocity distribution obtained using specified loss and deviation values throughout the blade rows. As it can be observed a successful prediction of spanwise axial velocity distribution was obtained when mixing is included in the analysis. The same result was also obtained for total pressure distribution, as mentioned above.

The computational performance of the new code was found to be very promising. In the analysis of Cambridge four stage compressor, 288 elements with 889 nodes was used. CPU time on a UNISYS A9F computer was 960 second. For NASA two stage compressor with 133 elements and 452 nodes, computations without mixing took 679 seconds. An increase of 30 % in computing time was experienced in the case when mixing analysis was included. No instabilities were observed in the mixing solution.

CONCLUDING REMARKS

The mixing model of Gallimore and Cumpsty was successfully applied to a finite element throughflow axisymmetric code. The program is accurate and fast in calculating the flow properties in annular duct, isolated stator and isolated rotor test cases.

For multi-stage axial compressor analysis, when empirical 2-D and 3-D losses and deviations and end wall blockage calculations are performed simultaneously with mixing analysis, satisfactory radial variations of properties can not be obtained. Spanwise loss and deviation distributions should be specified for all blade rows and their redistribution must be allowed along the compressor due to mixing.

In specifying the spanwise distribution of loss and deviation; profile, secondary flow and end wall effects should be considered. A properly proportioned and quantified loss and deviation profile in the spanwise direction should be capable of predicting the property changes with success if mixing is introduced. It must be noted that the mixing model calculates shear stresses and heat transfer using the variation of axial, tangential velocities and temperature in the radial direction. These properties are strongly affected by the entropy production and work input along the streamlines through the blade row. Therefore loss and deviation distributions including the effects of profile, shock and secondary flows must be as accurate as possible for obtaining accurate radial property variations.

REFERENCES

1. Adkins, G.G., and Smith, L.H.Jr., "Spanwise Mixing in Axial-Flow Turbomachines" ASME Jour. of Eng. Power., Vol. 104, 1982, p. 97.
2. Gallimore, S.J. and Cumpsty, N.A., "Spanwise Mixing in Multistage Axial Flow Compressors: Part I-Experimental Investigation" ASME Jour. of Turbomachinery, Vol. 108, 1986, p. 2.
3. Gallimore, S.J. "Spanwise Mixing in Multistage Axial Flow Compressors: Part II-Throughflow Calculations Including Mixing", ASME, Jour. of Turbo. 1986, p. 10.
4. Wisler, D.C., Bauer, R.C., and Okiishi, T.H., "Secondary Flow, Turbulent Diffusion, and Mixing in Axial-Flow Compressors" ASME, Jour. of Turbomachinery, Vol. 109, 1987, p. 455.
5. Smith, L.H., Jr. "Secondary Flow in Axial-Flow Turbomachinery" Trans. of the ASME, Vol. 77, No. 7, 1955, pp. 1055.
6. Lakshminarayana, B., and Horlock, J.H., "Review: Secondary Flow and losses in Cascades and Axial-Flow Turbomachines" Int. J. Mech. Sci., 1963, p. 287.
7. "Secondary Flows in Turbomachines" ,AGARD-CP-217, 1977.
8. Hawthorne, W.R. "The Growth of Secondary Circulation in Frictionless Flow" Proc. Camb. Phil. Soc., Vol. 51, No. 4, 1955, p. 737.
9. Hirsch, C. and Kool, P., "Measurement of the three-dimensional flow field behind an Axial Flow Compressor Stage" Trans. ASME, J. Eng. Power, 1977, p. 168.
10. Üçer, A.Ş., Yeğen, İ., and Durmaz, T., "A Quasi-Three-Dimensional Finite Element Solution for Steady Compressible Flow Trough Turbomachines", Trans., of the ASME, J. of Eng. for Power, 1983, p. 536.
11. Roberts, W.B., Serovy, G.K., and Sandercock D.M., "Design Point Variation of 3-D loss and Deviation for Axial Compressor Middle Stages" ASME paper 88-GT-57.
12. Koch, C.C., Smith, L.H., "Loss Sources and Magnitudes in Axial-Flow Compressors", Trans. of the ASME, J. of Eng. for Power, 1976, p. 411.
13. Stratford, B.S. "The use of Boundary Layer Technique to Calculate the Blockage from the Annulus Boundary Layers in Compressors", ASME paper 67-WA/GT-7.
14. Wu, C.H., "A General Theory of Three-Dimensional Flow in Subsonic and Supersonic Turbomachines of Axial-Radial and Mixed Flow Type", NACA TN 2604, 1952.
15. Bosman, C., and Marsh, H., "An Improved Method For Calculating the Flow in Turbo-Machines, Including a Consistent Loss Model", J. Mech. Eng. Sci., Vol. 16, 1974, p. 25.
16. Creveling, H.F., "Axial-Flow Compressor Computer Program for Calculating off-Design Performance", NASA CR 72472, 1968.

17 Çetin, M. Üçer, A.Ş., Hirsch, Ch., Serovy, G.K., "Application of Modified Loss and Deviation correlations to Transonic Axial Compressors" AGARD-R-745, 1987.
18. Gallimore S.J., "Spanwise Mixing in Multistage Axial Compressors" Ph. D. Dissertation, Univ. of Cambridge, 1985.
19. Denton, J.D. and Cumpsty, N.A., "Loss Mechanisms in Turbomachines", Inst. of Mech. Eng., C260/87, 1987.
20. Cumpsty, N.A., "Annulus Wall Boundary Layer Measurements in a Four Stage Compressor" ASME paper No. 85-GT-62.
21. Urasek, D.C., Gorrell, W.T., and Cunnan, W.S., "Performance of Two-Stage Fan Hawing Low-Aspect-Ratio, First Stage Rotor Blading", NASA TR-78-49, 1979.
22. Calvin, L.B., Lonnie, R., and Schmidt, J.F., "End Wall Boundary Layer Measurements in a Two Stage Fan", AGARD-CP-351,1983.

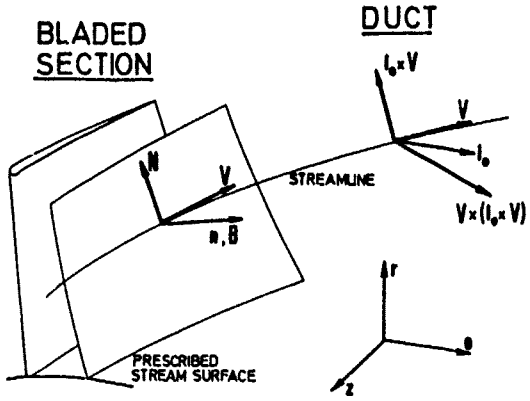


Fig.1 Flow through an Axial Turbomachine

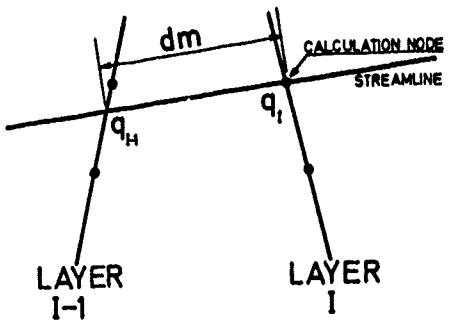


Fig.2 Streamline between two layers

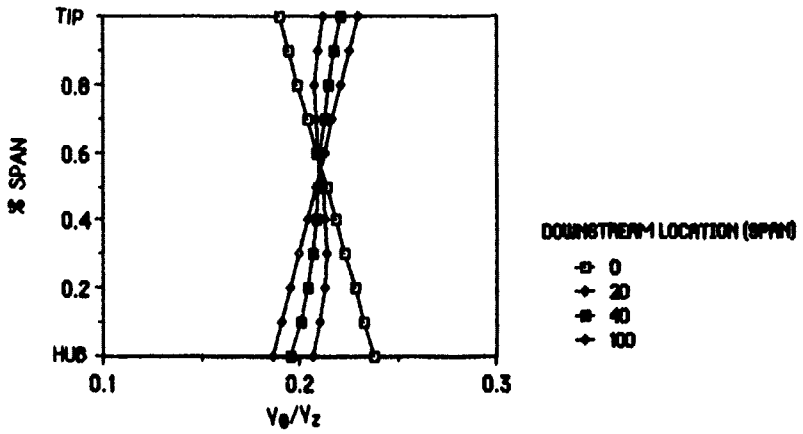


Fig.3 Swirling Flow in a Constant Area Annular Duct

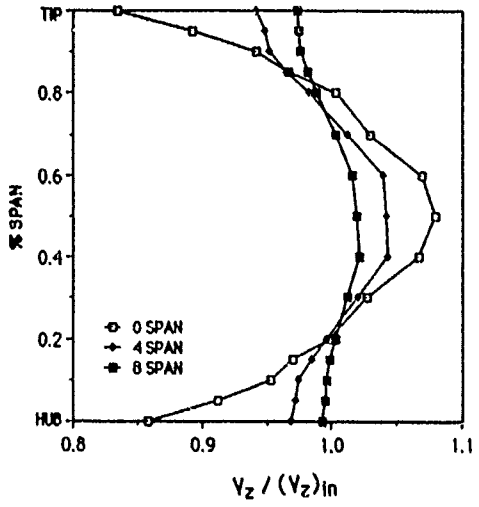


Fig.4 Axial Velocity Distributions Downstream of Stator

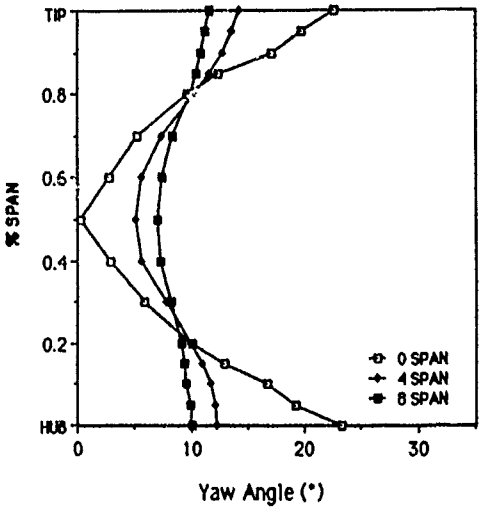


Fig.5 Yaw Angle Distribution Downstream of Stator

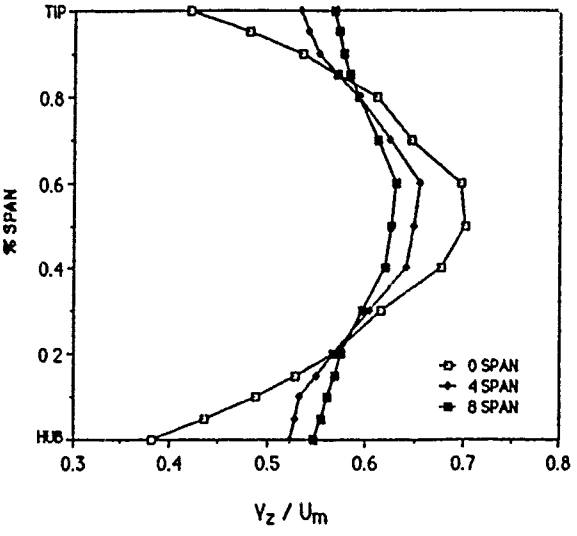


Fig.6 Axial Velocity Distribution Downstream of Rotor

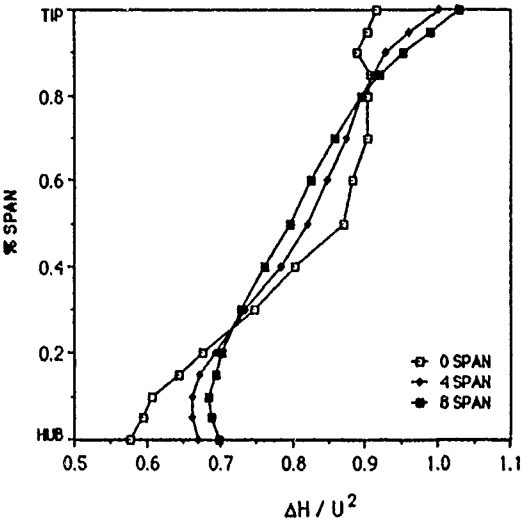


Fig.7 Total Enthalpy Distribution Downstream of Rotor

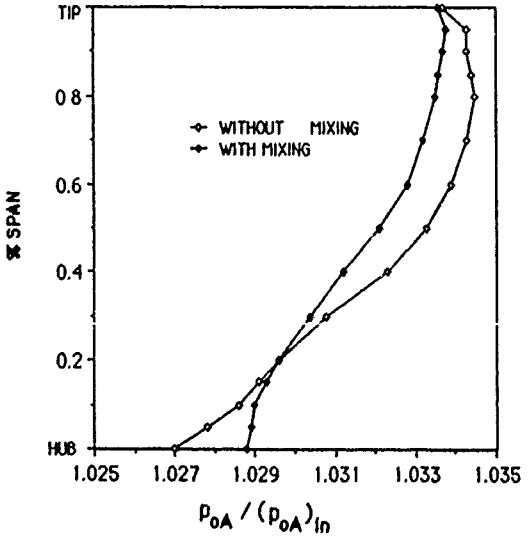


Fig.8 Total Pressure Distribution at the Exit of 4-Stage Cambridge Compressor

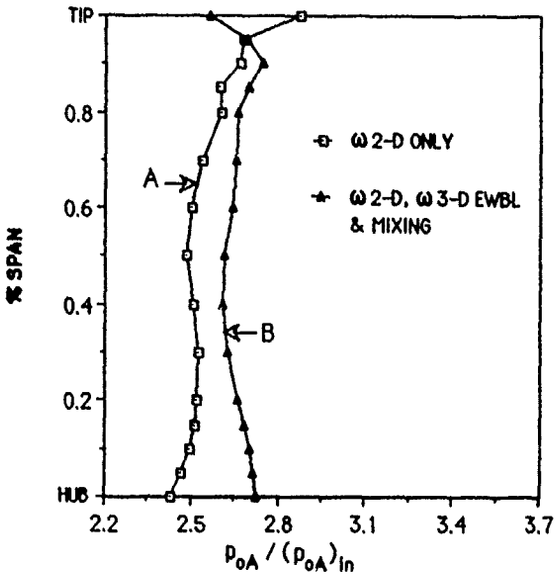


Fig.9 NASA 2-Stage, Second Stage Stator Exit

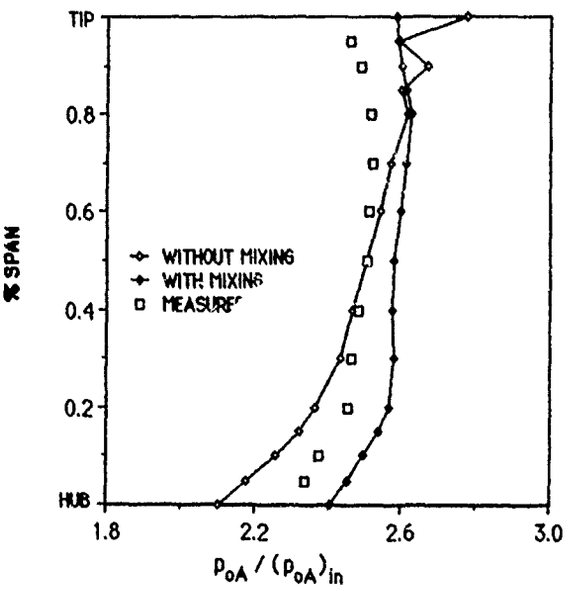


Fig.10 NASA 2-Stage, Second Stage Stator Exit

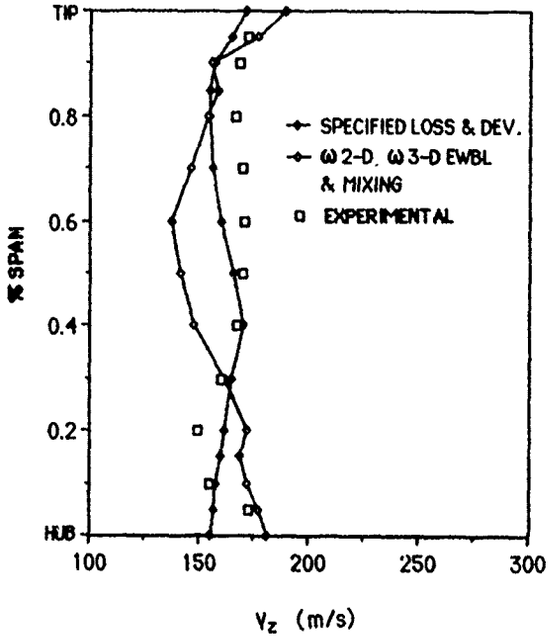


Fig.11 NASA 2-Stage, Second Stage Rotor Exit

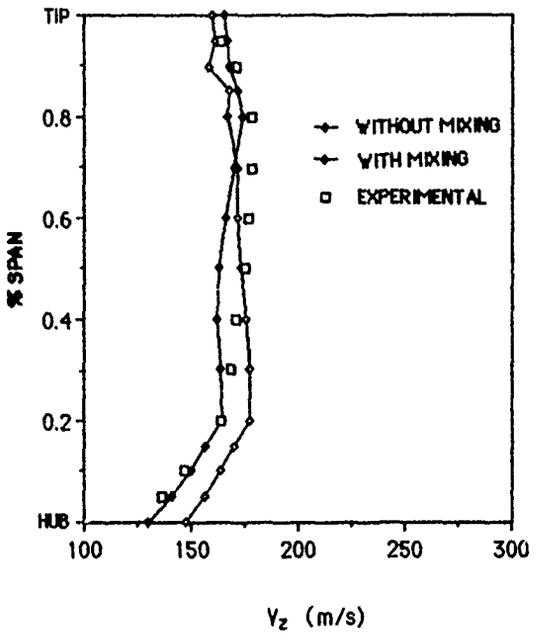


Fig.12 NASA 2-Stage, Second Stage Stator Exit, Mixing Calculations

PARABOLIZED CALCULATIONS OF TURBULENT THREE DIMENSIONAL FLOWS IN A TURBINE DUCT

P. FERRAND *, F. LEBOEUF *, F POMMEL *, E. PARKINSON *
* LMFA URA CNRS 263 ECL BP 163 69131 Ecully - FRANCE

1. INTRODUCTION

For a number of practical flows with a dominating convective direction, it is often possible to neglect the diffusive phenomenona in this direction. This hypothesis is particularly true in turbomachine ducts where the Reynolds numbers are usually very high.

In this case, the diffusive terms in the main convective direction (written ξ in the following) are eliminated. Concerning the velocity, the problem described by the Navier-Stokes equations becomes parabolic. However, in all the subsonic zones, the pressure tends to transfer the downstream information in the upstream direction, which is typical of an elliptical behaviour. As a consequence, eliminating those diffusive terms in the Navier Stokes equations is not sufficient to obtain a pure problem. The momentum equations have a parabolic nature and can be treated by a space marching resolution. On the opposite, the elliptic nature of the pressure equation has to be taken into account. In a subsonic flow, with highly curved ducts, it is then necessary to define an hybrid parabolic-elliptical method called "Quasi Elliptical" in the following [5].

The idea, based on parabolized methods recognizing the elliptical pressure effect, has already been used successfully by KULISA-BELLOIR [2,3] for local reverse flows. In this case, a boundary-layer model is used in strong interaction with a pressure calculation based on a small potential pertubations method generated by the viscous wall flow. The integral equation obtained with Green's theorem restores properly the elliptical effect on the wall. Moreover, DELERY and MARVIN [4] have shown the importance of this strong coupling, at the wall, if the elliptical pressure effect is to be restored in a supersonic boundary-layer.

This paper intends to present a new method calculating three dimensional flows in turbomachine ducts with a quasi-ellipticity hypothesis for the velocity field.

The main ideas of the method are presented ; then its specific aspects shall be detailed. At last, its capacity is viewed on a representative test case typical of a turbine duct.

2. BASIS OF THE METHOD

The momentum and continuity equations are first decoupled. As the diffusive terms are eliminated in the ξ direction, an upstream/downstream space-marching procedure, labelled "sweep", is hence used for the momentum equations. For each transversal plan (η, γ), a three dimensional pressure calculation insures the correct restitution of the pressure influence on the wall viscous layers.

For the current calculation station, written i-1/2 (refer to figure 1), the momentum equations are written between the stations i-1 and i and the stations i-2, i-1 and i. The first equations predict the velocity corrections $\delta \mathbf{v}$ in station i. All the different variables of station i-1 are fixed during this procedure (parabolic effect). The last equation calculates the static pressure corrections δp_c in the station i-1, with all the variables being fixed in the station i (elliptical effect). As the pressure is only estimated in the station i, an iterative upstream/downstream sweeping procedure is necessary.

However, to reinforce the far upstream/downstream boundary conditions transmission, a linearized one dimensional calculation allows a readjustement of the mass flow (correction $\delta \overline{V}$) and the static pressure (correction $\delta \overline{P_s}$) during the sweeps.

In opposition to most existing parabolized methods, this quasi-elliptical method enables the imposition of conditions on the stagnation upstream values, the transversal V_γ an V_η velocities and on the downstream static pressure. The mass flow thus becomes an unknown of the problem.

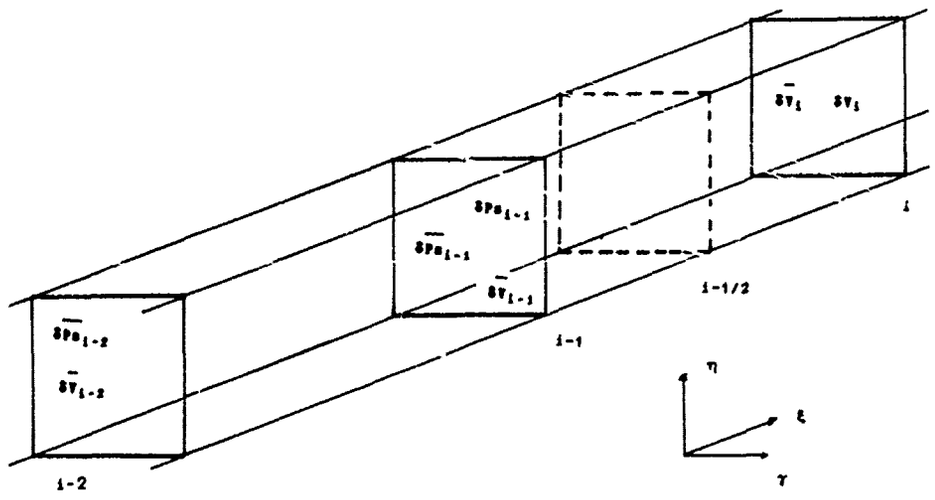


Figure - 1 Definition of the current calculation stations.

3. VELOCITY FIELD TREATMENT

The momentum equation is written in a weak conservative form in a transformed (ξ, η, γ) frame where ξ is the longitudinal direction of the flow and (η, γ) the transversal directions.

$$\frac{\partial q}{\partial t} + \frac{\partial E}{\partial \xi} + \frac{\partial F}{\partial \eta} + \frac{\partial G}{\partial \gamma} + H = \frac{1}{Re}\left\{\frac{\partial F_v}{\partial \eta} + \frac{\partial G_v}{\partial \gamma} + H_v\right\} \quad (1)$$

where $q = \left(\frac{\rho U}{J}, \frac{\rho V}{J}, \frac{\rho H}{J}\right)$ and J is the metric Jacobian of the transformation. E, F and G are the convective vectors, G_v and F_v are the diffusive vectors. The derivatives $\frac{\partial}{\partial \xi}$ have been eliminated from the diffusive terms according to the parabolization hypothesis. H and H_v are the vectors associated with the curvature of the initial frame and D contains the rotation terms. An algebraic turbulence model is introduced on the basis of BALDWIN and LOMAX' works [6].

A time implicit numerical scheme is used to solve system (1). The derivatives along ξ are discretized with second order relations centered in the station i-1/2.

Marching from upstream to downstream, system (1) must be verified between the stations ξ_{i-1} and ξ_i before treating the next domain (ξ_i, ξ_{i+1}). Consequently, the velocity correction in the upstream station ξ_{i-1} is considered as equal to zero ($\Delta q_{i-1} = 0$). At time iteration n, the discretized scheme along ξ is written :

$$\left\{I + h.A_i^n + h.\frac{\partial}{\partial \eta} B^n_{i-1/2} + h.\frac{\partial}{\partial \gamma} C^n_{i-1/2} + \varepsilon_{im}\frac{h}{J}\left\{\frac{\partial^2}{\partial \eta^2} + \frac{\partial^2}{\partial \gamma^2}\right\}\right\} \Delta q_i^n =$$

$$Res_i^n - \varepsilon_{ex}\frac{h}{4J}\left\{\frac{\partial^4}{\partial \eta^4} + \frac{\partial^4}{\partial \gamma^4}\right\} q_i^n \quad (2) \qquad (2)$$

where A, B and C are the Jacobian resulting from the linearization of the diffusive and convective vectors of (1). The discretizations along γ and η are second order centered. A numerical dissipation is added to stabilize the scheme. ε_{im} and ε_{ex} are the viscosity coefficients.

Two resolution schemes for the implicit part of (2) have been tested. The first one is a factorized BEAM & WARMING [7] scheme which uses three diagonal matrical systems of 3X3 blocs. Each matrix was treated with an LU decomposition proposed by PULLIAM and STEGER [8].

A Gauss-Seidel type resolution has also been written to treat the 3X3 blocs five-diagonals resulting from the direct discretization of system (2). A convergence accelerating tech ique, MMPE, based on SIDI's works [10], is then applied to the vector sequence issued from GAUSS-SEIDEL's method. This technique is detailed by BENBOUTA [9]. The obtained time computing gain with the MMPE method compared to the factorized method is approximately 4.2 in scalar mode and 8.9 in non-concurrent vectorized mode with an ALLIANT FX-80.

4. STATIC PRESSURE FIELD TREATMENT

The static pressure calculation method is exhaustively detailed in reference [5]. This method differs deeply from the classical methods used for parabolized equations. The main aspects of the incompressible formulation are presented in the following, the extension to the compressible case differs only by the expression of Θ in equation (3). The static pressure equation can be obtained by taking the divergence of the momentum equations.

$$\nabla^2 p = f(\Theta) + g(\vec{\Omega}) \qquad (3)$$

where $\Theta = \nabla.(\rho \vec{V})$ and $g(\vec{\Omega})$ mainly depend on the rotational $\vec{\Omega}$ of $\vec{V}$. $f(\Theta)$ is written :

$$f(\Theta) = -\left(\frac{\partial \Theta}{\partial t} + \nabla.(\Theta \vec{V})\right) + (\lambda + 2\mu).\Delta\left(\frac{\Theta}{\rho}\right) \qquad (4)$$

Assuming that, at time iteration n, the static pressure Ps^n verifies effectively (3), the solution of the momentum equations at time iteration n+1 generates a velocity divergence which is not compatible with (3) any more. Ps^{n+1} is then calculated from a correction which effectively checks $f(\Theta) = 0$.

$$Ps^{n+1} = Ps^n + \delta Ps$$

$$\nabla^2 \delta Ps = -f(\Theta) \qquad (5\text{-a})$$

If at convergence, the condition $f(\Theta) = 0$ implies effectively $\Theta = 0$, accelerating the convergence processing is possible in some cases by replacing (5-a) by a model equation where Θ is more directly introduced :

$$\nabla^2 \delta Ps = -f(\Theta) \simeq \nabla.(\Theta \vec{V}) \simeq 2J.\frac{\partial}{\partial \xi}\left(\frac{\Theta}{J} U^\xi\right) \quad (5\text{-b})$$

where J is the Jacobian of the geometrical transformation and u^{ξ} is the contravariant velocity component along ξ.

As mentionned in part 2, the unknown $\vec{V}$ is calculated in station ξ_i and Ps in ξ_{i-1}. There are three reasons for this choice :

- As the method is applied to compressible or incompressible subsonic flows, the proper information transfer from downstream to upstream is realized only if the longitudinal pressure gradient $\frac{\partial Ps}{\partial \xi}$ is downstream decentered (RUBIN [11]).

- Thus the obtained formulation is very compact as all the unknown and known terms belong to the same domain delimited by the stations (ξ_{i-1}, ξ_i).
- When solving the pressure equation (5-a) or (5-b), only the divergence Θ in $\xi_{i-1/2}$ is assumed non equal to zero as the upstream (ξ_{i-2}) and downstream (ξ_{i+1}) flows are supposed converged thus giving a zero divergence. From (5), the sign of the right-hand term changes when applying (5) at the stations ξ_{i-1} or ξ_i. It it thus verified that the numerical statibility is consequently improved when taking the pressure as an unknown in the station ξ_{i-1}.

Also, in order to take correctly into account the three dimensional elliptic effect associated with the pressure and to optimize its results on the boundary (as the viscous flow seems to be very sensitive to them), the resolution of the pressure equation (5) is decomposed in two steps : the pressure is first calculated on the boundary of the domain limited by the stations ξ_{i-2} and ξ_i, then a two dimensional equation is used in station i-1. This technique enables a real local three dimensional calculation of the boundary pressure with a limited computing requirement. So, the pressure is first calculated on the boundary with an integral equation deduced from (5) through Green's identity.

$$4\Pi T\ \delta Ps(M) = \int_\Gamma \frac{1}{r}\frac{\partial}{\partial n}(\delta Ps)\ d\Gamma - \int_\Gamma \frac{\partial}{\partial n}\left(\frac{1}{r}\right) d\Gamma + \int_\Omega \frac{1}{r} f(\Theta)\ d\Omega \qquad (7)$$

T is a coefficient function of the point M position in the space.
This equation (6) is discretized by decomposing the boundary in 9 nodes surfacic elements associated with quadratic interpolation functions. As the pressure is known on the boundary, it was found sufficient to use a two dimensional discretization of a finite differences type to obtain the pressure inside the domain at station i-1.
Concerning the boundary conditions, it is interesting to note that the different normal derivatives can be distinguished at a same point. It is particularly important when treating wall intersections (two normal derivatives) or corners (three normal derivatives).
Downstream, the pressure is imposed in ξ_i, thus giving $\delta Ps_i = 0$ in all cases. Upstream (ξ_{i-2}), the pressure field $\delta Ps_{i-2} = 0$ or its gradient $\frac{\partial \delta P_{i-2}}{\partial n} = 0$ can be either imposed. At last, on the lateral boundaries, a zero normal derivative is imposed on the walls, which is compatible with high Reynolds flows. Periodicity conditions can also be imposed.

5. ONE DIMENSIONAL MASSFLOW CORRECTION

For a subsonic iso-energy flow, the proper boundary conditions in the upstream section are the stagnation pressure Po and the two covariant velocity components V_η and V_γ. Downstream, imposing the static pressure Ps is interesting. The history of the flow in the duct, and particularly pressure losses, will fix the mass flow which then appears as an unknown of the problem. In classical parabolized methods, the mass flow is given as the velocity is completely fixed upstream. The downstream static pressure is then calculated by the numerical scheme.
In our parabolized method, (Po , V_η, V_γ) are estimated upstream and Ps downstream not only for all the duct but also partly when solving the system between the ξ_{i-1} and ξ_i stations. Ps is therefore imposed either from an initial guess or from the results of a preceding upstream/downstream sweep. In opposite, if V_{i-1} is imposed to initialize the calculus, it cannot be completely fixed as Ps_{i-1} is modified to verify the local mass conservation (equation (6)), the total pressure Po_{i-1} would be an unknown. The question is then to correct the V_{i-1} velocity to verify an unknown mass flow. The solution lies in the utilization a one dimensional mass flow correction using the information on the K_i total pressure loss coefficients between two stations ξ_i and ξ_{i-1}. For example, the following relation can be written for an incompressible case on a one dimensional basis for a flow averaged on the transversal surface (η, γ) :

$$Po_{i-1} = Po_i + K_i \cdot \rho\left(\frac{V_{i-1}^2 + V_i^2}{2}\right)$$

or

$$\frac{1 - K_i}{1 + K_i} \cdot Po_{i-1} + \frac{K_i}{1 + K_i} \cdot Ps_{i-1} - \frac{1}{1 + K_i} \cdot Ps_i = \frac{1}{2}\rho V_i^2$$

More generally, using the existing information between the stations $j < i$ and i, the obtained equation is :

$$a_j . Po_j + \sum_{k=j}^{i} b_{kj} . Ps_k = \frac{1}{2} \rho . V_i^2 \qquad (j=1, i) \qquad (8)$$

where the (a_j, b_{kj}) coefficients depend on the loss coefficients K_k $(k = j+1,i)$. This equation (8) can be used to uniformize a mass flow between the stations j and i and therefore between i-1 and i, thus giving the average values Ps_k $(k<i)$.

Let's first suppose that (8) is verified with a pressure Ps_j not corresponding to the desired value Ps_j^* . It is then necessary to calculate some pressure corrections δPs_k to add to the current values Ps_k $(k<i)$, and as well as the mass flow Q*, Ps_i being fixed.

By linearizing (8), one obtains :

$$\sum_{k=j}^{i} b_{kj}\, dPs_k - \rho\, d\left(\frac{V_i^2}{2}\right) = - a_j\, dPo_j$$

$$As \quad \rho\, d\left(\frac{V_i^2}{2}\right) = \rho \left(\vec{V_i} . \frac{\vec{dM}}{d\xi}\right) . \left(\vec{dV_i} . \vec{\nabla}\, \xi\right) = \left(\vec{V_i} . \frac{\vec{dM}}{d\xi}\right) \frac{dQ_i}{\mathcal{V}_i}$$

where $\mathcal{V}$ is the local volume between two stations (η, γ) .

Noting $\delta Q_i = Q^* - Q_i$

$$\sum_{k=j}^{i} b_{kj}\, dPs_k - \left(\vec{V} . \frac{\vec{dM}}{d\xi}\right)_i \frac{Q^*}{\mathcal{V}_i} = - a_j\, dPo_j + \left(\vec{V} . \frac{\vec{dM}}{d\xi}\right) \frac{Q_i}{\mathcal{V}_i} \qquad (9)$$

When applied to i and i-1 with j=i-1, this equation (9) uses both mass flows Q_i and Q_{i-1} as well as the difference $Po_{i-1}^* - Po_i$ and $\delta Ps_i = 0$ to give δPs_{i-1} and the new mass flow Q*.This method enables a fast mass flow uniformization between the two surfaces of the local calculus domain. It is used at each time-step. After convergence and verification of the equations between stations i-1 and i, the calculation goes on between i and i+1 with an imposed arbitrary Ps_{i+1} value, as was the obtained total pressure Po_i. It is hence natural to assume that Q* is different from the one obtained between i-1 and i. Consequently, when finishing each calculation in a station, it is possible to use (9) from the upstream station i=1 to i by setting j to 1. This method uniformizes the mass flow by taking into account the complete upstream history.

In order to also take into account the downstream pressure Ps_N, (8) is written once more as follows :

$$a_1 . Po_1^* + \sum_{k=1}^{i} b_{ki} . Ps_k - \rho \frac{V_i^{*2}}{2} = 0$$

where Ps_k^* are all the desired values and V_i^* corresponds to the mass flow Q*. Then a linearization based on the obtained state (Ps_k, V_i) gives :

$$a_1\, Po_1^* + \sum_{k=1}^{i} b_{ki}\, (Ps_k + dPs_k) - \frac{1}{2} \rho\, V_i^{*2} - \left(\vec{V} . \frac{\vec{dM}}{d\xi}\right) . \left(\frac{Q^* - Q_i}{\mathcal{V}_i}\right) = 0$$

$$\text{where} \sum_{k=1}^{i} b_{ki}\, dPs_k - \left(\vec{V} . \frac{\vec{dM}}{d\xi}\right)_i \frac{Q^*}{\mathcal{V}_i} = - a_1 Po_1^* - \sum_{k=1}^{i} b_{ki}\, Ps_k +$$

$$\rho \frac{V_i^2}{2} - \left(\vec{V} . \frac{\vec{dM}}{d\xi}\right)_i \frac{Q_i}{\mathcal{V}_i} \qquad (10)$$

Equation (10) thus enables to uniformize the mass flow in the complete duct and uses the upstream and downstream conditions $(Po_1, V_{1\eta}, V_{1\gamma})$ and P_{SN} ; it is written for i varying from 1 to N. After calculating these one dimensional δPs_k and δQ_k corrections, the local values are accordingly corrected :

$$\begin{cases} Ps_k(\xi_k, \eta, \gamma) = Ps_k(\xi_k, \eta, \gamma) + \delta Ps_k \\ V(\xi_k, \eta, \gamma) = V(\xi_k, \eta, \gamma) \cdot \left(1 + \frac{\delta Q_k}{Q^*}\right) \end{cases}$$

6. RESULTS

The method has been tested on two representative test cases in turbomachinery for which experimental data was available. Our main objective was here to validate qualitatively the method and especially to verify its convergence capacity in cases with high elliptical effects.

The first case is a 90° square duct with a high curvature (Dean number : 369). The fluid is water. The flow is turbulent (Reynolds number : 400000). The experimental measurements of TAYLOR and al. [12] enable velocity profiles comparisons. As no pressure results are given, the pressure was estimated to give approximately the experimental mass flow.

The mesh is regular with 21 grid points in each transverse directions and 40 along (Figure 4) ξ . The convergence was obtained after 35 upstream/downstream sweeps. All the variables (mass flow, pressure, ...) were then stabilized, as it is shown by the figure 2 where the evolution of the upstream mass flow difference is a function of the sweeps.

The velocity profiles of U_ξ and V_η (pressure side to suction side) are presented at the averaged radius at 4 different sections (30°, 60°,77.5° and 90°) from the duct centre (symetrical) ($Z^* \approx 0$) to the wall ($Z^* = 1$) (Figures 5 to 12).

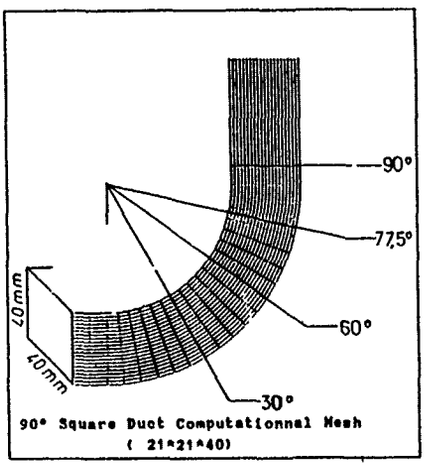


Figure 2

On one hand, the longitudinal velocity is correctly predicted at the centre for all 4 sections (Figures 5 to 8) ; on the other hand, a significant velocity deficit appears near the wall ($Z^* = 1$). This deficit is easily explained by the far too coarse grid near the walls. The turbulent boundary layers cannot be properly represented and this effect is seen by an arbitrary growing-up of the boundary layer generating an overestimation of the losses

The transversal evolution of V confirms the correct prediction at the duct centre, the differences again appearing near the walls (figures 9 to 12). The low number of grid points near the wall tends to overestimate and displace the transversal velocity peak inside the duct.

Despite this wall discrepancy, it is interesting to note that the levels are properly predicted even with secondary velocities representing 30% of the mass averaged longitudinal velocity.

The second test case is a turbine cascade for which velocity and pressure experimental results existed [13]. In opposition to the preceding test case, we felt important to mainly validate the static pressure evolutions.

The computing was made on an inter-blade duct of the cascade with its trailing and leading edges elongated (smoothing) by solid walls. No periodicity conditions were thus imposed, and the comparison is therefore only qualitative and restricted to the domain limited downstream by the trailing edge.

The mass averaged velocity is 15.05 m/s and the Reynolds number is 275000. There is a 63° deviation. The regular mesh is equivalent to the previous one (21X21X40) but is of an I-grid type (Figure 3).

Convergence problems occured during the sweeps as a transient reverse flow zone was created in the pressure side corner near the stations 6 and 8. The Flare approximation, used in this zone, permits the computing to converge in the current station. However this approach generates some fluctuations of the local pressure corrrections. These diseappear with difficultly along the sweeps.

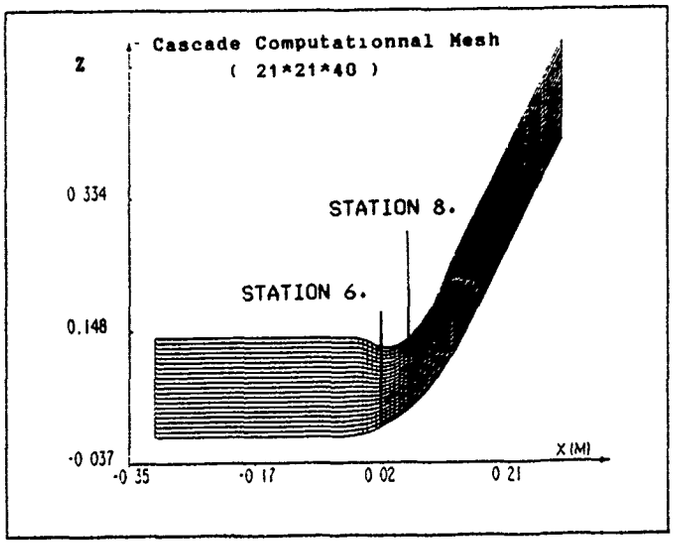


Figure 3

The obtained results, after 15 sweeps, are not yet converged. Despite this fact, there is a good agreement between the calculated and measured static pressures.

The amplitude of the pressure/suction sides pressure gradient is slightly overestimated in station 6 (as a too high level exists at the pressure side)(Figure 13).

On the opposite, in station 8 (figure 14), the transverse gradient is properly predicted (slightly underestimated). Figure 15 presents a comparison of the total pressure isolevels. An excessive loss is seen along the lateral wall/suction side because of the excessive pressure level at the pressure side and the thus created too high transversal velocities.

To establish a more thorough comparison for this test case, it seems necessary to modify the actual treatment of the reverse flows occuring during the sweeps. It is also necessary to use a more refined mesh near the wall.

7. CONCLUSION

A new method of calculating flows in geometrically complex ducts, typical of turbomachines, has been presented. It uses an upstream/downstream space marching procedure resulting of the parabolization of the equations. Different new aspects of the method are outlined. First of all, the treatment of the longitudinal pressure gradient decentring in subsonic zones implies calculating the pressure and the velocity in two different stations. The resulting numerical formulation is particularly compact. Secondly, the elliptical pressure effect, already existing because of the downstream decentring of the longitudinal pressure gradient, is reinforced by calculating the pressure on the boundary with an integral equation. This point is particularly important in order to predict correctly the viscous wall flows. The third point is the use of a one dimensional correction always allowing to take into account the global correct upstream and downstream boundary conditions.

The method has been validated is typical turbomachines ducts. A correct numerical behaviour and a good qualitative agreement between the numerical and measured results is shown.
Also it seems important to improve the actual treatment of the reverse flow zones appearing during the sweeps.
Sufficiently refined meshes are also found necessary to validate quantitavely the method.

ACKNOWLEDGMENTS

This research was supported by the Direction des Recherches et Etudes Techniques. The authors would also like to acknowledge the SNECMA for its interest and support on this action.

REFERENCES

1. DAVIS, R.L., CARTER J.E.
Counterrotating streamline pattern in a transitional separation bubble
AIAA, J. Vol 24 N° 5, PP. 850 - 851, May 1986

2. KULISA-BELLOIR P.
Etude théorique des écoulements visqueux en présence d'injections pariétales en vue du refroidissement des turbines.
Thèse de Doctorat - LYON 1 - Avril 1989

3. LEBOEUF F., KULISA-BELLOIR P., EL MARJANI A.
Viscous computations in turbomachines based on the use of integral equations
5 th International Conference on Numerical Methods in laminar and turbulent flow
Montreal - July 1987 - Pineridge Press (Ed TAYLOR, HABASHI, HAFEZ)

4. DELERY J., MARVIN J.G.
Shock wave boundary layer interactions
Agardograph AG-280 (1986)

5. PARKINSON E., POMMEL F., EL MARJANI A., FERRAND P., LEBOEUF F.
A quasi elliptical numerical resolution of the parabolic Navier-Stokes equations in Turbomachines, with the boundary element method.
6th conference on Numerical Methods in laminar and Turbulent Flow - SWANSEA - July 1989.

6. BALDWIN R.S., LOMAX H.
Thin layer approximation and algebraic model for separated turbulent flows
AIAA paper N° 78-257 (1978)

7. WARMING R.F., BEAM R.M.
On the construction and application of implicit factored schemes for conservation laws.
SIAM - AMS Proceeding, Vol 11, 1978

8. PULLIAM, T.H. STEGER J.L.
Implicit finite difference simulation of three dimensional compressible flows
AIAA J. vol 18 - 2, 1980

9. BENBOUTA N., FERRAND P., LEBOEUF F.,
Convergence acceleration for linear systems iterative resolution and applications to computational fluid dynamics.
High performance Computing. J.-L. Delhaye and E Gelenbe (Editors)
Elsevier Science Publishers B.V. (North Holland), 1989.

10. SIDI A. FORD R.F., SMITH D.A.
Acceleration of convergence of vector sequences
SIAM J. Num. Anal vol 23 n° 1 Feb. 1986

11. RUBIN S.G.
A review of marching procedures for parabolized Navier-Stokes equations
Numerical and physical Aspects of Aerodynamics flows
Springer Verlag, 1982.

12.TAYLOR A.M.K.P., WHITELAW J.H. YIANNESKIS
Measurements of laminar and turbulent flow in a curved duct with thin inlet boundary layers.
NASA Contractor Report 3367, 1981.

13.ONVANI A.
Etude expérimentale des écoulements secondaires en grille d'aubes de turbine en absence et en présence d'injections discrètes à la paroi.
Thèse de doctorat - LYON 1 - Septembre 1983

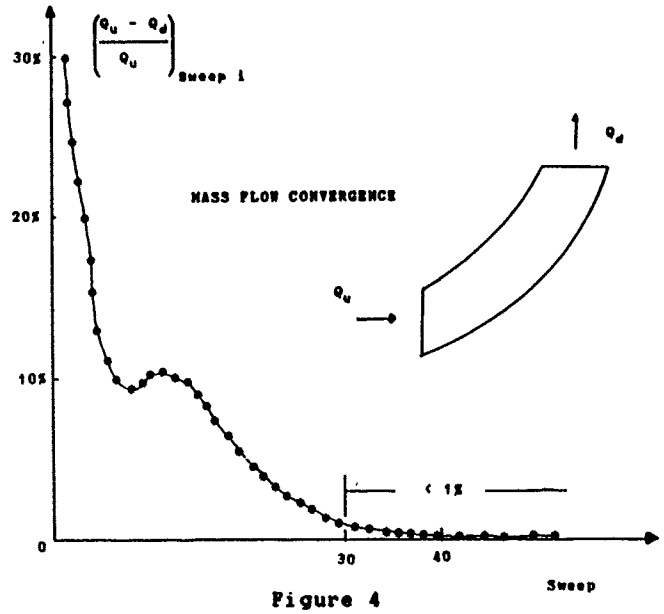


Figure 4

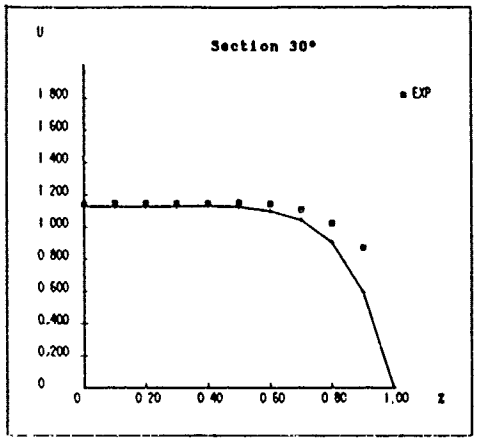


Figure 5

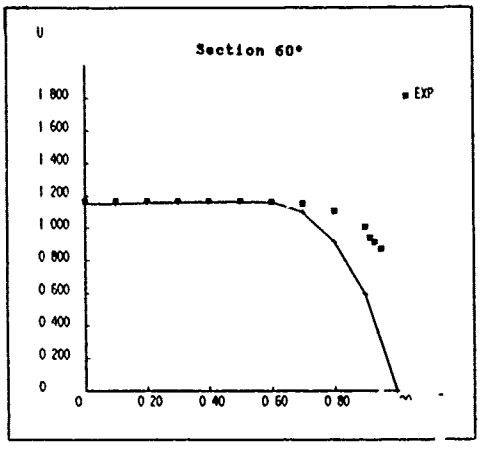


Figure 6

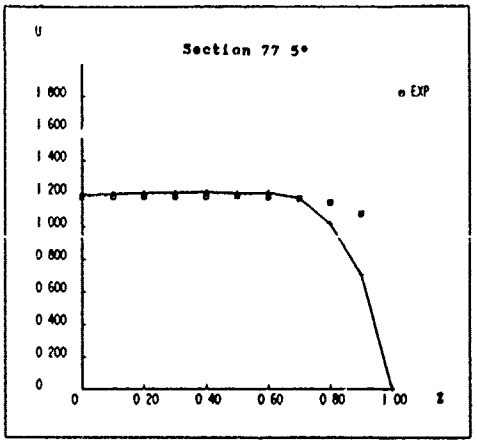


Figure 7

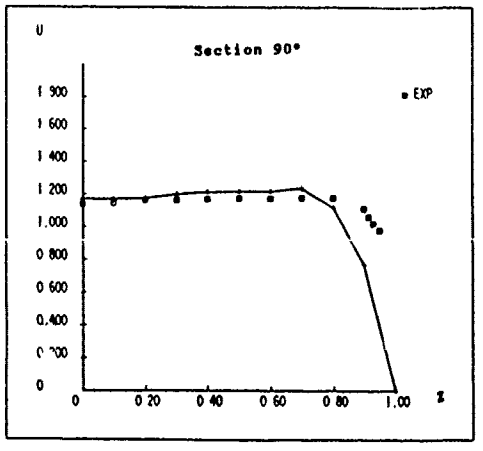


Figure 8

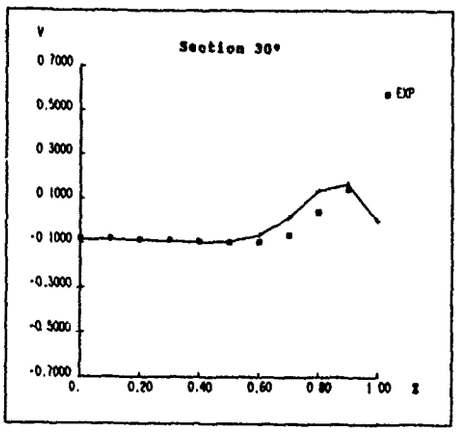


Figure 9

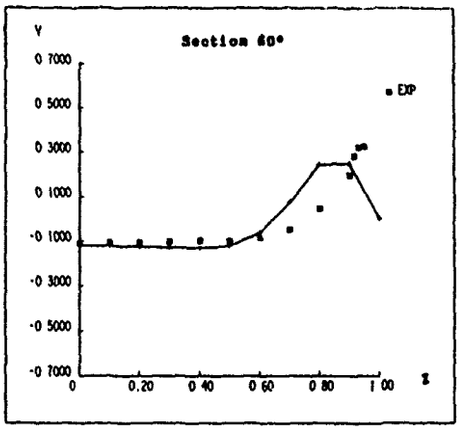


Figure 10

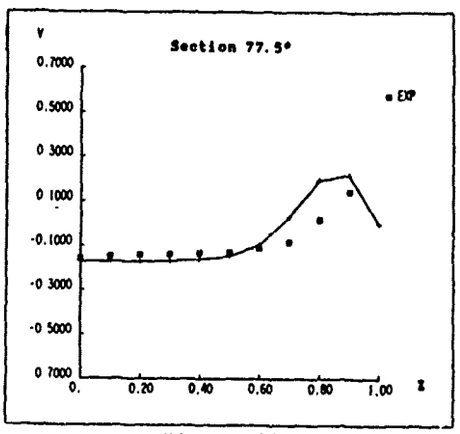


Figure 11

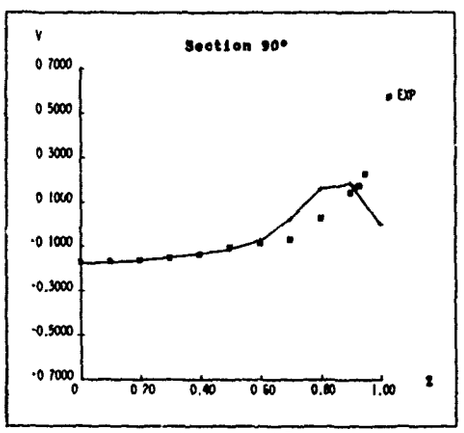


Figure 12

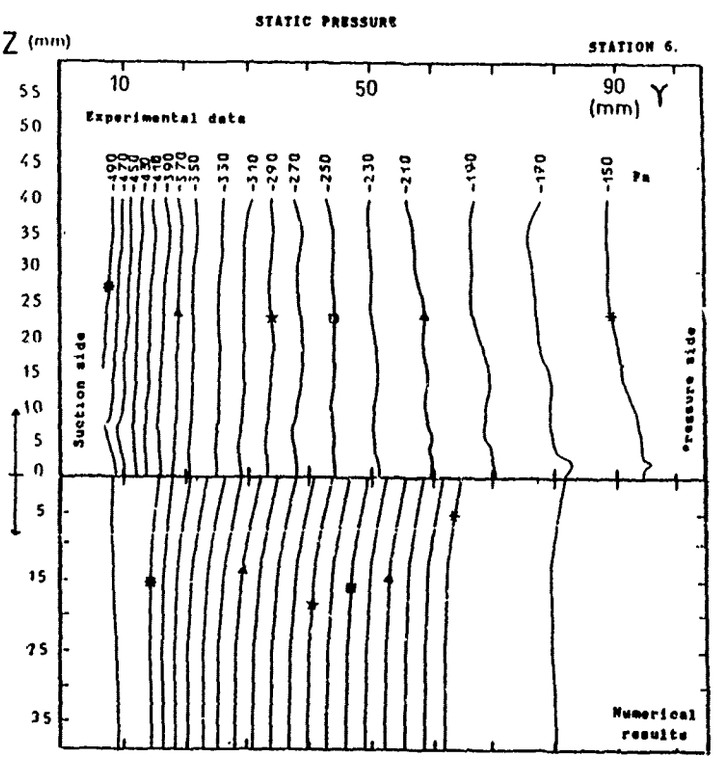


Figure 13

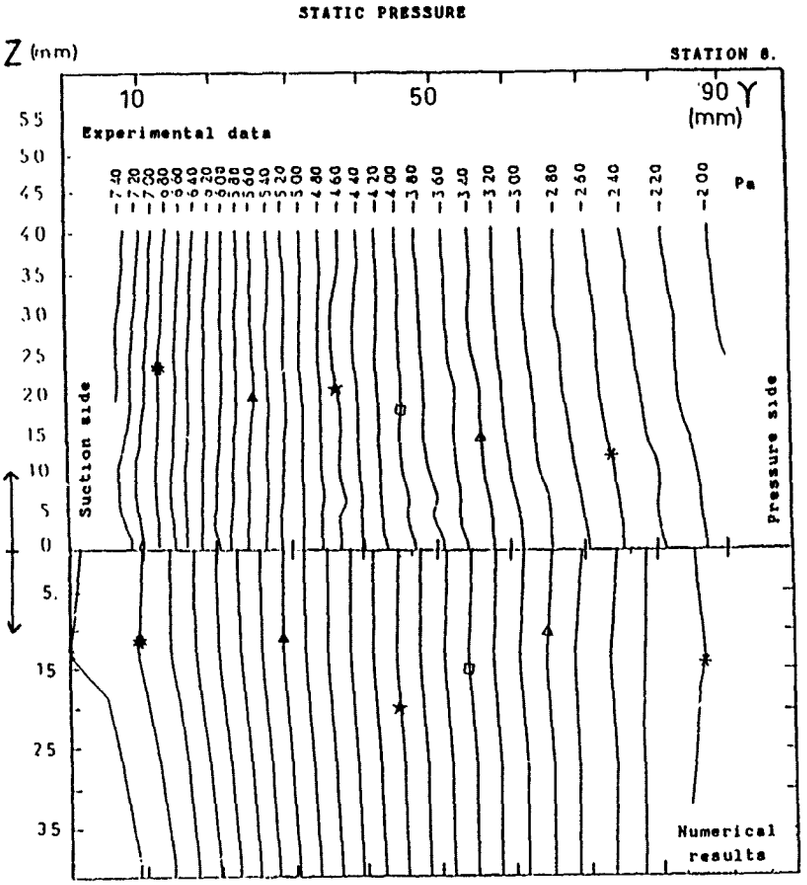


Figure 14

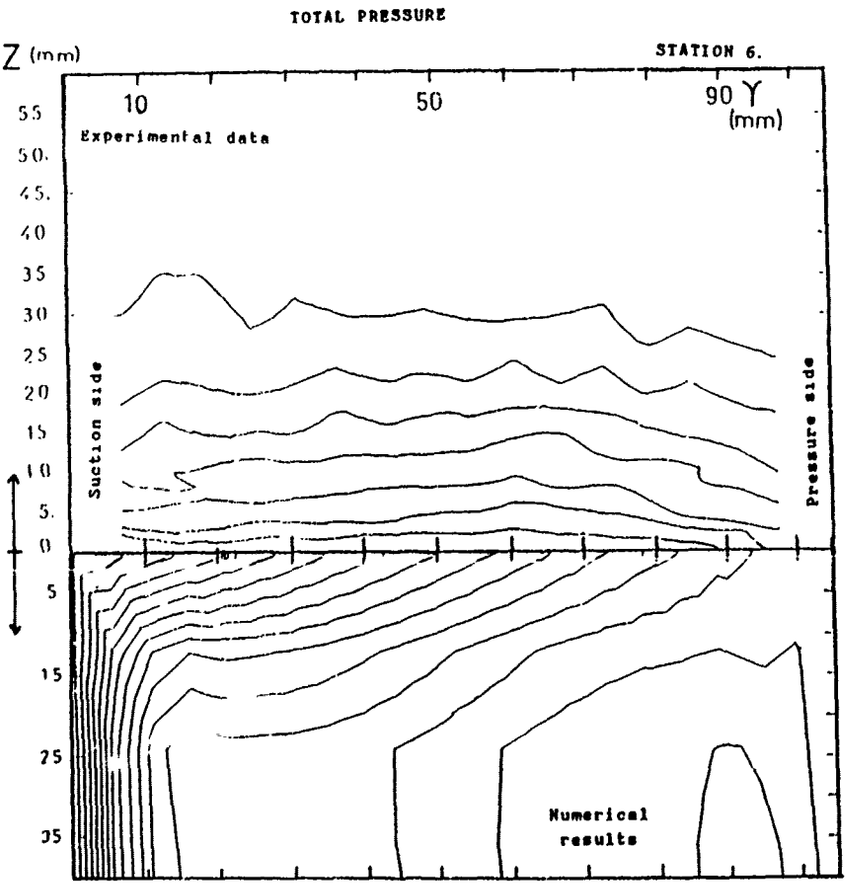


Figure 15

EXPERIMENTAL AND NUMERICAL STUDY ON BASIC PHENOMENA OF SECONDARY FLOWS IN TURBINES

by

R. Niehuis, P. Lücking and B. Stubert

MTU MOTOREN- UND TURBINEN-UNION MÜNCHEN GMBH

Dachauer Strasse 665
8000 München 50

GERMANY

SUMMARY

The recent understanding and the basic principles of secondary flow development in turbines, such as the formation of a horseshoe vortex and a passage vortex, are illustrated. This paper contains results of an experimental investigation of the three-dimensional flow within an annular cascade rig of an inlet guide vane of a low pressure turbine. Flow calculations with a three-dimensional Euler and a partially-parabolized Navier-Stokes code were performed, and the numerical results are discussed and compared with the experiment. Additionally, the mentioned computer codes were applied to calculate the three-dimensional flow within two different model configurations designed to expose the influence and the contribution of different secondary flow phenomena in the endwall region.

LIST OF SYMBOLS

$\vec{c}$	velocity vector	α_{z-u}	flow turning angle, $\alpha_{z-u} = \tan^{-1}(c_z/c_\varphi)$
H_{12}	boundary layer shape parameter, $H_{12} = \delta_1/\delta_2$	α_{z-r}	radial flow angle, $\alpha_{z-r} = \tan^{-1}(c_r/c_z)$
p	pressure	δ_1	displacement thickness
Re	Reynolds number based on chord length and exit flow	δ_2	momentum thickness
		ϱ	density
s^1,s^2,s^3	nonorthogonal curvilinear coordinates	μ	dynamic viscosity
z,r,φ	cylindrical coordinates in axial, radial and circumferential direction	$\vec{\omega}$	vorticity vector

Subscripts

z,r,φ	vector components in axial, radial and circumferential direction
s	secondary
t	stagnation
in	rig inlet condition

1. INTRODUCTION

Secondary flows in turbines are of significant practical importance because they produce considerable three-dimensional flow distortions and losses in the endwall regions of turbine blades. 30 - 50% of the total losses are due to the presence of secondary flows. In order to design blades with reduced secondary losses, a thorough understanding of the mechanism and the physical effects responsible for the generation and development of secondary flows is required.

During the past decades, many papers have appeared which describe the phenomena associated with secondary flows in turbomachines, and the structure of secondary flows in turbine blade passages is to date reasonably well understood. A comprehensive review article illustrating the state of the art on the subject with an extensive list of references has been published recently by Sieverding /1/. It is the purpose of this paper to investigate which of the various secondary flow phenomena predominates in the endwall region of turbine blades.

2. SECONDARY FLOW PHENOMENA IN TURBINES

The terminology 'secondary flow' is a loose definition for flow phenomena existing in endwall regions of turbomachinery blading. What is called secondary flow turns out to be part of a complex three-dimensional flow field in the endwall regions consisting of a more or less pronounced vortex system caused by different flow phenomena. Although these effects are present simultaneously and interfere with each other in typical turbomachinery blading, each of the dominant effects itself leads to the formation of a

- horseshoe vortex,
- passage vortex, and
- trailing edge vortex.

Additional vortices such as corner vortices or tip clearance vortices may be present in turbines, but will not be treated in this paper. Except for the tip clearance vortex all secondary flow phenomena are primarily due to viscous flow effects. Before illustrating the secondary flow phenomena in turbine cascades in more detail, let us briefly recall those flow phenomena responsible for the generation and the development of secondary flows.

A horseshoe vortex is generally formed when an oncoming boundary layer flow hits an obstacle, i.e., a body of finite thickness. It is due to the fact that the oncoming boundary layer cannot withstand the pressure gradient in front of the body and starts to separate upstream of the body. This process is associated with the formation of a vortex that rolls up the boundary layer and wraps itself around the body. Owing to its particular shape, it is called horseshoe vortex. The formation of a horseshoe vortex is always combined with the generation of a separation line at some distance upstream of the leading edge and around the body. This line can be easily visualized by surface oil flow techniques and is then an indication for the existence of a horseshoe vortex. Hornung & Perry /2/, who established a consistent vocabulary for the description of three-dimensional 'separated flows,' call the separation line a negative bifurcation line. In the following, the term 'bifurcation line' will be used, too, instead of the term 'separation line,' a term which is used and meaningful for the description of two-dimensional flow separation, but becomes inadequate for the description of phenomena such as reverse flow and vortical motions in three-dimensional flows. The term 'negative bifurcation line' is more suitable for the description of the above effects because it implies that the streamsurfaces on each side of this line and close to the endwall appear to combine and to form a single streamsurface leaving the wall and wrapping itself around the horseshoe vortex as illustrated in Fig. 1. (The obstacle in Fig. 1 is removed to show more clearly the salient features of the flow.) The term 'negative' is used because two streamsurfaces combine to a single streamsurface.

It is worth mentioning that for such kind of junction flows cases are known for which not a single horseshoe vortex is observed but a number of vortices, see e.g. Cornish /3/ and Abid & Schmitt /4/. In these cases the number of negative bifurcation lines increases according to the number of vortices so that these kind of leading edge vortex systems can be easily detected by surface oil flow techniques. Up to now, the effects are unknown which are reponsible for the generation of multiple horseshoe vortices. Different types of boundary layer profiles may be one reason. For turbine blades, however, just one horseshoe vortex is observed in almost all cases.

As mentioned before the formation of a horseshoe vortex is primarily due to the finite thickness of a body. Therefore, it exists even for very simple blades such as blades of finite thickness but without any flow turning. On the other hand, the generation of a passage vortex comes about just because of the turning of a flow. In order to illustrate this effect, consider an infinitely thin turning cascade with zero incidence as indicated in Fig. 2. Let the cascade be straight for simplicity. Except for the endwall regions and the surface of the blades, the flow through the cascade may be regarded as approximately inviscid. In this core flow region equilibrium exists between the centrifugal and the pressure force. The pressure in the endwall boundary layers is imposed by the pressure of the surrounding inviscid core flow. Owing to the fact that the flow velocity rapidly decreases in the endwalls boundary layer, the centrifugal force of a fluid element cannot withstand the pressure force unless the radius of curvature of the streamlines in the vicinity of the endwalls decreases. Therefore, the streamlines close to the endwall are deflected towards the suction surface as shown in Fig. 2. At the outer edge of the endwall boundary layers this deflection is compensated by a deflection in the opposite direction due to continuity effects so that two counterrotating vortices are generated in each passage, see Fig. 3. These vortices are called passage vortices.

Downstream of each blade a vortex sheet leaves the trailing edge. In classical secondary flow theory this corresponds to the trailing filament and trailing shed vorticity, see e.g. Hawthorne /5/ and Came & Marsh /6/. The trailing filament vorticity is due to the stretching of the inlet vortex filaments when passing through the cascade. The trailing shed vorticity is due to the spanwise change of blade circulation which itself is caused by the spanwise non-uniformity of the oncoming flow. The vortex filaments of the vortex sheet concentrate further downstream of the blade to form the so-called trailing edge vortex as illustrated in Fig. 4.

In turbine blade passages, the three above-mentioned secondary flow phenomena, causing individually the generation of a horseshoe, passage, and trailing edge vortex, exist simultaneously and interact with each other. Certainly, this is a non-linear interaction process and thus it is impossible to separate the individual effects. In Fig. 5 the secondary flow in the endwall region of a turbine blading is illustrated. The oncoming boundary layer separates in front of the blade leading edge and a horseshoe vortex as well as a negative bifurcation line are formed. They both wrap around the front part of each blade. Inside the blade passage they are influenced by the pitchwise pressure gradient between the suction and pressure sides so that they are shifted towards the suction surface during the passage. The negative bifurcation line on the endwall, too, is deflected towards the suction surface and usually meets the suction surface at the axial position of maximum pressure difference between pressure and suction surfaces. It continues on the suction surface associated with a deflection towards midchannel.

The pressure side leg of the horseshoe vortex, H_P, has the same sense of rotation as the passage vortex. Both phenomena act together and seem to merge. As a result only one vortex can be identified which has the sense of rotation of the pressure side leg of the horseshoe vortex and the passage vortex, respectively. The process can be explained as follows. The vortex starts as the pressure side branch of the horseshoe vortex and is then reinforced by the passage vortex effect. The suction side leg of the horseshoe vortex, H_S, of the neighboring blade, however, has the opposite sense of rotation in the blade passage as the passage vortex. Its development is certainly not supported by the passage vortex effect; on the contrary, it will be attenuated. In addition, it is shifted close to the suction surface and may interact with the boundary layer on the blade. Klein /7/ suggests that it dissipates completely, while Langston /8/ and Sieverding & Van den Bosche /9/ assume that it is preserved, although attenuated, and wraps itself around the passage vortex. In case it is preserved, two counterrotating vortices must be seen in the exit plane of the blade passage in addition to the trailing edge vortex. The latter is not included in Fig. 5.

Up to now, it is an open discussion whether the suction side leg of the horseshoe vortex dissipates or is preserved up to the exit of the passage. Certainly, a general answer will not be possible since this will depend on the particular flow conditions and the blade geometry. Furthermore, it is unknown to date whether the passage vortex effect dominates the horseshoe vortex effect or whether both effects contribute in the same order of magnitude to the generation and development of secondary flows in turbine blade passages. It is the purpose of this paper to discuss the latter problem.

3. DEFINITION OF SECONDARY FLOW AND SECONDARY VORTICITY

In the literature, a commonly accepted definition of 'secondary flow' is not available. According to Salvage /10/, 'secondary flow in turbomachines may be considered to be any flow the designer chooses to ignore in solving the basic equations of fluid motion.' Therefore, the definition of secondary flow is arbitrary and strongly linked with the definition of a primary flow. Depending on the effects which will be regarded as secondary, the primary flow may be defined in such a way that the difference between the real three-dimensional flow and the primary flow represents these secondary flow effects. In order to describe for instance the endwall secondary flow effects outlined above in

straight cascades, the flow direction at midspan is usually regarded as the primary flow direction and the flow normal to this direction as secondary. In case of twisted blades or annular cascades, this is no longer valid because the flow angle varies along the span. For such cases, a comparable definition is used in this paper to study the secondary flow effects, which turned out to be practical and yielded good results. The primary flow direction is defined by a quasi three-dimensional inviscid S1/S2 streamsurface calculation without endwall boundary layers, cf. Chap. 6.2. The flow perpendicular to this direction is regarded as secondary, consequently the vorticity of the secondary flow, called secondary vorticity, is the component of the vorticity vector in the direction of the primary flow. According to the above definition, the vorticity of the collateral boundary layer on the walls has no contribution to the secondary vorticity.

4. IDENTIFICATION OF SECONDARY VORTICES

In order to obtain an experimental insight into the secondary flow phenomena in turbines, the flow field behind or inside the blade passage is traversed at planes of interest with appropriate measurement probes, most commonly with pressure probes (e.g. 5- or 3-hole pressure probes). As a result the measured flow quantities such as velocity components, pressure, or flow angles are usually plotted in so-called contour plots, provided the resolution of the traverses is high enough. Binder & Romey /11/ reported a method to identify secondary vortices by means of contour plots of flow angles. Their theory is based on the fact that the secondary vortices in turbine passages behave approximately like a Rankine vortex, namely like a solid body vortex in the central part and a free vortex in the outer part, as illustrated in Fig. 6. A real vortex is similar to a Rankine vortex with the only difference that it exhibits a buffer zone between the two regions which smoothes out the discontinuities of the velocity gradients. Binder & Romey /11/ noticed that the isoclinal lines of a solid body vortex are parallel lines to the plane in which the flow angle is measured. The corresponding isoclinal lines of a free vortex are a pair of enclosing circles touching each other at the center of the vortex.

Analysing experiments and three-dimensional computational results, it turned out that the vorticity is another interesting quantity for secondary flow analysis. It is an experimentally observed fact that, at high Reynolds number, the convection of vorticity dominates the diffusion of vorticity and that the vorticity rapidly concentrates into vortex cores, see e.g. Perry & Hornung /12/. The typical vorticity distribution of a real vortex is sketched in Fig. 6 and is characterized by a distinct plateau in the region of the vortex core surrounded by an almost irrotational region. Using contour plots of vorticity, the location of secondary vortices can be easily identified by means of those flow regions where the vorticity locally exhibits extreme values. The advantage of this method is that only one contour plot is needed for the localization of vortices, and that the strength of the vortical motion can be estimated by the absolute values of vorticity. The only drawback of this method is that the vorticity is a quantity which can hardly be measured directly, but must be determined by calculating velocity gradients. Measurements with sufficient resolution are required to achieve adequate accuracy.

5. CALCULATION OF VORTICITY COMPONENTS

The vorticity is defined as

$$\vec{\omega} = \mathrm{rot}\ \vec{c} \tag{1}$$

For a cylindrical coordinate system the vorticity vector has the following components:

$$\omega_r = \frac{1}{r}\frac{\partial c_z}{\partial \varphi} - \frac{\partial c_\varphi}{\partial z}\ , \tag{2}$$

$$\omega_\varphi = \frac{\partial c_r}{\partial z} - \frac{\partial c_z}{\partial r}\ , \tag{3}$$

$$\omega_z = \frac{1}{r}\frac{\partial}{\partial r}(r\,c_\varphi) - \frac{1}{r}\frac{\partial c_r}{\partial \varphi}\ . \tag{4}$$

Assuming that the flow field is traversed in circumferential and radial direction at a fixed axial position, the axial component of the vorticity vector can be calculated by approximating the velocity gradients by finite differences. A difficulty arises for the other two components because gradients in z-direction are required, see Eq. (2) and (3). In most cases, however, these gradients cannot be determined directly because the flow field is traversed at one axial position only. Even if traverses are performed at different axial positions, the distance between the measurement planes is usually too large to calculate the remaining two vorticity components with sufficient accuracy. Gregory-Smith et al. /13/ proposed a method for the calculation of the vorticity components in radial and circumferential direction that does not require gradients in z-direction. This method, called Euler approximation in the following, will be outlined here and extended to compressible flows.

Consider the momentum equation of a steady, compressible, viscous flow in dimensionless form, see e.g. Lagerstrom /14/:

$$s\left[\mathrm{grad}\,\frac{c^2}{2} + (\mathrm{rot}\,\vec{c})\times\vec{c} + \mathrm{grad}\,p\right] = \frac{1}{Re}\left[\mathrm{Div}(\mu\,\mathrm{def}\,\vec{c}) - \frac{2}{3}\mathrm{grad}(\mu\,\mathrm{div}\,\vec{c})\right]\ . \tag{5}$$

Assuming high Reynolds number flow ($Re \to \infty$), the right hand side of Eq. (5) is negligibly small, i.e. the viscous terms are small compared to the other terms and the above equation reduces to

$$s\left[\mathrm{grad}\,\frac{c^2}{2} + (\mathrm{rot}\,\vec{c})\times\vec{c} + \mathrm{grad}\,p\right] = 0\ . \tag{6}$$

Using the definition of vorticity, cf. Eq. (1), Eq. (6) can be rewritten as

$$\vec{c}\times\vec{\omega} = \frac{\mathrm{grad}\,p}{s} + \frac{\mathrm{grad}\,c^2}{2}\ . \tag{7}$$

For incompressible flow this equation degenerates to

$$\vec{c} \times \vec{\omega} = \text{grad}\left(\frac{p}{\rho} + \frac{c^2}{2}\right) = \text{grad}\,\frac{p_t}{\rho} \quad , \tag{8}$$

an equation which is used in the derivation of Gregory-Smith et al. /13/. Taking the components in radial and circumferential direction of Eq. (7), we obtain:

$$\omega_\varphi = -\frac{1}{c_z}\left[\frac{1}{3}\frac{\partial p}{\partial r} + \frac{1}{2}\frac{\partial c^2}{\partial r} - c_\varphi \omega_z\right] \quad , \tag{9}$$

$$\omega_r = \frac{1}{c_z}\left[\frac{1}{3}\frac{1}{r}\frac{\partial p}{\partial \varphi} + \frac{1}{2}\frac{1}{r}\frac{\partial c^2}{\partial \varphi} + c_r \omega_z\right] \quad . \tag{10}$$

With these two equations the components of the vorticity vector in radial and circumferential direction can be calculated. In contrast to the vorticity definition of Eqs. (2) and (3), gradients in axial direction are not required anymore so that the complete vorticity vector can be determined even in cases where the flow field is traversed at one axial position only. It has to be mentioned that Eqs. (9) and (10) have a singularity at $c_z = 0$, i.e., in flow regions where c_z tends to zero (e.g. boundary layers very close to the wall). In those regions they are not applicable and no longer valid. The only assumption, however, used in this derivation is that the Reynolds number tends to infinity. For the flow regions of interest, this assumption turned out to be approximately valid, and the method produced good results, as shown later on.

6. COMPUTATIONAL METHODS

6.1 THE THREE-DIMENSIONAL EULER-CODE

All Euler calculations were made with an explicit time marching finite volume method to solve the three-dimensional Euler equations. The time integration consists of the so-called 'Damping Surface Technique', see Happel & Stubert /15/, and is first order accurate. A second order central nodal point scheme is used for spatial discretization. At the nonperiodic boundaries the equations are discretized using half-elements, resulting in first order accuracy. Depending on the geometry of the problem two types of grids can be generated. In the case of blunt body configurations a C-type grid is preferred, but for many turbomachinery cascades a H-grid seems to be sufficient if the leading edge region of the grid is not highly skewed.

The explicit one-step Euler calculations for a central discretization is unconditionally unstable. Therefore, the solution process must be stabilized by additional dissipative terms in the equations. The stabilization is accomplished by a periodic addition and reduction of so-called artificial viscosity which can be adjusted by a special damping parameter. Numerical studies have shown that this artificial viscosity has a strong influence on the vorticity distribution in the flow field. Since this paper is mainly concerned with secondary flow phenomena a minimum of artificial damping was used for the calculations although this produces some wiggles in the solution.

In all cases aerodynamic inlet boundary conditions are prescribed by radial distributions of circumferentially constant values, namely stagnation pressure, stagnation temperature and flow angles in radial and circumferential direction. In fact, the vorticity of the oncoming boundary layers is simulated by the total pressure distribution. Hence the task of a three-dimensional Euler calculation is to distribute this oncoming vorticity throughout the flow field without any production or reduction of global vorticity. The mass flow rate is obtained as a calculation result by the static pressure distribution at the outlet boundary. Therefore, at the midspan of the outlet boundary the pressure is fixed, and the radial equilibrium is computed every time step depending on the actual solution. In order to save computer time a grid refinement procedure is used. First, an initial solution is calculated on a coarse grid. The final solution is subsequently obtained by interpolation and calculation on successively finer grids. Generally, three grid levels are used for a complete calculation.

6.2 THE THREE-DIMENSIONAL PARTIALLY-PARABOLIZED NAVIER-STOKES CODE

In order to calculate the three-dimensional viscous (turbulent) flow through the turbomachinery cascades described above, a three-dimensional partially-parabolized Navier-Stokes code has been used that solves the Reynolds-averaged equations numerically with a space-marching pressure-correction method, see Lücking /16/. The differential equations of motion, energy, and possibly turbulence quantities are partially parabolized neglecting the diffusion into a previously defined main flow direction, i.e., derivatives with respect to this direction are cancelled in the diffusion terms. This implies that reverse flow should not occur in this special direction, and that separation areas can be treated only to a small extent and with approximations. Due to their parabolization the equations can be integrated space marching, i.e., the solution proceeds through the cascade or duct along the mean flow direction.

The other condition for the space marching solution is the knowledge of a pressure field. It is approximately prescribed as good as possible and is corrected during the calculation. Satisfying continuity is the measure for necessary changes to the pressure. The pressure corrections are performed in three steps - two of them during the marching solution to satisfy global and local continuity, and the third three-dimensionally after each sweep through the domain to obtain the elliptic coherence of the (subsonic) flow field. The partially-parabolic calculation is finished when the pressure corrections have become small after several passes through the channel.

As preparation for the partially-parabolic solution through a cascade a quasi-three-dimensional inviscid streamsurface calculation is performed. It consists of an iterative coupling of one mean hub-to-tip streamsurface and several blade-to-blade surfaces. The flow is two-dimensional along the surfaces. On each of them it is calculated by a finite difference method using the stream function, see Lücking & Gallus /17/. The quasi-three-dimensional calculation gives the solution domain for the partially-parabolic marching and transforms it into a numerical space using the streamlines as coordinate lines into the main flow direction S^1 and the intersections of the stream surfaces and S^1 = const. as secondary coordinates S^2 and S^3. The inviscid spatial pressure- and density-distribution is an ideal starting field for the calculation of the viscous flow. In many cases one single marching sweep is sufficient for practical purposes on the basis of a quasi-three-dimensional solution.

The basic equations for steady relative flow are developed for the nonorthogonal curvilinear coordinate system mentioned above. The equation of motion is multiplied by unit vectors in the S^1-direction, and normal to S^2 = const. and S^3 = const., respectively, to solve for the covariant velocity component in the primary flow direction and the contravariant components in the secondary flow directions. Parabolization and further simplifications are performed on the viscous terms. The viscosity of the fluid is either laminar or extended by turbulent eddy viscosity evaluated from a turbulence model. The equations are discretized with finite differences using central approximation for the diffusion terms and upwind approximation for the convection terms. Linearization and introduction of the boundary conditions leads to an algebraic system of equations for the flow values of the grid points on a S^1 = const. surface. The continuity is checked at the finite volumes formed by the mesh lines or coordinate lines. Necessary corrective fluxes are introduced by a modification of the velocity field induced by a correction of the pressure. A simplified equation of motion couples the velocity and pressure corrections.

7. EXPERIMENTAL INVESTIGATION OF AN INLET GUIDE VANE OF A LOW PRESSURE TURBINE

7.1 EXPERIMENTAL APPARATUS

The experiments described in this report were conducted at the high-altitude test facility of the university of Stuttgart. The inlet guide vane of a low pressure turbine was investigated in an annular cascade rig simulating the annular duct of a commercial jet engine. The annulus diverges in the range of the guide vane, see Fig. 7. The correct inlet swirl is established by preswirl vanes placed sufficiently far upstream of the guide vanes, such that the wakes have the chance to mix out. The blade profiles at hub and tip are shown in Fig. 8.

As indicated in Fig. 7 the flow field was traversed at 3 different axial positions, namely two upstream and one downstream of the guide vane. At these positions, area traverses were performed with five-hole pressure probes (probe head diameter 3.0 mm) mounted in radial traversing devices. Circumferential traverses were obtained by rotating those parts of the casing carrying the radial traversing devices. The resolution of the traverses was 28 points in circumferential direction covering 2.8 pitches of the preswirl vane in the inlet plane and 2.2 pitches of the guide vane in the exit plane. The radial traverses consisted of 16 points in the inlet plane and 19 points in the exit plane with an increased resolution in the endwall regions in each case. Besides the traverses, the static pressure distribution on the blade surface was measured on three quasi-streamlines (hub, mean, tip), and the flow was visualized by oil-and-dye injection on the blade surface as well as on hub and casing.

7.2 INLET CONDITIONS OF THE GUIDE VANE

The inlet conditions of the inlet guide vane were measured with five-hole pressure probes upstream of the leading edge (M.P. 2, cf. Fig. 7). In Fig. 9 a contour plot and the radial distribution of the measured total pressure related to the total pressure at the inlet of the test rig as well as the radial distribution of the Mach number are shown. The contour plot illustrates that the wakes and secondary vortices of the preswirl vanes are completely mixed out. The flow in circumferential direction is almost uniform, for all quantities the range of variation is less than 0.7% of the pitchwise averaged values. The boundary layers, both at the hub and the casing, are relatively thick and amount to 20% of the duct height in each case. The boundary layers are laminar according to the shape parameter H_{12}. At the hub the shape parameter was calculated as $H_{12} = 2.7$ and at the casing as $H_{12} = 2.2$.

7.3 EXPERIMENTAL RESULTS

The topology of the streamline pattern on the blade surface as well as on hub and casing visualized by oil-and-dye injection reveals that the endwall flow region of the inlet guide vane matches well with the secondary flow model outlined in Chap. 2, see Fig. 10. Both on hub and casing a negative bifurcation line is clearly visible in front of the leading edge of each blade indicating the generation and presence of a horseshoe vortex. Owing to the fact that only one negative bifurcation line is visible, just a single horseshoe vortex is formed in front of this turbine blade. Inside the blade passage the bifurcation line and other limiting streamlines on the endwall are strongly deflected towards the suction surface by the pitchwise pressure gradient. Behind the location, where the suction side branch of the bifurcation line and the bifurcation line of the neighboring blade meet the suction surface, these lines proceed on the suction surface with a deflection towards midchannel. They are ending in a separation bubble sitting in the rear part of suction surface. However, the deflection of the limiting streamlines towards midchannel behind the separation bubble continues to exist and is apparent on the photographs of the flow visualization. The flow in the endwall of the casing looks qualitatively similar to the one in the hub region. However, the distance between the negative bifurcation line and the leading edge is larger and the deflection of streamlines towards midchannel on the rear part of the suction surface of the blade is stronger, indicating a more intensive vortical motion.

This is also confirmed by the five-hole pressure probe measurements in the exit plane. In Fig. 11 the distributions of various flow quantities are shown in form of contour plots. The flow field behind different blades looks almost identical, indicating a good periodicity and an uniform inlet flow. Applying the earlier mentioned isoclinal method of Binder & Romey /11/, the location of the secondary vortices could be clearly identified by means of the flow angles $\alpha_{z\text{-}u}$ and $\alpha_{z\text{-}r}$. The center of each vortex is marked in Fig. 11. The distribution of the secondary vorticity calculated according to Chap. 5 is shown in Fig. 11, too. It is clearly visible that those regions where the secondary vorticity exhibits a plateau of extreme values, coincide with the location of the secondary vortices identified by the isoclinal method. The sense of rotation is apparent by the sign of the vorticity and is in agreement with the isoclinal method. Both in the endwall region of hub and casing, a pair of counterrotating vortices is visible behind each blade. The vortices indicated by I have the sense of rotation of the passage vortex and pressure side leg of the horseshoe vortex, respectively. It is probably composed of both. The remaining vortices (II) have the opposite sense of rotation and are located in the wake of each blade. A suction side leg of the horseshoe vortex could not be identified explicitly at the hub or at the casing. It is either dissipated during the passage or its vorticity is redistributed during the passage. The sense of rotation coincides with vortex II so that vortex II is likely to consist partly of the trailing edge vortex and partly of the suction side leg of the horseshoe vortex. In classical secondary flow theory, the streamwise vorticity of the passage vortex, called distributed vorticity according to Hawthorne /5/, is assumed to be uniform in pitchwise direction at the exit of the passage. However, the distribution of the measured vorticity at the exit of the guide vane clearly shows that this is not the case. On the contrary, the vorticity accumulates and is concentrated in the center of vortex I.

Although the inlet boundary layer thickness at hub and casing is almost identical, cf. Fig. 9, and the flow turning is slightly lower at the casing, it is apparent, that the secondary flow field at the casing is significantly stronger compared to the hub. The local extension of the secondary field is larger combined with higher loss in total pressure and stronger secondary vortices. The latter can be seen clearly by the higher density of the almost parallel isoclines in the center of the vortices. The change of the radial flow angle α_{z-r} across the secondary vortices at the casing, for instance, reaches values of approximately 40^0 compared to 20^0 at the hub. These significant differences between hub and casing are not completely understood. One reason may be the lower inlet total pressure at the casing.

It is interesting to note that the region of highest total pressure loss in the endwall flow region of the casing does not coincide with the location of the secondary vortices, but lies somewhere between passage and trailing edge vortex, see Fig. 11a. Obviously, this low momentum fluid is the inlet boundary layer material convected and accumulated by the vortical motion inside the blade passage. The hub endwall flow region, however, looks slightly different. It exhibits at least a loss region at the center of the trailing edge vortex. The passage vortex is very close to the endwall and could not be resolved completely by the five-hole pressure probe measurements.

8. NUMERICAL INVESTIGATION OF AN INLET GUIDE VANE OF A LOW PRESSURE TURBINE

The above mentioned three-dimensional calculation methods, namely the Euler and the Navier-Stokes code, were applied to the inlet guide vane described in Chap. 7 using the measured inlet conditions. During the calculations it turned out that the inlet conditions, especially the boundary layer profiles, have a strong influence on the solution and need to be carefully simulated in order to obtain good agreement with the experiment.

Results of the three-dimensional Euler flow calculation are presented in Fig. 12 in form of contour plots of various flow quantities in the exit plane of the guide vane (M.P. 3). The secondary vortices can be easily identified by means of the isoclinal method and the distribution of the secondary vorticity. As before, both methods yielded identical locations of the vortices. A comparison with the experimental results shows that the calculated flow field in the exit plane looks qualitatively very similar. Both, in the endwall region of hub and casing a pair of counterrotating vortices is present and the positions of the vortex centers are almost identical to the experiment. Vortex II was tracked upstream and was clearly found to originate from the trailing edge as assumed.

In the endwall region of the casing, the change of the two flow angles across the vortex centers compares well with the experiment. The vorticity of the secondary vortices, however, turns out to be slightly lower, but has a comparable distribution and is located at almost identical positions. In the hub endwall region the vortical motion of the secondary flow is predicted too weak by the Euler calculation according to the distributions of flow angles and vorticity. This may be due to the lower extension of the secondary flow field resulting in a decreased resolution of the numerical mesh.

In Fig. 12a the distribution of the total pressure is presented in the exit plane. Note that this is not the total pressure loss due to the artificial damping of the Euler solution, but the low momentum material of the inlet boundary layers. Similar to the experiment it is convected and accumulated by the vortical motion of the secondary flow. The regions with lowest total pressure are located between vortex I and II. The numerical total pressure loss is much lower than that and turns out to be in the order of magnitude of about one percent of the total pressure at the rig inlet P_{tin} as can be seen by means of the 'wake' downstream of each blade.

According to the contour plots in the exit plane, a suction side leg of the horseshoe vortex is not present. A three-dimensional calculation of streamlines even revealed that the generation of a horseshoe vortex could not be simulated in this case. This becomes apparent by the calculated wall streamline pattern on hub and casing, which does not exhibit any negative bifurcation line in front of the leading edge, see Fig. 13 a and b. This line is finally formed downstream of the leading edge, i.e., inside the blade passage. The H-type grid used is obviously too coarse to resolve the leading edge region sufficiently in order to enable the Euler code to simulate of a horseshoe vortex. The number of mesh points is at the limit of the computer capacity so that a further refinement is not possible. Nevertheless, the wall streamlines on the suction surface look qualitatively very similar to the oil flow visualization, cf. Fig. 10, although no horseshoe vortex is present in the calculation. Certainly, the separation bubble cannot be simulated by the Euler code, but the deflection of streamlines on the rear part of the suction surface towards midchannel agrees fairly well with the experiment. Even the stronger deflection at the casing is simulated correctly. However, both at hub and casing the calculation predicts slightly lower deflections confirming the results in the exit plane that the secondary vortices are a little stronger in the experiment. Another reason for the slight difference may be that the boundary layers on the blade are not simulated by the Euler calculation.

Owing to the fact that the Euler calculation is inviscid and did not even simulate the horseshoe vortex, the agreement between computational and experimental results is surprisingly good. Except for the small numerical total pressure losses, the Euler code is an inviscid flow calculation, which just simulates the convection process of the vorticity at the inlet during the passage of the guide vane. Diffusion and total pressure losses because of viscous effects are not present in the calculation. Obviously the three-dimensional flow field, at least in this inlet guide vane, primarily depends on the inlet boundary layers which obviously dominate the viscous effects inside the blade passage. Although the existence of the inlet boundary layers is caused by viscous effects, the generation and development of the passage vortex is mainly an inviscid process. Therefore, inviscid calculation methods are a valuable tool to calculate secondary flows and yield good results. Since no horseshoe vortex is present in the flow calculation, vortex I and II are identical with the passage vortex and the trailing edge vortex, respectively. Because the difference between numerical solution and experimental data is small, it can be concluded that also the vortices I and II present in the experiment, see Fig. 11, are primarily composed of the passage vortex and trailing edge vortex, respectively. This means that the secondary flow in the exit plane is controlled by the passage vortex, and the horseshoe vortex seems to be of minor importance. Otherwise the good agreement between computational and experimental data cannot be explained. Numerical simulations in two model configurations confirming this conclusion will be presented in the next chapter.

Additional flow calculations were performed with the parabolized Navier-Stokes code. It is a viscous flow calculation and is able to simulate the boundary layers on the endwalls as well as on the blades. Separated flow regions or regions with reverse flow, however, have to be approximated owing to the parabolization of the Navier-Stokes equations. Therefore, it is expected that the horseshoe vortex in front of the leading edge is not simulated completely by this method. Since not only the boundary layers at the inlet are laminar but also the boundary layers over the dominant part of the blade surface, a laminar Navier-Stokes flow calculation was regarded best fitted for this guide vane.

Some of the results in the exit plane of the guide vane are presented in Fig. 14. The distribution of the total pressure reveals that the total pressure loss in the wakes and secondary flow regions is predicted too high by the calculation. This is partly due to laminar separation on the suction surface of the blade. In reality the laminar separation is followed by a transition and turbulent reattachment, a process which cannot be simulated with the Navier-Stokes code. An additional separation, which is obviously not present in the experiment, occurs at the casing downstream of the blades and is due to the diverging annulus. These separated flow regions no longer appear when a turbulent Navier-Stokes calculation is performed. The mixing length turbulence model used, however, was not appropriate for this kind of flow. The solution appeared to be too viscous associated with a weak vortical motion in the endwall regions.

According to the distribution of the flow angles and the secondary vorticity of Fig. 14, the calculated flow field again looks at least qualitatively very similar to the experiment. It needs to be mentioned that the range of the vorticity in Fig. 14 b was limited in order to enhance the presentation of the secondary flow phenomena. The wakes and the flow region close to the casing exhibit large portions of vorticity outside the selected range due to the mentioned laminar flow separation. The location of the vortices II is almost identical to the experiment, and the vortices are of approximately equal magnitude. The vortex I at the casing appears to be too close to the endwall. But, similar to the Euler calculation, a pair of vortices is observed in the endwall regions behind each blade. Again, a horseshoe vortex is not visible explicitly, either in the contour plots of the exit plane or in the calculated streamline pattern on hub and casing. As before, the pattern does not exhibit any negative bifurcation in front of the leading edge, which confirms that no horseshoe vortex is present. A plot of the streamline pattern is not presented here because it is almost identical to the Euler solution. Nevertheless, the Navier-Stokes solution compares well with the experiment. This confirms again the conclusion that the passage vortex is the dominant secondary flow phenomenon in the endwall region. The horseshoe vortex appears to be of minor importance.

In Fig. 15 the radial distribution of the pitchwise mass-averaged flow angle of the two numerical results is compared to the flow angle obtained from experimental data. It can be clearly seen that the predicted flow angle outside the secondary flow regions is predicted too low by the Euler code and too high by the Navier-Stokes code. This can be explained as follows. The Euler code does not simulate the boundary layers on the blades resulting in an increased throat area. The Navier-Stokes code, on the contrary, calculates laminar separation and accordingly thick boundary layers, which results in a decreased throat area. The measured distribution lies between the two numerical solutions. In each case the difference is less than 2^0 compared to the experiment. The radial distributions of the numerical results look qualitatively similar to the experiment and the regions of underturning and overturning caused by the secondary flow are located at almost identical radial positions. Except for the Euler result, which predicts the underturning in the hub region almost correctly, the magnitude of underturning and overturning, however, is generally smaller compared to the experiment. This is certainly caused by the weaker secondary vortices of the computational results, already observed by means of the contour plots.

9. NUMERICAL INVESTIGATION OF BASIC SECONDARY FLOW PHENOMENA IN TWO MODEL CONFIGURATIONS

In the previous chapter it was concluded that the horseshoe vortex plays a minor role in the secondary flow regions at the endwall. The passage vortex appeared to be the dominant effect in the exit plane of the guide vane. In order to confirm this conclusion, the flow in two model configurations was studied numerically. Two model turbine cascades in an axisymmetric duct were designed with identical inlet conditions, number of blades, flow turning, and inlet boundary layers. One blade, denoted case A, has an infinitely small thickness while the other, case B, has a thickness distribution. The maximum thickness is rather large for a typical low pressure turbine blade nowadays, but has been chosen to enhance the effects. Both blades have no incidence to the oncoming flow so that in case A practically no horseshoe vortex is formed in front of the leading edge. Therefore the secondary flow region consists of a passage vortex only. On the contrary, the blade of finite thickness, case B, will lead to the generation of a horseshoe vortex and simultaneously a passage vortex. A comparison of both flow fields will exhibit the influence and importance of the horseshoe vortex.

The profiles of the two different blades are presented in Fig. 16 and do not vary along the span. For the three-dimensional flow calculations, an inlet boundary layer was prescribed at the hub only in order to achieve a high numerical resolution of the secondary flow region. The boundary layer thickness amounts to 25% of the blade height. The total pressure and temperature of the free stream are 1.0 bar and 300 K, respectively. The mass flow amounts to 58.1 kg/s. The flow turning of the blades is relatively small for the following reason. Owing to the experience with the three-dimensional flow calculations applied to the inlet guide vane, a C-type grid was regarded best fitted for the Euler flow calculations in case B in order to resolve the horseshoe vortex in front of the blade properly. It was necessary to restrict the flow turning to relatively small values to avoid highly skewed and distorted grids in the exit region of the blade. In case A again a H-type grid was used.

Both the Euler and the Navier-Stokes code were applied to case A and contour plots of secondary vorticity of both solutions are presented in Fig. 17. The Navier-Stokes code performs a viscous flow calculation and has no provision to suppress the boundary layer on the casing competely. In order to keep its influence as small as possible, the calculation started with a new boundary layer at the first mesh line. The boundary layer at the hub was defined by the radial total pressure distribution and is identical for the Euler and Navier-Stokes calculation. Comparing the secondary flow region at the hub reveals that both methods yield almost identical solutions in the exit plane, as can be seen from the distribution of secondary vorticity. There are two prominent vorticity plateaus belonging to the passage vortex (I) and to the trailing edge vortex (II). The location of these vortices is almost identical for both codes. However, the maximum vorticity of the passage vortex is slightly lower for the Navier-Stokes calculation and may be caused by viscous effects. Additionally, the Navier-Stokes code predicts the presence of a small corner vortex (IV) underneath the passage vortex, a vortex which is not present in the inviscid flow solution.

A result of the Euler solution inside the blade passage of case B is shown in Fig. 18. Clearly the secondary vorticity exhibits two plateaus of opposite sign, one representing the suction side leg of the horseshoe vortex and the other the passage vortex and pressure side leg of the horseshoe vortex, respectively. Although the size of vortex I is already much larger at this axial position, it definitely dominates the flow field in the exit plane of the cascade, see Fig. 19. Only a small portion of vorticity with an opposite sense of rotation to vortex I is present. Vortex I is shifted a little less towards the suction surface compared to case A and sits closer to the endwall. Also the vorticity is slightly lower, indicating a reduced vortex strength. This is further confirmed by the streamlines on the endwall which are deflected less towards the suction surface in case B. Obviously, the suction side leg of the horseshoe vortex in cascade B requires a part of the inlet boundary layer which in turn is not available to vortex I and causes its reduced strength. It

was noticed that close to the exit of the passage the vorticity of the suction side leg of the horseshoe vortex is redistributed and appears to be contained in the trailing edge vortex. A look at pitchwise averaged quantities shows that the difference in the exit plane of case A and B is small. The radial distribution of the pitchwise mass-averaged flow angle α_{z-y} is presented in Fig. 20. Because of the weaker vortex I the amount of underturning and overturning is slightly lower in case B. However, the difference between both cases is less than 1°. These results clearly demonstrate that for these relatively low turning cascades the passage vortex is the dominant secondary flow phenomenon in the exit plane. In real turbine blades the flow turning is usually higher so that the influence of the passage vortex increases further. A Navier-Stokes calculation was performed for case B, too, but it turned out that the generation of a horseshoe vortex could not be simulated adequately.

In Chap. 5 a method (Euler approximation) was outlined which allows the calculation of all vorticity components even in cases where the flow field is traversed at one axial position only. The Navier-Stokes solution of case A was used to estimate the accuracy and the potential of the procedure. In Fig. 17 the secondary vorticity was shown calculated according to the definition of the vorticity, see eq. (2) to (4), i.e., using velocity gradients in the radial, circumferential, and axial directions. Application of the proposed method yields the distribution of Fig. 21. In this case all vorticity components are calculated by velocity gradients in the radial and circumferential directions only. Gradients in the axial direction are not required. It can be clearly seen that the difference between Fig. 17 and 21 is negligibly small, except for the regions very close to the wall, i.e., in regions where the method does not hold as mentioned in Chap. 5. However, the method offers excellent results in the main part of the flow and even in the secondary flow regions.

10. CONCLUDING REMARKS

The generation and development of secondary flows in turbine cascades was investigated experimentally and numerically. The investigations revealed that in the endwall region of turbine blades the passage vortex effect is the dominant secondary flow phenomenon and dictates the flow in the exit plane. The horseshoe vortex turned out to play a minor role.

Furthermore, it was found that although the existence of the inlet boundary layers are caused by viscous effects, the rolling up process of the oncoming boundary layer material and the formation of secondary vortices is primarily an inviscid phenomenon. Inviscid flow calculations with an Euler code simulated well the convection of the vorticity contained in the inlet boundary layers. The numerical solution in the exit plane of the turbine cascade did not differ much from the experimental result. Certainly, the Euler code was not able to calculate the losses associated with the secondary flows.

The three-dimensional computational methods, namely the Euler and the partially-parabolized Navier-Stokes methods, are able to simulate the dominant secondary flow phenomena in typical turbine cascades at least qualitatively and are a valuable tool in the design process of blades with reduced secondary losses.

11. ACKNOWLEDGEMENT

The authors would like to express their gratitude to the German Ministry for Research and Technology who sponsored this research program.

12. REFERENCES

/1/ Sieverding, C.H. — Recent Progress in the Understanding of Basic Aspects of Secondary Flow in Turbine Blade Passages
ASME Paper No. 84-GT-78, June 1984

/2/ Hornung, H.; Perry, A.E. — Some Aspects of Three-Dimensional Separation, Part I: Streamsurface Bifurcations
Z. Flugwiss. Weltraumforsch. 8, Heft 2, 1984, pp. 77-87

/3/ Cornisch III, J.J. — Vortex Flows
AIAA Paper No. 83-1812, 1983

/4/ Abid, R.; Schmitt, R. — Experimental Study of a Turbulent Horseshoe Vortex using a Three Component Laser Velocimeter
AIAA Paper No. 86-1069, 1986

/5/ Hawthorne, W.R. — Rotational Flow Through Cascades, Part I: The Component of Vorticity
Quart. J. Mech. Appl.Math., Vol. 8, 1955, pp. 266-279

/6/ Came, P.M.; Marsh, H. — Secondary Flow in Cascades: Two Simple Derivations for the Components of Vorticity
J. Mech. Eng. Sci., Vol. 16, No. 6, 1974, pp. 391-401

/7/ Klein, A. — Untersuchungen über den Einfluß der Zuströmgrenzschicht auf die Sekundärströmung in den Beschaufelungen von Axialturbinen
Forsch. Ing.-Wes., Bd. 32, Nr. 6, 1966, pp. 175-188

/8/ Langston, L.S. — Crossflow in a Turbine Cascade Passage
ASME J. Eng. for Power, Vol. 102, No. 4, 1980, pp. 866-874

/9/ Sieverding, C.H.; van den Bosche, P. — The Use of Coloured Smoke to Visualize Secondary Flows in a Turbine-Blade Cascade
J. Fluid Mech., Vol. 134, 1983, pp. 85-89

/10/ Salvage, J.W. — A Review of Cascade Secondary Flow Effects
Von Kármán Institute, Lecture Series 72, 'Secondary Flows in Turbomachines', 1975

/11/ Binder, A.; Romey, R. — Secondary Flow Effects and Mixing of the Wake behind a Turbine Stator
ASME J. Eng. for Power, Vol. 105, No. 1, 1983, pp. 40-46

/12/ Perry, A.E.
Hornung, H.
Some Aspects of Three-Dimensional Separation, Part II: Vortex Skeletons
Z. Flugwiss. Weltraumforsch. 8, Heft 3, 1984, pp. 155-160

/13/ Gregory-Smith, D.G.
Graves, C.P.
Walsh, J.A.
Growth of Secondary Losses and Vorticity in an Axial Turbine Cascade
ASME Paper No. 87-GT-114, May 1987

/14/ Lagerstrom, P.A.
Laminar Flow Theory. In: High Speed Aerodynamics and Jet Propulsion
4th Ed., F.K. Moore, Princeton University Press, Princeton, 1964

/15/ Happel, H.W.
Stubert, B.
Computation of Transonic 3D Cascade Flow and Comparison with Experiments
AGARD CP No. 437, 1988

/16/ Lücking, P.
Partially-Parabolic Calculations of Three-Dimensional Viscous Flow Through Turbomachinery Cascades
Proc. 6th GAMM-Conf. on Num. Meth. in Fluid Mech., Vieweg, 1985

/17/ Lücking, P.
Gallus, H.E.
Numerische Berechnung der dreidimensionalen reibungsfreien und reibungsbehafteten Strömung durch Turbomaschinen
VDI-Berichte Nr. 487, 1983

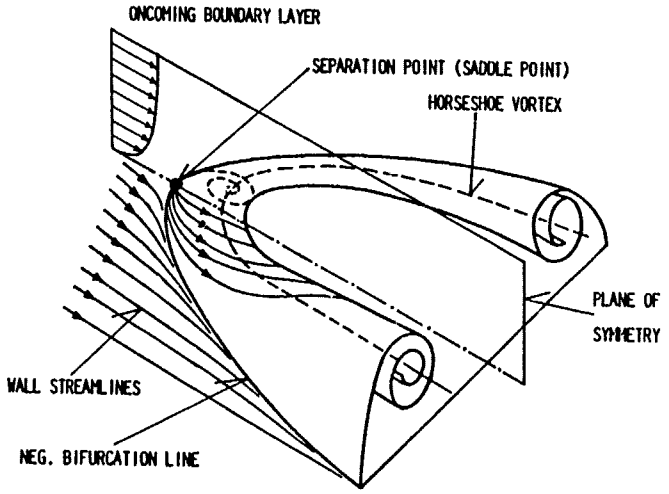


Fig. 1 Formation of a horseshoe vortex in front of an obstacle (obstacle removed)

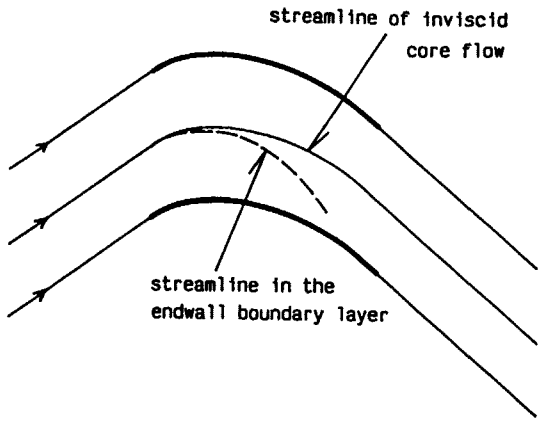


Fig. 2 Deflection of streamlines inside the endwall boundary layer

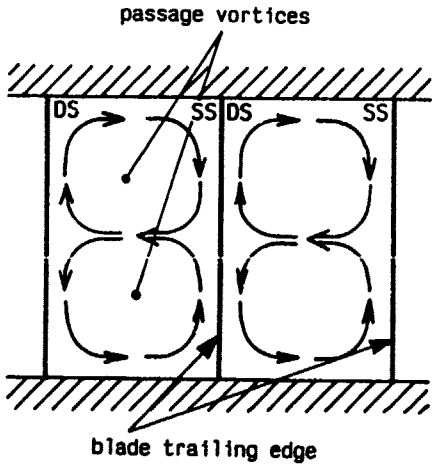


Fig. 3 Passage vortices in the exit plane of a straight cascade

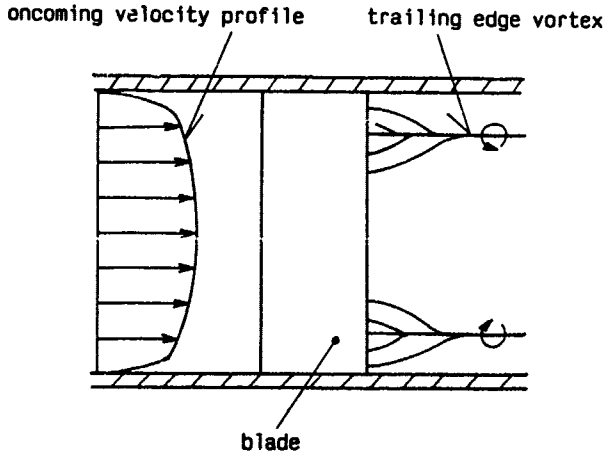


Fig. 4 Formation of trailing edge vortices

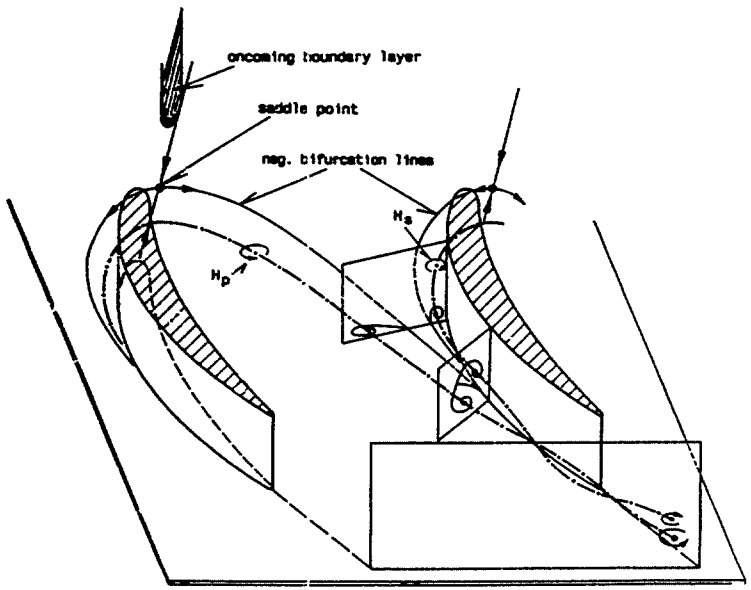


Fig. 5 Secondary vortices in a turbine cascade

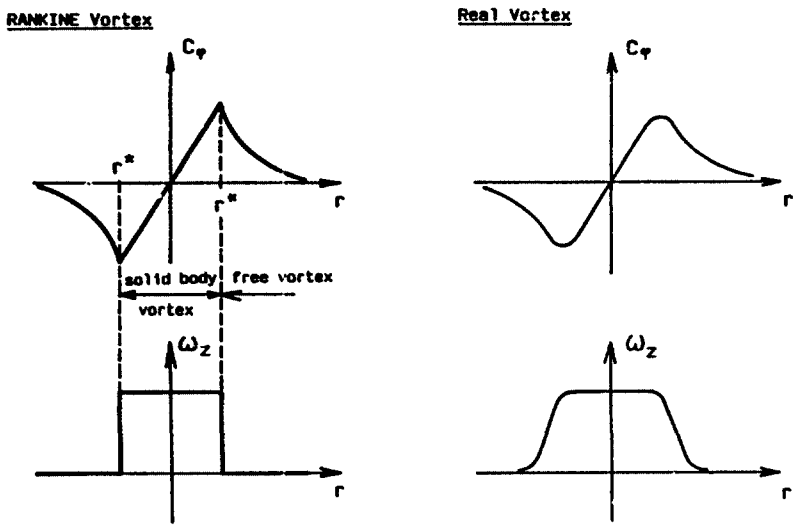


Fig. 6 Velocity and vorticity distribution of a Rankine vortex and a real vortex

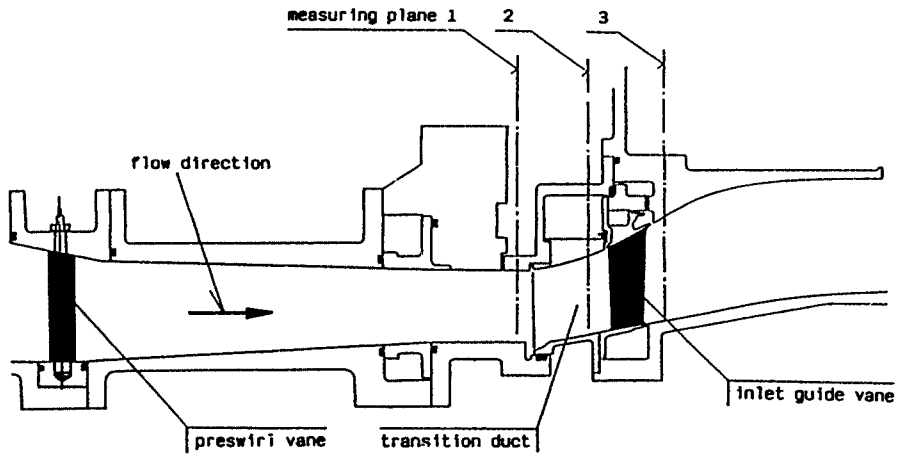


Fig. 7 Annular test rig with inlet guide vane of a low pressure turbine

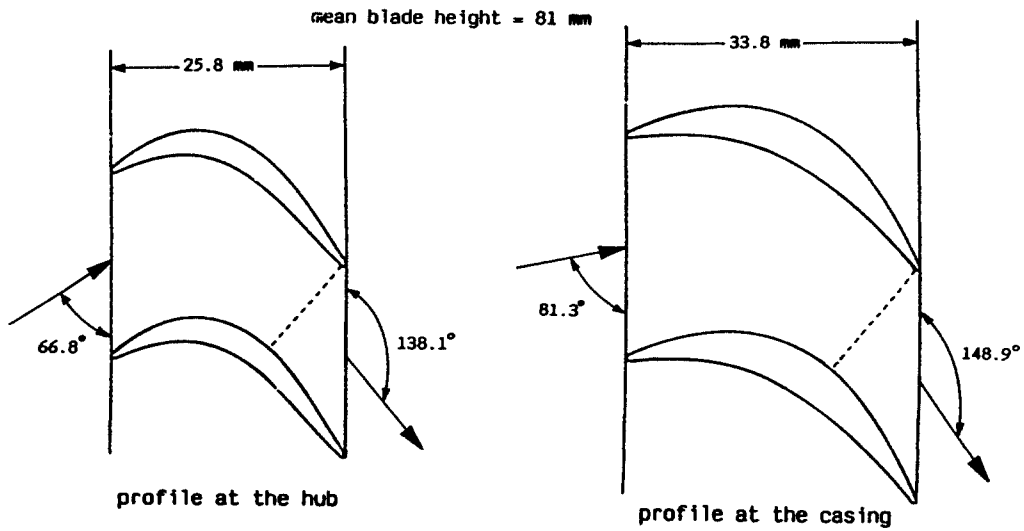


Fig. 8 Inlet guide vane geometry at hub and tip

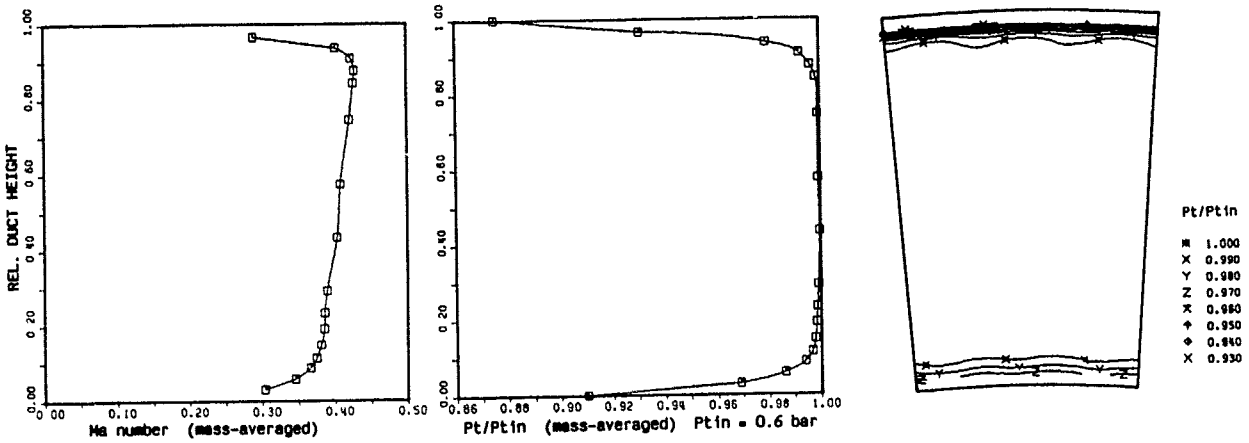


Fig. 9 Inlet conditions of the guide vane in M.P.2 (cf. Fig. 7)

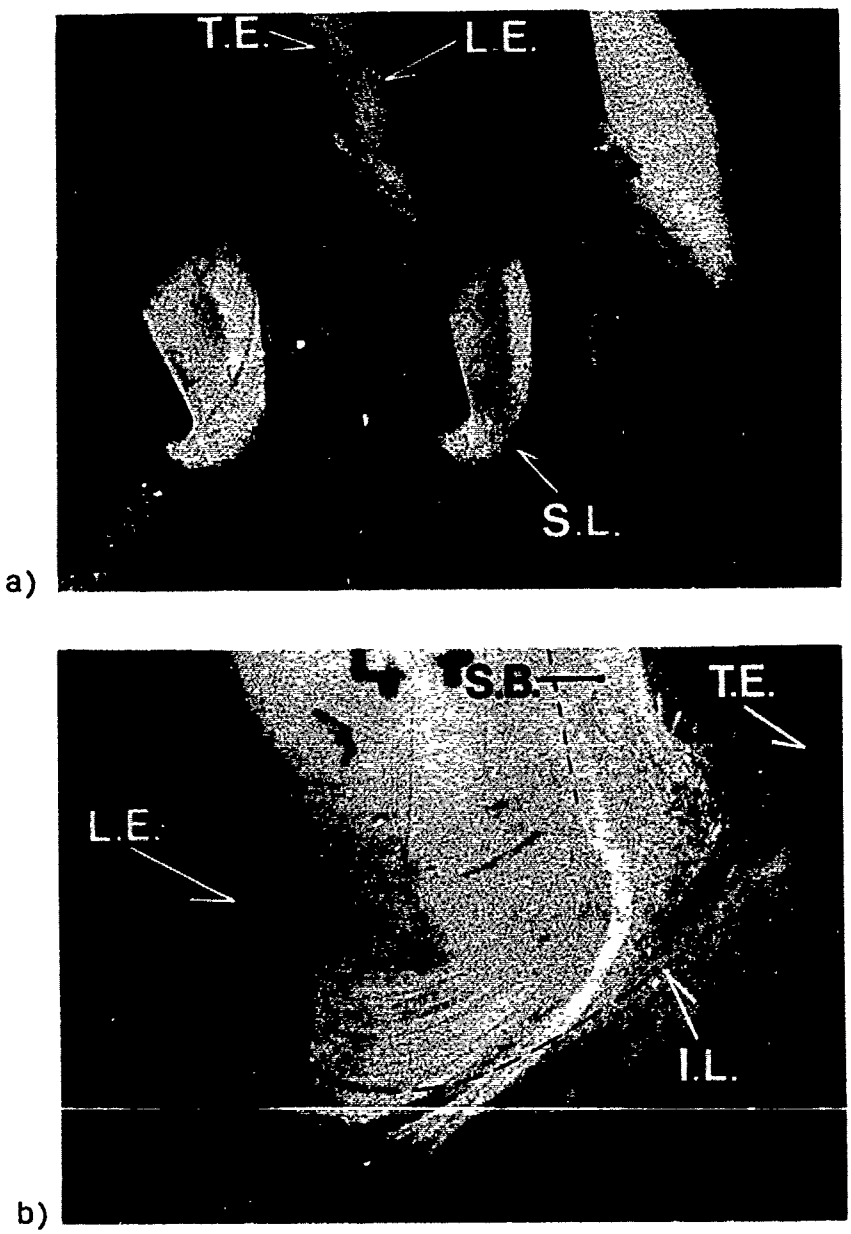


Fig. 10 Oil flow visualization in the hub region of the inlet guide vane
a) front view, b) side view (suction surface)
(notation: L.E. leading edge, T.E. trailing edge, S.L. separation line, I.L. intersection line of blade and platform, S.B. separation bubble)

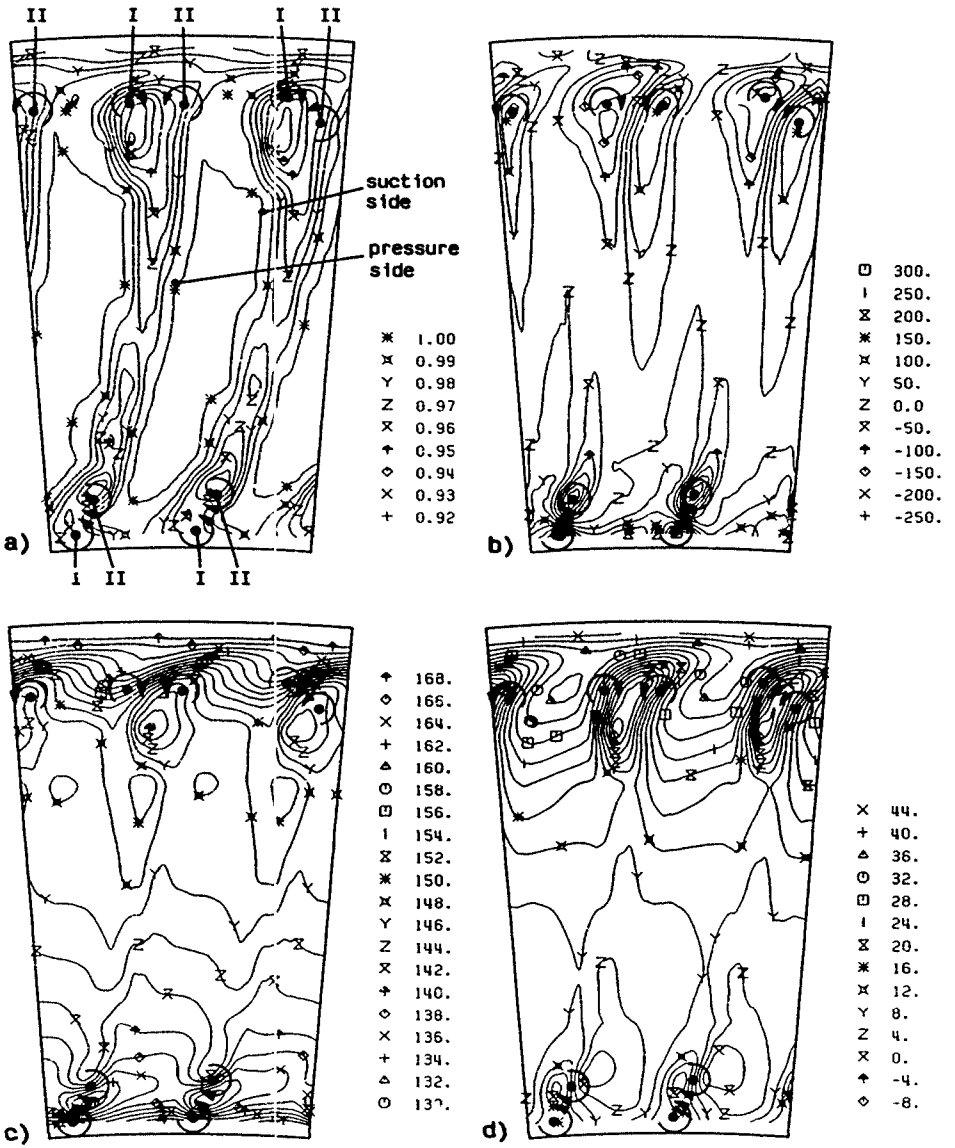


Fig. 11 Contour plots of measured flow quantities in the exit plane (M.P. 3, cf. Fig. 7) of the inlet guide vane

a) p_t/p_{tin} (p_{tin} = 0.6 bar), b) ω_s [10^2 1/s] c) α_{z-u}, d) α_{z-r}

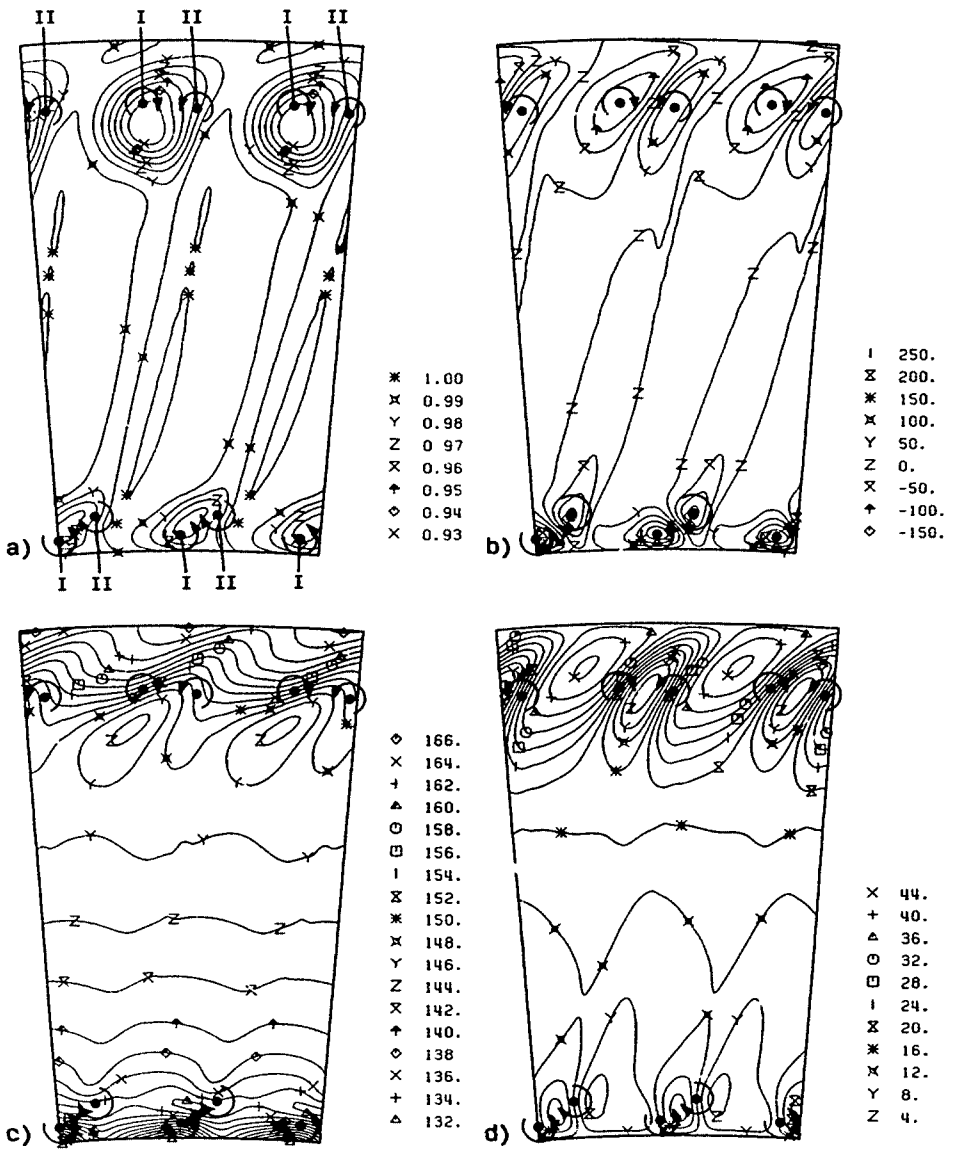


Fig. 12 3-d Euler calculation result in the exit plane of the inlet guide vane (M.P.3)

a) p_t/p_{tin} (p_{tin} = 0.6 bar), b) ω_s [10^2 1/s] c) α_{z-u}, d) α_{z-r}

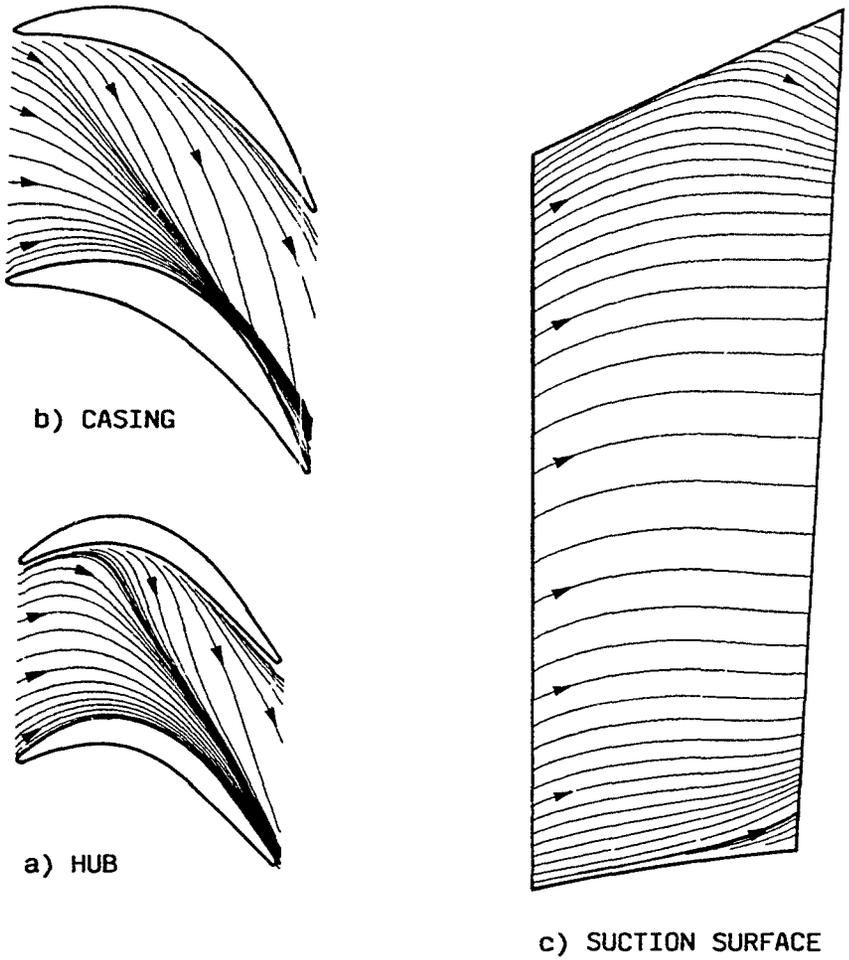


Fig. 13 Calculated wall streamlines on hub, casing, and suction surface (3-d Euler)

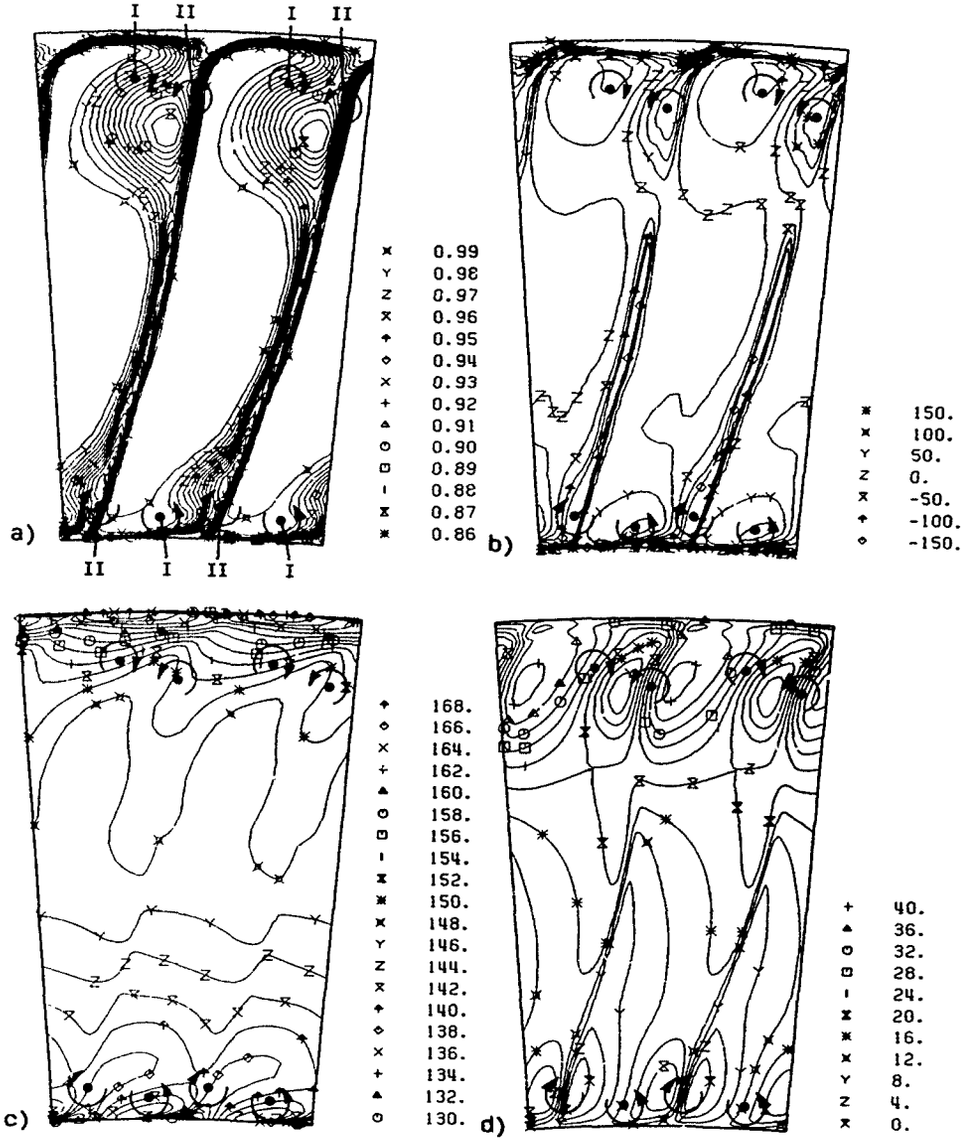


Fig. 14 3-d Navier-Stokes calculation result in the exit plane of the inlet guide vane (M.P.3)

a) p_t/p_{tin} (p_{tin} = 0.6 bar), b) ω_s $[10^2\ 1/s]$ c) α_{z-u}, d) α_{z-r}

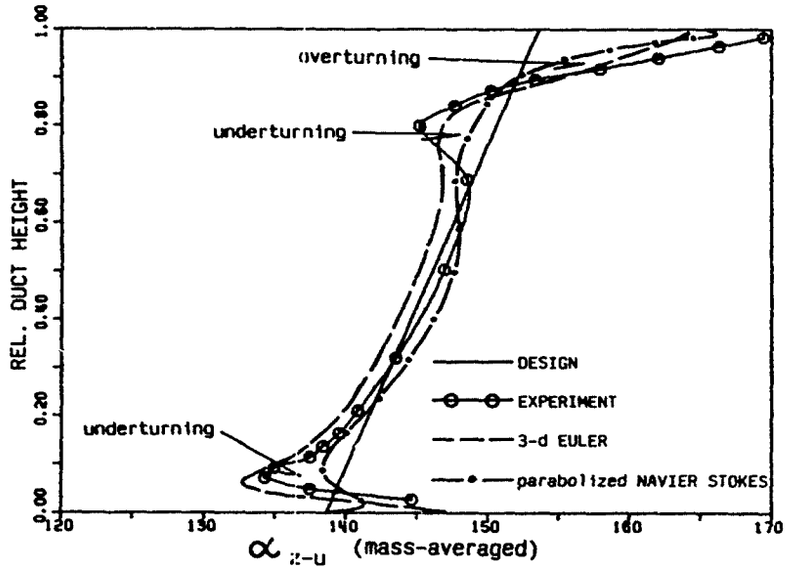


Fig. 15 Comparison of radial distributions of pitchwise mass-averaged flow angle α_{z-u} in the exit plane (M.P.3)

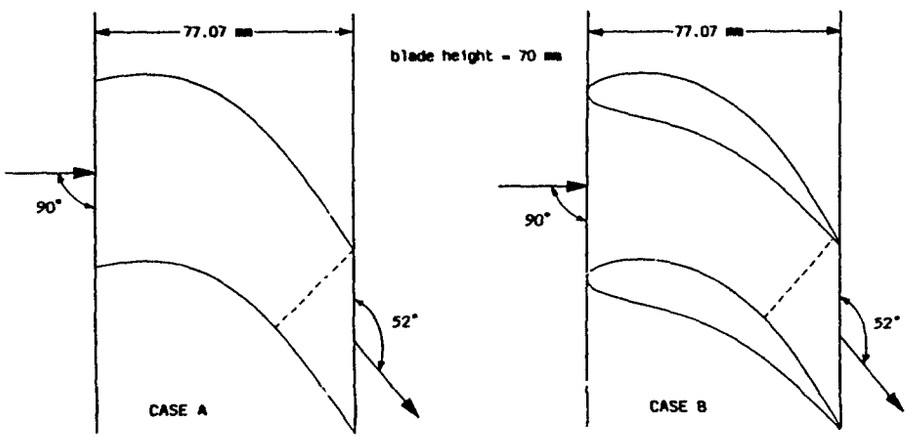


Fig. 16 Profiles of cascades A and B

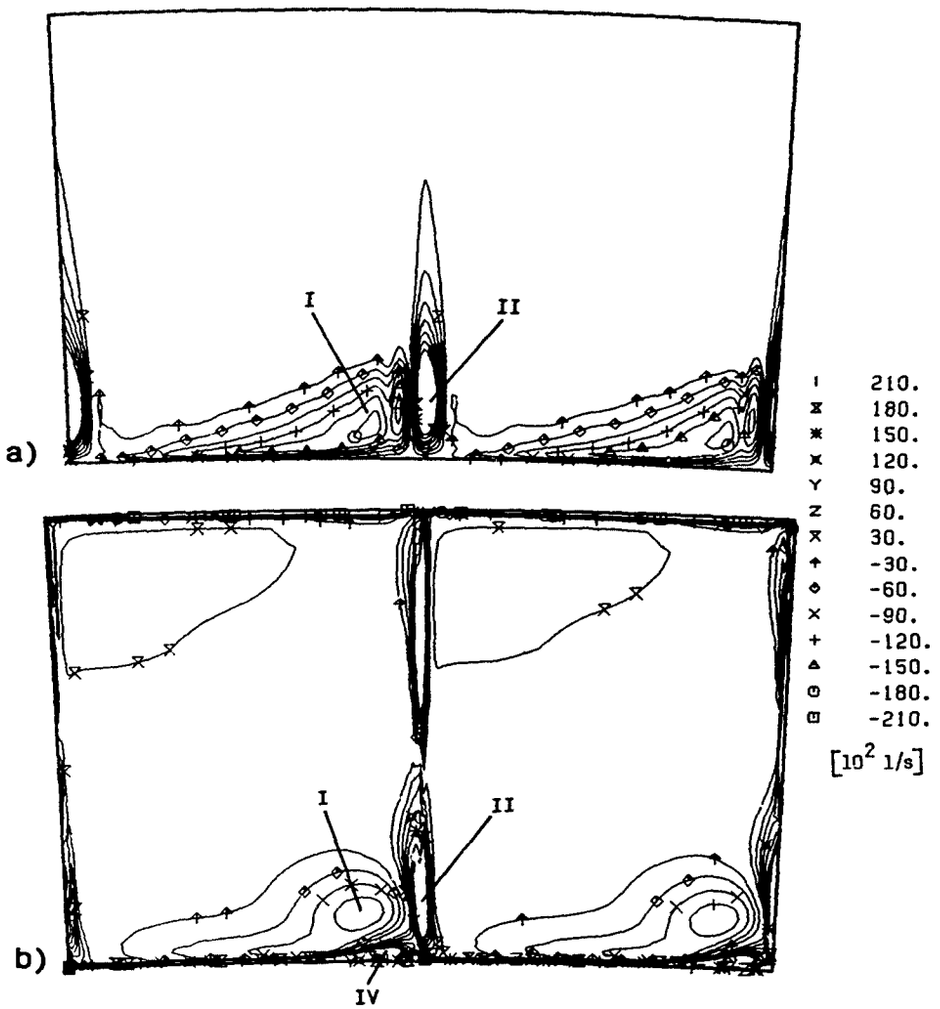


Fig. 17 Secondary vorticity in the exit plane of case A

a) 3-d Euler b) 3-d partially-parabolized Navier-Stokes

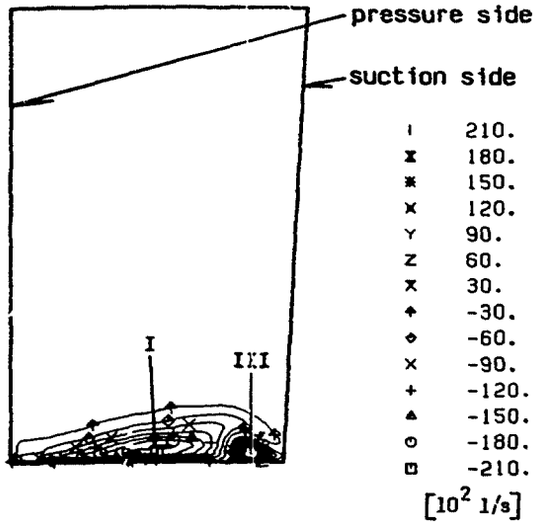


Fig. 18 Secondary vorticity inside the blade passage of case B (3-d Euler) (distance from the leading edge = 65 % axial chord length)

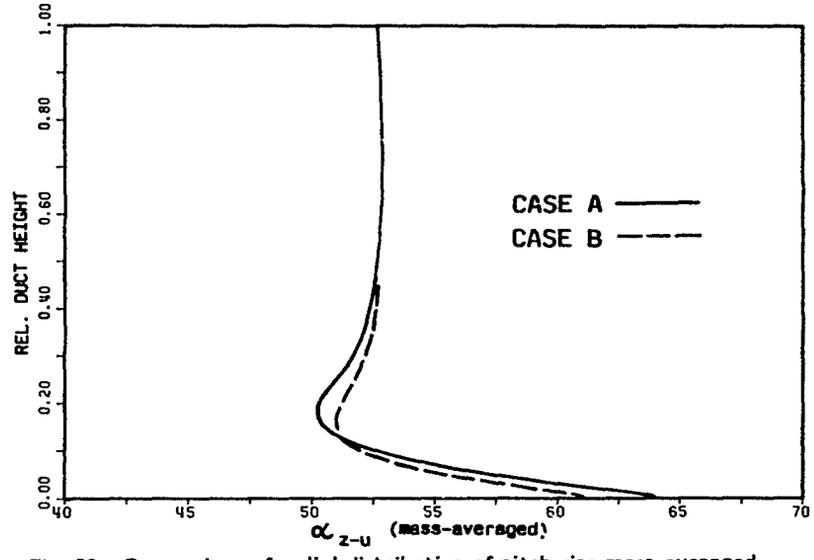


Fig. 20 Comparison of radial distribution of pitchwise mass-averaged flow angle α_{z-u} in the exit plane (Euler solution)

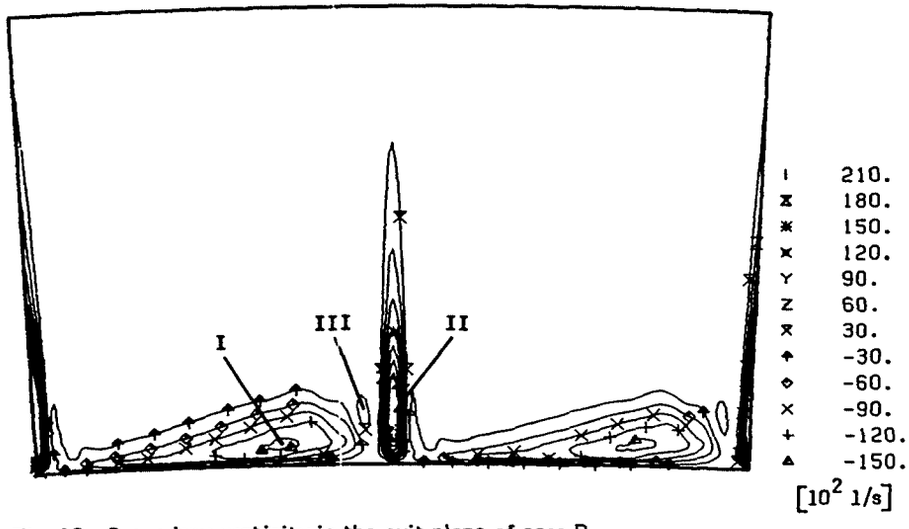


Fig. 19 Secondary vorticity in the exit plane of case B

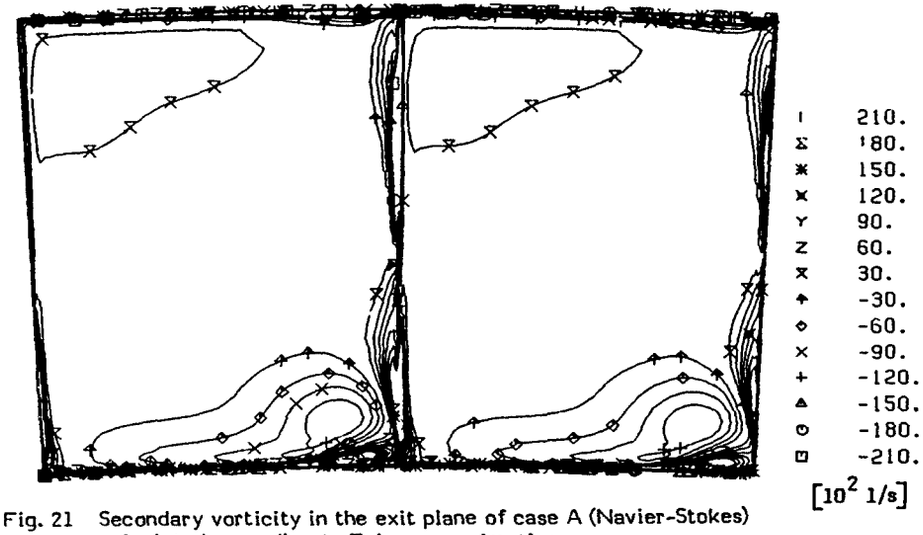


Fig. 21 Secondary vorticity in the exit plane of case A (Navier-Stokes) calculated according to Euler approximation

DISCUSSION

Langston, USA

You state that there is NO horseshoe vortex in Case A. Did you actually see this to be the case by looking at the results within the passage? As an experimentalist, I would expect to see a horseshoe vortex in case A. For example, See Fig 29 of Herzig, Hansend & Castello, NACA report 1163 (1953). They show a cascade of very thin (sheet metal) airfoils a zero angle of attack (zero incidence), very similar to your case A. Their smoke-flow visualization clearly shows evidence of a horseshoe vortex. We tried to point out in an earlier paper[1] that the formation of the horseshoe vortex does not depend on the airfoil leading edge radius, but on the axial chord and angle of attack of the airfoil. Please also see our comments on a paper by John Moore[2] at VPI on the effect of leading edge radius. One other comment concerns the "separate classification" of the passage vortex and the pressure side vortex. They are one-in-the-same. One becomes the other.

(1) Langston, Nice & Hopper, 1977 ASME Journal of Engineering for Power

(2) Moore & Ransmayr, 1984 ASME Part I

Author's Reply:

Thank you for your interesting comments. First of all, let me point out that I did not say that no horseshoe vortex is present for cascade A rather than practically no horseshoe vortex. I do agree with you that in reality (experimentally) of course a horseshoe vortex will be generated in front of the l.e. even if the cascade is composed of very thin blades, because the flow field in the l.e. region will exhibit a stagnation point. It's the associated pressure field which will be responsible for the generation of the horseshoe vortex. The numerical investigation of case A is somewhat different because this cascade consists truly of blades with zero thickness. Because of the inviscid treatment of the flow and the zero incidence, there is no stagnation point in front of the l.e. Possibly, a horseshoe vortex may be generated due to the pressure field caused by the blade loading. In our opinion however, for case A, its strength will be negligibly weak in relationship to the turning of the "shear flow" (passage vortex) and therefore assumed to be of no practical significance. Consequently, we regard the comparison of the flow fields within the two cascades to be meaningful to estimate the contribution of the horseshoe vortex and passage vortex to the secondary flow development in a typical turbine blading, at least qualitatively. Concerning the numerical Euler solution in case A. I was actually saying that no horseshoe vortex is present. This is based on the fact that no suction side leg of the horseshoe vortex was found by analyzing the flow field inside the blade passage (distribution of the various flow quantities in planes at different axial positions, streamlines, etc.). Concerning your last comment on "separate classification" of the passage vortex and the pressure side leg of the horseshoe vortex, I do absolutely agree with you. That is exactly what I wanted to point out during my presentation.

Cambier, France

What are the mesh topology you have used and the number of mesh points, for the Euler and for the Navier-Stokes calculation?

Author's Reply:

	rid	Axial	Radial	Circumferential
IGU Euler	ype	73	37	17
IGU Navier-Stokes	H-type	51	52	26
Cascade A Euler	H-type	73	29	23
Cascade B Euler	C-type	113[1]	29	25[2]

[1] grid points around the blade

[2] grid points in normal direction

Harvey, UK

How many grid points (for the 3D calculations) were within the inlet boundary layers? Also what was the height of the first grid points from the endwalls?

Author's Reply:

In case of the IGV about ten grid points were used in the boundary layers for the Euler calculations and about 20 for the Navier-Stokes calculations. The first grid point had a distance of 1% of the duct height for the Euler and 0.1% for the Navier-Stokes calculations. The numerical resolution of the inlet boundary of cascade A and B was increased for the Euler calculation and consisted of 20 grid points associated with a decreased distance of less than 1% for the first grid point from the side wall.

SECONDARY FLOWS AND REYNOLDS STRESS DISTRIBUTIONS

DOWNSTREAM OF A TURBINE CASCADE AT DIFFERENT EXPANSION RATIOS

Antonio Perdichizzi

Dipartimento di Meccanica
Università di Brescia
Via Valotti 9, 25060 Brescia (Italy)

Marina Ubaldi

Pietro Zunino

Dipartimento di Ingegneria Energetica
Università di Genova
Via Montallegro 1, 16145 Genova (Italy)

SUMMARY

This paper presents the results of an experimental investigation on secondary flows and turbulence in a plane located 30 per cent of an axial chord downstream of a turbine cascade. Mean velocity field, energy loss and Reynolds stress distributions have been measured with pressure and hot wire probes at different expansion ratios for three isentropic outlet Mach numbers M_{2is} = 0.3, 0.5, 0.7.

High levels of turbulence kinetic energy are found in the passage-shed vortex interaction region and in the corner vortex, while lower values are present in the wake. The turbulent shear stress distributions, analysed in details, are consistent with the mean strain field. As the Mach number increases, the turbulence kinetic energy level is significantly reduced. The $\overline{uv}$ and $\overline{vw}$ shear stresses show a similar trend, while the $\overline{uw}$ component remains of the same magnitude, revealing different contributions to the dissipation rate.

NOMENCLATURE

a_w	wire overheating parameter
B	blade axial chord
C	blade chord
H	blade height
H_{12}	boundary layer shape factor
M	Mach number
n,s,z	flow coordinate system, s direction of the undisturbed flow at midspan, n normal, z spanwise direction
p	pressure
q	turbulence kinetic energy coefficient
$Re_{\theta 1}$	Reynolds number based on the upstream boundary layer momentum thickness $Re_{\theta 1} = U_1\theta_1/\nu_1$
Re_{2is}	outlet isentropic Reynolds number based on the chord $Re_{2is} = U_{2is}C/\nu_2$
S	pitch
T	temperature
Tu	turbulence intensity
U, u	mean and fluctuating streamwise velocity components
U_1	upstream freestream velocity
U_{2is}	downstream isentropic velocity
U*	local mean velocity $U^* = \sqrt{U^2 + V^2 + W^2}$
V, v	mean and fluctuating transverse velocity components
W, w	mean and fluctuating spanwise velocity components
X, Y, Z	cascade coordinate system (figure 2)
β	flow angle with axial direction
β'	blade angle with axial direction
γ	stagger angle with axial direction
ζ	energy loss coefficient
θ	boundary layer momentum thickness
ν	laminar kinematic viscosity
ν_T	turbulent kinematic viscosity

Subscripts

e	freestream
is	isentropic condition
MS	midspan
s	static
t	total

1 upstream of the cascade
2 downstream of the cascade

Overbars

— time averaged

1. INTRODUCTION

The extensive flow investigations, performed during the last decade in large scale low speed turbine cascades [1-6], have provided detailed descriptions of secondary flow development and loss distributions and have suggested the guideline for understanding the physical aspects of the phenomenon.

Recently some results on turbulence and Reynolds stress distributions within and downstream of large scale cascades have become available [7-10]. These experimental investigations have clearly shown how turbulence and velocity fields are deeply related, giving further elements for a more thorough comprehension of the secondary flow process and the associated loss production mechanism. Moore et al. [7] identified the work of deformation of the mean motion operated by the Reynolds stress tensor as the main cause of the secondary loss generation.

Due to various experimental difficulties, at present, very few data concerning secondary flows in high subsonic and transonic cascades are available [11-14].

Some results about Mach number influence on vortex configuration, secondary loss production and vorticity distribution downstream of a turbine cascade are provided in [14]. Differences in the flow structure and in the loss generation process were observed even in the range of subsonic compressible flows. For the same cascade an experimental research program is now in progress with the aim of providing detailed results on turbulence and Reynolds stress tensor for expansion ratios ranging from incompressible to high subsonic flows.

The difficulties in obtaining good quality data on Reynolds stress distribution in high velocity tridimensional flows are well known. A large amount of effort was therefore spent to develop and verify the hot wire analysis method, to set up the instrumentation and to automatize all the measurement operations and the data acquisition procedure in order to reduce the large air consumption required for detailed field measurements at high Mach numbers.

The paper presents some first results obtained in a plane located at 30 per cent of an axial chord downstream of the blade trailing edge for three expansion ratios corresponding to M_{2is} = 0.3, 0.5, 0.7.

2. EXPERIMENTAL PROCEDURE

2.1 Experimental apparatus

The investigation was carried out in the transonic cascade test facility of the C.N.P.M. (Centro Nazionale di Propulsione, Milano). It is a blowdown type wind tunnel, fed with compressed air stored in high pressure tanks (200 bar). The tunnel is described in detail in [13]. An air storage capacity of 3100 kg allows for continuous operation for more than 200 s at the maximum flow rate of 12 kg/s. The air is accurately filtered

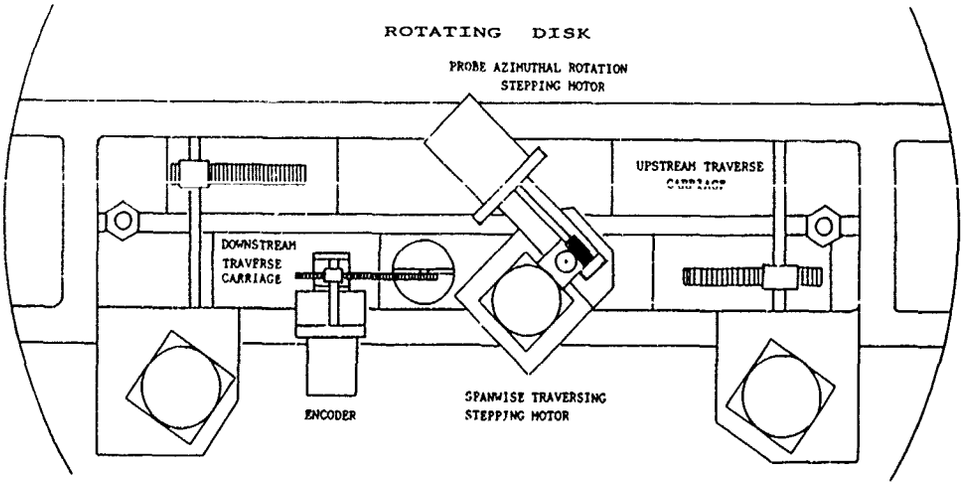


Fig. 1 Probe traversing mechanisms

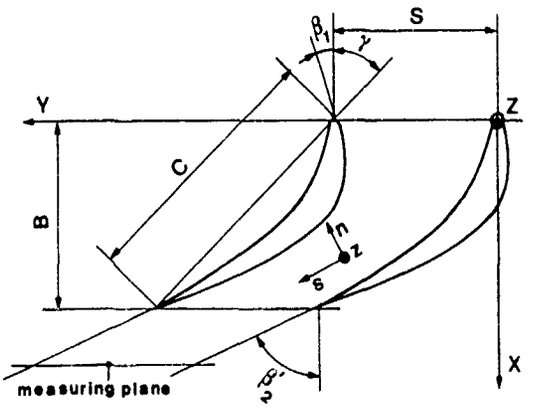


Fig. 2 Cascade geometry

Table 1 : Cascade geometry

Chord length	C	=	47.7	mm
Pitch to chord ratio	S/C	=	0.63	
Aspect ratio	H/C	=	1.05	
Inlet blade angle	β_1'	=	2.6	deg
Outlet blade angle	β_2'	=	66.0	deg
Stagger angle	γ	=	45.2	deg
Number of blades	N	=	12	

to prevent dirt from depositing on cascade and probes. Ten-micrometer pore sintered metal filters were recently installed in the settling chamber just for hot wire measurements.

The test section is 400 mm wide and 50 mm high. It allows installation of a relatively large number of blades (twelve in this case). Blades are mounted on a large rotating disk, that allows inlet flow angle variations and includes the probe traversing carriages. The opposite wall, equipped with static pressure taps, is made of plexiglas to allow easy control of probe positioning.

Cascade periodicity is obtained through an adjustable tailboard, and checked by means of downstream wall static pressure tappings. Two sliders, equipped with eccentric probe holders, allow a continuous selection of upstream and downstream measuring planes.

Data acquisition and probe positioning are fully automated and controlled by a HP 9000/319 microcomputer, to minimize the overall measuring time. Four stepping motors are used to perform the desired probe movements: two for the upstream and downstream pitchwise traverses, one for the spanwise traverse and the last one for the rotation of the probe about its own axis. The pitchwise position is continuously controlled by an encoder and the coordinate is also stored in the computer. The reference condition for the probe azimuthal rotation is obtained with a micrometric turning table. Each step of the probe positioning (translations and rotations) and of the data acquisition procedure was carefully optimized to minimize the overall acquisition time. Typical times for a complete measuring plane (20x10 points) are about 120 s for the five holes probe and 1800 s for the hot wire measurements. A schematical view of the traverse mechanisms is given in figure 1.

2.2 Cascade geometry and test conditions

The airfoil profile is a scaled down model of the midspan section of a steam turbine rotor blade. The profile coordinates are given in [14]. The relevant geometrical data of the cascade, shown in figure 2, are given in table 1.

The inlet flow conditions measured at X/B = -0.8 are given in table 2 for the three investigated isentropic outlet Mach numbers. In figure 3 the inlet Mach number is shown as a function of the isentropic outlet Mach number.

All the tests were performed with the natural turbulent boundary layer developed upstream of the cascade. Velocity profiles and turbulent kinetic energy distributions (figure 4) as well as integral parameters (table 2) remained similar for all the three test conditions.

Table 2: Test conditions

M_{2is}		0.3	0.5	0.7
T_{t1}	(K)	290	290	290
p_{t1}	(bar)	1.09	1.23	1.43
	(mm)	1.72	1.68	1.58
H_{12}		1.26	1.25	1.26
$Re_{\theta 1}$		5600	8400	9700
β_1	(deg)	-17.4	-17.4	-17.4
Tu	freestream	0.025	0.027	0.025
Tu	near wall	0.06	0.06	0.06
$Re_{2is} \cdot 10^6$		0.34	0.61	0.90

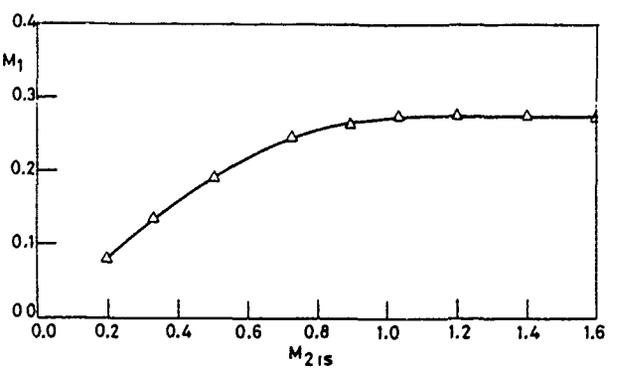


Fig. 3 Inlet Mach number

2.3 Instrumentation

Static pressure and mean velocities, measured by means of a miniature conical five holes probe [14], were used as reference data and for the evaluation of mean kinetic energy losses.

Mean velocities and Reynolds stresses were measured with a hot wire anemometer.The hot wire instrumentation consists of a DANTEC 55M10 constant temperature anemometer and of single sensor miniaturized hot wire probes. The instantaneous hot wire outputs are processed by a digital voltmeter (Solatron 7060) and a true rms voltmeter (HP 3456A) controlled by the HP 9000/319 microcomputer through a IEE488 board. Mean and rms data are stored on line in the computer memory and later analysed to obtain mean velocity and Reynolds stress components. The integration time was progressively reduced to 250 ms without finding differences with results obtained for an integration time of 2 s.

Two miniature hot wire probes, made by modifying DANTEC single sensor normal and slanted probes (models 55P11 and 55P12), are employed. Sensors are tungsten wires 5 μm diameter and 1.5 mm lenght. Standard probes were found to suffer of strain gage effects for Mach numbers larger than .5. On-line FFT of the signal performed by a spectrum analyser (Ono Sokki CF-920) showed disturbance peaks between 25 and 30 kHz. No spikes were detected below M_{2is} = 0.9 in the range 0-50 kHz after reduction of the needles length.

The system frequency response, deduced from a square wave test, was found higher than 50 kHz and therefore adequate in the present study to resolve turbulent disturbances with characteristic wavelengths larger than about one fifth of the upstream boundary layer thickness.

Preliminary tests in the wind tunnel sidewall turbulent boundary layer and power spectra carried out during the field measurements in the downstream plane up to M_{2is} = 0.8, showed that more than 90 per cent of the turbulence kinetic energy is contained within 30 kHz.

In all measurements the hot wires were operated at a high overheat ratio (a_w = 0.9) so that the contribution of total temperature fluctuations to the fluctuating voltage was small and the probe sensed essentially mass flow fluctuations.

The estimated experimental uncertainties are given in table 3. Repeatibility of the hot wire measurements, checked at a number of stations was good and always the results fell within the estimated experimental uncertainties.

2.4 Hot wire measuring technique

The hot wire measuring technique is based on the analysis of the signals of two single hot wire probes, oriented with the primary flow in a plane perpendicular to the probe axis.

For each measuring point, ten readings of mean and rms output voltages (seven for the slanted probe and three for the normal probe) are taken for different azimuth angles about their stems.

The wires were calibrated before and after each measuring session over the range of the wire Reynolds numbers of interest in a free jet calibration tunnel and the coefficients A, B, n of a relation for compressible flow, similar to the King's law for incompressible case, were obtained

$$E^2/(T_w - T_e) = A + B \cdot (\rho U)^n_{eff}$$

Once the operating temperature of the wire T_w is set, this law links the

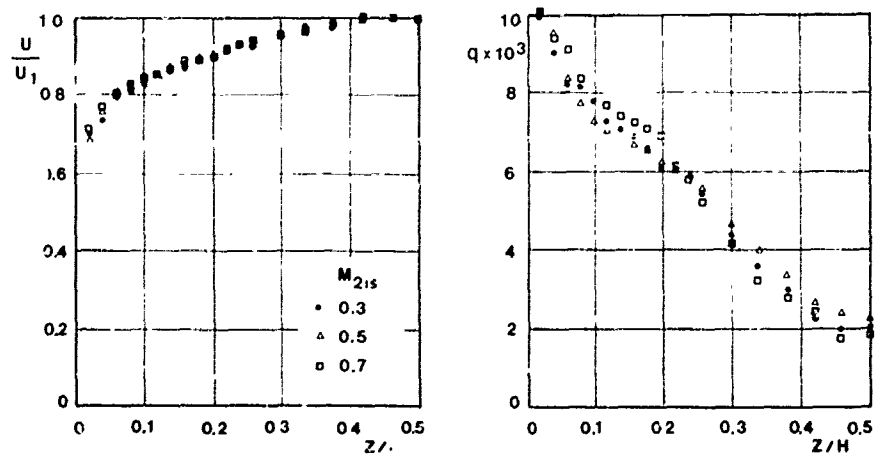


Fig. 4 Inlet boundary layer velocity profiles and turbulent kinetic energy distributions

Table 3: Estimated experimental uncertainties

Pitchwise position	± 0.05	mm
Spanwise position	± 0.1	mm
Stagnation pressure	± 0.5	% of $(p_{t1}-p_{s2})$
Static pressure	± 0.5	% of $(p_{t1}-p_{s2})$
Flow angles from pressure probe	± 0.1	deg
Mean velocity from hot wire	± 3	%
Flow angles from hot wire	± 1.5	deg
Reynolds normal stresses	± 15	%
Reynolds shear stresses	± 20	%

instantaneous output voltage of the anemometer E to the effective cooling mass flux $(\rho U)_{eff}$ of the fluid and allows accounting for the variations, during the experiment, of the equilibrium temperature T_e, that is close to the flow stagnation temperature.

The effective cooling mass flux is assumed to be related to the mass flux components, tangential and normal to the sensor in the plane of the prongs and normal to the sensor and the prongs, by the Jorgensen relationship [15]. The directional sensitivities of the employed probes were carefully investigated at different Mach numbers and flow angles with the aid of a fully automated mechanism for the probe positioning in the calibration tunnel. The directional coefficients of the Jorgensen law were found sensitive to the Reynolds number and to the velocity direction.

The analysis method, that relates mean velocity and Reynolds stress components to mean and rms voltages, is an extension to compressible flows of a previous procedure described in [16]. Through the probe directional coefficients, the mean and rms values of the effective cooling mass fluxes, measured for different probe rotations, are written in function of the mass flux components in a fixed system of coordinates. Two systems of equations are obtained for the mean and fluctuating quantities. These systems, that are over-defined, are solved by means of least squares techniques.

Finally the mean values of density and velocity components are calculated from the mean mass flux components, utilizing the local static pressure values measured by the five holes probe and the total temperature, assumed to be constant, measured upstream of the cascade. To deduce the density fluctuations and the Reynolds stress tensor components from the calculated fluctuating quantities, the ratio of the pressure fluctuation to the mean absolute pressure is assumed to be negligeable, if compared with the density relative fluctuation and the total temperature fluctuations are neglected, because of the nearly adiabatic condition of the flow [17].

3. RESULTS AND DISCUSSION

3.1 Measurement locations, coordinate systems and results

The measuring plane is located downstream of the cascade at X/B = 1.3. Ten pitchwise traverses were made, each of them consisting of twenty equidistant measuring points. Traverses are spaced 4 mm from midspan to 13 mm from the endwall and 2 mm from this position to 1 mm from the endwall.

An intrinsec system of coordinates s, n, z, where s is the direction of the mean velocity at midspan (streamline direction), n is the principal normal (transversal direction) and z is the binormal (spanwise direction) was used for mean velocity vector and Reynolds stress tensor. U, V, W and u, v, w are respectively the mean and fluctuating velocity components in s, n, z directions. The flow coordinate system is shown in figure 2 together with the cascade reference coordinate system (X, Y, Z).

The mean flow field is described in terms of secondary velocity plots and kinetic energy loss coefficient contours in the measuring plane. The secondary velocity vectors are the resultants of the secondary velocity components V and W. The local kinetic energy loss coefficient is defined as

$$\zeta = (U^{\dagger 2}_{2is}(Y,Z) - U^{\dagger 2}_{2}(Y,Z)) / U^{\dagger 2}_{2isMS}$$

and calculated from the pressure probe results.

Turbulence quantities are described as contour plots of the Reynolds stress tensor components, normalized by the squared upstream reference velocity U_1. The coefficient of turbulence kinetic energy q and the turbulence intensity Tu are defined as:

$$q = (u^2 + v^2 + w^2) / U_1^2 \qquad ; \qquad Tu = \sqrt{q/3}$$

The eddy viscosity hypotesis links the Reynolds shear stress components to the mean flow strain tensor by means of the following relations, in streamline curvature and convergence are neglected:

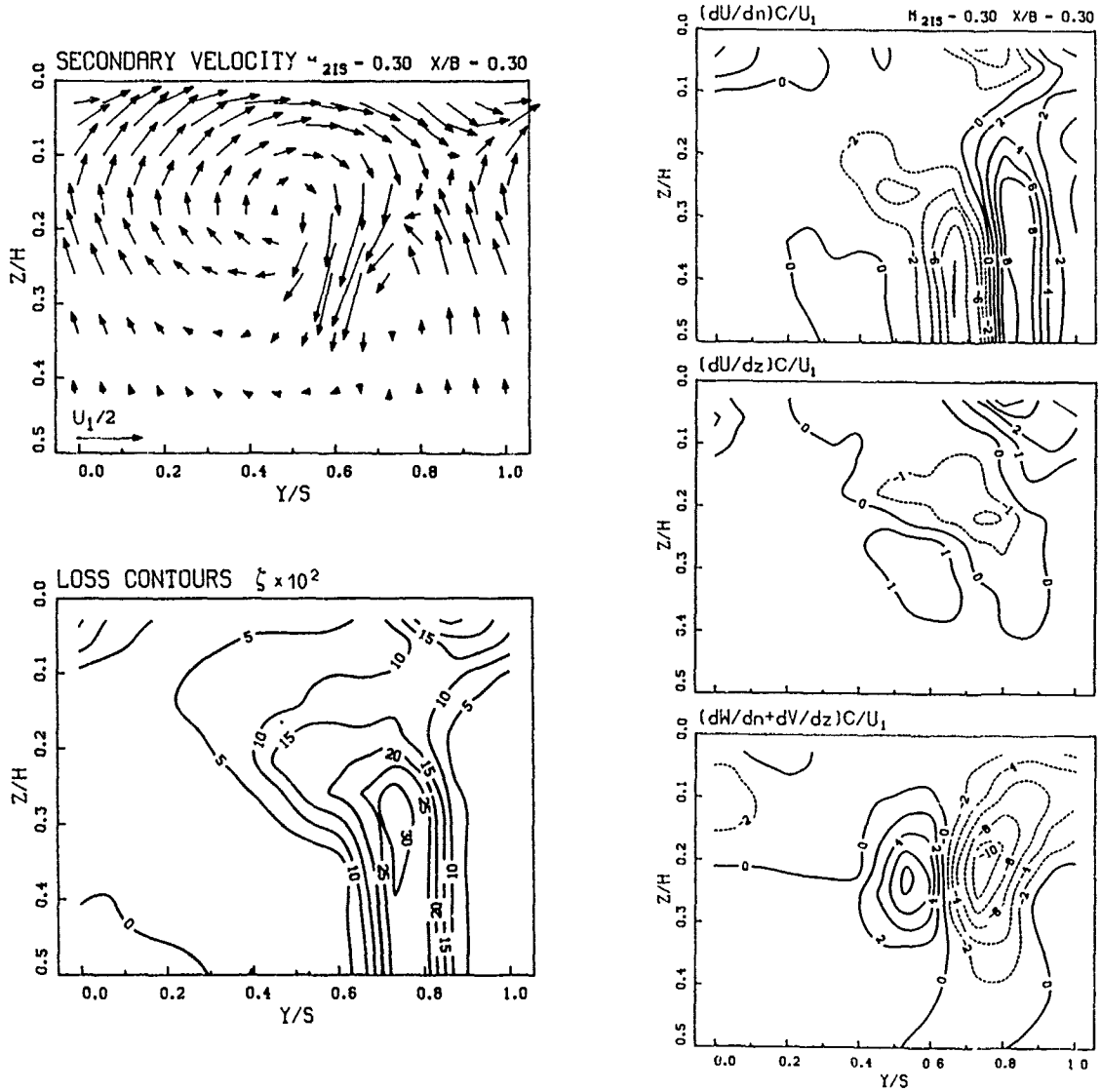


Fig. 5 Secondary velocity vectors, loss contours and mean velocity gradients for $M_{2is} = 0.3$

$$\overline{uv} = -\nu_T \cdot (\partial U/\partial n + \partial V/\partial s) \quad ; \quad \overline{uw} = -\nu_T \cdot (\partial U/\partial z + \partial W/\partial s)$$
$$\overline{vw} = -\nu_T \cdot (\partial V/\partial z + \partial W/\partial n) \qquad (1)$$

From the experimental data pertaining to only one plane, only the spanwise derivatives can be directely calculated. If the assumptions $\partial/\partial s << \partial/\partial n$, $\partial/\partial z$ is made, the transverse derivatives $\partial/\partial n$ can be evaluated from the tangential derivatives $\partial/\partial y$ and the three mean strain components can be approximated by the terms $(\partial U/\partial n)$, $(\partial U/\partial z)$, $(\partial V/\partial z + \partial W/\partial n)$. Contour plots of these quantities in the measuring plane are presented to support the qualitative analysis of the turbulence results.

3.2 Measurements for $M_{2is} = 0.3$

The experimental results for $M_{2is} = 0.3$ are given in fig. 5 and 6 respectively for mean flow and turbulence quantities.

3.2.1 Secondary flow vectors and kinetic energy loss

The secondary flow pattern shows the presence of three well distinct vortices. The clockwise rotating passage vortex occupies a large part of the spacing between two adjacent wakes. Its centre is located near the suction side of the passage, large transverse velocities of about 1/4 of the upstream reference velocity U_1 are found near the endwall. Larger spanwise velocities towards midspan, of the order of $U_1/2$, are present near the suction side of the blade wake, where the passage vortex interacts with an intense shed vortex rotating counterclockwise. Near the endwall, on the pressure side of the wake, the presence of the corner vortex is evident.

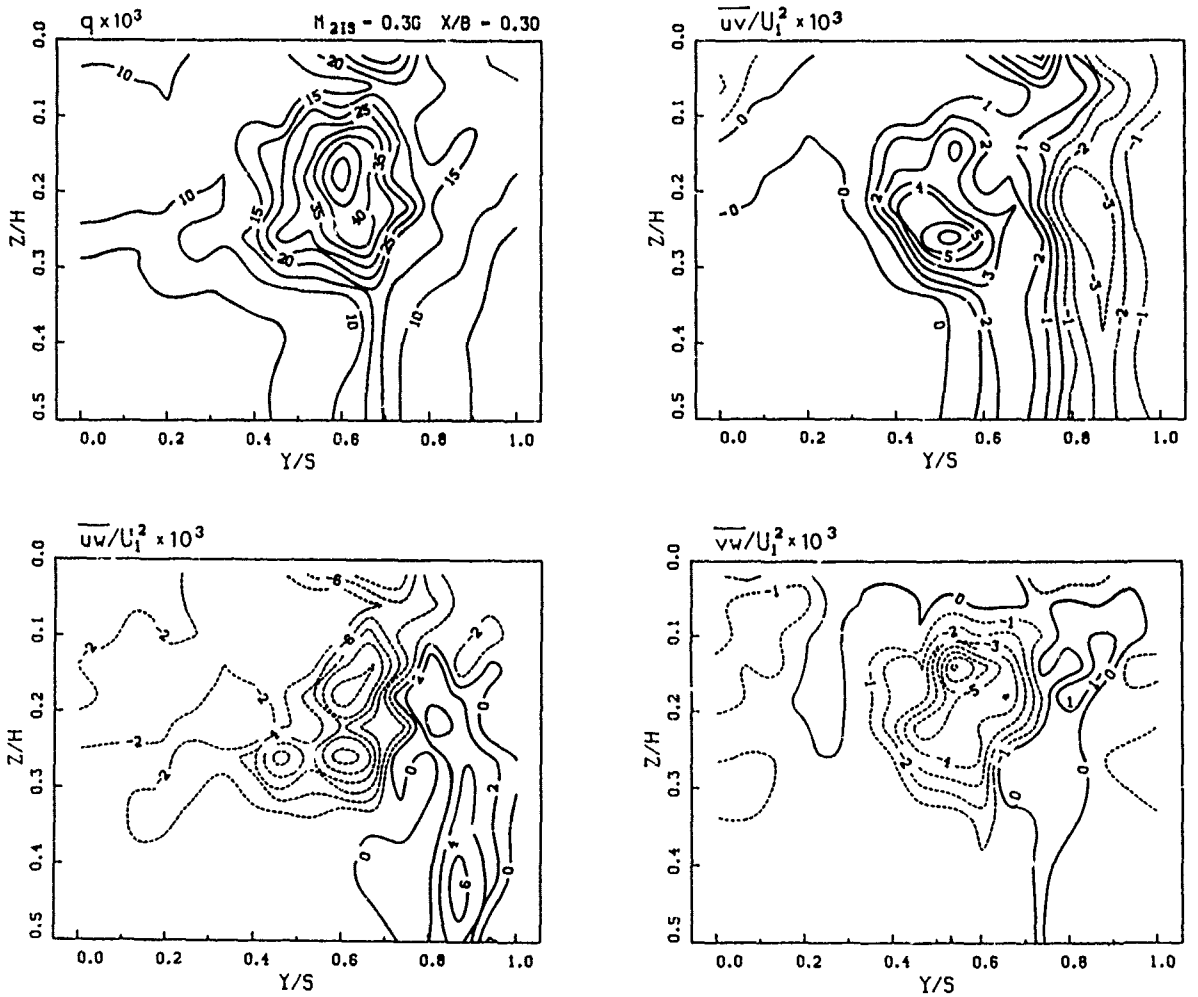


Fig. 6 Turbulence kinetic energy and Reynolds shear stress components for M_{2is} = 0.3

The mean kinetic energy loss coefficient contours identify a wake with high loss values up the 25 per cent of the downstream kinetic energy and show a peak of 30 per cent located at about Z/H = 0.3 and Y/S = 0.75 in a region where the losses generated by the interaction of the passage and the shed vortices may have been convected by the spanwise velocities.

Near the endwall, a second 25 per cent intensity peak is present in the corner vortex region. No distinct loss core related to the passage vortex is found at this plane; on the contrary, a wide zone with fairly large losses, containing the endwall low momentum fluid convected by the passage vortex, occupies all the suction side of the passage and merges into the wake.

3.2.2 Turbulent kinetic energy

Turbulent kinetic energy distribution resembles the mean kinetic energy loss plot, however some significant differences can be noticed. The wake is characterized by relatively low turbulence, that is about of the same intensity of that found in the upstream inlet boundary layer near the endwall (6-7 per cent) . Turbulence intensity on the suction side is higher than on the pressure side of the wake; the wake location is determined from the loss contour plot. This feature indicates a more turbulent development of the boundary layer on the blade suction side than on the pressure side. Midspan free stream turbulence intensity is found to remain of the same order (about 2.5 per cent) as the turbulence at the edge of the upstream inlet boundary layer.

A large and intense core of turbulence kinetic energy is located near the suction side leg of the passage vortex, with a local peak reaching 5 per cent of the reference kinetic energy (corresponding to a turbulence intensity of 13 per cent), that is five time larger than the near wall turbulence kinetic energy in the inlet boundary layer. A second more limited, but still intense, turbulence core is located in the corner vortex region.

The low turbulence intensity in the wake near midspan suggests that rather intense viscous dissipation of the turbulence kinetic energy takes place in the near wake region, upstream of the measuring plane.

The presence of a turbulent kinetic energy core in the passage vortex region may

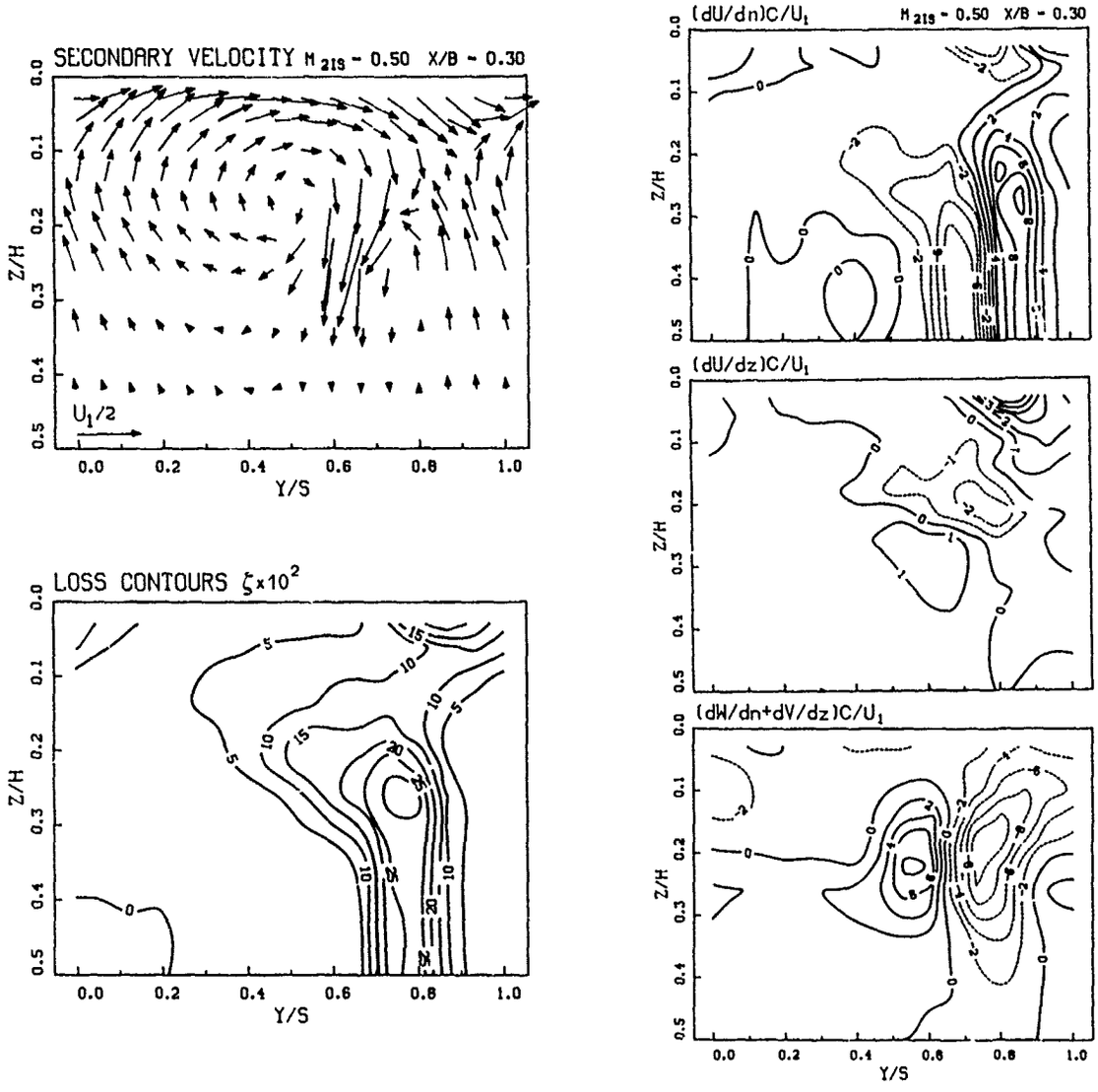


Fig. 7 Secondary velocity vectors, loss contours and mean velocity gradients for $M_{2is} = 0.5$

result from the action of convection operated by the passage vortex on the endwall quantities and by an intense production due to the concentration of Reynolds stresses in a region of relatively large mean velocity gradients. Actually the contour plots of (∂W/∂n +∂V/∂z) in figure 5 and $\overline{vw}$ in figure 6 show high values in this region and, as shown by Moore et al. in [7], the product of these two quantities is an important term in the dissipation mechanism of the secondary mean kinetic energy and hence in the turbulence kinetic energy production process.

3.2.3 Reynolds shear stresses

The $\overline{uv}$ Reynolds shear stress is mainly related to the non uniformity of the primary flow in the pitchwise direction. In the measuring plane, the streamwise flow is perturbed in the pitchwise direction essentially by the presence of the wake and of low momentum fluid associated with passage and corner vortices. Because of the positive direction of the n coordinate from the pressure to the passage suction side, these low momentum regions are characterized by negative transverse derivative ∂U/∂n on the left side, where the velocity decreases, and by positive values on the right side (figure 5). According to relations (1), the $\overline{uv}$ shear stress in figure 6 shows an overall distribution similar to ∂U/∂n, but with opposite sign. The peak values, that are positive and equal to 0.6 per cent of U_1, occur near the suction side leg of the passage vortex and in the corner vortex region, where large concentrations of turbulence kinetic energy were previously observed and where higher values of ν_T can be expected. From a different point of view, the presence of higher values of $\overline{uv}$ in the same region where the high turbulence kinetic energy is present can be explained as the result of similar transport and production mechanisms for both normal and shear stress components.

The $\overline{uw}$ is mainly associated with the non uniformity of the streamwise flow in spanwise direction. In a boundary layer the positive spanwise velocity gradient causes

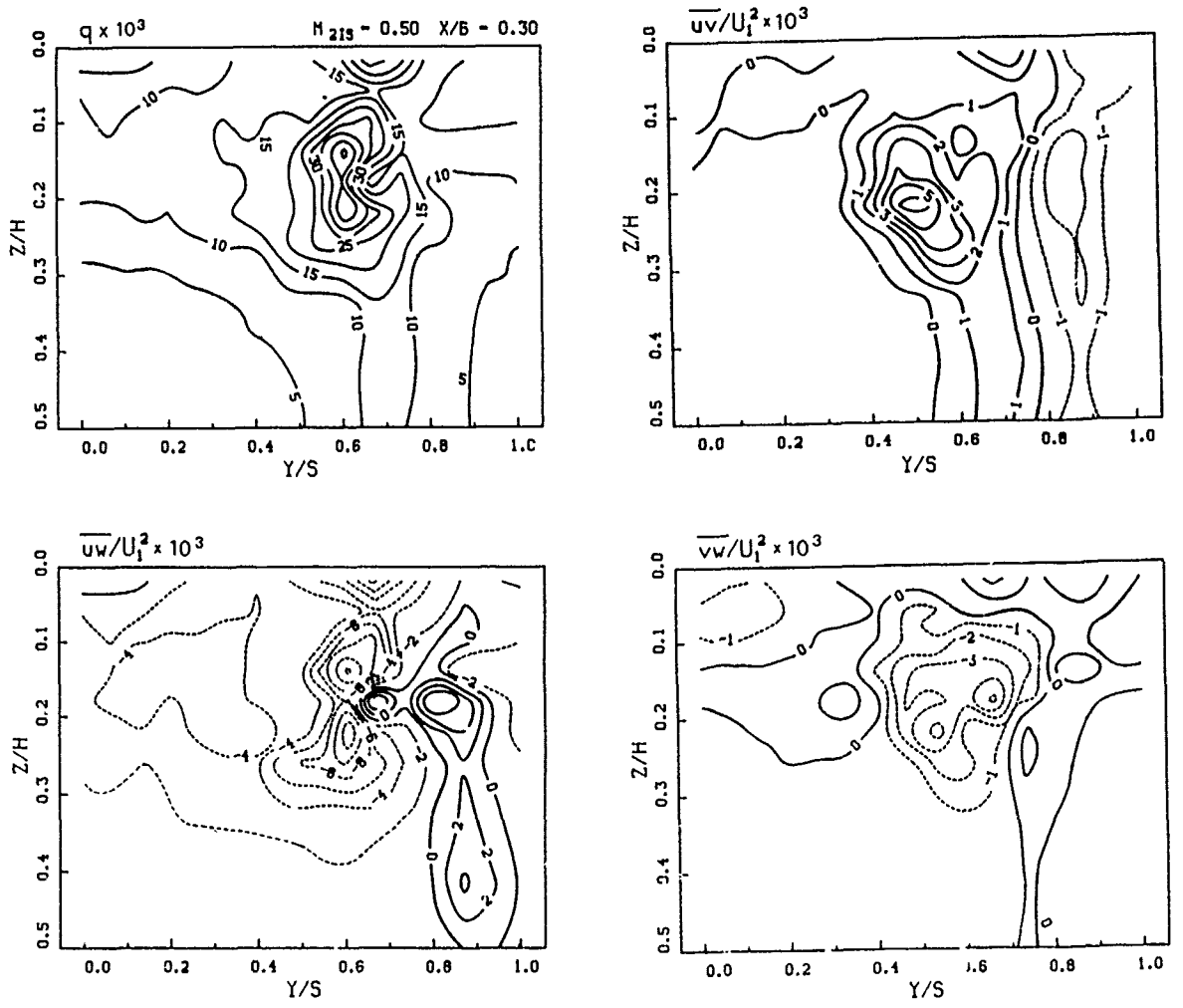


Fig. 8 Turbulence kinetic energy and Reynolds shear stress components for M_{2is} = 0.5

negative values of $\overline{uw}$. In the cascade the endwall boundary layer has been rolled up and convected by the passage vortex. Large negative values of $\overline{uw}$ therefore can be expected in the passage vortex region. However the local spanwise velocity gradients at the measuring plane, shown in fig. 5, are different from those of a boundary layer, because at this station the endwall boundary layer, subjected to a favourable velocity gradient in the cascade and swept by the passage vortex is very thin (less than 2 mm of thickness at mid passage) and therefore the near wall positive spanwise gradient of U cannot be sensed by the probes. The $\partial U/\partial z$ contour plot shows large positive values only in the corner vortex and a broad band of negative values in the region that precedes, in spanwise direction, the loss peak occurring in the wake. These negative derivatives are consistent with a narrow band of positive shear stresses located alongside the blade wake, to which negative values of $\partial W/\partial s$ may also have contributed. The negative $\partial W/\partial s$ derivatives are expected as a result of the decay of the high spanwise velocity W measured in the wake.

The $\overline{vw}$ shear stress is related to the spatial gradient of the secondary velocities in the secondary vorticity plane. In the $\overline{vw}$ distribution three distinct regions can be observed. A first one, showing low positive values near most of the endwall, is consistent with the reduction in spanwise direction of the transverse velocities that occurs near the endwall leg of the passage vortex (negative values of $\partial V/\partial z$ in a region where $\partial W/\partial n$ is low). A large core of high negative vw values is associated with the passage vortex through the inherent positive tranverse gradient of the spanwise velocity W (large positive $\partial W/\partial n$ in a region of low $\partial V/\partial z$). Finally positive contours, displayed along the wake, account for the shed vortex presence that is characterized, in the pressure side of the wake, by negative transverse gradients of the velocity W. This means that there is a significant deformation work associated with this shear stress component acting to dissipate the secondary kinetic energy. The largest values of $\overline{vw}$, that are negative, are located in the region of higher turbulence kinetic energy, just as those of the other shear stresses.

3.3 Tests at different Mach numbers

Tests were made at M_{2is} = 0.3, 0.5 and 0.7. The outlet Mach number variation was

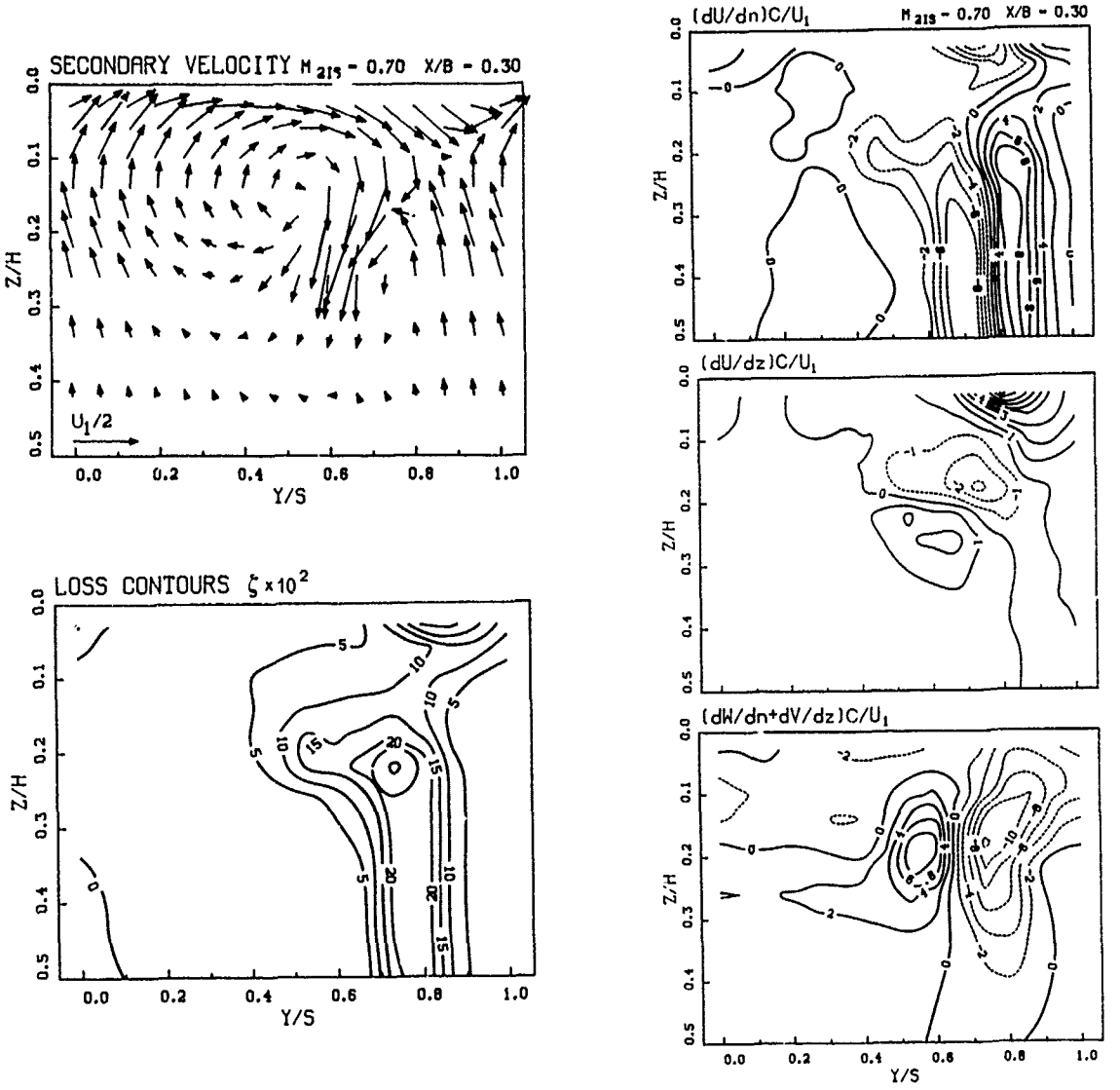


Fig. 9 Secondary velocity vectors, loss contours and mean velocity gradients for M_{2is} = 0.7

obtained by changing the inlet total pressure at nearly constant inlet total temperature and outlet static pressure. The change of the expansion ratio has a direct influence on the outlet Reynolds number and on the streamwise and transverse velocity gradients, which grow considerably, because of the compressibility effect, when the Mach number increases. These gradients are believed to mostly influence the secondary flow development and the outlet flow structure. The inlet boundary layer velocity profiles and the turbulence kinetic energy distributions were found to be quite similar for the three conditions, as shown in figure 4. The experimental results for mean flow and turbulence are given in figures 7 and 8 for M_{2is} = 0.5 and in figures 9 and 10 for M_{2is}= 0.7.

3.3.1 Mean quantities

The comparison of the kinetic energy loss contour plots of figures 5, 7 and 9 indicates that the increase of the expansion ratio results in a progressive reduction of overall losses when referred to the outlet velocities. As M_{2is} increases, the area of corresponding contours is reduced and the positions of the loss cores related to passage and shed vortices are found to be closer to the endwall. The secondary velocity vector plots show a rather similar secondary flow pattern for the three cases. Local velocities in the passage and in the shed vortices are about of the same order if referred to the inlet velocities. The corner vortex, on the contrary, becomes more intense as M_{2is} increases. If secondary velocities are referred to the outlet isentropic velocity, the intensity of the passage and the shed vortices decreases as M_{2is} increases, due to the larger inlet to outlet velocity ratios associated with the higher expansion ratios. This means that for larger Mach numbers secondary kinetic energy is a smaller fraction of the primary outlet kinetic energy. These remarks support the hypotesis that at higher expansion ratios both blade and cascade endwall boundary layers, subject to more

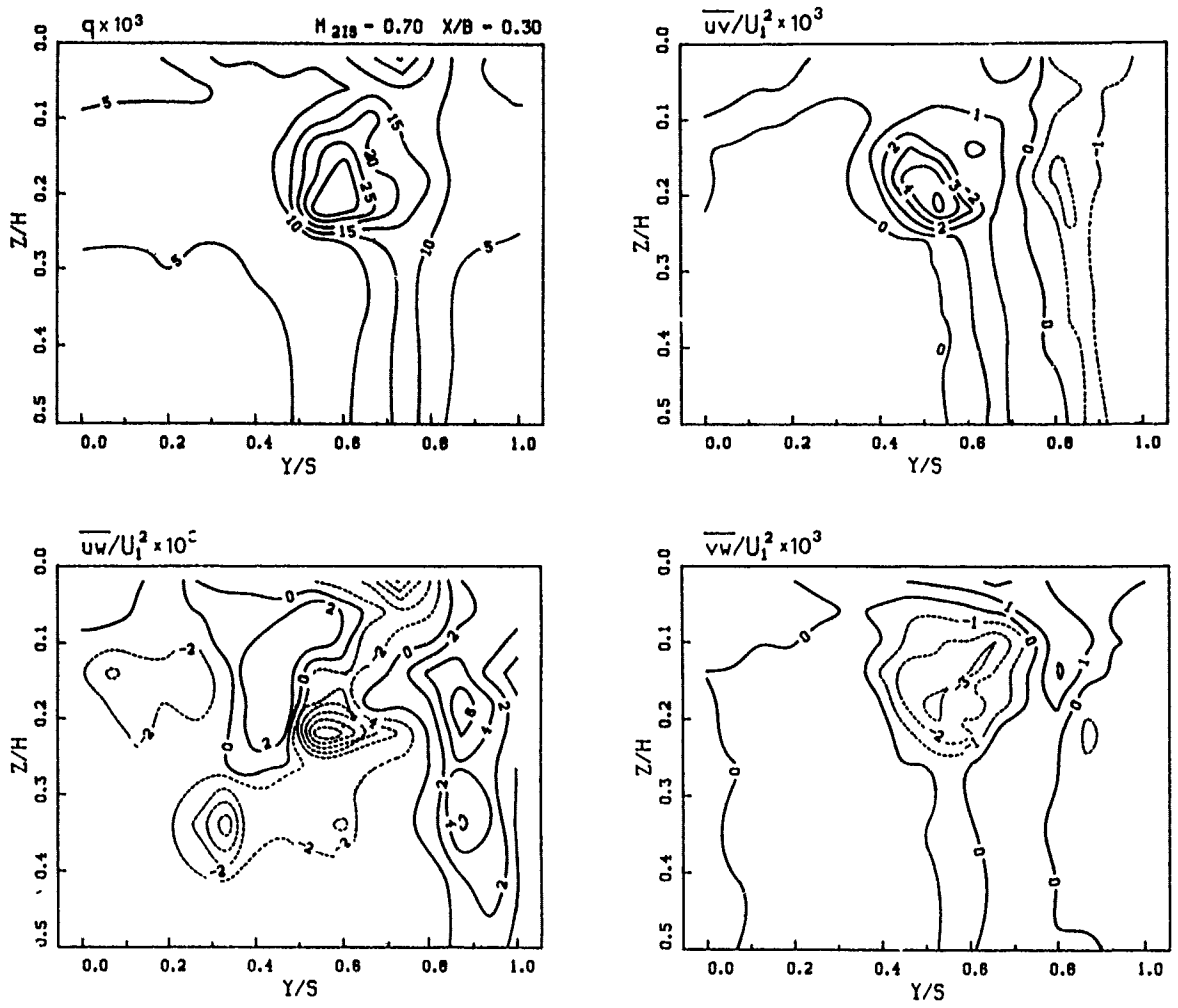


Fig. 10 Turbulence kinetic energy and Reynolds shear stress components for M_{2is} = 0.7

favourable streamwise velocity gradients and larger Reynolds numbers, grow less, resulting in a lower loss level and in a less intense passage vortex.

3.3.2 Turbulent quantities

Comparing turbulent quantities at different Mach numbers (figures 6, 8, 10), some of the previous observations are confirmed.

As M_{2is} increases, turbulence kinetic energy shows a significant reduction and its contours appear weakly displaced towards the endwall. The decrease in turbulence kinetic energy, observed also in the wake near midspan, indicates that larger flow acceleration, related to the higher expansion ratios, has a stabilizing influence on the turbulence in the blade boundary layer, as confirmed by the decreasing trend of the profile losses versus Mach number [14].

The Reynolds shear stress components, also for M_{2is} = 0.5 and 0.7 (figures 8 and 10), are consistent, at least in a qualitative way, with their respective spatial derivatives (figures 7 and 9), as in the case of M_{2is} = 0.3, just examined. Therefore a similar analysis applies, showing both similarities and some differences.

The $\partial U/\partial n$ derivatives of figures 5, 7 and 9 are nearly the same for the three cases examined, the only difference is a weak tendency of the contours to move towards the endwall as M_{2is} increases. Also the associated $\overline{uv}$ shear stress distributions of figures 6,8,10 look very similar and a weak displacement of the isovalue lines appears at higher values of Mach number. In spite of equal levels of mean velocity derivatives the $\overline{uv}$ contour values tend to decrease as M_{2is} increases, in agreement with the reduction of the turbulence kinetic energy observed in the passage vortex core and in the wake.

About the same features characterize the comparison for the $\overline{vw}$ shear stresses and the related velocity spatial derivatives. Here lower levels of $\overline{vw}$ in the passage vortex at constant mean motion deformation may indicate that at higher M_{2is} a less intense secondary kinetic energy decay occurs.

The uw shear stress and the corresponding strain tensor component, on the contrary, show a rather different behaviour as a function of M_{2is}. Both the positive spanwise gradients of U, associated with the corner vortex losses, and the negative ones, related to the relatively high momentum flow, squeezed between the endwall and the mid passage

loss core region, increase as M_{2is} rises. The $\overline{uw}$ shear stresses are about of the same order for all the three test conditions and the corner vortex peak values are even larger for higher M_{2is}, in contrast with the just described decreasing trend displayed by the other turbulent quantities examined. At $M_{2is} = 0.7$ a second region of positive shear stess, that appears near the mid passage, reduces the extension of the negative $\overline{uw}$ regions and tends to split the two negative cores associated with the passage and corner vortices. These positive $\overline{uw}$ shear stresses, acting in a region of negative values of the $\partial U/\partial z$ mean strain component, work to reduce the spanwise nonuniformity of the streamwise velocity, giving a contribution to the dissipation of the primary kinetic energy, not found at lower Mach numbers.

4. CONCLUSIONS

A detailed description of the turbulence field associated with the tridimensional flow in a plane downstream of a turbine cascade for different expansion ratios ranging from incompressible to high subsonic flow has been given.

Turbulence kinetic energy shows similar distributions for all the examined expansion ratios, with an intensity reduction as M_{2is} increases. Concentrations of turbulence kinetic energy are found in the corner vortex and in the passage/shed vortex interaction region, where the passage vortex has convected the endwall turbulence energy and where the larger amount of secondary kinetic energy is being dissipated.

A similar decreasing trend as the expansion rate increases is found for the $\overline{uv}$ and $\overline{vw}$ turbulent shear stresses, that for all the test conditions are consistent with the local gradients of mean velocity. The occurrence of peak values of these two quantities in the regions of larger turbulence intensity suggests that similar transport and production mechanisms have affected both normal and shear stress components. As the expansion ratio increases, the reduction of $\overline{uv}$ and $\overline{vw}$ shear stresses and the nearly constance of the associated mean strains result in a lower rate of dissipation of primary and secondary kinetic energy.

A rather different trend characterizes the $\overline{uw}$ shear stress. At low Mach number its distribution depends more on the convection process, due to the passage vortex, than on the local gradients of mean velocity. As Mach number increases the $\overline{uw}$ components become more consistent with the mean strain and therefore a larger dissipation of the primary kinetic energy is believed to take place.

Further indications confirming these features and giving an organized picture of the expansion ratio effects are expected by a more quantitative analysis performed at different planes.

REFERENCES

[1] Marchal P., Sieverding C.H., "Secondary Flows within Turbomachinery Bladings", in "Secondary Flows in Turbomachines", AGARD CP 214, 1977.

[2] Langston L.S., Nice M.L., Hooper R. M., "Three-Dimensional Flow within a Turbine Cascade Passage", ASME Journal of Engineering for Power, Vol. 99, Jan. 1977, pp. 21-28.

[3] Bario F., Leboeuf F., Papailiou K.D., "Study of Secondary Flows in Blade Cascades of Turbomachines", ASME Journal of Engineering for Power, Vol. 104, Apr. 1982, pp. 497-509.

[4] Gregory-Smith D.G., Graves C.P., "Secondary Flows and Losses in a Turbine Cascade", in "Viscous Effects in Turbomachines, AGARD CP 351, 1983.

[5] Moore J., Adhye R.Y., "Secondary Flows and Losses Downstream of a Turbine Cascade", ASME Journal of Engineering for Gas Turbines and Power, Vol. 107, Oct. 1985, pp. 961-968.

[6] Yamamoto A., "Production and Development of Secondary Flows and Losses in Two Types of Straight Turbine Cascades. Part 1: A Stator Case. Part 2: A Rotor Case", ASME Journal of Turbomachinery, Vol. 108, 1987, pp. 186-200.

[7] Moore J., Shaffer D.M., Moore J.G., "Reynolds Stresses and Dissipation Mechanisms Downstream of a Turbine Cascade", ASME Paper 86-GT-92, 1986.

[8] Zunino P., Ubaldi M., Satta A., "Measurements of Secondary Flows and Turbulence in a Turbine Cascade Passage", ASME Paper 87-GT-132.

[9] Zunino P., Ubaldi M., Satta A., Peisino E., "A Comparison Between Measurements and Turbulence Models in a Turbine Cascade Passage", ASME Paper 88-GT-226.

[10] Gregory-Smith D.G., Graves G.P., Walsh J.A., Fulton K.P., "Turbulence Measurements and Secondary Flows in a Turbine Rotor Cascade", ASME Paper 88-GT-244, 1988.

[11] Sieverding C.H., Wilputte Ph., "Influence of Mach Number and End Wall Cooling on Secondary Flows in a Straight Nozzle Cascade", ASME Journal of Engineering for Power, Vol. 103, Apr. 1981, pp. 257-263.

[12] Hodson H.P., Dominy R.G., "Three-Dimensional Flow in a Low-Pressure Turbine Cascade at Its Design Condition", ASME Journal of Turbomachinery, Vol. 109, Apr. 1987, pp. 177-185.

[13] Bassi F., Perdichizzi A., "Secondary Flow Development Downstream of a Transonic Cascade ", Proceedings 1987 Tokyo Gas Turbine Congress, 1987.
[14] Perdichizzi A., " Mach Number Effects on Secondary Flow Development Downstream of a Turbine Cascade", ASME Paper 89-GT-67, 1989.
[15] Jorgensen F.E., "Directional Sensitivity of Wire and Fiber-film Probes", DISA Information No. 11, May 1971, pp. 31-37.
[16] Zunino P., Ubaldi M., Satta A., "Un metodo per la misura delle velocità medie e delle tensioni di Reynolds in componenti di turbomacchine mediante sonde a filo caldo", Proceedings of the 43rd ATI Congress, Sept. 1988.
[17] Horstman C.C., Rose W.C., "Hot-Wire Anemometry in Transonic Flow", AIAA Journal, Vol. 15, March 1977, pp. 395-401.

ACKNOWLEDGMENTS

The authors are grateful to prof. C. Osnaghi for his precious suggestions.
The authors would like to thank the technical staff of C.N.P.M., C. De Ponti, G.B. Daminelli and C. Guarnieri for the appreciated support to the experimental work. Particular thanks to A. Basa and V. Dossena, students in Mechanical Engineering, for the valuable contribution provided to the research work.
Finally the authors wish to thank F. Tosi Industriale S.p.A. for having provided the cascade.

DISCUSSION

Moore, USA

1. The authors are to be complemented on an excellent piece of experimental work. I believe this can contribute to an improved understanding of turbulence, and to improved models for turbulence in turbine blade rows.

2. Are the authors planning to use their data to test current turbulence models?

Author's Reply:

The authors wish to thank Professor Moore for his kind comment. Measurements in other planes ranging from $x/b = 1.1$ up to 1.9 are planned to be carried out in the near future. We are going to use these data to evaluate the contributions of the deformation work due to Reynolds stresses to the loss production downstream of the cascade. Distributions of quantities like eddy viscosity, mixing length and turbulence production terms will also be evaluated from the experimental data to test current turbulence models.

AN INVESTIGATION OF SECONDARY FLOWS IN NOZZLE GUIDE VANES

R.G. Dominy
School of Engineering and
Applied Science
University of Durham
Durham DH1 3LE
United Kingdom

S.C. Harding
Rolls-Royce plc.
Filton
Bristol BS12 7QE
United Kingdom

SUMMARY

Much of the energy loss that occurs in turbine nozzles is associated with the strongly three-dimensional secondary flows that result from the interaction between the surface boundary layers and the nozzle row with its associated pressure field. A study is made of three alternative nozzles, each performing the same duty, with different degrees of three-dimensionality in their designs to control secondary flows. The chosen nozzle guide vanes are fully representative of the current generation of high hub-tip ratio aero engine nozzles in which the proportion of the overall loss that is attributable to secondary flows is high. A computational analysis of all three nozzles is presented including predictions from three alternative viscous, three-dimensional methods. These detailed measurements and predictions demonstrate the significant influence of the vane geometries on the magnitude and the distribution of the secondary losses.

LIST OF SYMBOLS

C = chord
Cx = axial chord
h = passage height (span)
M = Mach number
p = static pressure
Po = total pressure
Re = Reynolds Number
s = pitch
U = velocity
x = axial distance
y = tangential distance
Y = total pressure loss coefficient
z = spanwise distance
β = pitchwise flow angle (from axial)
δ^* = boundary layer displacement thickness
θ = boundary layer momentum thickness
ρ = density

subscripts

∞ = free stream
1 = inlet
2 = traverse plane
2s = downstream isentropic
3 = pitchwise mixed out
4 = downstream infinity (i.e. pitch & spanwise mixed out)

INTRODUCTION

A part of the loss of available energy that occurs in axial flow turbines arises from the essentially two-dimensional flow of the fluid over the blade sections. Typically this accounts for less than half of the total fluid dynamic loss in the turbine although the proportion varies significantly with turbine geometry. These two dimensional flows have been widely investigated both experimentally and computationally. The remaining 'three-dimensional' losses result from such influences as rotation and radial pressure gradients, tip clearances, seal leakage, heat transfer, interactions between rotors and stators and wall boundary layers. In the absence of tip leakage and rotation effects the blade passage corner flow depends critically upon the boundary layers on the annulus walls at the inlet to the blade row. Secondary flows develop which redistribute the 'old' loss in the inlet boundary layers and which result in the growth of new wall boundary layers with their associated loss generation.

Moves towards higher pressure ratios and higher temperature cycles in modern aero engines result in smaller core mass flows for a given thrust with correspondingly smaller components. This leads to low aspect ratio, high hub/tip ratio designs in which the proportion of the overall loss that is attributable to secondary flows is high. Manufacturers are also driven towards low aspect ratio designs with their associated three dimensional losses by commercial and reliability considerations which require turbines to be designed with the minimum number of vanes and blades. The requirement to be able to control and minimise secondary flows and losses is therefore vitally important.

The existence of secondary flows and loss mechanisms within axial flow turbines has long been recognised and many investigations (e.g. [1]-[4]) have been undertaken to understand these phenomena and their effects. As a result the main parameters which influence the growth of secondary flows and losses are now known (e.g. [5]) even if their relative importance is not fully understood. Thus it is possible to attempt to inhibit their generation by attention to both the overall and detailed design of turbines (e.g. [6],[7]). Methods of controlling three-dimensional losses include end-

wall profiling, leaned and bowed blades, fillets, boundary layer fences and unloading of the blade tips. In many investigations of these effects the results have been inconclusive.

Correlations of secondary loss are available (e.g. [8],[9]) but by their very nature correlations cannot be used to predict ways of reducing new loss generation by the use of detailed blading design beyond the confines of the database from which the correlation is derived.

The redistribution of the inlet boundary layer loss can be predicted with varying degrees of accuracy (e.g. [10],[11]) and numerical computer codes designed to predict the generation of new losses in three-dimensional flows are now available (e.g. [12] - [14]) but these are, as yet, in their infancy.

Although numerous publications are available relating to secondary flow investigations the majority are limited to either incompressible flows (e.g. [15]-[17]) or linear cascades (e.g. [18]-[21]). Those that are relevant to transonic nozzle flows generally make useful additions to the available data but often fail to provide sufficient information to enable detailed validation of prediction methods.

In this investigation secondary flows are studied in nozzles that are fully representative of current designs which incorporate secondary flow control features. Detailed flowfield measurements are presented together with an initial evaluation of the latest generation of viscous, three-dimensional numerical prediction methods. The predictions presented in this study have been generated using the Denton [13], Dawes [14] and Moore [12] codes. The results from the former two methods have been provided by the authors of those codes whilst the predictions from the Moore code have been provided by Rolls-Royce plc [22].

EXPERIMENTAL DETAILS

The experiments described in this report were conducted in the Transonic Cascade Facility of the Whittle Laboratory, Cambridge [23]. The wind tunnel is part of a closed circuit within which the density and pressure ratio can be varied independently. Within the system a new annular cascade research rig has been constructed specifically for this investigation [24]. The air is supplied to the test section via a contraction and a short, parallel duct and is exhausted through a radial diffuser into a large plenum. The general arrangement is shown in figure 1. The scale of the rig was governed largely by the restrictions that were imposed by the available air supply but conveniently this allows an annulus size to be chosen that is representative of the full scale core of a medium sized aero engine (40kN sea level dry static thrust class). Geometric details of the parallel-walled working section and of the three alternative blade designs are given in table 1.

Each cascade contained 34 blades. The first, datum cascade used straight, constant section vanes, each stacked about its centroid (figure 2). The profile selected was designed to operate with an axial inlet flow and to provide a nominal 65 degrees of turning. The aspect ratio was 0.7 and the hub/tip ratio was 0.87. Blade designs 2 and 3 were fully three-dimensional designs in which the blade profiles changed significantly across their spans. In both designs the blade camber at both the hub and the tip was reduced relative to a nominal, mean geometry whilst the camber was correspondingly increased near mid-span. Such an arrangement induces spanwise pressure gradients which distort the secondary flows giving rise, in principal, to a more uniform redistribution of the low energy fluid that is associated with the inlet wall boundary layers as it passes through the blade passages. The cross passage pressure gradients at the walls are also reduced which has a further influence upon the secondary flow behaviour and upon the development of the boundary layers on the hub and casing. Unlike the straight vane the blade section was not constant across the span. However, the two '3-D' blade designs shared the same cross section at each radial station but differed as a result of minor deviations from a nominal stacking about their throats (figure 3).

A single passage of each cascade was instrumented with 0.25mm diameter static pressure tappings which were located at mid-span. Typically between 12 and 20 tappings were located on each surface. Limited static pressure measurements were also made at alternative radial positions. The static pressure tappings at the cascade inlet were located 0.35 axial chord lengths upstream of the cascade leading edge plane. A conventional pitot was positioned at the same axial location. The inlet stagnation temperature (approximately ambient) was measured using a thermocouple located upstream of the contraction and working section.

The small scale of the blade passages and their associated flow phenomena dictated the requirement for probe miniaturisation in order to achieve acceptably high resolution and to minimise any probe induced flowfield disturbances. Considerable effort has therefore been put into the construction of accurate and reliable miniature probes. Four different types of pneumatic probe have been employed during this investigation. The first of these was a fixed-direction, 5-hole, 90 degree conical probe with an overall diameter of 1.85mm. This was used to traverse the cascade exit flowfield at nominal axial locations of 104% C_x and 140% C_x. Calibration of the probe was carried out

in the new transonic probe calibration facility at the Whittle Laboratory [25]. Immediately downstream from the trailing edge plane a five element total pressure rake (tube diameter 0.8mm, spacing 2.0mm) provided further information about the secondary flow field and losses. Within the blade passages only a single, 0.8mm diameter pitot probe was used in order to minimise blockage effects. The fourth type of probe was a flattened pitot, 0.14mm thick, which was used to traverse the blade surface boundary layers and also the wall boundary layers at entry to and exit from the cascades.

The facility is provided with a fully automated, computer controlled data acquisition system. Probe movement, for example, can be achieved using one linear and two angular traverse mechanisms all of which are mutually independent. All pressures are measured using a Scanivalve system.

Oil and dye surface flow patterns were obtained using a mixture of silicone oil and a fluorescent pigment which was photographed under ultraviolet illumination. Two colours were used, one on the blade surfaces and the other on the endwalls upstream from the inlet boundary layer separation line. It was therefore possible to trace the passage of the inlet endwall fluid through the cascade. Where possible this is identified on the black and white photographs reproduced here.

The current investigations were conducted at exit isentropic Mach numbers of 0.83 and 0.95 and at a common value of Re/C of $2.25 \times 10^7 m^{-1}$ corresponding to actual Reynolds numbers of 9×10^5 (Vane 1) and 1.0×10^6 (Vanes 2 and 3). The free-stream turbulence intensity at inlet to the cascade was 0.8%.

Hub Diameter	0.357 m
Tip Diameter	0.412 m
Passage Height	0.028 m
Hub / Tip Ratio	0.867
Annulus Area	0.033 m^2
Number of Blades in Cascade	34
Blade Chord (Vane 1, Constant Section) ...	0.040 m
Axial Chord (Vane 1)	0.025 m
Blade Chord (Vanes 2 & 3 ; mid-span)	0.044 m
Axial Chord (Vanes 2 & 3 ; mid-span)	0.031 m
Inlet Flow Angle	0.0 deg.
Mean Exit Flow Angle (Nominal)	65.0 deg.
Reynolds Number (Vane 1 ; Cascade Exit) ..	9.0×10^5
Reynolds Number (Vane 2,3 ; Cascade Exit).	1.0×10^6
Mach Numbers (at Cascade Exit)	0.83,0.95

Table 1 : Cascade Geometry

RESULTS AND DISCUSSION

Constant Section Vane : Midspan Flow. The measured mid-span isentropic Mach number distribution at the 0.83 exit Mach number condition for the datum, constant section vane is presented in figure 4. These results reveal that the the profile is relatively mid-loaded showing two distinct, suction side velocity peaks, the greater velocity occurring at the more downstream position where the peak suction surface Mach number just exceeds unity. The diffusion that follows the first velocity peak is insufficient to cause the boundary layer to separate but the diffusion at the back of the suction surface gives rise to a short separation bubble near 65% chord. There is no clear evidence of the influence of a shock interaction which would, in any case, be weak. The boundary layer on the suction surface at the trailing edge has the typical characteristics of an attached, turbulent boundary layer with a displacement thickness of 0.27mm (δ^*/C = 0.007) and a momentum thickness of 0.14mm. On the pressure surface continuous acceleration from the blade leading edge results in a laminar boundary layer over the entire surface. At the trailing edge its measured displacement thickness is 0.08mm although in such a thin boundary layer measurement errors are likely to be relatively large. Although the mid-span results may give an indication of the two-dimensional nature of the flow they are of limited value in such a low aspect ratio nozzle where the secondary flows are dominant.

Surface Flow Visualisation. Surface oil flow visualisation in two and three-dimensional flow studies is a well established investigative tool. It is of course recognised that although important and useful, these flow patterns only provide information about the nature of the near surface flow and care must therefore be taken when inferences are made regarding the main body of the flow. Conclusions which are drawn are supported by other measurements or by other investigations of similar phenomena (e.g. [1]-[7],[18]). The general nature of the secondary flow is shown clearly by the blade suction surface flow visualisation (figure 5) at the same flow condition. It is immediately apparent that little, if any, of the surface flow may be considered to be two-dimensional. The spanwise influence of the passage vortices, bounded by a well defined separation lines is clearly visible. In particular the asymmetry of the flow under the influence of the radial pressure gradient that is generated in the nozzle row is evident. At the trailing edge 35% of the blade span is directly influenced by the casing passage vortex compared with less than 20% at the hub

end of the vane. Between these clearly defined secondary flow regions the nominally two-dimensional surface flow is interrupted by a boundary layer separation line running diagonally across the blade. At mid-span the separation line occurs at approximately 65% chord, confirming the interpretation of the surface Mach number distribution. On the hub side of the blade immediately upstream of the separation line is a region of almost radial flow which reflects the low axial momentum of the near-surface flow in this region and the relative strength of the radial pressure gradient.

Inlet Boundary Layer. The velocity profiles of the incoming hub and casing boundary layers, obtained at mid-pitch on the cascade leading edge plane, are plotted in figure 7. The integral parameters of these boundary layers are given in table 2. They were obtained using the compressible form of the appropriate expression or integral. These results show that the upstream boundary layers are turbulent with shape factors (δ^*/θ) of 1.57 and 1.44 on the hub and casing respectively. The corresponding values of displacement thickness-chord ratio (δ^*/C) are 0.006 and 0.008. The boundary layers are thus typical of those found at inlet to model turbines (e.g. [26]) and of those measured by other investigators during cascade studies (e.g. [3],[4]). The relevance of these parameter values in relation to actual turbines remains uncertain since the appropriate data do not appear to exist.

Inlet Mach Number	0.23
Inlet Reynolds Number (based on vane 1 chord) ...	3.25×10^5

	Hub	Casing
Displacement Thickness (mm) ...	0.224	0.327
Momentum Thickness (mm)	0.142	0.228
Shape Factor	1.578	1.436

Table 2 : Inlet Boundary Layers

Exit Flowfield. The truly three-dimensional nature of the flow is revealed by the contours of total pressure loss coefficient ($P_{01} - P_{04}$) / ($P_{04} - p_4$) at exit from the cascade (figure 6). The two passage vortices are clearly defined as is the wake in the nominally two-dimensional flow region between the vortices. The asymmetric nature of the flow resulting from the radial pressure gradient leads to clearer definition of the of the passage vortex near the tip where the flow is 'stretched' across the span than at the hub. At this axial location (104% Cx) the passage vortices confine the '2-D' wake to the region between 20% and 65% span, a result which identically matches the estimate made from the surface flow visualisation. Near the hub there is little distinction between the loss core associated with the passage vortex and the high loss endwall fluid whilst near the tip the two loss regions remain more recognisable. The variation across the span of the pitchwise integrated total pressure loss coefficient deduced from the traverse data of figure 6 is plotted in figure 8. The quantities shown have been obtained by a constant area mixing calculation at each spanwise position. Even though the measurements do not extend right to the wall it is clear that the greatest losses are associated with the endwall fluid. The total pressure loss contours of figure 6 have been integrated over the area of the traverse giving an overall loss of 0.045. A constant area mixing calculation has been used in which the conservation of mass, momentum and energy were employed. The addition of the endwall losses that are not included in the traversed area gives an overall loss of approximately 0.078. These wall losses are based on boundary layer data obtained from multiple traverses by a flat, fixed direction pitot tube. and the overall loss figure should only be taken as an indication of the true loss. Details of the casing flow obtained from the flat pitot data are presented in figure 9. Of particular interest is a distinct region of high loss close against the wall near the mid-pitch position. Evidence of such a feature is also found upstream within the passage itself at 80% Cx although here it is located closer to the suction side of the passage (figure 10). Usually a loss concentration near one endwall may be expected to be swept towards the suction side as the flow proceeds downstream, not towards the pressure side as appears to occur here. Studies of the flow further upstream in an attempt to trace the source of the loss zone are inconclusive. Mid-passage loss cores of this type have been observed by other investigators [27] and whilst arguably of only minor importance in terms of the contribution to the overall loss within the nozzle row much greater significance may be attached to the heat transfer implications. Surface oil flow visualisation provides no indication as to its origin or even to its very existence but a little further evidence of a deviation from a conventional endwall boundary layer may be found in the velocity profile of the casing boundary layer at mid-pitch in the trailing edge plane (figure 11). Typically a turbulent or maybe transitional boundary layer would be expected here and although the integral parameters that are stated match such a boundary layer closer examination reveals the reducing near wall velocity gradient that is usually associated with a boundary layer at the point of separation. No further details relating to this phenomenon were observed.

Further downstream from the cascade where the secondary flows have developed, no longer constrained by the blade surfaces, the centre line of the wake becomes distorted as the fluid rotates. At 140% Cx this is clearly apparent (figure 12) as is the decay of the intense loss cores that were evident closer to the trailing edge. The tip vortex core is seen to have moved radially inwards from 80% span to 70% span whilst the hub

passage vortex shows little sign of radial migration and has merged with the endwall fluid. Further detail is provided by the spanwise loss distribution shown in figure 8. The corresponding variation of pitchwise averaged tangential flow angle is shown in figure 13. The influence of the passage vortices is superimposed upon the general reduction of turning from hub to tip again showing the relatively smaller extent of the influence of the hub side flow. The use of a five-hole probe for these measurements precluded near wall measurements and thus little of the overturning that results from the passage vortices is evident. Nowhere can there reasonably be said to be two-dimensional flow.

'3-D' Results : Vane 2. The three-dimensional geometry of vane design 2 is shown in figure 3. Surface flow visualisation for this vane operating at the same exit isentropic Mach number (0.83) reveals that despite the different appearance of this vane the general nature of the flow, albeit on the surface of the blade only, differs little from that of the datum, constant section vane (figure 14). Again a discontinuity is seen which runs across the centre part of the blade between the boundaries that are imposed by the secondary flows at hub and tip and immediately upstream from the discontinuity is a region of nearly radial (inward) flow signifying low axial momentum of the flow. For this vane it is less clear whether the apparent discontinuity signifies separated flow which very rapidly re-attaches or whether this is just a more extreme example of local low streamwise shear stresses. In figure 4 the mid-span blade surface Mach number distribution reveals a more aft loaded section. The interpretation of this information should be made with caution in view of the changing character of the blade section across its span. At mid-span the velocity peak, which occurs at 50% chord, is followed by an initially gentle diffusion which leads to a separation at approximately 70% chord and almost immediate re-attachment.

The differences between the flowfields generated by this nozzle and the first design become more apparent upon examination of the loss contours just downstream from the trailing edge plane (figure 15). The curvature of the wake is a consequence of the bowed trailing edge that is associated with this particular vane geometry (figure 3). Two features are of particular significance. The first is the much greater containment of the passage vortices within the wake than is achieved using the constant section vane and the second is the apparently reduced endwall loss. Study of the spanwise distribution of the total pressure loss coefficient reveals that a consequence of the partial containment of the loss cores within the wake and the spanwise pressure gradients that are induced by this vane geometry there is a more uniform distribution of the secondary losses across the annulus (figure 16). The integrated total pressure loss derived from these measurements is 0.043. The overall loss including an estimate of the near-wall losses based on limited boundary layer data is 0.068. A comparison of figures 8 and 16 reveals that the effect of unloading the blade tips upon the magnitudes of the endwall losses is dramatic. This latter effect is confirmed by measurements of the casing flow (figure 17) made using a flat pitot probe which show greatly reduced loss in comparison with the measurements presented in figure 9. The results of figure 17 also show how the thickness of the endwall boundary layer varies across the pitch. The variation occurs because the fluid nearest the suction side of the wake will have originated further upstream than that near the pressure side thus allowing greater growth. There is, however, no sign of the near-wall loss concentration that was observed from the corresponding measurements made on the constant section vane. A further effect of reducing the blade camber towards its tips whilst increasing the camber near mid-span is shown by the greatly increased spanwise exit flow angle variation (figure 18) relative to the datum vane.

The effect of increasing the exit isentropic Mach number from 0.83 to 0.95 is demonstrated most clearly by blade suction surface oil flow visualisation (figure 19). At this higher Mach number the separation that occurs over the middle part of the blade between the boundaries imposed by the passage vortices is more clearly defined. The separation occurs at the same chordwise position as it did at the lower Mach number flow condition (approximately 75% chord) but in this case re-attachment is not immediate, there being clear evidence of a closed separation bubble which is bounded by a re-attachment at approximately 81% chord. This is confirmed by the measured mid-span blade surface Mach number distribution (figure 20). This much longer region of separated flow allows the some of the endwall fluid at the casing to migrate towards the hub under the influence of the spanwise pressure gradient. This is shown clearly in the oil flow visualisation photograph (figure 19). Two colour flow visualisation demonstrates that the spanwise surface flow in the separation bubble has its origin in the cascade inlet casing boundary layer. Upstream from the separation line the strong component of radial flow that was evident at the lower Mach number is now absent. The total pressure loss contours (figure 21) and the related spanwise loss distribution measured at 104% Cx (figure 22) are almost indistinguishable from those at the lower Mach number implying that the proportion of the inlet boundary layer fluid that is redistributed across the passage in the separation bubble is small. The integrated loss over the area of the traverse remains almost unchanged at 0.044.

'3-D' Results : Vane 3. The geometry of the third vane is essentially similar to that of the second design, differing only in its stacking. An effect of this re-stacking, which was implemented primarily for mechanical and not aerodynamic reasons, is shown by the mid-span surface Mach number distribution (figure 4). The new distribution has a 'flat-top' character with a much reduced peak Mach number (0.94

compared to 1.00 for vane 2) and consequently less diffusion on the back surface of the blade. The reduced diffusion eliminates the separation that was in evidence in both of the other vanes at this flow condition. This observation is confirmed by oil flow visualisation (figure 23). The differences between the flows relating to these two vanes confirms the need to consider such flows as fully three-dimensional and not simply as a set of independent two-dimensional flows at different radial stations. Figure 24 shows the total pressure loss contours immediately downstream from the trailing edge (104% Cx) which differ from those of figure 15 as a result of the different stacks of the alternative vanes but in other respects, notably the magnitude and position of the secondary flow features there is little difference. Figure 25, showing the spanwise variation of total pressure loss identifies a small radially inward shift of the loss core that is associated with the casing side passage vortex and the integrated loss over the traversed area is a little higher than that of vane 2 at 0.047. There is probably little significance to this apparent loss increase since small positional changes of the area traversed would be sufficient to account for such a difference. Approximations of the losses associated with the endwall fluid outside the traversed area lead to an estimated overall loss of 0.070; a figure which is still significantly less than that of the datum, constant section vane.

'3-D' Viscous Flow Predictions. The calculations presented here have been generated using three alternative, three dimensional viscous codes namely those of Moore and Moore [12,28], Dawes [14] and Denton [13]. The Moore Elliptic Flow Program (MEFP) solves the Navier-Stokes equations in three dimensions using a finite volume method [28]. A rectangular grid is adopted which is deformed to fit the boundaries of the calculation domain. For this study a 58x17x25 grid was used, its size limited by computer capacity. The Dawes approach is also a Navier-Stokes solver using a finite volume method to solve three-dimensional, viscous, compressible flow problems [14]. The Denton method differs by extending a well proven inviscid, three-dimensional time-marching Euler solver to simulate viscous effects by the use of a distributed body force. Predictions have been made for all three cascades using the Moore code whereas only predictions relating to the second vane are available to the author in relation to the Dawes and Denton codes. The latter predictions were performed by the codes respective authors at the Whittle Laboratory, Cambridge using a common data set including the flowfield grid structure and therefore direct comparisons between the two are particularly valid. A denser grid (90x15x29) has been used than for MEFP and this must be taken into consideration when assessing the results. Computations using the Moore code were performed independently by Rolls-Royce plc. All calculations were performed using inlet free-stream turbulence and wall boundary layers to match the experimental measurements. Since this study is primarily concerned with the influence of blade geometry upon the redistribution of the incoming losses and then generation of new losses the most illuminating description of the flowfield is provided by the predicted total pressure loss contours at exit from the blade passage. Figure 26 shows the loss contours predicted by MEFP at 126% Cx for each of the three vane designs at the same, subsonic exit Mach number (approx. 0.8). This lies between the two measurement planes adopted for the experimental investigation. For the constant section vane the secondary flows are clearly underpredicted and as a consequence both the extent of the passage vortices and the distortion of the blade wake which they induce are underestimated. The apparent weakness of the passage vortices is reflected in the corresponding mass averaged spanwise loss distribution (figure 28). A loss peak at 80% span is seen but no distinct loss core is evident at the hub side of the passage where there is a continuous spanwise loss increase from the nominally two-dimensional wake through the endwall fluid to the hub. The mid-span loss is approximately double that recorded experimentally resulting in a close, albeit possibly fortuitous, agreement between the predicted overall loss (7.5%) and the measured value (7.8%). In view of the underprediction of the extent of the secondary flows for the constant section vane it would be surprising if significant information relating to the redistribution of the inlet wall fluid were to be obtained from flowfield predictions for three-dimensional vane designs. In practice, however, the spanwise loss distribution that is presented in figure 28 reveals that this flowfield is more accurately modelled. In particular the loss cores associated with the passage vortices are well defined and they match the measured distribution for vane 2 (figure 16) both in magnitude and position. The calculation also correctly predicts the much reduced endwall losses arising from the less severely loaded tips. Overall the integrated loss over the entire passage is 7.0% , again a figure which closely matches the wind tunnel measurements despite a mid-span loss which remains approximately double the measured value. For both cascades the predicted endwall losses are less than the measured values but, as mentioned previously, the loss measurements close to the wall may only be treated as approximations whilst the accuracy of the calculations near the hub and casing is limited by the chosen grid. The exit flow from the third cascade is also predicted well in terms of the secondary flow distribution relative to the previous two cascades (figure 28). At the hub side of the passage the peak loss associated with the passage vortex increases to 10.5% at 25% span. The corresponding point of peak loss in the measured distribution occurs closer to the hub but is, of course, measured in a plane lying closer to the trailing edge. The measurements suggest that the natural radial migration of the passage vortex loss core is approximately balanced by the radially inward pressure gradient in this cascade.

Calculations have been performed on the second cascade using all three computational methods. Figure 27 shows total pressure loss contours immediately downstream from the trailing edge as predicted by Denton and Dawes. Both methods display passage vortices

extending across a greater spanwise distance than is suggested by MEFP and of the three sets of results it is the Dawes code that generates the most clearly defined vortices. However, in terms of quantitative losses there is little difference between any of the methods. It has already been shown that MEFP generates an acceptable loss distribution across the passage and Dentons results display an even closer resemblance to the experimental data (figure 29). No equivalent data set from the Dawes calculation was available to the author.

Blade suction side velocity vectors for this vane have been derived from the three computational methods (figure 30) and may be compared to the suction side surface oil flow visualisation for this vane (figure 14). MEFP displays only relatively weak radial velocity components relative to both the flow visualisation and the alternative predictions although the scale of the vector plots exaggerates the apparent underestimation. Denton too displays significant radial flows over only the rear half of the blade surface. By far the strongest near-surface radial velocity components and those most closely matched to the flow visualisation are generated by the Dawes code.

CONCLUSIONS

It is shown that three-dimensional considerations in the design of low aspect ratio, transonic nozzle guide vanes allow a significant degree of control over the redistribution of the total pressure losses associated with the incoming wall boundary layers and over the generation of new loss within blade passages. The reduction of the blade loading towards the hub and the tip reduces the cross passage pressure gradients resulting in reduced loss generation at the endwalls. No significant loss increase is observed near mid-span where the blade loading is increased relative to the datum to compensate for the unloaded tips. A further result of the resulting pressure field is to stretch the passage vortices across the span resulting in a more uniform loss distribution across the passage and in a loss distribution that is largely coincident with the blade wake. It may therefore be argued that a downstream rotor experiences a more uniform incident flow across the annulus with high loss fluid spatially confined in the circumferential direction. Acting in opposition to these benefits is a greater variation in the nozzle exit flow angle across the span. The overall loss just downstream from the trailing edge plane is reduced from 7.8% to 6.8% as a result of the three dimensionality of the second vane in relation to the straight, constant section geometry of the first, datum vane. The precise stacking of the blade sections of the three-dimensional design is of less significance in respect of the overall nozzle total pressure loss although differences are observed in the detailed nature of the flow resulting from alternative stacks.

Current three-dimensional, viscous flow calculation methods are shown to identify the secondary flow phenomena that exist in these nozzles. The MEFP code from which the greatest range of predictions were available demonstrates correct comparitive flowfield predictions for straight and contoured vanes although the extent and magnitude of the passage vortices tend to be underestimated. The calculated losses, integrated over the entire passage closely match the measured results although the relative contributions of the losses associated with the nominally two-dimensional wake, the passage vortices and the endwall differ. Both the Denton and particularly the Dawes predictions provide a better representation of the extent of the flow area over which the inlet loss is redistributed at exit from the cascade. For these cascades, where a relatively small proportion of the overall loss is attributed to the inlet flow there is little difference between the three prediction methods in terms of the loss distribution at exit from the cascades. The nominal profile loss at mid-span is overestimated by both of the prediction methods for which these data are available to the author (MEFP and Denton) although the Denton results are closer to the measurements. However direct comparisons between the calculations and the measurements for the nominally two-dimensional mid-span flows may be expected to show such differences because of the fully turbulent condition assumed during the calculations.

For low aspect ratio, highly three-dimensional nozzles guide vanes such as those presented in this study there is little doubt that fully three-dimensional, viscous flow calculations are essential for reliable analysis of the flowfield.

REFERENCES

1. Herzig, H.X., Hansen, A.G. and Costello, G.R., 'A Visualisation Study of Secondary Flows in Cascades', NACA Report 1163, 1953.

2. Sjolander, S.A., 'The Endwall Boundary Layer in an Annular Cascade of Turbine Nozzle Guide Vanes', Carleton University, Canada, TRME/A75-4, 1975.

3. Langston, L.S., Nice, M.L. and Hooper, R.M., 'Three Dimensional Flow Within a Turbine Cascade Passage', ASME J. of Engineering for Power, Vol.99, 1977, pp 21-28.

4. Marchal,P. and Sieverding, C.H., 'Secondary Flows Within Turbmachinery Bladings', AGARD CP-214, Paper No.11, 1977.

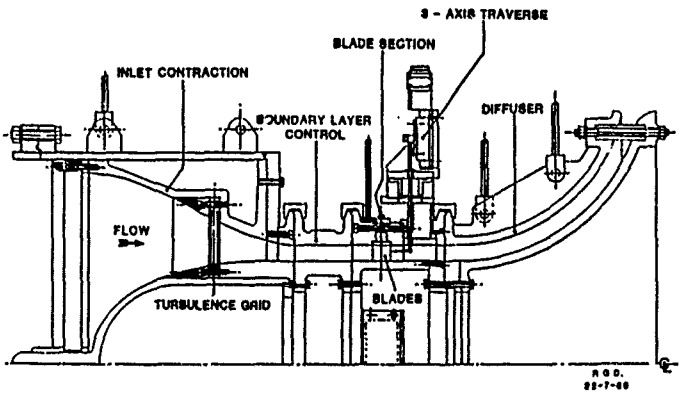
5. Sieverding, C.H., 'Recent Progress in Understanding of Basic Aspects of Secondary Flows in Turbine Blade Passages', ASME paper No. 84-GT-78, 1984.

6. Haas, J.E., 'Analytical and Experimental Investigation of Stator Endwall Contouring in a Small Axial Flow Turbine', NASA Technical Paper 2023, 1982.

7. Atkins, M.J., 'Endwall Profiling in Axial Flow Turbines', Ph.D. Thesis, Cambridge, U.K. 1985.
8. Dunham, J., 'A Review of Cascade Data on Secondary Losses in Turbines', J. Mech. Eng. Sci., Vol.12, No.1, 1970, pp. 48-59.
9. Dunham, J. and Came, P.M., 'Improvements to the Ainley-Mathieson Method of Turbine Performance Prediction', ASME J. of Engineering for Power, Vol.92, 1970, pp. 252-256.
10. Hawthorne, W.R., 'Secondary Circulation in Fluid Flow', Proc. R. Soc., Vol.206, 1951, pp. 374-387.
11. Denton, J.D., 'An Improved Time Marching Method For Turbomachinery Flow Calculation', ASME J. of Engineering for Power, Vol.105, 1983, pp. 514-524.
12. Moore, J. and Moore, J.G., 'A Calculation Proceedure for Three Dimensional Viscous Compressible Duct Flow', ASME J. of Fluids Eng., Vol.101, 1979, p415.
13. Denton, J.D., 'The Use of a Distributed Body Force to Simulate Viscous Effects in 3D Flow Calculations', ASME Paper No. 86-GT-144, 1986.
14. Dawes, W.N., 'Application of Full Navier-Stokes Solvers to Turbomachinery Flow Problems', VKI Lecture Series 1986-02, 1986.
15. Boletis, E., 'Effects of Tip Endwall Contouring on the Three-Dimensional Flow Field in an Annular Turbine Nozzle Vane : Part 1 - Experimental Investigation', ASME Paper No. 85-GT-71, 1985.
16. Sieverding, C.H., Van Hove, W. and Boletis, E., 'Experimental Study of the Three-Dimensional Flow Field in an Annular Turbine Nozzle Guidevane', ASME Paper No. 83-GT-120, 1983.
17. Yamamoto, A. and Yanagi, R., 'Production and Development of Secondary Flows Within a Three-Dimensional Turbine Stator Cascade', ASME Paper No. 85-GT-217, 1985.
18. Hodson, H.P. and Dominy, R.G., 'Three-Dimensional Flow in a Low-Pressure Turbine Cascade at its Design Condition', ASME Paper 86-GT-106, 1986.
19. Hodson, H.P. and Dominy, R.G., 'The Off-Design Performance of a Low-Pressure Turbine Cascade', ASME Paper No. 86-GT-188, 1986.
20. Moore,J. and Adhye, R.Y., 'Secondary Flows and Losses Downstream of a Turbine Cascade', ASME Paper No. 85-GT-64, 1985.
21. Sonoda, T., 'Experimental Investigation on Spatial Development of Streamwise Vortices in a Turbine Inlet Guide Vane Cascade', ASME Paper No. 85-GT-20, 1985.
22. Rolls-Royce plc. Private Communication.
23. Gostelow, J.P. and Watson, P.J., 'A Closed Circuit Variable Density Air Supply for Turbomachinery Research', ASME Paper No. 76-GT-62, 1976.
24. Dominy, R.G., 'The Whittle Laboratory Transonic Annular Cascade Wind Tunnel', 9th Symposium on Measuring Techniques for Transonic and Supersonic Flow In Cascades and Turbomachines, Oxford. U.K., 1988.
25. Hodson, H.P. and Dominy, R.G., 'An Investigation Into the Effects of Reynolds Number and Turbulence upon the Calibration of 5-Hole Cone Probes', 9th Symposium on Measuring Techniques for Transonic and Supersonic Flow In Cascades and Turbomachines, Oxford. U.K., 1988.
26. Hunter, I.H., 'Endwall Boundary Layer Flows and Losses in an Axial Turbine Stage', ASME J. of Engineering for Power, Vol.104, 1982, pp. 184-193.
27. Rolls-Royce plc. Private Communication.
28. Northall, J.D., Moore, J.G. and Moore, J., 'Three-Dimensional Viscous Flow Calculations for Loss Prediction in Turbine Blade Rows', I.Mech.E. 'Turbomachinery-Efficiency Prediction and Improvement', 1987, pp 63-72.

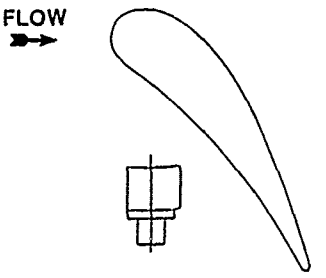
ACKNOWLEDGEMENT

The work described was supported by Rolls-Royce plc. and the British Science and Engineering Research Council. The contributions of Dr.J.D.Denton and Dr.W.N.Dawes are greatly appreciated.



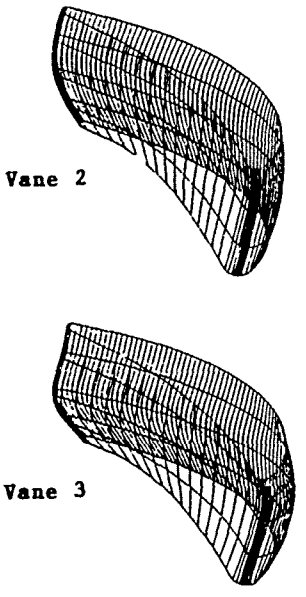
The Whittle Laboratory Transonic Annular Cascade Rig

Figure 1



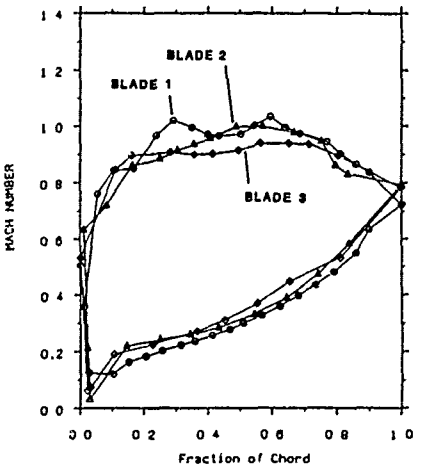
Constant Section Vane Geometry

Figure 2



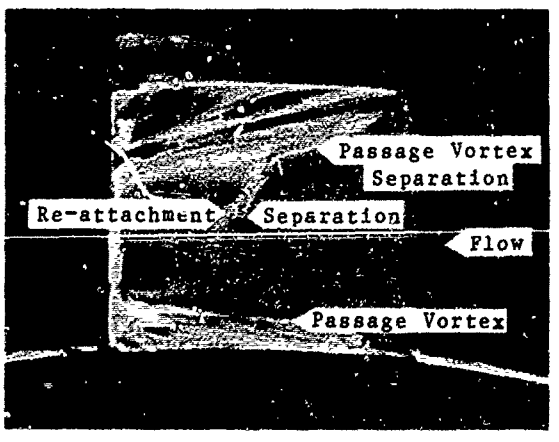
3-D Vane Geometries

Figure 3



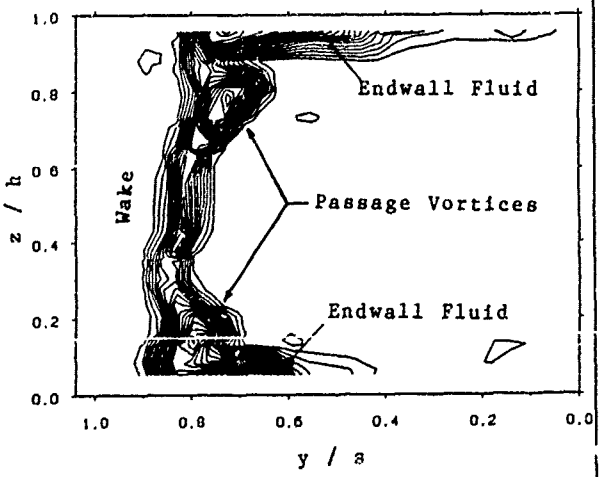
Measured Blade Surface Mach Number Distributions (M_2 = 0.83)

Figure 4



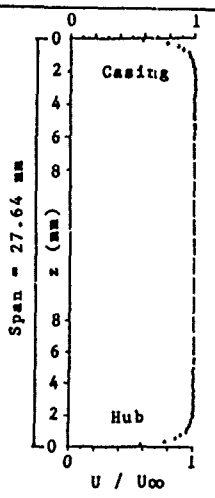
Suction Surface Flow Visualisation Viewed in Axial Direction From Downstream (Vane 1, M_2 = 0.82)

Figure 5



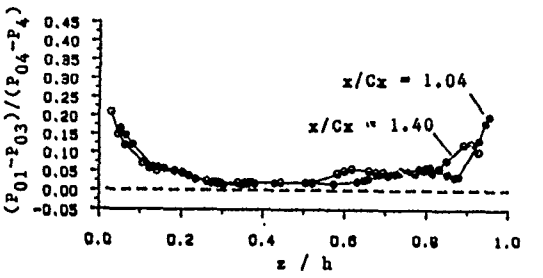
Measured Total Pressure Loss Coefficient Contours (Vane 1, x/Cx = 1.04, Contour Interval = 0.03, M_2 = 0.83)

Figure 6



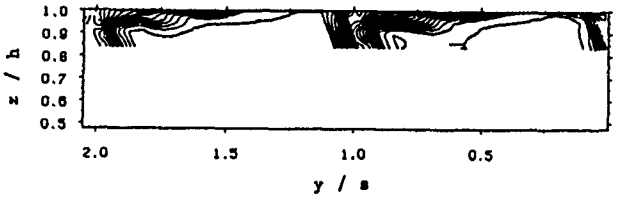
Inlet Boundary Layers

Figure 7



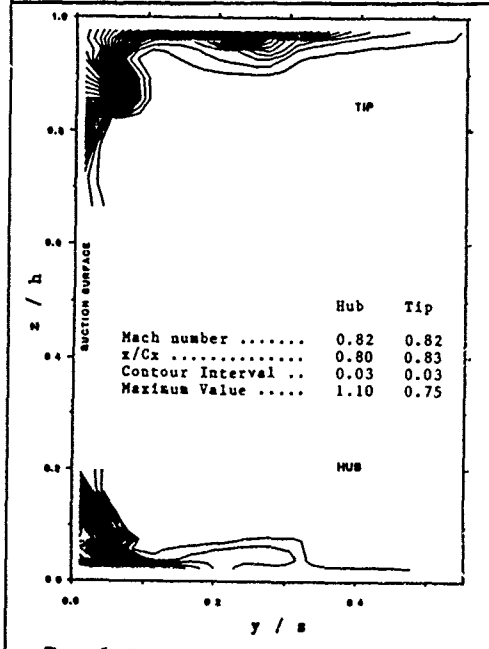
Spanwise Mixed-out Stagnation Pressure Loss
(Vane 1, M2 = 0.83)

Figure 8



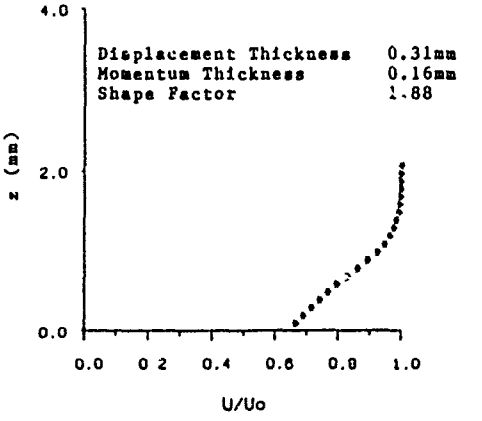
Near Casing Total Pressure Loss Coefficient Contours
(Vane 1, M_2=0.83, x/Cx=1.12, Contour Interval=0.03)

Figure 9



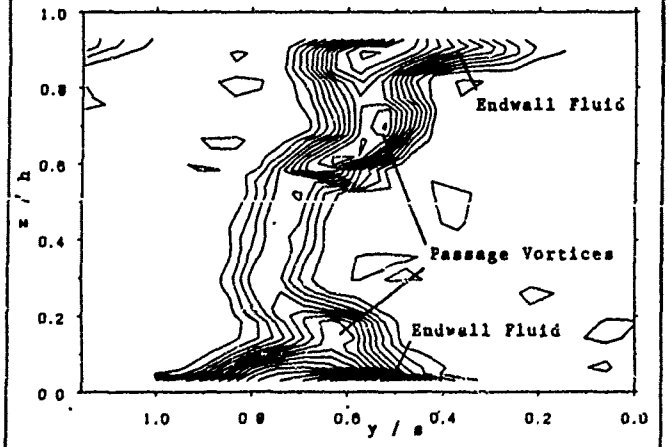
Total Pressure Loss Coefficient Contours

Figure 10



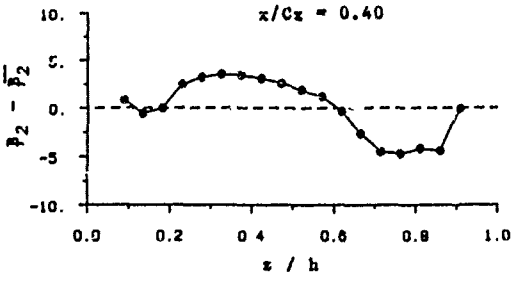
Mid-Pitch Casing Boundary Layer
(Vane 1, x/Cx = 1.00, M_2 = 0.83)

Figure 11



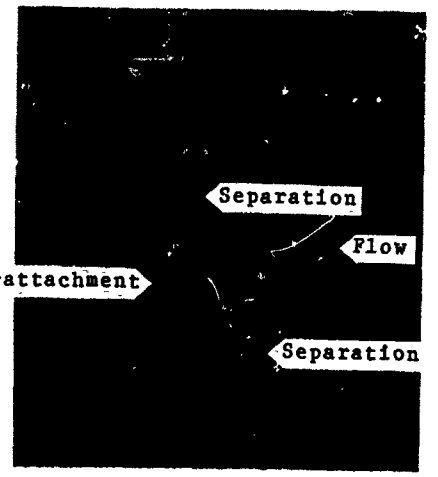
Total Pressure Loss Coefficient Contours
(Vane 1, x/Cx=1.40, Contour Interval=0.03, M_2=0.83)

Figure 12



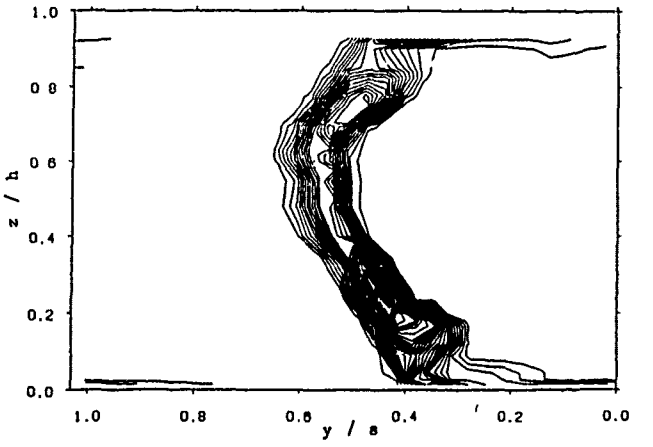
Spanwise Variation Of Pitchwise Flow Angle
(Vane 1, M_2=0.83)

Figure 13



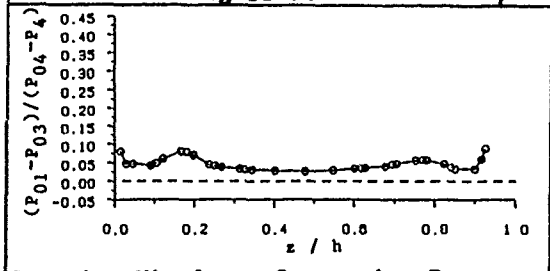
Suction Surface Flow Visualisation
(Vane 2, M_2=0.82)

Figure 14



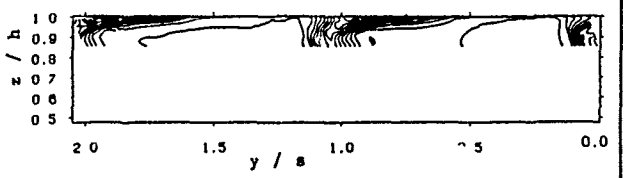
Total Pressure Loss Coefficient Contours
(Vane 2, x/Cx=1.04, Contour Int.=0.03, M_2=0.83)

Figure 15



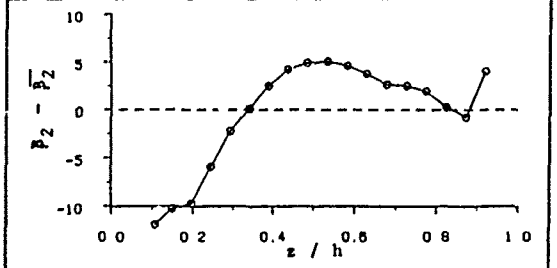
Spanwise Mixed-out Stagnation Pressure Loss (Vane 2, M_2=0.83, x/Cx=1.04)

Figure 16



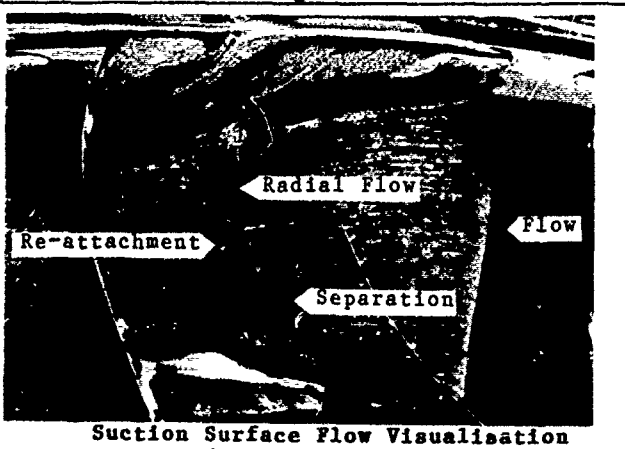
Near Casing Total Pressure Loss Coefficient
(Vane 2, M_2=0.83, x/Cx=1.10, Contour Int.=0.03)

Figure 17



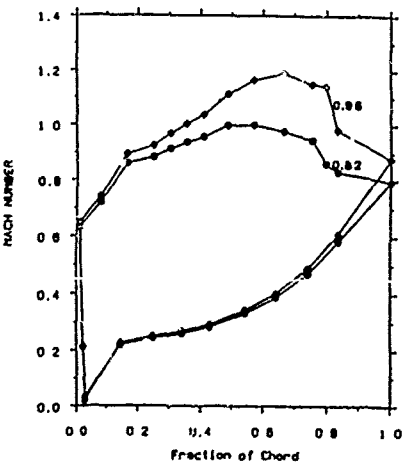
Spanwise Variation of Pitchwise Flow Angle (Vane 2, M_2=0.83, x/Cx=1.04)

Figure 18



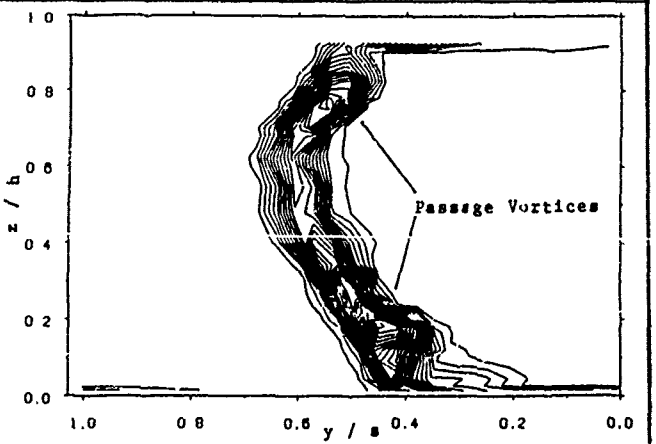
Suction Surface Flow Visualisation
(Vane 2, M_2=0.95)

Figure 19



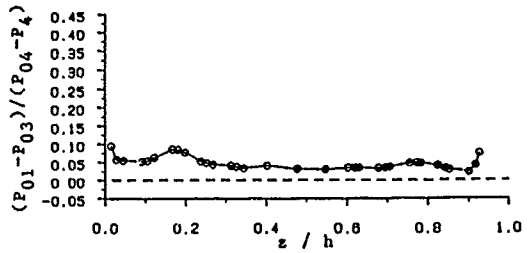
Measured Blade Surface Mach Number Distribution (Vane 2)

Figure 20



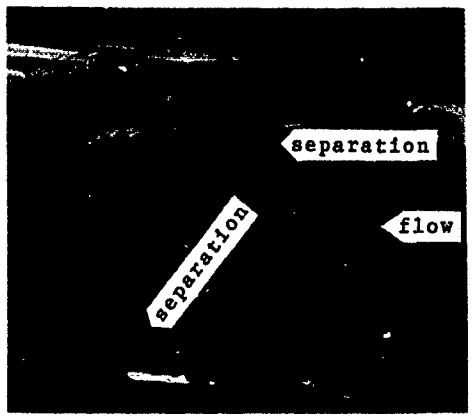
Total Pressure Loss Coefficient Contours
(Vane 2, x/Cx=1.04, Contour Int.=0.03, M_2=0.95)

Figure 21



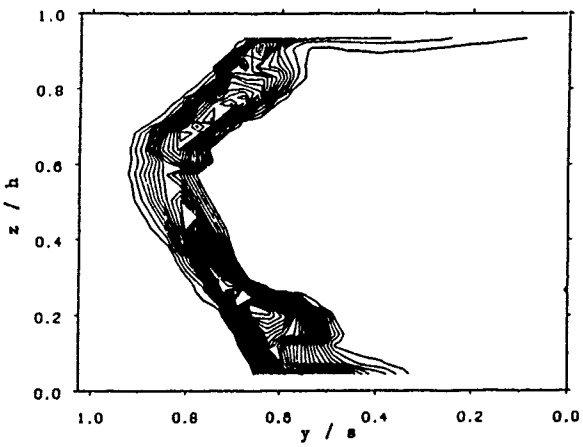
Spanwise Mixed-out Stagnation Pressure Loss (Vane 2, M_2=0.95, x/Cx=1.04)

Figure 22



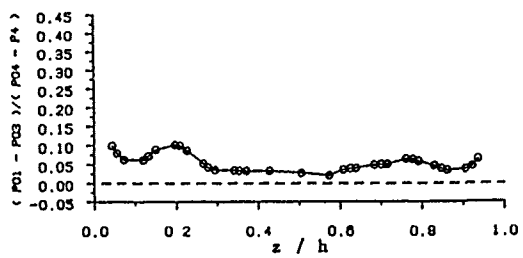
Suction Surface Flow Visualisation (Vane 3, M_2=0.83)

Figure 23



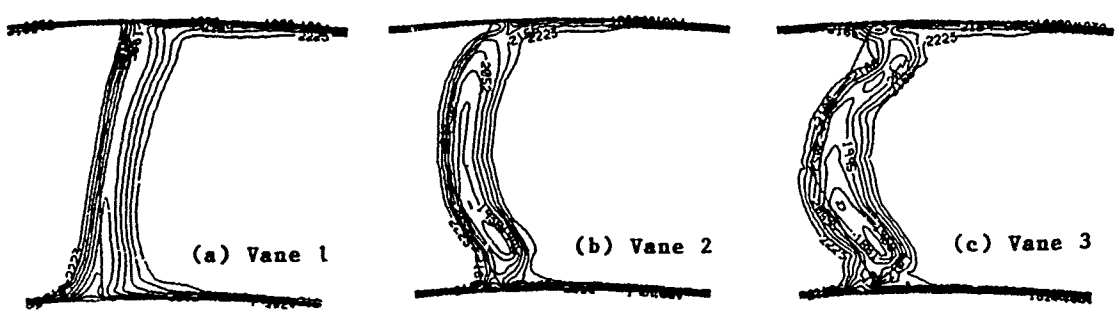
Total Pressure Loss Coefficient Contours (Vane 3, x/Cx=1.04, contour Int.=0.03, M_2=0.83)

Figure 24



Spanwise Mixed-out Stagnation Pressure Loss (Vane 3, M_2=0.83, x/Cx=1.04)

Figure 25



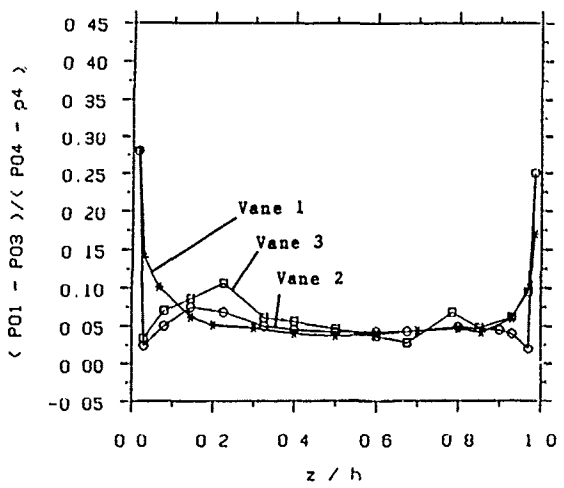
Total Pressure Loss Contours : MEFP (z/Cx=1.26)

Figure 26



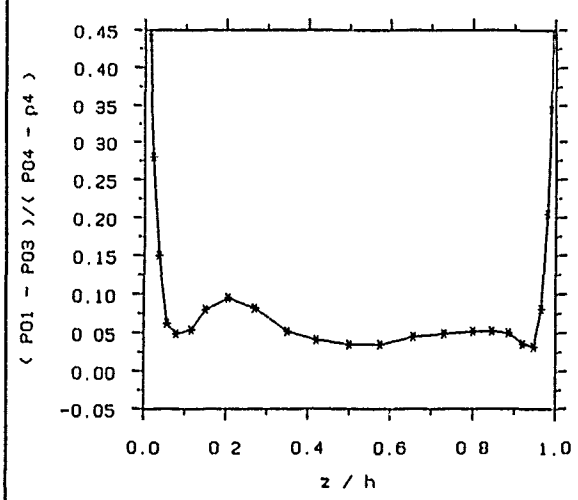
Total Pressure Loss Contours (Vane 2, x/Cx=1.02, M_2=0.83)

Figure 27



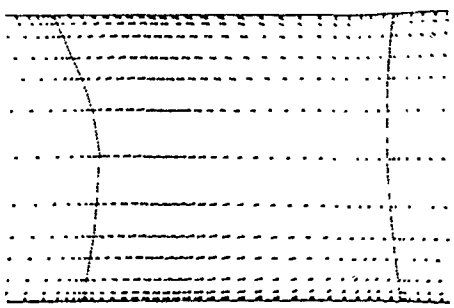
MEFP : Spanwise Mixed-out Stagnation Pressure Loss (x/Cx=1.26)

Figure 28

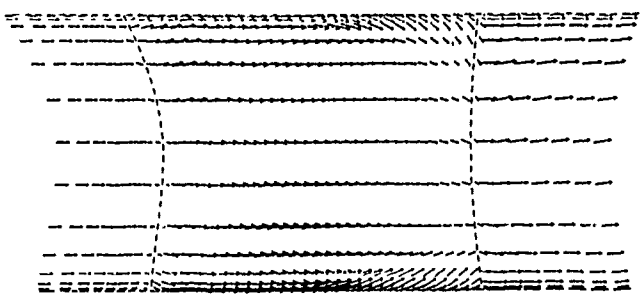


Denton : Spanwise Mixed-out Stagnation Pressure Loss (Vane 2, M_2=0.83, x/Cx=1.02)

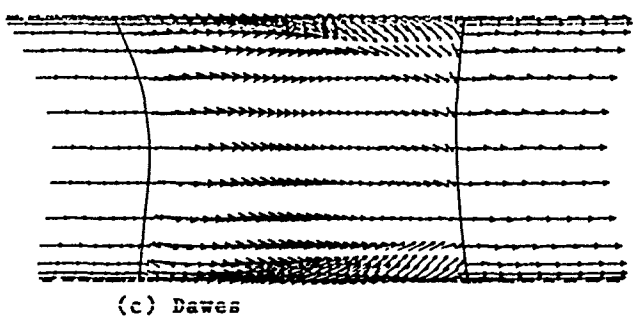
Figure 29



(a) MEFP



(b) Denton



(c) Dawes

Suction Side Near Surface Velocity Vectors (Vane 2)

Figure 30

DISCUSSION

Hah, US

I heard your presentation very interestingly. Experimental data (Fig 6 and Fig 12) show that the vortex system does not decay between 4% and 40% downstream. However, numerical results at 26% (Fig 26) show that the vortex system is completely washed out. Can you present numerical results at 4% and 40% downstream of the blade?

Author's Reply:

I have presented the loss contours at 26% Cx since this is the only axial location at which loss contours for all three vanes were available to me. Given a little time and effort it should be possible to extract the results corresponding to the measurement planes.

Moustapha, Canada

1. What are the differences between vane 2 and 3 in terms of stacking? Did you use any lean for these designs?

2. The reduction in losses due to the "3D design" is relatively small: were you able to explain with this reduction the measured improvement in turbine stage efficiency?

Author's Reply:

1. Although I was not personally involved in the design of these blades, I understand that both vanes 2 and 3 have a nominal throat stack. The difference between the vanes derives from deviations from this nominal stacking which seems to be based on intuition.

2. I'm not sure that I would regard a reduction of NAV loss from 7.8% to 6.8% as small. This improvement is of similar magnitude to the gains seen in the turbine stage tests.

Langston, USA

Were all three sets of calculations predictions or were they (some or all) postdictions? (That is, did the calculators [some or all] see the experimental results before they performed their calculations?)

Author's Reply:

I believe that all of the calculations were performed with at least some knowledge of the experimental results. In my experience, true predictions are rare indeed!

Chen, Switzerland

Figs 14 and 19 of the paper revealed a radial flow through the axis of the separation bubble. Usually, a flow through the core of a vortex, here the separation bubble, will enhance it due to vortex stretching effect, just like the longitudinal spiral vortex of a delta wing. Would this radial flow also energize the swirling moment of the separation bubble and then make its re-attachment much earlier?

Author's Reply:

It is my belief that the energy associated with the separation bubble and

crossflow is so small as to be insignificant in terms of the mechanism that you refer to. The best evidence that I have for this view is a video of smoke visualization in the "LA" cascade that was presented at the ASME meeting in Dusseldorf to demonstrate the secondary flows in the cascade. (see Ref 18)

Moore, USA

1. You presented exit flow angle data for vanes 1 and 2. How did the exit flow angle vary with vane 3?

2. What turbulence models were used for the calculations with the codes of Moore, Dawes and Denton?

Author's Reply:

1. The exit flow angle distribution across the span of vane 3 is similar to that of vane 2 but with slightly increased turning near mid-span and reduced turning closer to the casing.

2. The calculations using the Moore code used a Prandtl mixing length turbulence model. I am not sure of the turbulence models that were adopted by Dawes and Denton.

SECONDARY FLOW PREDICTIONS FOR A TRANSONIC NOZZLE GUIDE VANE

by
G.C.Horton
Propulsion Department
Royal Aerospace Establishment, Pyestock
Farnborough, Hampshire, England

SUMMARY

To improve turbine efficiency it is necessary to design the blading to control the flow, including the secondary flow, and hence reduce the losses. A method is therefore required to predict the three-dimensional flow, with losses, within turbine geometries. Three-dimensional viscous flow programs offer the capability of doing this.

Such a program (as developed by Dawes) is available at the Royal Aerospace Establishment, Pyestock. It has been used to analyse the flow through a transonic turbine nozzle guide vane which has been tested in cascade at Pyestock. The predictions are compared with surface pressure and downstream traverse results to assess the ability of the program to predict secondary flows and losses in a highly loaded nozzle guide vane operating at representative engine conditions.

1 INTRODUCTION

To increase turbine efficiency it is necessary to reduce the total pressure losses within the blading passages. The loss within the nozzle guide vane (ngv) row can in general be divided into four components; profile loss, secondary loss, trailing edge loss and, when supersonic flows are present, shock loss. The relative importance of each of these depends on the requirements and design of the particular turbine. Of particular interest in the context of a high pressure, low aspect ratio turbine is that loss attributable to the secondary flows, the secondary loss.

The nature of the secondary flows is illustrated in Fig 1. The boundary layer which has formed on the endwall upstream of the turbine separates at a saddle point ahead of the leading edge and forms the two legs of the horseshoe vortex. One leg sweeps around the suction surface and is largely dissipated by viscous actions. The other leg sweeps across the passage to the suction surface of the adjacent blade. As most of the fluid in the endwall boundary layer is entrained into this leg of the vortex, a new boundary layer forms on the endwall downstream. This new boundary layer is also swept across the passage by the blade-to-blade pressure gradient reinforcing the horseshoe vortex and forming the passage vortex. The formation and subsequent mixing of these flows incur loss, the secondary loss, and also cause the exit flow distribution to be significantly non-uniform in the circumferential direction resulting in further losses being generated in downstream blade rows.

A variety of techniques for controlling secondary flows and hence reducing secondary losses have been investigated by different researchers with some success. These techniques have included leaning the blade and profiling the endwall[1,2]. In order that such techniques may be incorporated into future engine designs a method is needed for accurately predicting the secondary flows and losses and also the effect of changes in geometry on them.

Various methods have been used to predict secondary flows. Rotational inviscid techniques, such as time marching, have been shown to be capable of predicting these flows but some features are not modelled well and the methods are not able to give predictions of losses. Only three-dimensional viscous flow methods offer the likelihood of accurately modelling the secondary flows and losses. This paper details the modelling of the flow through a turbine ngv with such a program and the comparison of the results with experiment.

2 EXPERIMENTAL DETAILS

The geometry that was to be analysed was the nozzle guide vane of the RAE High Rim Speed Turbine[3]. This is a high work, high blade speed single stage research turbine with transonic blading which has been tested with comprehensive aerodynamic instrumentation in a continuous running cold flow turbine rig. The ngv has also been tested in annular cascade in a short duration facility, the RAE Isentropic Light Piston Cascade[4], at representative engine Mach numbers and Reynolds numbers. The theoretical modelling is compared with the results from these latter measurements

Details of the ngv design are shown in Fig 2. The exit angle varies along the span with a mid-height value of 75 degrees and reducing slightly towards each endwall. The trailing edge is stacked on a curve to give a concave suction surface to encourage off-loading of the sections near the endwalls. The design exit Mach number at the hub was 1.02 but matching problems with the rig resulted in a value of 1.14 being adopted as the datum for the tests. The ngv ring contains 40 vanes giving a pitch/axial chord ratio of 1.20 and an aspect ratio (height/true chord) of 0.62. Tests were also performed at exit Mach numbers of 0.94 and 1.29 and at three different Reynolds numbers at the datum Mach number. Static pressure measurements were taken on the vanes and endwalls at each

condition and an area traverse was also performed at a plane one axial chord downstream of the trailing edge at the datum condition. This area traverse was built up from a series of circumferential sweeps, each of which was performed during a run of the rig and took approximately 0.5 second. The total pressures were measured using a three-hole probe fitted with high response miniature transducers. These measurements constituted the first use of this mechanism on this rig and the signal/noise ratio was rather lower than had been hoped for.

The correlations that were used during the design of the turbine gave a profile loss for the ngv of 0.04. The effect of secondary losses and endwall boundary layers were modelled at the design stage by further assuming that the loss increased to 0.30 near the endwalls, giving an overall mean loss of 0.08. Until the acquisition of the Dawes program, no method was available at RAE Pyestock for predicting the three-dimensional losses of this ngv.

3 THEORETICAL MODELLING

The program that is installed at RAE Pyestock is a three-dimensional viscous time marching program based on that developed by Dr Dawes of the Whittle Laboratory, Cambridge[5] with further development by the author. This program solves the thin shear layer form of the time dependent Navier Stokes equations for a time-independent solution using an implicit time marching algorithm. The eddy viscosity is modelled using a three-layer mixing length formulation based on the method of Baldwin and Lomax[6]. Spatial discretisation is accomplished using a body-fitted H-mesh.

The further development of the program at Pyestock has mainly involved extending it to include extra options, a principal one being to enable the user to specify the position of the start and end of laminar-turbulent transition on the blade surfaces. The endwall boundary layers may also be specified to be laminar or turbulent ahead of the blade transition locations. The other modifications are chiefly associated with tailoring the program to the computer system on which it is run at RAE Pyestock and also some changes have been made to the input and output which do not affect the results of the computation.

The program is run at RAE Pyestock on a FPS-164 attached processor with 2.5Mwords of storage. This allows a total of approximately 46000 mesh points which have been distributed in the following manner in all the computations reported in this paper:

Axial	73 mesh points
Blade-to-blade	25 mesh points
Radial	25 mesh points.

The leading and trailing edges are positioned at axial planes 14 and 63, with the grid extending 0.55 axial chords upstream of the leading edge and 0.67 downstream of the trailing edge. The perspective view showing the geometry of the ngv in Fig 2 also illustrates the intersection of the calculation grid with the blading surfaces. This also shows the refinement which was applied to the grid near the blade surfaces and endwalls, and also near the leading and trailing edges. This was to give improved resolution of the flow details in these important regions and resulted in a radial grid spacing at the wall of 0.4% of vane height and also a blade-to-blade spacing of 0.4% pitch at the vane surfaces. The axial grid spacing at the leading and trailing edges was 0.3% axial chord.

Previous experience of the program had shown that 2000 time steps were needed to ensure adequate convergence. The criterion for adequate convergence was that the mass flow should be conserved to within 1.0% of inlet flow throughout the flow field and that the other properties, such as total pressure loss, should be varying only slowly with time step number. The results being reported are all taken at 2000 time steps, at which point the mass flow was conserved to within 0.26% of inlet flow for the datum case. One run was continued to 3000 time steps to examine the effect of doing so on the solution. Only minimal changes were seen leading to confidence that 2000 time steps were indeed adequate for convergence to be obtained. The program was run with the artificial viscosity factors reduced to half the value recommended by the author of the program as experience had shown that this did not affect the stability of the program and that the predictions of secondary flows were enhanced by doing so.

4 RESULTS

The mid-height distributions of isentropic Mach number of the vane surfaces are compared with the experimental values in Fig 3 for the three different exit Mach numbers, all at the design Reynolds number. The results on the pressure surface are excellent at all three conditions. At the low Mach number condition the suction surface Mach number is slightly overpredicted for much of the vane chord, though the results downstream of 70% axial chord are in very good agreement with the experiment. The slight overprediction of the Mach number over the first 50% of chord is also evident at the other two conditions. However, downstream of mid-chord the differences between experiment and prediction are more marked with the analysis failing to correctly capture the overexpansion and recompression that is seen in the experiment where the trailing edge shock impinges on the suction surface at the higher Mach number conditions. This is probably associated with poor modelling of the trailing edge base region and would be improved with an increase in the number of mesh points used to model the trailing edge geometry.

The plots at 5% and 95% vane height show generally similar results. The over-expansion/recompression at about 65% axial chord in the experimental results at 5% height is probably due to the effect of the passage vortex impinging on the suction surface at this point. There is some indication that the program has picked up this feature at the design Mach number condition though it appears to be about 10% axial chord further downstream than in the experiment. There is no indication that the feature is modelled at the other flow conditions.

The predicted velocities near the outer endwall, as illustrated in Fig 4 show the saddle point ahead of the leading edge and the crossflow in the passage corresponding to the formation of the passage vortex. For clarity the vectors on some of the grid lines have been omitted from this Figure. The relatively low crossflow is due to the design philosophy of the vane; as it is rear-loaded near the endwalls the cross-passage pressure gradient which drives the secondary flows is only small. The velocities near the suction surface (Fig 5) show the manner in which the passage vortices impinge the suction surface at approximately 50% axial chord followed by a region of strong spanwise flow away from the endwalls.

The development of the total pressure loss contours along the vane passage for the design Mach number, design Reynolds number condition is illustrated in Fig 6. The effect of the sweeping of the endwall boundary layer across the passage by the blade-to-blade pressure gradient can be seen in the plane at 40% axial chord as a thickening of the endwall boundary layer towards the suction surface side of the passage. Two loss cores can be seen to be beginning to form in the suction surface - endwall corners. These loss cores then grow and move along the suction surface away from the endwalls and by the plane at 95% chord they have almost merged with the thick mid-height suction surface boundary layer. The endwall and pressure surface boundary layers have also grown considerably by this plane.

Fig 7 shows the secondary velocity vectors on the same planes. The secondary velocities are defined here as the absolute velocity minus the component parallel to the 'quasi-streamlines' which form part of the calculation grid. The flow across the endwalls and up the suction surface can be seen to develop through the passage, though this flow is confined to a thin layer next to the solid surfaces with various vortices outside this layer.

A photograph of some oil dot flow visualisation is shown in Fig 8 together with a similar view of the geometry on which the predicted near-surface velocities are shown. The region near the outer endwall that has been affected by the secondary flow can be clearly seen and corresponds well to the region bounded by the secondary flows in the prediction.

The circumferential variation of total pressure at the downstream plane is shown for two different heights in Fig 9 together with the relevant circumferential sweeps from the experiment. The prediction and experiment are shown at slightly different axial positions (0.67 axial chord downstream of the trailing edge for the prediction compared with 1.0 axial chord for the experiment) so they have been aligned by lining up the position of the minimum in each set. The levels of total pressure (and hence loss) match up well, particularly at the 25% height location. The wake appears to be wider in the experiment than in the prediction; this is not altogether surprising as the experimental results are from further downstream than the prediction and some mixing-out of the wake would be expected between the two axial locations. Such good agreement is not apparent in the comparison at 50% height, in particular the wake is very smeared in the experiment but is still well defined in the prediction. The maximum and minimum levels still agree quite well however which is encouraging with regard to the ability of the program to successfully predict the losses. The full set of circumferential sweeps has been combined into an area traverse and the results plotted as contours of total pressure in Fig 10 together with a similar plot from the prediction. Because of the design of the traverse probe it was not possible to obtain readings near the endwalls and this is reflected in the blank areas near the walls in the experimental plot. Unfortunately a high degree of noise was evident in the experimental measurements so some regions have been shaded in both plots to allow easier comparison between prediction and experiment. The general shape and width of the wake is modelled quite well though the experiment shows the highest loss regions near the endwalls whereas the prediction shows the highest loss near mid-height. The large regions of low total pressure on the extreme right-hand side of the experimental results are due to the measurement technique rather than real regions of high loss. Overall the levels of total pressure have been modelled very well. Fig 11 shows a comparison of the radial variation of circumferentially averaged total pressure between prediction and experiment. The predicted peaks of total pressure just outside the endwall boundary layers are probably caused by freestream fluid being swept into the suction surface/endwall corner region to replace the boundary layer which has been swept onto the vane surface by the secondary flow. The very high level of these peaks suggests that there is also probably some numerical error in this region. The prediction and experiment are in good agreement in the mid-height region of the vane but the experimental values tend to reduce near the endwalls whereas the prediction does not. In fact the predicted distribution does not exhibit the expected regions of secondary loss near the endwalls. It is believed that this is due to the low aspect ratio nature of the design having resulted in the losses being spread out across the span of the vane. These comparisons of predicted and experimental total pressure measurements suggest that the program could be used to give predictions of loss during the design of a new turbine with a reasonable degree of confidence.

The total pressure loss at mid-height is predicted to be 0.075 with the secondary loss being 0.003. These give an overall loss of 0.078. These compare with the values derived from the correlations at the design phase of 0.040 (mid-height) and 0.080 overall. The analysis predicts a significantly higher mid-height loss than had been assumed with a similar reduction in secondary loss. It is clearly important to be able to predict the radial distribution of loss at the design stage, and this prediction method evidently has the potential to do so.

5 CONCLUSIONS

A three-dimensional viscous flow program has been applied to the calculation of the flow through a transonic nozzle guide vane geometry. Good agreement has been obtained with experimental isentropic Mach number distributions at three different conditions, though it appears that an insufficient number of mesh points were used near the trailing edge to successfully capture a shock which appears there in the experiment. The predictions of secondary flows show the development of the features found in experimental flows along the vane passage and a comparison of the predicted total pressures with those from a downstream area traverse suggests that the program could be used to give predictions of loss as part of a turbine design process.

REFERENCES

1. F.C. Kopper and R. Milano "An experimental investigation of endwall profiling in a turbine vane cascade", AIAA paper 80-1089 (1980)

2. H.C. Liu, T.C. Booth and W.A. Tall "An application of 3-D viscous flow analysis to the design of a low aspect ratio turbine", ASME paper 79-GT-53 (1979)

3. R.C. Kingcombe, J.D. Bryce and N.P. Leversuch "Design and test of a high blade speed, high work capacity transonic turbine", in AGARD Conference Proceedings CP-421 (1987)

4. A.J. Brooks, D.E. Colbourne, E.T. Wedlake, T.V. Jones, M.L.G. Oldfield, D.L. Schultz and P.J. Loftus "The isentropic light piston annular cascade facility at RAE Pyestock", in AGARD Conference Proceedings CP-390 (1985)

5. W.N. Dawes "A numerical method for the analysis of 3D viscous compressible flow in turbine cascades; application to secondary flow development in a cascade with and without dihedral", ASME paper 86-GT-145 (1986)

6. B.S. Baldwin and H. Lomax "Thin layer approximation and algebraic model for separated turbulent flows", AIAA paper 78-257 (1978)

Copyright
©
Controller HMSO London
1989

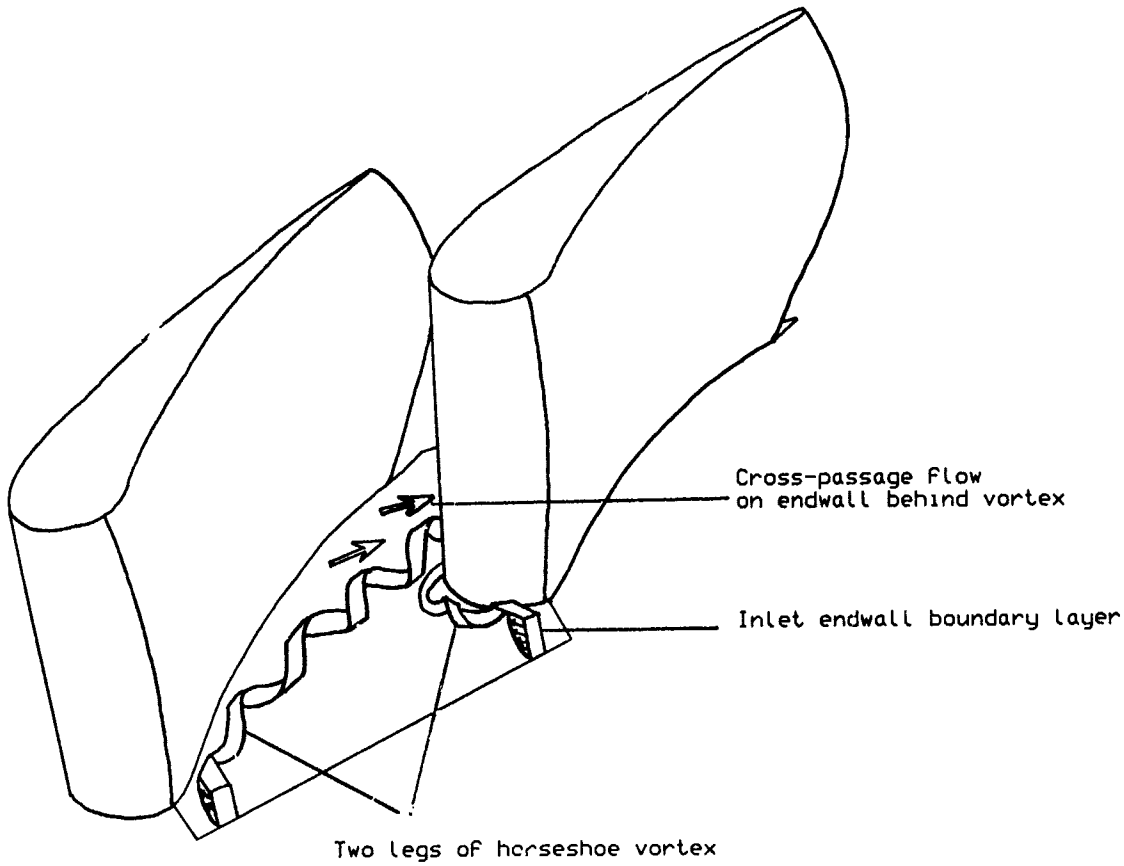


Fig 1. Illustration of turbine secondary flows

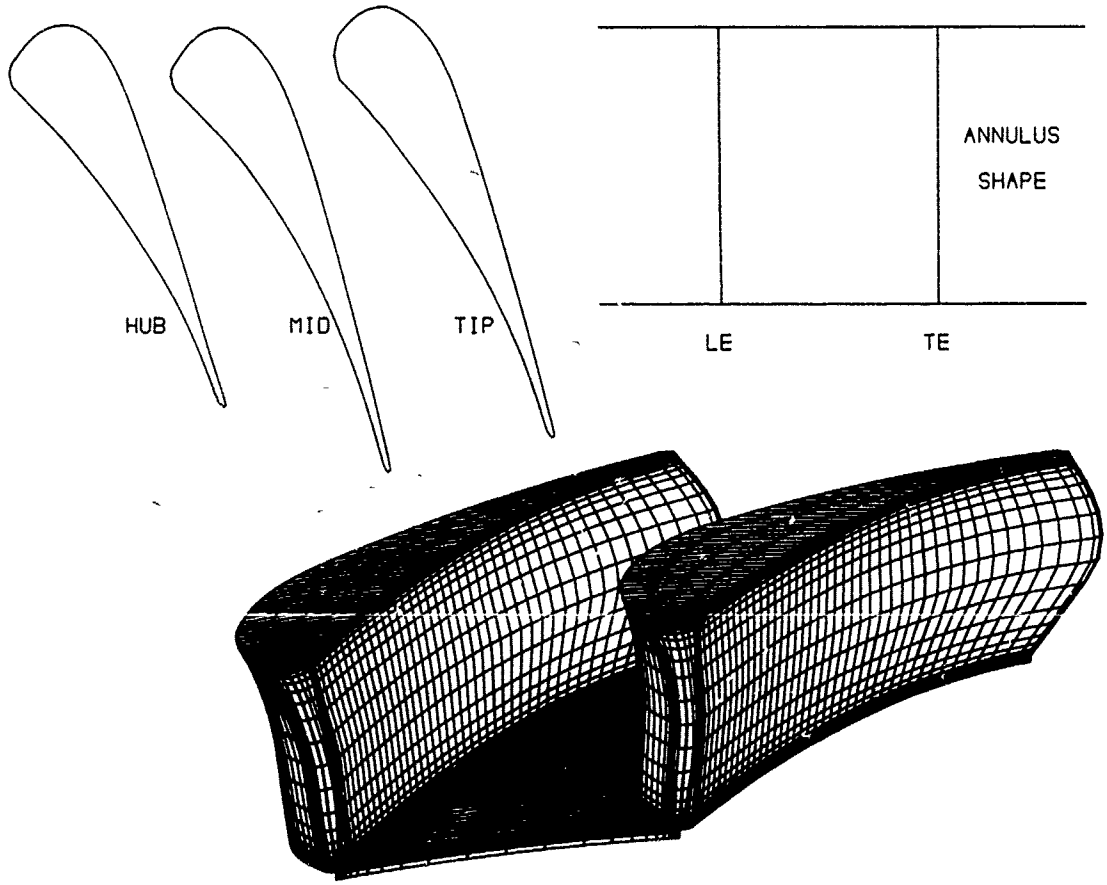


Fig 2. Illustration of ngv geometry

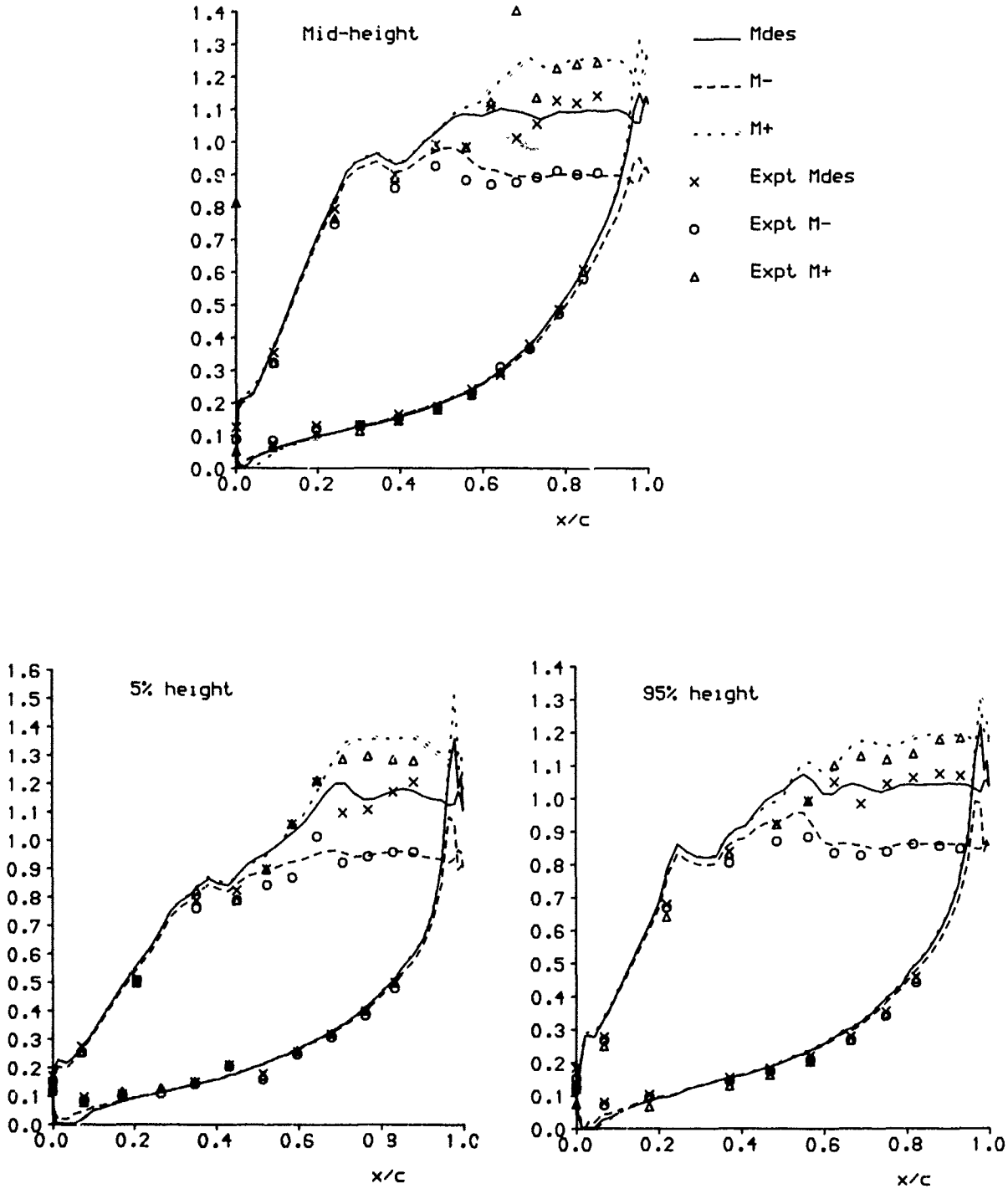


Fig 3. Comparison of isentropic Mach number distributions with experiment

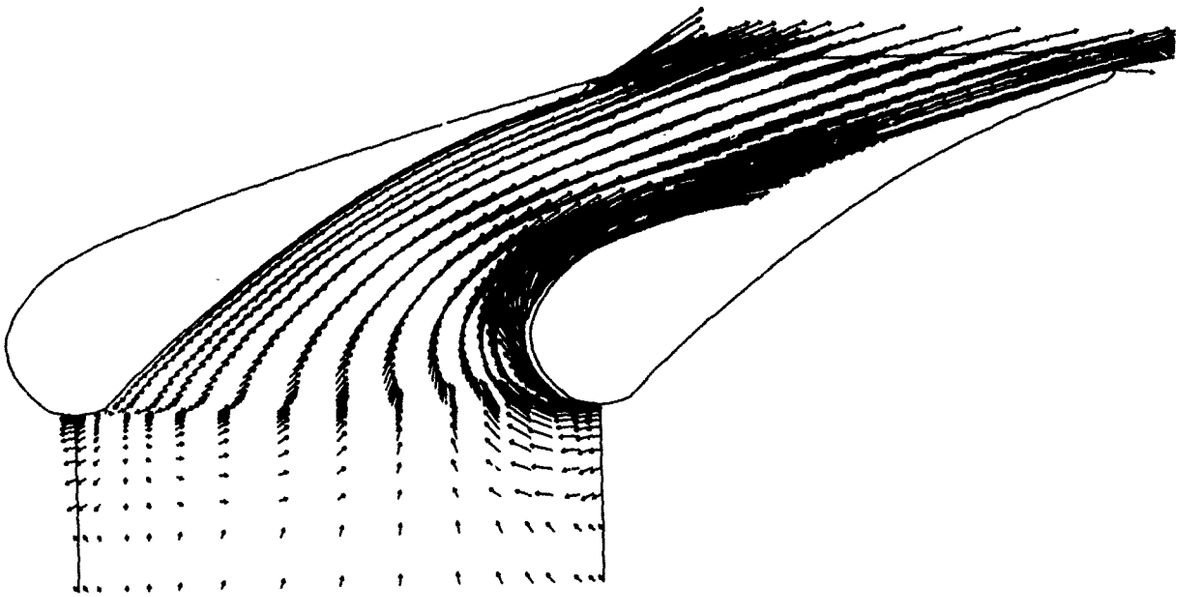


Fig 4. Velocity vectors near outer endwall

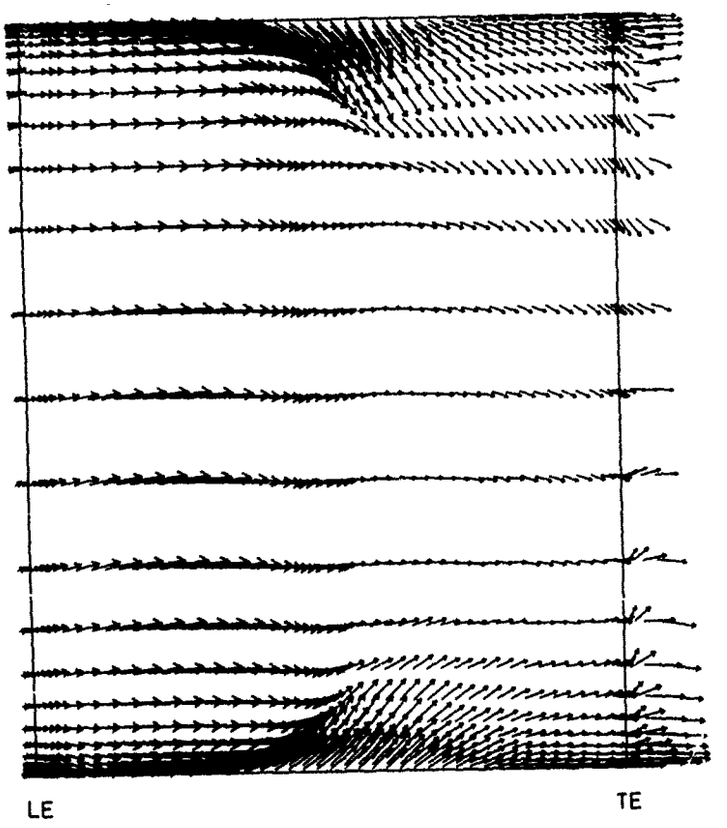
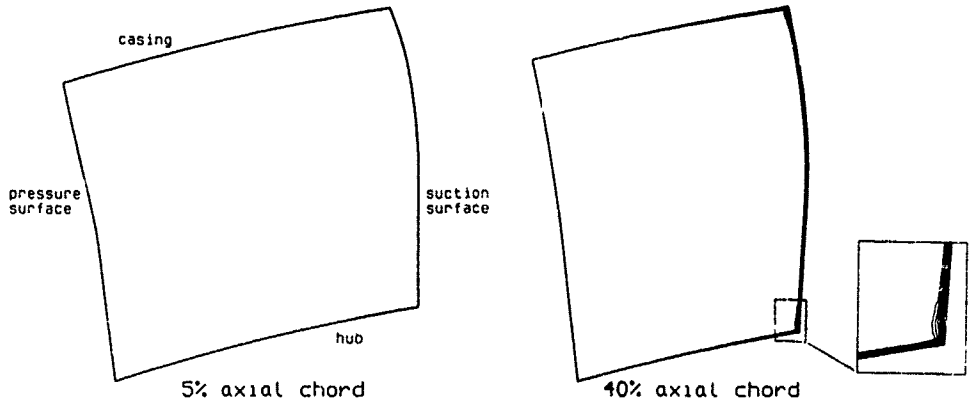


Fig 5. Velocity vectors near suction surface



Contour interval = 0.05

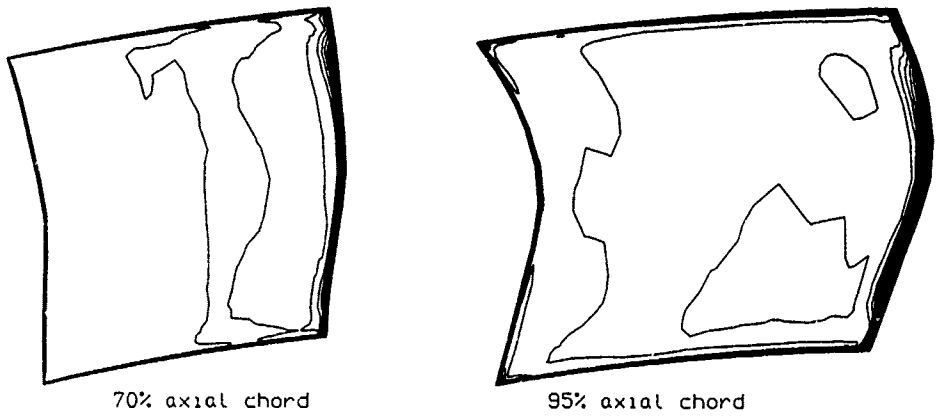


Fig 6. Development of loss contours along passage

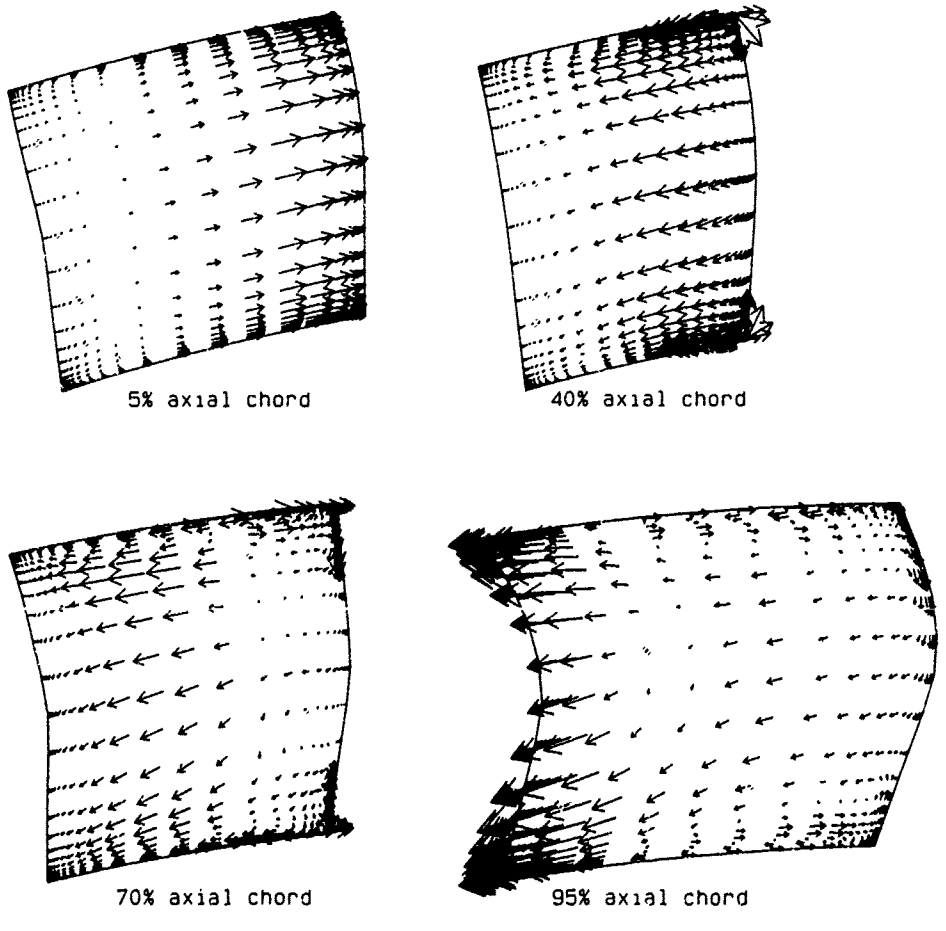
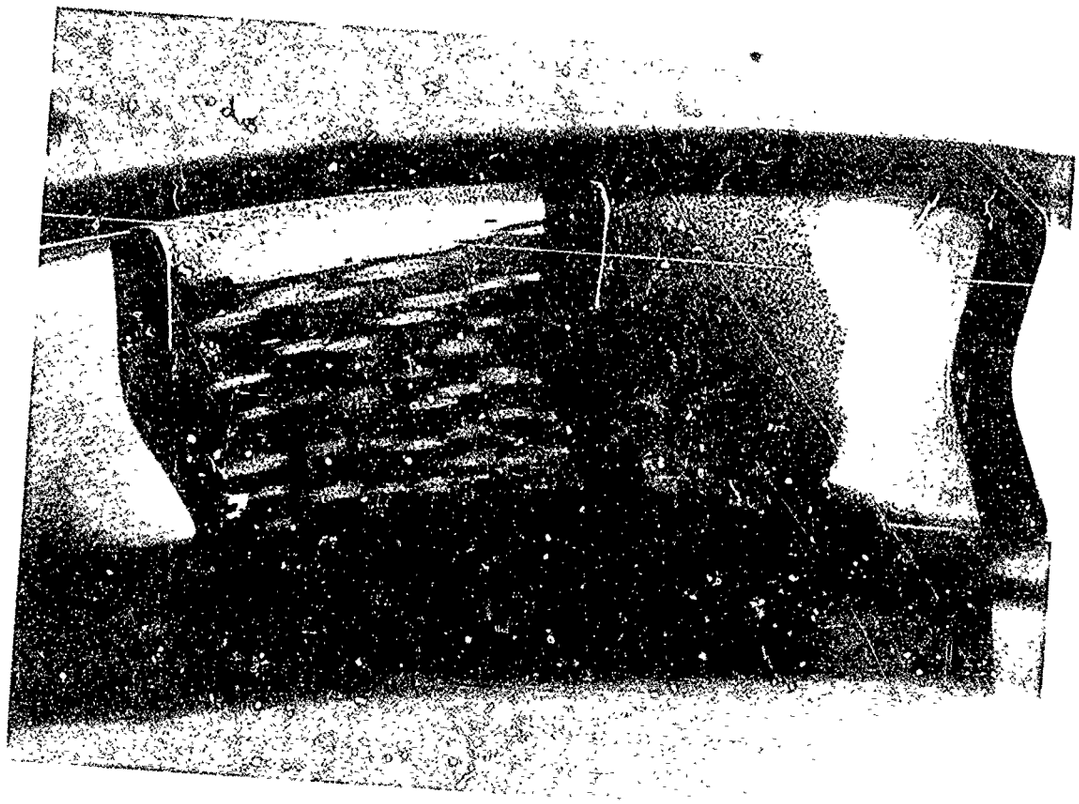


Fig 7. Development of secondary velocities along passage



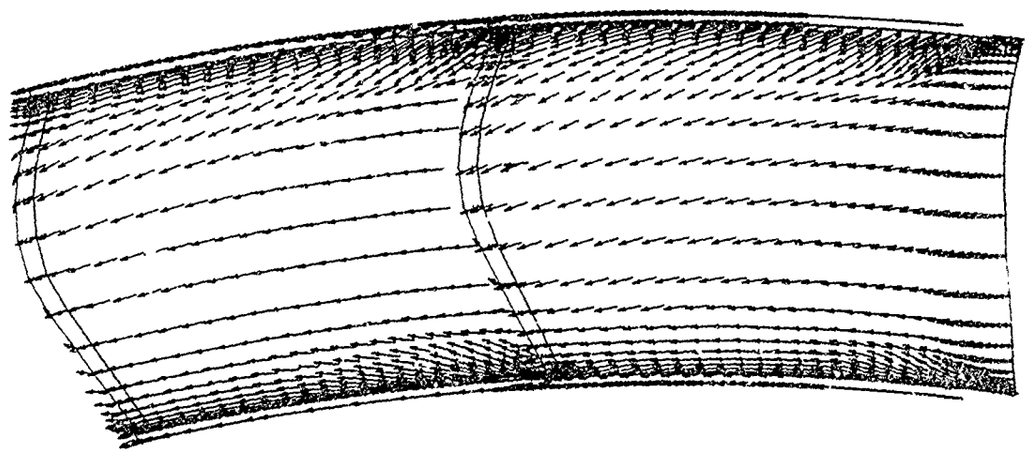
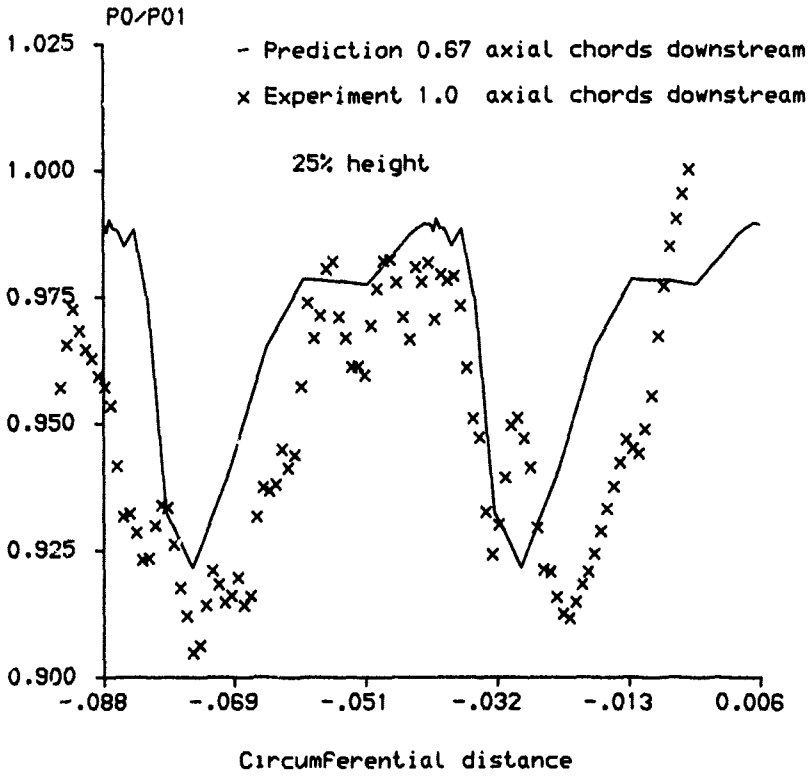


Fig 8. Oil dot flow visualisation and velocity vectors on similar view



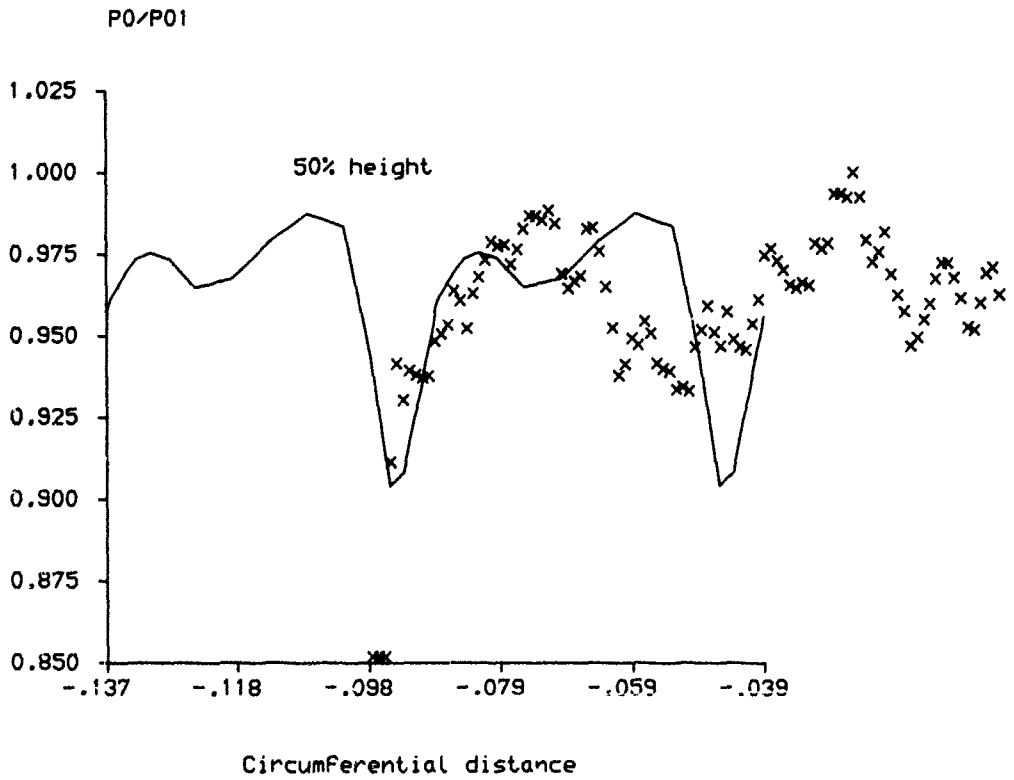


Fig 9. Circumferential variation of total pressure at exit plane

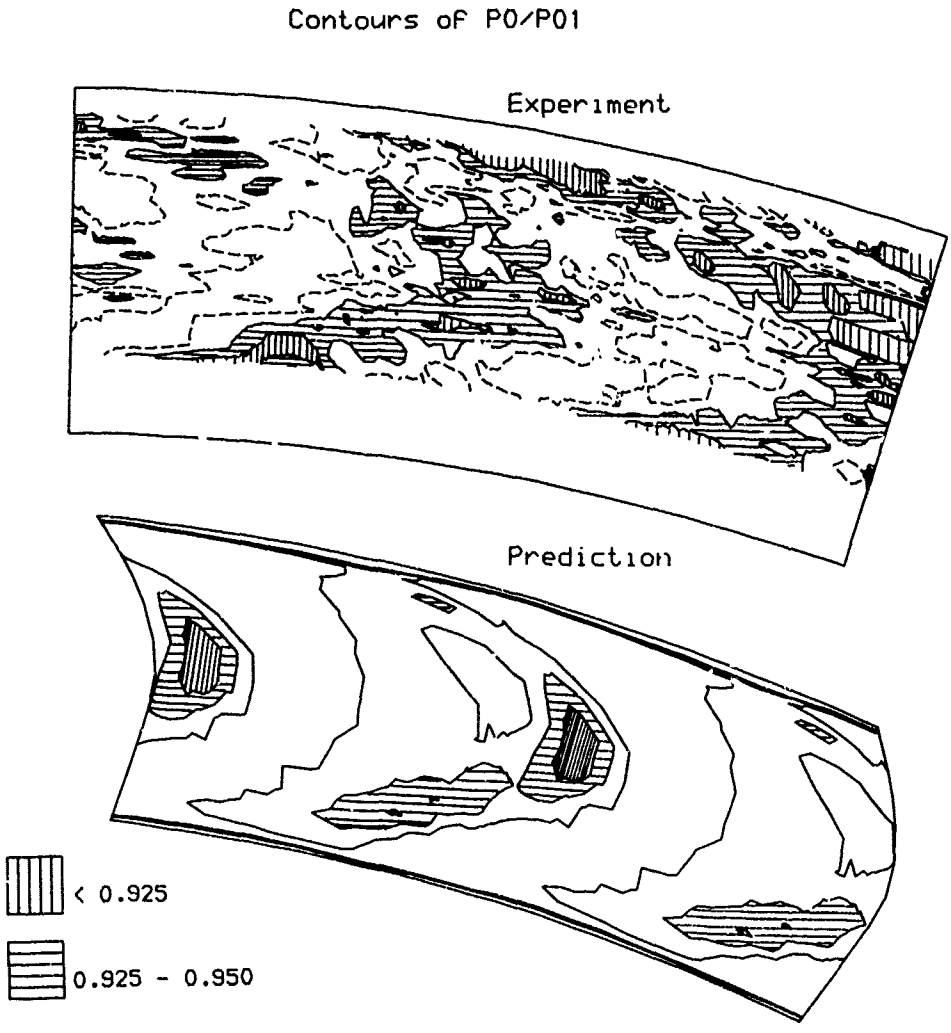


Fig 10. Contours of total pressure on downstream plane

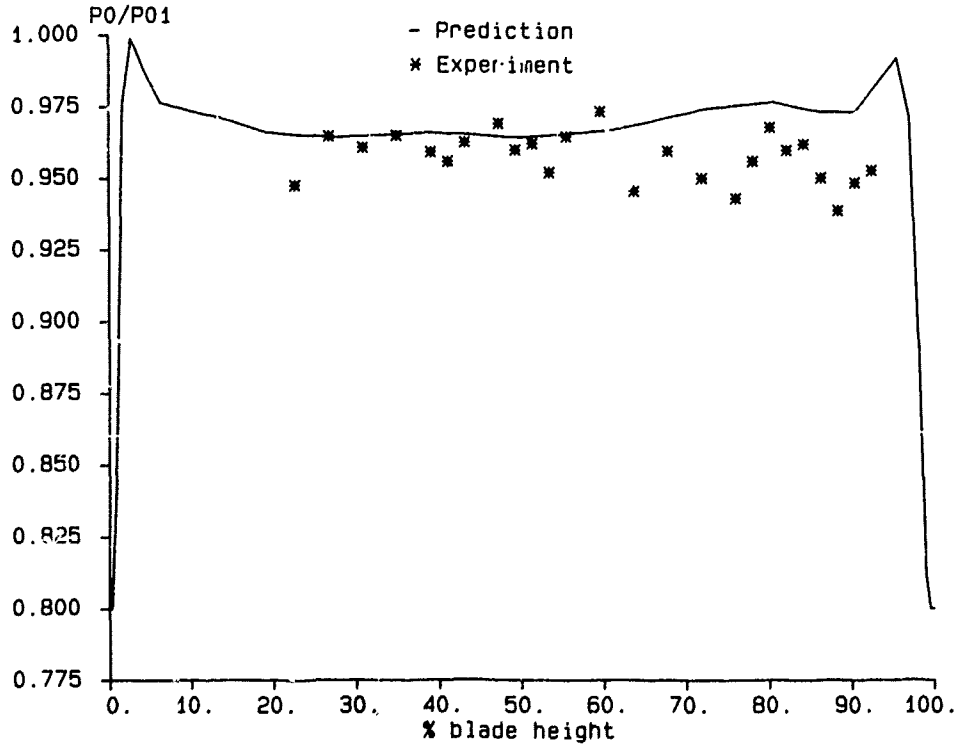


Fig 11. Radial variation of circumferentially averaged total pressure

DISCUSSION

Sieverding, Belgium

Referring to Figure 9, could you explain the non-periodicity of the measurements? What type of probe did you use?

Author's Reply:

The probe used for these measurements was a three hole probe with small Kulite transducers mounted near the probe tip. Some more recent measurements have been performed with the transducers mounted further from the probe tip and the probe closer to the blade trailing edge. These measurements have shown better, more periodic definition of the blade wakes so it appears that the lack of periodicity in the experimental results presented is due to a form of noise associated with the probe design and placement.

Servaty, Germany

You have used an H-type grid with great distortions at leading and trailing edge.

1. Is there a special treatment concerning these points in the numerical algorithm?

2. Did you consider using an O-type grid?

Author's Reply:

1. No special treatment is used in these regions. A periodic boundary condition is applied upstream of the leading edge and downstream of the trailing edge with a solid surface boundary condition applied between the two.

2. The program was originally developed by Dr Dawes with the current H-grid. It would be interesting to try it on an O-grid but time has not permitted this yet.

Hansen, USA

You attribute the discrepancy between experiment and prediction to inadequate computational grid spacing for accurate shock capturing. What change in grid spacing would be required for the requisite shock capturing?

Author's Reply:

Some previous computations using a two-dimensional version of the program on a similar Ngv geometry had shown adequate shock capturing with about 120 axial grid points. This calculation used about 8 grid points to model the trailing edge. I would estimate that this number of grid points would be adequate for shock capturing in the 3-D program.

SECONDARY FLOW IN A TURBINE GUIDE VANE WITH LOW ASPECT RATIO

by

D. Wegener, J. Quest and W. Hoffmann
DLR - Institut für Antriebstechnik
Linder Höhe, 5000 Köln 90, West-Germany

ABSTRACT

The flow field of an annular turbine cascade with low aspect ratio (0.6) is investigated by means of experiments and numerical calculations. An advanced computer code was applied to solve the three dimensional Reynolds averaged Navier-Stokes equations. Detailed measurements with 5-hole probes and an advanced Laser-Two-Focus velocimeter (L2F) were carried out to evaluate the numerical solution of the flow field. Flow visualizations on the endwalls and on the blade surfaces complement the experimental data and help to understand the secondary flow phenomena.

The results show that this 3D-NS-calculation is an efficient tool to predict complex secondary flow phenomena.

SYMBOLS

c	velocity
c_q	absolute velocity $(c_{ax}^2 + c_u^2)^{0.5}$
H	blade height
l_m	axial chord length (midspan)
$\dot{m}$	mass flow rate
$\dot{m}_{red}$	reduced mass flow rate $\dot{m} \cdot (\bar{T}_{t0})^{0.5} \cdot (\bar{p}_{t0})^{-1}$
Ma	Mach number
p	pressure
R	radius, spanwise coordinate
T	temperature
Tu	turbulence level
x	axial coordinate
α	flow angle with respect to pitchwise direction
ζ	total pressure loss coefficient $(\bar{p}_{t0} - p_{t4,loc}) / (\bar{p}_{t0} - \bar{p}_4) \cdot 100$ %

Subscripts

ax	axial direction
loc	local value
pr	primary flow
sec	secondary flow
t	total
u	pitchwise direction
0	upstream conditions
1, 2, 3, 4	measuring planes (Fig. 3)

Superscripts

(-)	pitchwise averaged value
(=)	average over the entire measuring plane

INTRODUCTION

The requirements for high performance and high efficiency turbomachines necessitate an optimization of all turbomachinery components. In the case of turbines it is well known that secondary flows are significantly influencing the loss generation inside the rotating and stationary blade channels (about 30 - 50 %). In addition to that these effects are influencing the deflection and the heat transfer at the blade surfaces /1, 2/. Therefore detailed knowledge about turbine secondary flows is a prerequisite for a further improvement of todays turbine efficiencies. One important tool for understanding and predicting secondary flows are the solutions of three dimensional Navier-Stokes calculations (3D-NS) for compressible flow. Experimental investigations can help to verify the calculated flow field at locations of interest.

An advanced 3D-NS-Code developed by Dawes /3/ was applied to detailed flow studies in a subsonic turbine guide vane with low aspect ratio. The flow field was also investigated with conventional probes and advanced L2F-velocimeter in four planes which has been selected identically to the calculation grid geometry. Detailed comparisons between measured and calculated data were carried out.

TEST RIG AND INSTRUMENTATION

Fig.1 illustrates the test rig geometry and the arrangement of the measuring planes. The test rig is an annular turbine cascade with a tip-diameter of 400 mm and a hub-to-tip ratio of 0.79. It is supplied with cold air from a distant compressor station. The maximum total pressure is 2.0 bar and maximum total inlet temperature is 315 K. The operation point is settled by measuring the mass flow rate, the total pressure and the total temperature upstream of the stator.

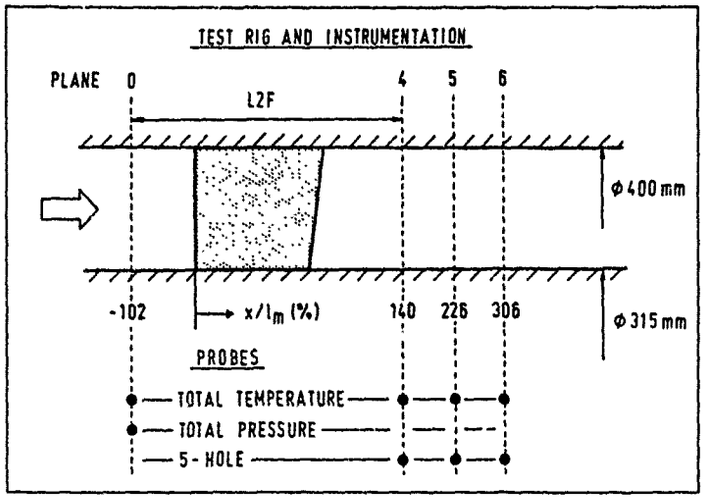


Fig. 1: Test rig and instrumentation of turbine annular cascade

The results of detailed investigations show that the inlet flow of the stator is uniform (at plane 0) /4, 5/. The flow direction is axial and the spanwise total pressure distribution is constant between 5% and 95% blade height. The pitchwise traversing of a total pressure probe shows a nearly constant pitchwise total pressure distribution at hub, midspan and tip. The conventional probes used in the test rig are mounted in computer controlled actuators which allow spanwise and pitchwise traversing in the measuring planes 4, 5 and 6.

The L2F-velocimeter developed at DLR /6/ was applied for detailed flow field investigations inside of the stator. The L2F-velocimeter was mounted on a table which is driven by actuators for axial and spanwise traversing. Pitchwise traversing is achieved by turning the stator hub. Flow measurements are possible with natural seeding, however to shorten the measuring time seeding has been applied which was especially useful close to the walls where the boundary layers are developing.

The flow patterns on the surfaces of the blades, the hub and the casing are also investigated by means of the oil tracing technique. Good results have been achieved by using a mixture of oil (SHELL T 220), titanium dioxyd powder and a little of oleic acid.

Fig. 2 shows the performance map of the stator as a result of overall tests with conventional probes in plane 4 /7/. The reduced mass flow rate and the total pressure loss coefficient are plotted as a function of the outlet Mach number $\overline{Ma}_4$. The data of Table 1 are representing the operating point for which the measurements and calculation to be presented were carried out. Measurement accuracy is illustrated in Table 2.

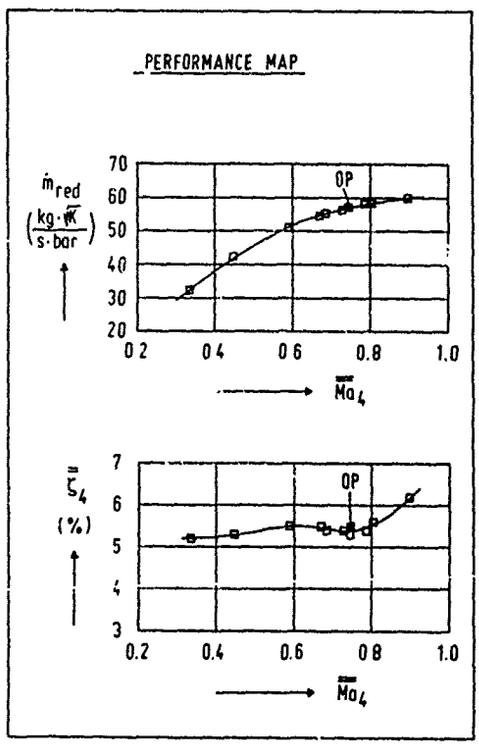


Fig. 2: Performance map of stator (OP = operating point)

Table 1: Characteristic data for operating point OP (Fig. 2)

inlet Mach number	0.18
outlet Mach number	0.74
total pressure (inlet)	1.7090 bar
total temperature (inlet)	299.6 K
inlet flow angle	90.0 °
outlet flow angle	20.1 °
mass flow rate	5.7 kg/s
Reynolds number (based on l_m)	1.0×10^6
inlet turbulence intensity	4.4 %

Table 2: Measurement accuracy

flow angle	absolute	± 0.25 °
(5-hole)	reproducible	± 0.25 °
(L2F)	reproducible	± 0.1 °
pressure	absolute	± 0.1 mbar
temperature	static	± 0.5 K
	dynamic	± 0.5 K
velocity (L2F)	relative	< ± 1.0 % (depending on Tu-level)

NUMERICAL PROCEDURE

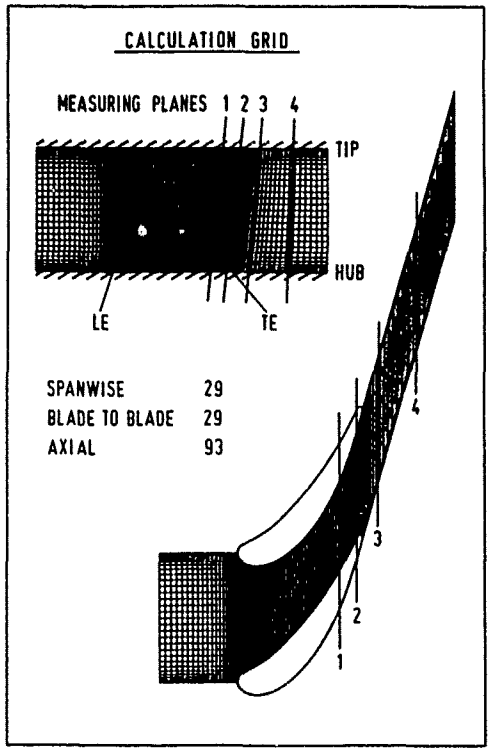


Fig. 3: Mesh geometry and locations of measuring planes

The 3D-viscous stator flow is simulated by the solution of the Reynolds averaged Navier-Stokes equations. Fig. 3 shows the mesh structure in the meridional plane and on an axis symmetric blade-to-blade surface. Due to the boundary layers the grid points are clustered to both endwalls as well as on the blade surfaces. The locations of the four measuring planes that fit exactly into the mesh geometry are also indicated. Planes 1 and 2 (inside the stator) are located at x/l_m = 81 % and 95 %. Planes 3 and 4 are located downstream of the stator and their axial positions are x/l_m = 111 % and 140 %.

This 3D-NS-Code has an option for using the FAS-multigrid technique to force convergence. For this turbine case, however, a faster convergence is obtained without using the multigrid option which is due to the strong sustained acceleration in the blade passage. A converged solution of the stator flow field with a total grid point number of about 78000 needs 3000 timesteps. This corresponds to 4 1/2 hours c.p.u.-time on a CRAY X-MP (6.9×10^{-5} sec/ grid point/ time step). The input for the 3D-calculation is taken from detailed measurements and consists of the spanwise distributions of total pressure, total temperature and flow angles at the inlet (plane 0) and of the static pressure at the stator exit (plane 4). The output of the 3D-NS-Code is a large dataset containing information about the velocity components, densities, static pressures at the centers of all volume elements. This makes it necessary to have sophisticated graphic software for a time saving post processing. Such a graphic tool for flow field visualization, running on a mainframe computer, was developed at the Institute for Propulsion Technology of DLR /8/.

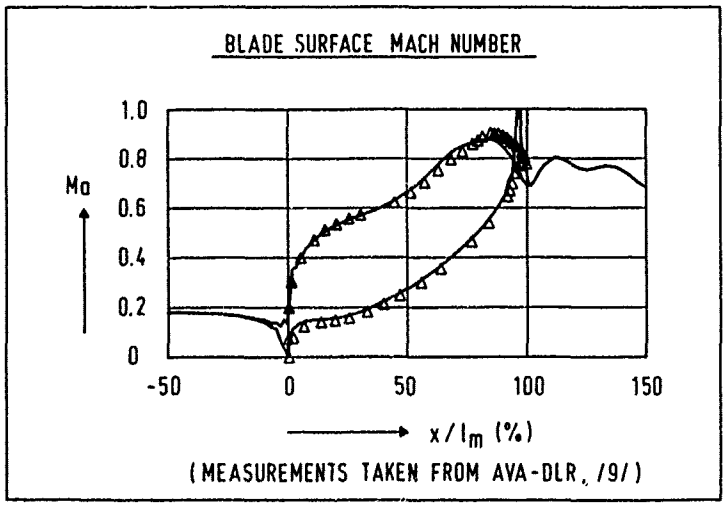


Fig. 4: Isentropic blade surface Mach number at midspan

Fig. 4 shows a comparison between the isentropic blade surface Mach number at midspan taken from the calculation and the measurement (triangle). This Mach number is calculated from the mean total pressure at the inlet and from the static pressure distribution along the blade surfaces. The static pressure measurements at the blade surfaces were carried out for a plane turbine cascade with the identical blade shape at the AVA (DLR) /9/. The agreement between the calculated distribution and the measured values is very good. The small wiggles at the leading edge (LE) are probably due to the non-uniform spacing of the mesh in axial direction. The same is due to the varying outlet Mach number between x/lm = 100 % and 150 %. A further optimization of the mesh geometry should provide better results but has not been carried out yet.

COMPARISION BETWEEN MEASURED AND CALCULATED DATA

The reliability of the 3D-NS-code was checked by a comparison between measured and calculated data before its results were used for a detailed flow field analysis. Fig. 5 and 6 show comparisons between calculated and measured spanwise distributions of axial and circumferential velocities for planes 1 - 4. Planes 1 and 2 are located in the bladed area close to the stator trailing edge (Fig. 3), whereas planes 3 and 4 are already located downstream of the trailing edge. The spanwise distributions are achieved by pitchwise area-averaging the local values at a given radius /10/.

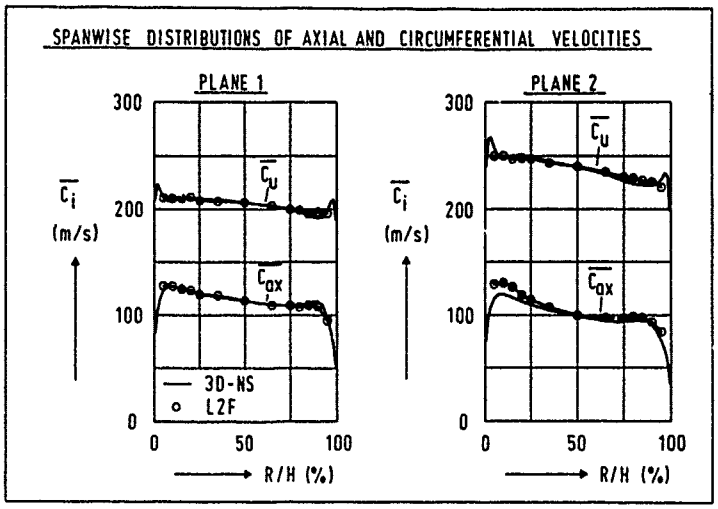


Fig. 5: Spanwise distributions in planes 1, 2

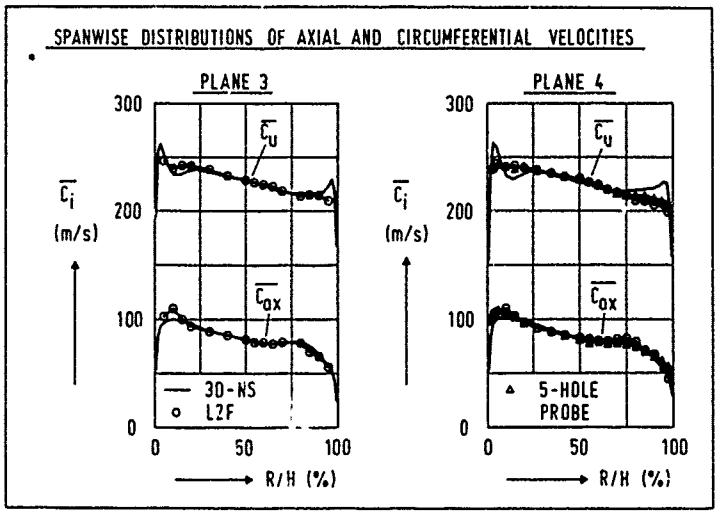


Fig. 6: Spanwise distributions in planes 3, 4

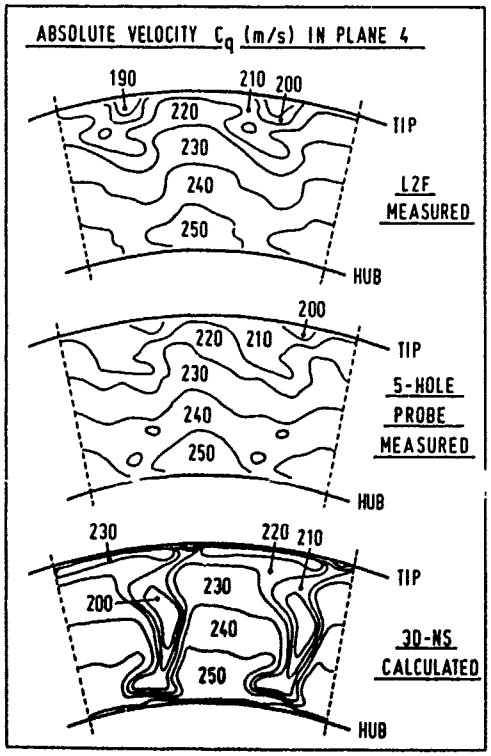


Fig. 7: Distribution of absolute velocity in plane 4

A very good agreement between the calculated and measured distributions is obtained in planes 1 and 2. Only at the endwalls, i. e. at hub and tip, the calculated values deviate from the measured ones. Fig. 6 shows on the left-hand side the spanwise distributions in plane 3. The agreement is good except the calculated peaks at hub and tip which are higher compared to those in plane 1 and 2. On the right-hand side of Fig. 6 the calculated distributions in plane 4 are compared with those taken from the L2F-measurements and in addition taken from the 5-hole-probe measurements. The measured distributions agree well which proves the reliability of the used instrumentation.

The calculated distributions of the axial velocity correspond well with the measured ones. The fact that the axial velocity is predicted well by the calculation is supported by the comparison of the total mass flow rate through the cascade. Measurements with a mass flow orifice show a deviation less than 3 % when compared to the calculated flow rate. The circumferential velocity distribution agrees well from 25 % to 75 % blade height. In the endwall regions the calculated values differ much from the measured data.

Fig. 7 shows the local distributions of the absolute velocity in plane 4 which is defined here as the vector sum of the axial and circumferential velocity. The velocity distributions of one spacing are doubled for better illustration. The upper and middle plots show the distributions taken from the L2F-measurements and 5-hole-probe measurements. The measured data are in good agreement. Comparing these distributions to the calculated data shown at the bottom of the figure one can realize striking differences. The clear shape of two wake regions is remarkable and proves that the calculation predicts losses too high caused by the trailing edge. Except these wake regions the calculated velocities fit well to the measured ones in the main flow. At the tip the code predicts remarkably high velocities up to 230 m/s that are obviously responsible for the peaks in the spanwise distribution of the circumferential velocity in Fig. 6.

Looking at the mesh given in Fig. 3, it should be noted that in this application the insufficiently large stretching of the mesh supports the transport and growth of numerical errors that are dominant at the trailing edge.

SECONDARY FLOW ANALYSIS

An overview of basic aspects of secondary flows in turbine blade passages is given in /2/. The development of secondary flow through a blade passage is described in the following secondary flow model /11/. The inlet boundary layer separates near the leading edge and forms a leading edge vortex also called horseshoe vortex with two legs, i.e. a pressure side leg and a suction side leg. The pressure side leg seems to be responsible for a fluid motion from pressure side to suction side at the endwall within the blade passage. The passage vortex which forms independently from the leading edge vortex due to the deflected inlet boundary layer (see passage vortex in curved ducts) turns in the same sense as the pressure side leg of the leading edge vortex. A detailed investigation of the formation of these two vortices is given in /12/ and shows that these vortices cannot continue to exist separately next to each other. They will combine to form a single vortex which is called passage vortex in the following. The suction side leg of the leading edge vortex turns in the opposite sense to the passage vortex and is much smaller. It remains in the suction surface-endwall corner due to the radial and transverse pressure gradients and may be dissipated by viscosity.

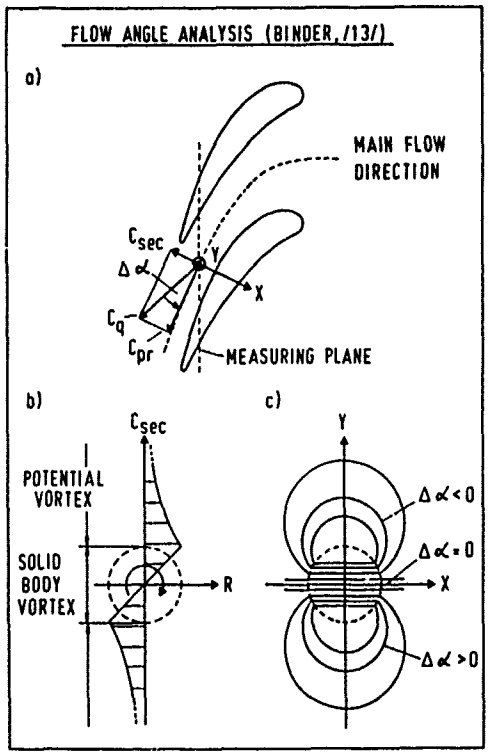


Fig. 8: Identification of a vortex by flow angle analysis

The identification of vortices in a three dimensional flow field can be achieved in different ways. Considering the experimental data obtained from 5-hole probe measurements and L2F-measurements it is possible to identify vortices by analysing the flow angle distributions in the measuring planes /13/. Fig. 8a shows a typical turbine blade-to-blade section. The measuring plane is perpendicular to the machine axis and the secondary flows are defined to be perpendicular to the main flow direction. In a plane perpendicular to the main flow direction a cylindrical vortex consisting of a solid body vortex and a potential vortex part (Fig. 8b) is associated with an isocline pattern shown in Fig. 8c. This pattern results from overlapping a system of parallel isoclines and a system of circles touching each other in the vortex centre. In general measurements are carried out in planes that aren't perpendicular to the main flow direction. So the isocline pattern has a different shape in this plane, i. e. the isoclines are parallel to each other in the solid body vortex area and are of elliptical shape in the potential vortex area.

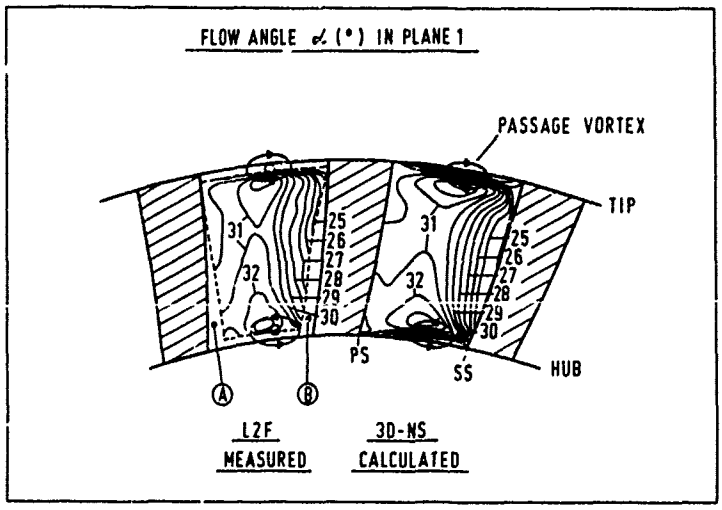


Fig. 9: Distribution of flow angle in plane 1 (isoclines)

Fig. 9 shows the calculated and measured flow angles in plane 1. The L2F-measurement data were taken for this comparison. The correspondence between the two isocline patterns is very good. They indicate two passage vortices at hub and tip. Their sense of rotation is given by the directional markers. Due to the radial leaning of the blades measurements were not possible in region "A" near pressure side. The minimum measurement distance from the endwalls was 2.1 mm which corresponds to 5 % blade height. Since the L2F-system works in a backscattering mode a closer approach to the hub wall was not possible because of the high reflexions although the surface was coloured black. At the endwalls it is in addition difficult to seed the flow streamlines with particles. High components of radial velocities prevent the use of the two-dimensional L2F- velocimeter in region "B" near suction side.

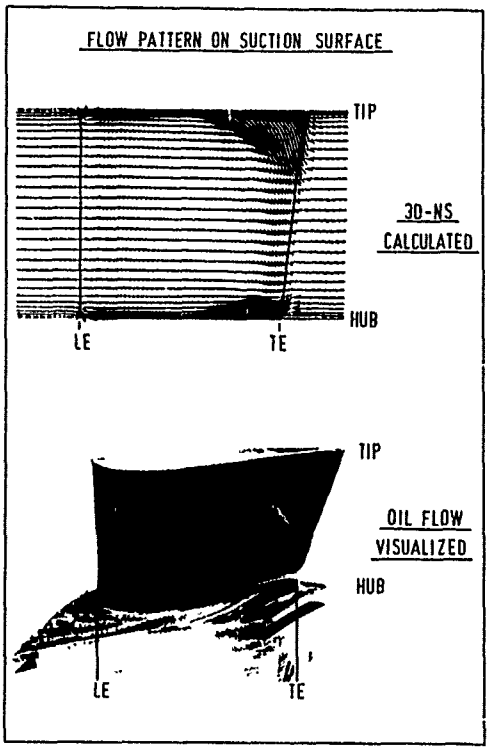


Fig. 10: Flow pattern on suction surface of guide vane

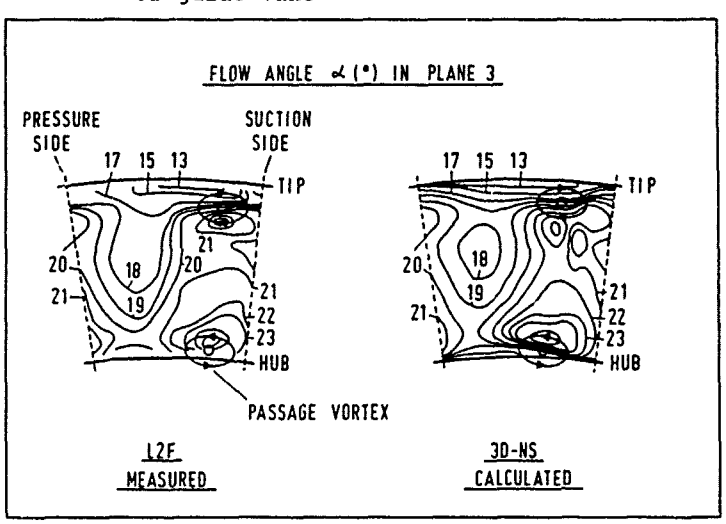


Fig. 11: Distribution of flow angle in plane 3 (isoclines)

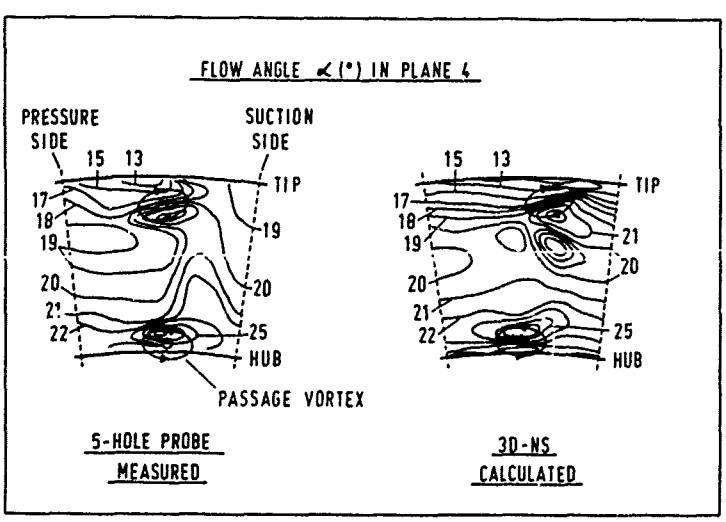


Fig. 12: Distribution of flow angle in plane 4 (isoclines)

Fig. 10 illustrates calculated and measured flow patterns on the suction surface. The calculated flow field shows two regions of high radial velocities at hub and tip at the rear part of the blade surface. The region at the hub is smaller than that at the tip which is due to the radial pressure gradient. The picture below taken by an oil tracing technique shows also two regions of strong radial velocity components. But the extensions of these areas are different when compared to the calculated regions. The wedge-shaped area of tracing lines on the lower part of the surface is caused by a big particle and doesn't represent the real flow field. The calculated and measured flow fields on the pressure side correspond well to each other and do not show remarkable radial velocity components.

The oil tracing technique at hub (Fig. 10) shows a saddle point near leading edge and the shapes of two endwall separation lines belonging to the legs of a weak leading edge vortex. The vector plot of the calculated flow field at hub indicates also the existence of a suction side leg of the leading edge vortex which dissipates at about x/l_m = 40 %. The development of the pressure side leg of the leading edge vortex is difficult to analyze. Up to now neither the calculation nor the measurements give detailed information about its development. This seems to be due to the thin inlet boundary layer generating only a weak leading edge vortex which is believed to attribute only a small rate to the overall secondary flow loss production.

Fig. 11 shows the flow angles calculated and measured by the L2F-velocimeter in plane 3. The agreement between both distributions is quite good. The two systems of parallel isoclines at hub and tip indicate the two passage vortices already known from plane 1 (Fig. 9).

Fig. 12 illustrates the comparison of the calculated and the by 5-hole probes measured flow angles in plane 4. They agree quite well except in the main flow region. But the two passage vortices again can be clearly identified by the isocline patterns. The existence of these vortices in plane 4 has been additionally proved by L2F-measurements.

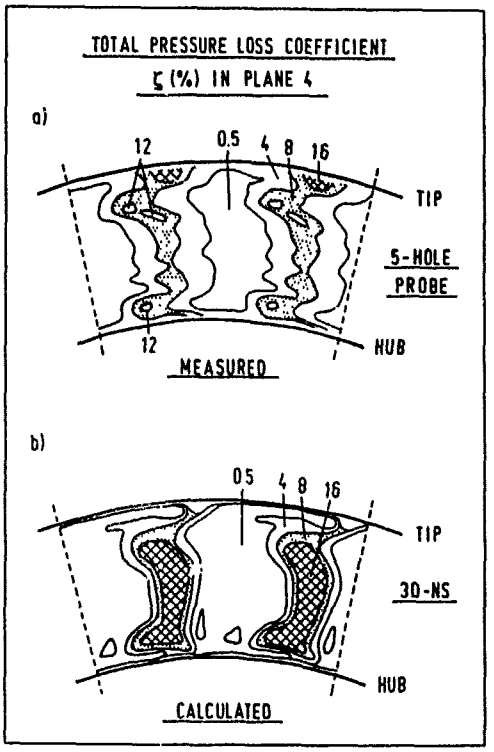


Fig. 13: Distribution of total pressure loss coefficient in plane 4

Fig. 13 shows the loss distribution in plane 4. The 3D-NS calculated total pressure loss coefficient is plotted against the results based on 5-hole-probe measurements.

In Fig. 13a high losses are concentrated to the wake regions of the turbine guide vanes. These are inclined to the radial direction due to the spanwise distribution of flow angle and due to the different axial distances between the trailing edge and the measuring plane (axial leaning of trailing edge). High loss regions of 12 % and 16 % are caused by secondary flows.

The calculated distribution in Fig. 13b differs much from the measured one. A large region of very high losses (16 %) is predicted. The measurements are showing much lower losses in these areas. The present work is concentrated to check the influence of the computational grid on calculated results. It has to be pointed out that the presented calculations are based on a not adapted grid which might cause uncertainities in predicted losses.

CONCLUSIONS

The comp. isons between measured and calculated flow field data resulted in an overall good agreement and contributed to a better understanding of the flow phenomena in this annular turbine cascade with low aspect ratio. Additionally these comparisons have shown that a further improvement of calculated results seems to be possible by using a modified mesh structure. The following aspects were found:

1) The secondary flows in this blade passage consist of two passage vortices at hub and tip. Due to the thin inlet boundary layer the leading edge vortices are weak. The suction side leg of this vortex at hub dissipates at about x/l_m = 40 % while the development of the pressure side leg cannot be described up to now.

2) The applied 3D-NS-code is able to predict the secondary flow phenomena in the blade passage. But for detailed numerical flow studies a much finer mesh is necessary.

3) The correspondence between measured and calculated velocities is already quite good. Only the predicted velocities near hub and tip are too high which probably will be improved by using the finer mesh structure.

4) The loss prediction is not satisfying yet, an improvement seems also to be possible by optimizing the mesh geometry at the trailing edge and in the downstream region.

ACKNOWLEDGEMENTS

The authors wish to express their gratitude to R. Schodl and his team for their support in L2F-measuring technique, W. Karnatschke, M. Roske and K. Peters who did the measurements.

REFERENCES

/1/ SHARMA, O.P.
BUTLER, T.L.
"Predictions of Endwall Losses and Secondary Flows in Axial Flow Turbine Cascades"
ASME Paper No. 86-GT-228

/2/ SIEVERDING, C.H.
"Recent Progress in the Understanding of Basic Aspects of Secondary Flows in Turbine Blade Passages"
ASME J. Eng. Gas Turbines and Power, Vol. 107, 1985

/3/ DAWES, W.N.
"Development of a 3D Navier Stokes Solver for Application to all Types of Turbomachinery"
ASME Paper No. 88-GT-70

/4/ WEGENER, D.
ROGGE, H.
KARNATSCHKE, W.
BIRKHÖLZER, H.
"Beurteilung der Zuströmverhältnisse und der Fünflochsonden-Meßtechnik im Turbinenprüfstand VT-1B"
DFVLR, IB 325-09-87, Köln, 1987

/5/ ROSKE, M.
"Beschreibung der Konstruktion eines Leitgitterprüfstandes und der zugehörigen Anlage zur Meßwerterfassung und Versuchsablaufsteuerung"
DFVLR, IB 325-14-87, Köln, 1987

/6/ SCHODL, R.
"A Laser-Two-Focus (L2F) Velocimeter for Automatic Flow Vector Measurements in the Rotating Components of Turbomachines"
ASME Journal of Fluids Eng., Vol. 102, No. 4, 1980

/7/ QUEST, J.
"Über die Berücksichtigung der räumlichen Strömung beim Entwurf von Turbinenleiträdern"
DFVLR, IB 325-20-86, Köln, 1986

/8/ KRAIN, H.
HOFFMANN, W.
"Verification of an Impeller Design by Laser Measurements and 3D-Viscous Flow Calculations"
ASME Paper No. 89-GT-159

/9/ HENN, M.I.
GIESS, P.-A.
"Messung der aerodynamischen Kenndaten des ebenen Turbinen-Leitradgitters VT-1B"
DFVLR, IB 222-87 A 13, Göttingen, 1987

/10/
"Propulsion and Energetics Panel Working Group 1: on Suitable Averaging Techniques in Non-Uniform Internal Flows"
AGARD-AR-182, Chap. 5: Conclusions and Recommendations

/11/ LANGSTON, L.S.
"Crossflows in a Turbine Cascade Passage"
ASME J. of Eng. for Power, Vol. 102, 1980

/12/ MARCHAL, Ph.
SIEVERDING, C.H.
"Secondary Flows within Turbomachinery Bladings"
AGARD-CP-214, 1977

/13/ BINDER, A.
ROMEY, R.
"Secondary Flow Effects and Mixing of the Wake Behind a Turbine Stator"
ASME J. of Eng. for Power, Vol. 105, No. 1, 1983

DISCUSSION

Howard, UK

1. The comparison of losses at plane 4 suggests that in the experiment the wake is mixing out faster than in the prediction.

2. Have comparisons at other axial planes been made to study the wake mixing experiment compared to prediction?

Author's Reply:

Five hole probe measurements in planes 4, 5 and 6 show that the wake is totally mixed out in plane 6, i.e., at about two axial chord lengths behind stator exit. The numerical approach is based on a mesh given in Fig 3 which has downstream only an axial extension of 2/3 of axial chord length. I believe that the short downstream mesh is responsible for this different mixing out behavior.

Adamczyk, USA

Did you attempt to incorporate a transition model in you numerical simulation?

Author's Reply:

No, I don't. Our numerical approach is based on the unchanged 3D-NS-code we applied from Prof Dawes.

MEASUREMENT OF THE FLOW FIELD IN THE BLADE PASSAGE AND SIDE-WALL REGION OF A PLANE TURBINE CASCADE

E. Detemple-Laake

Deutsche Forschungsanstalt
für Luft- und Raumfahrt e.V.
Institut für Experimentelle Strömungsmechanik
Bunsenstr. 10
D-3400 Göttingen
F. R. Germany

SUMMARY

The transonic flow through a plane cascade consisting of profiles designed for a highly loaded gas turbine rotor of a high pressure stage is investigated. The experiments presented here are part of an entire test program performed in a special wind tunnel at the DLR. This paper describes the measurements of the side-wall pressure distribution in a blade passage. The parameters varied are the inlet flow angle and the downstream isentropic Mach number. Based on the results of schlieren photographs of the flow field and surface oil flow patterns on the blades and the side-wall the experimental results are interpreted.

NOMENCLATURE

M_{2S}	isentropic Mach number of the cascade exit flow
β	inlet flow angle
$p_{s/0}$	side-wall pressure
p_{t1}	total pressure of the inlet flow
x	coordinate normal to the cascade outlet plane
y	coordinate parallel to the cascade outlet plane
l_x	axial profile chord
t	blade pitch
φ	viewing angle

INTRODUCTION

In the plane cascade wind tunnel EGG of the DLR Göttingen various measurement techniques are used to investigate transonic flow fields within plane cascades. On the one hand the development of the flow field resulting from the shock wave boundary layer interaction is studied, on the other hand the development of the flow field along the blade from the middle of the passage to the side-wall is studied.

A sequence of joint investigations of a highly loaded turbine cascade consisting of profiles designed by MTU was performed by the DLR Institute for Experimental Fluid Mechanics Göttingen and MTU München. The measurement techniques used comprise: surface pressure measurements, trailing edge wake traverse measurements, schlieren visualization (Dietrichs et al. (Ref.1)), infrared image technique, surface oil flow visualization (Bräunling et al. (Ref.2)), heated thin-film measurements (Kost et al. (Ref. 3)).

The main objective of the present investigations is to extend this existing knowledge of the flow field within the blade passage to the flow phenomena resulting from side-wall effects and three dimensional separation. A systematic experimental investigation of the side-wall pressure has been performed with four different inlet flow angles β = 120°, 140°, 150°, 155° at various downstream Mach numbers in the range $0.8 \leq M_{2S} \leq 1.3$. The experimental results are interpreted with respect to the existing flow models describing secondary flow effects (Sieverding (Ref.4)) and shock-wave boundary layer interactions (Delery and Marvin (Ref.5)).

EXPERIMENTAL METHODS

The experiments were carried out in a plane cascade wind tunnel of the DLR Göttingen (Fig. 1). The test facility is described by Heinemann (Ref.6). The wind tunnel is a suction type tunnel with an open circuit which operates intermittently or continuously. The testing time is about 50 seconds for high Mach numbers (M $\sim$ 1.3), for lower Mach numbers the wind tunnel operates continuously. Figure 2 shows a typical arrangement of the test section. The test section can accomodate 8-12 blades of high deflection geometry and about 20 blades of low deflection geometry. The blade chord length is 60 mm, the blade height is 125 mm. The blades are fabricated in brass.

The side-wall pressures were measured in one passage by use of two exchangable side-walls with 170 and 196 pressure tappings, respectively. Figure 3 shows the configuration of the pressure tappings of 0.4 mm diameter in 5x5mm grids. The flow field in the midspan is visualized by schlieren technique. The schlieren optic is arranged conventionally. The surface oil flow pictures were taken by coating the blade and side-wall surfaces with a mixture of titanium dioxide powder and baby oil. An overview of the visualization techniques is given among others by Merzkirch (Ref. 7).

EXPERIMENTAL RESULTS AND CONCLUSIONS

The experiments were carried out with a plane cascade consisting of profiles designed for a highly loaded gas turbine rotor of a high pressure stage. The cascade was designed for 130° inlet flow angle with respect to axial direction. The test program comprised the variation of the isentropic downstream Mach number M_{2S} (based on the pressure in the test chamber) and the inlet flow angle β. The side-wall pressures (Fig. 3) have been measured at seven Mach numbers in the range $0.8 \leq M_{2S} \leq 1.3$ with four inlet flow angles β = 120°, 140°, 150°, 155°. The presentation of experimental results is mainly confined to the flow fields for β = 120° at M_{2S} = 0.9, 1.0, 1.25.

Figure 4 illustrates the development of the midspan flow field with increasing Mach number in the case of negative incidence. In the subsonic case, M_{2S} = 0.9, the flow is strongly accelerated along the suction side. As a result of the expansion of the flow down to the throat local supersonic regions develop - indicated by the weak compression fans - which are terminated by a normal shock. The wake consists of the boundary layers coming from the pressure side and suction side forming a vortex street. At the leading edge the pressure side separation and the local expansion region in suction side direction are revealed. Profile pressure distributions (Ref.1) and oil flow patterns (Fig. 5) show a laminar separation bubble on the suction side which is not visible in the schlieren picture. With increasing Mach number a trailing edge shock occurs at M_{2S} = 1.0. With further increase of the Mach number the trailing edge shock becomes stronger and more oblique. At M_{2S} = 1.25 a typical transonic flow pattern for plane cascades develops. Trailing edge shocks are formed in the near wake. The right shock is deflected by the upper wake. The left shock is reflected at the lower suction side as a sequence of compression-expansion-compression waves due to the wedge-shaped thickened boundary layer. The laminar boundary layer has lifted due to the adverse pressure gradient and a separation bubble has developed. Finally at M_{2S} = 1.3 the flow is fully separated and no reattachment occurs. Detailed explanations of the flow structures in the cascade investigated are given in Ref.1 and Ref.2.

The associated flow structures on the blade suction side and on the side-wall are shown in Figures 5 and 6. In the case of negative incidence for all Mach numbers separation bubbles exist on the suction side, here clearly revealed by the blade surface oil flow patterns.

Figure 5 shows a subsonic case. The rolling up of the side-wall boundary layer in front of a blade into the leading edge horseshoe vortex causes the separation saddle point, i.e distinct flow regions are delimited by the 3D separation lines and the stagnation streamline. Along the stagnation streamline the inlet boundary layer divides into the fluid entering the suction leg of the horseshoe vortex and the fluid forming the pressure leg which merges with the passage vortex in the passage. The two major separation lines ahead of the leading edge are the liftoff line of the horseshoe vortex and the boundary layer separation line ahead of the horseshoe vortex. They merge while swinging around the leading edge.

The suction leg of the horseshoe vortex is swept onto the suction surface behind the leading edge due to the transverse pressure gradient in the blade passage. The associated separation line interferes with the suction side: the vortex leg moves on the blade suction side towards the midspan and touches the separation bubble (Fig. 5, top). The separation line is visible up to the trailing edge.

The pressure leg of the horseshoe vortex is deflected towards the suction side of the adjacent blade due to the transverse pressure gradient. On its way the pressure leg merges with the existing passage vortex to one single vortex. In the suction surface flow pattern the side-wall side separation line denotes the separation of the passage vortex from the suction surface. On the side-wall side of the separation line of the passage vortex - in the corner of suction side and side-wall - the separation of the suction side endwall corner vortex is revealed. The side-wall flow pattern (Fig. 5, bottom) shows the

associated separation line originating downstream of the intersection point of the suction leg with the suction surface. Also a pressure side endwall corner vortex is indicated by a reattachment line on the side-wall along the corner of pressure side and side-wall.

Figure 6 shows the supersonic case. In principle the oil flow patterns show qualitatively the same features. Additionally, the trailing edge shock traces are revealed which coincide with the shock locations in the midspan which are known from schlieren pictures (Fig. 4) and thin-film measurements (Refs.2 and 3). The skin-friction lines are strongly deflected in the shock foot regions. They turn parallel to the shock direction and then continue downstream of the shock in outlet flow direction. The lines' crossing of the shock traces indicates an interaction without separation. The development of the structures at increased inlet flow angle causes the saddle point as well as the intersection point on the suction surface to move dependent on the flow direction. Additionally, the suction side corner vortex is greater.

Figures 7, 8, and 9 show the side-wall pressure distributions in a passage for $\beta = 120°$. Three different viewing angles φ (see Fig. 3) are chosen to show the pressure fields from different points of view. The side-wall pressure distribution at $M_{2S} = 0.9$ (Fig. 7) reveals:

- a weak pressure maximum due to the trailing edge expansion (□) as can be seen in the schlieren picture (Fig. 4);
- a weak pressure maximum at the location of the saddlepoint (•) as can be seen in the side-wall flow pattern (Fig. 5);
- pressure decrease across the passage towards the suction side;
- a local pressure maximum next to the suction surface (o).

At $M_{2S} = 1.0$ (Fig. 8) the pressure differences are greater due to the increased Mach number. The development of the pressure field at the leading edge and across the passage is qualitatively similar to the previous case. Additionally, the side-wall pressure distribution shows:

- a greater local pressure maximum next to the suction surface (o);
- the shock trace (---) of the shock upstream of the trailing edge which can be seen in the schlieren picture (Fig. 4).

In the supersonic case at $M_{2S} = 1.25$ (Fig. 9) the pressure field shows:

- the local pressure maximum next to the suction surface (o) coincides with the location of the separation bubble as shown by schlieren pictures (Fig. 4) and thin-film measurements (Ref.2);
- the trailing edge shock traces in the near wake (---) in agreement with the schlieren pictures (Fig. 4).

For comparison of the extreme inlet flow conditions at $\beta = 120°$ and $\beta = 155°$ Figure 10 shows the midspan flow field, the suction side flow pattern, and the side-wall pressure distribution for $\beta = 155°$ at $M_{2S} = 1.25$. While the flow structures develop qualitatively analoguous for $\beta = 120°$, 140°, 150° at $\beta = 155°$ the flow separates at all Mach numbers at the suction surface downstream of the leading edge starting with a shock. Schlieren pictures and oil flow patterns reveal in connexion with pressure measurements and thin-film measurements (Ref.3) that at the nose of the profile a separation bubble exists and the flow reattaches turbulent shortly behind the separation. The fully turbulent boundary layer resists the pressure rise due to the impingement of the shock from the upper blade and no separation bubble occurs. The oil flow pattern reveals on the one hand that the suction leg moves nearer to the midspan and its separation line is deflected by the shock, and on the other hand that the passage vortex extends to the midspan. The side-wall pressure distribution also indicates the characteristic change of the flow around the leading edge with a local pressure maximum at the separation (o). In comparison to pressure distributions for $\beta = 120°$ the suction side local pressure maximum (o) also exists at the shock impingement point but in contrast in this case no separation occurs.

REFERENCES

1. Dietrichs, H.-J.; Hourmouziadis, J.; Malzacher, F.; Bräunling, W.: Flow Phenomena in Transonic Turbine Cascades. Detailed Experimental and Numerical Investigation. Proc. 8th ISABE, Cincinnati, Ohio, USA, 1987.

2. Bräunling, W.; Quast, A.; Dietrichs, H.-J.: Detection of Separation Bubbles by Infrared Images in Transonic Turbine Cascades. ASME Paper 88-GT-33, 1988.

3. Kost, F.; Bräunling, W.; Schüpferling, E.; Göhl, R.: Detection of Separation Bubbles by Heated Thin-Film Sensors in Transonic Turbine Cascades. Proc. 9th Symp. on Measuring Techniques for Transonic and Supersonic Flows in Cascades and Turbomachines, Oxford, U.K., 1988.

4. Sieverding, C.H.: Secondary Flows in Straight and Annular Turbine Cascades. In: Thermodynamics and Fluid Mechanics of Turbomachinery, Vol.II, Dordrecht/Boston/Lancaster, Martinus Nijhoff Publishers, 1985, pp. 621-664.

5. Delery, J.; Marvin, J.G.: Shock-Wave Boundary Layer Interactions. AGARD-AG-280, 1986.

6. Heinemann, H.-J.: The Test Facility for Rectilinear Cascades (EGG) of the DFVLR. DFVLR Report IB 222 - 83 A 14, 1983.

7. Merzkirch, W.: Techniques of Flow Visualization. AGARD-AG-302, 1987.

ACKNOWLEDGEMENT

The author wishes to express her gratitude to Dr. W. Bräunling who took the oil flow pictures

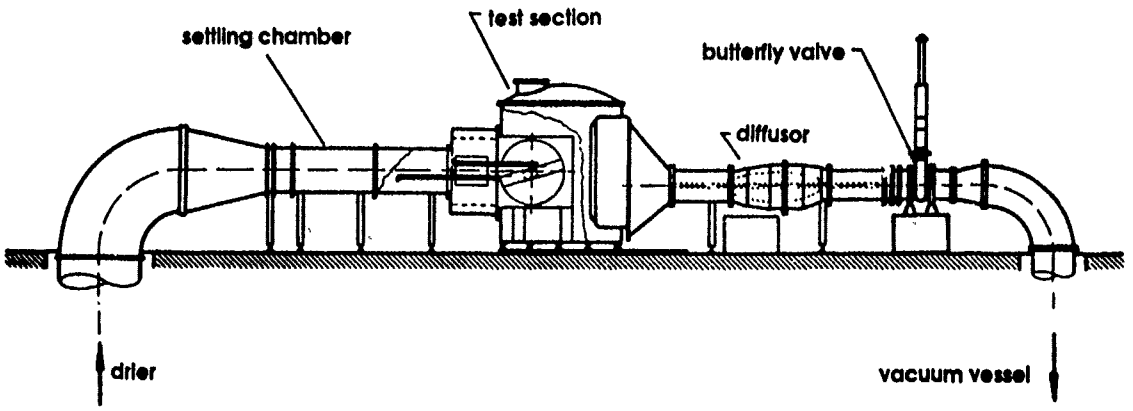


Fig. 1 Plane cascade wind tunnel EGG

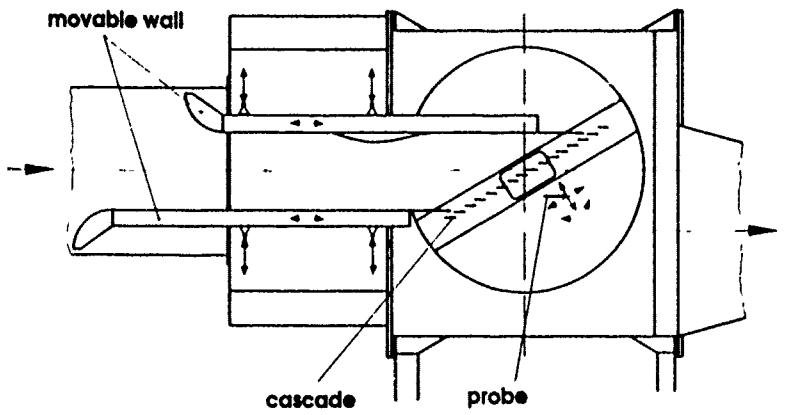


Fig. 2 Test section

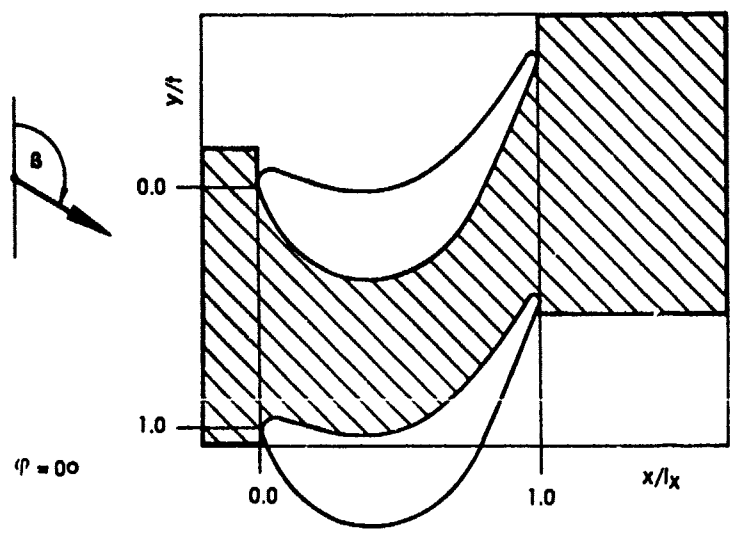


Fig. 3 Side-wall pressure tappings

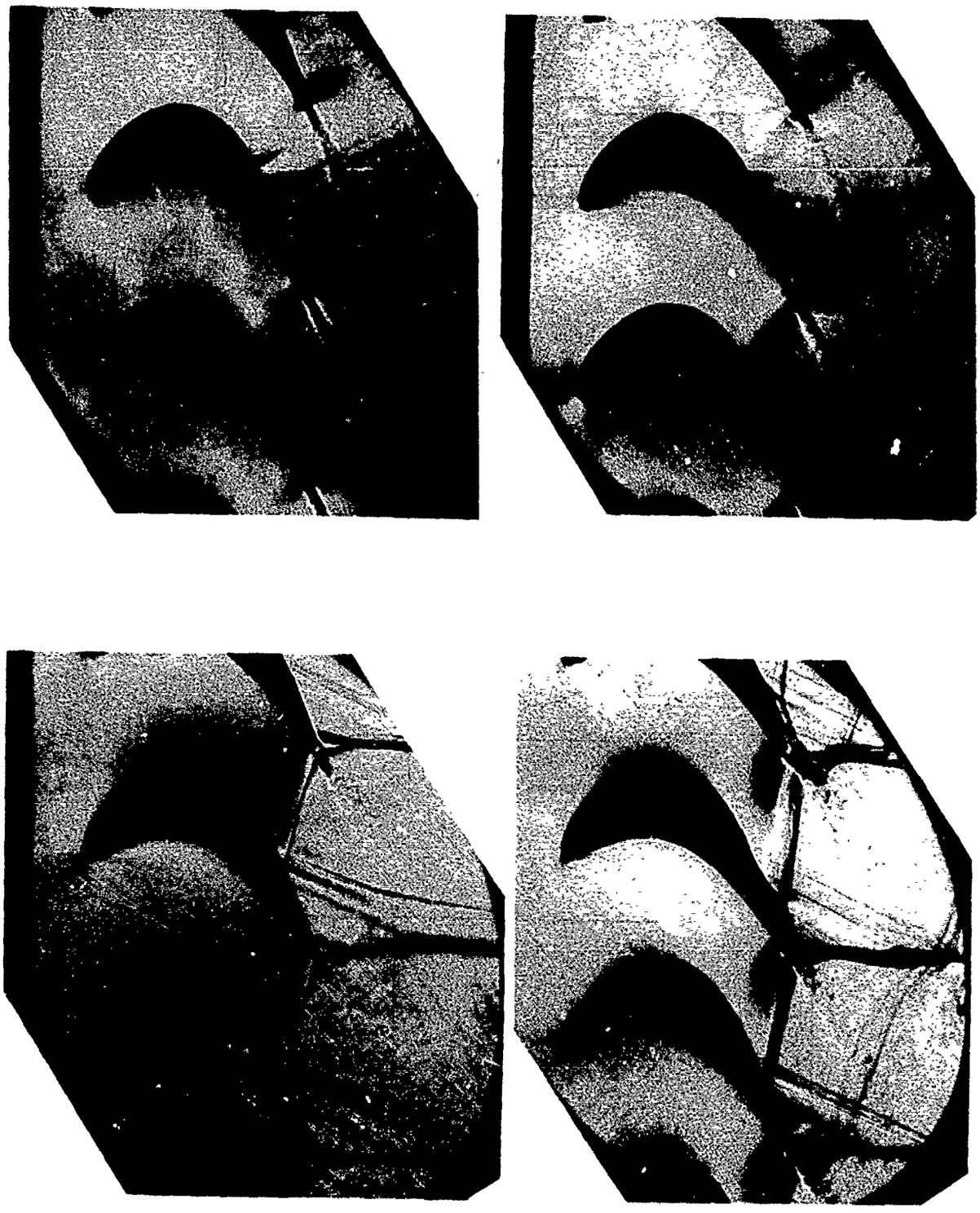


Fig. 4 Schlieren pictures: $\beta = 120°$, $M_{2S} = 0.9$ (upper left), $M_{2S} = 1.0$ (upper right), $M_{2S} = 1.25$ (lower left), $M_{2S} = 1.3$ (lower right)

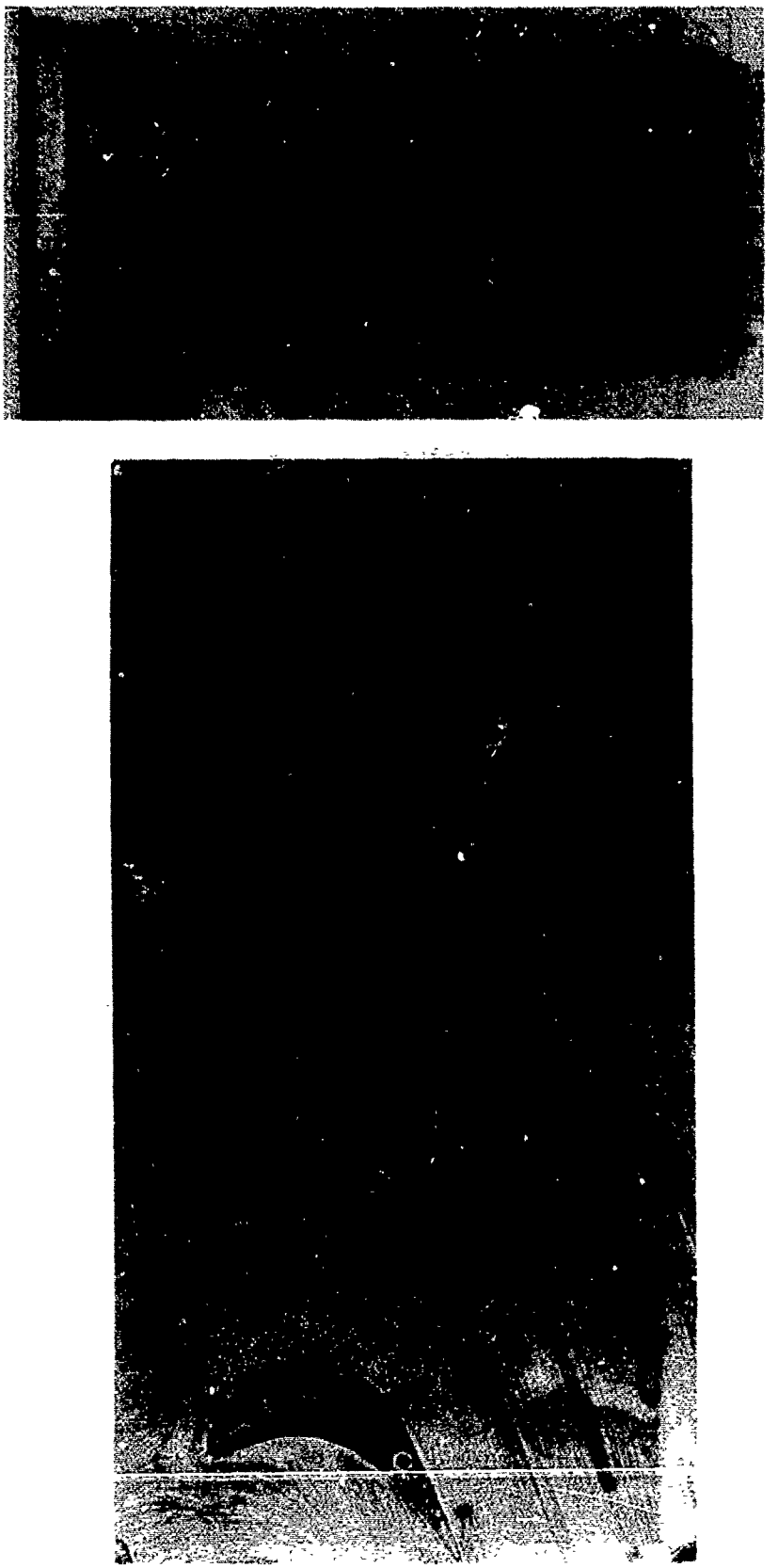


Fig. 5 Surface oil flow patterns: $\beta = 120°$, $M_{2S} = 0.72$; suction side (top), side-wall (bottom)

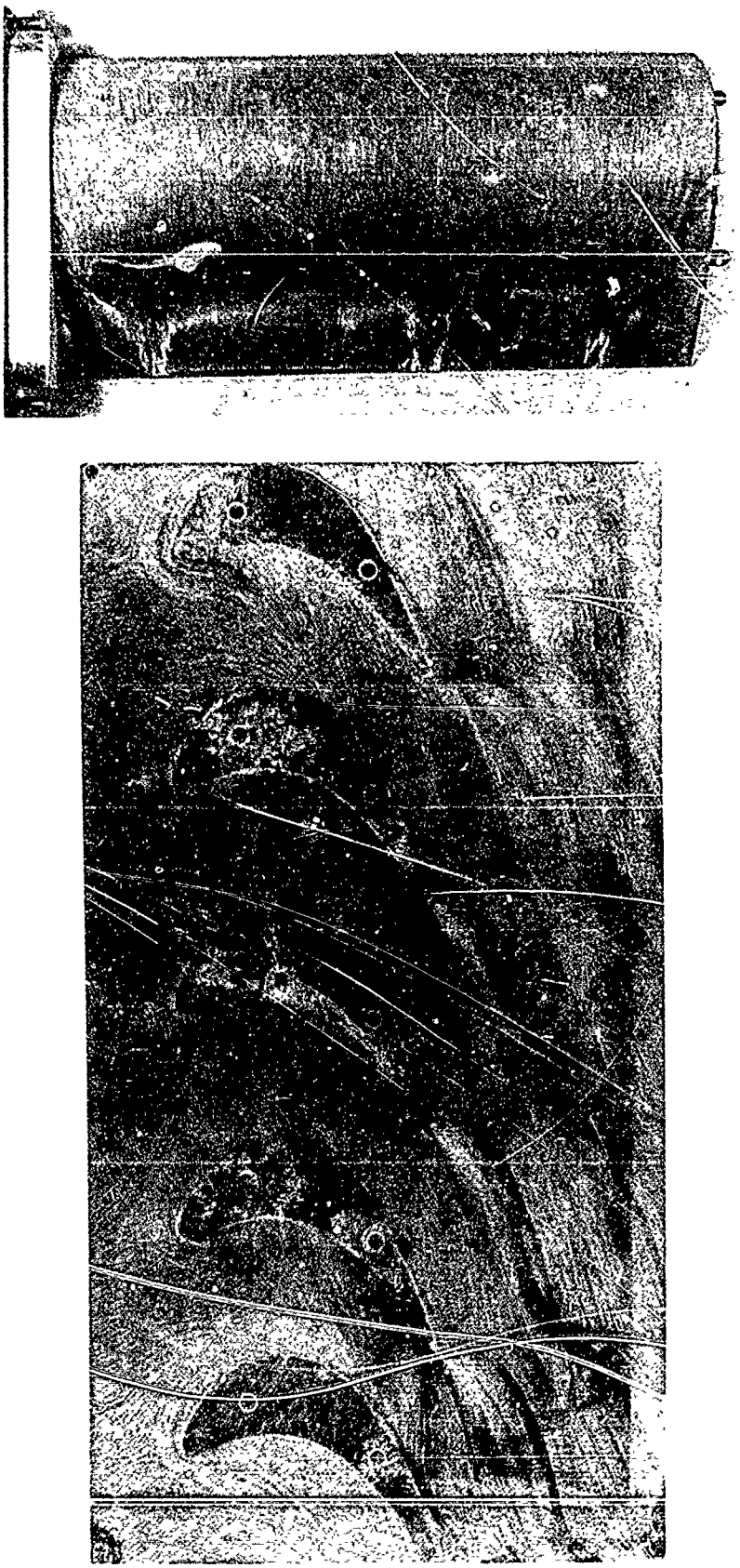


Fig. 6 Surface oil flow patterns. $\beta = 120°$, $M_{2S} = 1.25$; suction side (top), side-wall (bottom)

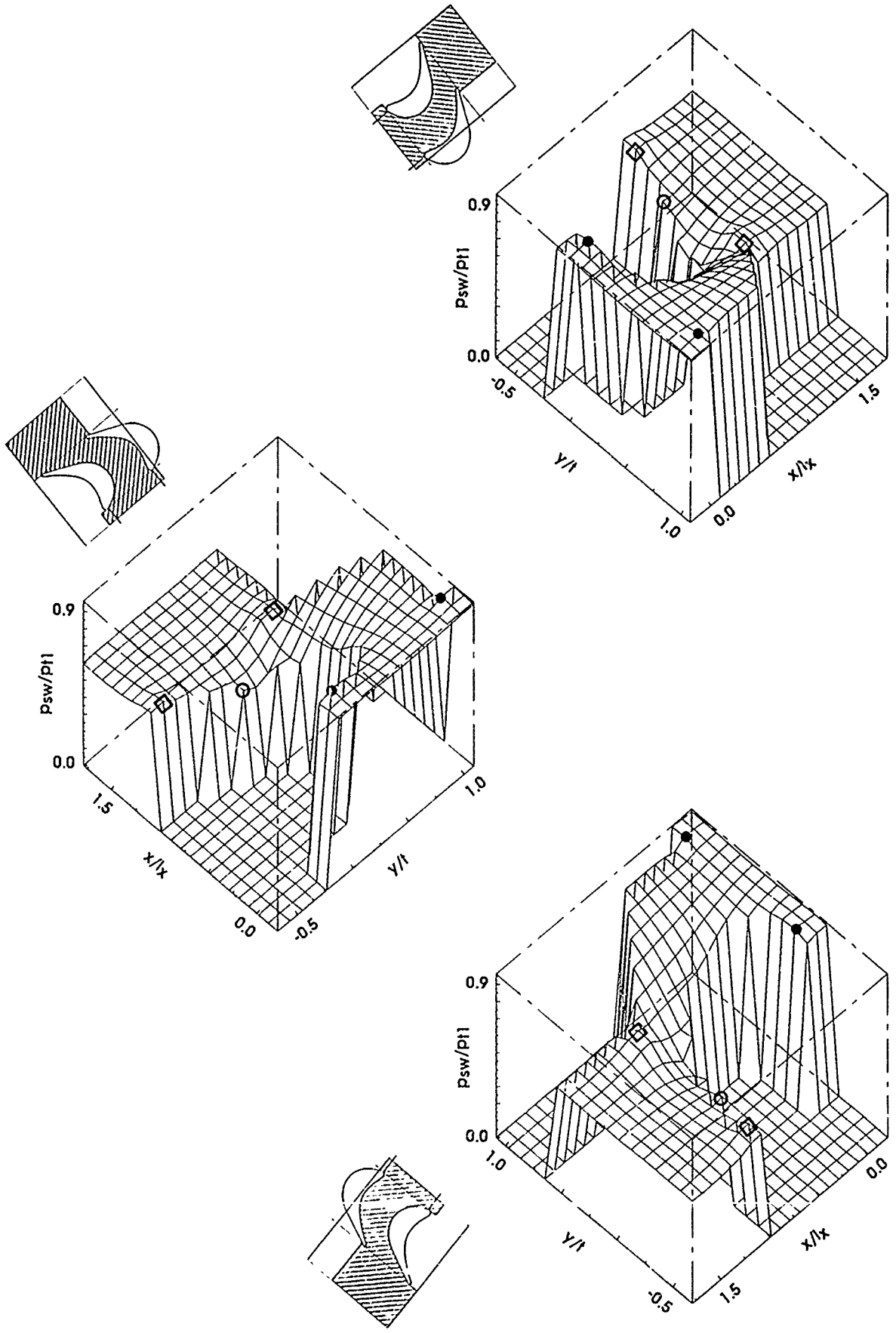


Fig. 7 Side-wall pressure distribution: $\beta = 120°$, $M_{2S} = 0.9$, $\varphi = 45°$ (top), $\varphi = 135°$ (left), $\varphi = 225°$ (bottom)

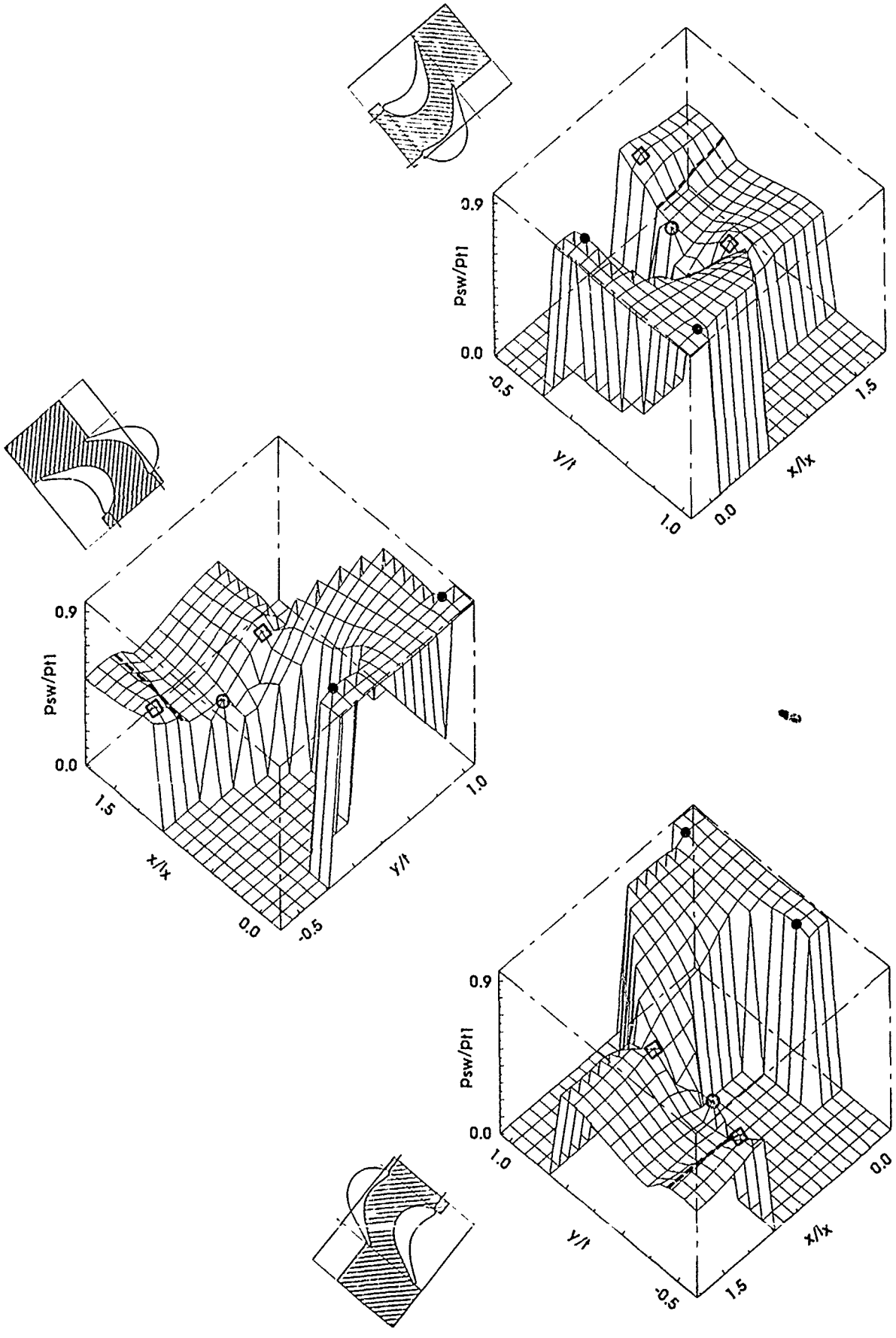


Fig. 8 Side-wall pressure distribution: $\beta = 120°$, $M_{2S} = 1.0$; $\varphi = 45°$ (top), $\varphi = 135°$ (left), $\varphi = 225°$ (bottom)

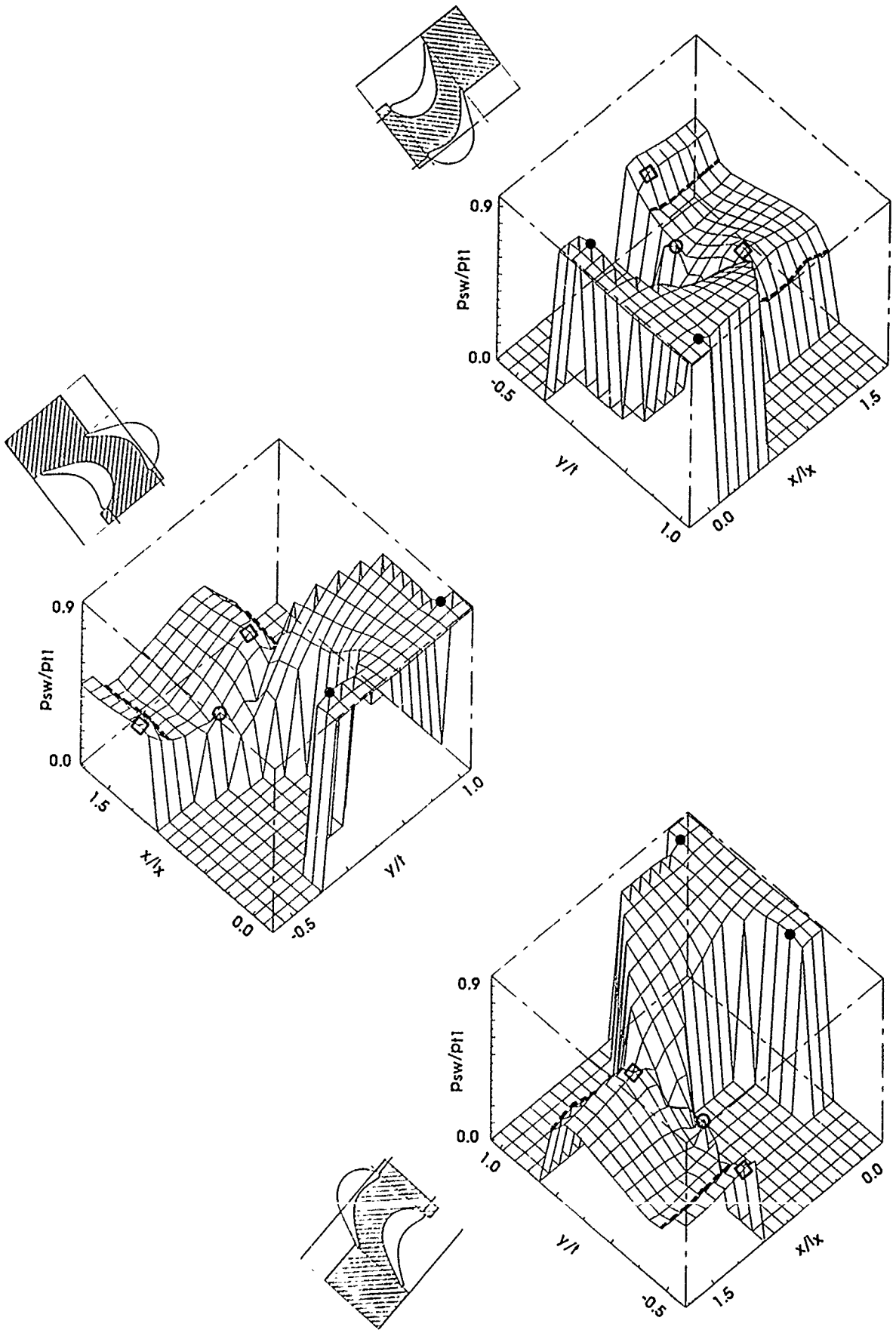
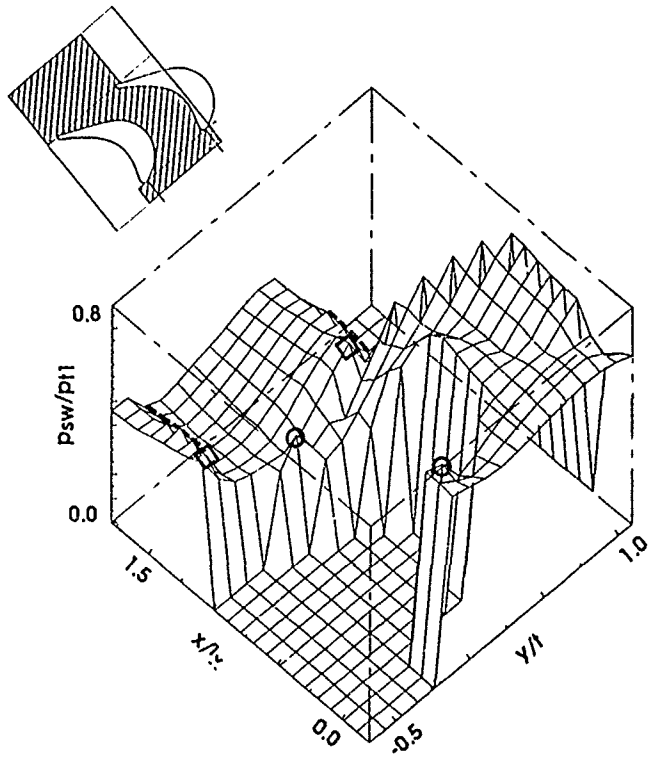


Fig. 9 Side-wall pressure distribution: $\beta = 120°$, $M_{2S} = 1.25$; $\varphi = 45°$ (top), $\varphi = 135°$ (left), $\varphi = 225°$ (bottom)







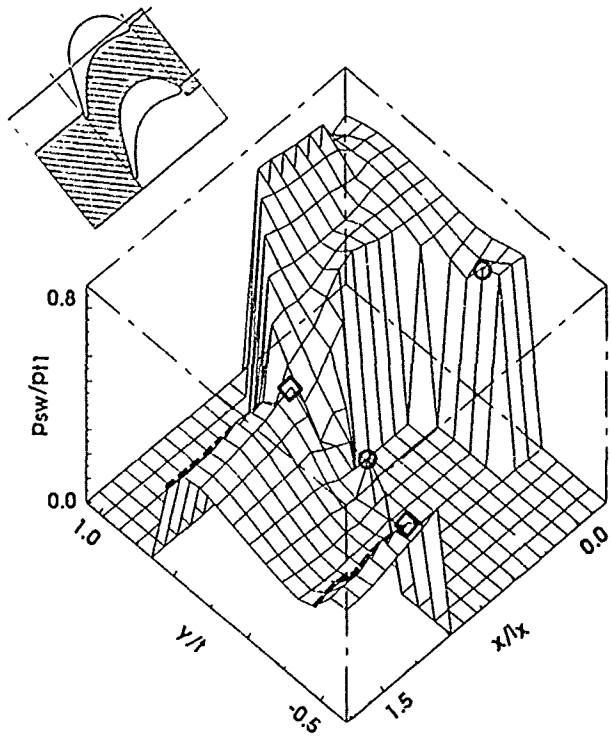


Fig. 10 Schlieren picture, surface flow pattern, side-wall pressure distribution. $\beta = 155°$, $M_{2S} = 1.25$; $\varphi = 135°$ (top), $\varphi = 225°$ (bottom)

DISCUSSION

Ahmed, UK

You mention you had difficulties in getting seeding in your L2F measurement volumes. What sort of seeding material did you use and what was the arrangement to get the seeding particles in the measurement volumes?

Author's Reply:

I mentioned that we only had difficulties in getting seeding close to the suction surface in plane 1 at x/ℓ_m=81%. The seeding of our L2F - measurement volumes is achieved by a probe which is mounted further upstream of plane 0. This probe is supplied with oil droplets by a seeding generator.

Sieverding, Belgium

You showed colored schlieren pictures with a lammar shock B.L. interaction. On what ground do you suppose that transition takes place between the apex of the separated zone and the reattachment point?

Author's Reply:

From other experimental results (see Ref 1-3), it is known that the boundary layer separates laminar and reattaches turbulent. Thus the transition occurs within this separated region. Taking into account the photograph of the separation bubble which shows a thickened boundary layer downstream of the apex, we suggest that the thickened boundary layer indicates that transition has occurred.

Jones, UK

You referred to two separation lines ahead of the leading edge of the blade. The downstream separation you associate with the horseshoe vortex. Do you have information about the flow between the two separation lines? Was any vertical motion observed in this area?

Author's Reply:

The only information I have are those from oil flow patterns and s wall pressure distributions. They do not allow any conclusion concerning flow structure and vortical motion.

Moustapha, Canada

Did you measure the losses as a function of inlet angle change? It will be nice to report these data.

Author's Reply:

These losses were measured by Dr Braunling. The data have been published in a DLR-Internal Report

Centrifugal Impeller Geometry and its Influence on Secondary Flows

by

H. Krain
W. Hoffmann

DLR, Institut für Antriebstechnik
Linder Höhe, 5000 Köln 90, West-Germany

1. ABSTRACT

Detailed experimental and theoretical flow field studies are carried out for two 30 deg., high pressure ratio impellers having the same blade geometry but different shroud contours. An advanced Laser-Two-Focus Velocimeter is used to obtain experimental data (8), the theoretical investigations are performed with a 3D-viscous code (4) that was coupled with a postprocessor primarily suitable for turbomachinery flow field studies (2). Comparisons between measured and calculated data are carried out and the influence of the flow channel variation on the through flow velocity patterns and secondary flow structures are discussed.

SYMBOLS

A^+	constant damping factor, $A^+ = 26$	V	finite volume
C_{Kleb}	Klebanoff constant $C_{Kleb} = 0.3$	$\vec{v}$	absolute velocity
C_{WK}	constant, $C_{WK} = 0.25$	$\vec{w}$	relative velocity
C_{mL}	velocity component perpendicular to laser beam axis	y, y^+	coordinate normal to the wall, $y = \sqrt{\tau_w/\rho_w}/\mu_w$
c_p , c_v	constants of specific heat	y/t	dimensionless blade pitch
e	volume-specific total energy	z	axial coordinate
$F(U)$	flux	z/b	dimensionless channel depth
$F(y)$	function, Eq. (7) on page 8	z_R	rotor blade number
h	static enthalpy, $h = (\kappa/\kappa - 1)p/\rho$	α	constant, $\alpha = 0.0268$
I	rothalpy, $I = h + (w^2)/2 - (\Omega r)^2/2$	δS	surface element of finite volume
l	mixing length, $l = ky$, $k = 0.41$	δV	finite volume element
$\dot{m}$	mass flow rate	ρ	density
n	finite volume surface normal	κ	$\kappa = c_p/c_v$
n/n_0	shaft speed / design speed	μ	viscosity
PS	pressure side	μ_{turb}	eddy viscosity
p	pressure	τ	stress tensor
r	radial coordinate	π_t	total /total pressure ratio
S	surface of finite volume	φ	circumferential coordinate
SS	suction side	Ω	constant angular velocity
T	temperature	$\vec{\omega}$	$\vec{\omega} = 1/2\nabla\times\vec{v}$
t	time	$\nabla\times$	differential operator: rotor
u	circumferential velocity	$_w$	value taken at the wall

2. INTRODUCTION

The flow character of advanced centrifugal compressor impellers is typically governed by fully 3D-viscous flow effects being primarily due to the complex flow channel geometry and to the high loading of these components. Strong curvature effects in conjunction with boundary layer developments are causing significant secondary flows in both the hub-to-tip and blade-to blade planes. Coriolis forces, tip clearance effects as well as strong decelerations of the relative flow in the shroud area are additionally contributing to the development of pronounced cross flows. The loss productions and the performance characterstics of centrifugal compressors are believed to be strongly dependent on secondary flow development inside the impellers. The interdependence between secondary and primary flows have been experimentally studied with the L2F-velocimeter for a 30 deg, backswept impeller, (1), (8). These studies revealed that

the through flow velocity pattern was disturbed in areas of pronounced vortex development. This points to an impeller efficiency drop in the areas of high secondary flow development and to a reduction of the flow range of the overall machine, especially if vaned diffusors are used that are generally applied for high pressure ratio compressors ($\pi_t > 3$). For these reasons a secondary flow control during the design process of centrifugal impellers seems to be a prerequisite for a further improvement in efficiency and flow range. This, however, necessitates the development of reliable tools capable to predict and analyse such effects during the design process. Todays advanced 3D-viscous calculation methods in combination with increasing computer capacities are offering the possibilities to solve the problem indicated, (4), (5), (6) and (7). However, presently it is not well known whether the available 3D-viscous codes can be reliably applied to complex flow situations like those occuring in centrifugal compressor impellers. For example, it is not quite clear up to now, whether the simple turbulence models applied are sufficient to describe flow phenomena like wake development, separation and backflow that are known to occur frequently in centrifugal impellers. Therefore these methods should be checked against reliable measurement data before becoming a regular design tool. This paper describes the application of an impeller design procedure, (2), containing Q3D calculations on hub-to-tip and blade-to-blade stream surfaces, boundary layer calculations as well as 3D-viscous calculations. The design procedure was applied to two different impeller designs that have been experimentally investigated with the help of laser velocimetry, (8). Both the experiments and the calculations give insight into the secondary flow development of the two impellers. The influence of the flow channel geometry on secondary flows has been studied and it was found that a detailed control of secondary flow during the design process should be possible by the application of 3D-viscous codes which probably would contribute to a further efficiency improvement of impellers and to a significant cost reduction during the development process of advanced centrifugal compressors.

3. TEST IMPELLERS

3.1 GEOMETRICAL DATA

Two 30 deg. backswept impellers have been used for the flow studies. Both had the same blade- und hub geometry and were operated at the same mass flow rate and shaft speed but differed in their shroud contour shape. The second impeller was a redesign of the first one. The detailed blade geometry of the first impeller is submitted in Table 1, containing the pressure- und suction surface coordinates of the blades. Figure 1 shows a comparison of the meridional cross sections for both impellers.

	PRESSURE SIDE					
	HUB			TIP		
I	X (MM)	Y (MM)	Z (MM)	X (MM)	Y (MM)	Z (MM)
1	0.00	-27.76	35.41	0.00	-65.64	91.67
2	6.40	-26.03	39.76	5.36	-57.95	96.86
3	12.70	-24.40	43.97	10.53	-51.16	101.01
4	18.90	-22.82	48.15	15.52	-45.07	104.49
5	24.98	-21.23	52.36	20.35	-39.55	107.51
6	30.93	-19.62	56.64	25.04	-34.50	110.22
7	36.76	-17.97	61.01	29.61	-29.82	112.73
8	42.44	-16.25	65.49	34.05	-25.46	115.10
9	47.98	-14.45	70.08	38.39	-21.36	117.40
10	53.37	-12.57	74.79	42.64	-17.48	119.66
11	58.59	-10.59	79.62	46.80	-13.77	121.93
12	63.64	-8.49	84.56	50.88	-10.21	124.22
13	68.52	-6.28	89.62	54.89	-6.75	126.57
14	73.22	-3.93	94.79	58.82	-3.39	128.99
15	77.72	-1.44	100.06	62.68	-0.07	131.51
16	82.03	1.20	105.43	66.47	3.20	134.13
17	86.14	4.00	110.88	70.18	6.48	136.88
18	90.04	6.97	116.41	73.80	9.77	139.76
19	93.73	10.12	122.00	77.34	13.11	142.80
20	97.20	13.46	127.66	80.79	16.52	146.00
21	100.45	16.99	133.35	84.12	20.04	149.38
22	103.48	20.73	139.07	87.32	23.68	152.93
23	106.27	24.68	144.81	90.37	27.49	156.67
24	108.83	28.85	150.54	93.25	31.48	160.60
25	111.15	33.25	156.26	95.92	35.66	164.72
26	113.23	37.88	161.94	98.36	40.13	169.01
27	115.07	42.75	167.58	100.52	44.83	173.46
28	116.66	47.87	173.14	102.37	49.80	178.06
29	118.00	53.26	178.62	103.86	55.06	182.78
30	119.09	58.91	183.98	104.95	60.62	187.60

	SUCTION SIDE					
	HUB			TIP		
I	X (MM)	Y (MM)	Z (MM)	X (MM)	Y (MM)	Z (MM)
1	0.00	-23.88	38.14	0.00	-63.92	92.88
2	6.40	-21.66	42.31	5.36	-55.46	98.31
3	12.70	-19.63	46.30	10.53	-48.11	102.50
4	18.90	-17.74	50.24	15.52	-41.65	105.90
5	24.98	-15.94	54.21	20.35	-35.89	108.78
6	30.93	-14.19	58.24	25.04	-30.70	111.34
7	36.76	-12.44	62.38	29.61	-25.97	113.68
8	42.44	-10.67	66.63	34.05	-21.60	115.89
9	47.98	-8.86	71.01	38.39	-17.53	118.03
10	53.37	-6.97	75.52	42.64	-13.70	120.16
11	58.59	-4.99	80.16	46.80	-10.04	122.29
12	63.64	-2.91	84.94	50.88	-6.53	124.47
13	68.52	-0.72	89.84	54.89	-3.12	126.71
14	73.22	1.60	94.86	58.82	0.21	129.04
15	77.72	4.05	99.99	62.68	3.50	131.46
16	82.03	6.63	105.22	66.47	6.75	134.00
17	86.14	9.35	110.56	70.18	10.01	136.66
18	90.04	12.21	115.98	73.80	13.28	139.47
19	93.73	15.23	121.47	77.34	16.59	142.44
20	97.20	18.40	127.04	80.79	19.95	145.57
21	100.45	21.73	132.66	84.12	23.38	148.89
22	103.48	25.24	138.32	87.32	26.92	152.40
23	106.27	28.93	144.02	90.37	30.57	156.10
24	108.83	32.82	149.73	93.25	34.37	160.01
25	111.15	36.92	155.43	95.92	38.34	164.12
26	113.23	41.26	161.12	98.36	42.53	168.42
27	115.07	45.84	166.76	100.52	46.95	172.90
28	116.66	50.69	172.34	102.37	51.65	177.53
29	118.00	55.82	177.83	103.86	56.66	182.29
30	119.09	61.26	183.21	104.95	62.02	187.15

Table 1. Blade coordinates of the first impeller.

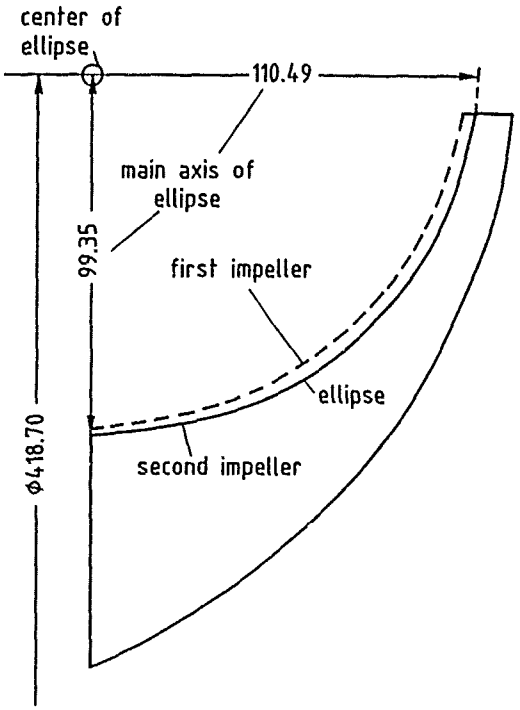


Figure 1. Meridional cross sections of both impellers

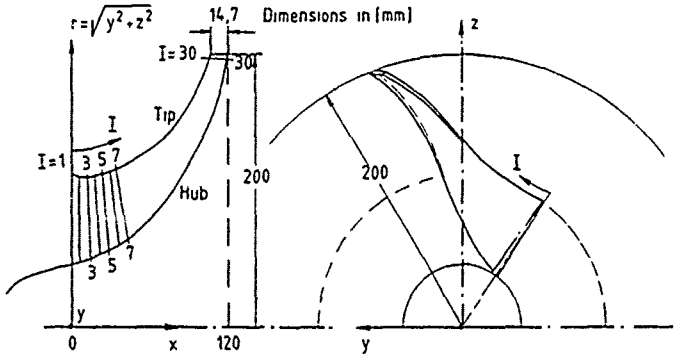


Figure 2. Generation of blade surfaces.

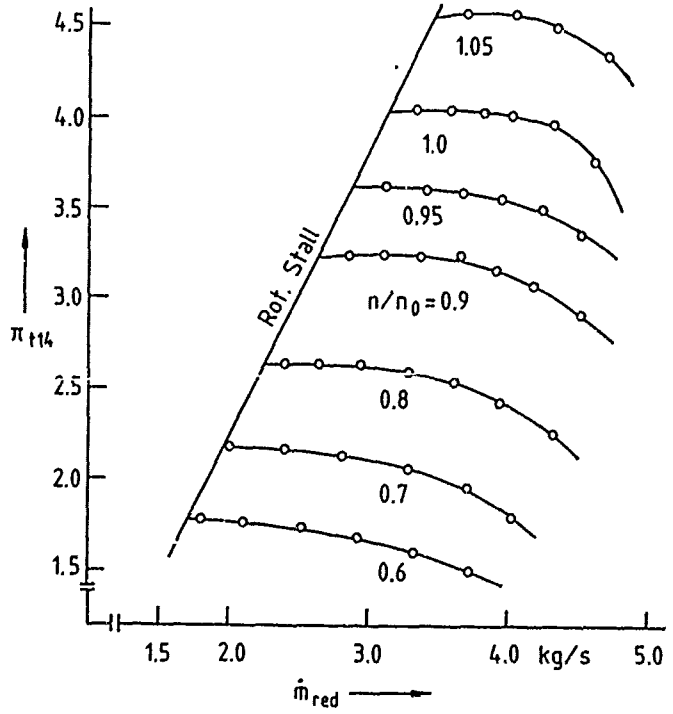


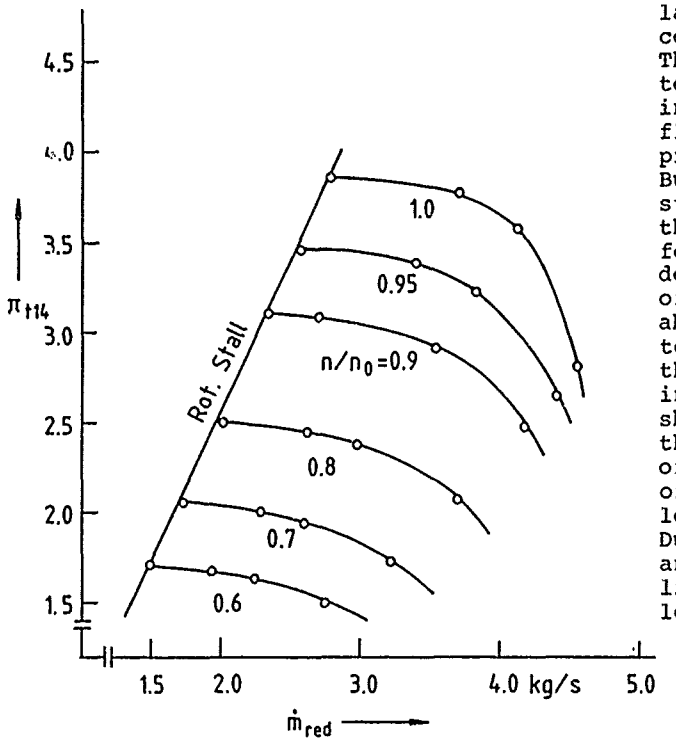
Figure 3. Performance map of the first stage.

The blade surfaces are composed of straight line elements, which ensures, that the impeller can be manufactured in a flank -milling mode on a 5-axis numerically controlled milling machine (Fig. 2).

The blade leading edge is generated by radially varying circles that are tangent to the blade surfaces. The main impeller dimensions and operating conditions for the measurements and calculations are as follows: d_2 = 400 mm, z_R = 22363 rpm, $\dot{m}$ = 4.0 kg/s. The specific speed of the first impeller was N_s = 80 (US units). Both impellers were manufactured from aluminium and operated up to a maximum shaft speed of 23481 rpm. During the tests the impellers were coupled with diffusers of constant areas adopted to the specific impeller geometry each. Tip clearance for the design point was measured to be 0.5 mm at the inlet and 0.2 mm at the exit. For the 3D-viscous calculations a linear clearance distribution was assumed from inlet to exit.

3.2. PERFORMANCE CHARACTERISTICS

The performance characteristics of both stages are submitted in Figures 3 and 4. Detailed conventional measurements were carried out for the first stage that included mass flow rate, total and static pressure, temperature as well as flow angle measurements. The development of static pressure was taken from rotor inlet to the diffuser exit. Total temperatures were measured at the compressor inlet and exit and assumed constant throughout the diffuser for calculating the impeller efficiency. For these calculations a mean static pressure derived from 24 circumferentially distributed measurement positions was used. The maximum total/total isentropic impeller efficiency was 94%. The flow angle and total pressure distribution at the diffuser exit was measured with 6 circumferentially distributed 3-hole probes that have been moved in the axial direction. From the measurement arrangement described the performance map shown in Figure 3 has been derived.



The experimental investigations for the second impeller were mainly concerned with laser measurements. Therefore only limited conventional measurements were carried out. These included total pressure and total temperature measurements at the impeller inlet nescessary for shaft speed and mass flow corrections. Additionally, the total pressure was measured at the diffuser exit. But for these measurements only one stationary Pitot-tube was used. From this simple arrangement the second performance map shown in Figure 4 has been derived. Nevertheless, the comparison of, of both maps gives useful information about the different compressor characteristics. Obviously the flow range of the second stage has been significantly increased by changing the compressor shroud contour. As expected, for the the same shaft speed the pressure ratio of the second stage is lower than that of the first stage which is due to the lower energy input per mass flow rate. Due to the higher absolute design flow angle at the impeller exit, the surge line for the second stage has shifted to lower mass flow rates.

Figure 4. Performance map of the second stage.

4. TEST RESULTS

4.1 INSTRUMENTATION

The internal flow fields of both impellers were analysed with the Laser-Two-Focus Velocimetry developed at DLR. This measurement system gives information about the magnitude and direction of the absolute velocity vector and its turbulent components.

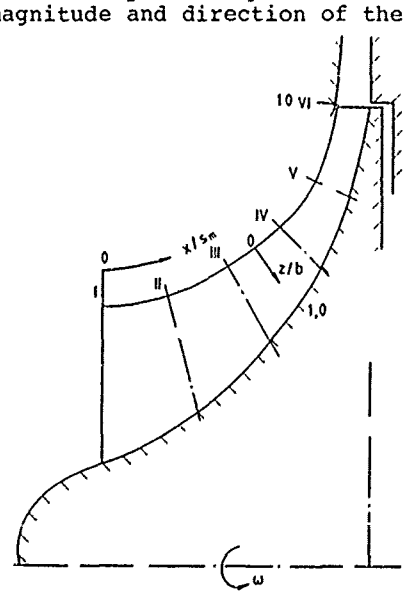


Figure 5. Arrangement of measurement planes.

The relative velocity components can be easily derived from the velocity triangle that can be constructed with the help of the known circumferential rotor velocity. Generally the error of mean absolute velocity measurements is less than ± 1 % and the uncertainty in flow angle measurements is usually less than ± 1 deg.. Only in pronounced wake areas an increased uncertainty has to be taken into account. Here the error in absolute velocity can raise up to ± 3 %, and an error in flow angle measurement up to ± 3 deg. can occur. However, pronounced jet/wake flows did not occur inside the flow channels of the two rotors investigated excluding increased L2F-uncertainties in the specific applications. From the velocity triangle it can be derived that the uncertainty in relative flow angle for the backswept impellers is less than ± 0.5 deg.. Additional information about the L2F-measurement technique and its application to complex turbomachinery flow conditions are described in (9). Measurements in both impellers were carried out in 6 planes equally spaced along the shroud contour. Figure 5 gives the the arrangement of the measurement planes for the first rotor.

Plane windows inserted parallel to the shroud contour were used for measurements. Thus all measurement planes were perpendicular to the shroud. Extensive laser measurements were carried out for the first impeller at 70, 90 and 100 percent shaft speed and also for each speed measurements close to surge at BEP and close to choke were carried out. For the redesigned impeller, however, L2F-measurements were limited to only one operating point (n/n_0 = 1.0, m = 4.0 kg/s) which was the design point for the first impeller.

4.2 MEASUREMENT RESULTS

Information about the vortex flow in rotating turbomachinery components can be obtained from L2F-measurements by plotting lines of constant relative flow angle. This is

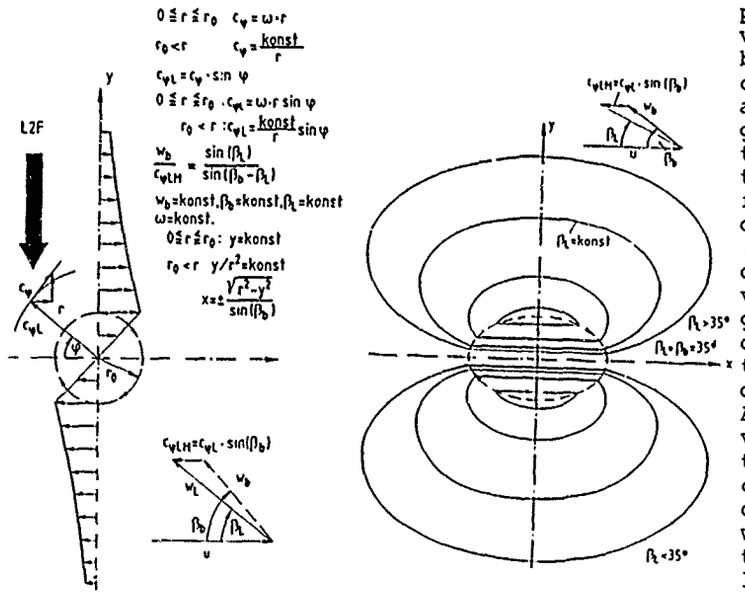


Figure 6. Sketch of vortex flow model (1).

illustrated in Figure 6, taken from (1). The appearance of the isocline pattern gives information whether a vortex flow is present or not. The basic equations for a real vortex, composed of a solid body vortex and a potential vortex part are given in the same figure. From these equations it can be derived that lines of constant relative flow angle are parallel to each other in the solid body vortex area ($0<r<r_0$), whereas the isoclines are of elliptic type in the potential vortex area ($r>r_0$). The derivative given in Figure 6 has been carried out for a main through flow direction that is inclined against the drawing plane (β_L = 35 deg.). According to this result the vortex center is always located in the middle of the parallel isoclines. The approach presented was originally applied by Binder (10) who derived similar equations for a through flow direction perpendicular to the drawing plane. This approach has been used to analyse the vortex flow inside the flow passages of the two backswept impellers. A real vortex was assumed to be present when an isocline pattern like that shown in Figure 6 occured. It should be mentioned that the measurements were taken in planes orientated in the circumferential direction. Therefore the analysis of the vortex flow could also only be carried out in these planes. Very often, however, secondary flows are plotted in planes perpendicular to the main flow direction or perpendicular to a somehow defined main channel direction which makes it difficult to compare secondary flow patterns. The shape of the secondary flow pattern depends strongly on the view direction and can extremly change when the view direction changes. Therefore from the simple approach presented in Figure 6 only an overall information about the presence of a vortex flow can be extracted, but it is not to be expected that such a detailed information as that of 3D-calculations can be obtained from this approach. That is also due to the rather limited measurement data used for the interpolation procedure. Nevertheless, vortex flow patterns derived from measurements in two different impellers, drawn in the same way and plotted on the same planes, as done here, should give information in which way the secondary flows are changing when different impeller geometries are applied.

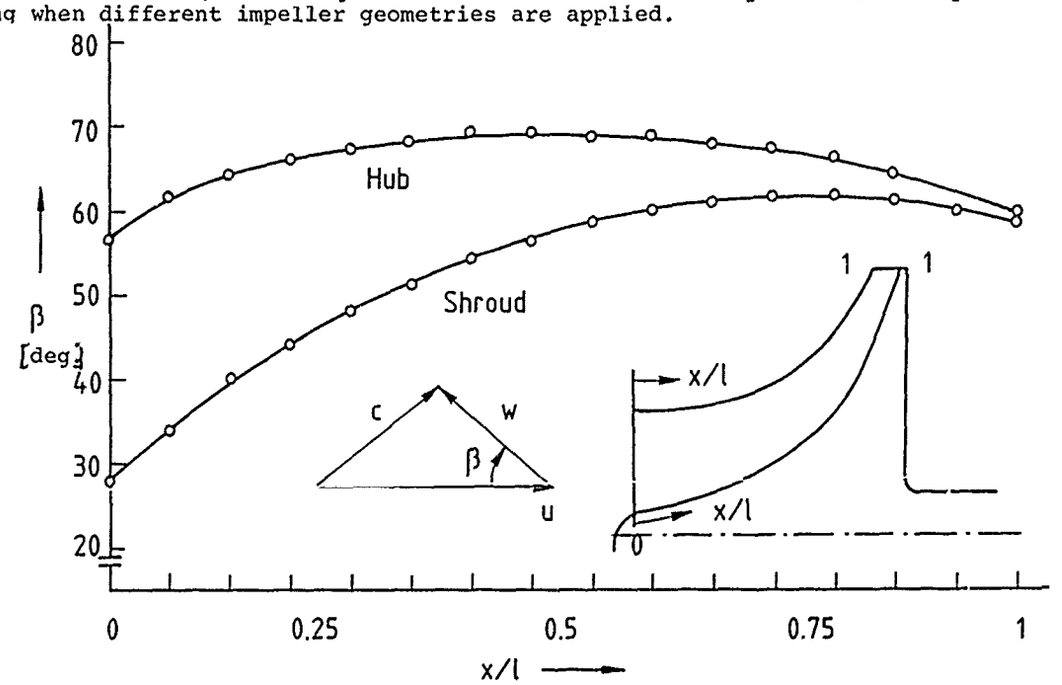


Figure 7. Blade angle distribution for the second rotor.

Figure 7 at first shows the blade angle distibution for both impellers. High blade angle variations are present in the shroud area where a turning of about 32 deg. occurs which does not include the turning in the meridional plane that is in the range of 84 deg.. This illustrates that strong 3D-effects are to be expected in these impellers.

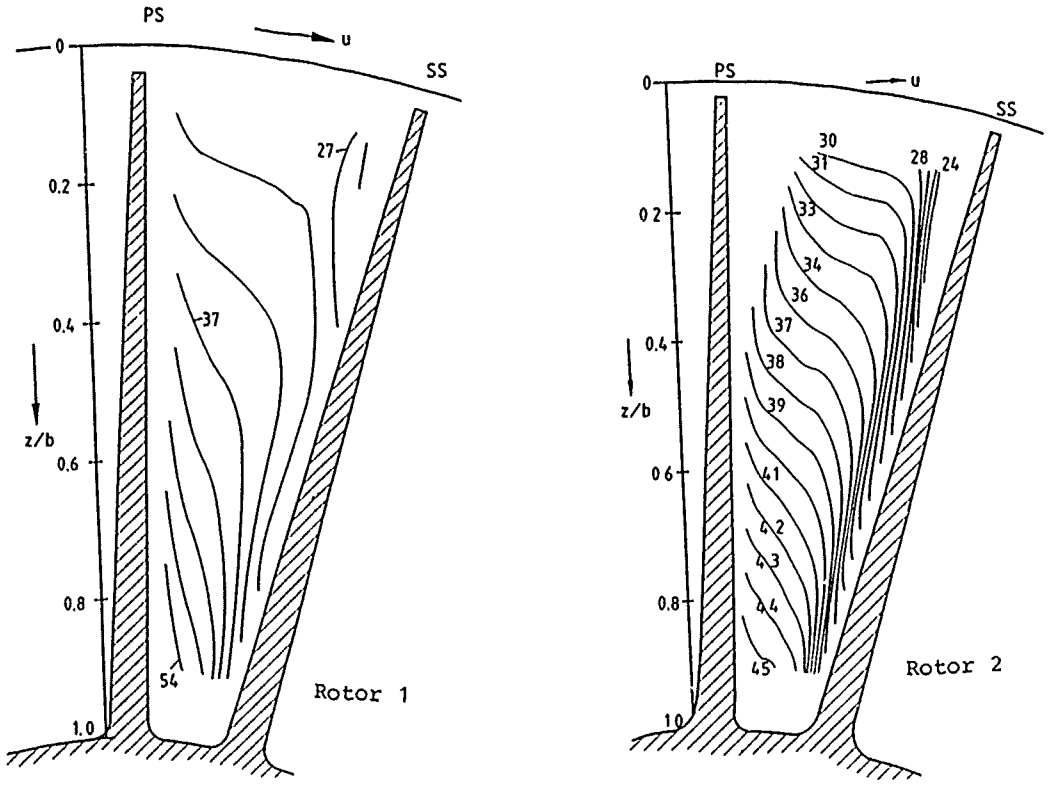
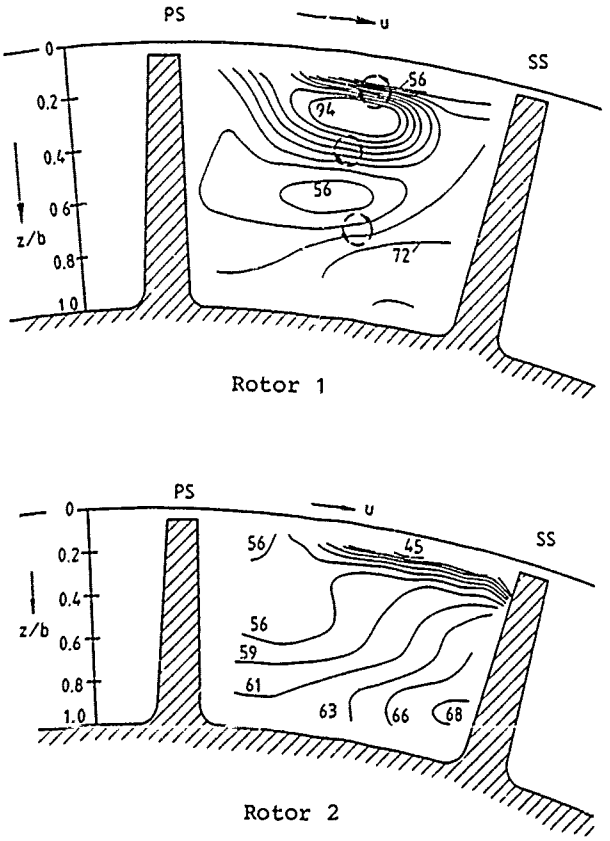


Figure 8. Isocline patterns for plane I of both impellers.



The measured flow angle distributions at the inlet (plane I) are shown for both impellers in Figure 8. The patterns are actually results of an interpolation between a limited number of measurement points. About 65 measurement points were available for these interpolations. In principal both isocline patterns are very similar to each other and no closed isoclines pointing to a real vortex are seen. The relative flow angle at the hub of the second impeller is lower than that of the first impeller which is equivalent to a slightly lower through flow close to the hub of the second impeller. A comparison with Figure 7, illustrating the blade angle distribution, reveals that the blade and flow angles of both impellers are in the same range pointing to a blade congruent flow for the operating point under consideration. A different situation occurs at plane IV located at 60 percent flow path length for which the corresponding isocline patterns are shown in Figure 9.

Figure 9. Isocline patterns for plane IV of both impellers.

In this area the mean flow angle levels are similar for both impellers and they are in good agreement with the angle prescribed by the blade (Figure 7), however, the isocline structure is different for both impellers. The pronounced channel vortex flow occuring at this measurement plane in rotor 1 and indicated by the isoclines of elliptic type is not seen for the second rotor. In contrast, similar isocline structures are present in the shroud areas of both impellers indicating that no principal change in secondary flows is obtained in this region where secondary flows are mainly governed by tip clearance effects that are strongly dependent on blade loading. Since the blade geometry is the same for both designs the blade loading characteristic will also be similar for both rotors resulting in similar tip clearance effects at the same measurement positions. A similar situation occurs at the impeller exit (plane VI) for which the measured isocline distributions are plotted in Figure 10.

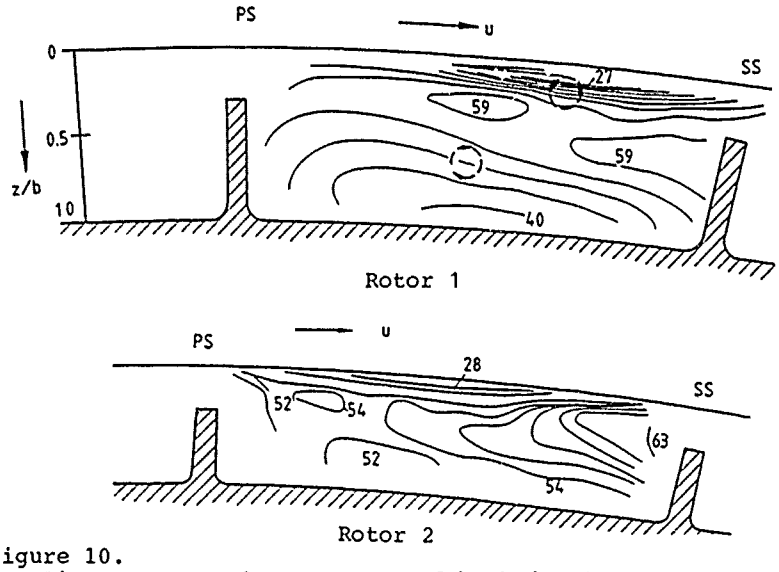


Figure 10.
Isocline patterns for plane VI of both impellers

Although the isocline structure has slightly changed inside of the flow channel, the concentration of parallel isoclines pointing to a strong vortex development is again present in the shroud regions of both impellers. Obviously, distinct changes in the secondary flow characteristic at this plane were mainly obtained in the center of the flow channel whereas the secondary flows due to tip clearance effects have again conserved their features. The results obtained are showing that secondary flows can be influenced by changes of the flow channel geometry. Probably an even stronger reduction in secondary flows could be possible by an additional variation of the blade geometry. In this case an improvement of impeller efficiencies could be expected, because secondary flows are strongly contributing to the loss production of impellers. Additionally they are influencing the primary flow pattern at the exit of the impeller that controls the flow range of the machine. Therefore, developping theoretical tools capable to predict reliably the secondary flow development in impellers seems to be a valuable step forward.

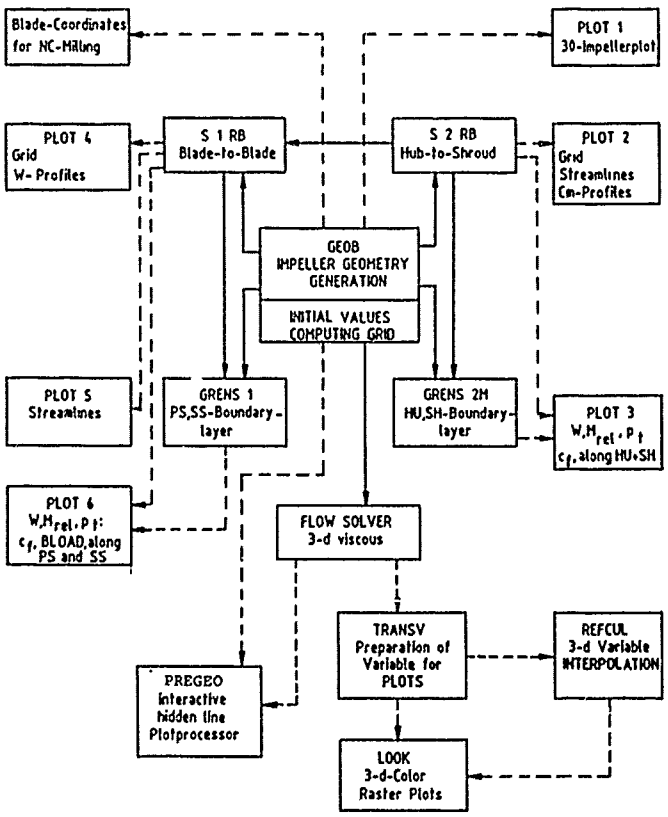


Figure 11. Block diagram for the impeller design, flow field calculations and 3D-data visualization.

5. NUMERICAL APPROACH

5.1 DESIGN PROCEDURE

The impeller design proceeds in running iteratively modular programs of the design procedure, Figure 11, starting in GEOB on a set of 16 input parameters for analytical functions describing hub- and shroud meridional contours and the blade geometry. The fluid dynamic variables corresponding to the designed flow channel are calculated on hub-to-shroud and on blade-to-blade surfaces at different radial positions. The latter take care of input data from GEOB and the hub-to-shroud calculation. A feed-back of the blade-to-blade solution to the hub-to-shroud calculation is not provided. The boundary layer calculations for pressure and suction sides of the blades and for the hub and shroud surfaces are independent of the flow calculation. In this flow calculation, viscous effects are already incorporated through aerodynamic blockage. The boundary layer calculations are carried out to indicate whether separation occurs or not. Secondary flow and vortex development cannot be predicted by this S1/S2-flow solution.

In principal, it is possible to replace this S1/S2-calculation by the 3D-viscous time-dependent flow solution mentioned below, but iterative loops of the Navier-Stokes code are too expensive and time-consuming and would typically need 45 times of CPU-time of one S1/S2-solution on a supercomputer. Thus, in this approach, the impeller is designed to a relative optimum running a lot of fast S1/S2-calculations. Finally, the 3D-viscous flow field is simulated by a solution of the Navier-Stokes equations.

5.2 3D-VISCOUS FLOW CALCULATIONS

The following time-dependent Navier-Stokes equations (1) have been solved with respect to a steadily rotating frame of reference and cylinder coordinates r, φ and z by the code of Dawes (4) that has been modified for efficient use on CRAY-type vector processing computers for which a speedup of 1.5 has been achieved up to now for a typical 3D-solution, measured against the auto-vectorized version. An even higher acceleration seems to be possible by vectorizing the remaining scalar calculation of viscous terms, that needs 42 % of the overall CPU-time for a converged solution.

$$\int_V \frac{\partial U}{\partial t}\,\delta V + \oint_S \left\{ \sum_{r,\varphi,z} F(U)\,n \right\} \delta S + \int_V G(U)\,\delta V = 0 \qquad (1)$$

with

$$U = \begin{pmatrix} \rho \\ \rho w_r \\ \rho w_\varphi r \\ \rho w_z \\ e \end{pmatrix}, \quad G(U) = \begin{bmatrix} 0 \\ \rho\left(w_\varphi^2/r + \Omega^2 r + 2\Omega w_\varphi\right) \\ -2\rho\Omega r w_r \\ 0 \\ 0 \end{bmatrix}, \quad F_r(U) = \begin{bmatrix} \rho w_r \\ \rho w_r w_r - \tau_{rr} + p \\ \rho w_r w_\varphi r - \tau_{r\varphi} \\ \rho w_r w_z - \tau_{rz} \\ \rho w_r I \end{bmatrix}$$

and

$$F_\varphi(U) = \begin{bmatrix} \rho w_\varphi \\ \rho w_\varphi w_r - \tau_{\varphi r} \\ \rho w_\varphi w_\varphi - \tau_{\varphi\varphi} + p \\ \rho w_\varphi w_z - \tau_{\varphi z} \\ \rho w_\varphi I \end{bmatrix}, \quad F_z(U) = \begin{bmatrix} \rho w_z \\ \rho w_z w_r - \tau_{zr} \\ \rho w_z w_\varphi - \tau_{z\varphi} \\ \rho w_z w_z - \tau_{zz} + p \\ \rho w_z I \end{bmatrix}$$

and

$$e = \frac{p}{\kappa - 1} + \frac{\rho}{2}\left[w_r^2 + w_\varphi^2 + w_z^2 - (\Omega r)^2\right]$$

$$\tau_{rr} = 2\mu\frac{\partial w_r}{\partial r} \qquad \tau_{\varphi r} = \mu\left[r\frac{\partial}{\partial r}\left(\frac{w_\varphi}{r}\right) + \frac{1}{r}\frac{\partial w_r}{\partial \varphi}\right] \qquad \tau_{zr} = \mu\left(\frac{\partial w_r}{\partial z} + \frac{\partial w_z}{\partial r}\right)$$

$$\tau_{r\varphi} = \tau_{\varphi r} \qquad \tau_{\varphi\varphi} = 2\mu\left(\frac{1}{r}\frac{\partial w_\varphi}{\partial \varphi} + \frac{w_r}{r}\right) \qquad \tau_{z\varphi} = \mu\left(\frac{\partial w_\varphi}{\partial z} + \frac{1}{r}\frac{\partial w_z}{\partial \varphi}\right)$$

$$\tau_{rz} = \tau_{zr} \qquad \tau_{\varphi z} = \tau_{z\varphi} \qquad \tau_{zz} = 2\mu\frac{\partial w_z}{\partial z}$$

These equations are interpreted as Reynold-averaged Navier-Stokes Equations with viscosity and static pressure formally replaced in the following way, where the turbulent kinetic energy has been added to the static pressure:

$$\mu \leftarrow \mu + \mu_{turb} \qquad p \leftarrow p + \frac{2}{3}\rho\overline{v'^k v'^k} \qquad (2)$$

In the program the eddy viscosity μ_{turb} is derived from a modified Baldwin-Lomax turbulence model with

$$\mu_{turb_{inner}} = \rho l^2 |\omega| \quad \text{with} \quad l = \kappa y\left[1 - \exp\left(-y^+/A^+\right)\right] \qquad (3)$$

for an inner region $y \le y^+$. For an outer region $y > y^+$, the modified Clauser formula

$$\mu_{turb_{outer}} = \rho\alpha F_w F_{Kleb} \qquad (4)$$

has been applied. Switching between these two formulas occurs at positions y^+ with $\mu_{turb\ inner} = \mu_{turb\ outer}$. The Klebanoff intermittency factor is chosen to be

$$F_{Kleb} = \left[1 + 5.5\,(C_{Kleb}\, y/y_{max})^6\right]^{-1} \tag{5}$$

and F_w is

$$F_w = \min\left(y_{max}\, F(y)_{max}\ ,\ C_{WK}\, y_{max}\, v^2_{DIFF} / F(y)_{max}\right) \tag{6}$$

with F_{max}, the maximum of function (7) and v_{DIFF} the maximum difference of the absolute velocities on a y^+-coordinate line and

$$F(y) = y|\omega|\left[1 - \exp(-y^+/A^+)\right] \tag{7}$$

Stable solutions were reached after 2000 and 2600 time steps for the first and the redesigned impeller, respectively. Both impeller flow channels were discretized into 16 x 16 x 94 blade-to-blade, span- and streamwise finite volumes with ? volumes filling the tip clearence gap, Figure 12.

The blade tip gap was formed by reducing blade thickness smoothly to zero. In the finite tip gap volumes, circumferential periodicity has been assumed for the calculation of boundary values. With respect to the metal geometries tested, the computing grids did not fit exactly the spinner shape, the leading- and trailing-edges and the sharp edges at the blade tips due to grid point number restrictions. Grid refinement in these flow regions and the response of the numerical code on that have not been studied up to now. This may be important for an even more precise numerical analysis of the channel boundary- and tip gap flows, that drive secondary flow.

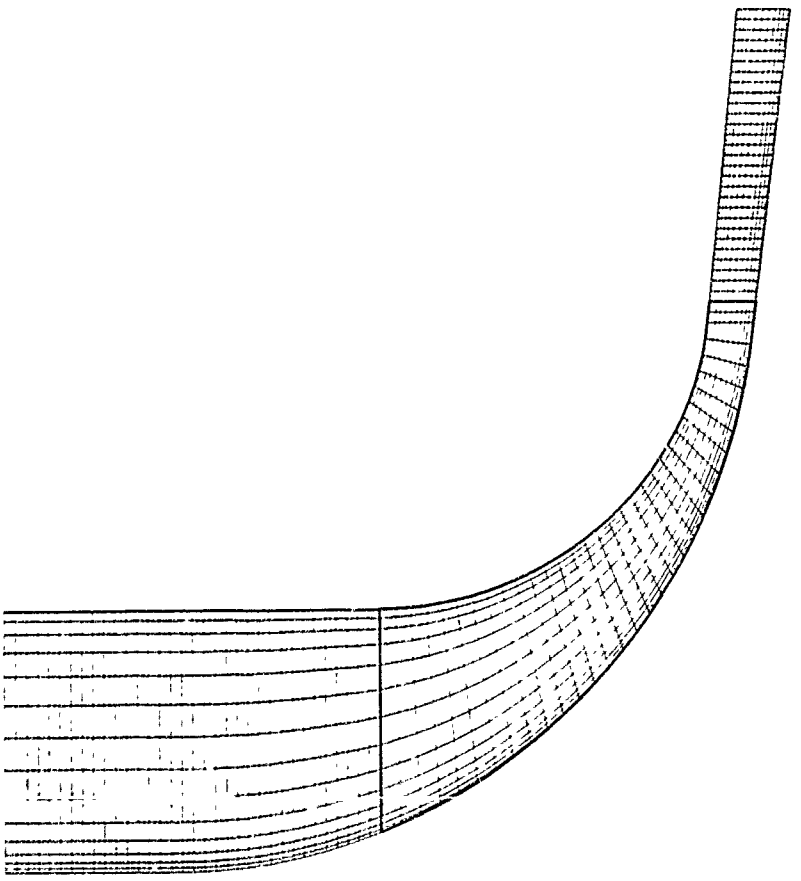


Figure 12. Grid used for 3D calculations.

5.3 POSTPROCESSING

The solutions have been postprocessed by a modular and partly interactive program system (2) (lower right part of Figure 11). With this a flexible 3D grafic and numeric analysis of the primary and secondary variable field has become possible. Although computing times of postprocessing routines are small compared to that for a single converged Navier-Stokes solution, postprocessing demands for a large amount of time selecting and producing evident graphics of flow variables based on a complex spatially wounded geometry as that of a backswept radial impeller. To reduce this amount of work, some special turbomachinery applications have been implemented that are automatically processed. For ease of secondary flow studies flow vectors can be plotted on crossflow surfaces. Such a surface shows the secondary velocity in a plane normal to the viewpoint direction that is implicitely defined by the program. In this case, the viewpoint direction may be defined as local mean flow direction which is the mean direction of the four channel corner tangents. The following secondary flow pictures are examples of this approach. Any other definition is possible, but each definition produces its specific projected view of the relative velocity, hence its own picture of secondary flow.

5.4 SECONDARY FLOW ANALYSIS

A detailed comparison between measured and calculated 3D results carried out for the first rotor revealed predominantly good agreement between measured and calculated through flow velocity profiles. Additionally, a reasonable cross flow structure was predicted for the boundary layer development along the blade surfaces (2). The encouraging agreement obtained suggests that the code can also be used for particular secondary flow studies that could give more insight into the flow mechanisms of the two impellers under consideration. For these studies the output of the postprocessor (Figure 11, Program LOOK) has been used. With this program secondary flow plots have been generated for specific cross sections. Before going into these details an additional comparison between measured and calculated through flow velocity profiles is shown for both rotors in Figures 13 and 14.

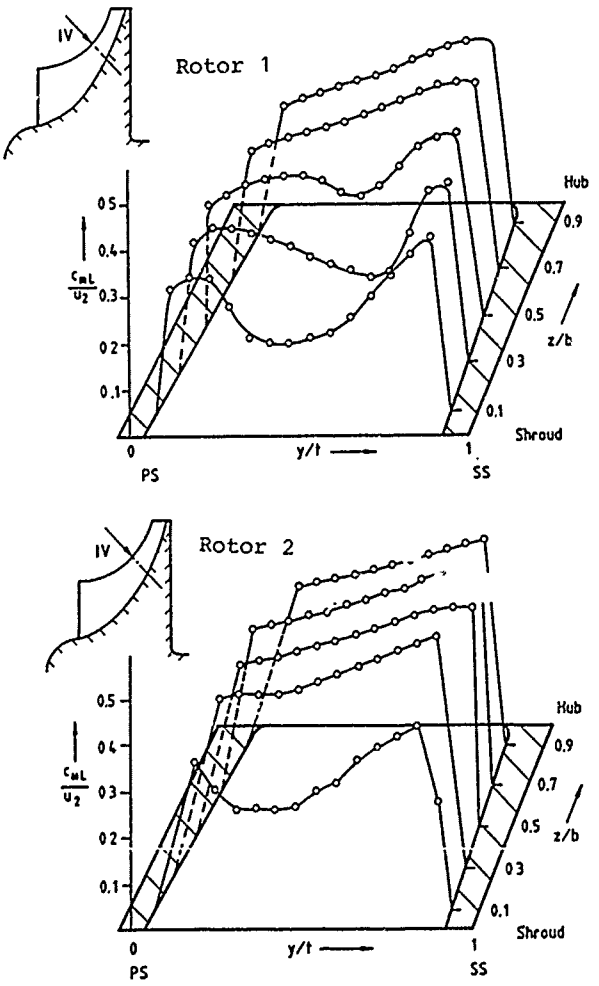


Figure 13. Comparison of measured through flow velocity profiles for both impellers at 60 percent flow path length.

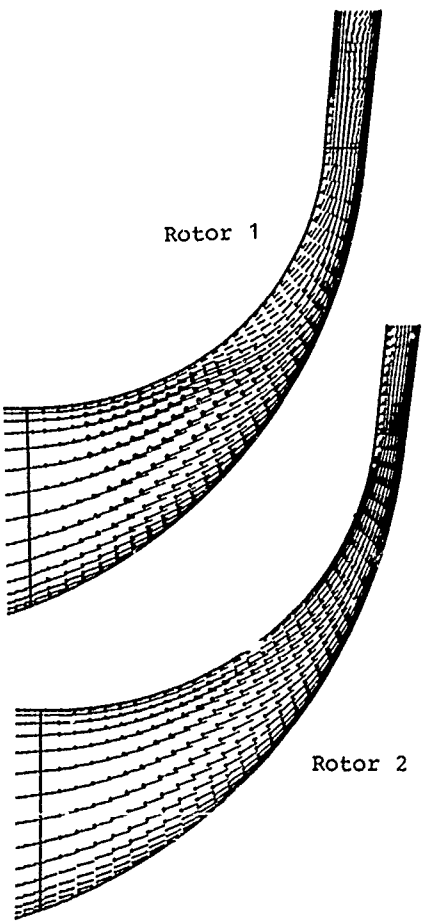


Figure 14. Calculated meridional velocity distribrution for both impellers on mid-pitch planes.

Figure 13 shows the measured meridional velocity profiles for the two impellers at measurement plane IV, located at 60 per cent flow path length and Figure 14 illustrates the calculated meridional velocities for both designs on mid-pitch surfaces. The measurements clearly show significant differences in the velocity profiles of the two impellers. The disturbed profiles of the first rotor that are extending from the shroud up to 50 per cent flow channel depth (z/b = 0 - 0.5) have smoothed out for the second rotor. The second rotor has only a slightly disturbed velocity profile in the vicinity of the shroud which seems to be due to tip clearence effects. The disturbance in this region, however, is also smaller than for the first rotor. A very regular profile occurs for the second rotor inside of the flow channel that was the aim of the redesign approach. For the redesign the Q3D-calculation procedure was used because at that time the 3D-viscous calculation method was not available.
The 3D-method was applied to calculate the flow field of the second rotor when the measurements were already taken. The calculations indeed confirmed the measurement results what is shown in Figure 14. The calculated meridional velocity distributions are indicating a distinct low velocity region in the shroud area of the first rotor that is not predicted for the second rotor. At 60 percent flow path length the calculation indicates a very smooth velocity distribution from hub to shroud for the second rotor what corresponds fairly well with the measurements of Figure 13. Obviously the 3D code is capable to predict correctly flow phenomena that are very important to be known during the design process. Especially the knowledge whether a wake development inside the impeller is to be expected or not is of importance to the designer of these machines who generally wants to avoid this effect. The measured and calculated results are suggesting that the 3D-code in conjunction with an appropriate geometry generation procedure could help to solve this problem.

The following Figures will give additional information about the secondary flow development inside the flow passages of both impellers. Here the secondary flows are plotted on cross flow planes that are perpendicular to a mean flow-channel direction. The mean flow-channel direction is defined by the directions of the tangents at the four corner points of a cross flow plane. The relative flow vectors are perpendicularly projected on these cross flow planes. In this paper the result of this projection is called "Secondary Flow". It should be mentioned again that the secondary flow structure can look quite different if the projection is only slightly changed which makes it sometimes difficult to compare calculated secondary flow patterns. These difficulties, however, do not occur for the comparisons to be presented for the two rotors which is primarily due to the fact that both rotors had the same blade geometry and that the comparisons are carried out at the same meridional flow path positions. Figure 15 shows an arrangement of cross flow planes inside of the impeller flow channel. Those planes are labeled from 34 to 66. Cross flow plane 34 is located just aft of the impeller leading edge, plane 66 is located close to the exit. Secondary flow patterns, meridional velocity distributions, Mach number distributions, loss distributions etc. can be plotted with the help of the postprocessor at any plane. The numbers L = 35, 42, 55 and 65 in Figures 16 to 19 correspond with the cross flow plane arrangement of Figure 15 and thus illustrate the exact location of the planes inside of the flow channel. Cross flow planes ahead and aft of the rotor that can also be chosen are not shown in Figure 15.

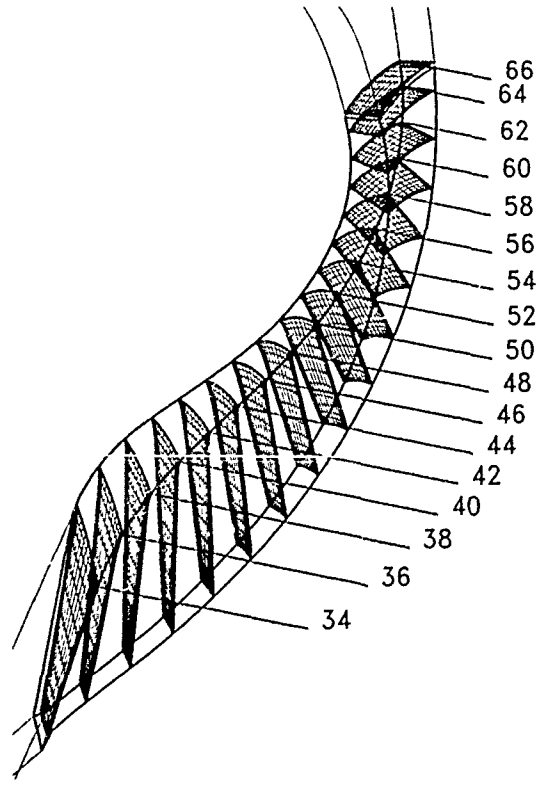


Figure 15. Arrangement of cross flow planes in the impeller area.

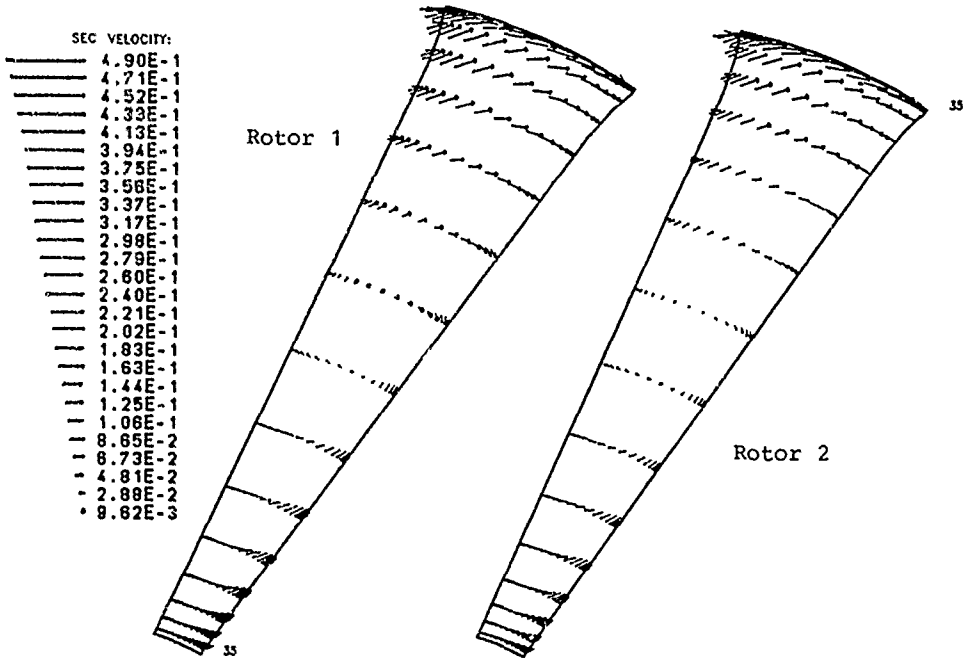


Figure 16. Calculated secondary flows for both impellers at cross flow plane 35 (Fig. 15)

Figure 16 shows the calculated secondary flows for both impellers at plane 35 located just aft of the leading edge. The analysis was carried out for the same operating point ($\dot{m}$ = 4.0 kg/s, n/n_0 = 1) and the length of the secondary flow vectors is scaled in both cases to the rotor tip speed which was equal for the two impellers. Therefore a direct comparison is possible between the two secondary flow patterns. The rotor is moving in the clockwise direction thus the pressure side of the blade is located on the left and the suction side on the right. The Figure indicates very similar patterns for both impellers. Secondary flows seem to be very small inside of the flow channels which corresponds with the measurement results of Figure 8 that are also showing negligible secondary flows in the inlet areas of both impellers. At this position the tip clearence flows are also low which is due to the small blade loading in this region.

Since the changes of the flow channel geometry were rather small in the inlet area (Figure 1) the calculated secondary flows are also quantitatively in good agreement what was to be expected. A similar situation occurs at plane 43 located at about 30 percent flow path length (Figure 17).

At this position a main channel vortex is predicted for both rotors that seems to be driven by tip clearence effects and boundary layer flows along the hub and the suction side of the blade. Compared to plane 35 tip clearence flows are now higher which is due to the increasing blade loading.
Vortex flow patterns of different appearance are predicted for plane 55 located at 66 percent flow path length (Figure 18).

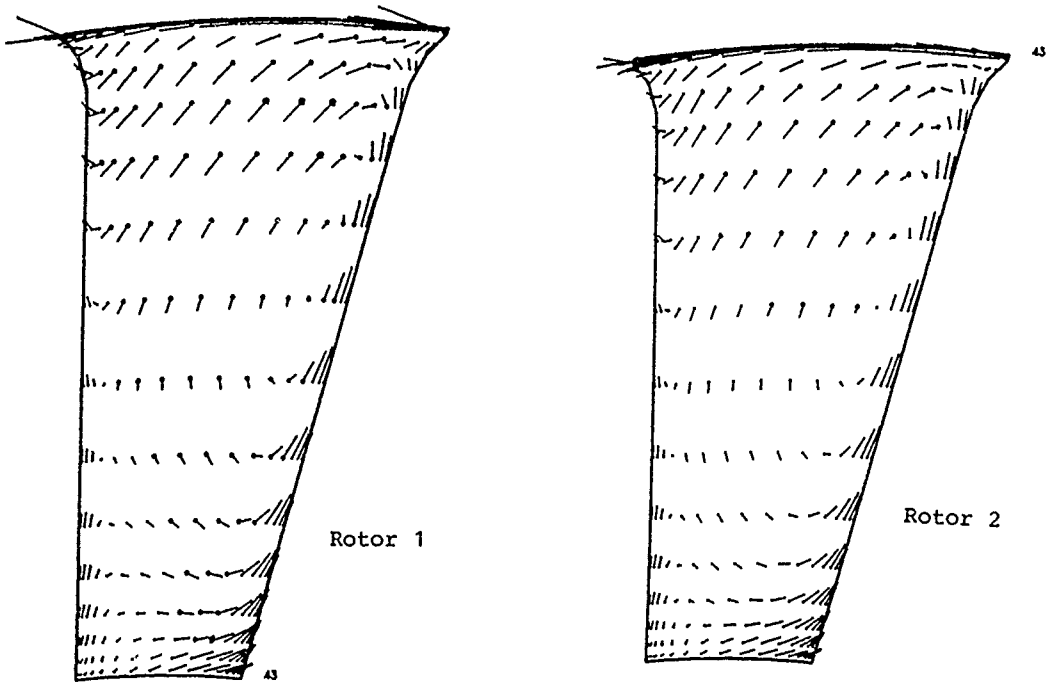
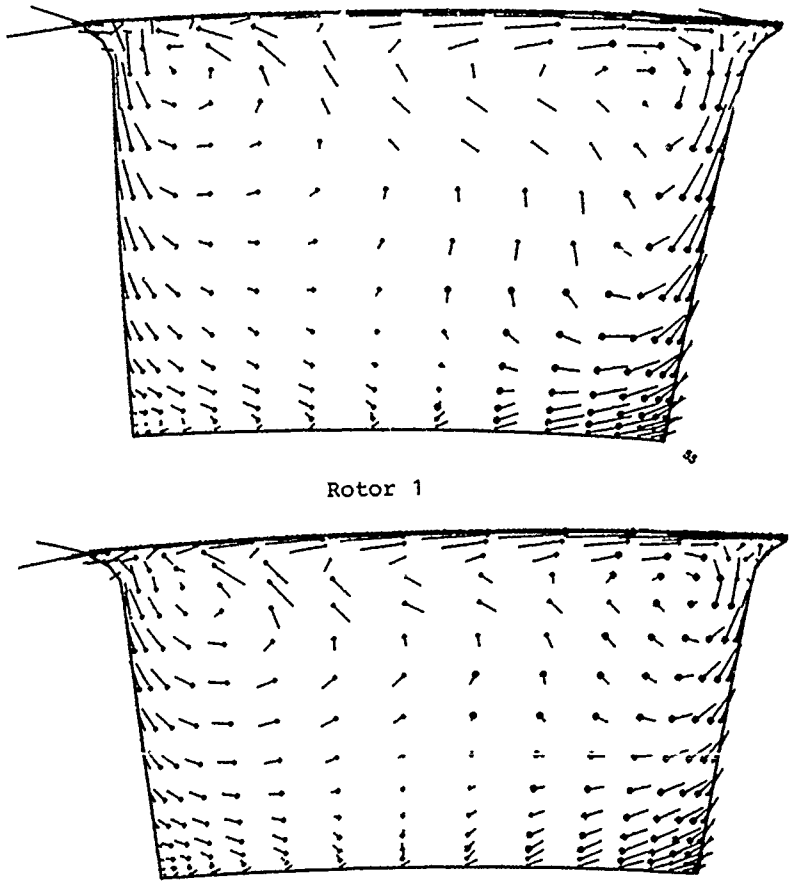
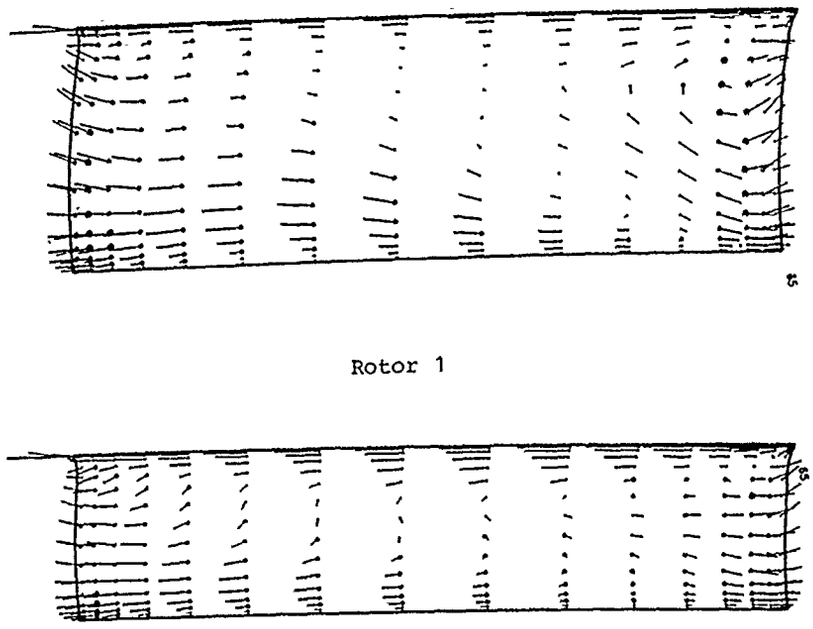


Figure 17. Calculated secondary flows for both impellers at cross flow plane 43 (Fig. 15)



At this position two corner vortices are predicted for both rotors that are generated by tip clearance and boundary layer flows. However, in rotor 1 these vortices are extending far deeper into the channel area than in rotor 2 what is mainly true for the vortex in the shroud/suction side area. In rotor 2 the distinct vortex development is more concentrated in the shroud area what qualitatively agrees with the measurement results discussed in Figure 9. The corner vortices, however, were not resolved with the laser measurement technique what is mainly due to the limited number of measurement points close to the channel boundaries. Principally the same vortex structure occurs for both rotors but the extension of the vortices is different. In total a rather small secondary flow development seems to be present in both rotors. Expecially in the second rotor the secondary flow is totally suppressed in the middle of the flow channel.

Figure 18. Calculated secondary flows for both impellers at cross flow plane 55 (Fig. 15)



Rotor 1

Rotor 2

The situation close to the rotor exit is illustrated in Fig. 19. In both cases cross flows are mainly directed in the negative circumferential direction which is due to the slip effect generally occuring at the exit of centrifugal impellers. According to this result and excluding the near shroud region, cross flows appear to be lower at the exit of rotor 2 than at the exit of rotor 1 what can be deduced from the length of the velocity vectors. Primarily in the shroud /pressure side area cross flows are more pronounced in rotor 1 than in rotor 2. Furthermore the shroud /suction side corner vortex is clearly developed in rotor 1, whereas in rotor 2 this vortex is degenerated to two cross flow layers moving in the opposite direction.

Figure 19. Calculated secondary flows for both impellers at cross flow plane 65 (Fig. 15)

6. CONCLUSIONS

The secondary flow studies carried out for the two backswept rotors having different shroud contours but the same blade geometry gave insight into basic flow characteristics of these impellers. The experimental as well as the theoretical results indicated noticeable differences in the secondary flow structure of both rotors and were qualitatively in good agreement. The main differences in secondary flow structure were observed in the center of the flow channels, whereas the corner vortex development in the shroud area was similar for both impellers being mainly due to tip clearance and boundary layer flows that are generating vortices of this type. However, the change of the flow channel hight significantly influenced the through flow velocity pattern. By varying this hight it was possible to eliminate the low kinetic energy area present in the first rotor which resulted in a wider flow range of the machine and in a smoother velocity profile at the rotor exit what was proved by laser measurements as well as by 3D-viscous calculations. Probably, the secondary flow development in the second rotor could have been even more suppressed if an additional variation in blade geometry would have been carried out since secondary flows are also strongly dependent on blade curvature effects. The results optained are suggesting that the 3D-viscous code can be used for secondary flow control during the design process of future impellers.

REFERENCES

(1) Krain, H.,
Swirling Impeller Flow, Transactions of the ASME, Vol. 110, pp. 122-128, (1988).

(2) Krain, H., Hoffmann, W.,
Verification of an Impeller Design by Laser Measurements and 3D-Viscous Flow Calculations, ASME-paper 89-GT-159,Toronto, (1989).

(3) Krain, H.,
A CAD-Method for Centrifugal Compressor Impellers, ASME Journal of Engineering for Gas Turbine and Power, Vol. 106, pp. 482-488, (1984).

(4) Dawes, W. N.,
Development of a 3D Navier Stokes Solver for Application to all Types of Turbomachinery, ASME-Paper 88-GT-70, (1988).

(5) Hah, C., Krain, H.,
Secondary Flows and Vortex Motion in a High-Efficiency Backswept Impeller at Design and Off-Design Conditions, ASME-Paper 89-GT-181, Toronto, (1989).

(6) Moore, Joane G.,
An Elliptic Calculation Procedure for 3D Computation Techniques Applied to Internal Flow in Propulsion Systems, (1985).

(7) Moore, John,
Performance Evaluation of Flow in Turbomachinery Blade Rows, AGARD Lecture Series No. 140, 3D Computation Techniques Applied to Internal Flows in Propulsion Systems, (1985).

(8) Schodl. R.,
A Laser-Two-Focus (L2F) Velocimeter for Automatic Flow Vector Measurements in the Rotating Components of Turbomachines, ASME-Paper in Measurement Methods in Rotating Components of Turbomachinery, pp. 139-147, (1980).

(9) Krain, H., Schodl, R., Binder, A. and Dunker, R.,
Successes in the Application of Laser Velocimetry to Turbomachinery Studies. Principal LS No. 1, Concepts ETI, Inc. 1986, pp. 5.1-5.22.

(10) Binder, A.,
Instationary Flow Effects in the Rotor of a Turbine, Thesis, University of Aachen, DFVLR-FB-85-66, p. 157 (in German).

DISCUSSION

Hoffmann, Germany

A question by Dr Joan Moore concerning the color plots of the two impeller designs.

Author's Reply:

In the colored figure (shown only in the oral presentation) showing in crossflow planes the meridional velocities, each crossflow plane solution is scaled individually to the maximum and minimum value occurring in that specific plane. By this a higher resolution in isocolor is achieved. Moreover, color tables are different for each impeller shown. This is due to the different tip speeds of the two impellers to which the color maps have been referenced. The intention to show these figures was not to compare directly their velocities, but to demonstrate, that the wake development could be supressed for the redesigned impeller.

Skoe, Norway

Were the number of grid points in the clearance region sufficient to predict realistic clearance losses? Have you made systematic "numerical tests" to investigate the relation between aerodynamic blade loading and clearance losses (test results indicate an adverse effect)? Additionally, what was the relative polytropic efficiency difference between the two rotors?

Author's Reply:

Only two volume elements were used in the gap for the initial calculations to model clearance effects. This is the minimum number of elements for getting information about clearance flow. But a much higher grid line number, probably between six and seven should be used for systematic clearance loss predictions. Up to now, this has not been done but will be tried in the future. Detailed conventional measurements giving information about impeller efficiency were only carried out for the first rotor whereas the measurements for the second rotor were primarily dealing with laser measurements. From the laser measurements, an impeller efficiency cannot be derived. Therefore a quantitative comparison between the rotor efficiencies is not possible. However, since the relative flow in the redesigned rotor is less decelerated than in the original impeller, it is to be expected that we lost one or two points in impeller efficiency.

Chen, Switzerland

The authors of this paper are to be congratulated for the finding of the vortices in the corner of the shroud surface. The discusser is also very happy to see that the argument made by him and his co-authors in the ASME paper of 1988 at Amsterdam (88-GT-120) about the appearance of the longitudinal vortex in the corner "suction-surface/shroud" is confirmed by the present investigation at the original impeller, which would correspond to the impeller investigated by the discusser. The discusser made that time color injection into the outlet of the impeller at the design point and found that the colored dye travelled backwards along the corner mentioned onto the inlet region. Since a sharp pulse was also found in the dynamic pressure along the said corner, the discusser argued that a longitudinal vortex arises in this corner guiding the high pressure of the outlet through its core onto the inlet region.

Author's Reply:

It is interesting to learn that you have found similar vortex structures as we in the shroud/suction side area of your impeller by using a different type of measurement technique. Nevertheless, there seem to be specific flow effects present in your impeller, because we did not measure backflow in either of our impellers.

CALCUL DE L'ECOULEMENT TRIDIMENSIONNEL TURBULENT DANS UN AUBAGE RECTILIGNE DE TURBINE

par

L. CAMBIER et B. ESCANDE
Office National d'Etudes et de Recherches Aérospatiales (ONERA)
B.P. N° 72 - 92322 Châtillon CEDEX (France)

RESUME

La présente communication est consacrée à la simulation numérique de l'écoulement tridimensionnel turbulent dans un aubage rectiligne de turbine, par résolution des équations de Navier-Stokes compressibles moyennes et complétées par un modèle de turbulence algébrique. La méthode numérique se caractérise par l'utilisation d'un schéma de différences finies explicite centré, associé à une phase multigrille d'accélération de convergence. La décomposition du domaine de calcul en un sous-domaine en O autour de l'aube et deux sous-domaines en H à l'amont et à l'aval permet d'assurer une bonne description des bords d'attaque et de fuite arrondis, tout en plaçant les frontières amont et aval du domaine de calcul suffisamment loin de l'aube. Les résultats obtenus dans un maillage comportant plus de 300 000 points (dans un domaine limité par un plan de symétrie) mettent en évidence des phénomènes complexes d'écoulements secondaires, analogues qualitativement à ceux observés dans une expérience réalisée à vitesse plus faible.

ABSTRACT

The paper deals with the numerical simulation of a three-dimensional turbulent flow in a linear turbine cascade, by solution of the Reynolds-averaged compressible Navier-Stokes equations with an algebraic turbulence model. The numerical method is characterized by an explicit centered finite difference scheme, associated with a multigrid convergence acceleration. The splitting of the computational domain in an O-type subdomain around the blade and two H-type subdomains upstream and downstream allows an accurate description of the round leading edges and trailing edges, while setting the upstream and downstream boundaries of the domain sufficiently far from the blade. The results obtained in a mesh containing more than 300,000 points (in a domain bounded by a symmetry plane) show complex phenomena of secondary flows, qualitatively similar to the phenomena observed in an experiment carried out at a lower flow velocity.

1. INTRODUCTION

L'amélioration des performances des moteurs nécessite aujourd'hui la mise en oeuvre d'une simulation numérique de l'écoulement dans une roue de turbomachine présentant une valeur prédictive sûre. Pour obtenir une description correcte d'un écoulement aussi complexe, il serait souhaitable de prendre en compte simultanément les effets de la viscosité du fluide, le caractère tridimensionnel de l'écoulement et les phénomènes instationnaires. Les travaux menés à l'ONERA dans le domaine de la résolution instationnaire ou pseudo-instationnaire des équations d'Euler ou de Navier-Stokes compressibles ont conduit au cours des dernières années à l'analyse de l'écoulement dans une roue de turbomachine en régime permanent [1] de fluide visqueux bidimensionnel, et en régime permanent [2] ou instationnaire [3] de fluide parfait tridimensionnel.

Les ordinateurs actuels ne semblent pas encore assez puissants pour permettre la résolution des équations de Navier-Stokes tridimensionnelles dans un maillage adéquat, pour le calcul d'écoulements instationnaires de turbomachines. Les premiers essais effectués par Rai (voir par exemple, [4]) sur un cas d'interaction rotor-stator et dans des maillages sans doute encore insuffisants ont conduit à des coûts de calcul beaucoup trop élevés pour des applications industrielles.

En revanche, il est dès maintenant possible de résoudre les équations de Navier-Stokes tridimensionnelles en régime permanent. Plusieurs publications récentes [5 à 9] sont d'ailleurs relatives à des analyses d'écoulements stationnaires de turbomachines fondées sur cette résolution.

La présente communication est consacrée au calcul d'un écoulement tridimensionnel stationnaire de turbomachine par résolution des équations de Navier-Stokes compressibles moyennes et complétées par un modèle de turbulence algébrique. La méthode numérique qui ne sera que brièvement rappelée se caractérise par l'utilisation d'un schéma de différences finies explicite centré, auquel on adjoint une phase d'accélération de convergence de type "multigrille", et par la mise en oeuvre d'une approche par sous-domaines. Le code "Navier-Stokes 3D" [11] a été réalisé à partir du code "Euler 3D" [2] et du code "Navier-Stokes 2D" [10], [1] précédemment développés à l'ONERA. Une comparaison satisfaisante des résultats du calcul avec des données expérimentales détaillées, sur un cas d'interaction onde de choc-couche limite turbulente dans un canal tridimensionnel, a été présentée dans [11] et a constitué une première validation du code "Navier-Stokes 3D".

L'application traitée ici concerne le calcul de l'écoulement turbulent dans une grille rectiligne de turbine placée entre deux parois planes parallèles. Cette configuration a fait l'objet d'une étude expérimentale à l'Ecole Centrale de Lyon [12, 13] qui a permis en particulier de mettre en évidence l'importance des effets liés aux écoulements secondaires. Or, la réduction des pertes liées à ces écoulements est essentielle pour accroître l'efficacité des turbomachines, et une prédiction correcte des écoulements secondaires par voie numérique est donc d'un grand intérêt.

Dans le calcul présenté, une grande attention a été portée au choix du maillage. La décomposition (Fig.1) du domaine de calcul en un sous-domaine en O autour de l'aube et deux sous-domaines en H respectivement situés en amont et en aval permet à la fois d'assurer une bonne description des régions de bord d'attaque et de bord de fuite et de placer les frontières amont et aval du domaine de calcul à des distances suffisamment grandes de l'aube. L'existence d'un plan de symétrie permet de réduire le domaine de calcul qui s'étend (Fig. 1) d'une paroi latérale au plan de symétrie et qui est discrétisé à l'aide d'un maillage comportant plus de 300 000 points.

Dans l'expérience, le nombre de Mach en amont de la grille est égal à 0,044 et l'effet de la compressibilité du fluide est négligeable. Eu égard à des difficultés de convergence prévisibles liées à la très faible valeur de ce nombre de Mach, un premier calcul a été tenté sans succès pour un nombre de Mach amont égal à 0,15, et les résultats présentés dans cette communication ont été obtenus pour une valeur du nombre de Mach amont encore plus élevée, et égale à 0,27. Le nombre de Mach aval étant alors égal à 0,7, l'effet de la compressibilité n'est plus négligeable et, par conséquent, seule une comparaison qualitative du calcul avec l'expérience sera présentée.

2. MODELE MATHEMATIQUE ET RESOLUTION NUMERIQUE

Equations de Navier-Stokes moyennes

Le modèle mathématique mis en oeuvre pour la simulation numérique d'écoulements tridimensionnels compressibles turbulents est formé des équations de Navier-Stokes compressibles moyennes et complétées par un modèle de turbulence algébrique de type longueur de mélange. Les équations de Navier-Stokes permettant de décrire l'écoulement moyen s'écrivent sous la forme suivante :

$$
\begin{aligned}
&\frac{\partial \rho}{\partial t} + div\,(\rho \overline{V}) = 0 \\
&\frac{\partial \rho \overline{V}}{\partial t} + div\,(\rho \overline{V} \otimes \overline{V} + p\overline{\overline{I}}) = div\,(\overline{\overline{\tau}} + \overline{\overline{\tau}}_R) \\
&\frac{\partial \rho E}{\partial t} + div\,(\rho E \overline{V} + p\overline{V}) = div\,[(\overline{\overline{\tau}} + \overline{\overline{\tau}}_R).\overline{V} - \overline{q} - \overline{q}_t]
\end{aligned}
\qquad (1)
$$

Dans ces équations, ρ, $\overline{V}$ et E désignent respectivement la masse volumique, la vitesse de l'écoulement et l'énergie totale par unité de masse.

En supposant que le fluide considéré est un gaz parfait à chaleurs spécifiques constantes de rapport Cp/Cv = γ , la pression statique p est reliée à ρ, $\overline{V}$ et E par la loi d'état :

$$
p = (\gamma - 1)\rho\left(E - \frac{V^2}{2}\right) \qquad (2)
$$

Le fluide étant en outre supposé Newtonien et vérifiant l'hypothèse de Stokes, le tenseur des contraintes $\overline{\overline{\tau}}$ et la densité de flux de chaleur $\overline{q}$ ont pour expression :

$$
\begin{aligned}
&\overline{\overline{\tau}} = -2/3\,\mu\,(div\overline{V})\,\overline{\overline{I}} + \mu\,[\nabla\overline{V} + (\nabla\overline{V})^T] \\
&\overline{q} = -\lambda\,\nabla T
\end{aligned}
\qquad (3)
$$

où μ est le coefficient de viscosité moléculaire qui varie en fonction de la température selon la loi de Sutherland, et λ est le coefficient de conductibilité thermique qui est donné par $\lambda = \mu Cp/Pr$ (le nombre de Prandtl Pr est supposé constant et égal à 0,72).

Les expressions du tenseur des contraintes de Reynolds $\overline{\overline{\tau_R}}$ et de la densité de flux de diffusion turbulente d'enthalpie $\overline{q_t}$ sont données par le modèle de turbulence.

Modélisation de la turbulence

Les résultats présentés dans cette communication ont été obtenus à l'aide d'un modèle de turbulence algébrique pour lequel le tenseur $\overline{\overline{\tau_R}}$ et le vecteur $\overline{q_t}$ sont reliés aux gradients de vitesse et de température par des expressions analogues à (3), c'est-à-dire :

$$
\begin{aligned}
&\overline{\overline{\tau}}_R = -2/3\,\mu_t\,(div\overline{V})\,\overline{\overline{I}} + \mu_t\,[\nabla\overline{V} + (\nabla\overline{V})^T] \\
&\overline{q}_t = -\frac{\mu_t\,C_p}{Pr_t}\,\nabla T
\end{aligned}
\qquad (4)
$$

Le nombre de Prandtl turbulent Pr_t est supposé constant et égal à Ø,9. Le coefficient de viscosité turbulente μ_t est donné par le modèle de longueur de mélange initialement développé par Michel, Quémard et Durant [14] dans le cadre de l'approximation de couche limite et pour des écoulements bidimensionnels. μ_t a pour expression :

$$\mu_t = \rho l^2 F^2 \omega \tag{5}$$

où l, F et ω désignent respectivement la longueur de mélange, la fonction correctrice de sous-couche visqueuse et le module du rotationnel de la vitesse.

La quantité ω remplace la dérivée suivant la direction normale à la paroi de la composante tangentielle de la vitesse, qui intervient dans le modèle original [14]. La longueur de mélange l est donnée par :

$$l = 0{,}085\,\delta\, th\left(\frac{K}{0{,}085}\frac{d}{\delta}\right) \qquad \text{avec K = Ø,41,} \tag{6}$$

où d et δ désignent respectivement une distance aux parois et une épaisseur de couche limite dont la détermination sera expliquée plus bas.

La fonction F, destinée à représenter l'amortissement de la turbulence au voisinage des parois, est donnée par :

$$F(\zeta) = 1 - \exp\left(-\frac{\sqrt{\zeta}}{26K}\right) \quad \text{avec} \quad \zeta = \rho l^2 \frac{\mu + \mu_t}{\mu^2}\omega \tag{7}$$

ce qui conduit à une définition implicite de μ_t.

Dans le modèle original [14], les quantités d et δ apparaissant dans l'expression de la longueur de mélange (6) désignent sans ambiguité la distance à la paroi et l'épaisseur de la couche limite. Pour l'application tridimensionnelle présentée ici, la distance à la paroi est remplacée par une distance modifiée tenant compte de la présence de plusieurs parois, et l'épaisseur de la couche limite est remplacée par la valeur de cette distance modifiée, en un point Mv de la frontière de la couche visqueuse.

Pour l'application traitée dans cette communication, la détermination de d et δ dépend du sous-domaine considéré. Dans le sous-domaine en O, la distance d est obtenue à l'aide de la formule :

$$d = \frac{2d_1 z_1 d_2 z_2}{d_2 z_2\sqrt{d_1^2+z_1^2} + d_1 z_2\sqrt{z_1^2+d_2^2} + d_2 z_1\sqrt{d_1^2+z_2^2} + d_1 z_1\sqrt{d_2^2+z_2^2}} \tag{8}$$

A l'intrados de l'aube considérée A_l (voir la figure 2), d_1 et d_2 désignent respectivement les distances du point M à la paroi intrados de l'aube A_k et à la paroi extrados de l'aube consécutive A_{k-1}. A l'extrados de l'aube A_k, d_1 et d_2 désignent alors les distances du point M à la paroi intrados de l'aube A_{k+1} et à la paroi extrados de l'aube A_k. Les quantités z_1 et z_2 désignent les distances du point M aux deux parois latérales.

La formule (8) qui a été établie à l'origine par Buleev [15] dans le cas d'une tuyère à section rectangulaire est utilisée ici par extension pour un canal interaube. Cette formule présente la propriété souhaitée suivante : quand une des distances, d_1 par exemple, tend vers Ø, alors que les autres distances sont fixes, la distance d se comporte comme d_1.

La frontière de la couche limite est déterminée de la manière suivante : dans chaque section de maillage (Y,Z) où les coordonnées Y et Z représentent les indices des points de discrétisation (Fig.3), on recherche, en allant en direction du coin, le point B de la bissectrice où le tourbillon ω devient supérieur à une valeur ω_0. La section (Y, Z) est alors divisée en trois régions comme il est indiqué sur la figure 3. Dans la région II, on recherche pour chaque ligne de maillage Y = cste et en allant vers la paroi, le point P où ω devient supérieur à ω_0. Dans la région III, on procède de façon analogue.

Le choix du point Mv associé au point M où est appliqué le modèle et permettant de déterminer la valeur de δ (voir plus haut) est alors le suivant. Si le point M appartient à la région I, le point Mv est choisi en B. Si le point M appartient à la région II, par exemple au segment QR (Fig. 3), le point Mv est choisi sur la frontière de la couche limite en P. La région III est traitée de manière similaire à la région II.

Dans les sous-domaines en H amont et aval, situés à une distance notable de l'aube, la distance d est obtenue à l'aide de la formule simplifiée :

$$d = \frac{z_1 z_2}{z_1 + z_2} \tag{9}$$

qui se déduit de (8) en considérant que z_1 et z_2 sont petits par rapport à d_1 et d_2. La recherche de la frontière de la couche limite se fait uniquement selon les lignes de maillage orthogonales à la paroi latérale.

Méthode numérique

La méthode numérique utilisée [11] est dérivée de la méthode présentée par Vuillot [2] pour les équations d'Euler tridimensionnelles et par Cambier, Couaillier et Veuillot [10] pour les équations de Navier-Stokes bidimensionnelles.

Les équations (1) sont discrétisées à l'aide d'un schéma explicite centré de type Lax-Wendroff à deux pas, les termes dissipatifs étant pris en compte à l'instant t^n pour le calcul de la solution à l'instant $t^{n+1} = t^n + \Delta t$ (technique attribuée à Thommen [16] et largement répandue). La discrétisation en espace des termes de divergence et des termes dissipatifs est décrite dans [11].

Une viscosité artificielle [2] consistant en un terme non-linéaire du second ordre et un terme linéaire du quatrième ordre est ajoutée aux équations.

Pour accélérer la convergence vers une solution stationnaire, on applique la technique bien connue du pas de temps local (calculé à partir d'un critère de stabilité prenant en compte les limitations de type CFL et de type diffusif), et on utilise une méthode d'accélération multigrille. Cette méthode est fondée sur les travaux présentés initialement par Ni [17] pour les équations d'Euler bidimensionnelles, et a été développée à l'ONERA pour les équations d'Euler bidimensionnelles [18] et tridimensionnelles [19], et pour les équations de Navier-Stokes bidimensionnelles [10]. La méthode multigrille appliquée au système (1) consiste à intégrer sur des grilles grossières, un système aux résidus fondé sur la dérivation en temps des équations de fluide parfait seulement. Ainsi, la phase multigrille développée pour les équations d'Euler tridimensionnelles est utilisée sans modification pour le système (1). Le calcul présenté dans cette communication a été réalisé en utilisant deux grilles grossières dans chacun des trois sous-domaines.

Le traitement des conditions aux limites amont et aval et des raccords entre sous-domaines (y compris la frontière de périodicité) est effectué à l'aide de la technique des relations caractéristiques développée de façon rigoureuse pour des systèmes hyperboliques [20], et appliquée par extension dans le cadre des équations de Navier-Stokes [10].

3. CALCUL DE L'ECOULEMENT DANS UNE GRILLE RECTILIGNE DE TURBINE

Conditions aérodynamiques

L'expérience ([12], [13]) a été réalisée dans la soufflerie de grille d'aubes plane installée au Laboratoire de Mécanique des Fluides de l'Ecole Centrale de Lyon. Elle a permis une étude portant sur les écoulements secondaires, en absence et en présence d'injections à la paroi. Le calcul a été effectué sans représentation des injections pariétales.

Le profil constant des aubes est celui d'une grille distributrice de turbine à gaz. L'aubage présente une hauteur $2L = 274$ mm, une corde de 163 mm, un pas interaube de 141 mm et un angle de calage, compté par rapport à la direction axiale Ox, de 41°30'.

Les conditions aérodynamiques expérimentales données dans un plan situé à 24 mm en amont du front de grille sont les suivantes : nombre de Mach égal à 0,044, direction de la vitesse selon Ox, nombre de Reynolds (calculé à partir de la corde et de la vitesse extérieure à la couche limite) égal à 165 000. La couche limite se développant sur la plaque plane qui constitue la paroi latérale $z = 0$ mm atteint dans le plan $x = -24$ mm une épaisseur importante, égale à 50 mm.

Comme il a été dit dans l'introduction, le calcul a été effectué à un nombre de Mach amont beaucoup plus grand que dans l'expérience, et égal à 0,27. En revanche, la similitude en nombre de Reynolds a été respectée grâce à une diminution des longueurs (dimensions de la grille et épaisseur de couche limite amont) dans un rapport égal au rapport des vitesses.

Conditions aux limites

Sur la frontière amont, on impose la direction de la vitesse (selon Ox), la température totale (à sa valeur dans les conditions génératrices) et le profil de pression totale. Ce dernier profil est déduit d'un profil initial de vitesse longitudinale en supposant que la pression statique est constante et calculée à partir des données de la pression totale notée p_{t1} et de la vitesse à l'extérieur de la couche limite. Le profil initial de vitesse est lui-même obtenu à partir de la formule de Whitfield [21] faisant intervenir l'épaisseur de la couche limite, son épaisseur de déplacement, son paramètre de forme et le coefficient de frottement pariétal dont les valeurs sont extraites de [12]. On peut noter que le profil de vitesse est un peu modifié en cours de calcul et dépend de la condition aux limites imposée sur la frontière aval et décrite dans le paragraphe suivant ; en revanche, le profil de pression d'arrêt n'est pas remis en cause.

Sur la frontière aval, on impose la valeur de la pression statique. La valeur choisie ($p_2 = 0{,}7065\ p_{t1}$) a été obtenue en écrivant la conservation du débit par rapport à l'amont, et en estimant les valeurs de l'angle de la vitesse et de la pression d'arrêt dans cette section où les valeurs expérimentales étaient inconnues.

Sur la paroi de l'aube et sur la paroi latérale $z = 0$, on impose la condition d'adhérence et la valeur de la température (prise égale à la température génératrice). La pression statique est calculée en supposant nulle sa dérivée le long de la ligne de maillage passant par le point considéré et pratiquement

normale à la paroi.

Enfin, une condition de symétrie est appliquée sur le plan de symétrie z = L.

Maillage

Les aubes étant non vrillées et présentant un profil constant, le maillage tridimensionnel (Fig. 4) a été obtenu par empilement de maillages bidimensionnels identiques. Sur les deux frontières de raccord entre le sous-domaine en O (autour de l'aube) et les deux sous-domaines en H (situés en amont et en aval), il y a correspondance des points de maillage, ce qui permet d'éviter de faire des interpolations pour l'application de la technique de raccord et assure donc une meilleure régularité de la solution à la traversée de ces deux frontières. En revanche, sur la frontière de périodicité, il n'y a pas correspondance des points de maillage, car cette correspondance se ferait nécessairement au prix d'une dégradation de la qualité du maillage.

Les maillages des trois sous-domaines ont été obtenus grâce à une méthode d'optimisation variationnelle [22] permettant d'améliorer grandement la régularité et l'orthogonalité de maillages initiaux construits algébriquement. Le maillage bidimensionnel comprend 13 x 25 points dans le sous-domaine en H amont, 161 x 53 points dans le sous-domaine en O et 33 x 21 points dans le sous-domaine en H aval, soit 9551 points au total. Le maillage tridimensionnel correspond à un empilement de 33 maillages bidimensionnels et comprend donc 315 183 points.

Les resserrements opérés au voisinage des parois pour une discrétisation correcte des couches limites conduisent à des tailles de maille égales environ à $0{,}2\ 10^{-4}$ Cx sur l'aube (près du bord d'attaque) et à $1{,}6\ 10^{-4}$ Cx sur la paroi latérale (Cx désigne l'encombrement axial de l'aube).

Résultats

Les résultats présentés ont été obtenus après une décroissance des résidus supérieure à trois ordres de grandeur. Le temps CPU sur un ordinateur CRAY-2 est égal environ à vingt micro secondes par itération et par point, ce qui conduit à un temps de l'ordre de dix heures pour les résultats présentés.

La figure 5 représente les distributions de pression sur l'aube pour quatre valeurs de z : z = 0 (paroi latérale), z = 0,041 L, z = 0,178 L et z = L (plan de symétrie). Alors que la pression n'est pratiquement pas modifiée sur la quasi-totalité de l'intrados quand z varie, la pression à l'extrados connaît en revanche de fortes variations et augmente, sur la majeure partie de l'extrados, quand on s'approche de la paroi latérale. Ce comportement lié aux effets secondaires correspond tout à fait aux constatations expérimentales [12, 13]. Par ailleurs, dans les trois plans autres que la paroi latérale, le calcul met en évidence dans la région du bord de fuite, correctement discrétisée par le maillage en O, une chute de la pression du côté intrados correspondant à l'accélération de l'écoulement dans la région à forte courbure, suivie d'une recompression rapide associée au décollement de bord de fuite.

Les courbes iso-nombre de Mach dans le plan de symétrie sont représentées sur la figure 6. Cette figure montre en particulier la bonne description, par le maillage en O, de l'écoulement dans la région du bord d'attaque, et la régularité des courbes iso-nombre de Mach dans le sillage à la traversée de l'interface entre le sous-domaine en O et le sous-domaine en H aval.

La figure 7 représente les vecteurs vitesse obtenus par le calcul dans le plan de symétrie. Sur les tracés des vecteurs vitesse présentés dans cette communication, il faut noter que les points correspondent aux origines des vecteurs. Par ailleurs, l'échelle de longueur des vecteurs est propre à chaque tracé et ne donne donc qu'une indication du module de la vitesse relative au tracé considéré. Enfin, les vecteurs ne sont pas tracés en tous les points de maillage.

L'agrandissement du champ de vecteurs vitesse au voisinage du bord de fuite (Fig. 8) met en évidence la présence de deux tourbillons contrarotatifs dans le proche sillage.

Dans le plan de maillage situé au voisinage immédiat de la paroi latérale, les vecteurs vitesse représentés sur la figure 9 ont une allure très différente de ceux tracés dans le plan de symétrie. L'examen de la figure 9 montre la présence d'un col (désigné par la lettre C) en amont de l'aube, associé à l'existence d'un courant de retour allant du bord d'attaque de l'aube vers ce point C. Ce décollement de la couche limite provient de l'important gradient de pression contraire subi par l'écoulement sur la paroi latérale lorsqu'il approche du bord d'attaque de l'aube. Ce comportement classique, correspondant à la naissance d'un tourbillon en fer à cheval, a été décrit au cours des dernières années par résolution numérique des équations de Navier-Stokes dans le cas de la configuration plus simple d'un cylindre sur une plaque plane, en régime laminaire [23] ou en régime turbulent [6].

On peut noter par ailleurs sur la figure 9 la forte augmentation du module de la vitesse dans la région du bord d'attaque par rapport à l'écoulement en amont. Une bonne description de ce phénomène nécessite l'utilisation d'un maillage très fin dans la direction z au voisinage de la paroi latérale. Dans le calcul présenté, l'épaisseur de la maille près de la paroi latérale correspond à une division par 6 de l'épaisseur initialement choisie dans un essai préliminaire et adaptée au profil de couche limite en amont. L'influence sur la solution d'une réduction supplémentaire de la taille de maille (qui reste probablement encore trop importante) devra être soigneusement étudiée dans l'avenir.

Dans le plan de maillage passant par le bord d'attaque de l'aube, près du coin formé par ce bord d'attaque et la paroi latérale plane, le comportement de l'écoulement calculé est illustré par les figures 10a à 10d qui représentent le maillage, les lignes iso-nombre de Mach, les lignes iso-pression totale et le champ de vecteurs vitesse. En particulier, l'examen des lignes iso-pression d'arrêt (Fig. 10c) montre l'enroulement de la partie interne de la couche limite autour d'un noyau de pertes élevées.

Sur la figure 10d représentant les vecteurs vitesse, on voit clairement l'enroulement de l'écoulement dans le coin, le mot "enroulement" n'étant peut-être pas parfaitement approprié dans la mesure où l'écoulement s'échappe du plan considéré dans la direction tangentielle à l'aubage. La figure 11 présentant un fort agrandissement des vecteurs vitesse dans le coin indique la présence, en plus du tourbillon principal, d'un petit tourbillon secondaire contrarotatif.

Les vecteurs vitesse sur la surface de maillage immédiatement voisine de la paroi de l'aube sont représentés sur les figures 12, 13 et 14 respectivement dans la région du bord d'attaque, du côté extrados et du côté intrados.

On peut constater à nouveau sur la figure 12 la grande valeur de la composante verticale de la vitesse près de la ligne de bord d'attaque. Du côté extrados, l'examen de la figure 13 montre la forte déviation de l'écoulement vers le milieu de l'aube et l'important ralentissement dans la partie arrière. En revanche, du côté intrados (Fig. 14), l écoulement est quasi-bidimensionnel sur la majeure partie de l'aube.

L'écoulement est représenté enfin (Fig. 15 à 18) sous forme de courbes iso-pression d'arrêt et de vecteurs vitesse dans deux plans parallèles au front de grille.

Pour le premier plan situé à l'intérieur de la grille en une abscisse égale à 86% de l'encombrement axial, l'écoulement calculé est comparé aux résultats expérimentaux [12] sur les figures 15 et 16. L'examen des courbes iso-pression d'arrêt (Fig. 15) montre que l'épaisseur de la couche limite sur la paroi latérale est beaucoup plus faible dans le calcul que dans l'expérience. Ceci est sans doute dû en partie à l'accélération plus forte de l'écoulement calculé, liée au changement de conditions aérodynamiques. En revanche, l'allure des courbes calculées présente une certaine similitude à celle observée dans l'expérience (à l'exception des régions proches des parois où les mesures ne sont pas disponibles), et le calcul prédit de manière conforme à l'expérience des pertes plus importantes du côté extrados.

Les vecteurs vitesse représentés sur la figure 16 témoignent de la présence dans le calcul du tourbillon de passage qui occupe, comme dans l'expérience, tout le canal interaubes.

Les résultats du calcul sont également présentés dans un plan situé à une distance égale à 52% de l'encombrement axial en aval du bord de fuite. Deux canaux ont été tracés par périodicité. L'allure des courbes iso-pression d'arrêt (Fig. 17) et des vecteurs vitesse (Fig. 18) est classique pour ce type d'écoulement avec un noyau dans le sillage correspondant à une perte de pression d'arrêt, et la présence d'un tourbillon étendu.

4. CONCLUSION

Les résultats présentés dans cette communication ont montré que la méthode numérique utilisée, appliquée dans un maillage fin associant deux sous-domaines en H et un sous-domaine en O, conduit à une description précise de l'écoulement dans une grille de turbine, et permet de mettre en évidence des phénomènes complexes d'écoulements secondaires. En raison du changement de conditions de l'écoulement lié au caractère compressible des équations résolues, seule une comparaison qualitative limitée avec l'expérience a été effectuée. Cette comparaison peut être considérée comme encourageante, mais une validation plus poussée du code est bien entendu nécessaire pour pouvoir l'utiliser comme un outil prédictif. Cette validation constituera la suite immédiate de nos travaux.

REFERENCES

[1] - L. CAMBIER et J.P. VEUILLOT. Computation of Cascade Flows at High Reynolds Number by Numerical Solution of the Navier-Stokes Equations. AIAA Paper 88-0364, 1988 and ONERA TP n° 1988-3.

[2] - A.M. VUILLOT. A Multi-Domain 3D Euler Solver for Flows in Turbomachines. Proceedings of the 9th ISABE Symposium, Athens, Sept. 1989 (à paraître).

[3] - A. FOURMAUX, G. BILLONNET, A. LE MEUR et A. LESAIN. Simulation des écoulements tridimensionnels et instationnaires dans les turbomachines. Equations. AGARD/PEP 74th A Meeting on Unsteady Aerodynamic Phenomena in Turbomachines, Luxembourg, 1989.

[4] - N.K. MADAVAN, M.M.RAI et S. GAVALI. Grid Refinement Studies of Turbine Rotor-Stator Interaction. AIAA Paper 89-0325, 1989.

[5] - C. HAH. Numerical Study of Three-Dimensional Flow and Heat Transfer Near the Endwall of a Turbine Blade Row. AIAA Paper 89-1689, 1989.

[6] - R.V CHIMA et J.W. YOKOTA. Numerical Analysis of Three-Dimensional Viscous Internal Flows. AIAA Paper 88-3522, 1988.

[7] - W.N. DAWES. Development of a 3D Navier-Stokes Solver for Application to all Types of Turbomachinery. ASME Paper 88-GT70, 1988.

[8] - S.V. SUBRAMANIAN et R. BOZZOLA. Numerical Simulation of Three-Dimensional Flow Fields in Turbomachinery Blade Rows Using the Compressible Navier-Stokes Equations. AIAA Paper 87-1314,1987.

[9] - K. NAKAHASHI, O. NOZAKI, K. KIKUCHI et A. TAMURA. Navier-Stokes Computation of Two and Three-Dimensional Cascade Flow Fields. AIAA Paper 87-1315, 1987.

[10] - L. CAMBIER, V. COUAILLIER et J.P. VEUILLOT. Résolution numérique des équations de Navier-Stokes à l'aide d'une méthode multigrille. La Recherche Aérospatiale n° 1988-2, pp. 23-42, 1988.

[11] - L. CAMBIER et B. ESCANDE. Navier-Stokes Simulation of a Shock Wave-Turbulent Boundary Layer Interaction in a Three-Dimensional Channel. AIAA Paper 89-1851, 1989 and ONERA TP n° 1989-82.

[12] - A. ONVANI. Etude expérimentale des écoulements secondaires en grille d'aubes de turbine en absence et en présence d'injections discrètes à la paroi. Thèse de doctorat de 3ème cycle, Université Claude Bernard- LYON 1, 1983.

[13] - F. BARIO, F. LEBOEUF, A. ONVANI et A. SEDDINI. Aerodynamics of Cooling Jets Introduced in the Secondary Flow of a Low Speed Turbine Cascade. ASME Paper 89-GT192, 1989.

[14] - R. MICHEL, C. QUEMARD et R. DURANT. Application d'un schéma de longueur de mélange à l'étude des couches limites turbulentes d'équilibre. ONERA NT n° 154, 1969.

[15] - N.I. BULEEV. Theoretical Model of the Mechanism of Turbulent Exchange in Fluid Flows. Teploperedacha, pp. 64-98, Moscou, URSS, 1962 and AERE Translation 957, Atomic Energy Research Establishment, Harwell, England, 1963.

[16] - H.U. THOMMEN. Numerical Integration of the Navier-Stokes Equations. ZAMP, Vol. 17, pp. 369-384, 1966.

[17] - R.H. NI. A Multigrid Scheme for Solving the Euler Equations. AIAA Journal, Vol 20, pp. 1565-1571, 1982.

[18] - V. COUAILLIER. Solution of the Euler Equations : Explicit Scheme Acceleration by a Multigrid Method. Proceedings of the 2nd European Conference on Multigrid Methods, GAMM, Cologne, Oct. 1985 and ONERA TP n° 1985-129.

[19] - V. COUAILLIER. Multigrid Method for Solving Euler and Navier-Stokes Equations in Two and Three Dimensions. Proceedings of the 8th GAMM Conference on Numerical Methods in Fluid Mechanics, Delft, Sept. 1989 (à paraître).

[20] - H. VIVIAND et J.P. VEUILLOT. Méthodes pseudo-instationnaires pour le calcul d'écoulements transoniques.ONERA Publication n° 1978-4, 1978.

[21] - D.L. WHITFIELD. Analytical Description of the Complete Turbulent Boundary Layer Velocity Profile. AIAA Paper n° 78-1158, 1978.

[22] - O.P. JACQUOTTE. Génération, optimisation et adaptation de maillages multidomaines autour de configurations complexes. AGARD 64th FDP, Loen (Norvège), 1989 and ONERA TP n° 1989-72.

[23] - M.R. VISBAL. Numerical Investigation of Laminar Juncture Flows. AIAA Paper 89-1873, 1989.

REMERCIEMENTS

Le travail présenté ici a été effectué sous contrat de la "Direction des Recherches, Etudes et Techniques" de la Délégation Générale pour l'Armement.

Les auteurs expriment leurs remerciements à B. PETOT, de la SNECMA, pour la fourniture d'une initialisation algébrique des maillages, à O.P. JACQUOTTE, de l'ONERA, pour son programme d'optimisation de maillage et à F. LEBOEUF, de l'Ecole Centrale de Lyon, pour la communication des résultats expérimentaux.

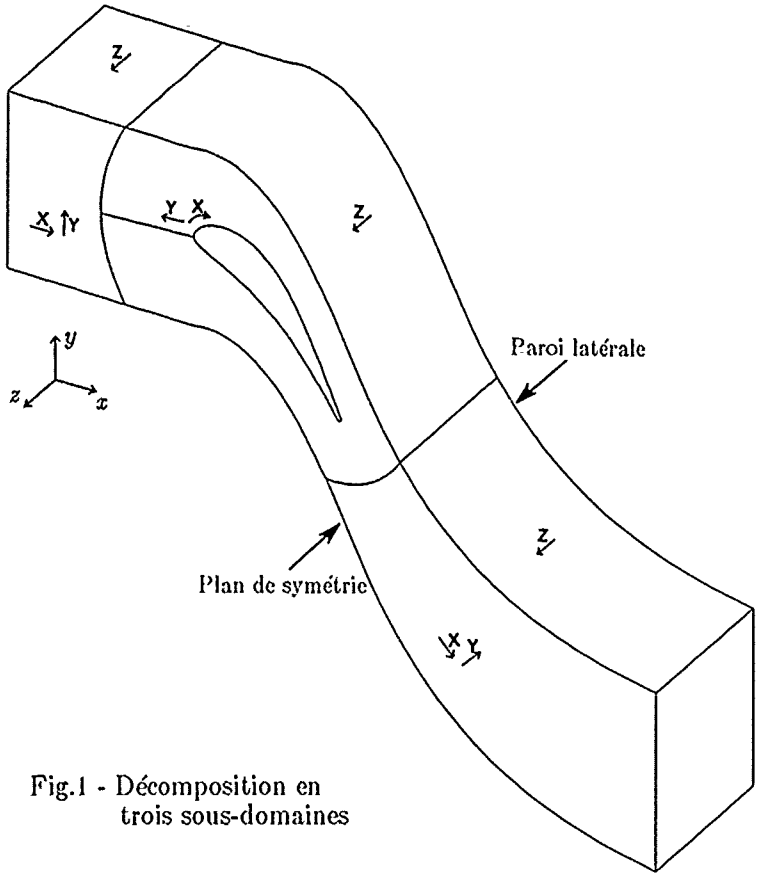


Fig.1 - Décomposition en trois sous-domaines

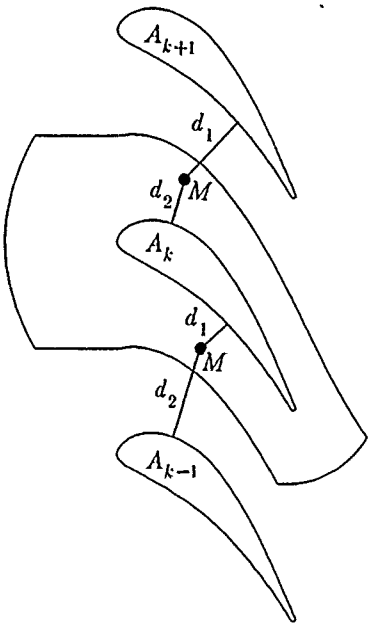


Fig.2 - Schéma explicatif pour le calcul de la distance aux parois

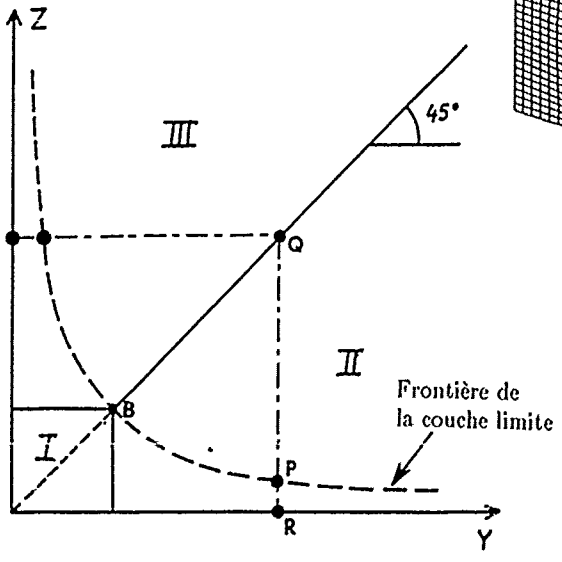


Fig.3 - Evaluation de l' épaisseur de couche limite

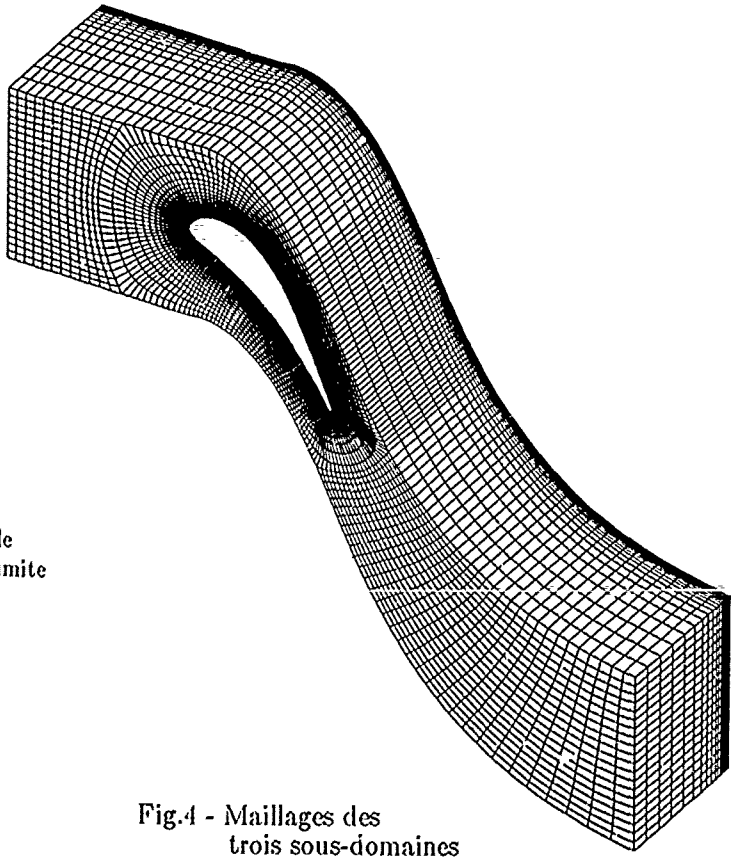


Fig.4 - Maillages des trois sous-domaines

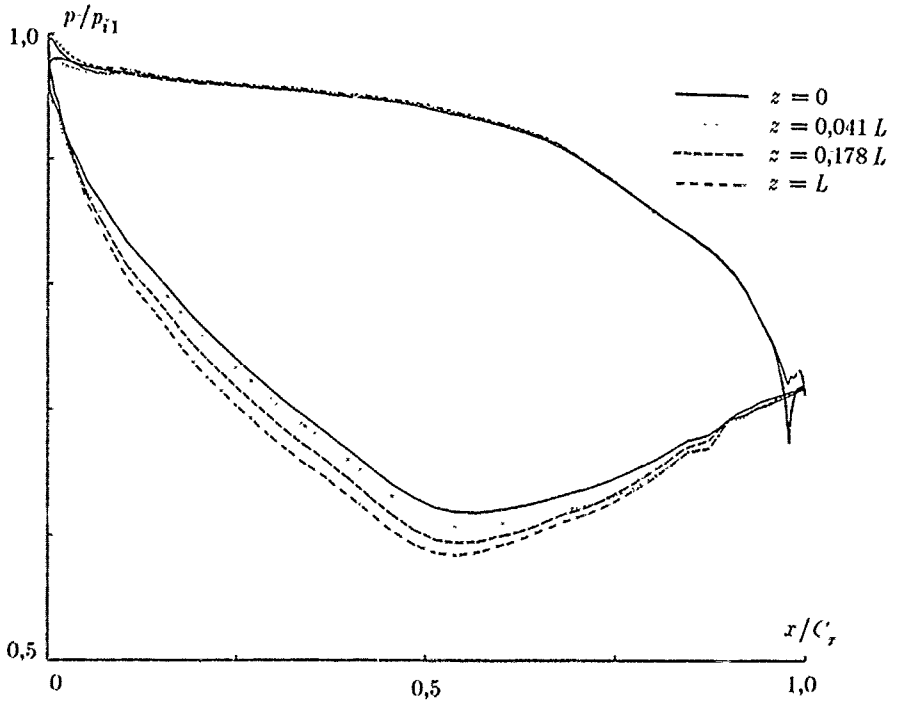


Fig.5 - Distributions de pression sur l' aube

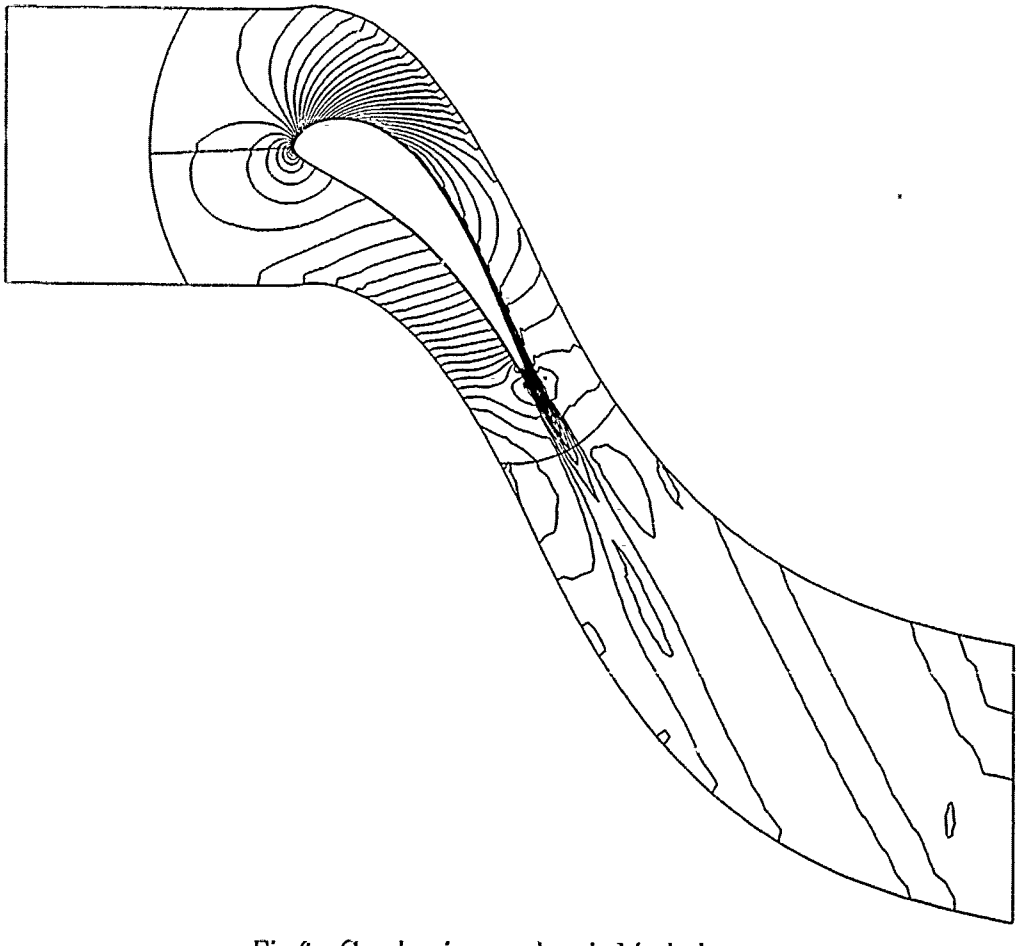
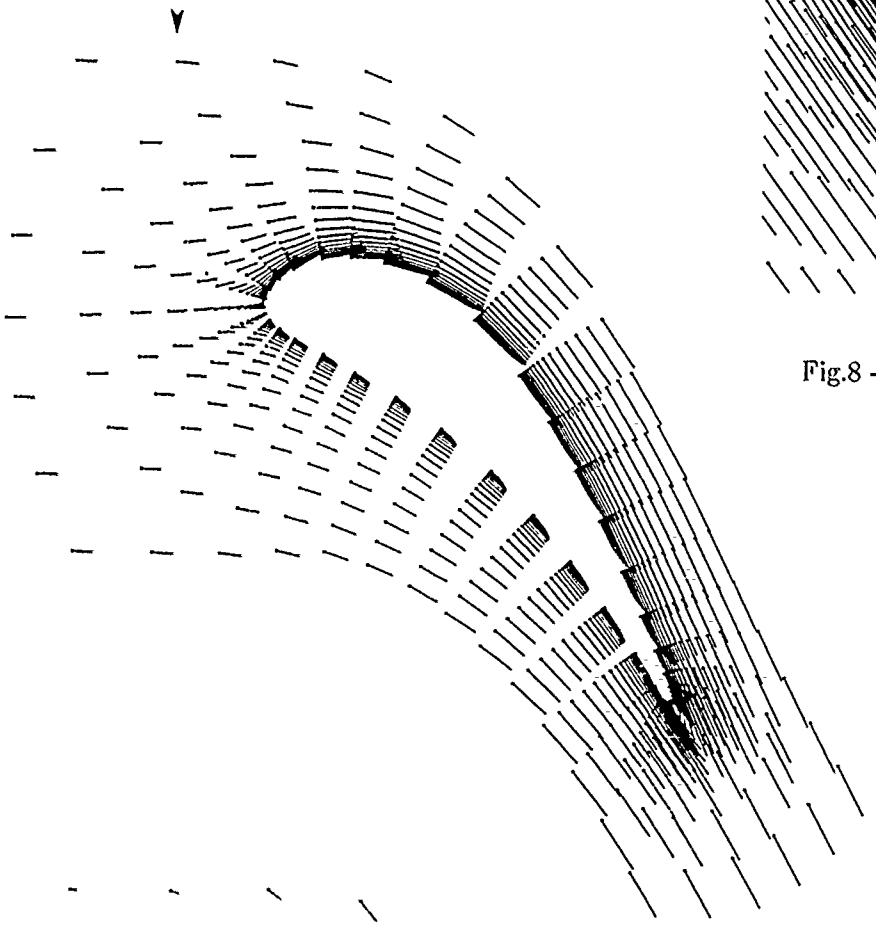


Fig.6 - Courbes iso-nombre de Mach dans le plan de symétrie ($\Delta M = 0{,}025$)

Fig.7 - Vecteurs vitesse dans le plan de symétrie



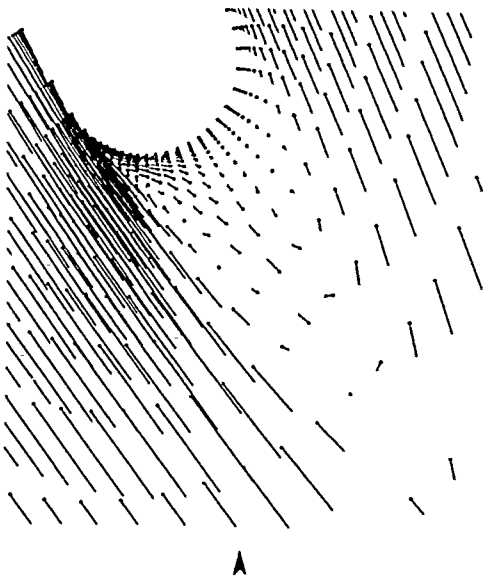


Fig.8 - Vecteurs vitesse dans le plan de symétrie Agrandissement au voisinage du bord de fuite

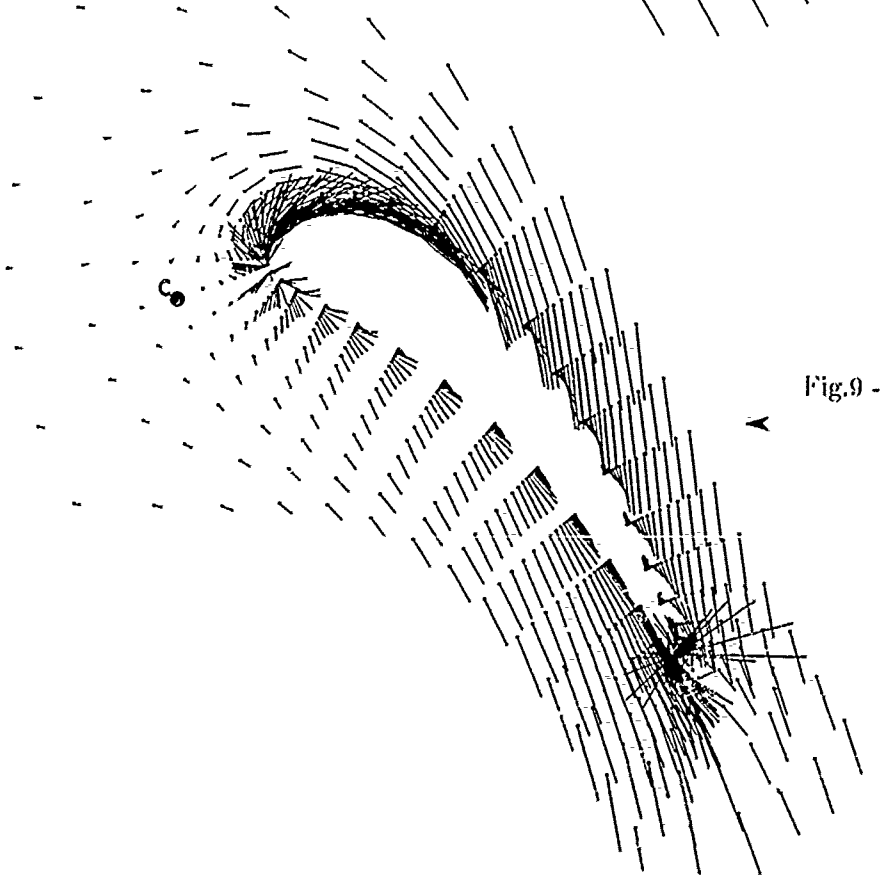


Fig.9 - Vecteurs vitesse dans le plan de maillage immédiatement voisin de la paroi latérale

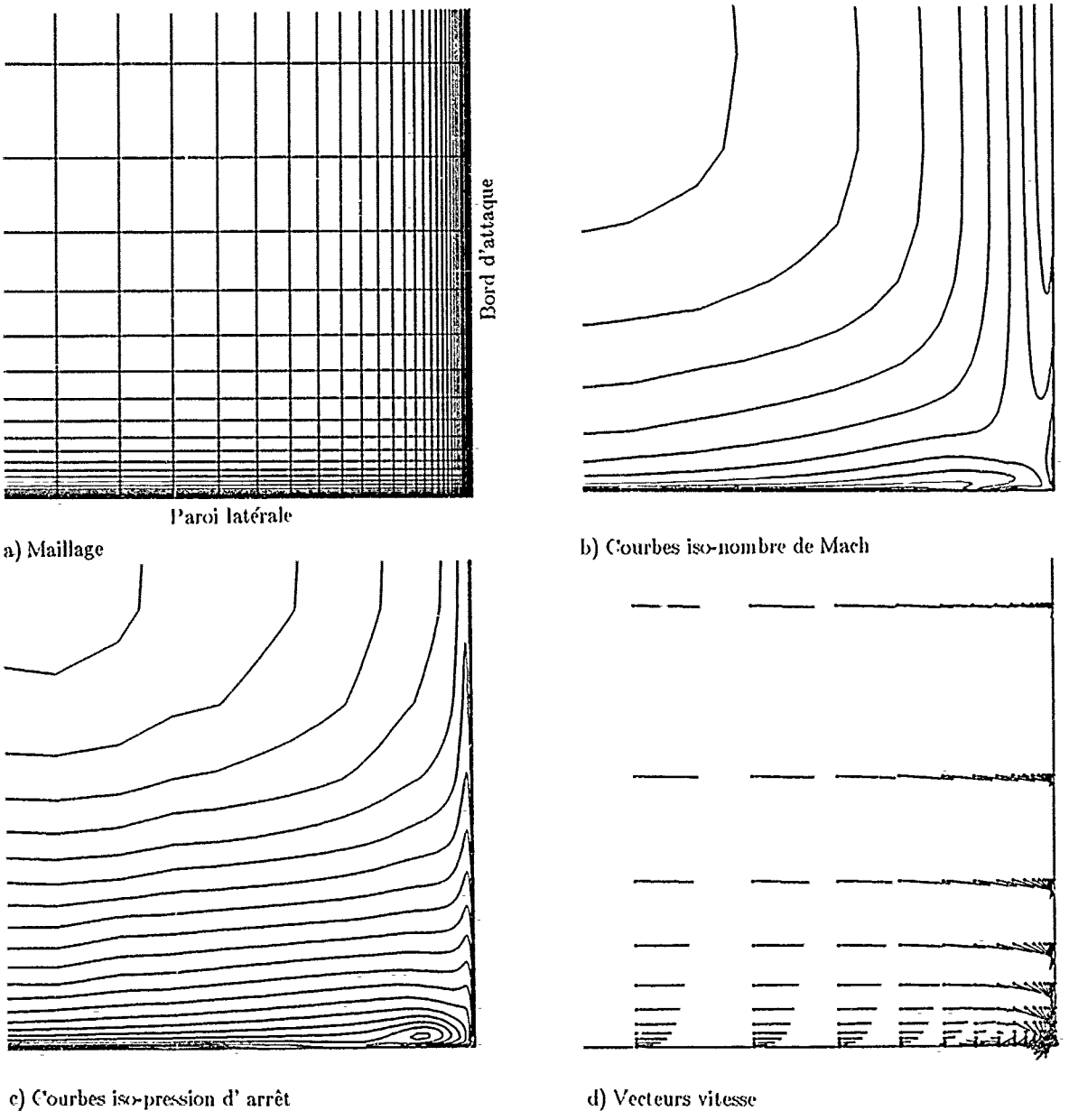


Fig.10 - Ecoulement calculé dans le coin formé par la paroi latérale et le bord d' attaque de l' aube

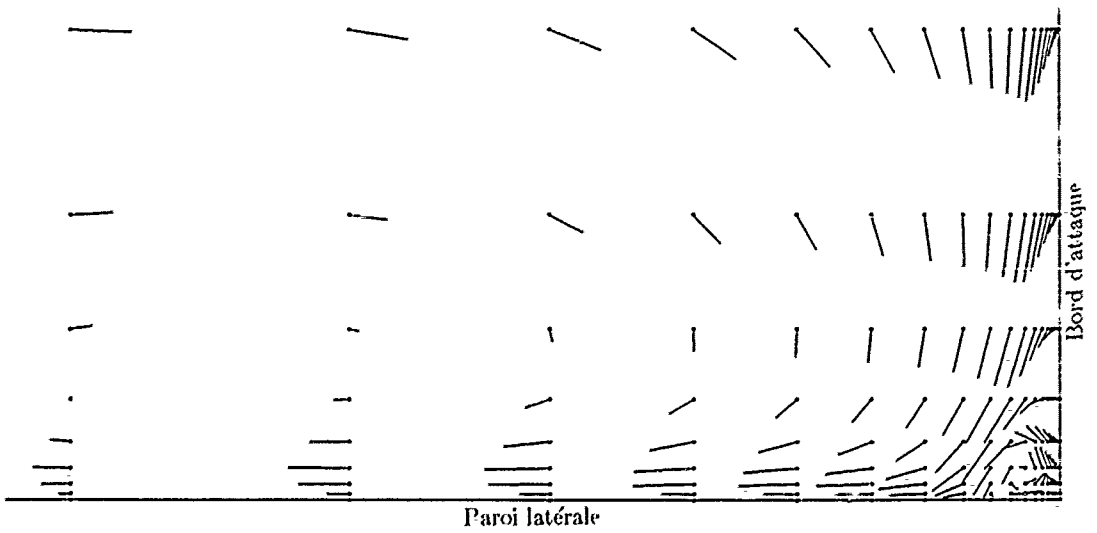


Fig.11 - Vecteurs vitesse - Agrandissement près du point de jonction entre la paroi latérale et le bord d'attaque de l' aube

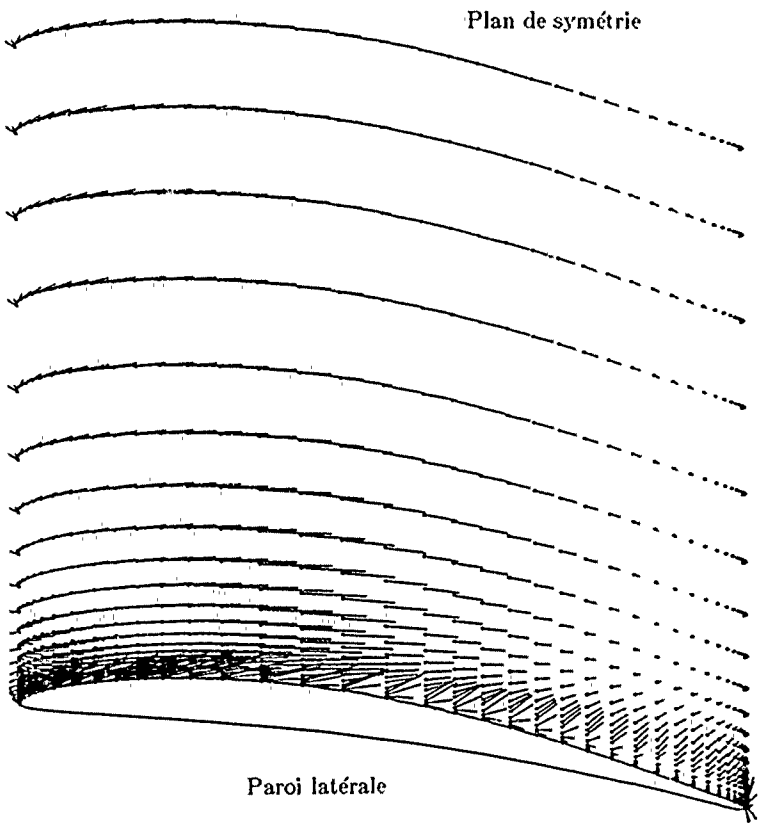


Fig.13 - Vecteurs vitesse - Surface de maillage voisine de la paroi de l' aube - Côté extrados

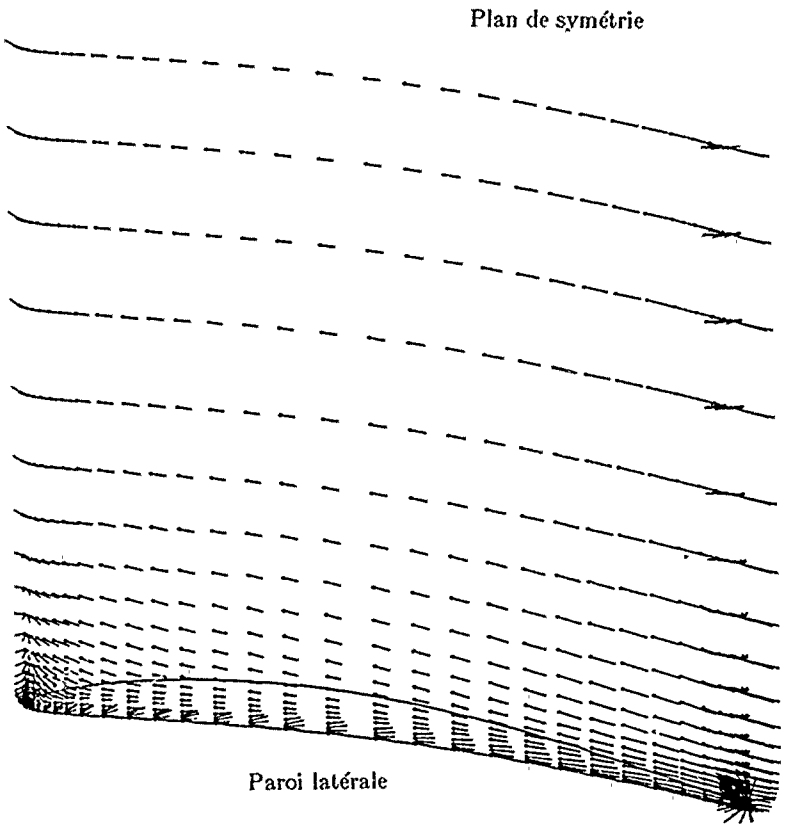
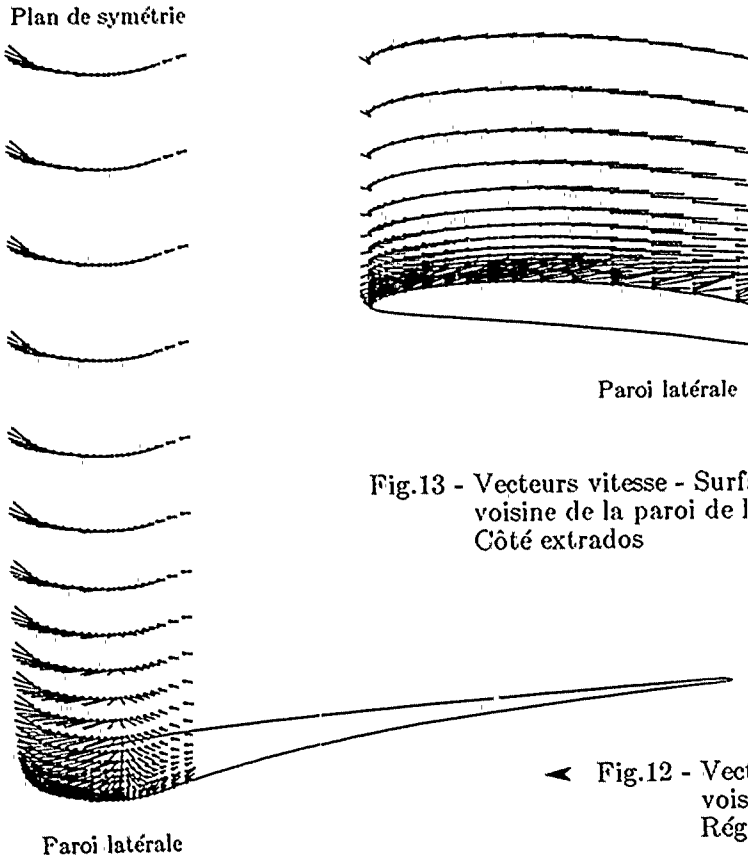


Fig.14 - Vecteurs vitesse - Surface de maillage voisine de la paroi de l' aube - Côté intrados



◄ Fig.12 - Vecteurs vitesse - Surface de maillage voisine de la paroi de l' aube - Région du bord d' attaque

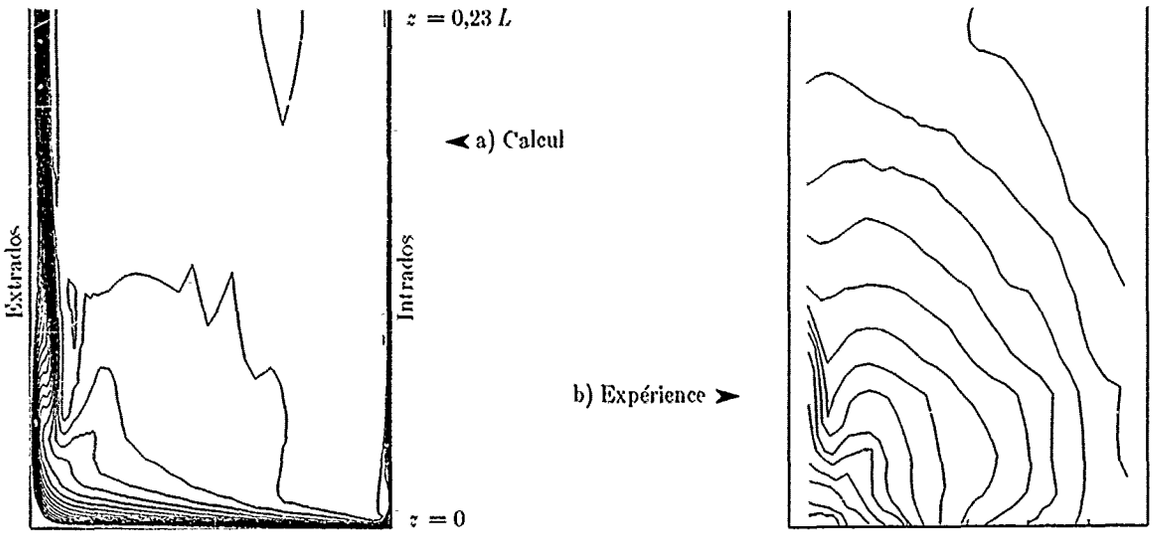


Fig.15 - Courbes iso-pression d' arrêt dans le plan $x = 0{,}86\ C_r$
(Echelle dilatée dans la direction z)

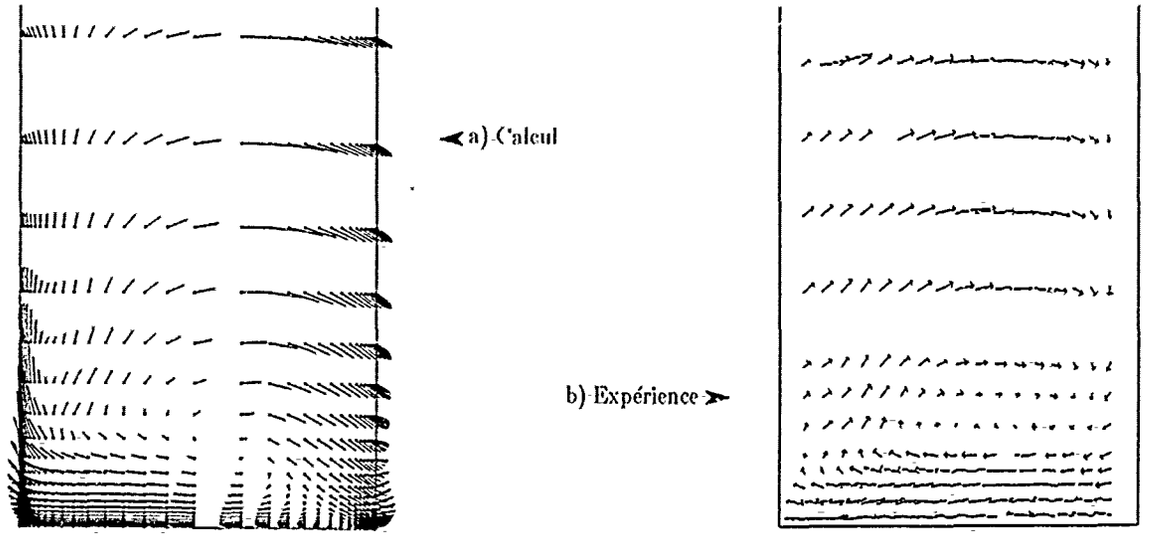


Fig.16 - Vecteurs vitesse dans le plan $x = 0{,}86\ C_r$
(Echelle dilatée dans la direction z)

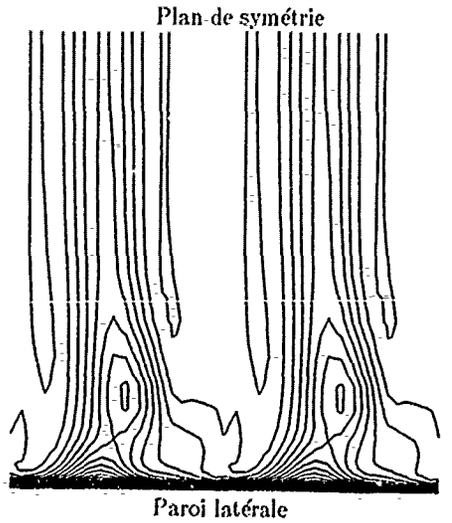


Fig.17 - Courbes iso-pression d' arrêt dans le plan $x = 1{,}52\ C_r$

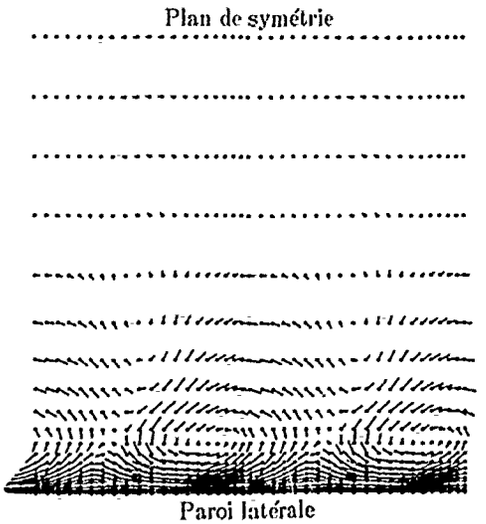


Fig.18 - Vecteurs vitesse dans le plan $x = 1{,}52\ C_r$

DISCUSSION

Savini, Italy

1. Can you comment about comparison with experimental total pressure contours downstream of trailing edge?

2. Was the multigrid effective for this computation?

3. How did you treat the wake region in the O-mesh subdomain?

Author's Reply:

1. Due to the different flow conditions, we have done a limited comparison between computation and experiment; in particular, we have not compared the total pressure contours downstream of the trailing edge. Besides, the total pressure contours downstream of the trailing edge were available in the experiment only in one section very close to the trailing edge (at a distance equal to 0.024 C_x).

2. The multigrid acceleration technique was tested in Ref 10 for a 2-D Navier-Stokes calculation and was found to yield in that case an acceleration factor of about 3. We have not tried to do the present 3-D computation without multigrid because it would have been too costly. I think that the acceleration factor is slightly smaller in the 3-D computation than it was in the above mentioned 2-D calculations.

3. There is no special treatment for the wake region in the O-subdomain. In particular, the turbulence model is applied in the same way at any point of the O-subdomain, as it is described in the paper.

Hoffmann, Germany

Did you try a calculation with an H-type grid instead of your O-type grid equivalent to that of your O-grid? If yes, did you achieve a comparable accuracy near the trailing and/or leading edges. Using such a fine H-type grid as you did with the O-type, to my opinion, may yield in comparable accurate results.

Author's Reply:

I did not try a calculation with an H-type grid. However, I am convinced that, with an equivalent number of mesh points, an O-type grid is capable of providing improved solution accuracy when compared with an H-type grid. The use of an O-type grid allows the minimizing of the discretization errors at the leading and trailing edges.

Erkilet, Turkey

From the paper I understand that, you assumed $Pr_t = 0.2$ $Pr = 0.9$. May I learn, how did you assume these values?

Author's Reply:

We assumed from general information given in literature. Do you have a comment for those values?

Comment: As far as I know, for turbulent turbomachinery flows, it is advised to assume values about 1.

Papailiou, Greece

1. Which is the number of nodes for your calculation?

2. Can you give some more details about the physical meaning of the distance d?

Author's Reply:

1. The number of nodes is equal to 315,183.

2. The distance d is used to account for the turbulent length scale corresponding to the presence of several walls. More details about its physical meaning may be found in Buleer's paper [15].

CALCUL DES ECOULEMENTS SECONDAIRES DANS UNE TURBINE AXIALE

J. BERNARD -- F. FALCHETTI
SNECMA, Centre de Villaroche
77550 MOISSY CRAMAYEL - FRANCE

RESUME

L'estimation des écoulements secondaires est un objectif majeur pour la conception des aubes de turbine et l'analyse de leurs performances. Une méthode de calcul des écoulements secondaires, développée initialement pour les compresseurs multi-étages, a été appliquée en grilles d'aubes de distributeur et sur un étage de turbine basse pression. La méthode, couplée à un calcul méridien classique, détermine correctement la vorticité secondaire, et la correction locale de la triangulation qui lui est associée. La détermination des pertes secondaires et du blocage reste insuffisante car liée à un calcul intégral des couches limites de paroi. La méthode peut néanmoins être utilisée conjointement aux corrélations usuelles et dans ce cadre son emploi permet une meilleure adaptation des grilles d'aubes successives lors de la conception. L'analyse des performances d'un aubage, et notamment la prévision détaillée des écoulements secondaires, exige bien sûr l'emploi de méthodes de résolution des équations de Navier-Stokes tridimensionnelles.

ABSTRACT

Satisfactory prediction of secondary flow effects can be considered a major objective in the design and analysis of turbine blades. A method, initially developed for the computation of secondary flows in multi-stage compressors, is briefly presented together with results obtained on a turbine nozzle cascade and on a low pressure turbine stage. Satisfactory results are obtained for the secondary vorticity as well as for the local variations in the velocity triangles. However, secondary losses and blockage are not well predicted due to the integral character of the wall boundary layer calculation used in the model. However use of the method together with current correlations can yield interesting results especially as far as successive blade row adaptation is concerned. For detailed predictions of blade row performance, in particular secondary flow effects, the turbine designer must implement more complex methods developed for the resolution of the three-dimensional Navier-Stokes equations.

Nomenclature

B	= coefficient de blocage
h	= hauteur de veine
h_m, h_b	= métriques
$k_{i,j}$	= courbure ($= \frac{1}{h_i h_j} \frac{\partial h_i}{\partial U_j}$)
(m,b,θ)	= système de coordonnées curvilignes axisymétriques
p	= pression statique
P	= pression totale
(s,b,n)	= système de coordonnées intrinsèques, orthogonal
u_m, u_b	= coordonnées selon les directions m et b
T	= température totale
$\vec{v}$	= vitesse absolue
$\vec{w}$	= vitesse relative
(z,r,θ)	= système de coordonnées cylindriques
α	= angle absolu de l'écoulement ($= \tan^{-1}(v_\theta/v_m)$)
β	= angle relatif de l'écoulement ($= \tan^{-1}(w_\theta/w_m)$)
β'	= angle du profil
δ	= épaisseur de la couche limite
δ^*_m	= épaisseur de déplacement méridienne $\left(= \frac{1}{\pi r_0 \rho_0 w_{m_0}} \int_0^h r (\rho \hat{w}_m - \rho w_m)\, db\right)$
δ^*_n	= épaisseur de déplacement transversale $\left(= \int_0^h \frac{\rho w_m}{\rho_0 w_{m_0}} db\right)$
δq	= déficit de débit ($= 2\pi B (r \rho \hat{w}_m)_0 \delta^*_m$)
$\Delta D_m, \Delta D_\theta$	= composantes du déficit de force d'aubage
ΔD_{3m}	= déficit de pression statique
ϕ	= angle entre les directions z et m
$\vec{\omega}$	= vitesse angulaire de rotation
$\vec{\Omega}$	= vorticité relative ($= \vec{\nabla} \wedge \vec{w}$)
ρ	= masse volumique
ν_t	= viscosité cinématique turbulente
σ	= tenseur des tensions visqueuses

indices inférieurs :

o	= valeur à la paroi
m,b,θ	= composantes d'un vecteur dans le système de coordonnées axisymétriques
s,b,n	= composantes d'un vecteur dans le système de coordonnées intrinsèques
δ	= valeur à la limite extérieure de la couche visqueuse

indice supérieur :

Λ	= relatif à l'écoulement sain non visqueux

INTRODUCTION

Les objectifs croissants de charge et de rendement pour les turbines de moteur d'avion impliquent une estimation correcte des pertes. Les pertes secondaires doivent en particulier être connues dès le stade de la définition de la triangulation d'un projet de turbine. Or les calculs méridiens servant à établir cette triangulation ne prennent pas en compte les effets visqueux associés aux parois du moyeu et du carter; ceci conduit le concepteur à appliquer des corrections très globales sur la triangulation. A partir de corrélations semi-empiriques ou l'expérience du constructeur, l'effet de blocage et les pertes dûs aux couches limites se développe r la veine sont pris en compte par un coefficient, et par une correction globale des pertes d iées. Le problème de la désadaptation locale en pied et en tête de grilles d'aubes successi rdé qu'en termes de tenue à l'incidence.

Une approche plus complète du cal ues phénomènes secondaires est en fait souhaitable dès le stade de la definition de la triangulation : la correction du calcul méridien sous l'effet des écoulements secondaires est seule capable d'aboutir à l'estimation correcte de la triangulation, notamment en pied et en tête des aubages. L'objectif doit donc être de disposer non seulement de l'évolution axiale du blocage associé aux couches limites du moyeu et du carter, mais aussi de l'évolution radiale des pertes et de l'angle de sortie de l'écoulement liée à la présence des écoulements secondaires.

Un code de calcul des écoulements secondaires a été développé à l'Ecole Centrale de Lyon et à la SNECMA <1> pour le cas des compresseurs monoetages. Une adaption du code aux compresseurs multi-étages a été realisee <2>. L'objet de ce présent travail concerne l'application de ce code à des écoulements de turbine afin d'en déterminer la validité.

Dans un premier temps les caractéristiques de la méthode seront présentées en insistant sur les hypotheses simplificatrices entrant dans la modélisation. Celles-ci pourront être discutées au vu des resultats obtenus pour des écoulements de turbine. Le comportement du code sera en effet analysé sur des configurations industrielles de grille d'aubes et d'étage de turbine sur lesquelles des résultats expérimentaux sont disponibles.

Cette analyse doit permettre de comprendre le domaine d'application et les limitations de ce type d'approche. Les perspectives plus générales quant au calcul des phénomènes secondaires seront également abordées sous l'éclairage de l'expérience acquise à la SNECMA.

1 - METHODE DE CALCUL

La méthode de calcul utilisée est décrite en détail par Leboeuf-Brochet <1>. Nous reprendrons ici les caracteristiques principales de la méthode en insistant sur les points particulièrement importants dans le cadre d'une application en grille d'aubes de turbine.

1.1. Une approche de type couche-limite

L'ecoulement est represente par un modèle à trois zones . deux zones visqueuses au voisinage des parois du moyeu et du carter, séparées par une zone saine où l'écoulement méridien classique est peu perturbé (voir figure 1). Notons toutefois que le calcul de la zone saine tient compte des effets visqueux liés à la présence des profils.

Les écoulements secondaires présents dans les deux zones visqueuses sont appréhendés par une correction visqueuse apportee à l'écoulement sain. Le niveau d'approximation du calcul des écoulements secondaires est comparable à celui du calcul méridien . la méthode détermine ainsi la valeur moyennée en azimut des effets secondaires dans tout le plan méridien.

Les couches visqueuses sur le moyeu et le carter sont traitées séparément, l'écoulement extérieur de reference etant la valeur a la paroi de l'écoulement sain. L'écoulement complet est reconstitué en fin de calcul par superposition. Un couplage classique écoulement méridien - couches visqueuses est réalisé par des injections de débit pariétales au moyeu et au carter, représentant le blocage (voir fig. 2).

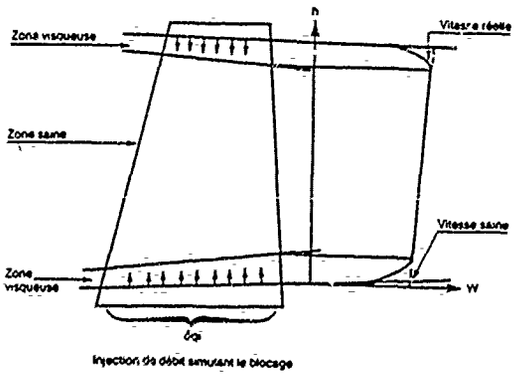


Fig. 1 Modélisation de l'écoulement méridien

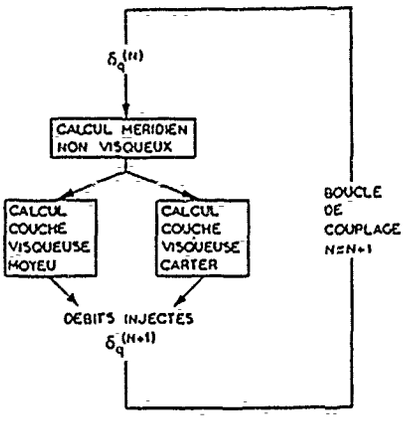


Fig. 2 Couplage calcul méridien-écoulement secondaire

1.2. CALCUL DES COUCHES VISQUEUSES

La corrélation visqueuse relative à chaque paroi est obtenue en résolvant un système d'équations dérivées des équations de Navier-Stokes compressibles stationnaires et parabolisées dans la direction de l'écoulement. La connaissance de l'écoulement sain à la paroi définit une direction privilégiée de l'écoulement secondaire. Cette propriété est utilisée pour décomposer ce dernier en un écoulement longitudinal suivant cette direction et un écoulement transversal directement lié à la vorticité secondaire (tourbillon de passage).

On utilise ainsi un système de coordonnées méridiennes (m, b, θ) et un système de coordonnées intrinsèques (s, b, n) lié à chaque aubage (fig. 3). Un traitement particulier est appliqué dans les plans de calcul situés entre deux grilles et où on passe d'un repère fixe à un repère mobile ou inversement.

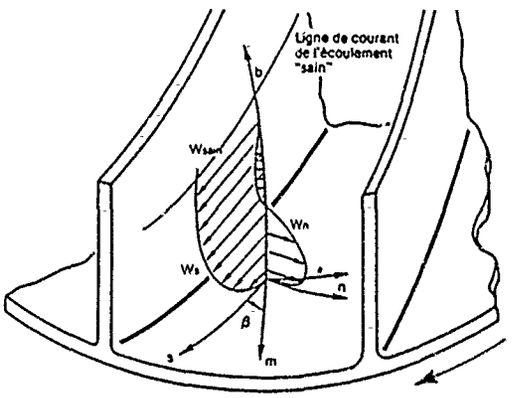


Fig. 3 Systèmes orthogonaux de coordonnées

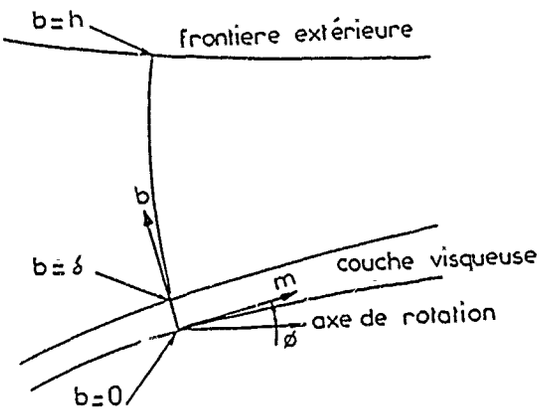


Fig. 4 Intégration des équations suivant l'envergure

La méthode est enfin basée sur une approche intégrale de la couche limite. Les équations décrivant l'évolution de la couche limite sont :

- l'équation intégrale de continuité moyennée en azimut :

$$(1)\qquad \frac{\partial}{\partial u_m}\int_0^{\delta} Br\,\rho W_m\,db = (Br\,\rho W_m)_\delta \left(\frac{\partial \delta}{\partial u_m} - h_m \frac{W_b}{W_m}\right)_\delta$$

Le second membre de cette équation représente l'entraînement du fluide dans la couche limite, modélisé par une loi de Head <3>.

- les deux composantes selon m et θ de l'équation intégrale de quantité de mouvement, moyennée en azimut, écrites sous forme déficitaire par rapport à l'écoulement sain, et intégrées jusqu'à la frontière extérieure (voir fig. 4).

$$(2)\qquad \frac{\partial}{\partial u_m}\int_0^h Br\left(\rho \hat{W}_m^2 - \rho V_m^2\right)db - \left[Br\,h_m\left(\rho \hat{V}_b \hat{W}_m + \tau_{bm}\right)\right]_{b=0} - \int_0^h Bh_m \sin\phi\left(\rho \hat{V}_\theta^2 - \rho V_\theta^2 + \tau_{\theta\theta}\right)db = \Delta Q_{1m} + \Delta Q_{3m}$$

$$(3)\qquad \frac{\partial}{\partial u_m}\int_0^h Br\left(\rho \hat{V}_\theta \hat{W}_m - \rho V_\theta V_m\right)db - \left[Br\,h_m\left(\rho \hat{V}_\theta \hat{W}_b + \tau_{b\theta}\right)\right]_{b=0} + \int_0^h Bh_m \cos\phi\left(\rho \hat{V}_\theta \hat{W}_b - \rho V_\theta W_b + \tau_{\theta b}\right)db$$
$$+ \int_0^h Bh_m \sin\phi\left(\rho \hat{V}_\theta \hat{W}_m - \rho V_\theta W_m + \tau_{\theta m}\right)db = \Delta Q_{1\theta}$$

Le vecteur D_i représente l'effet visqueux sur la force d'aubage. Dans une zone libre d'aubage, ce terme est nul et (2) et (3) sont résolues directement. En zone aubée il est nécessaire de se donner la direction du vecteur D_i.

$$(4)\qquad \Delta Q_{1m} + (1-\varepsilon)\tan\beta'\ \Delta Q_{1\theta} = 0$$

où le coefficient ε représente un écart de D_i par rapport à la perpendiculaire au profil.

Les trois équations de base (1), (2), (3) ne permettent pas une résolution du champ aérodynamique complet : il est nécessaire de déterminer les trois composantes de la valeur moyennée en azimut du vecteur vitesse. L'approche intégrale retenue nous conduit à décrire la composante longitudinale W_s par un profil analytique. Le choix s'est porté sur un profil de Kühn et Nielsen <4>.

Une description analytique des profils de vitesse W_s et W_b semble cependant plus difficile. La composante tranversale W_s, directement liée à l'existence de la vorticité secondaire (tourbillon de passage) est alors obtenue par une méthode différentielle basée sur la résolution d'une équation de transport de la vorticité secondaire longitudinale Ω_s :

$$(5)\qquad \frac{1}{Br\,\rho\, h_b h_m}\frac{\partial}{\partial u_m}\left(Br\,h_b\,\rho W_m \Omega_s\right) - (\Omega_s + 2\omega_s)\left[\frac{\cos\hat{\beta}}{Br\,h_m}\frac{\partial B\rho V_s}{\partial u_m} + k_{sn}W_n - \frac{W_n}{Bh_m}\sin\hat{\beta}\frac{\partial B\rho}{\partial u_m}\right]$$
$$+ (\Omega_b + 2\omega_b)\left(V_s k_{sb} - \frac{1}{Bh_b}\frac{\partial BW_s}{\partial u_b}\right) + (\Omega_n + 2\omega_n)\left(V_s k_{sn} + \frac{\sin\hat{\beta}}{Bh_m}\frac{\partial BW_s}{\partial u_m}\right) = \frac{\nu_t}{\theta}\frac{\partial^2 B\Omega_s}{\partial b^2}$$

Il est nécessaire de résoudre dans le plan transversal une équation de Laplace :

(6) $$\Delta\psi = -\Omega_\theta$$

la fonction de courant vérifiant :

(7) $$W_n = -\frac{\partial\psi}{\partial b}$$

Si la composante W_θ représente directement l'effet de la vorticité secondaire, il n'en est pas ainsi pour la composante W_θ (moyennée en azimut). Seules les fluctuations azimutales de W_θ pourraient être déduites de la connaissance de la vorticité. Ainsi cette composante est quant à elle obtenue en résolvant une forme appropriée de l'équation de continuité, traduisant l'épaississement de la couche limite :

(8) $$\rho_{ref} W_b(b) - \rho_{ref} W_b(0) = \frac{\partial}{\partial m}\int_0^b \rho_{ref} W_m \, db$$

Le terme W_θ (O) étant nul sauf dans le cas de prélèvement ou d'injection pariétale de débit pour la ventilation interne du moteur.

Le calcul de la vitesse est complété par ceux de la pression statique et de la température totale. L'écart de pression statique avec l'écoulement sain est calculé en résolvant la composante selon b de l'équation de quantité de mouvement. La fluctuation azimutale de W_θ, d'un ordre de grandeur nettement supérieur à sa valeur moyenne n'est cependant pas prise en compte. La température totale T, qui intervient dans le calcul de la masse volumique est obtenue en résolvant une forme non visqueuse de l'équation de l'énergie; en particulier, les transferts thermiques pariétaux ne sont pas modélisés par la méthode.

La parabolisation des équations réduit les temps de calcul nécessaires, mais peut conduire à des instabilités numériques. Les effets elliptiques négligés, liés surtout au champ de pression statique sont restitués de façon approchée en résolvant une équation supplémentaire relative à l'écoulement sain, en même temps que les équations pour l'écoulement visqueux. En pratique cette équation se présente comme une équation en $\widehat{W}_\theta$ et calcule les effets linéarisés de blocage et de courbure sur l'écoulement sain; ceux-ci sont provoqués par les variations entre deux itérations de couplage du déficit de débit représentant la couche limite. L'effet complet est bien entendu restitué par le couplage au calcul méridien.

Après discrétisation, cette équation supplémentaire s'écrit sous une forme vectorielle:

(9) $$\left[\widehat{W}_{m_i}\right] = A\left[\delta q_j\right] + B$$

de nature elliptique et assure ainsi la stabilité du calcul.

La description de la méthode de résolution adoptée pour cet ensemble d'équations (1) à (9) n'apporterait pas d'éclairage sur le travail réalisé, le comportement numérique étant satisfaisant dans l'ensemble des cas présentés. Le lecteur intéressé pourra se reporter à une description donnée dans <1> et dans <2>.

2 - TESTS DE LA METHODE AXISYMETRIQUE

2.1. Grille d'aubes de distributeur de turbine basse pression

La première application présentée ici est le calcul des écoulements secondaires pour une grille d'aubes de distributeur de turbine basse pression. Cette géométrie a pu être testée en soufflerie de grille annulaire, et des résultats expérimentaux disponibles permettent une comparaison des résultats de calcul aux valeurs mesurées.

La géométrie de l'aube, fortement tridimensionnelle est présentée en fig.5. L'aubage est subsonique : le nombre de Mach à l'amont vaut 0.5, le nombre de Mach à l'aval vaut 0.65. La déviation de l'aubage est relativement forte pour un distributeur ($\Delta\beta = 85°$) ce qui correspond à une application réaliste pour le test de la méthode en grille d'aubes de turbine.

Les mesures disponibles sont les suivantes : conditions génératrices de la soufflerie, profils radiaux de pression totale et de l'angle de l'écoulement à l'entrée et à la sortie de la grille d'aubes, mesures de pression statique aux parois du moyeu et du carter d'une part, sur la section du profil à mi-hauteur de veine d'autre part (non utiles dans le cadre de ce travail). Une attention particulière aux mesures proches des parois moyeu et carter à été portée, afin de déterminer l'effet des écoulements secondaires sur les performances de la grille.

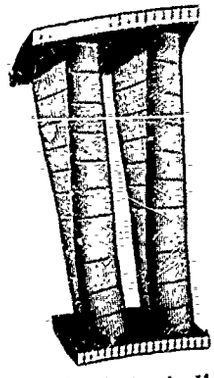


Fig. 5 Géométrie de l'aubage
Vue arrière

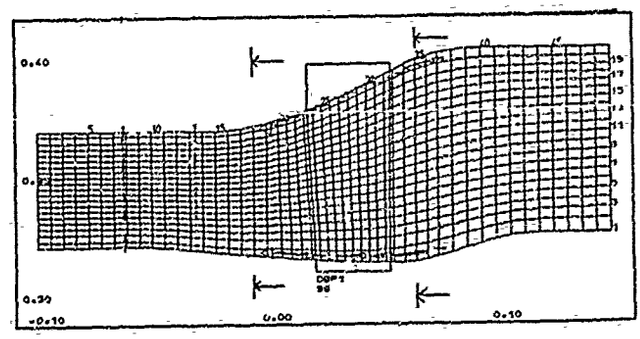


Fig. 6 Veine méridienne et plans de mesures

Un calcul méridien, couplé au calcul des écoulements secondaires, a été réalisé. La géométrie de la veine, le maillage de calcul et les injections modélisant le couplage sont représentés en fig.6. Le maillage "vertical" est commun aux deux codes, mais le code d'écoulements secondaires est évidemment plus resserré au voisinage des parois, une vingtaine de points de calcul se trouvant dans la zone visqueuse.

Le comportement numérique de la méthode couplée a été satisfaisant. Cinq itérations de couplage seulement sont nécessaires, grâce à l'équation d'interaction fluide visqueux - écoulement sain présente dans la méthode de calcul des écoulements secondaires.

Les mesures de pression totale et d'angle à l'amont (fig.7 et 8) ont servi à l'initialisation du calcul d'écoulement secondaire dans le premier plan (plan 18 du maillage). Les résultats dans le plan 35 du maillage, correspondant au plan de mesures à l'aval de l'aube, sont présentés en fig.9 et 10.

On peut constater sur ces résultats une adéquation correcte de l'angle de sortie calculé à l'angle de sortie mesuré (voir fig.10). Au moyeu la concordance est très bonne, quelques écarts subsistant au carter. L'angle de sortie dépend bien sûr du rapport de la vitesse transversale W_t à la vitesse longitudinale W_z. Ici, compte-tenu des écarts entre l'écoulement secondaire et l'écoulement sain ne dépassant pas quelques degrès, le bon accord de l'angle de sortie dénote essentiellement un calcul satisfaisant de la vitesse transversale W_t, par le biais de la vorticité secondaire Ω_t.

Les résultats sont moins bons pour ce qui concerne la pression totale. L'évolution radiale de la pression totale, déduite de l'évolution radiale de la vitesse W et de la pression statique, présente un écart important entre valeurs calculées et valeurs mesurées, dans les zones visqueuses proches du moyeu et du carter (voir fig.9). Ce résultat provient pour l'essentiel d'une mauvaise adéquation du profil de vitesse analytique pour décrire ces couches visqueuses.

Enfin des écarts de pression statique à l'aval de la grille d'aube démontrent un calcul du blocage insuffisant (voir fig.11 et 12). L'évolution de la couche limite, décrite par une méthode intégrale, n'est pas correctement prédite. Par le biais du couplage au calcul méridien par injections pariétales, les corrections de débit sont erronées et conduisent à une valeur trop faible de la pression statique.

2.2. Etage de turbine basse pression

La deuxième application du code a été réalisée pour un calcul des écoulements secondaires dans le premier étage d'une turbine basse pression. Cette géométrie a été testée en banc de turbine et les résultats disponibles permettent une comparaison des résultats de calcul aux valeurs mesurées.

La géométrie du distributeur est plus simple que dans le test précédent, mais l'écoulement est de même type : subsonique, le nombre de Mach valant environ 0.5 à l'amont, 0.60 à l'aval; la déviation est du même ordre : $\Delta\beta = 90°$. Pour ce qui concerne la roue mobile, l'écoulement relatif est également subsonique, le nombre de Mach relatif valant 0.35 à l'amont, 0.66 à l'aval. La déviation, quant à elle, vaut $\Delta\beta \approx 80°$. Cet étage de turbine est représentatif du premier étage d'une turbine basse pression de moteur civil.

Les mesures disponibles pour la validation de la méthode sont moins nombreuses et moins fines que dans le cas précédent. La veine d'essais est équipée de trois plans de mesure, à l'amont du distributeur, entre les deux grilles et à l'aval de la roue mobile, notés 480, 490, et 49A respectivement.

Les conditions génératrices de l'écoulement sont connues, ainsi que les profils radiaux de pression totale, angle et température totale de l'écoulement aux plans 480, 490 et 49A. Derrière les aubages des mesures en bossage (déplacement radial de la sonde, azimut fixe) et en lumière (intégration azimutale des sillages sur un pas à diverses profondeurs d'immersion de la sonde). Les mesures proches des parois n'ont cependant pas été effectuées avec toute la précision souhaitable ici. Enfin, notons que les mesures de température totale n'ont pas été exploitées dans ce travail sauf pour s'assurer de la cohérence du calcul méridien par rapport au point de fonctionnement de la turbine.

Comme précédemment le calcul méridien, couplé au calcul des écoulements secondaires, a été réalisé, avec autant de cohérence qu'il est possible pour reconstituer le point de fonctionnement de la turbine. La veine et le maillage de calcul sont représentés en fig.13. Les plans de mesure 480, 490, 49A correspondent respectivement aux plans de maillage 17, 30, et 37.

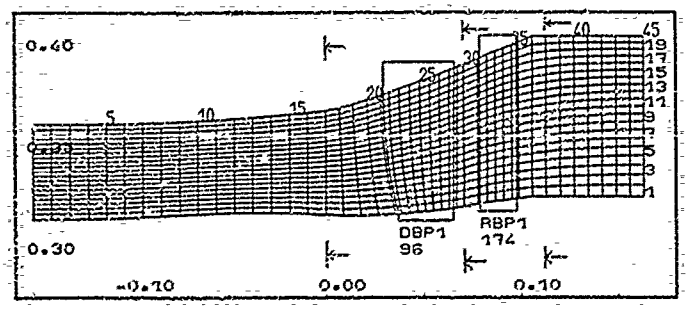


Fig. 13 Veine méridienne et plans de mesure

Le comportement numérique de la méthode couplée a été satisfaisant. Sept itérations de couplage ont été réalisées.

Les mesures de pression totale et d'angle au plan 480 ont servi à l'initialisation du calcul des écoulements secondaires dans son premier plan. Ces résultats sont présentés fig.14 et 15.

Les résultats au plan de mesure 490, à l'aval du distributeur, sont présentés fig.16 et 17 pour la pression totale et l'angle de l'écoulement. On note comme précédemment un calcul réaliste de l'angle de sortie, associé à une évaluation des pertes moins précise. Dans ce cas cependant, il faut noter des écarts de pression totale dans la zone saine, dûs à des écarts importants des valeurs mesurées entre les plans 480 et 490, non pris en compte par le calcul méridien. De plus la conclusion sur l'angle de sortie est plus difficile compte tenu de l'absence de mesures fiables au voisinage des parois.

Les résultats au plan 49A, à l'aval de la roue mobile sont présentés fig.18 et 19, pour la pression totale et l'angle de sortie. Là encore les conclusions sont rendues difficiles par l'interprétation des mesures. Pour ce qui concerne l'angle, on notera que l'écoulement sain recoupe plutôt les valeurs mesurées en bossage. Par contre l'allure de l'écoulement à la paroi, au moyeu et au carter, s'accorde plutôt aux mesures déduites de l'intégration de sillages. Pour ce qui concerne la pression totale, l'accord entre le calcul et les mesures est très satisfaisant, notamment pour les sillages intégrés. Bien que mal calculée au plan 490, la pression totale semble bien évaluée au plan 49A, ceci étant en fait en grande partie dû à l'ajustement du calcul méridien au point de fonctionnement de la turbine.

Enfin un résultat intéressant concerne l'évolution du blocage, représentée par l'évolution de la pression statique aux plans 480, 490, 49A. (voir fig.20, 21, 22). On note un désaccord assez important au plan intermédiaire, montrant une sous-estimation du blocage produit par les couches limites à la traversée du distributeur. Cependant au plan 49A l'accord calcul-expérience est à nouveau satisfaisant, laissant présager une estimation correcte du blocage à la traversée de l'étage. Cependant l'incertitude sur l'accord du calcul concernant l'angle de l'écoulement au plan 49A entache ce dernier résultat d'une marge d'incertitude importante.

Ce dernier test montre l'obtention de résultats réalistes dans l'ensemble mais des essais en turbine plus précis seraient nécessaires pour conclure; ceci d'autant plus que des écarts locaux importants ont été démontrés, notamment pour les pertes et le blocage, tant pour un distributeur isolé que pour un étage complet.

3 - ANALYSE DES RESULTATS. PERSPECTIVES POUR LE CALCUL DES PHENOMENES SECONDAIRES EN TURBINE

3.1. Domaine d'application de la méthode

Les résultats obtenus en grille d'aubes de distributeur d'une part, sur le premier étage d'une turbine basse pression d'autre part, permettent de délimiter sur un certain nombre de points le domaine d'application de la méthode axisymétrique.

Il faut noter tout d'abord que la discussion ne porte que sur les turbines subsoniques, la méthode n'ayant pas été testée sur des aubages transsoniques; aucune prise en compte des chocs n'est d'ailleurs incluse dans la méthode.

Le premier point démontré, largement positif, est une bonne adéquation de l'équation de transport de la vorticité secondaire pour le calcul du champ de vitesse transversale W_t. Ce résultat semble pouvoir être expliqué par le caractère essentiellement "potentiel" du mécanisme de formation du tourbillon de passage. Certains auteurs obtiennent une estimation très correcte des écoulements secondaires, au moins pour le champ des vitesses, à l'aide de méthodes de calcul tridimensionnelles en fluide parfait : les travaux de Boletis et Arts <5> pour une grille d'aubes de turbine basse vitesse, et ceux de Bassi, Osnaghi, Perdichizzi, Savini <6> corroborent largement cette hypothèse.

En revanche, le calcul de la couche limite pariétale, au moyeu et au carter, se heurte à des obstacles plus sérieux. Il ne semble pas que l'hypothèse de couche limite retenue soit suffisament pertinente, ni la méthode intégrale suffisament précise, pour un calcul pleinement satisfaisant du blocage et des pertes secondaires.

Ceci peut être aisément confirmé par une revue expérimentale de la nature des phénomènes secondaires. Gregory-Smith et Graves <7> ont réalisé des mesures tridimensionnelles détaillées des phénomènes secondaires en turbine. On peut aisément vérifier que le champ de pression statique est fortement influencé par la présence du tourbillon de passage (voir fig. 23). D'autre part, la production des pertes est liée à des phénomènes tridimensionnels localisés : présence de lignes de décollement et de recollement tridimensionnelles sur la plate-forme et sur l'extrados (voir fig. 24), convection de fluide de basse énergie au sein du tourbillon de passage, interaction de celui-ci avec la couche limite à l'extrados (voir fig. 25).

Cependant, le manque de précision au niveau des pertes et du blocage ne condamne pas l'emploi de la méthode pour le calcul de conception des turbines. On peut noter en effet que la méthode donne des résultats intéressants pour ce qui concerne l'angle de sortie; par ailleurs, l'imprécision du calcul du blocage ne pénalise pas le calcul au niveau du plan de sortie de l'étage de turbine; enfin, l'estimation des pertes secondaires peut être obtenue par les corrélations utilisées largement par les constructeurs.

En conclusion, la combinaison calcul méridien - méthode axisymétrique - corrélations expérimentales semble prometteuse pour la conception des turbines. Le problème de l'ajustement de la triangulation aux effets visqueux tridimensionnels est notamment abordé de façon satisfaisante; l'adaptation locale en pied et en tête des grilles d'aubes successives est possible.

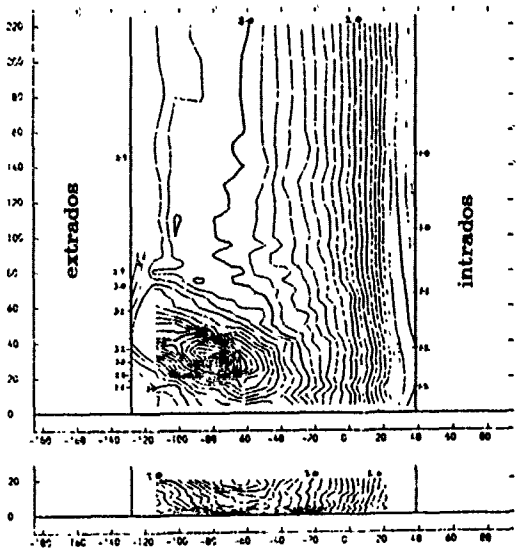


Fig. 23 Champ de pression statique dans un canal interaube de turbine

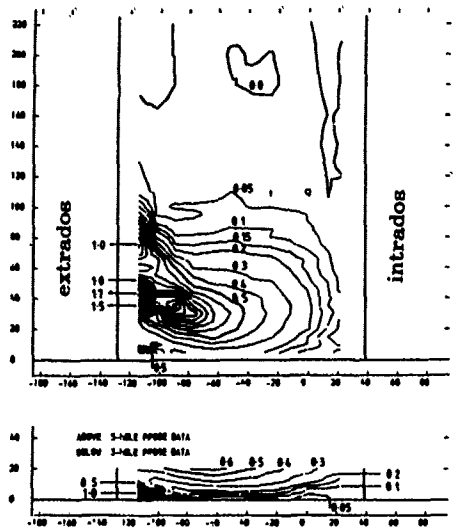
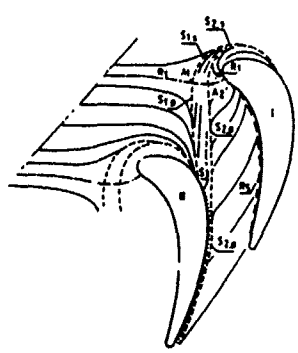


Fig. 25 Champ de pression totale dans un canal interaube de turbine

Ces résultats d'ensemble, que l'on peut juger positifs compte tenu de la simplicité de la formulation (quelques secondes de calcul IBM 3090 pour un étage de turbine) devront bien entendu être confirmés sur des tests incluant des turbines complètes de quatre ou cinq étages.

Une amélioration de la méthode reste sans doute possible par une meilleure modélisation des couches visqueuses, de la "couche limite" longitudinale notamment. Cependant ceci ne sera réalisable qu'au prix d'une lourdeur accrue. Enfin il n'est pas assuré qu'une méthode de type axisymétrique soit capable d'estimer correctement la production des pertes secondaires, phénomène essentiellement tridimensionnel.



S : lignes de décollement

R : lignes de recollement

Fig. 24 Lignes de courant à la paroi d'une aube de turbine

3.2. Calcul des écoulements visqueux tridimensionnels en grille d'aubes de turbine

Parallèlement aux travaux précédents, portant sur des méthodes légères, adaptées à la conception des turbines multi-étages, le développement de méthodes de calcul des écoulements visqueux tridimensionnels est une priorité.

La prévision de ces écoulements est en effet essentielle pour l'analyse des performances d'un aubage :

- prévision fine des écoulements secondaires, incluant la description du tourbillon en fer-à-cheval, des lignes de décollement associées, du tourbillon de passage, des lignes de courant au voisinage des plates-formes et des profils.

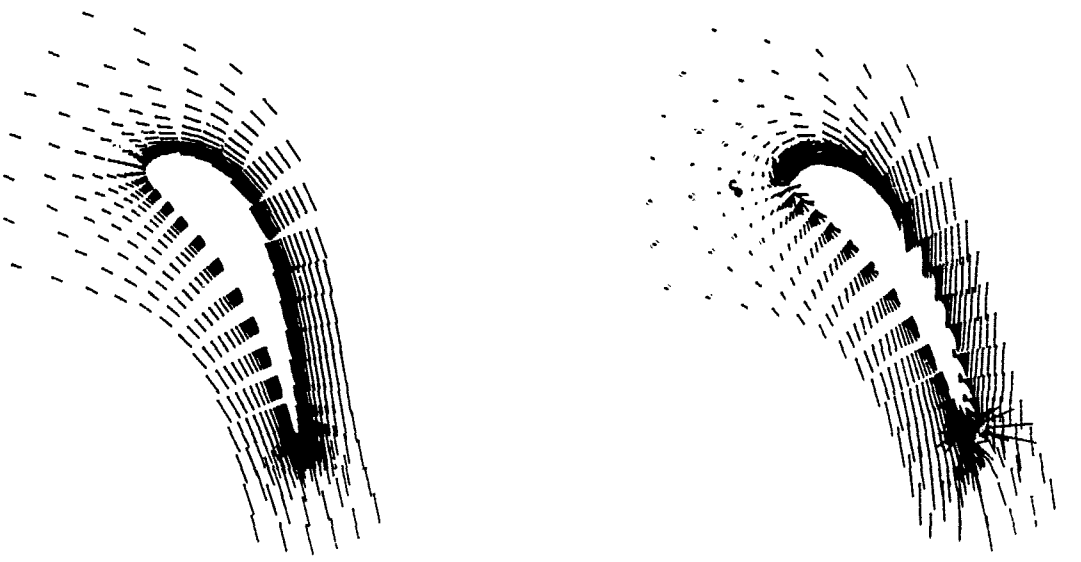
- prévision fine des pertes de l'aubage incluant les pertes de profil et pertes secondaires; la connaissance de la localisation des pertes doit permettre de mieux comprendre et mieux contrôler leur production. L'optimisation aérodynamique tridimensionnelle des aubages dépend de ces deux points.

- prévision fine des effets thermiques tridimensionnels : redistribution du profil radial de température à l'entrée de la grille d'aubes, évolution dans le canal interaube d'un pic de température derrière un injecteur, transferts thermiques pariétaux sur les aubes et les plates-formes.

Compte tenu de cet objectif multiple, la SNECMA a engagé un effort important pour la résolution des équations de Navier-Stokes compressibles moyennées stationnaires en grille d'aubes de turbine. Cet effort, complémentaire du travail présenté au paragraphe 2, aboutit dès aujourd'hui à des applications industrielles.

Le développement d'un code Navier-Stokes parabolisé tridimensionnel a été entrepris à l'Ecole Centrale de Lyon, pour le calcul des écoulements secondaires en grille d'aubes de turbine ventilées. Une première application est en cours sur une grille d'aubes de distributeur basse vitesse <8>.
Le développement d'un code Navier-Stokes tridimensionnel à l'ONERA, soutenu par la SNECMA, permet aujourd'hui une application en grille d'aubes de distributeur <9>. Les résultats montrent un calcul correct de l'écoulement tridimensionnel y compris au voisinage de la plate-forme (voir fig. 26).

Ces applications, qui doivent aboutir aux objectifs cités plus haut, présagent pour la SNECMA la possibilité d'appliquer une panoplie de méthodes adaptées au calcul des écoulements secondaires à divers stades d'un projet: méthodes légères, axisymétriques, pour les calculs de conception multi-étages, méthodes tridimensionnelles, bien plus coûteuses, pour l'analyse des performances d'un aubage.



Vitesses à mi-hauteur **Vitesses au voisinage de la paroi**

Fig. 26 Calcul de l'écoulement tridimensionnel visqueux dans une turbine

CONCLUSION

La prévision des écoulements secondaires est un objectif majeur pour la conception des aubes de turbine et pour l'analyse de leurs performances.

Une méthode de calcul axisymétrique des écoulements secondaires, initialement développée à l'ECL et à la SNECMA pour les compresseurs multi-étages, a été appliquée sur deux configurations de turbine : une grille d'aubes de distributeur de turbine basse pression et un premier étage de turbine basse pression.

Des comparaisons calcul/expérience ont permis de mettre en évidence les qualités ainsi que les limitations de la méthode. Le calcul correct de la vorticité secondaire (tourbillon de passage) permet d'employer avec succès la méthode pour la correction locale de la triangulation en pied et tête d'aube, ce qui rend possible une meilleure adaptation des grilles d'aubes successives. Le calcul de la couche limite longitudinale, au moyeu et au carter est plus difficile et la méthode ne rend pas compte avec précision des pertes secondaires et de l'évolution du blocage.

Cependant l'emploi de cette méthode, couplée au calcul méridien classique d'une part, aux corrélations de pertes secondaires d'autre part répond à l'objectif de prédiction globale des phénomènes secondaires au stade de la conception d'un projet de turbine.

Des méthodes plus lourdes sont bien entendu nécessaires pour l'analyse des performances d'un aubage. La connaissance de l'écoulement visqueux tridimensionnel est désormais indispensable pour l'optimisation aérodynamique et thermique d'un aubage de turbine. La SNECMA s'est associée à des programmes de recherche, à l'ECL et à l'ONERA, pour la résolution des équations de Navier-Stokes tridimensionnelles. Des applications industrielles de ces codes sont aujourd'hui disponibles.

Ainsi l'objectif de prévision des écoulements secondaires peut être atteint grâce à une panoplie de méthodes complémentaires : les méthodes légères correctives d'un calcul méridien, sont indispensables lors de l'établissement de la triangulation d'un projet de turbine; les méthodes tridimensionnelles lourdes et coûteuses, permettent une analyse fine de l'écoulement visqueux.

REMERCIEMENTS

Cette étude est financée par la SNECMA. Les auteurs tiennent à remercier A. RIBERE pour avoir réalisé une grande partie des calculs présentés dans ce travail; le Docteur F. LEBOEUF, pour ses encouragements et suggestions precieuses au cours de cette étude; M. CAMBIER et Mme ESCANDE, pour les documents relatifs aux calculs qu'ils ont réalisés; la hiérarchie de la Direction des Recherches et Etudes avancées, pour son soutien.

REFERENCES

(1) : F. LEBOEUF, J. BROCHET : "The Use of a Secondary Flow Computation in the Compressor Design Process", AIAA/SAE/ASME/ASEE 21st Conference of Monterey California, 1985.

(2) : F. FALCHETTI, J. BROCHET : "Calcul des écoulements secondaires dans un compresseur multi-étages", AGARD CP 421, 1987.

(3) : M.R. HEAD : "Entrainment Approach", VKI Short Course on "Turbulent Boundary Layers", March 1968.

(4) : C.D. KUHN, J.N. NIELSEN : "Prediction of Turbulent Separated Boundary Layers", AIAA, 6th Fluid and Plasma Dynamic Conference, July 1973.

(5) : E. BOLETIS : "Effects of Tip Endwall Contouring on the Three-dimensional Flow Field in an Annular Turbine Nozzle Guide Vane : Part I - Experimental Investigation", ASME paper n°85-GT-71.

(5) bis : T. ARTS : "Effects of Tip Endwall Contouring on the Three-dimensional Flow Field in an Annular Turbine Nozzle Guide Vane : Part II - Numerical Investigation", ASME paper n°85-GT-108.

(6) : F. BASSI, C. OSNAGHI, A. PERDICHIZZI, M. SAVINI : "Secondary Flows in a Transonic Cascade : Comparison between Experimental and Numerical Results", Journal of Fluids Engineering, à paraitre.

(7) : D.G. GREGORY-SMITH, C.P. GRAVES : "Secondary Flows and Losses in a Turbine Cascade", AGARD CP 351, 1983.

(8) : P. FERRAND, F. LEBOEUF, F. PAUMEL, E. PARKINSON : "Calculs Parabolisés d Ecoulements Turbulents Tridimensionnels dans une Turbine", AGARD 74 B Specialist Meeting, paper B 4; à paraitre.

(9) : L. CAMBIER, B. ESCANDE : "Calcul de l'Ecoulement Tridimensionnel Turbulent dans un Aubage Rectiligne de Turbine", AGARD 74 B Specialist Meeting, paper B 13; à paraitre.

TESTS SUR DISTRIBUTEUR BP

□□□□□□□ MESURES

——— CALCULS

– – – – – ECOULEMENT SAIN

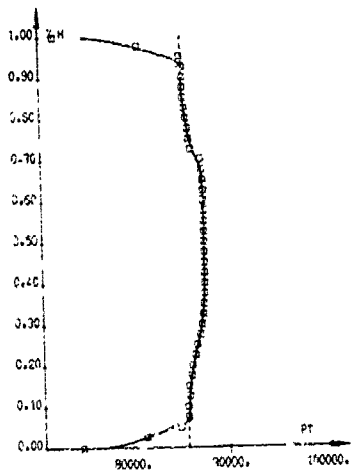


Fig. 7 plan amont
PRESSION TOTALE

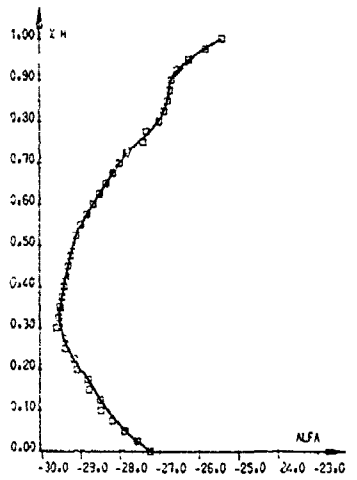


Fig. 8 plan amont
ANGLE DE L'ECOULEMENT

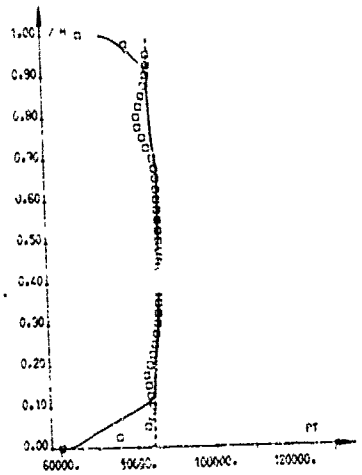


Fig. 9 plan aval
PRESSION TOTALE

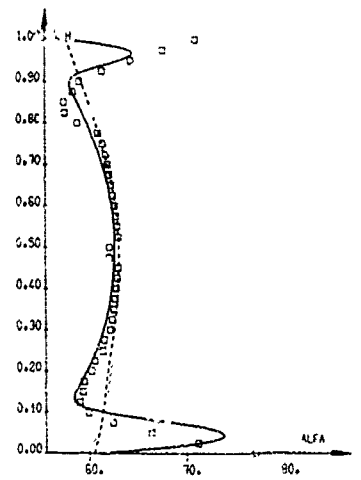


Fig. 10 plan aval
ANGLE DE L'ECOULEMENT

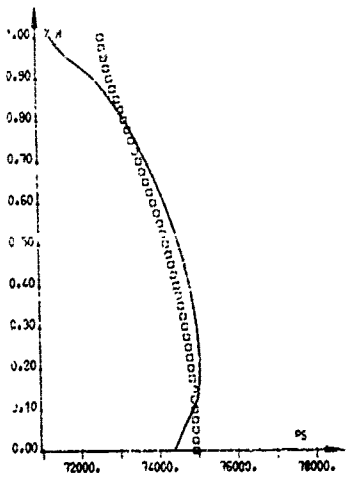


Fig. 11 plan amont
PRESSION STATIQUE

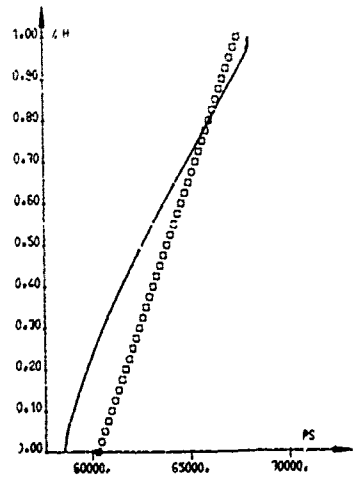


Fig. 12 plan aval
PRESSION STATIQUE

TESTS SUR UN ETAGE

———— MESURES (A : SILLAGES, B : BOSSAGES)

□□□□□□□ CALCULS

- - - - - - - ECOULEMENT SAIN

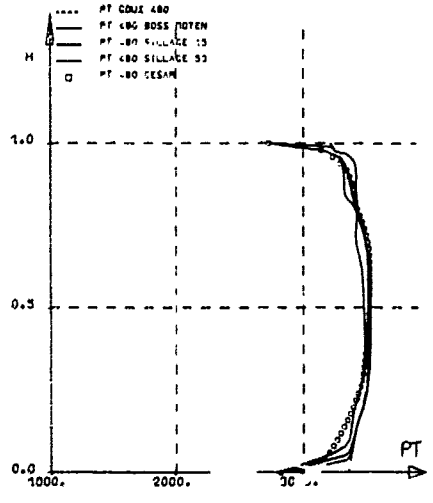


Fig. 14 plan 480
PRESSION TOTALE

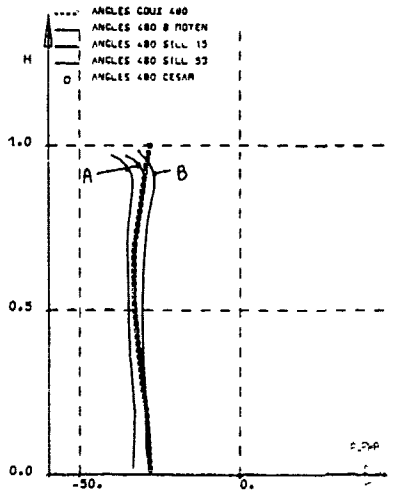


Fig. 15 plan 480
ANGLE DE L'ECOULEMENT

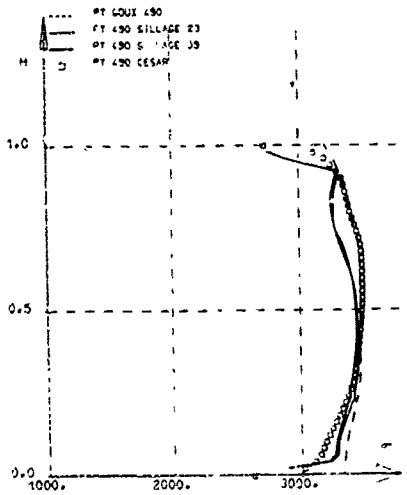


Fig. 16 plan 490
PRESSION TOTALE

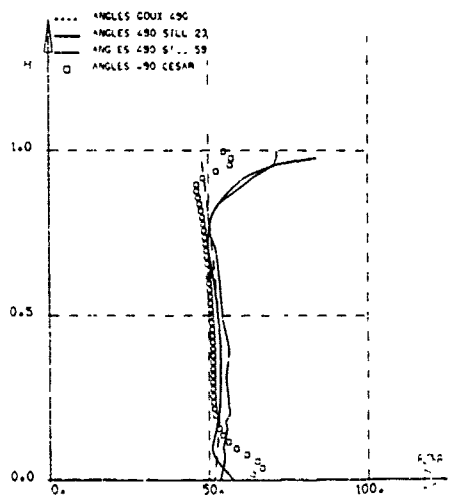


Fig. 17 plan 490
ANGLE DE L'ECOULEMENT

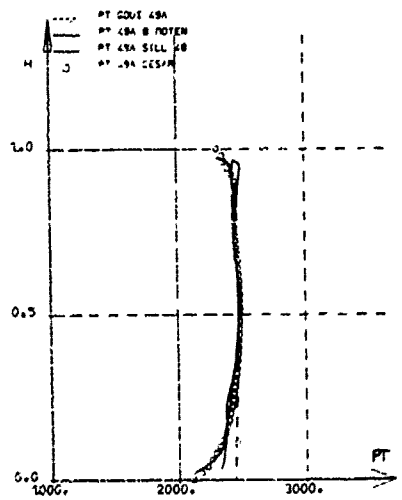


Fig. 18 plan 49 A
PRESSION TOTALE

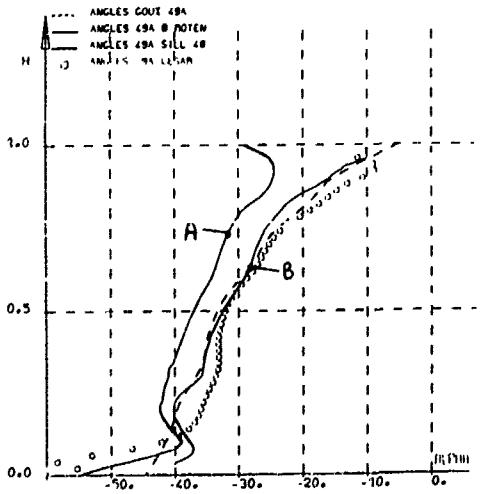


Fig. 19 plan 49 A
ANGLE DE L'ECOULEMENT

TESTS SUR UN ETAGE
EVOLUTION DU BLOCAGE

□□□□□□□ **CALCULS**

——————— **MESURES**

- - - - - - - **ECOULEMENT SAIN**

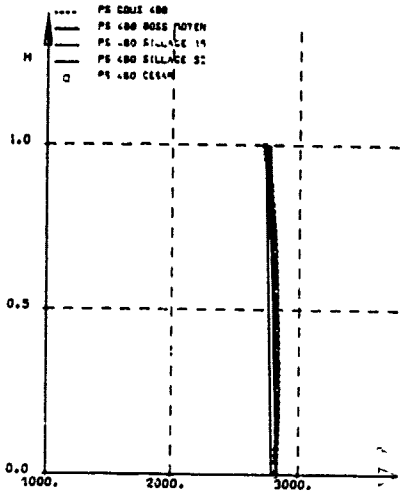


Fig. 20 plan 480
PRESSION STATIQUE

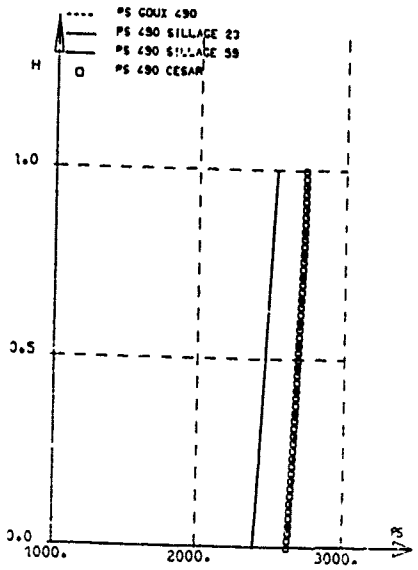


Fig. 21 plan 490
PRESSION STATIQUE

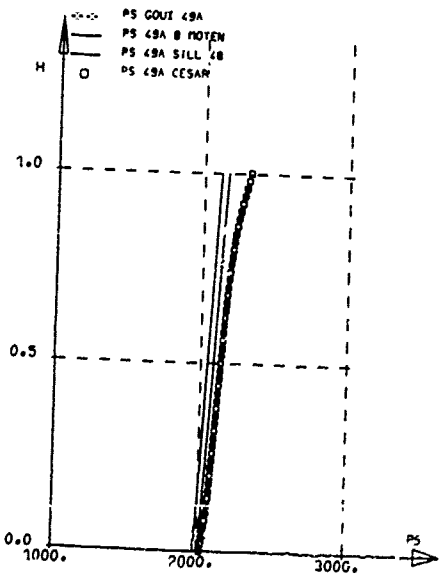


Fig. 22 plan 49 A
PRESSION STATIQUE

GENERATION AND DECAY OF SECONDARY FLOWS AND THEIR IMPACT ON AERODYNAMIC PERFORMANCE OF MODERN TURBOCHINERY COMPONENTS

by

C.Hah
GE Corporate Research and Development
P.O.Box 8
Schenectady, New York 12301
United States

Summary

A three-dimensional viscous flow code is used to distinguish aerodynamic performance of different designs of turbomachinery components. Two designs of a high-pressure-ratio turbine nozzle and a centrifugal compressor impeller are numerically studied to investigate detailed flow development and overall aerodynamic performance. The present study indicates that the current viscous code can differentiate aerodynamic performance of various designs of turbomachinery components.

Introduction

Computational fluid dynamics are frequently used for the analysis and design of turbomachinery components. Various methods, such as streamline curvature, potential flow, Euler, and Navier-Stokes, are an integral part of computer-aided engineering systems. As computer architecture becomes more powerful, increasingly complex Navier-Stokes methods are used to get more realistic pictures of the flow. Although Navier-Stokes methods are more expensive than Euler methods or Euler-boundary layer methods, they provide invaluable information when the design is pushed beyond the current envelope of correlations.

Various previous numerical studies based on Navier-Stokes solutions [1-4] have shown great promise for the prediction and evaluation of aerodynamic performance of newly designed components. One of the purposes of doing viscous flow computation is to estimate aerodynamic performance parameters of a particular component. To predict aerodynamic performance correctly, various important viscous flow phenomena (boundary layer development, secondary flow generation, flow separation, shock-boundary layer interaction, etc.) must be adequately represented in the solution. Because the currently available physical models (flow transition, turbulent shear stress, turbulent heat flux, etc.) are rather restricted, the numerically predicted value of aerodynamic performance parameters, especially aerodynamic losses, are not always exactly the same as the experimentally measured values. However, it is believed that the differences in aerodynamic performance of different designs can be predicted numerically using Navier-Stokes solutions.

In this study, a relatively well-established numerical method for Reynolds-averaged Navier-Stokes solutions is applied to compare numerically the aerodynamic performance of slightly different designs. Designs for a high-pressure-ratio turbine nozzle and two different centrifugal impeller designs are used for comparison purposes.

Governing Equations and Turbulence Modeling

The following Reynolds-averaged Navier-Stokes equations are solved for the current problem:

$$\frac{\partial}{\partial x_i}(\rho U_i) = 0 \tag{1}$$

$$\frac{\partial}{\partial X_j}(\rho U_i U_j) + 2\rho\,\epsilon_{ijk}\,\Omega_j U_K = -\frac{\partial p}{\partial x_i} + \frac{\partial}{\partial x_j}\left[\mu\left(\frac{\partial U_i}{\partial x_j} + \frac{\partial U_j}{\partial x_i} - \frac{2}{3}\frac{\partial U_k}{\partial x_k}\delta_{ij}\right) - \rho\overline{u_i u_j}\right] + F_i \tag{2}$$

$$\frac{\partial}{\partial x_j}(\rho U_j e) = \frac{\partial}{\partial x_j}\left[\left(\frac{\mu}{Pr}\right)_{eff}\frac{\partial T}{\partial x_j}\right] - \frac{\partial}{\partial x_j}(pU_j) + U_i F_i + \frac{\partial}{\partial x_j}\left[U_i\mu\left(\frac{\partial U_i}{\partial x_j} + \frac{\partial U_j}{\partial x_i} - \frac{2}{3}\frac{\partial U_k}{\partial x_k}\delta_{ij}\right)\right] \tag{3}$$

$$P = \rho RT \tag{4}$$

where U_i = mean velocity, u_i = fluctuating velocity, e = total energy, Ω_i = angular velocity,

$$\left(\frac{\mu}{Pr}\right)_{eff} = \left(\frac{\mu}{Pr}\right)_{laminar} + \left(\frac{\mu}{Pr}\right)_{turbulent}$$

and

$$e = C_v T + \frac{1}{2}U_i U_i$$

A modified k-ε, two-equation model is used to estimate Reynolds stresses and heat flux. The turbulence model is extended to the solid wall following the studies of Chien [5]. The following additional transport equations are solved to calculate turbulent stress terms:

$$\frac{\partial(\rho U_i k)}{\partial x_i} = \frac{\partial}{\partial x_i}\left(\frac{\mu_{eff}}{\sigma_k}\frac{\partial k}{\partial x_i}\right) - \rho\,\overline{u_i u_j}\,U_{i,j} - \rho\varepsilon - \frac{2\mu k}{\rho^2} \tag{5}$$

$$\frac{\partial(\rho U_i \varepsilon)}{\partial x_i} = \frac{\partial}{\partial x_i}\left(\frac{\mu_{eff}}{\sigma_\varepsilon}\frac{\partial \varepsilon}{\partial x_i}\right) + C_1\frac{\rho\varepsilon}{k}(\overline{u_i u_j}\,U_{i,j}) - \frac{\rho\varepsilon}{k}\left(c_2 f\varepsilon + \frac{2\nu k e^{-c_4 u^* l/\nu}}{l^2}\right) \tag{6}$$

where

$$\mu_{eff} = \mu + C_\mu(k^2/\varepsilon)\,[1 - \exp(-c_3 u^* l/\nu)]$$

and

$$f = 1 - \frac{0.4}{1.8}\,e^{-(k^2/6\nu\varepsilon)^2}$$

No attempt was made to optimize constants of the turbulence modeling equations for this study. Therefore, standard values of various constants of the turbulence model are used; the values are

$$C_\mu = 0.09,\ C_1 = 1.35,\ C_2 = 1.8,\ \sigma_k = 1.0,\ \sigma_\varepsilon = 1.3,\ C_3 = 0.0115,\ C_4 = 0.5$$

Numerical Scheme and Boundary Conditions

Equations 1 through 6 are solved numerically with a fully conservative control volume approach. The finite difference equations are formulated in terms of Cartesian momentum (ρU_i), static pressure (p), total internal energy (e), turbulence kinetic energy (k) and turbulence energy dissipation rate (ε). The numerical fluxes through control volume surfaces are estimated with a quadratic upwinding scheme and so the formal spatial accuracy is third order on smoothly varying meshes. The steady-state solution is obtained through the elliptic relaxation of the finite difference equations and each relaxation consists of one semi-implicit prediction and two implicit correction steps. During each iteration, pressure-based correction equations are used to ensure global conservation.

With the static pressure field at the previous iteration, the momentum conservation equations are solved using the following equation on nonorthogonal body-fitted coordinates:

$$\begin{aligned}\frac{1}{J}\frac{\partial}{\partial\xi}(G_1\phi) + \frac{1}{J}\frac{\partial}{\partial\eta}(G_2\phi) + \frac{1}{J}\frac{\partial}{\partial\psi}(G_3\phi) &= \frac{1}{J}\frac{\partial}{\partial\xi}\left[\frac{\Gamma'_\phi}{J}D_{\xi\xi}\phi_\xi + \frac{\Gamma'_\phi}{J}D_{\xi\eta}\phi_\eta + \frac{\Gamma'_\phi}{J}D_{\xi\psi}\phi_\psi\right] \\ &+ \frac{1}{J}\frac{\partial}{\partial\eta}\left[\frac{\Gamma'_\phi}{J}D_{\eta\xi}\phi_\xi + \frac{\Gamma'_\phi}{J}D_{\eta\eta}\phi_\eta + \frac{\Gamma'_\phi}{J}D_{\eta\psi}\phi_\psi\right] \\ &+ \frac{1}{J}\frac{\partial}{\partial\psi}\left[\frac{\Gamma'_\phi}{J}D_{\psi\xi}\phi_\xi + \frac{\Gamma'_\phi}{J}D_{\psi\eta}\phi_\eta + \frac{\Gamma'_\phi}{J}D_{\psi\psi}\phi_\psi\right] + \tilde{S}_\phi\end{aligned} \tag{7}$$

where Γ'_ϕ is the diffusion coefficient, G_i is a velocity component along the transformed coordinates (ξ,η,ψ), and $\tilde{S}_\phi$ consists of additional body force terms and pressure terms. A 3-point central difference approximation is used for all the diffusion terms and a modified quadratic upwinding scheme is used for convection terms.

Because the coefficients of the finite difference equation (7) are based on the values at the previous step, the resulting ρU_i does not satisfy mass conservation. Two correction steps are needed to satisfy the mass conservation at each iteration. The concept of pressure-implicit splitting is used for the correction of p and eU_i after the prediction step.

The two correction steps are as follows:

$$(\rho U_i)^{**} - (\rho U_i)^{*} = \Delta_p^{-1}\,\Delta_i(P^{*} - P^{n}) \tag{8}$$

$$(\rho U_i)^{n+1} - (\rho U_i)^{**} = A_p^{-1}\,\Sigma A_{pm}\,[(\rho U)^{**} - (\rho U)^{*}] - \Delta_i\,(P^{n+1} - P^{*}) \tag{9}$$

For equations (8) and (9), the mass conservation condition is imposed as

$$\Delta_i(\rho U_i)^{**} = \Delta_i(\rho U_i)^{n+1} = \Delta_i(\rho U_i)^{**} = 0 \tag{10}$$

By combining equation (10) with equations (8) and (9), Poisson-type equations are obtained for $(P^{*} - P^{n})$ and $(P^{**} - P^{*})$ and the value of $(\rho U)_i^{n+1}$, P^{n+1} is calculated with the corrected pressure. With the correction step in equations (8)-(10), density is handled rather implicitly and (ρU_i) and P are updated. A single implicit step is used to calculate k, ε, and e with the corrected values of ρU_i and p.

The computations were carried out on I-O type composite grids. With the I-grid, spatial periodicity of the grid at the periodicity surface is not forced and the physical flow periodicity condition is handled inside the flow solver by a high-order

interpolation of variables. Good orthogonality of the grid can be maintained near the blade surface and at periodic surfaces, which is essential for accurate solution of transonic viscous flow inside turbine blade rows with high turning. Near the blade surface, an O-grid is wrapped around the blade. This inner O-grid is used mainly to represent the high gradient of variables near the surface. With the I-O type grid, dimensionless wall distance (y^+) at the first node can be in the order of 1 to 5 with an acceptable overall grid size.

At the inflow boundary, the distribution of total pressure, total temperature, and inlet flow angles are fixed. At the outflow boundary, the static pressure is fixed at one location. For the turbulence, the experimental value of turbulent kinetic energy is used at the inflow boundary and the equilibrium condition is used to estimate the inflow condition of the turbulence dissipation rate. Residuals of each finite difference equation are integrated over the entire domain. When the integrated residuals of all the equations are required by four orders of magnitude from their initial value, the solution is considered to be converged. The code is vectorized on Cray-XMP and has an option to run out-of-core solution (solid-state-disk storage on Cray-XMP) for large-scale problems.

Two High-Pressure-Ratio Axial Turbine Nozzles

The current turbomachinery design practices are still mainly based on quasi-three-dimensional methods. Various correlations for the viscous effect are built on these methods, which are also based on past experiences. The current standard design procedures work well as long as the design is within the envelope of valid correlations. As expected, the current quasi-three-dimensional methods become less reliable when the aerodynamic or geometric parameters are changed drastically beyond past experience.

The basic flow structure in turbine blade passage is believed to be fairly well understood [6,7]. Various numerical studies based on fully three-dimensional Navier-Stokes analysis [2,3] have also indicated that the entire flowfield can be predicted with the accuracy for design applications.

Two different designs of a high-pressure ratio turbine nozzle are numerically simulated to determine whether the numerical solution can distinguish differences in aerodynamic performances.

The geometry of two nozzles is shown in Figure 1. Nozzle A, with 42 blades, and nozzle B, with 24 blades, were both designed to operate at a pressure ratio of 2.1. Nozzle B was designed to reduce the overall weight of the stage. As expected, nozzle A has very good aerodynamic performance. However, experimental test results of nozzle B indicate significant deterioration of aerodynamic performance, which is quite contradictory to the design intention. Figure 2 shows static pressure distributions on the blade surface for both nozzles. Mach number contours near the hub are compared in Figure 3: Nozzle A shows conventional Mach number distribution and usual supersonic shock system near the trailing edge, a weak shock on the pressure side, and a strong shock on the suction side that propagates toward the next blade row, even after strong interaction with the wake. However, nozzle B does not indicate such a conventional shock system near the trailing edge. The velocity vectors near the hub are compared in Figure 4: Flow separation is clearly shown for nozzle B, which might contribute to the relatively high aerodynamic loss. Radial distribution of total pressure loss is compared in Figure 5. The current numerical solutions for the two high-pressure-ratio turbine nozzles indicate that the numerical solution can distinguish aerodynamically good design from aerodynamically bad designs, which conventional correlation-based methods cannot correctly identify.

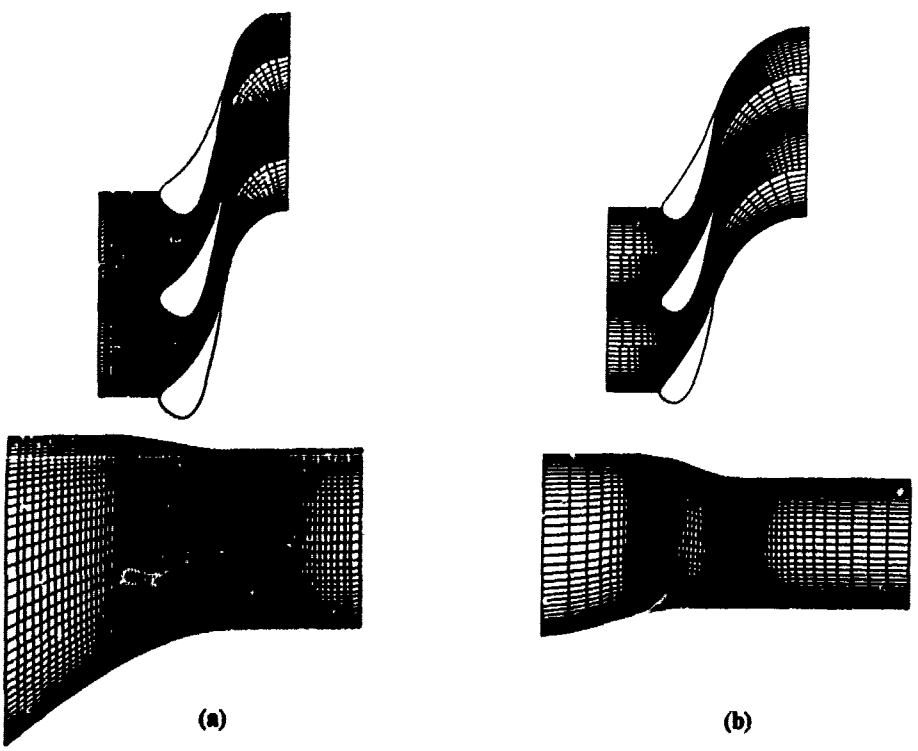
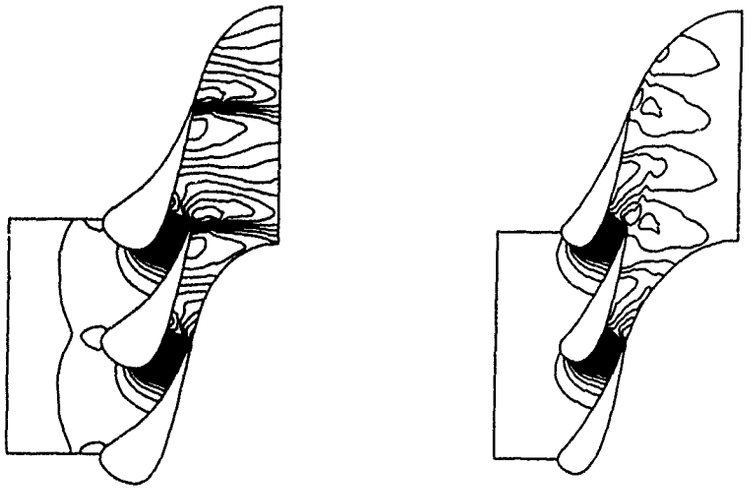
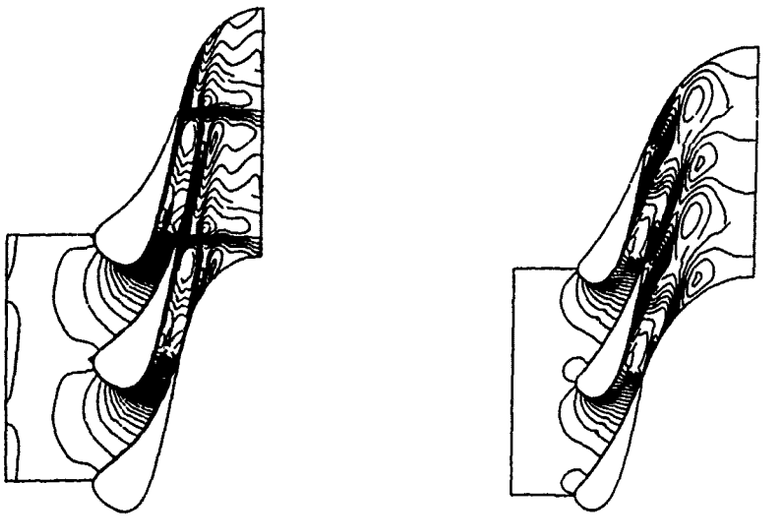


Figure 1. Computational grids for two nozzles.



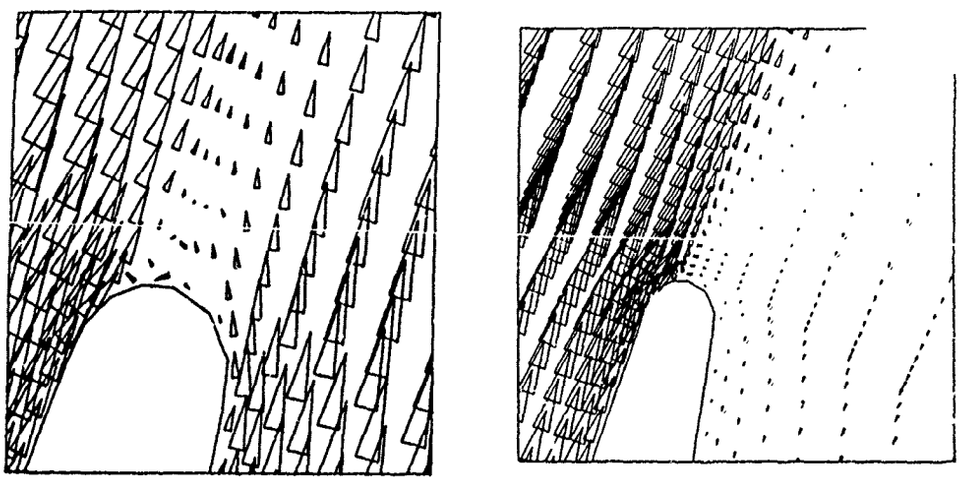
(a) (b)

Figure 2. Comparision of static pressure contours near the hub.



(a) (b)

Figure 3. Comparision of Mach number contours near the hub.



(a) (b)

Figure 4. Comparision of velocity vectors near the hub.

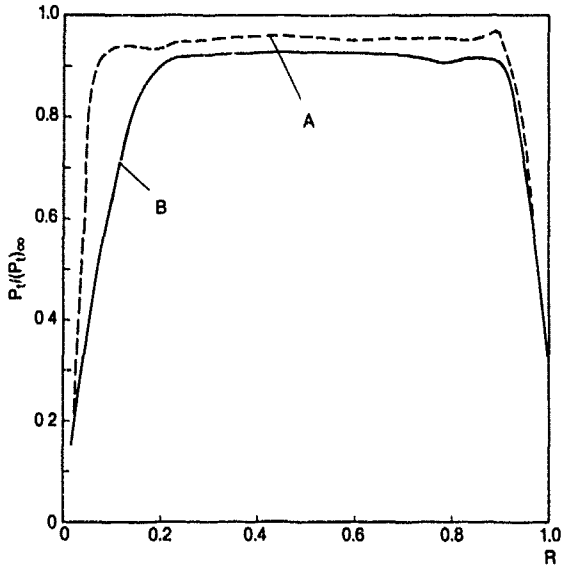


Figure 5. Comparison of spanwise distribution of total pressure loss.

Two Backswept Centrifugal Impellers

The development of an aerodynamically efficient centrifugal compressor stage is essential for the high-performance small gas turbines. The flow inside the centrifugal compressor stage is very complex and various three-dimensional viscous flow phenomena dominate the flowfield. Experimental investigations with the well-developed optical measurement techniques [8,9] have further shown the complex nature of the flowfield (flow separation, large vortex motion, different exit flow profiles, etc.). In recent years, various studies have been made to calculate the flows inside Eckardt's backswept impeller [4,10] and Krain's backswept impeller [11,12] with full three-dimensional Navier-Stokes code. As reported earlier, the impeller exit velocity profiles from these two impellers are distinctively different. Eckardt's impeller shows a traditional jet/wake type profile at design and choke flow condition while Krain's more advanced impeller shows smoother profiles at all operating conditions.

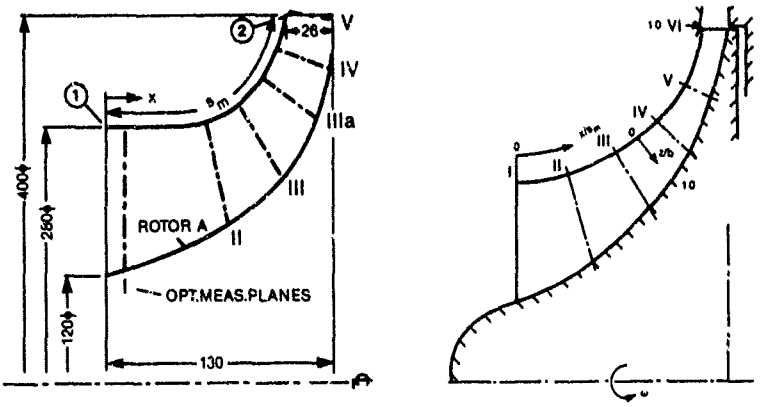
As detailed numerical studies of these impellers at design condition have been published previously [10,11], the aerodynamic performances of Eckardt's impeller and Krain's impeller at off-design conditions (choke condition) are compared numerically. Figure 6 shows both impellers. The detailed geometry and test conditions are given in [8,9]. Eckardt's impeller has 20 blades, and Krain's impeller has 24 blades. Both impellers have 30° backswept geometries and operate with vaneless diffusers. The computations were carried out on H-type grids with the same number of nodes (26 × 31 × 51 in blade-to-blade, spanwise, streamwise directions). Six span-wise nodes are located inside the tip-clearance regions for both impeller calculations. Figure 7 shows meridional impeller shapes and measurement planes where comparisons are made.

For the current study, detailed development of vortex motion and secondary flow inside the impeller is investigated using the numerical solution. Krain [9] and Hah and Krain [11] have used the shape of the lines of constant relative flow angles (iso-clines) to identify the existence of a vortex.



Eckhardt **Krain**

Figure 6. Eckardt's and Krain's impellers.



Eckhardt **Krain**

Figure 7. Measurement planes.

The basic equations for the isoclines of a real vortex moving with the relative velocity W_b are derived in Figure 8a. The result of the analysis for a through flow inclined against the drawing plane ($\beta = 35°$) is shown in Figure 8b. According to this analysis the isoclines are parallel to each other in the solid body vortex area and are elliptical in the potential vortex area. The vortex center is always located in the middle of the parallel isoclines. A real vortex, which consists of a solid-body vortex and a potential vortex part, is assumed to be present when isoclines similar to those shown in Figure 8b are identified.

In Figure 9, circumferentially averaged shroud static pressure distribution is compared for the two impellers, and typical distribution of wall static pressure at this operating condition is observed. As shown in Figure 9, the overall impeller performance is very well predicted for both impellers. A detailed flow angle analysis is given in Figure 10. At Plane I, the impellers show no effect of tip-clearance and similar distribution of contours are observed. From Plane I to Plane III, two vortex systems are developed near the shroud. The pressure-side vortex of Eckardt's impeller is more clearly formed and its location is nearer to the center of the passage than is Krain's impeller. For both impellers, this vortex is formed because of tip-clearance flow and this difference in vortex structure might be due to the relatively stronger tip-clearance effect in Eckardt's impeller. From Plane III to the exit Plane IV, three distinctive vortex systems are developed for both impellers. However, the relative magnitude and location of the vortices are quite different between the impellers. Compared with Krain's impeller, the vortices of Eckardt's impeller are rather concentrated near the shroud and toward the center of the blade passage. The vortices represent velocity gradient, so some high-velocity gradient is expected near the pressure side of the centerline in Eckardt's impeller from Figure 10f. The exit relative total velocity component is compared with the experimental data in Figure 11. The agreement between experimental data and numerical prediction in Figure 11 is very good for both impellers considering the complex nature of the flowfield. The current numerical study indicates that the distinctive difference of flowfield in two different centrifugal impellers can be numerically predicted.

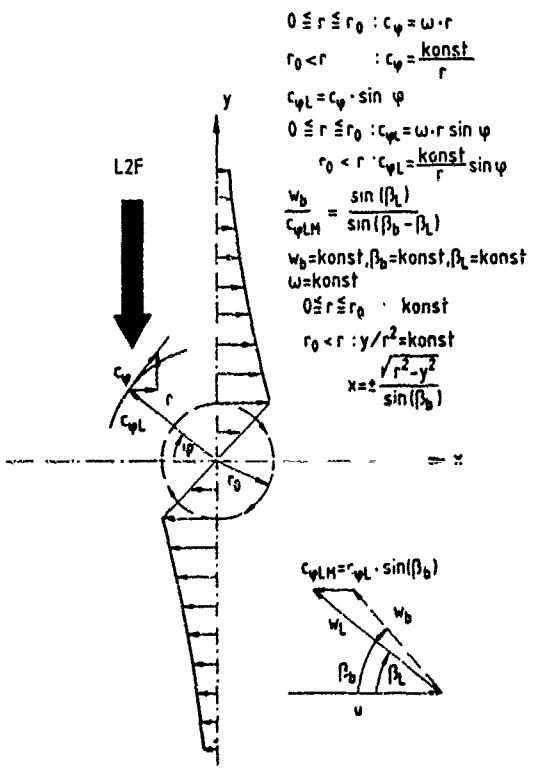


Figure 8a. Measurement of vortex flow with L2F measurement technique.

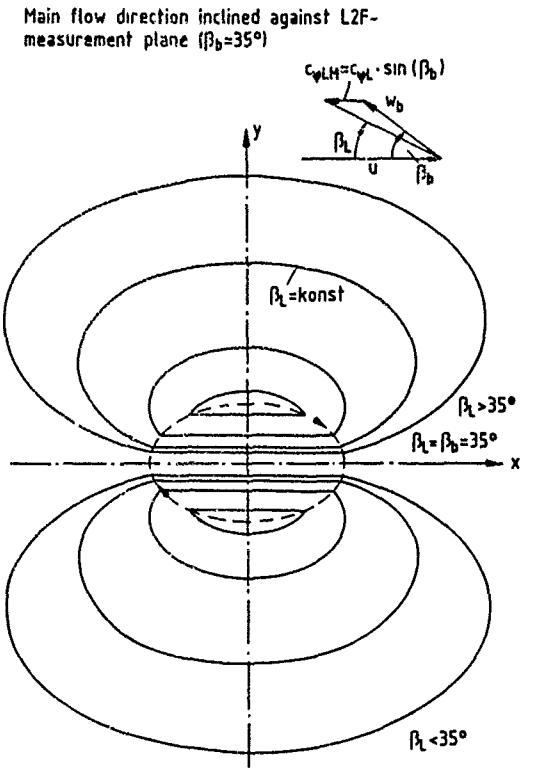
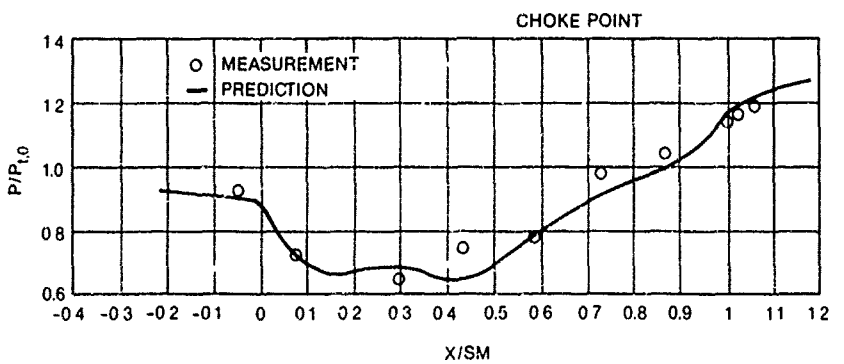
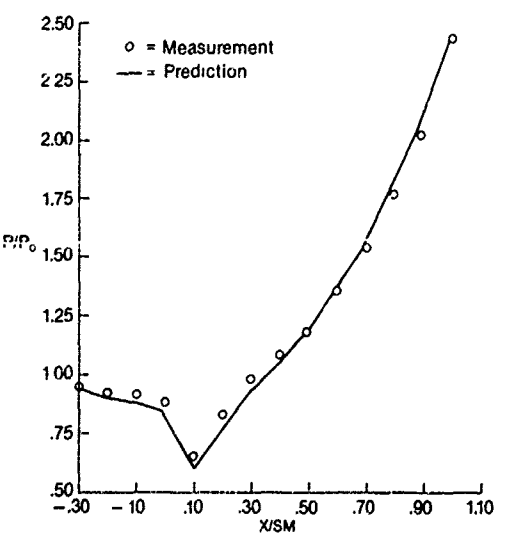


Figure 8b. **Isocline structure for a real vortex, composed of a solid body and a potential vortex.**



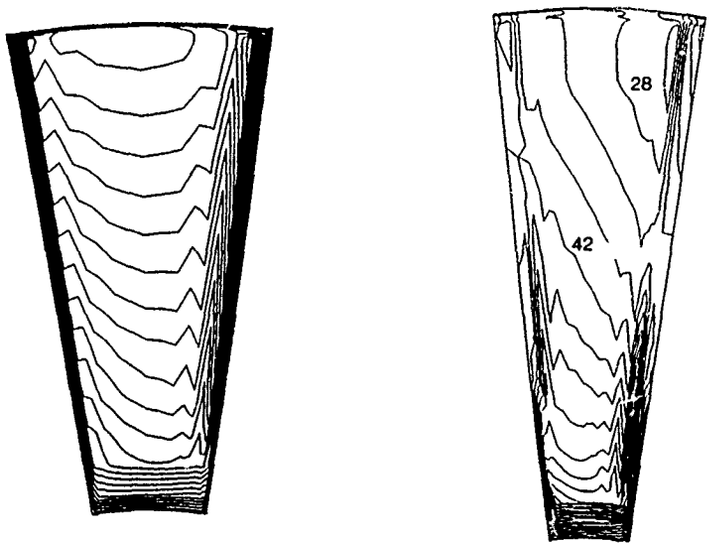
Eckardt

Figure 9a. **Comparison of circumferentially averaged shroud static pressure at choke condition.**



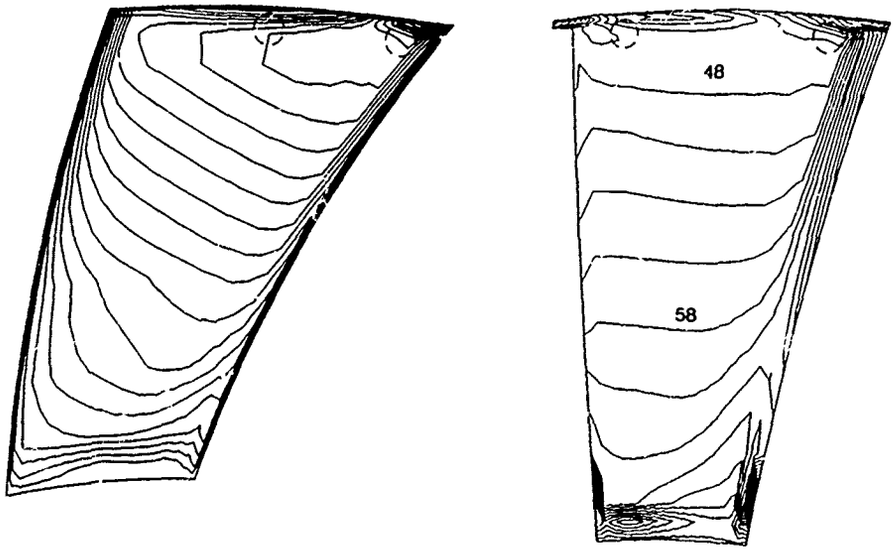
Krain

Figure 9b. **Comparison of circumferentially averaged shroud static pressure at choke condition.**



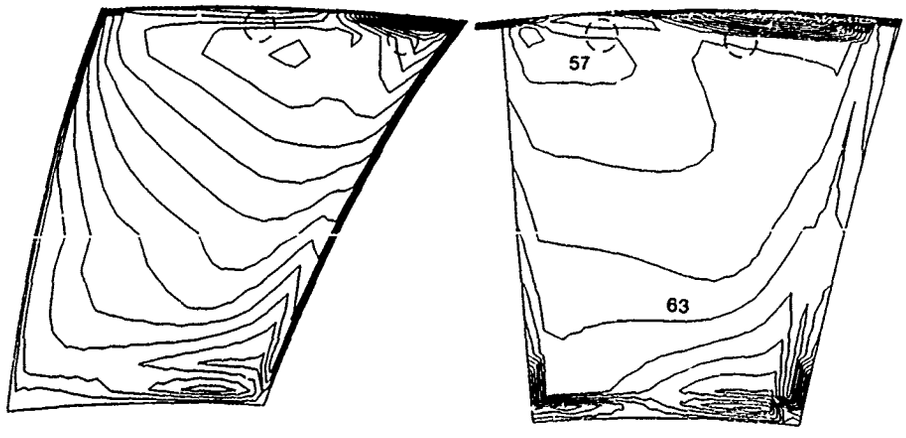
Eckhardt Krain

Figure 10a. Comparison of isocline pattern at Plane I.



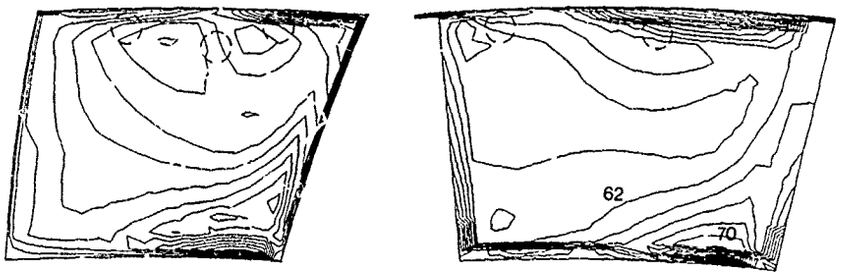
Eckhardt Krain

Figure 10b. Comparison of isocline pattern at Plane II.



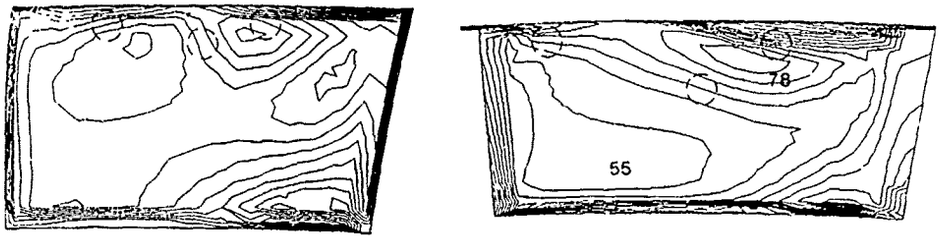
Eckhardt Krain

Figure 10c. Comparison of isocline pattern at Plane III.



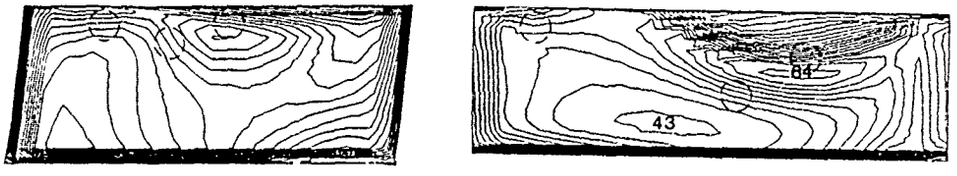
Eckhardt Krain

Figure 10d. Comparison of isocline pattern at Plane IV.



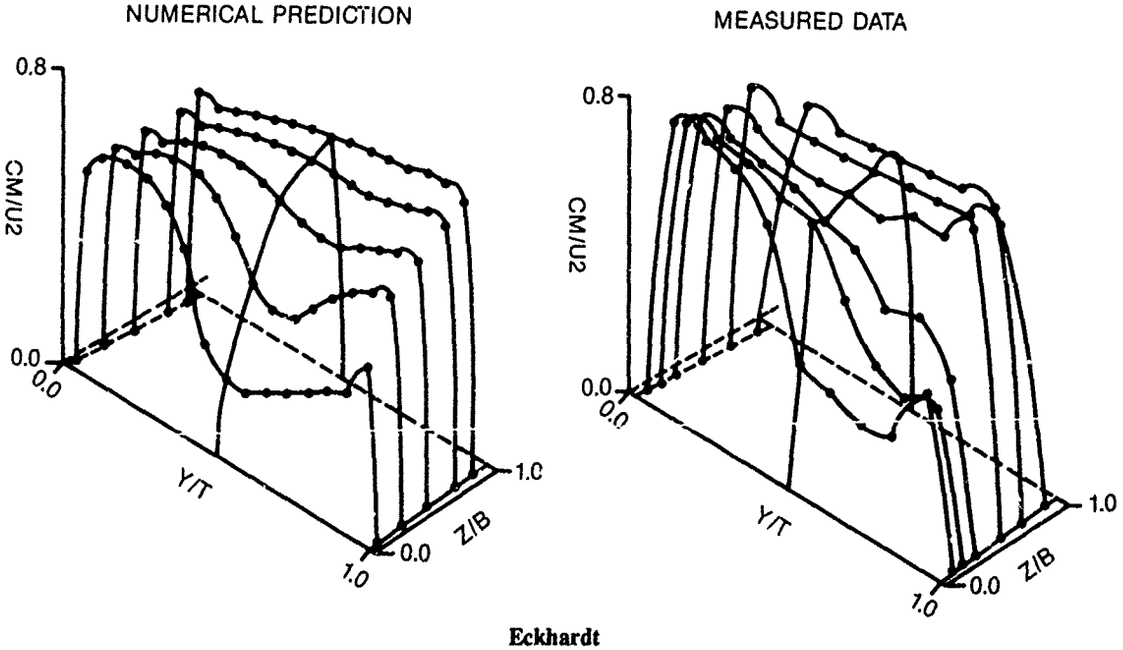
Eckhardt Krain

Figure 10e. Comparison of isocline pattern at Plane V.



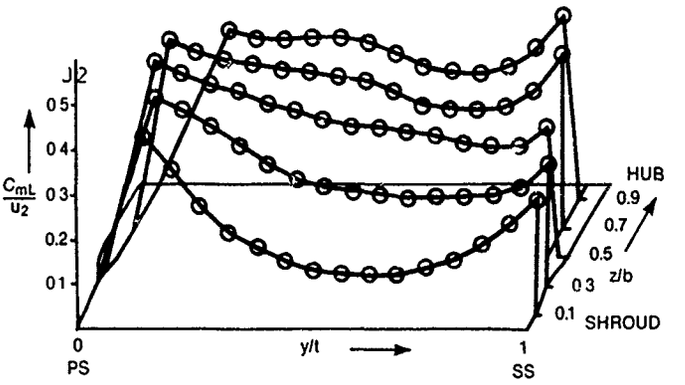
Eckhardt Krain

Figure 10f. Comparison of isocline pattern at Plane VI.

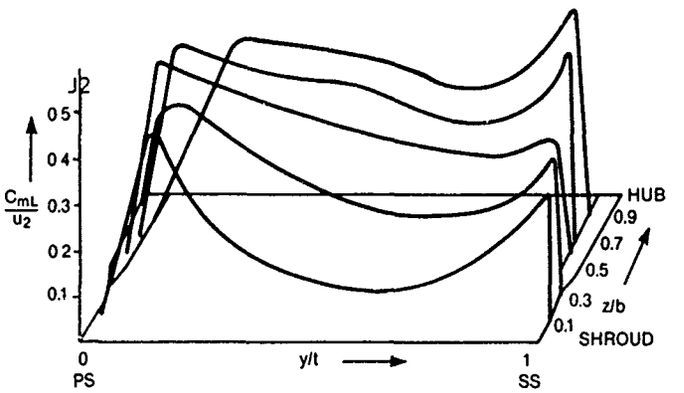


Eckhardt

Figure 11a. Comparison of meridional velocity profiles at impeller exit (choke condition).



MEASUREMENT BY KRAIN



VISCOUS FLOW SOLUTION

Krain

Figure 11b. Comparison of meridional velocity profiles at impeller exit (choke condition).

Concluding Remarks

The current study presented the results of the application of a three-dimensional viscous flow code to distinguish aerodynamic performance of different designs of turbomachinery components. Two different designs of a high-pressure-ratio turbine nozzle and a centrifugal impeller are used for verification purposes. Detailed examination of the numerical solutions indicates that the current three-dimensional Reynolds-averaged Navier-Stokes code does properly predict the differences in aerodynamic performance of the different designs, which other correlation-based methods or inviscid methods do not predict. The current work concludes that the Reynolds-averaged Navier-Stokes method can indeed be applied to the real design work of turbomachinery components. Designers can examine and verify several candidate designs numerically before any final verification test. Therefore, the overall development cycle can be significantly shortened.

References

[1] Moore, J., and Moore, J.G., "Performance Evaluation of Linear Turbine Cascades Using Three-Dimensional Viscous Flow Calculations," ASME paper 85-GT-65, 1985.

[2] Hah, C., "A Navier-Stokes Analysis of Three-Dimensional Turbulent Flows Inside Turbine Blade Rows at Design and Off-Design Conditions," *Trans. ASME, Journal of Engineering for Gas Turbines and Power,* Vol. 106, 1984, pp. 421-429.

[3] Dawes, W.N., "Development of a 3D Navier-Stokes Solver for Application to All Types of Turbomachinery,"" ASME paper 88-GT-70, 1988.

[4] Rhie, C.M., Delaney, R.A., and Mckain, T.F., "Three-Dimensional Viscous Flow Analysis for Centrifugal Impellers," *J. Propulsion,* Vol. 1, No. 4, 1985, pp. 257-258.

[5] Chien, K.Y., "Predictions of Channel and Boundary-Layer Flows With a Low-Reynolds Number Turbulence Model," *AIAA Journal,* Vol. 20, No. 1, 1982, pp. 33-38.

[6] Sieverding, C.H., "Recent Progress in the Understanding of Basic Aspects of Secondary Flow in Turbine Blade Passages," *ASME Journal of Engineering for Gas Turbines and Power,* Vol. 107, 1985, pp. 248-252.

[7] Langston, L.S., Nice, M.L., and Hooper, R.M., "Three-Dimensional Flow Within A Turbine Cascade Passage," *ASME Journal of Engineering for Power,* Vol. 99, No. 1, Jan. 1977.

[8] Eckardt, D., "Detailed Flow Investigations Within a High Speed Centrifugal Compressor Impeller," *ASME Journal of Fluids Engineering,* Vol. 98, 1976, pp. 390-402.

[9] Krain, H., "A Study on Centrifugal Impeller and Diffuser Flow," *ASME Journal of Engineering for Power,* Vol. 103, No. 4, 1981, pp. 688-697.

[10] Hah, C., Bryans, A.G., Moussa, Z., Tomsho, M.E., "Application of Viscous Flow Computations for the Aerodynamic Performance of a Backswept Impeller at Various Operating Conditions," *Trans. ASME Journal of Turbomachinery,* Vol. 110, No. 3, 1988, pp. 303-311.

[11] Hah, C., and Krain, H., "Secondary Flows and Vortex Motion in a High-Efficiency Backswept Impeller at Design and Off-Design Conditions," ASME paper 89-GT-181, to appear in *ASME Transaction.*

[12] Krain, H. and Hoffmann, W., "Verification of an Impeller Design by Laser Measurements and 3D Viscous Flow Calculation," ASME paper 89-GT-151.

DISCUSSION

Skoe, Norway

1. Are the number of gridpoints within clearance region sufficient to calculate realistic clearance loss, and the adverse effect of loading (on clearance loss)?

2. How is comparison between test & analysis for design point operation?

3. Is the code capable of treating splitter blades which is usually used on high performance centrifugal rotors for elevated pressure ratios?

Author's Reply:

1. We have six grid points inside tip-clearance and I think that the overall effects of tip-clearance on the main flow can be properly represented.

2. We published the results at design condition in the ASME paper 89-GT-181 and the results were very encouraging.

3. As all our current impellers have flow-splitter, the code is written to handle flow-splitters.

Leboeuf, France

Can you comment about the turbulent low Reynolds number effect included in your code?

Author's Reply:

The low Reynolds number modification of our standard two-equation turbulence model is intended to solve the transport equations to the solid wall without any assumption of profiles. Generally, this modification improves prediction of separated flow region especially near the trailing edge. Also, it simulates the effect of freestream turbulence qualitatively well when the freestream turbulence is above 1~2%.

Papailiou, Greece

Do you perform accurate unsteady computations with the appropriate accuracy for the unsteady terms?

Author's Reply:

Yes, we use a scheme which is second-order accurate in time when we perform unsteady time-accurate calculations.

Hansen, USA

As you look forward from today and into the future, what is your own best thinking about turbulence models that should be used for complex turbomachinery flows?

Author's Reply:

Thank you for your question about a very important issue of turbomachinery CFD. As you know very well, the turbulent flow inside turbomachinery is significantly influenced by the effects of curvature and rotation. Also,

flow transition must be properly modeled for the heat transfer computation on the turbine blades. With the currently available computers, three-dimensional flow computation inside turbomachinery with large eddy simulation or direct simulation of turbulence becomes impractical because of unrealistic amount of computing time. As we should produce useful computations for design purposes with reasonable cost, rather simpler mixing length or two-equation type model is used currently. Further research efforts to improve rather simpler models for complex flow application are essential for successful CFD for turbomachinery.

SECONDARY FLOW CALCULATIONS FOR AXIAL AND RADIAL COMPRESSORS

DOUVIKAS,D., Assistant
KALDELLIS,J., Assistant
PAPAILIOU,K.D., Professor

NATIONAL TECHNICAL UNIVERSITY OF ATHENS,
Lab. of Thermal Turbomachines,
P.O.Box 64069, 15710 Athens, Greece.

ABSTRACT

A secondary flow calculation method is presented, the development of which has recently been completed in the Thermal Turbomachines Lab. of the National Technical University of Athens. This method makes use of the meridional vorticity transport equation, the momentum integral equation and the mean kinetic energy integral equation. Emphasis is placed upon the use of a coherent two-zone model and care is taken to describe adequately the flow inside an unbounded (external), semi-bounded (annulus) and fully-bounded (bladed) space. The hub and tip secondary flow development is calculated simultaneously, so that, use of an approximate model for the interaction between the viscous shear layer and the external flow, permits to adapt this last flow field to the growth of the wall shear layers during the computational procedure. Not only the meridional but also the peripheral blockage is taken into account during this procedure. An additional approximate viscous-inviscid interaction model is used, when shocks are present in the passage.

An attempt is made to place the method in historical perspective. Then, after its brief description, comparisons with experimental results are presented along with the appropriate discussion in order to evaluate the capabilities of the method.

1. INTRODUCTION

The meridional flow model has been proved successful for the calculation of the flow field in single- and multi-stage compressors. The same flow model has been proved successful for the computation of the external flow field in turbines. However, for the wall shear layer case in turbines, the meridional flow model which utilizes circumferentially averaged quantities has been found to be inadequate and fully three-dimensional analyses have been proposed instead. It remains to be seen how these approaches will deal with the unsteady effects in the peripheral direction and the corresponding circumferential mixing, when one or more stages are considered.

Coming back to the compressor case, the main effort in the past decades has been directed towards producing a wall shear layer calculation method compatible with the meridional flow one used to calculate the external "inviscid" flow. Railly[1] was the first to develop equations for the wall shear layer behaviour in accordance with the meridional plane model. Although he identified the additional unknowns resulting from the loss of information related to the circumferential integration of the flow equations (appearance of the force defect, "fluctuation" and pressure terms as they were named later[2], he failed to recognize their importance. Being unable at that moment to propose an adequate modelling, he decided to drop them out altogether. The importance of the force defect term was recognized some years later by L.H. Smith[3] on the basis of experimental evidence from multistage compressors. Mellor[2], then, reconsidering Railly's analysis, was able to formulate a closed problem taking into account the force defect terms but neglecting the "fluctuation" and the pressure terms. Not being able to propose detailed assumptions needed for closure, he proceeded to an additional integration in the axial direction for a distance equal to an axial chord. Observing that, for compressor configurations, secondary vorticity was large at the inlet of each blade row but diminished drastically as the flow proceeded towards the trailing edge, he assumed a collateral shear layer at each blading exit (zero secondary vorticity). He relaxed, this assumption for the case of non zero tip clearance and formulated the corresponding correction on the basis of secondary vorticity theory. He, then, argued that the blade defect force was normal to the mean blade direction. Essentially, using these assumptions, he was able, in the frame of an integral formulation, to reproduce the qualitative and quantitative behaviour of the wall shear layers[2],[4]. The same method was used later[5], where Head's entrainment equation was added, in order to compute multistage compressor wall shear layer behaviour successfully.

Mellor's method, although attractive formally, could not take into account the flow field situation inside the blade passage, considering integral flow properties only at each blade row inlet and exit. Additionally, the assumptions used did not permit the calculation of the secondary flow behaviour of a single blade row. Following Mellor's work a series of experiments was undertaken and available experimental results were used (this work is reported in references (5) to (18)), in order to establish semi-empirical information, in an effort to obtain closure relaxing the restrictions of his formulation.

The analysis of the experimental results was performed using the two-zone model. Through this analysis it was possible to establish the following facts:

a) the circumferentially averaged longitudinal velocity profile, viewed in the reduced form proposed by Mellor[2] could be described with adequate accuracy for engineering purposes by the classical two-dimensional turbulent boundary layer velocity profile family.
b) the defect force vector was locally normal to the blade mean camber line.
c) the transverse velocity profile was s-shaped following Hawthorne's theory (see, for instance, ref.(18)).
d) the defect force vector was the most important of the three additional unknown terms resulting from the circumferential integration, the"fluctuation" and pressure found to be only correction terms, in the cases where these could be evaluated.

The above mentioned experimental facts pointed towards establishing a method, which could be integral in the longitudinal direction but had to be differential in the transverse one. This ought to be so, because the transverse velocity profile shape depends upon the passage geometry. The various stages of development of this method can be found in references (9),(11),(12),(13),(15),(16),(17),(18) and (44). Using a two parameter velocity profile family for the description of the longi-

tudinal velocity profile, two integral equations were necessary. The momentum integral equation in the meridional direction and Head's entrainment equation were used for this purpose. This last equation was found to be particularly suitable for a circumferentially averaged formulation. For the calculation of the transverse velocity field, the secondary vorticity transport equation was used in a single form (Squire and Winter's formula was utilized at the very beginning) disregarding viscous terms. A linear matching to the solid wall no slip condition was employed in order to simulate the viscous part of the transverse profile.

Initially, Horlock's[21] s-shaped velocity profile family was tried, but quickly it was abandoned in profit of Hawthorne's approximate solution, in spite of the fact that this could not produce Johnston's[22] triangular transverse velocity profile, when the passage walls were removed to infinity.

Considering a calculation step (Section 1, where all quantities are known and Section 2, where the various viscous quantities are calculated), the following simple algorithm may demonstrate the basis of the corresponding calculation procedure:

STEP1 Assume a longitudinal velocity profile at Section 2.

STEP2 Establish the streamlines between stations 1 and 2 and calculate the secondary vorticity increase between the two stations. Use, for this, the secondary vorticity transport equation. Having the secondary vorticity at station 2 compute the corresponding transverse velocity profile.

STEP3 Use the longitudinal and transverse profiles at station 2 and compute all integral quantities appearing in the two momentum equations and the entrainment equation.

STEP4 Use the peripheral component of the momentum equation in order to compute one of the defect force components. The others are computed from the condition of perpendicularity to the mean blade camber surface of the blade force vector.

STEP5 Search for a longitudinal velocity profile, repeating STEPS 2 and 3, for which the meridional momentum integral equation and the entrainment equation are satisfied.

Since the above theoretical development started, until the last contribution cited above, it was possible to improve the sophistication of the calculation procedure. This was due to the increased understanding of the secondary flow behaviour coupled with increasing availability of fast computing equipment. We may cite here as examples the inclusion of viscous terms in the secondary vorticity transport equation, the inclusion of the pressure term in the calculation procedure or, finally, the inclusion of adequate viscous-inviscid interaction techniques, in order to avoid computational failure when flow separation takes place.

Considering the cascade cases that have been computed, one can see that secondary flow behaviour is accurately predicted even for high turning turbines. It was the viscous part of the calculation that failed in this last case rather than the secondary vorticity inviscid part. On the other hand, losses are underestimated in highly loaded compressor cascades, probably because the flow model does not include explicitely the dissipation taking place in the suction side corner vortex. It is interesting to note that good prediction of tip clearance flow was realized using the model developed by Lakshminarayana[23]. Considering the compressor cases for which computations were performed, we can see that secondary flow behaviour is, as well, adequately well predicted.

In spite of the success of the method described above, it was felt that additional improvements could be achieved. At the same time, the problem of the shock-secondary flow interaction, appearing for high speed machines, could be successfully treated using as basis the existing theoretical development. The corresponding investigation that was undertaken resulted in a calculation method, which presented several improvements in respect to the existing one. However, the same basic methodology, was concerved. This new method is described in the following section.

2. THE PRESENT CALCULATION METHOD (refs.(24) to (31)).

The method presented in this work was developed in the Thermal Turbomachinery Lab. of the Athens National Technical University for the past seven years. The formulation was developed as previously, using the difference of the circumferentially averaged equations for the external "inviscid" and the real viscous flow fields. Care was taken from the very beginning to neglect as few terms as possible and remain, thus, as close as possible to the Navier-Stokes equations for turbulent flow.

The reasons for undertaking this new development will be made clearer below. As was said above, the general structure of the calculation method follows that already described. "Fluctuation" terms were neglected, although this is still an open question, while the pressure term is calculated using the third momentum equation. Calculated are also the three defect force components (until now only two were considered in the plane tangent to the axisymmetric stream surface of the external flow) and in this way, dihedral effects are taken into account.

Local static pressure differences arise in the viscous flow region because of the non-zero value of the normal defect force term and the additional terms appearing in the third momentum equation for non-zero rotational speed. A basic characteristic of the two-zone model, however, is the identity of the static pressure fields of the external and the real flow outside of the viscous flow region. This ensures the parabolicity of the two-zone deficit formulation (difference between real and external flow fields). On the other hand, the external and the real flow possessing the same total conditions outside of the region influenced by hub and tip wall viscous effects, it follows that the velocity field for the real and external flow must be identical there. This result is in direct contradiction with the existance of an s-shaped transverse velocity profile, mentioned previously, and the results of the secondary flow theory applied to internal flow problems.

An investigation was undertaken in order to understand the reasons for this contradiction, the results of which are reported in detail in references (25),(26) and (27). It is possible to indicate where lies the problem by the following analysis. Consider the two-dimensional flow sketched in Fig. (1a). In addition to the real flow velocity profile, the inviscid flow field is presented for both zero and non-zero wall shear layer blockage. In both cases the external flow total conditions are identical and equal to those of the real flow outside of the wall shear layer regions. In the first case, however, the velocity field of the external and the real flow being identical outside of the shear layer regions, the static pressures of the two fields are identical (in fact, they differ slightly inside the shear layer regions). In the second case, however, the velocity fields differ and so differ the static pressure fields. Global mass flux conservation across the passage results to zero displacement

thickness for this last case. Neglecting modifications of the effective wall curvature due to displacement effects, all differences vanish when the upper wall moves to infinity (external flow case). Consider now Fig.(1b), where the flow in the transverse plane is sketched for a bladed passage. Initially (Fig.(1b,a)) the external transverse velocity field is equal to zero by definition (zero transverse mass flux). When, due to three-dimensional effects, the mass flux inside the shear layer increases in the transverse direction (Fig.(1b,b)), the external flow velocity field must move accordingly, in order to create the necessary opposide mass flux, which will conserve the zero mass flux condition in the transverse direction (and zero total displacement thickness). If the lateral walls did not exist (or if they were moved to infinity) we would have the case of Fig.(1b,c), which applies to external aerodynamics. For this case no reaction of the external flow field is visible.

In order to ensure that the static pressure fields of the external and the real flow are identical outside of the wall viscous shear layer, it is necessary to include the above mentionned opposite mass flux to the external flow. Then the corresponding increase in the external flow velocity will result to the appropriate decrease in the external flow static pressure.

Fig.(1b,d) is added in order to differentiate between what was done before and what Fig.(1b,b) is done in the present method.

The analysis presented in ref.(27) demonstrates that instead of the transverse velocity profile, it is much easier, for computational reasons, to consider the peripheral velocity profile of the circumferentially averaged flow. This profile may be deduced by a simple quadrature from the meridional vorticity component distribution, when the integration constant is known. For this reason, the meridional vorticity component transport equation is used in the present method. In this way, Hawthorne's computational procedure is not anymore necessary along with the assumption that the secondary flow alone verifies the continuity equation in each transverse plane.

According to the theoretical development of ref.(27)(and the above discussion), the peripheral velocity profile is decomposed into two parts. The first one belongs to the viscous wall shear layer and is totally confined inside a strip of width δ, the shear layer thickness. The second one belongs to the external flow and denotes its reaction to the blockage in the peripheral direction introduced by the modification of the mass flux inside the wall shear layer in the same direction. This external flow profile part restores the total mass flux in a manner compatible with the degree of confinement excerced to the flow by the physical boundaries and ensures the identity of the external and real flow static pressure fields outside of the viscous region. The external flow reacts to both the upper and lower wall shear layer peripheral blockage and, thus, it is necessary that the hub and tip shear layer development is performed simultaneously. This is the case for the present method.

From what was said above, in addition to the well established meridional blockage, which increases the velocity-density product in the meridional direction, the peripheral blockage must be taken into account, modifying the external flow angle. The two blockage effects are independent from one another.

The present method utilizes an approximate procedure, which accounts for this viscous-inviscid interaction and gives a good estimate of the modifications that the external flow must undertake during the calculation procedure, in order to account for both blockage effects. As, however, at present, no meridional external flow calculation accounts for the peripheral blockage effects, computations are carried out for the first iteration only, using the approximate procedure mentioned above and the meridional external flow calculation results obtained with zero wall shear layer blockage. This viscous-inviscid approximate interaction procedure has been built in the present calculation method, protecting it as well from failure, when flow separation is encountered.

The analysis of ref.(27) demonstrates that for a given meridional vorticity profile, the peripheral blockage alone decides about the peripheral viscous profile shape (circumferentially averaged) regardless of the degree of geometrical confinement (external aerodynamics (unbounded space), annular duct (semibounded space) and bladed (rotating or non rotating) region (fully bounded space)).

This has quite a few important consequences:

a) The case of a vortex structure coming out of a bladed region is greatly simplified, because one is not obliged to distinguish between this structure, which will be conserved downstream and the essentially different velocity field, which will be developed because of the additional secondary vorticity created downstream

b) The case of external aerodynamics (Johnston's profile) is a particular case of the present development and is established when the confining walls are moved to infinity.

c) The fact that the whole shear layer profile is confined inside a distance δ from the wall, which is not modified when one passes from an absolute to a relative coordinate system (and vice-versa), facilitates particularly the calculation, when rotating parts are present.

Of course, when a bladed region is entered, the flow is adapted to local conditions because of the change in peripheral blockage. The external flow field in respect to which the calculation will be performed is then modified and this generally gives rise to non zero defect force terms at the inlet of the particular space considered, that have to be specified, if compatible initial conditions are to be used.

Another feature, which distinguishes the present method from what was done before is the use of the total kinetic energy integral equation instead of the entrainment equation of Head. This equation was developed and adopted in view of extending the method to cases, where the two viscous shear layers are merging (the reasons are explained in ref.(28)). The computational algorithm of the present calculation method is a completely inverse one. It computes, as well, simultaneously the lost work and the corresponding total temperature increase, something which was done previously after the calculation was completed.

When a shock is present in the passage, an approximate procedure is used in order to overcome difficulties related to its presence. The shock case is idealized in the sense that it is considered normal to the external flow direction, while its strength is conserved. Then, the approximate theory of Panaras and Inger[32] is used (see also ref.(33)), modified accordingly (refs.(24) and (31)) in order to give an estimate of the wall static pressure distribution resulting from this kind of viscous-inviscid interaction. Otherwise, the wall shear layer calculation method remains the same. Unfortunatelly, it was not possible to find experimental results in order to check the accuracy of this approximate procedure estimating the shock-secondary flow interaction.

In what follows, comparisons between theoretical and experimental results will be presented and discussed.

3. COMPARISON BETWEEN THEORETICAL AND EXPERIMENTAL RESULTS. DISCUSSION.

A cascade experiment is considered first (Case B of Flot[34]). The leading of the blading is quite high and separation occurs near the trailing edge on the blade suction side. This experiment constitutes a severe test for the loss producing mechanisms of the calculation method. The computation was realized using as external flow field the one resulting from an inviscid two-dimensional cascade calculation corrected for the blade suction and pressure side boundary layers. Fig.(2a) gives a schematic representation of the test cascade and Figures (2b) and (2c) comparisons between theory and experiment concerning overall and detailed parameters of the wall shear layer (more details can be found in ref.(29)).

On the same figures some older predictions are reported in order to demonstrate the progress that has be realized with the present calculation method. It is rather surprizing that the two-dimensional turbulent boundary layer velocity profile family is capable to describe the circumferentially averaged experimental shear layer velocity profiles so well. On the other hand, use of the meridional vorticity transport equation along with the total kinetic integral equations seems to result in a better prediction of both the peripheral velocity profile and the shear layer momentum thickness. Still, however, the losses (momentum thickness) are not predicted accurately enough. Probably this happens, because the corner vortex dissipation mechanism is not represented in the method with the necessary accuracy.

The flow field in a radial compressor is considered next. This compressor was designed in the Fluid Mechanics Lab. of the Ecole Centrale of Lyon and manufactured by NEU Co. The design details and experimental results are reported in refs (37) and (18). The compressor stage is presented schematically in Fig. (3a), where the positions where measurements were performed (and comparisons between theory and experiment are presented), are, as well indicated. The utilization of a small size scroll created circumferential non uniformities in the vaneless diffuser space. Consequently, valid comparisons between theory and experiment could be performed only for the station immediately downstream of the rotor exit. The calculation, more details of which can be found in refs. (25) and (30), was carried out using the meridional plane flow field issued from a streamline curvature meridional external flow calculation method with no wall shear layer presence. The calculation results describe the shear layer evolution along with the modified external flow field, resulting from the approximate interaction procedure incorporated in the secondary flow calculation itself. No additional (second) iteration was performed using the external flow calculation. Fig.(3b) present comparisons between prediction and experimental results for the spanwise evolution of the various flow quantities at the rotor exit. Care has been taken to start the calculation with such shear layer initial conditions, so that matching of predicted quantities and experimental results was ensured at the rotor inlet. Solid lines of the figures represent the pitchwise averaged flow field as computed by the present method. The "stars" represent the results of the external flow field calculation without wall shear layer presence and the squares represent the experimental results. The total temperature was not measured during the experiment. The "experimental" values presented here are all issued from Euler turbine equation considerations.

The agreement between theory and experiment at the rotor exit can be termed quite good. The predicted increase of total temperature inside the shear layer is qualitatively correct. For the reasons evoked above, no quantitative comparison can be made concerning this parameter.

Although comparisons can only be made at the exit station of the rotor, it is interesting to examine the evolution of the velocity field inside the rotating wheel relative to the blading. This evolution is presented in Fig.(4) for four calculated stations (47%, 73%, 87% and 100% of the meridional chord). Good inlet and outlet flow field agreement gives a good chance that the evolution presented in Figure (4) represents reality.

The above presented comparison demonstrates that the secondary flow losses and secondary vorticity have been well predicted. In addition the wall shear layer combined meridional and peripheral blockage effect was correctly estimated, although small. No correction for the presence of the suction side corner vortex seems to be here necessary, while peripheral non-uniformities seem to contribute little.

We consider next the flow fields of two axial flow compressor stages. The first of these, ECL1, is transonic (schematic representation in Fig.(5a), along with the measurement stations) and the second one, ECL3, is supersonic (schematic representation in Fig.(5b), along with the measurement stations). Both possess inlet guide vanes. Reference (34) gives details about the measurements and the experimental set up for the compressor ECL1, while corresponding information about compressor ECL3 can be found in ref.(35). More details about the comparisons presented here can be found in refs (24) and (31). Both wall shear layer calculations were based on the meridional external flow field issued from a meridional flow calculation performed with no wall shear layer blockage. The calculation results describe, as previously, the shear layer evolution along with the modified external flow field, resulting from the approximate interaction procedure incorporated in the secondary flow calculation itself. No additional (second) iteration was performed using the external flow calculation. Figures (6) to (8) present some comparisons between prediction and experimental results for the spanwise evolution of certain flow quantities at the rotor and stator exits. Again, solid lines of the figures represent the pitchwise averaged flow field as computed by the present method. The "stars" represent the results of the external flow field computation without wall shear layer presence and the squares represent the experimental results.

At the exit of the rotor of compressor ECL1, agreement between computed and experimental results can be termed quite good (Fig.(6a)). The well predicted overall blockage is quite important and one can remark the changes due to the peripheral blockage both upon the flow angle and the energy level at the rotor exit. The details of the shear layers are relatively well predicted, especially the exit flow angle. Still, the total temperature level inside the shear layers is underestimated, indicating that the computation of the lost work needs reexamination.

It is interesting to note that the real flow static pressure distribution follows closely that of the external flow.

At the exit of the stator, agreement between computed and experimental results is good (Fig.(6b)). The external flow quantities agree well with the real ones inside the "inviscid" flow region, so that the same remark as before can be made for the overall blockage prediction. The details of the wall shear layers are well predicted. We can observe the same discrepancy for the total temperature value, as for the rotor exit station. The same reasons are advanced.

In Fig.(7a), the evolution of the velocity field inside the rotor is examined as it was done for the radial compressor case. Again good inlet and outlet flow field agreement gives a good chance that this evolution represents reality.

The comparisons presented above concern the meridional/peripheral velocity fields and the longitudinal one. Other approaches, though, utilize secondary vorticity and the corresponding transverse velocity profile. A comparison of computed and experimental results for such a profile is presented in Fig.(7b) for the exit of the rotor. The agreement is good and one can remark the important difference, which exists between the initial and modified (by the combined effect of the meridional and peripheral blockage) transverse external flow field.

Comparisons between theory and experiment at the rotor and stator exits of supersonic compressor ECL3 are presented in Fig.(8). The comparisons are good and the effect of blockage is quite smaller in this case. It is interesting, though, to remark here that, for the calculation of the rotor tip shear layer it was necessary to apply the approximate viscous inviscid interaction procedure to which reference was made in Section 2.

This procedure redistributed the jump in static pressure concentrated in the shock, the position of which was fixed by the external flow calculation. It was in this way that the shear layer calculation could negotiate the static pressure increase of the shock wave. The static pressure distribution along the solid wall, resulting from the viscous inviscid interaction computational procedure, which was actually used for the calculation of the tip wall shear layer, is presented in Fig.(9). It can be seen that the interaction region occupies a good part of the blade axial chord. No experimental results exist to our knowledge, which permit the validation of this part of the computation.

In ref.(38) and (20) approximate methods for the calculation of the development of wall shear layers along rotating bodies of revolution, as well as shear layers that develop along a stationary part followed by a rotating part of a body of revolution, are developed. Full use of these methods in the calculation method described above would improve it in the case of rotating parts inside annular free spaces.

In future years, it is possible that methods solving the three-dimensional Navier-Stokes equations become available. These will not be capable to substitute the meridional flow model approach, which in our opinion will constitute for a long time still if not the exclusive, certainly an intermediate computational tool in the compressor design process. On the other hand, recent investigations, both theoretical and experiment (refs.(40),(41) and (42)) demonstrate that intense mixing takes place in the spanwise direction for multistage machines. Mixing in the peripheral direction (see not only ref.(42) but the discussion that followed the presentation of the paper) is being recognized as an important factor. Finally, merging of the two wall shear layers is currently encountered in both radial and the high pressure part of advanced axial flow compressors.

It is believed that the method presented above may constitute a good test bed for examing appropriate models, which could take into account these additional flow effects. It is also, believed that an extension of this methodology to the turbine case could be proved quite useful for the design engineer.

4. CONCLUSIONS

In this paper the work concerning the development of a secondary flow calculation method, which was done in the Turbomachinery Lab. of the National Technical University of Athens, was presented. An effort was done in order to put it in perspective in respect to work that has been realized before elsewhere.

The method that was described above solves the peripherally averaged flow equations and makes use of the two-zone model. It computes the hub and tip shear layers simultaneously and utilizes an approximate viscous-inviscid interaction calculation procedure, which modifies for blockage the initial external meridional flow field, as the computation marches downstream. In fact, the viscous-inviscid approximate interaction procedure is incorporated in the wall shear layer calculation method, giving it the possibility to match with any external meridional flow calculation, even when flow separation is present. In addition, this approximate procedure gives to the external flow meridional streamlines the possibility to be displaced during the viscous flow calculation, which uses as coordinate system the initial external streamlines and their normals.

An improved two-zone model is proposed, which introduces the notion of the peripheral blockage. This notion is beneficial in more than one way. External and internal flow problems are treated on a common basis and a clearer definition of each wall shear layer is possible, facilitating computations which involve changes in coordinate systems (absolute to relative and vice-versa). New matching conditions are developed and difficulties at inlet and exit of blade rows are avoided.

Instead of the traditional secondary vorticity, the meridional component is used, the transport of which is computed taking into account viscous terms. The corresponding peripheral velocity profile is derived through a simple quadrature.

The total kinetic energy equation has substituted the entrainment equation used until now. Although this equation is not as easily applicable, it seems that its use improves calculation results, allowing at the same time the possibility to treat the case of merging wall shear layers.

The method was applied to various cases, for which experimental results were available. A highly loaded compressor cascade was considered first, followed by one radial compressor and two one-stage axial compressor cases. The wall shear layer calculation was performed using as external flow field the one resulting from "inviscid" flow calculations without wall blockage. Comparison between computed and experimental results was good. It made it clear that the viscous shear layer calculation method was capable to compute correctly the blockage effects, demonstrating the importance of the peripheral part of the blockage. In addition, a good description of the details of the wall shear layers was obtained.

REFERENCES

1 RAILLY,J.W., HOWARD,J.H.G.,"Velocity Profiles Development in Axial Flow Compressors", Journal of Mechanical Engineering Science, Vol.4, June 1962.

2 MELLOR,G.L., WOOD,G.M.,"An Axial Compressor End-Wall Boundary Layer Theory", Journal of Basic Engineering, Vol.93.

3 SMITH,L.H.,"Casing Boundary Layers in Multistage Compressors Proceedings", Symposium on Flow Research on Blading, Brown Boveri Ltd., Baden, Switzerland, 1969.

4 MELLOR,G.L., BALSA,T.S., "The Prediction of Axial Compressor Performance with Emphasis on the Effect of Annulus Wall Boundary Layers", AGARD AG-164, 1972.

5 PAPAILIOU,K.D., ROBERTS,B., "On the behaviour of Blading in the Small Reynolds Number Regime", ASME Paper 70-WA-G-II, 1970.

6 FLOT,R., PAPAILIOU,K.D.,"Ecoulements Secondaires dans les Compresseurs Axiaux", IIe Colloque d'Aerodynamique Applique, AAAF, 1974.

7 PAPAILIOU,K.D., FLOT,R., MATHIEU,J.,"Secondary Flows in Compressor Blading", ASME Paper 76-GT-57, 1976, ASME Trans., Journal of Engineering for Power, Vol.99, pp 211-229, 1977.

8 BOIS,G., LEBOEUF,F.,COMTE,A.,PAPAILIOU,K.D.,"Experimental Study of the Behaviour of Secondary Flows in a Transonic Compressor", AGARD CP-214, 1977.

9 LEBOEUF,A., COMTE,A., PAPAILIOU,K.D.,"Calculation Concerning the Secondary Flows in Compressor Bladings", AGARD CP-214, 1977.

10 BOIS,G.,VOUILLARMET,A., DUCHEMIN,J., PAPAILIOU,K.D.,"Analyse Experimentale de l'Ecoulement dans un Etage de Machine Centrifuge", Presente au "Centrifugal Compressors, Flow Phenomena and Performance", AGARD Congress 7-9 May 1980, AGARD CP 282.

11 COMTE,A., OHAYON,G., PAPAILIOU,K.D.,"Method for the Calculation of the Wall Shear Layers Inside the Passage of a Compressor Cascade with and without Tip Clearance", ASME Paper 81-GT-168, ASME Trans., Journal of Engineering for Power, Vol.103/3, 1981.

12 BARIO,F.,LEBOEUF,F., PAPAILIOU,K.D.,"Study of Secondary Flows in Blade Cascades of Turbomachines", ASME Paper 81-GR/GT-3, ASME Trans. Journal of Engg. for Power, pp 497-503, 1982.

13 VOUILLARMET,A., PAPAILIOU,K.D., BOIS,G.,"Experimental Analysis and Theoretical Approach for the Three Dimensional Viscous Flow in a Centrifugal Compressor", presente au "Symposium on Energy and the Environment", Patras University, 1981.

14 BOIS,G.,LEBOEUF,F.,COMTE,A.,PAPAILIOU,K.D.,"Measurements of Secondary Flows in a Transonic Axial-Flow Compressor, Measuring Techniques in Transonic and Supersonic Cascades and Turbomachines", Editor: A.Bolcs and T. Fransson, Proc. of the Symp. held in Lausanne on Nov. 18-19, 1976.

15 LEBOEUF,F.,BARIO,F.,BOIS,G.,PAPAILIOU,K.D.,"Experimental Study and Theoretical Prediction of Secondary Flows in a Transonic Axial Flow Compressor", ASME Paper 82-GT-14.

16 LEBOEUF,F., "Computation of Secondary Flows in an Axial Flow Compressor including inviscid and viscous Flow Computation", ASME Paper 84-GT-244, Amsterdam, 1984.

17 BOIS,G., VOUILLARMET,A.,"Analyse de l'Ecoulement Delivré par le rouet d'un compresseur Centrifuge", AAAF, 21eme Colloque d'Aerodynamique Appliquée, Ecully, Nov. 1984.

18 VOUILLARMET,A.,"Contribution à l'Etude et à la Comprehension de l'Ecoulement Visqueux dans un Compresseur Centrifuge", Thèse de Docteur Ingénieur, Ecole Centrale de Lyon, 1979.

19 HAWTHORNE,W.R.,"The Applicability of Secondary Flow Analysis to the solution of internal flow problems, Fluid Mechanics of internal flow", edited by G. Sovren, Elsevier Publ., Co., 1967.

20 PAVIS,S.,KTENIDIS,P.,PAPAILIOU,K.D.,"Boundary Layer Development Passing from a Stationary to a Rotating Axisymmetric Surface", presented in the 8th ISABE International Symposium, Cincinnati, Ohio, 1987.

21 HORLOCK,J.H.,"Cross Flow in Bounded Three-Dimensional Turbulent Boundary Layers", Cambridge Univ., GUED/A, Turbo/TR28, 1971.

22 JOHNSTON,J.P., "The Turbulent Boundary Layer in a plane of symmetry in a Three-Dimensional Flow", Journal of Basic Engg., ASME Transactions, Series D, Vol. 82, No 3, Sept. 1960.

23 LAKSHMINARAYANA,B.,"Methods of Predicting the Tip Clearance Effects in Axial Flow Turbomachinery", Journal of Basic Engg., ASME Transactions, Vol.92, 1970.

24 KALDELLIS,J.,"Shock/Secondary Flow Interaction in Modern Axial Flow Compressors", Ph.D. Thesis, NTUA, 1988.

25 DOUVIKAS,D.,"Secondary Flows in Radial Compressors", Ph.D. Thesis, NTUA, 1988.

26 KOTIDIS,P.,CHAVIAROPOULOS,P.,PAPAILIOU,K.D.,"An Investigation of the Transverse Velocity Profile in the Case of Internal Viscous Aerodynamic Problems", ASME Paper 84-GT-60, 1984.

27 DOUVIKAS,D., KALDELLIS,J.,PAPAILIOU,K.D.,"The Circumferential Velocity Profile for Secondary Flow Calculations", ASME Paper 87-GT-255, 1987.

28 HARLAFTIS,S.,LEBOEUF,F.,PAPAILIOU,K.D.,"Experimental and Theoretical Investigation of Turbulent Asymmetric Shear Layer Interaction in a Two-Dimensional Smooth Wall Passage", ASME, 106th WAM, Nov. 1985.

29 KALDELLIS,J.,DOUVIKAS,D., PAPAILIOU,K.D.,"A Secondary Flow Calculation Method Based on the Meridional Vorticity Transport Equation", ASME Paper 88-GT-260, 1988.

30 DOUVIKAS,D.,KALDELLIS,J.,PAPAILIOU,K.D., "A Secondary Flow Calculation Method for one stage centrifugal Compressor", Paper to be presented in 9th Intern. Society of Air Breathing Engines (ISABE), Athens, September 1989.

31 KALDELLIS,J., DOUVIKAS,D., FALCHETTI,F., PAPAILIOU,K.D.,"A Secondary Flow Calculation Method for One Stage Axial Transonic Flow Compressors, Including Shock-Secondary Flow Interaction", Paper to be presented at the 1989 ASME IGTI, Toronto, Canada Accepted for publication in the ASME-Transactions.

32 PANARAS,A.G., INGER,G.R.,"Transonic Normal Shock Turbulent Layer Interaction in Pressure Gradient Flows", ASME Paper 77-GT-34, 1977.

33 KALLAS,J.,"Shock/Boundary Layer Interaction , Ph.D. Thesis, NTUA, 1987.

34 LEBOEUF,F., NAVIERE,H., "Etudes Experimentales et Theoriques des Couches Visqueuses Pariêtales dans un Compresseur monoètage trannsonique", AGARD CP 351, Paper 20.

35 GOUTINES,M., NAVIERE,H.,"Conception et Essais d'un Etage de Tête d'un Compresseur HP Avance", in Advanced Technology for Aero Gas Turbine Components, AGARD CP-421, Paris, 1987.

36 PAPAILIOU,K.D.,"A Contribution to the Calculation of Secondary Flows in an Axial Compressor", Proc. 6th Intern. Symposium of Air Breathing Engines (ISABE), Paris, June 1983.

37 BOIS,G.,PAPAILIOU,K.D.,"A Contribution to the Study of the Study of the Design of an Industrial Centrifugal Compressor", ASME Paper 84-GT-60, 1984.

38 LAMBROPOULOS,L., KTENIDIS,P., PAPAILIOU,K.D.,"Boundary Layer Development on Rotating Bodies of Revolution", Proceedings Symposium AGARD sur "Les Effets Visqueux dans les Turbomachines", Copenhagen, June 1983, AGARD CP 351.

39 SOCKOL,P.M., "End-Wall Boundary Layers Prediction for Axial Compressor", AIAA Paper 78-1139, 1978.

40 GALLIMORE,S.J., "Spanwise Mixing in Multistage Axial Flow Compressors:Part II-Through-Flow Calculations Including Mixing", ASME Paper 86-GT-21, 1986.

41 ADKINS,G.G., SMITH,L.H.,"Spanwise Mixing in Axial-Flow Turbomachines", Journal of Engg. for Power, Vol.104,1982.

42 WISLER,D.C.,BAUER,R.C.,OKIISHI,T.H.,"Secondary Flow, Turbulent Diffusion and Mixing in Axial-Flow Compressors", ASME Journal of Turbomachines, Vol.109, October 1987.

43 BROCHET,J., FALCHETTI,F.,"Secondary Flow Computation in Multistage Axial Flow Compressors", 8th ISABE, Cincinnati, Ohio, 1987.

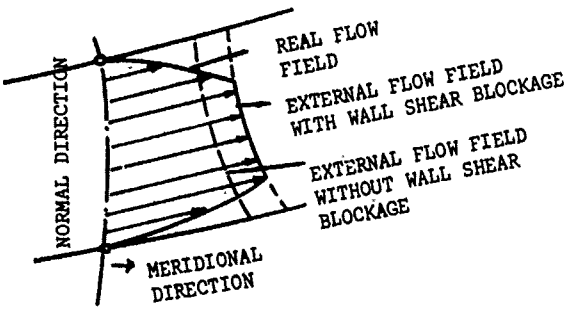
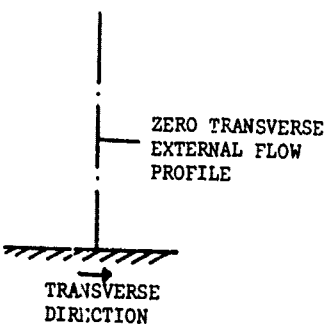
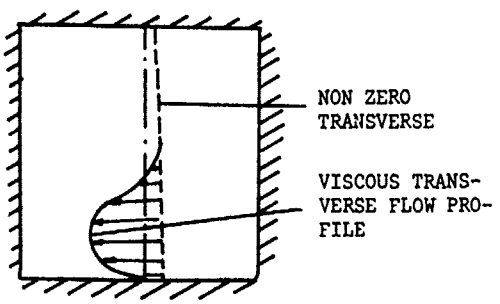


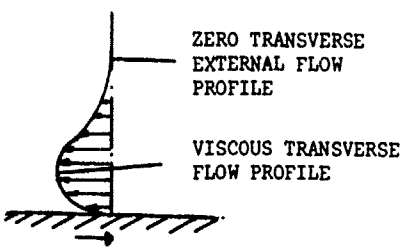
FIG.1a Circumferentially averaged meridional real flow velocity profile and corresponding external flow one modified by blockage effects, considered at the same station. The two-zone model is built up matching the static pressure field of the "inviscid" external and the real flow fields. In addition the circumferentially averaged meridional external flow velocity profile without wall shear layer blockage in presented.



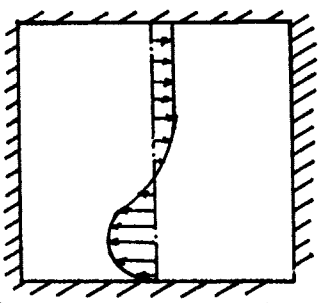
(a) When an inviscid calculation is performed, the corresponding transversa velocity is taken by definition equal to zero.



(b) When a circumferentially mean transverse viscous velocity profile appears in a fully bounded space, the external flow is perturbed and reacts. This "reaction modifies the admitted external flow angle and the static pressure.



(c) When a transversa velocity profile appears in an unbounded space the external flow field is not perturbed by its presence.



(d) Previously, the total velocity field modification in the transverse direction was attributed to the transverse viscous velocity profile. S-shaped transverse velocity profiles were, thus, constructed. In this manner, the kinetic energy of the viscous shear layer was artificially increased, as well as its total energy, because the static pressure in the longitudinal is taken equal with that of the transverse direction.

FIG.1b Schematic Explanation of the Transverse Blockage Effect as Considered in the Present Work.

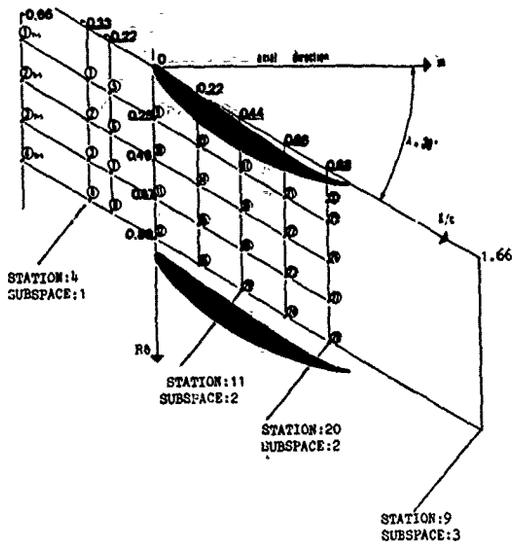
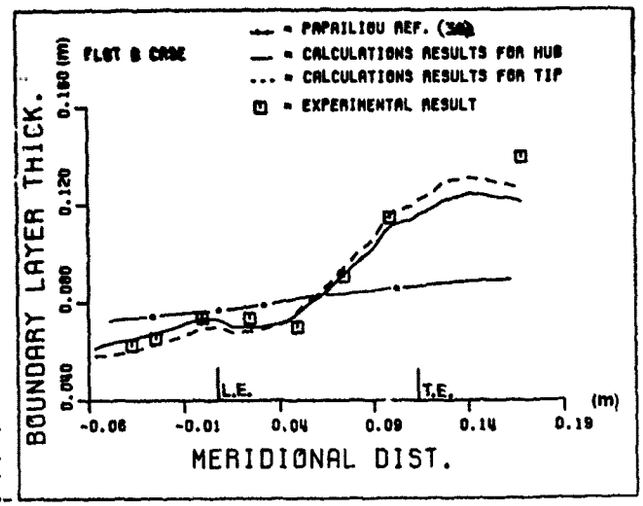
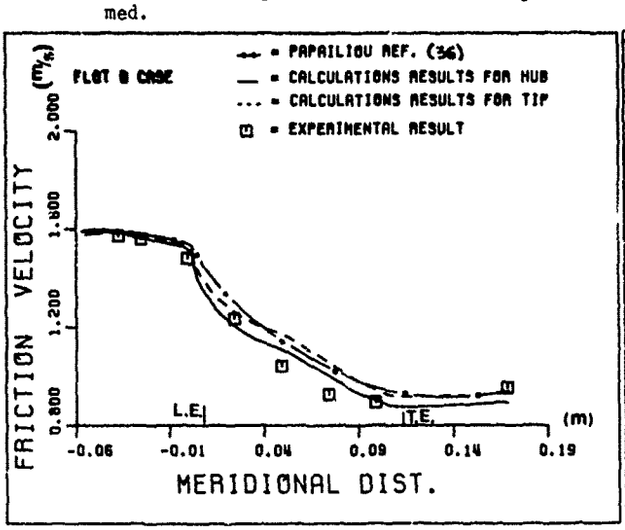
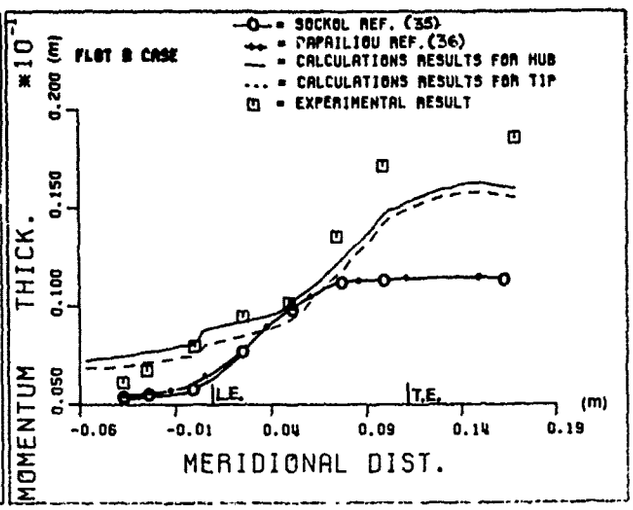
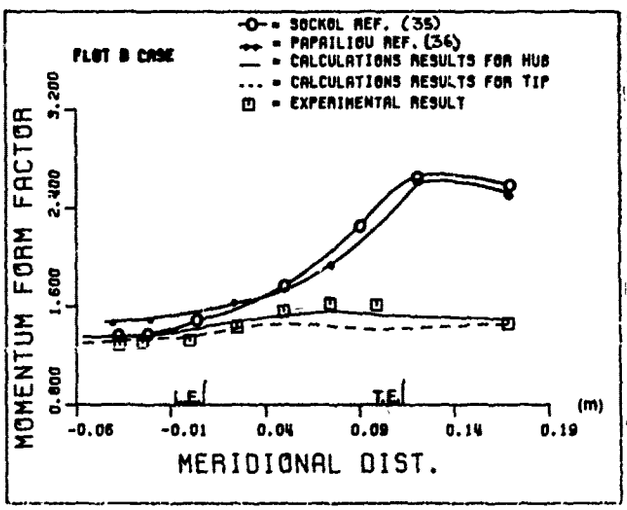


FIG.2a The Schematic representation of the experimental cascade indicating the computational stations, where the comparison of the theoretical and experimental results was performed.









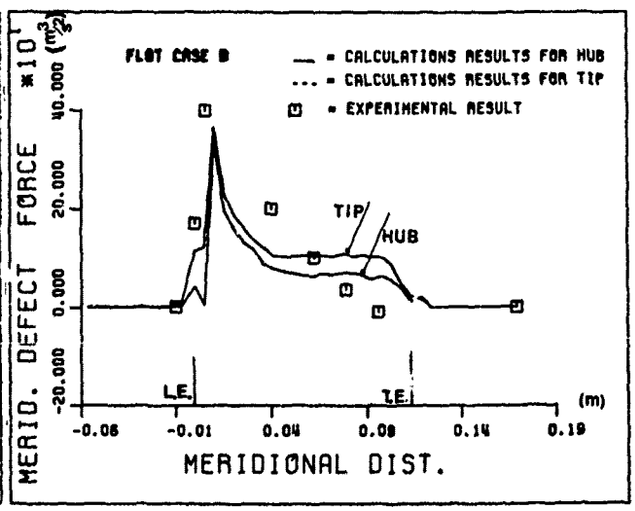
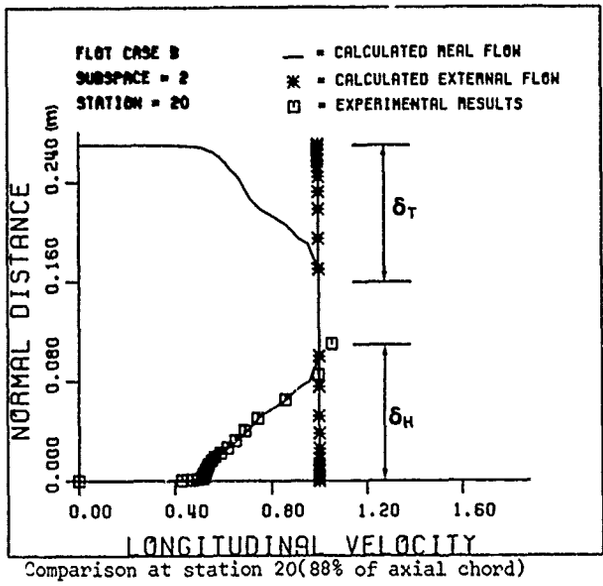
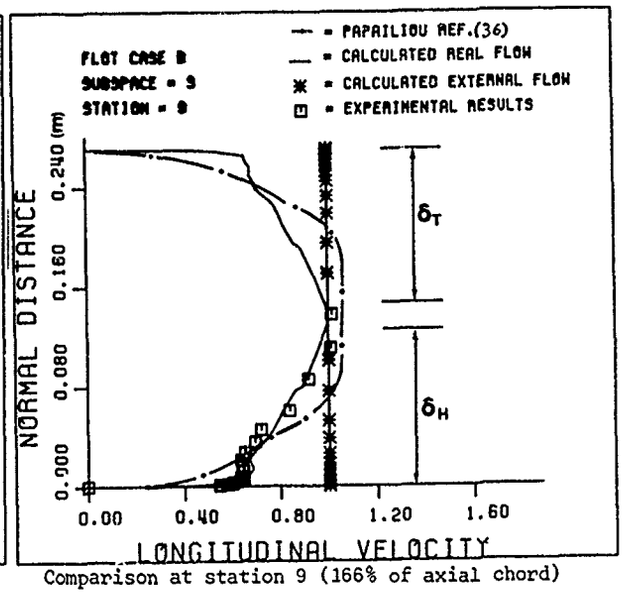


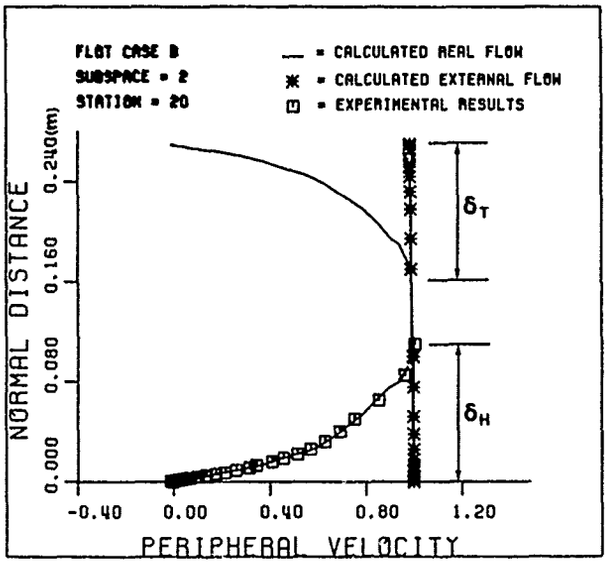
FIG.2b Comparison between calculation and experiment. Overall shear layer quantities.



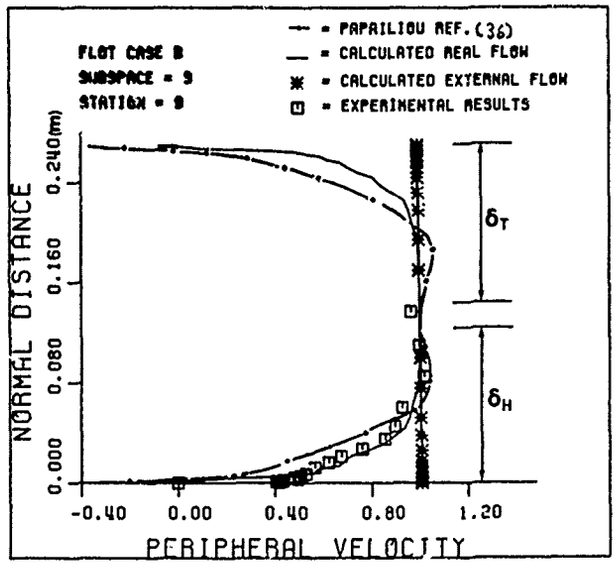
Comparison at station 20(88% of axial chord)



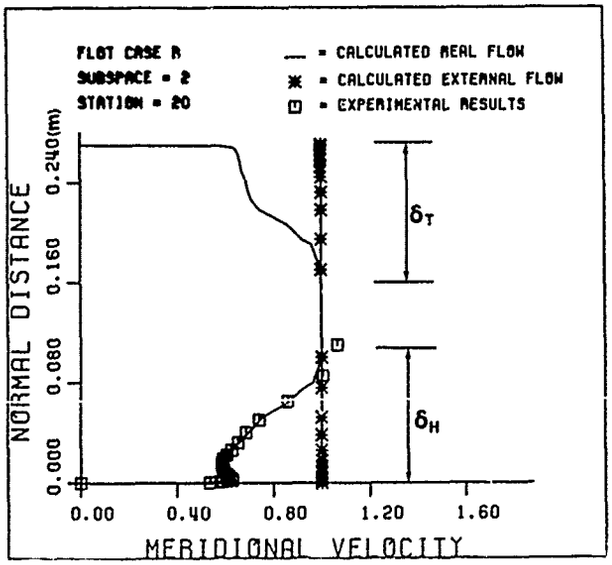
Comparison at station 9 (166% of axial chord)



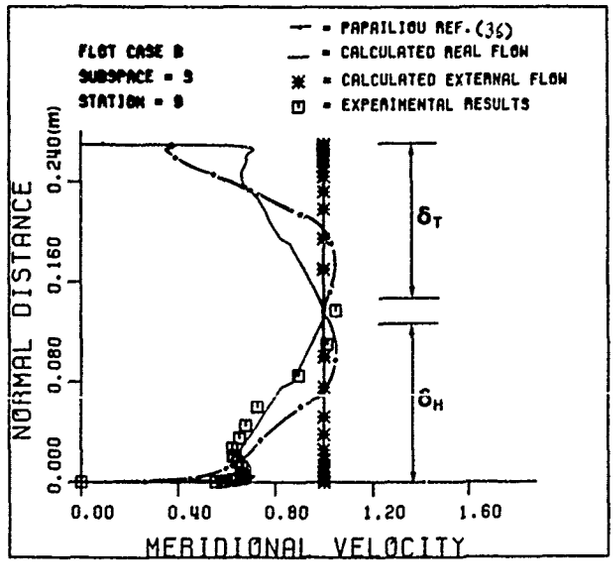
Comparison at station 20 (88% of axial chord)



Comparison at station 9 (166% of axial chord)



Comparison at station 20(88% of axial chord)



Comparison at station 9 (166% of axial chord)

FIG.2c Comparison between theory and experiment. Meridional, peripheral and longitudinal velocity profiles at given stations of Fig.2b. Nondimensional quantities are presented on the basis of the corresponding external flow velocity component.

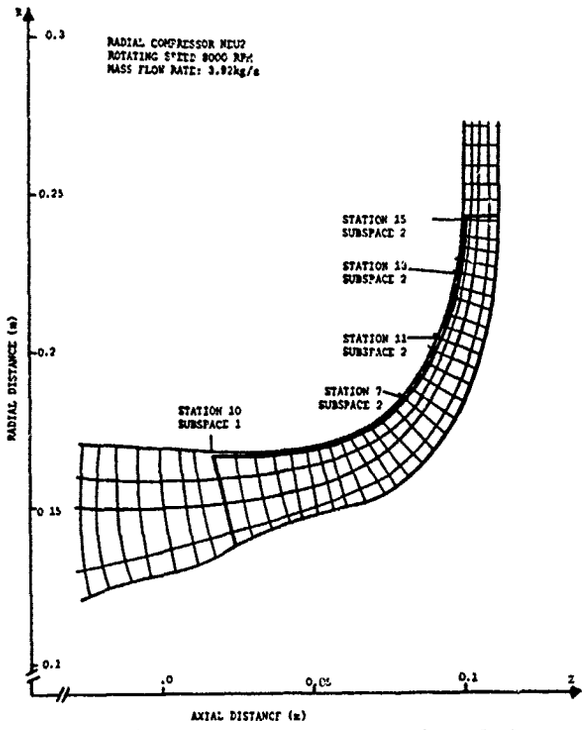
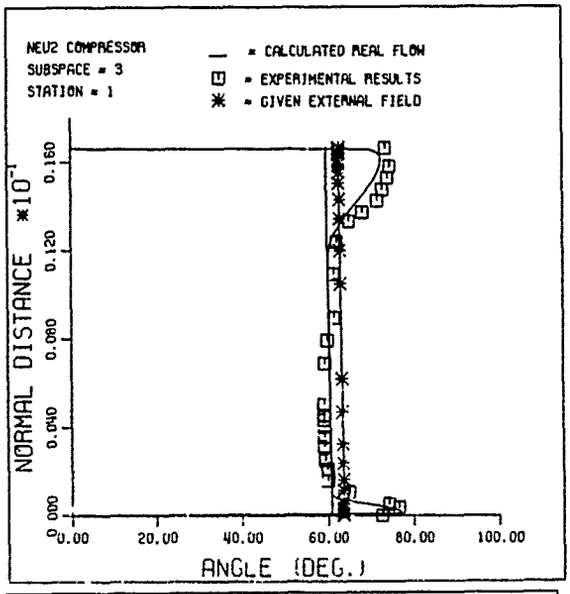
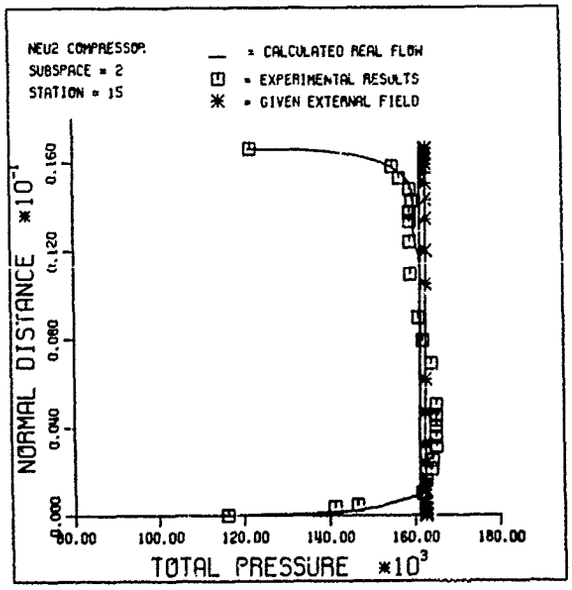
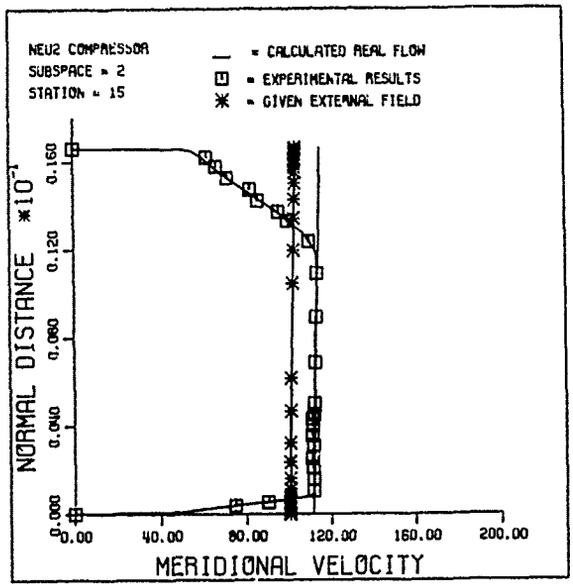
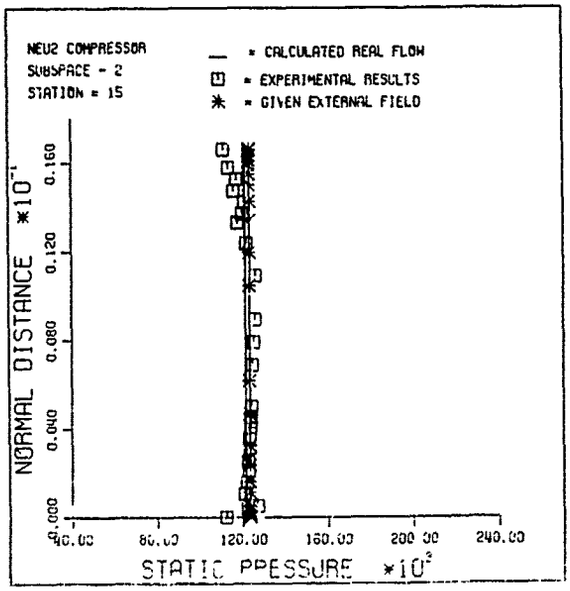


FIG.3a Meridional plane representation of the radial compressor NEU2 where the computation stations are present.









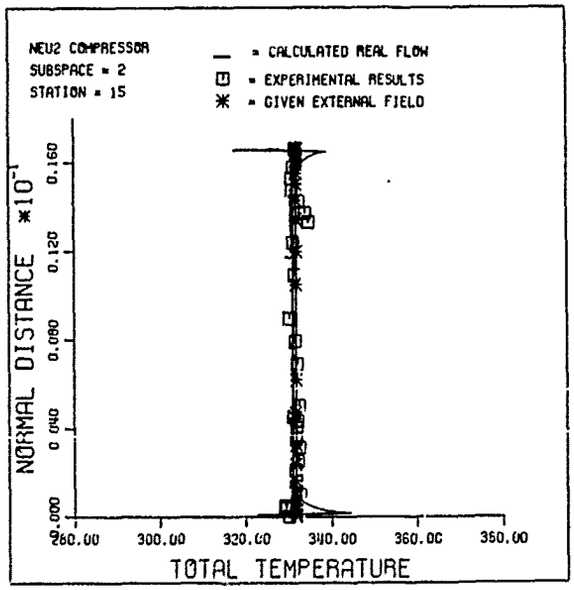
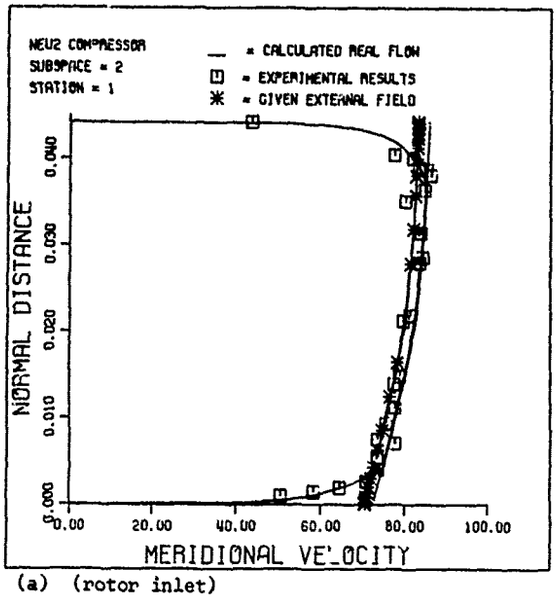
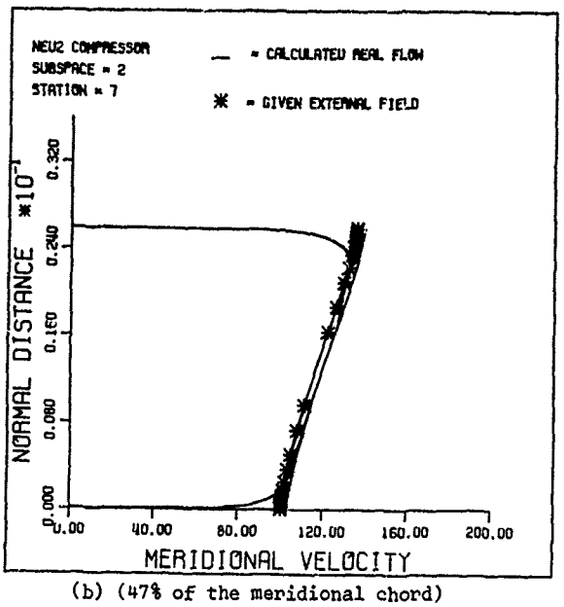


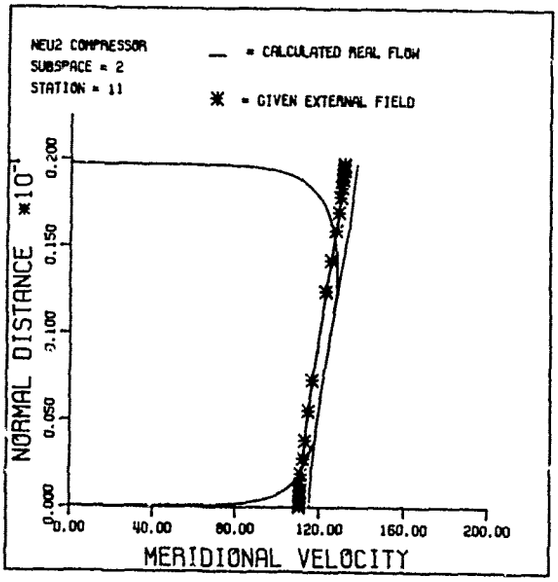
FIG.3b Comparison between theory and experiment at radial rotor exit (station 15, subspace 2, Fig.3a))



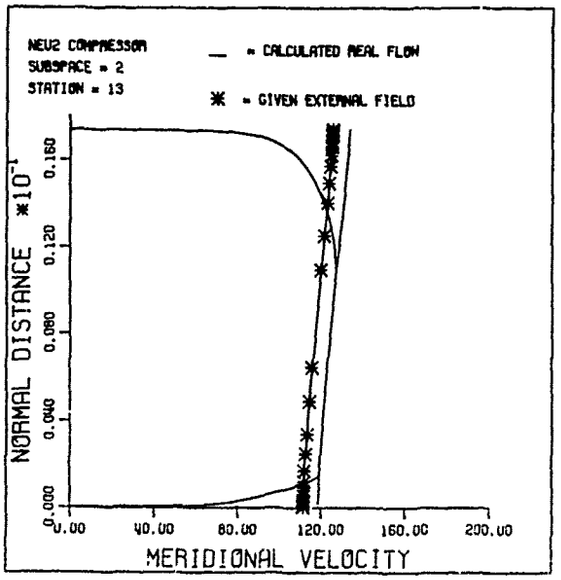
(a) (rotor inlet)



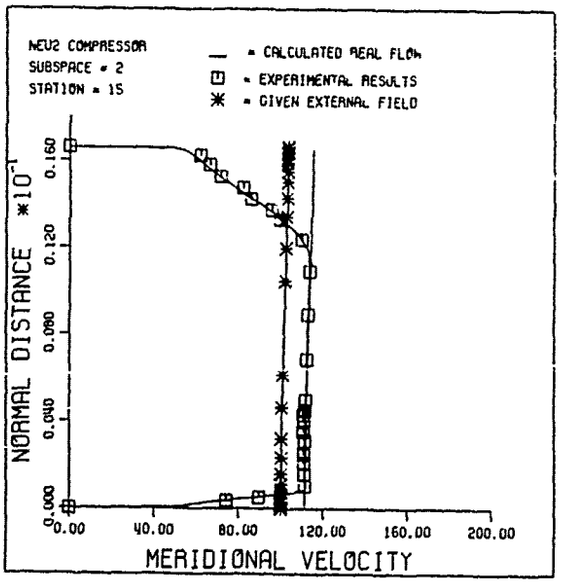
(b) (47% of the meridional chord)



(c) (73% of the meridional chord)



(d) (87% of the meridional chord)



(e) (rotor exit)

FIG.4 Evolution of the meridional velocity profiles inside the rotor of the radial compressor.

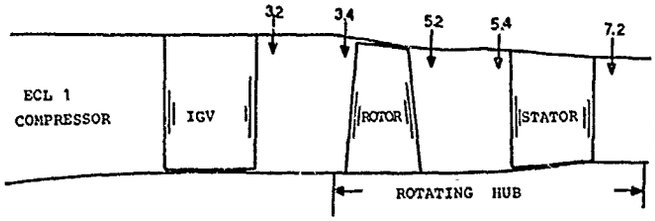


FIG.5a Schematic Representation of the ECL1 Transoni Axial Compressor (Meridional Plane)

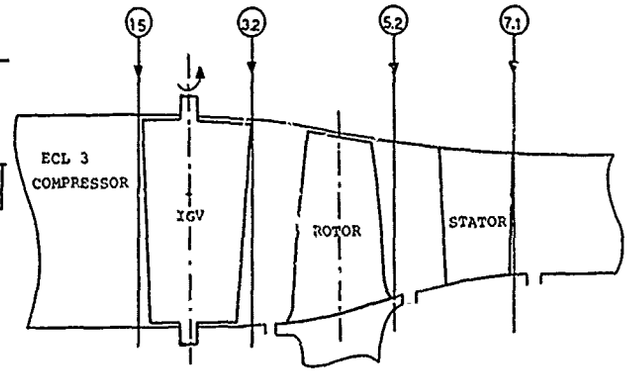
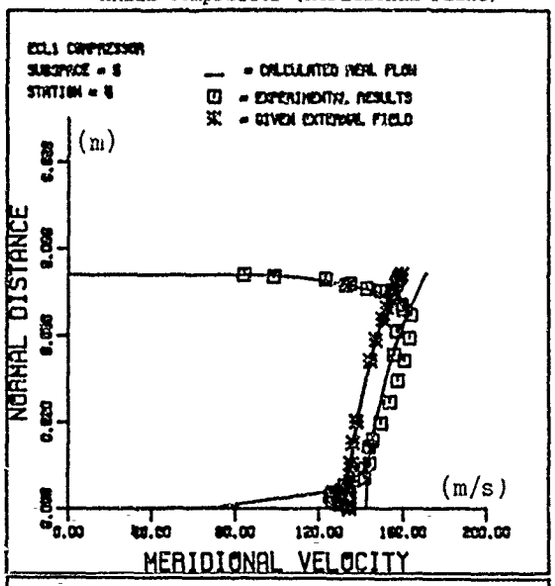
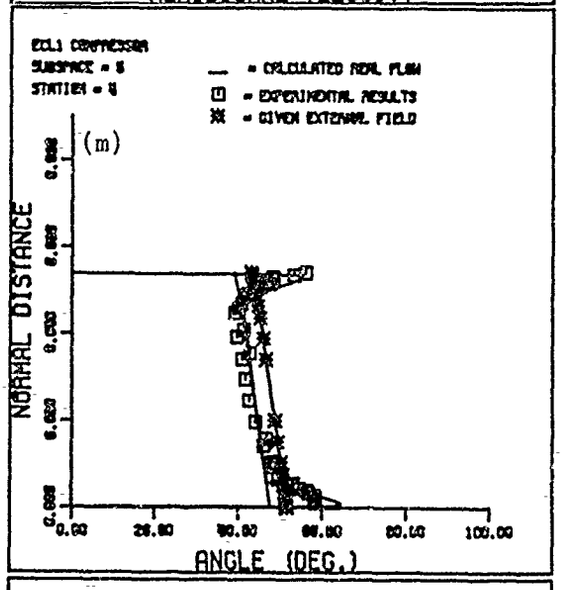
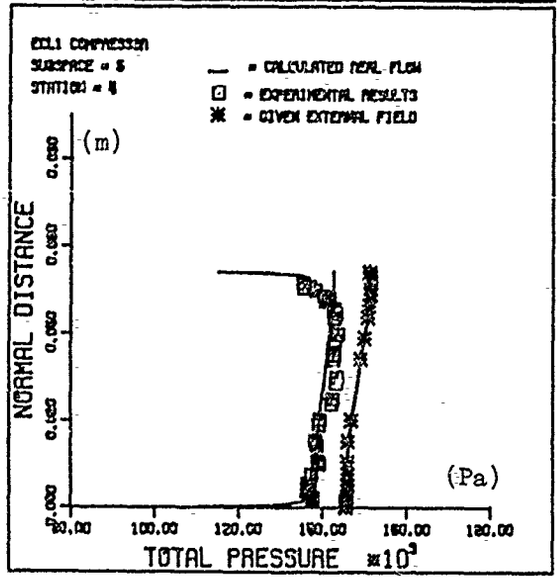
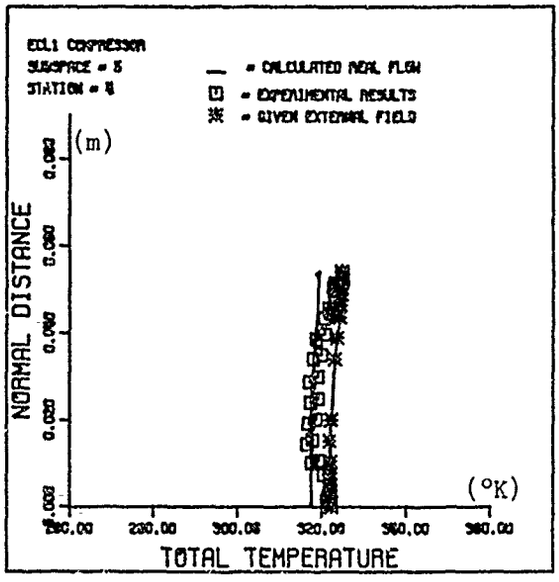


FIG.5b Schematic Representation of the ECL3 Supersonic Axial Compressor (Meridional plane)









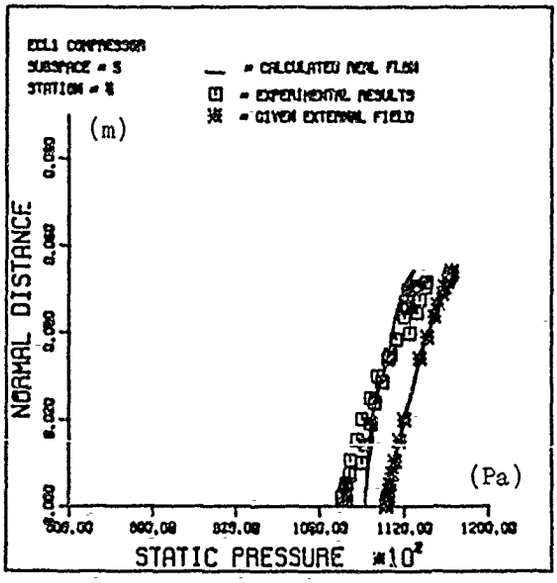
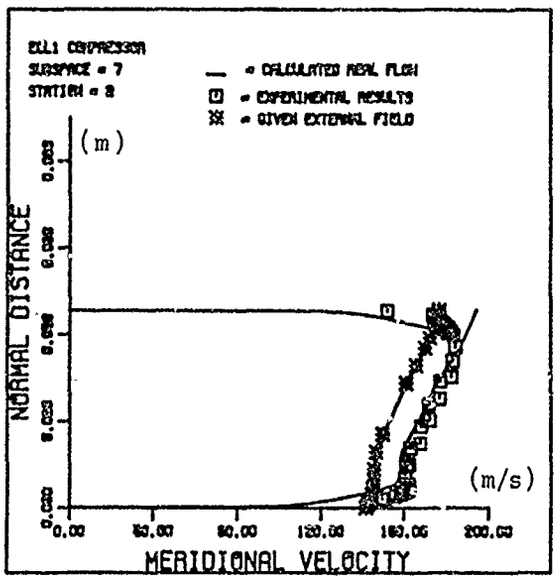
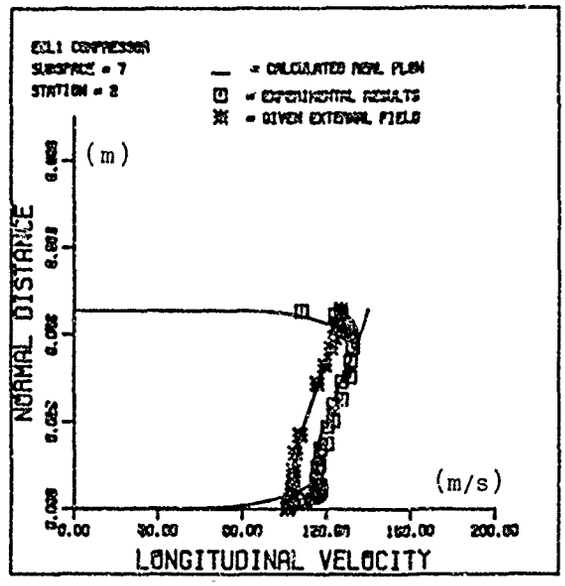
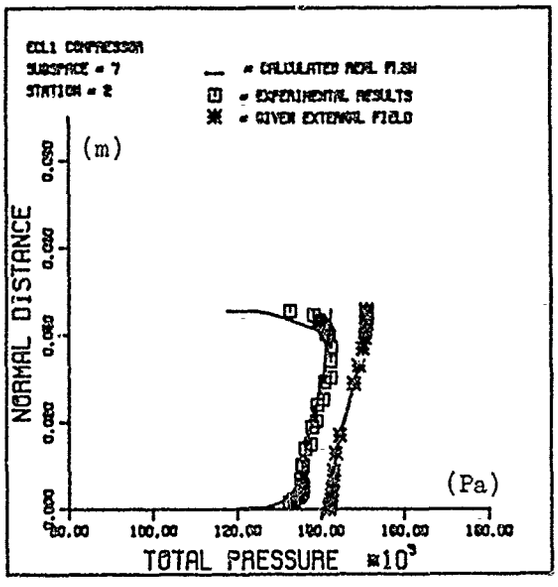
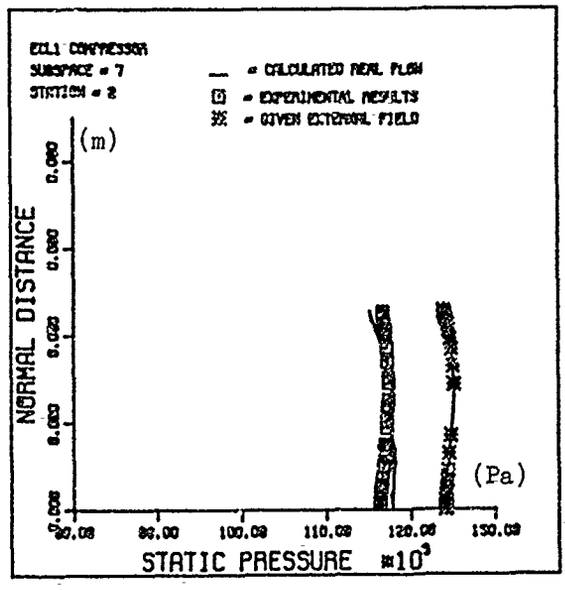


FIG.6a Comparison between theory and experiment, at the exit of the rotor.(Station 5.4, Fig.(5a)).









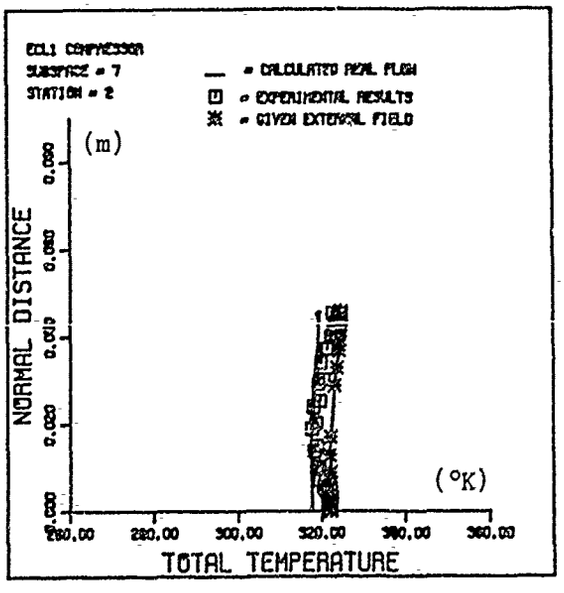


FIG.6b Comparison between theory and experiment, at the exit of the stator. (Station 7.2, Fig.(5a)).

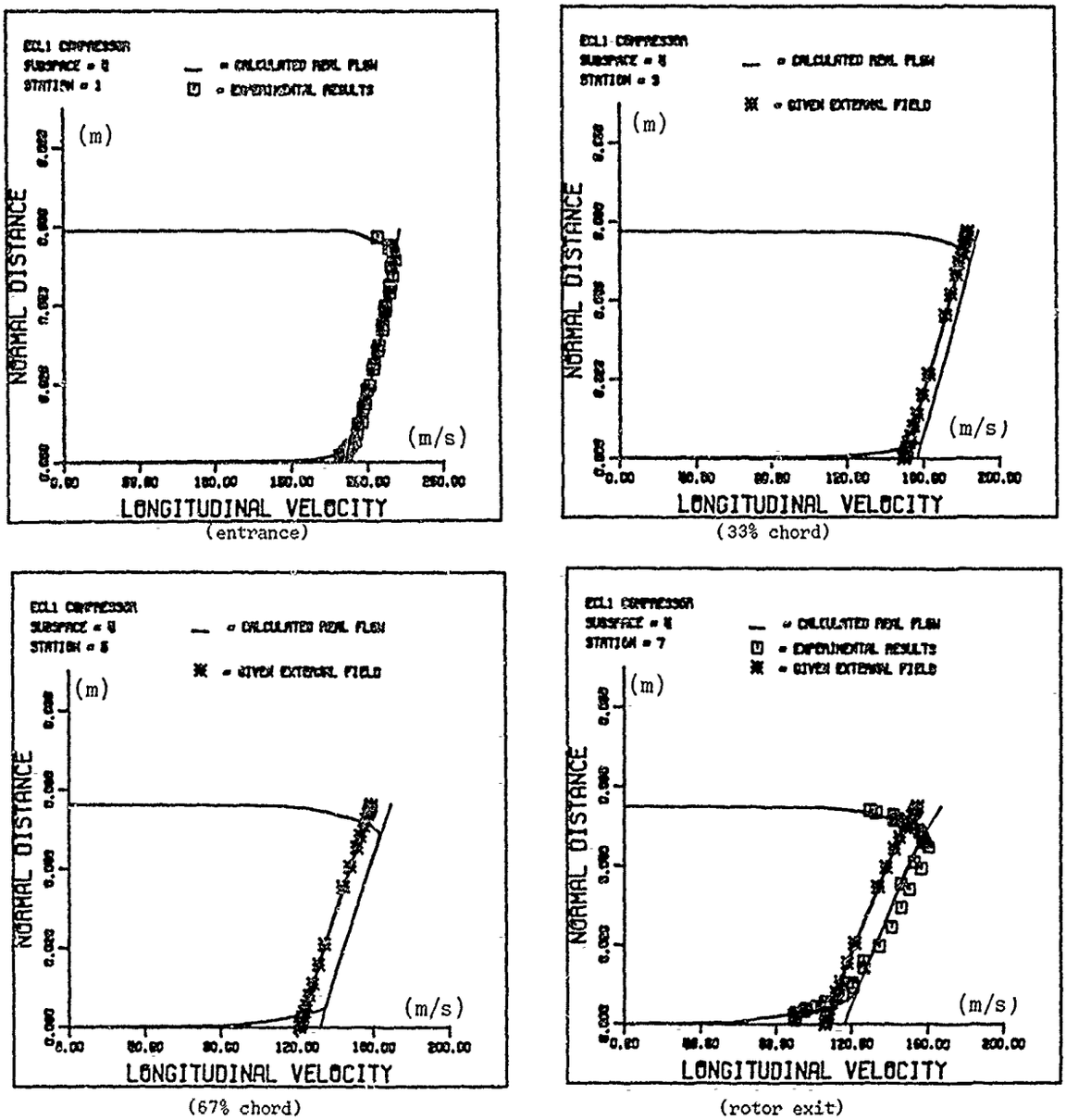


FIG.7a The Evolution of the Longitudinal Velocity Profiles Inside the Rotor. (Relative to the blading coordinate system of reference)

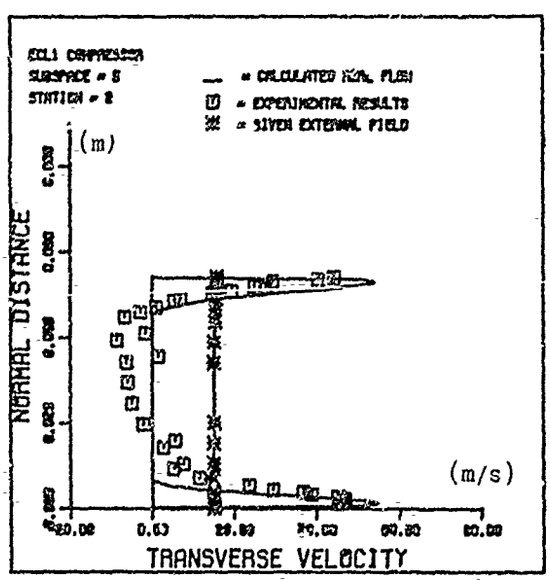
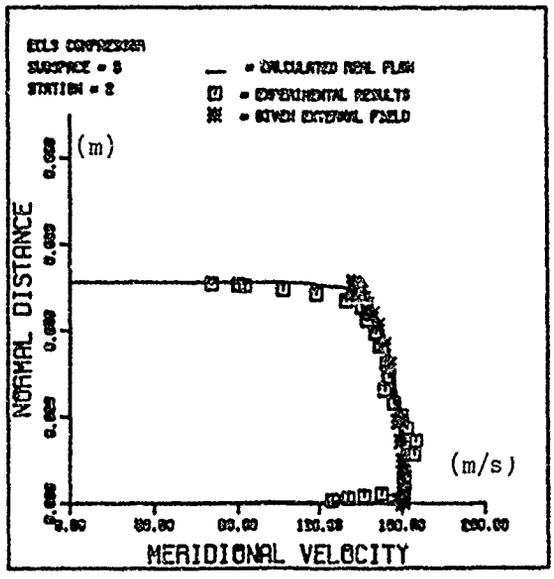
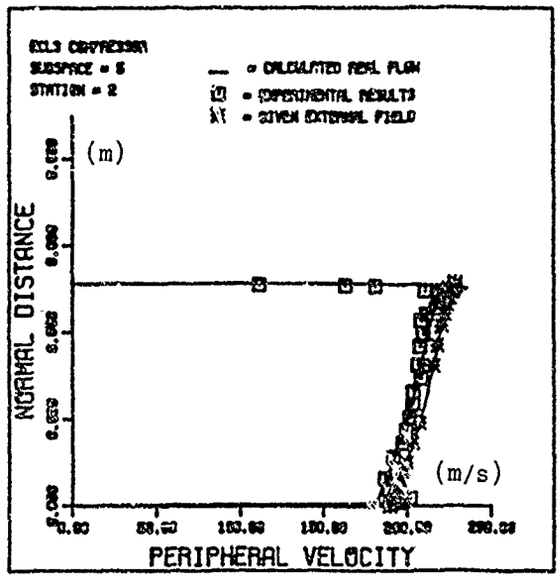
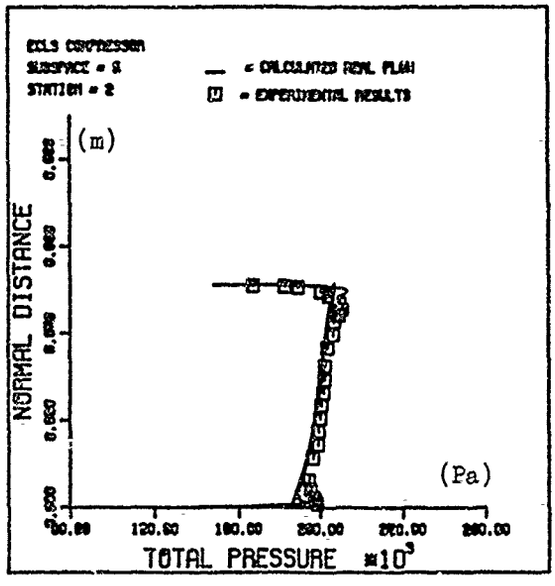
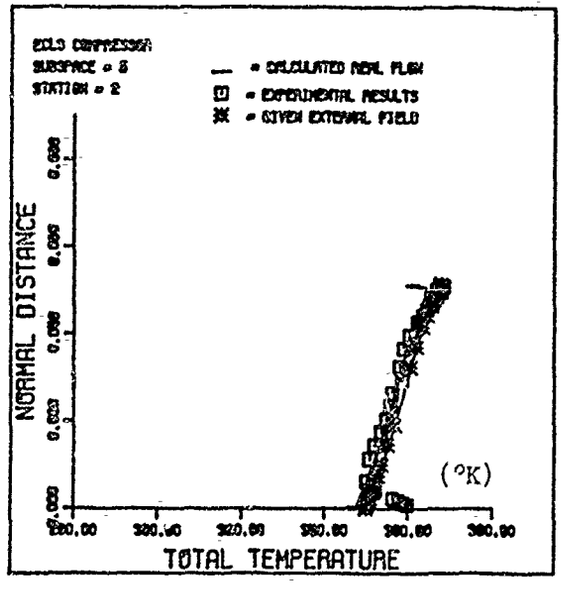


FIG.7b Comparison between theory and experiment. Transverse Velocity Profile at the exit of the rotor.









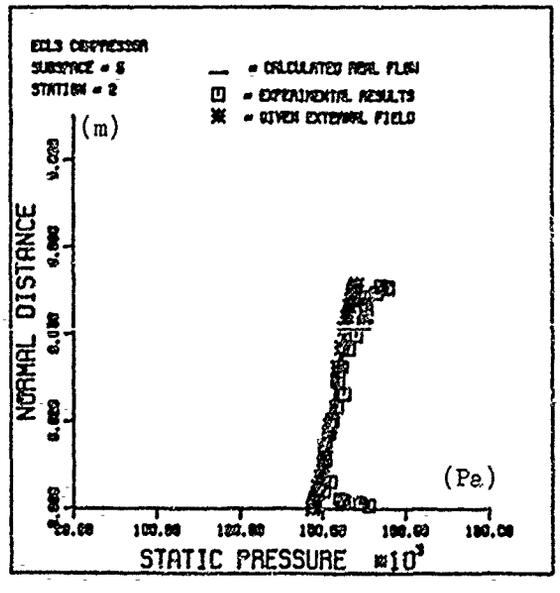
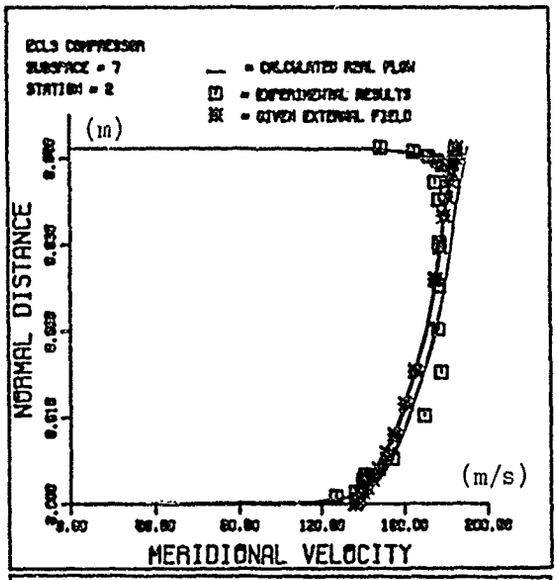
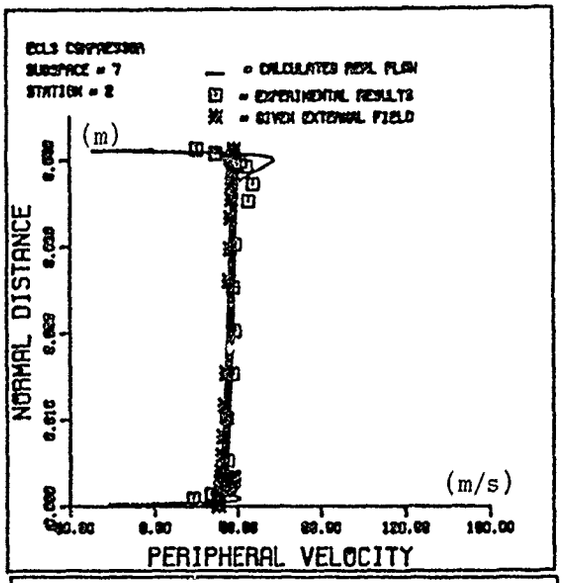
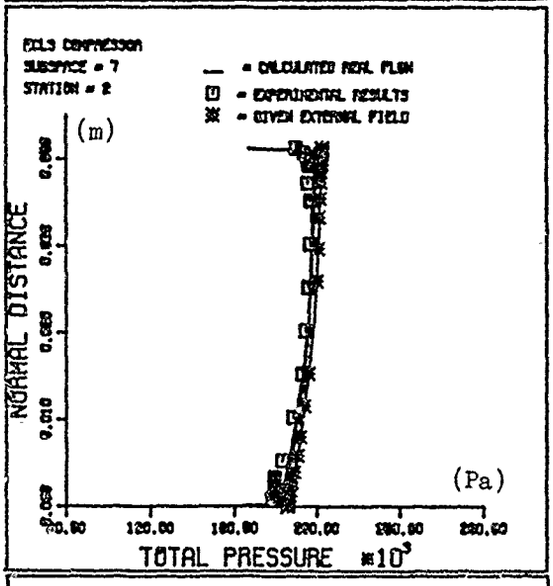
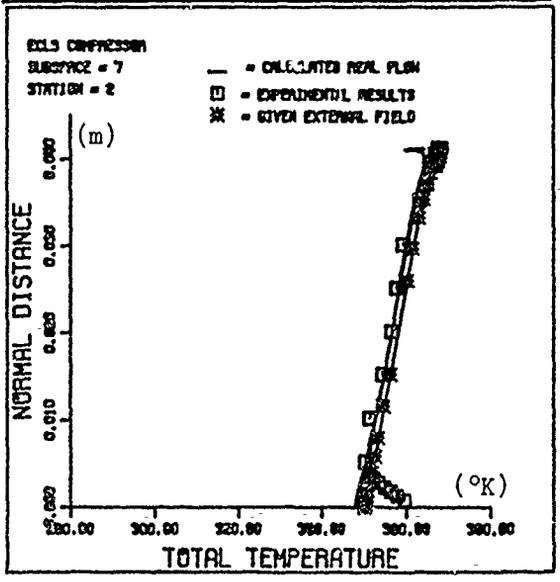


FIG.8a Comparison between theory and experiment at the exit of the rotor (Station 5.2, Fig. (5b))









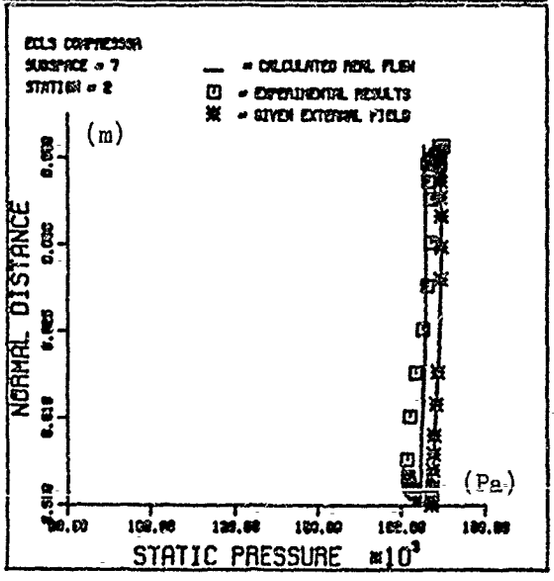


FIG.8b Comparison between theory and experiment at the exit of the stator. (Station 7.2, Fig.(5b))

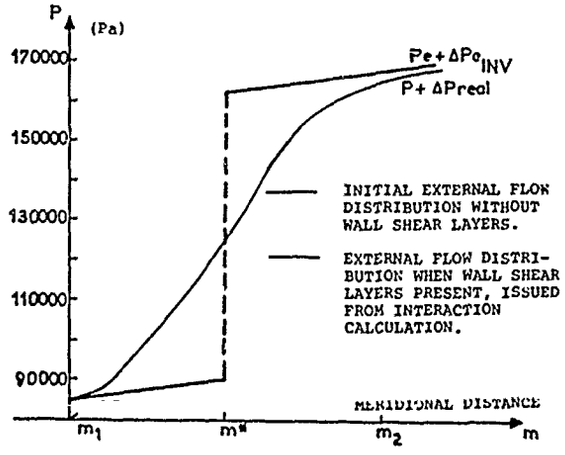


FIG.9 Inviscid Wall Static Pressure Distribution Inside the Shock - Secondary Flow Interaction Region near the Tip.
$m=m_2$ AT 25% of Axial Chord
$m=m_2$ AT 75% of Axial Chord

The Numerical Simulation of Multistage Turbomachinery Flows

J. J. Adamczyk
National Aeronautics and Space Administation
Lewis Research Center
Cleveland, Ohio 44135, U.S.A.

T. A. Beach, M. L. Celestina,
R. A. Mulac, and W. M. To
Sverdrup Technology,
Cleveland, Ohio 44135, U.S.A.

Summary

A study is undertaken to assess the need to account for momentum and energy transport by the unsteady deterministic flow field in modeling the time-averaged flow state within a blade row passage embedded in a multistage compressor. It was found that, within the endwall regions, large-scale three-dimensional unsteady structures existed which caused significant transport of momentum and energy across the time-averaged stream surface of a stator flow field. These experiments confirmed that the transport process is dominated by turbulent diffusion in the midspan region. A model was then proposed for simulating this transport process, and a limited study was undertaken to assess its validity.

Introduction

Currently, the flow model most often used in the design and analysis of multistage turbomachinery is based on a quasi-three dimensional representation of the flow field whose origins can be traced back to the early fifties (Smith, Ref. (1)). This model decomposes the flow field into three components; the first of these components is associated with the axisymmetric or through-flow field, the second with the blade-to-blade cascade flow, and the third with the secondary flow field. Each of these flows has been carefully investigated, and no attempt will be made to summarize the extensive literature on these subjects.

The nonaxisymmetric component of the flow field is the result of the blade-to-blade cascade flow and the secondary flow field. The combined effects of the nonaxisymmetric component from both of these flows will be combined in the present work. Smith, Ref. (2), showed that the nonaxisymmetric flow produced a transport of momentum across the axisymmetric stream surfaces. He further showed that this transport process is associated with a stress which he denoted as "g." Based on estimates derived from subsonic cascade theory, Smith concluded that for designs of the time, the effect of this transport process on the through-flow was minimal. Later, Sera and Sera and Kerrobrock, Refs. (3) and (4), reexamined the problem for a high-speed rotor. They showed that the "g" stress, as defined by Smith, contributed to the loss in performance of their rotor, and that it needed to be accounted for. More recently, a paper by Adkins and Smith, Ref. (5), updated Smith's original paper. Their study concluded that significant transport of both momentum and energy across the axisymmetric stream surfaces took place, especially in the rear stages of high-performance multistage machines. They related this transport to the nonaxisymmetric component of the cascade and secondary flow field and developed a mixing model to account for the transport process.

The subject was further studied by Galimore, Ref. (6), and Galimore and Cumsty, Ref. (7). They also concluded, based on experimental measurements taken in a multistage research compressor, that significant transport of both momentum and energy across axisymmetric stream surfaces occurred, but that the transport process was due to turbulent mixing. They, too, proposed a diffusion model for this process. Wisler et al., who performed a further experimental study Ref. (8), concluded that both Adkins and Smith and Galimore and Cumsty were correct and showed that both diffusion models gave comparable results. In the midspan region of a multistage machine, the transport process was observed to be dominated by turbulent diffusion. Near the endwalls, the transport process associated with the nonaxisymmetric flow field was comparable to that due to turbulent diffusion. Since the publication of the last article, mixing by either turbulent diffusion or secondary flow transport, or both, is now routinely accounted for in nearly all quasi-three dimensional multistage flow models. Thus although the need to account for mixing in the quasi-three-dimensional model has been firmly established, what has not been settled is the need to incorporate similar models into the three-dimensional flow simulators currently being developed.

With the advent of supercomputers, researchers are attempting to extend quasi-three-dimensional models to three-dimensions. The motivation for this work is to reduce the degree of empiricism required for the simulation of multistage machinery and to enhance the understanding of three-dimensional flows, especially those that occur in the endwall regions. Of the proposed models, those that attempt to define the time-averaged flow field within a typical passage of a multistage machine seem the most promising for design applications, given today's computer capabilities. It has been shown that flow mixing in these models is associated with the transport of momentum and energy across the time-averaged stream surfaces by turbulence and the unsteady deterministic flow field. The object of the work to follow is to estimate the magnitude of this transport process and to establish the need for including a model of this process in the developing three-dimensional multistage simulation codes.

Analysis

The present analysis is based on the work reported in Ref. (9) and the more recent work in Ref. (10). The starting point for the current work is the Navier-Stokes equations expressed in cylindrical coordinates with an inertial frame of reference. Unfortunately, at large Reynolds numbers, these equations are associated with a turbulent flow state, while our interest is in describing the time-averaged flow field within a typical passage of a blade row embedded in a single or multistage configuration. In Ref. (9), a procedure was developed for deriving the field equations governing this flow state, starting from the Navier-Stokes equations. To form a foundation for the present work, a brief outline of this procedure will be given, the mathematical details can be found in Ref. (9). The derivation begins by "removing" or "filtering out" all time scales which are uncorrelated with the shaft rotation time period. This step is accomplished by executing an ensemble average of a large number of data samples, each of a length equal to the shaft rotation time period. The application of this averaging procedure to the Navier-Stokes equations then yields their familiar Reynolds averaged form. These filtered equations govern an unsteady deterministic flow state whose time period by construction is equal to that of one shaft revolution. Note that all unsteady flow phenomena whose frequencies are unrelated to shaft speed cannot be described by this equation system. However, because the Navier-Stokes equations are nonlinear, the effect of the time-unresolved structures on the time-resolved structures cannot be completely eliminated by a simple filtering operation. The time-unresolved structures make their presence known through a series of correlations known as the Reynolds stress This stress is a direct measure of the transport of momentum across the time-resolved stream surfaces by the time-unresolved flow structures.

The next step removes or filters out the unsteady flow structures from the time-resolved flow state. This filtering step is executed with respect to both the stationary frame of reference and the rotor frame of reference. Thus two time-averaged flow states will exist: one with respect to the stationary blade rows; the other with respect to the rotating blade rows. The averaging or filtering process simply involves averaging the time-resolved flow state over a cycle of one shaft rotation with respect to the stationary and rotational frame of reference. Those blade rows which are moving relative to the frame of reference are smeared by this averaging procedure; those that are stationary remain distinct. Applying this filtering operation to the equations governing the time-resolved flow state produces a number of mathematical expressions through which the time-resolved flow state can influence the time-averaged state. These expressions are in the form of a series of correlations. a body force and an energy source. The body force and energy source are related to the aerodynamic and thermal loading acting on the blade rows which are moving with respect to the frame of reference; the correlations which appear in the momentum equations are in the form of a Reynolds stress. They are associated with the transport of momentum across the time-averaged stream surfaces by the time-resolved flow structures. Like their time-unresolved counterparts, these correlations are associated with mixing, and their relevance will be assessed in the section that follows.

The final averaging operation removes passage-to-passage variation from the time-averaged flow states. The resulting flow state is referred to as the "average passage" flow field. The derivation of the governing equations, starting from the time-averaged flow field equations, can be found in Ref. (9). The additional correlations, body forces, and energy sources associated with this equation set will not be dealt with in the present analysis, but will be addressed in future work.

The ensemble and time-averaging operations suggest that the velocity field u_i in the stationary frame of reference may be expressed as

$$u_i(r,\theta,z,t) = \bar{\bar{u}}_i^{(S\,k)}(r,\theta,z) + \sum_{n=1}^{N}[\bar{\bar{u}}_i^{(S\,n)}(r,\theta,z) - u_i^{(AX)}(r,z)] + \tilde{u}_i(r,\theta,z) + \sum_{m=1}^{M}[\bar{\bar{u}}_i^{(R\,m)}(r,\theta-\Omega t,z) - u_i^{(AX)}(r,z)] + \hat{u}_i(r,\theta,z,t) + u_i'(r,\theta,z,t) \quad (1)$$

where r, θ, and z are the radial, tangential, and axial coordinates respectively; Ω is the shaft rotational speed; and t is time. The velocity component $u_i'(r,\theta,z,t)$ is associated with the time-unresolved flow field. The subscript i denotes the conventional tensor notation for a vector. Its ensemble average by definition is zero. The momentum transported by this field across the time-resolved stream surfaces produces a Reynolds stress of the form $\overline{\rho u_i' u_j'}$, where ρ is the fluid density, and the single overbar denotes the ensemble average. This stress is periodic in time, with a period equal to one cycle of the shaft revolution. The combination

$$\sum_{m=1}^{M}[\bar{\bar{u}}_i^{(R\,m)}(r,\theta-\Omega t,z) - u_i^{(AX)}(r,z)] + \hat{u}_i(r,\theta,z,t) \quad (2)$$

represents the unsteady component of the time-resolved velocity field. The velocity component $\bar{\bar{u}}_i^{(R\,m)}$ under the summation sign represents the time-averaged velocity field in a typical passage of the m'th rotor. Its time mean value is equal to the axisymmetric component $u_i^{(AX)}$. The component $\hat{u}_i$ is associated with the rotor-stator and the rotor-rotor interaction field and can be shown to be a function of $\bar{\bar{u}}_i^{(R\,m)}$ and $\bar{\bar{u}}_i^{(S\,n)}$ where $u_i^{(S\,n)}$ is the time-average velocity field in a typical passage of the n'th stator. The velocity components in Eq. (2) can transport momentum across the time-averaged

stream surface. In Ref. (9), this transport process was shown to produce a mixing stress of the form

$$R_{ij} = \overline{\{\rho u_i{}^{\prime\prime} u_j{}^{\prime\prime} + \rho u_i{}^{\prime\prime}\hat{u}_j + \hat{\rho u}_i\, u_j{}^{\prime\prime} + \hat{\rho u}_i\,\hat{u}_j\}} + \overline{\overline{\rho u_i{}' u_j{}'}} \tag{3}$$

where

$$u_i{}^{\prime\prime} = \sum_{m=1}^{M} [\bar{\bar{u}}_i^{(R_m)}(r,\ \theta-\Omega t,z) - u_i^{(AX)}(r,z)] \tag{4}$$

The single bar over the expressions which appear within the brackets represents a time average; the double overbar over the remaining term denotes the time average of an ensemble average. The stress $\overline{\rho u_i{}^{\prime\prime} u_j{}^{\prime\prime}}$ is independent of θ and is associated with the nonaxisymmetric component of the "average passage" velocity field of each rotor. The work of Adkins and Smith may be viewed as an attempt to model the mixing due to this stress. In the present work, it will be evaluated directly. The remaining stresses which make up R_{ij} are associated with rotor-stator interaction, rotor-rotor interaction, and mixing due to the time-unresolved flow field. These terms arise in part due to wake chopping and turbulent diffusion and will be modeled by a Boussinesq diffusion model, as suggested by the work of Galimore and Cumsty, Ref. (7). The diffusion coefficient will be set according to the data published by Galimore, Ref. (6). The force associated with the gradient of the stress $\frac{d\rho u_i{}^{\prime\prime} u_\theta}{dx_j}$, which appears in the tangential momentum equation, will serve as a measure of the stress R_{ij} away from solid boundaries. Its effect will be evaluated by comparing its gradient to the tangential component of the blade force.

The time-averaged energy equation also contains a source term and energy correlations. The correlations arise because of the transport of total enthalpy across the time-averaged stream surfaces by both the time-resolved and the time-unresolved velocity field. The source term is the result of the work done by the blade force and the heat transfer at the blade surface. Applying the same decomposition that was used for the velocity to the total enthalpy H_o yields,

$$\begin{aligned} H_o(r,\theta,z,t) = {} & \bar{H}_o^{(S_k)}(r,\theta,z_k) + \sum_{n=1}^{N} [H_o^{(S_n)}(r,\theta,z) - H_o^{(AX)}(r,z)] \\ & + \tilde{H}_o(r,\theta,z) \\ & + \sum_{M} [\bar{\bar{H}}_o^{(R_m)}(r,\theta-\Omega t,z) - H_o^{(AX)}(r,z)] \\ & + \hat{H}_o(r,\theta-\Omega t,z) - H_o'(r,\theta,z,t) \end{aligned} \tag{5}$$

The ensemble and time-averaging operation applied to the energy equation yields the correlation

$$G_i \equiv \overline{\{\rho u_i{}^{\prime\prime} H_o{}^{\prime\prime} + \rho u_i{}^{\prime\prime} H_o + \rho u_i H_o{}^{\prime\prime} + \rho u_i H_o}} + \overline{\rho u' H_o'} \tag{6}$$

where

$$H_o{}^{\prime\prime} = \sum_{M} [H_o^{(R_M)}(r,\theta-\Omega t,z) - H_o^{(AX)}(r,z)] \tag{7}$$

As was noted for the momentum correlations, the correlation $\overline{\rho u_i{}^{\prime\prime} H_o{}^{\prime\prime}}$ can be directly evaluated based on the average passage flow field. The remaining correlations will be modeled by a Boussinesq diffusion model. The diffusion coefficient will be assumed to be related to the momentum diffusion coefficient through a Prandtl number of order one. The impact of the correlation $\overline{\rho u_i{}^{\prime\prime} H_o{}^{\prime\prime}}$ on the solution will be assessed by comparing the value of its divergence to the work done by the blade forces. This assessment is undertaken in the next section.

Results

The compressor used in this study is a high-speed five-stage research compressor, of which only the first two stages will be analyzed. The pressure ratio across these stages exceeds three. Both of the simulated stages are transonic, with the second stage starting to take on the characteristics of an embedded stage. The initial set of results to be presented will illustrate the predictive capability of the current model; the data to be used in the figures came from measurements recorded at the leading edge of the first and second stator. The first figure shows the total pressure rise across the first rotor as a function of span. The square symbols denote the data, the solid line is the prediction, and two or more symbols at a given spanwise location represent the circumferential scatter in the data. Notice that the level of the predicted total pressure rise across the rotor is slightly lower than measured, and the shape of the predicted curve is in good agreement with the data. The location of the local minimum at 38 percent is predicted, and the location of the maxima near the endwalls is also in good agreement with the data. It is believed that the predicted level of the total pressure rise across the first rotor could be raised by simply increasing the specified back pressure at the exit of the second stage.

The next figure shows the total temperature rise across the first rotor. Once again, the square symbols are the experimental measurements. The agreement between prediction and measurement is quite good, and the indicated ability to predict the performance of the first rotor provides a degree of credibility for the simulation. The next two figures show the total pressure and total temperature distribution entering the second rotor. The performance of the first stator, as judged by the loss in total pressure, is very satisfactory. The hub endwall flow shows no sign of separation, and the total

temperature distribution shows less of a variation than at the exit of the first rotor. Note that this result is quite apparent in the tip region. The simulation assumed no heat transfer to the solid surfaces and a finite clearance over both rotor tips. The previous results are thus an indication of the mixing produced by the nonaxisymmetric component of the flow field downstream of the first rotor.

Figures (5) and (6) show the total pressure and total temperature distribution at the exit of the second rotor. Here the predicted total pressure level is deficient in the hub and slightly overestimated in the tip. The low level inboard of 30 percent of span is caused by a separated flow region along the suction surface of the rotor. This separated region also causes an excessive total temperature over the measurements.

The source of the excess in both total pressure and temperature over the measurements for the region outboard of 50 percent span, is unknown. An examination of the results from the second stator simulation results showed no evidence of flow separation or regions of high loss which could be related to the shape of the predicted total pressure distribution at the exit of the rotor. Because this examination was inconclusive, further study will be required. The results derived from the second stage simulation will have to be thought of as typical of off-design operation.

To establish the degree of flow mixing present in both rotor simulations, the tangential component of the body force and the divergence of the momentum correlation $\overline{\rho u_i'' u_\theta''}$ associated with the average-passage flow field will be evaluated along with the energy source and the divergence of the energy correlation $\overline{\rho u_i'' H_o''}$. Figure (7) shows contours of the combined values of the tangential component of the body force and the di ergence of the correlation $\overline{\rho u_i'' u_\theta''}$. Both of these terms appear in the tangential momentum equation, and, as was noted in the previous section, the divergence of $\overline{\rho u_i'' u_\theta''}$ is a measure of the mixing of tangential momentum. The outline of the rotor appears in the left portion of the figure, while the first stator is to the right of the rotor. Figure (8) shows the contour levels of the tangential component of the body force produced by the aerodynamic loading acting on the first rotor. The sign of this component is negative over most of the bladed region. It vanishes, as it must, outside of this region. The difference in the value of the contours which appear in Figures (7) and (8) is equal to the divergence of the correlation $\overline{\rho u_i'' u_\theta''}$. Outside of the region swept out by the rotor, the value of $\frac{\partial}{\partial x_i} \overline{\rho u_i'' u_\theta''}$ is small, with the exception of the region downstream of the rotor and outboard of 85 percent of span. In this region, its value is comparable to the value of the tangential component of the blade force inboard of midspan. Furthermore, this correlation appears to act over a region which extends to near the stator trailing edge. Their effect, which can be shown to be cumulative over the time-averaged path line of a fluid particle, is non-negligible. These results further suggest that very little mixing due to the unsteady deterministic flow field occurs inboard of 85 percent of span. Turbulent mixing, however, would be present in the region.

The next two figures show the contour levels for the combined values of the energy source and the divergence of the correlation $\rho u_i'' H_o''$, and the contour values of the energy source. As in figure (8), the energy source, which is a function of the rotor aerodynamic loading, vanishes outside of the region swept out by the rotor. The difference between the contours in these two figures is equal to the divergence of the energy correlation $\overline{\rho u_i'' H_o''}$. Outside of the rotor blade region, the energy correlation, like the momentum correlation, appears to be significant only in the tip region. In the tip region, its effect appears to extend to near the stator trailing edge.

The next four figures (i.e., Figures (12)-(15)) clearly illustrate the mixing which can be attributed to the second rotor. The format of these figures is identical to that for Figures (7)-(11). The mixing associated with the average-passage flow field of the second rotor, unlike that of the first, is non-negligible in both endwall regions. The flow mixing which occurs in the hub is mainly due to the separated flow region near the trailing edge of the suction surface, while the mixing in the tip is the result of the leakage flow. Both of these mixing regions seem to extend to near the trailing edge of the second stator. At midspan, the wakes are thin, and the flow is nearly two-dimensional, which results in a low level of mixing by the unsteady deterministic flow field. These results are completely consistent with the work of Weisler et al., Ref. (8), and are also consistent with the work of Galimore and Cumsty, Ref. (7). They further suggest that the mixing, which both sets of authors associated with turbulence, might have a strong component which is associated with the unsteady time-resolved flow field. The proof of this conjecture will require detailed measurements or a three-dimensional unsteady viscous flow simulation. A final observation regarding these results: It is apparent that the correlations associated with the nonaxisymmetric component of the second rotor average-passage flow field has a minimal impact on the time-averaged flow field of the upstream stator.

A number of researchers have attempted to develop interblade row boundary conditions to permit the simulation of more than one blade row. These simulations, like the present, attempt to describe the time-averaged flow field in a typical passage of a blade row. The boundary conditions allow the transfer of the axisymmetric components of the flow variables between the rows; however, the nonaxisymmetric component is quite often overlooked. This boundary condition appears to be based on the assumption that the flow between the blade rows relaxes to an axisymmetric state within the interblade row region, and experimental evidence suggests that this might be reasonable for fan stages with wide separation between rotor and stator. However, as the present results show, this assumption is inappropriate for core compressors.

The final two figures show the absolute total temperature distribution at the exit of both rotors. These figures clearly show the three-dimensional structures which impact the time-averaged flow field within the stators. In the tip region, these structures are the result of the leakage flow, which is responsible for the high total temperature region to the right of midpassage. This same region also happens to be a region of high loss. The velocity field associated with the leakage flow transports energy across the time-averaged stream surfaces of the stator flow field; the result

of this transport process is the energy correlations shown in Figures (9) and (13). In the hub of the second rotor, there is also a region of high total temperature, which is the result of the boundary layer separating from the suction surface of the rotor. The thick wake which evolves from the separated region has a significant radial velocity component within it. As the wake convects downstream, this velocity component transports momentum and energy across the time-averaged stream surfaces of the stator flow field. This transport process yields a stress which acts on the stator time-averaged flow field. The physical extent of this stress field is shown in Figure (11). These results and those on the previous figures clearly show the need to take account of the stress and energy correlation produced by the time-resolved flow field in simulations of multistage compressors.

Conclusions

An assessment of the effect of the unsteady flow field within a multistage compressor on the time-averaged performance was attempted. It had previously been shown that the unsteady flow state impacts the time-averaged flow state through a stress tensor, a body force, an energy source, and an energy correlation. In this study, the magnitude of the body force resulting from the aerodynamic loading acting on a blade row was compared to the gradient of the stress tensor associated with the unsteady time-resolved flow field generated by the blade row. Both of these quantities appear in the time-averaged form of the momentum equations. In addition, the magnitude of the work done by these forces was compared to the divergence of the energy correlations produced by the unsteady time-resolved flow field. It was found that both the stress tensor and the energy correlations were non-negligible in the endwall regions, a finding consistent with that of Ref. (8). In the midspan region, both the stress tensor and the energy correlation were small; again, this finding is consistent with that in Ref. (8). These results suggest that turbulence or the time-unresolved flow field is the primary source of flow mixing in the midspan region. The stress tensor and energy correlations were found to be strongly dependent upon the three-dimensional structure of the time-resolved unsteady flow field The mixing associated with stress field and the energy correlations extended to a region near the trailing edge of the downstream stator. The influence of the correlations associated with the time-resolved flow field upon the upstream blade row was negligible.

This study has shown the need to understand and model the unsteady flow processes which impact the performance of multistage blade rows. Further studies are needed before this subject is understood to the point where semi-empirical models which explicitly account for the effects of the unsteady flow on blade row performance can be used to develop designs which take advantage of these effects to enhance performance.

Acknowledgement

The authors wish to express their appreciation to Mr. P. Tramm and Mr. R. Alverson of Allison Gas Turbine Division of General Motors and to Dr. A. Sehra of Textron Lycoming for their many helpful suggestions.

References

1. Smith, L. H., Jr.: Secondary Flow in Axial-Flow Turbomachinery. Trans. ASME, Vol. 77, No. 7, Oct. 1955, pp. 1065.

2. Smith, L. H., Jr.: The Radial-Equilibrium Equation of Turbomachinery. J. Eng. Power, Vol. 88, No. 1, Jan. 1966, pp. 1-12.

3. Sehra, A. K.: Boundary Layer and Wake Modifications to Compressor Design Systems: The Effect of Blade-to-Blade Flow Variations on the Flow Field of a Transonic Rotor. GT/PLD-144, M.I.T. Gas Turbine and Plasma Dynamics Lab., 1979.

4. Sehra, A. K., Kerrebrock, J. L.: Blade-to-Blade Flow Effect on Mean Flow in Transonic Compressors. AIAA Journal, April 1981.

5. Adkins, G. G., Jr.; and Smith, L. H., Jr.: Spanwise Mixing in Axial-Flow Turbomachines. J. Eng. Power, Vol. 104, No. 1, Jan. 1982, pp. 97-110.

6. Gallimore, S. J.: Spanwise Mixing in Multistage Axial Compressors. Ph.D. Dissertation, Dept. of Engr., University of Cambridge, Sept. 1985.

7. Gallimore, S. J.; Cumpsty, N. A.; Spanwise Mixing in Axial-Flow Turbomachines. Trans. ASME, J. Eng. Power, Vol. 109, July 1986, pp. 2-9.

8. Wisler, D. C., Bauer, R. C., Okiishi, T. H.: Secondary Flow, Turbulent Diffusion, and Mixing in Axial Flow Compressors. ASME Paper GT-16, 1967.

9. Adamczyk, J. J.: Model Equation for Simulating Flows in Multistage Turbomachinery. NASA TM-86869 and ASME 85-GT-226, Nov. 1984.

10. Adamczyk, J. J.; Celestina, M. L.; Beach, T. A ; Barnett, M.: Simulation of Three-Dimensional Viscous Flow Within a Multistage Turbine. NASA TM-101376 and ASME 89-GT-152.

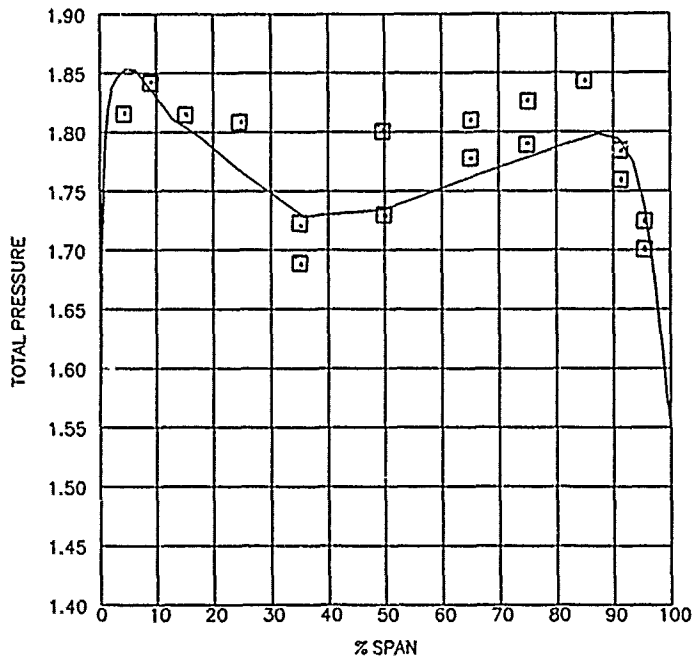


Fig. 1: Absolute Total Pressure Distribution At The Exit Of The First Rotor

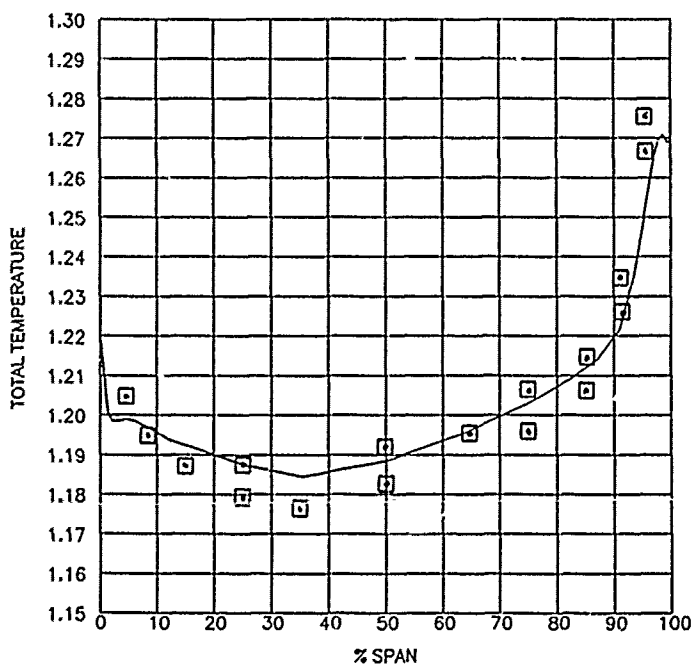


Fig. 2: Absolute Total Temperature Distribution At The Exit Of The First Rotor

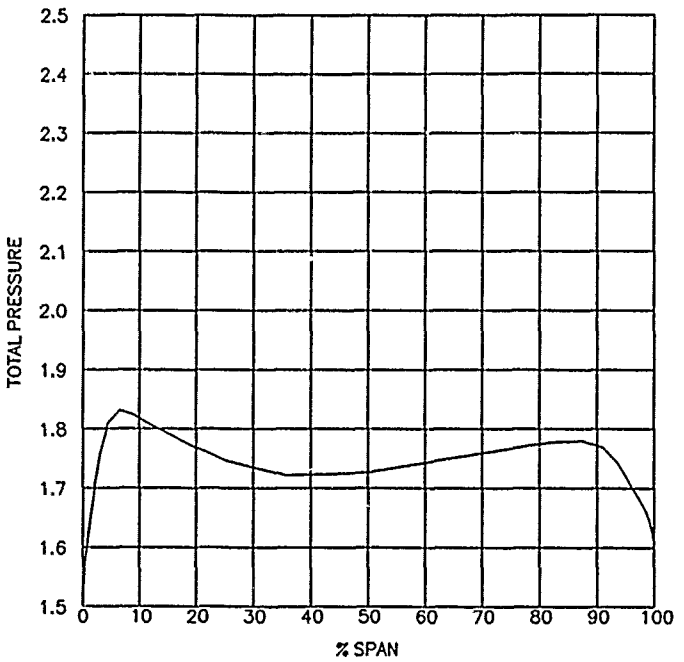


Fig. 3: Absolute Total Pressure Distribution At The Inlet To The Second Rotor

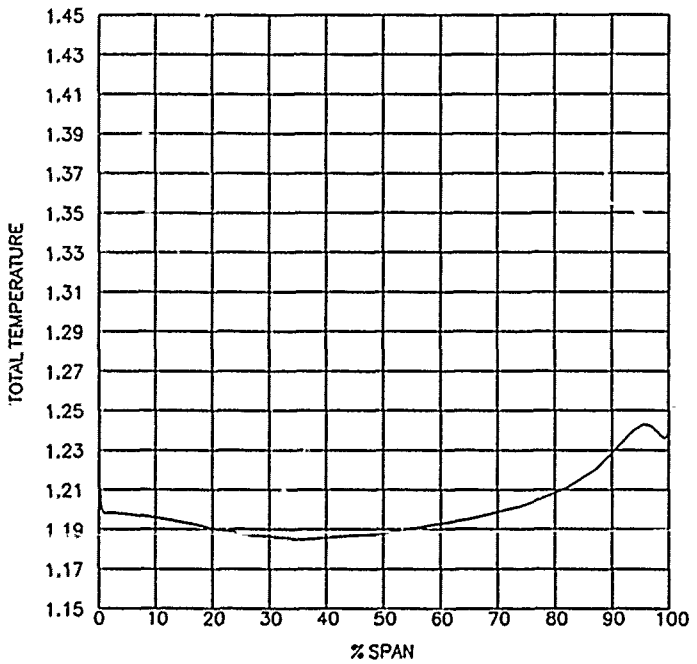


Fig. 4: Absolute Total Temperature Distribution At The Inlet To The Second Rotor

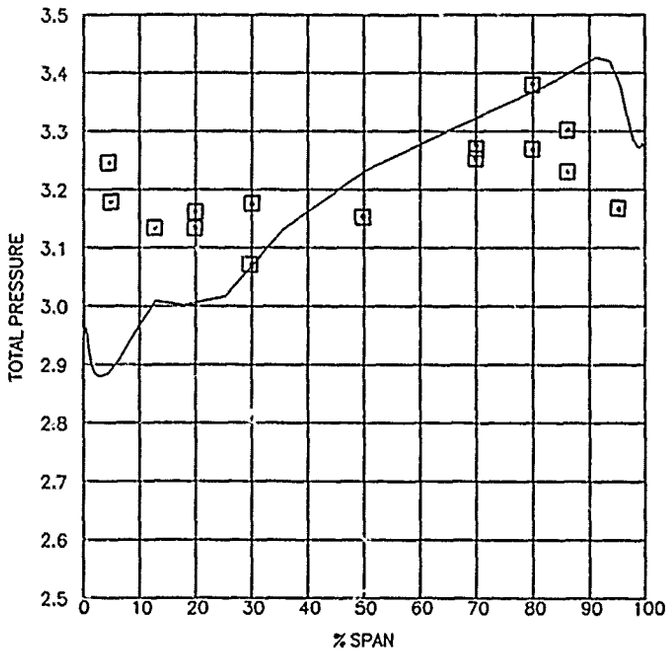


Fig. 5: Absolute Total Pressure Distribution At The Exit Of The Second Rotor

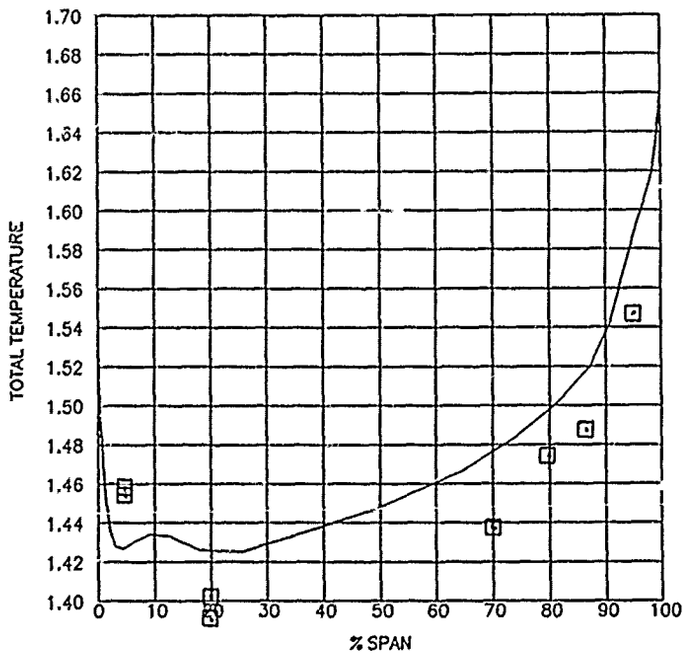


Fig. 6: Absolute Total Temperature Distribution At The Exit Of The Second Rotor

MOMENTUM CORRELATION - ROTOR 1

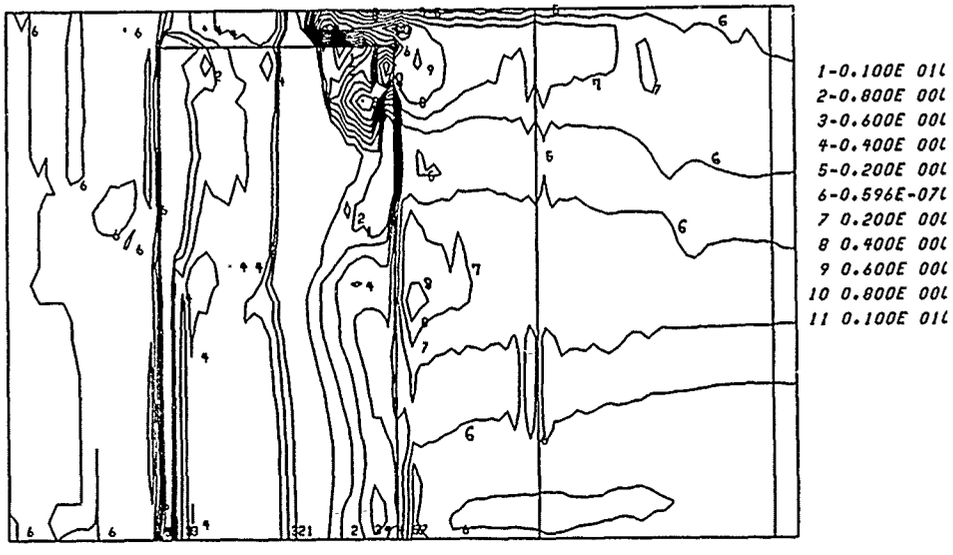


Fig. 7: Distribution Of The Tangential Momentum Correlation $\frac{\partial \overline{\rho u_\theta'' u_\theta''}}{\partial x_\theta}$

BODY FORCE - ROTOR 1

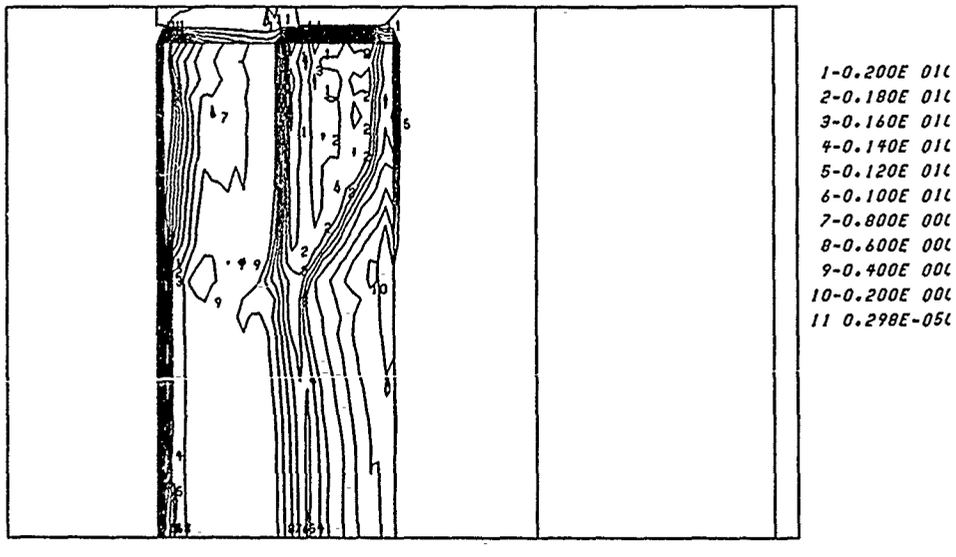


Fig. 8: Distribution Of The Body Force In The Tangential Direction

ENERGY CORRELATIONS - ROTOR 1

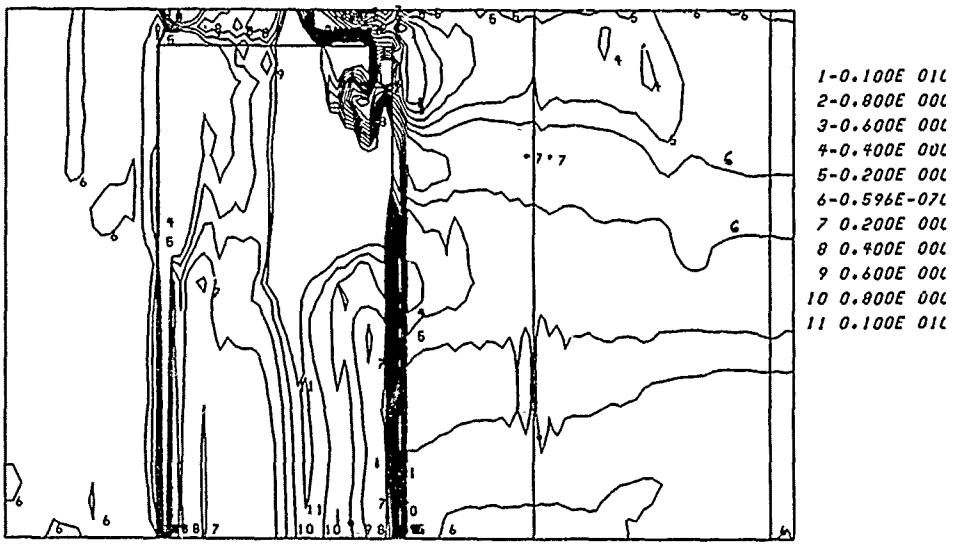


Fig. 9: Distribution Of The Energy Correlation $\partial \overline{\rho u_i'' H_o''} / \partial x_i$

ENERGY SOURCE - ROTOR 1

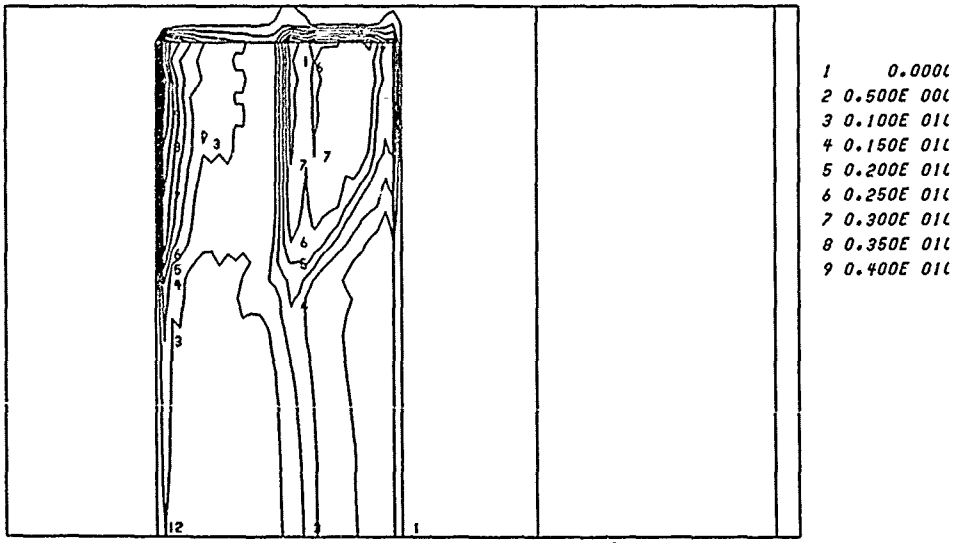


Fig. 10: Distribution Of The Energy Source

MOMENTUM CORRELATION - ROTOR 2

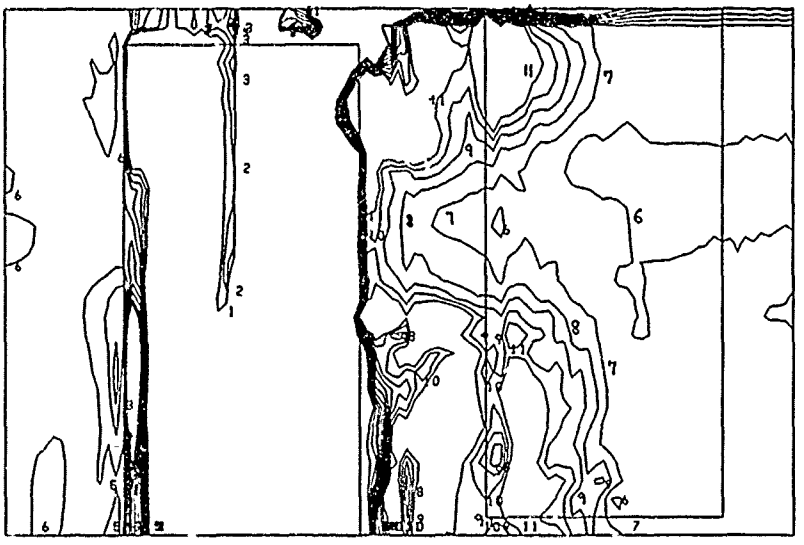


Fig. 11: Distribution Of The Tangential Momentun Correlation $\frac{\partial \overline{\rho u'' u_\theta''}}{\partial x_i}$

BODY FORCE - ROTOR 2

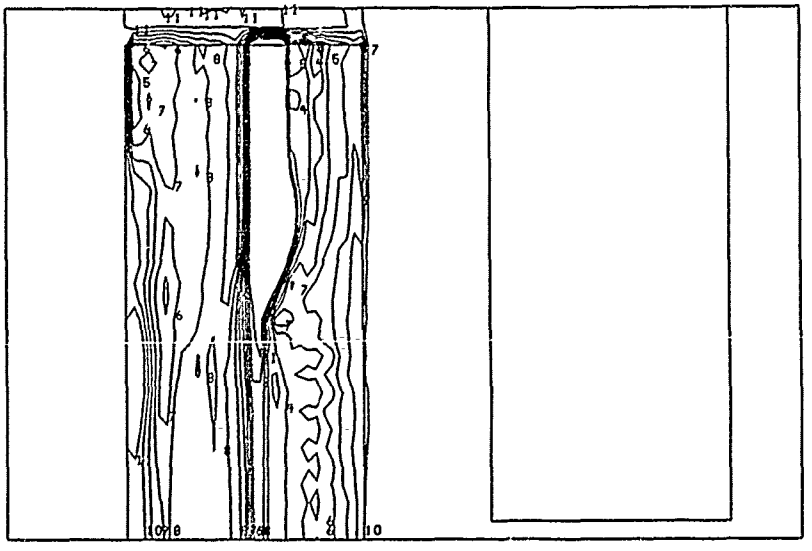


Fig. 12: Distribution Of The Body Force In The Tangential Direction

ENERGY CORRELATIONS - ROTOR 2

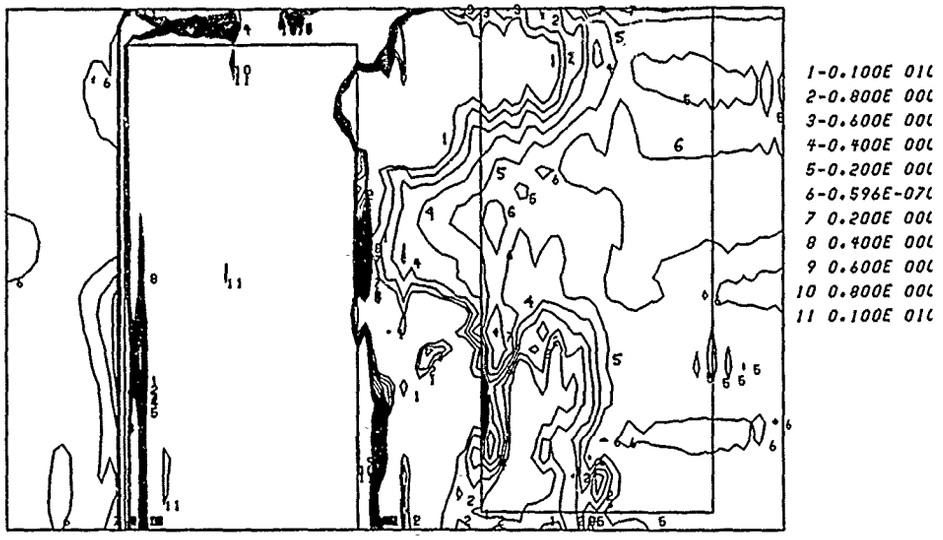


Fig. 13: Distribution Of The Energy Correlation $\frac{\partial \overline{\rho u_i'' H_o''}}{\partial x_i}$

ENERGY SOURCE - ROTOR 2

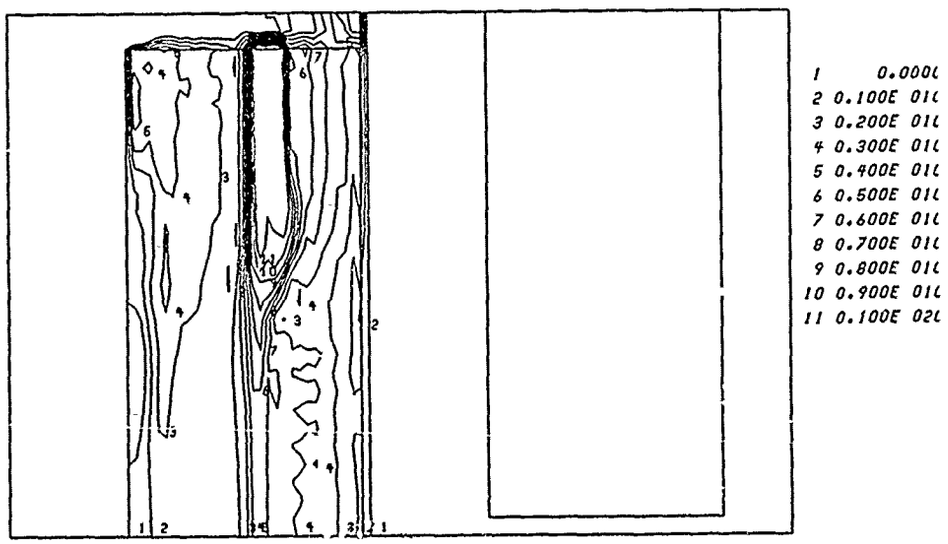


Fig. 14: Distribution Of The Energy Source

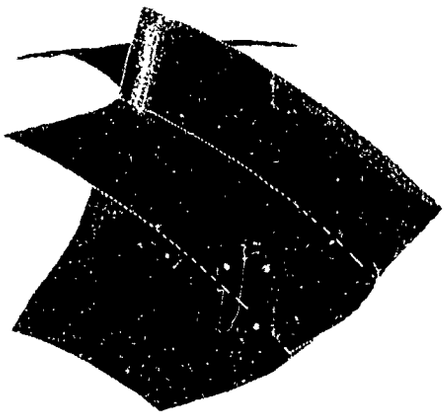


Fig. 15: Total Temperature Distribution At The Exit Of The First Rotor

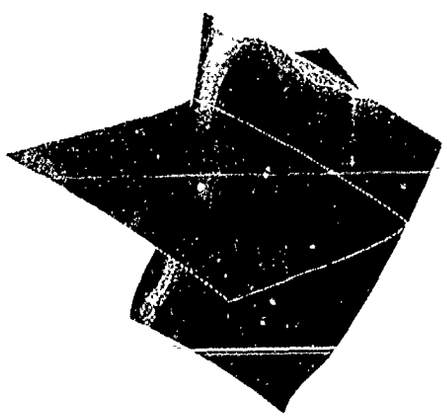


Fig. 16: Total Temperature Distribution At The Exit Of The Second Rotor

RESEARCH ON CASCADE SECONDARY AND TIP-LEAKAGE FLOWS - PERIODICITY AND SURFACE FLOW VISUALIZATION

by
L.S. Langston
Professor
University of Connecticut
Department of Mechanical Engineering
Storrs, CT 06269
US

Summary

Large scale planar cascade experimental studies have been used for some years now to sort out and measure three-dimensional flows in axial flow turbines. In particular, these planar cascades have been and are used for secondary flow studies and more recently for tip-clearance studies. This paper focuses on the topics of cascade periodicity and the use of surface flow visualization in planar turbine cascades, in these studies.

Since results from these cascade experimental studies are based on a planar cascade that usually has few airfoils (4-6), the topic of how periodicity is achieved in a finite cascade is an important one. One method of achieving periodicity in a 4-airfoil cascade is discussed.

The use of surface flow visualization in these cascade studies has been prominent. A commentary is given on three techniques that have been used, and on the interpretation of the results from each technique.

Nomenclature

a - ordinary point on attachment line

b_x - axial chord (0.281 m)

c_p - static pressure coefficient, $(p-p_o)/1/2\ U_o^2$

D - cylinder diameter

p - static pressure

s - ordinary point on separation line

S - airfoil surface distance divided by leading edge radius (1.50 cm)

S_s - saddle point of separation

u - velocity in the x-direction

U_o - free stream or upstream velocity

v - velocity in the y-direction

w - velocity in the z-direction

x - coordinate normal to cascade leading edge; axial

y - coordinate normal to endwall; spanwise

z - coordinate parallel to cascade leading edge; gapwise

} Nondimensionalized by b_x

ρ - density

τ_{yx} - wall shear stress in y = 0 plane in x-direction

τ_{yz} - wall shear stress in y = 0 plane in z-direction

Introduction

For many years, experimenters studying the complex three-dimensional flow in axial flow turbines have made use of simple planar (linear) cascades of turbine airfoils. One such four-bladed cascade is shown in cross section in Figure 1. Since axial turbine three-dimensional flows (or "secondary" and "tip-clearance" flows as they are generically called) are quite complicated, it has been found beneficial to use this simpliest geometry to sort them out, much as the classic "flat plate" is used in two-dimensional flows.

Planar cascade flow studies of turbine three-dimensional flows go back at least to the work of Herzig et al[1] at NACA and to Armstrong[2] at Cambridge. Because of the overall favorable (negative) pressure gradient in an axial flow turbine, simple planar cascade flows faithfully exhibit many of the most important features of actual turbine flows. Such is not the case for an axial flow compressor, because of its overall unfavorable (positive) pressure gradient. In general, compressor planar cascade flows may not accurately represent "engine" conditions in a compressor, because portions of the flow may be operating under conditions of impending (or actual) flow separation. Thus, small (or large) disturbances in the engine environment, not present in a cascade experiment, can give rise to steady or unsteady flows that are not easily representable by a simple compressor cascade.

The three-dimensional flow in a planar turbine cascade is usually thought of in terms of the "primary flow" and the "secondary flow". The primary flow consists of the flow that most closely follows two dimensional (usually midspan) inviscid streamlines in the cascade, and the corresponding two-dimensional region (if that exists) of the boundary layers on the cascade airfoil surfaces. The secondary flow then includes all that is not "primary", i.e. the so-called three-dimensional flows. These include endwall boundary layers (i.e. the region of flow on the non-airfoil bounding surfaces of a cascade) and any portion of the primary flow region that is strongly effected by the latter.

Tip-leakage flows occur because of airfoil tip clearances (i.e. leakage from pressure to suction surfaces between the tip of a moving blade and a fixed endwall, or between the tip of a stator and a moving endwall). Either is simulated in a planar cascade by leaving a gap between the cascade airfoil tips and an adjacent endwall (which is usually stationary, but can be made to move, e.g. a belt). The resulting "tip leakage" flow in the planar cascade will modify both the secondary flow and the primary flow.

For the case of a planar cascade that is used to model pure secondary flows (i.e. no tip clearance), the endwall regions give rise to the now well-known (and documented) horseshoe vortex system. One interpretation of this system, as given by Langston, Nice and Hooper[3] is shown in Fig. 2. This figure shows that at the endwall of the cascade, the inlet boundary layer separates and forms a horseshoe vortex. One leg of this vortex (sometimes called the "pressure" leg), drawn into a cascade passage, is "fed" by the passage pressure-to-suction endwall flow and becomes the passage vortex. The other leg (called the "suction" leg) is drawn into an adjacent passage and has an opposite sense of rotation to the larger passage vortex. This smaller vortex is labeled as a counter vortex in Fig. 2 and can be thought of as a "planet" possibly rotating about the axis of the passage vortex (the "sun"). Thus the position of the counter vortex relative to the passage vortex may be different than that shown in Fig. 2 (see Marchel and Sieverding[4]). The ribbon arrows in the figure have been drawn to exaggerate vortex motion. The actual rotation of the vortices is much less than shown (about two rotations for the passage vortex).

More complicated endwall flows than that shown in Fig. 2 have been discussed by Sieverding[5] and these will be considered later in this paper. There has been a large body of work on tip-clearance flows in planar cascades (e.g. Moore and Tilton[6], Bindon[7], Yamamoto[8], and Yaras and Sjolander[9]) but as yet no "simple" picture has emerged to be a counterpart to the no-gap cascade of Fig. 2.

At least three reviews of turbine secondary flows have been written. One written by Salvage[10] covers the literature on secondary flows up until the early 1970's. Some topics in turbine cascade flows have been reviewed by Gostelow[11] for much of the literature up to 1980-82. The most recent and comprehensive review was done by Sieverding[5] who reviewed and summarized the literature up to about 1983.

Since Sieverding's review there has been a fairly large number of papers presented and published (about 5-10 per year) on three-dimensional flows in turbine cascades. In light of this most recent work (since 1983) and that which was reviewed by Salvage, Gostelow, and Sieverding, the objective of this paper is to review and comment on the following turbine planar cascade experiment topics:

1) The question of cascade periodicity.

2) The use of surface flow visualization in planar cascade studies.

The question of cascade periodicity for non-infinite cascade experiments is an important one. Data from detailed turbine cascade experiments are being used as "test cases" against which numerical (computer) solutions of either the Euler or the Navier-Stokes equations are being compared (e.g. Hah[12]).

The use of surface flow visualization is and has been important in discovering and sorting out complex cascade flows. A commentary is given on three of the flow visualization methods that have been used and on the interpretation of the results of each.

The Question of Periodicity

The obvious way to achieve periodicity in a linear cascade is to have as many airfoil passages as possible. But of course, given a certain size airfoil passage, more airfoils mean more airflow, and hence, a larger air supply. Typically a turbomachinery company will test an "engine scale" cascade with 10-15 airfoils, using the middle three or four passages as the "test section", from which aerodynamic data is taken. Both ends of the cascade then provide the approximation to a periodic flow field for the cascade middle section.

However, in the large scale planar cascades that have come to characterize experimental studies of turbine cascade secondary flows, (e.g. Langston et al[3], Marchel and Sieverding[4], and Yamamoto[13]) the number of airfoils are reduced because:

a) It is necessary to increase the scale of the experiment (airfoils on the order of 5-10 times engine size) so that details of the complicated secondary flow field can be measured accurately while minimizing the effect of the instrumentation (e.g. pressure probes) on the flow .

b) There is a requirement to achieve Reynolds number similarity (based on axial chord and inlet or exit velocity) while keeping the total flow rate to the cascade within reasonable limits (size of the air supply).

A typical four-airfoil cascade used to study secondary flows, taken from Langston et al[3], is shown in Fig. 1. This particular cascade will be used as an example of at least one way to make part of such a cascade periodic. It had an aspect ratio of about 1.0, an axial chord of about 0.3m, and was tested at an axial chord Reynolds number of about 10^6 (inlet velocity 34m/sec at atmospheric conditions).

Because of the few airfoils, a four-airfoil cascade is not periodic in every airfoil passage. The overall turning of the flow entering and leaving the cascade in Fig. 1 is determined by the airfoil shape and spacing (solidity). The overall inlet flow angle is set by adjusting the cascade angle relative to the inlet duct. However, the detailed flow entering each cascade passage can vary depending on the passage's proximity to wind tunnel bounding walls. Thus, once the cascade inlet angle is set (44.7° in Fig. 1) the cascade flow can be adjusted to achieve center passage periodicity by trial-and-error positioning of the two boundary layer bleeds and the two tailboards. These four "adjustments" are not independent, because setting one (e.g. the longer tailboard) can effect the others (e.g. the low blead flow).

Figure 3 shows the final pitchwise static pressure distribution at the exit of the cascade, taken on an endwall at about 0.1 of an axial chord downstream of the trailing edge plane in the axial direction. (Like measurements were taken in front of the cascade, but due to the lower velocities there, the leading edge position did not yield as sensitive a measurement). At best, one can say that the pressure distribution has a "psuedo-periodic" behavior, being effected by such things as the boundary layer on the longer tailboard (e.g. the lower pressures between airfoils 3 and 4).

However, the criterion used for cascade periodicity was not the repeatibility of the wakes in Fig. 3. (This figure does represent the flow conditions under which the cascade was tested.) Rather, tailboards and blades were adjusted until the static pressures at midspan on the middle airfoils 2 and 3 agreed with one another (on both suction and pressure sides) and with a potential flow solution for an infinite cascade (as shown in Ref. 3 there was a midspan region that closely approximated an inviscid irrotation flow outside of the airfoil boundary layers). This agreement is shown in Fig. 4 as a plot of static pressure coefficient on airfoils 2 and 3 as a function of non-dimensional airfoil surface distance from the leading edge-mean camber line intersection, in the region of the airfoil leading edge. Airfoils 2 and 3 were also interchanged in the cascade (i.e. removed and repositioned) as a check for pressure tap location and pressure tap consistancy.

The midspan pressure distributions in Fig. 4 show infinite cascade behavior for airfoils 2 and 3 in two important ways:

1) There is very good agreement at midspan between the infinite cascade potential solution (the continuous curve in Fig. 4) and the measured pressures on airfoils 2 and 3.

2) The position of the leading edge stagnation points on both airfoils are the same and agree with the infinite cascade potential flow solution. This guarantees that the midspan region of the passage between airfoils 2 and 3 has the same mass flow rate as the potential flow calculation. (It should be noted from Fig. 4 that more than one pressure tap is needed to experimentally locate the stagnation point!)

Figure 5 shows the complete chordwise static pressure distribution on the pressure side of airfoil 3 and on the suction side of airfoil 2, for various spanwise locations. As in Fig. 4, there is good agreement with infinite cascade potential flow at midspan (50%), except near the trailing edge where viscous effects (trailing edge separation) start to effect the flow. As discussed in more detail in Ref. 3, the pressure distribution at other spanwise locations (25%, 12.5% and 2.3%) show the effects of the passage vortex (secondary flow) formed on the endwall of the cascade.

The above discussion shows at least one approach for insuring that one passage and two airfoils in a four-airfoil cascade behaves as if they were in an infinite (truly periodic) cascade. Two items are critical:

1) A region of midspan flow in the cascade passage had small viscous and rotational effects so that it could be compared to a two-dimensional inviscid calculation for an infinite cascade.

2) It was very important that there was a sufficient number of midspan pressure measurements on the airfoils (especially in the leading edge region) to insure that the periodicity conditions existed for at least one airfoil passage. This included accurately locating the stagnation streamlines at the midspan leading edges.

Thus, when experimenters report that their finite cascade was checked for periodicity, they should show that they have addressed these two key points. Without this check of periodicity, any attempt to duplicate their results experimentally or analytically may not be successful. Non-periodicity will cause a difference in the mass flow between passages, differences in incidence angles between airfoils, and differences in pressure distributions between airfoils.

The Use of Surface Flow Visualization

Because of the complexity of three-dimensional flows in turbine cascades, surface flow visualization has been used quite extensively to document and explain cascade passage flows. A surface flow visualization test is relatively easy to do, and if detailed measurements are to be made in the cascade passage, the flow visualization results are extremely valuable in telling the experimenter how to properly aline pressure probes, hot wire probes etc., when measurements are taken near cascade surfaces.

However, the interpretation of surface flow visualization results needs to be done carefully with a knowledge of the strong points and of the limitations of the test method used. Usually, one wants to find limiting streamline patterns (also called surface streamlines) by looking at the surface shear stress lines displayed by the flow visualization (be it oil, traces of ink, etc.) on a solid surface. As can be shown (e.g. see Howarth[14]), limiting streamlines and wall shear stress lines coincide, except at singular points (where the shear stress is zero). That is, the slope of limiting streamline z = z(x) on a solid xz surface bounding a three-dimensional flow (laminar or turbulent) is given by

$$\left.\frac{dz(x)}{dx}\right|_{y=o} = \lim_{y\to o} \frac{w}{u} = \left.\frac{\tau_{yz}}{\tau_{yx}}\right|_{y=o} = \frac{\left.\frac{\partial w}{\partial y}\right|_{y=o}}{\left.\frac{\partial u}{\partial y}\right|_{y=o}}$$

where y is normal to the surface, u and w are velocities in the x and z directions, and τ_{yx} and τ_{yz} are the corresponding components of wall shear stress for (in this case) a Newtonian Fluid. In the limiting process ($y \to o$) used to derive (1), $\partial w/\partial y$ and $\partial u/\partial y$ can not both be equal to zero (but either one could be zero, such as on a separation line). Thus at a singular point (e.g. the saddle point where the horseshoe vortex of Fig. 2 forms) and where the wall shear stress is zero, Eqn. (1) doesn't hold. Surface flow visualization will not yield accurate limiting streamline information at or very close to the singular point.

Most of the surface flow visualization techniques that have been used in turbine cascade studies are of the "mechanical interaction" class as defined by Merzkirch[15]. Following Merzkirch's terminology the "oil-dot", "the oil-dot-film" and "the oil-film" methods are three mechanical interaction techniques that have been used by turbine cascade experimenters, and will be discussed here.

I. Oil-Dot Technique

An example of the oil-dot technique for surface flow visualization is shown in Fig. 6. This figure, taken from Langston et al[3], shows the results of injecting dots of india ink (the "oil" dot in this case) onto the plexiglas endwall of a turbine cascade while the cascade was being operated at design airfoil conditions. The shear forces on and near the endwall then drive an ink droplet from each dot along the endwall to paint out the limiting streamline pattern shown in Fig. 6. The horseshoe vortex saddle point, S_{s1}, can be clearly seen (along with a neighboring saddle point S_{s2}, to show periodocity and the location S_{s1} to show where S_{s1} moved when the cascade incidence angle was increased). Arrows and dotted lines have been drawn in the figure to show flow direction and the location of separation and attachment lines. In agreement with the above discussion about the singular behavior of Eqn. (1), no ink dot could be made to flow at or very close to the saddle point S_{s1}.

The oil-dot technique is also used with a more viscous oil dot than the ink of Fig. 6. In this way the dots can be placed, before the airflow is turned on. However, the oil (or oil mixture) must be viscous enough so that it isn't significantly affected by the nonsteady start-up period, before steady flow is achieved.

The advantage of this discrete oil dot method is that the resulting oil traces are streaklines such that one can clearly see the true origin of each trace. Traces that do not accurately represent limiting streamlines can be easily identified. Examples of misleading (but identifiable!) traces are the ink splattering and traces that cross one another, both shown in the upper portion of the cascade passage between airfoils 2 and 3 in Fig. 6. These were caused by wake shedding from the probe used to inject the ink onto the endwall.

II. Oil-Dot-Film Technique

This technique, developed by Langston and Boyle[16], makes use of an ink dot pattern that is put onto the surface to be tested (either directly on the test surface or by use of a glued-on drafting film). The surface is then sprayed with a thin continuous film of clear, low-viscosity oil (oil of wintergreen) that acts as a solvent and starts to "dissolve" the ink dots.

When the air supply is turned on and quickly brought up to operating conditions, the oil and the dissolved ink flow in response to shear forces. Each ink dot acts as a well-defined stationary source of ink to produce a clear ink trace of a shear stress line. When the oil has been blown downstream or has evaporated, a permanent picture of a network of ink streaklines is left on the test surface.

This technique has been used in turbine cascade studies (e.g. Gaugler and Russell[17] and Boyle et al[18]). It works best on horizontal, upward facing surfaces, and requires some care to use the low viscosity film on non-horizontal surfaces. The oil-dot-film technique yields distinct, unambigious streaklines as does the oil-dot method, but is has the added advantage of yielding streaklines in regions of very low shear, where other methods of surface flow visualization won't work. (For example see Langston and Boyle[16] and the jet engine inlet studies of Shin et al[19]).

III. Oil-Film Technique

The oil-film technique (again using Merzkirch's terminology) has been the method most used by experimenters to document turbine cascade limiting streamline patterns. Among many others, it has been used by Marchal and Sieverding[4], Gregory-Smith et al[20], Jilek[21], and Harrison[22] for secondary flow studies, and by Moore and Tilton[6] for tip leakage studies.

The cascade surface is coated with a layer or film of a mixture of oil (e.g. diesel oil or a heavier motor oil) and a powdered pigment (e.g. titanium dioxide), as uniformly as possible. The air supply is turned on and run so that any initial brush marks, finger prints, etc. disappear. The test continues until the experimenter judges that a good "picture" of the shear stress lines has been obtained, but not long enough so that the oil film has been essentially blown away, leaving few or no shear stress lines.

An excellent example of the results of the oil film technique is shown in Fig. 7. This shows the flow visualization done by East and Hoxey[23] on the endwall in front of a 0.6 m diameter cylinder mounted in a wind tunnel, run at 61m/sec. This flow visualization picture clearly shows the saddle point formed by the horseshoe vortex. This is analogous to the saddle point S_{s1} in Fig. 6, where airfoil 3 is the "cylinder". The cascade horseshoe vortex is formed nonsymmetrically due to the cascade pressure field.

This very popular oil film method has the advantage of yielding a "picture" of an entire surface fairly easily and quickly. However it has three serious draw backs:

1) The judgement of when the oil film has painted out the "best" flow visualization picture is left up to the experimenter. The author has used the method and considers such a judgement quite subjective. Leaving the air supply on for longer periods of time can yield a "clearer" picture, but some details (e.g. separation lines) may have been blown away. Dickinson[24] shows an excellent sequence of six photos of an oil film flow visualization as it develops in a wind tunnel on the endwall around a symmetrical airfoil from time zero to 40 minutes. His sequence shows shear stress lines appearing and then disappearing, with no clear criterion as to when the shear stress line picture is "complete".

2) In flow situations involving upstream separation and downstream attachment, it is not always clear where the oil mixture in a particular region originated. Was the oil mixture there to begin with or was it deposited by attachment from some upstream separation region? This ambiguity was not a feature of the first two techniques discussed above. (By painting different surfaces with different colored oil mixtures, this ambiguity can be turned into a means of finding where the flow leaves one surface and impinges on another).

3) Areas that accumulate the oil mixture can be mistaken for separation lines. That can be easily seen in the oil film flow visualization of East and Hoxey in Fig. 7. There is only one saddle point shown, formed by the intersection attachment line running from right-to-left upstream of the cylinder, and the separation line that swings circumferencially around the cylinder. The dark area around the cylinder is <u>not</u> a separation line, but a <u>line of accumulation</u> of the oil mixture. This was shown by Eckerle and Langston[25] using direct flow field measurements and using the oil-dot-film technique. Their cylinder experiment, designed to study the formation of the horseshoe vortex of Fig. 2, was very similar to that of East and Hoxey. Figure 8 shows a sketch of their cylinder experiment and the horseshoe vortex they measured. Also shown in Fig. 8 is a sketch of their flow visualization results. (The actual results are shown in detail in Ref. 26.). This sketch clearly shows only one endwall saddle point and one associated separation line. The line in Fig. 8 labeled as the "accumulation line" is simply a region where pressure gradients are such that the reverse flow near the endwall is strongly decelerated. This corresponds to the dark area of accumulation in the East and Hoxey of Fig. 7. If the airflow had been allowed to continue in the East and Hoxey experiment, the true separation line might have disappeared, leaving the accumulation line to be erronously interpreted as a separation line. It should be emphasized that this "line of accumulation" as defined in Ref. 25 and 26 is not a "new" topological limiting streamline feature (such as a separation line). It is simply a by-product of the particular flow visualization technique used.

The above discussion has brought out the point that the <u>method</u> of surface flow visualization is critical in obtaining accurate surface shear stress pictures. One final comment can be made about the importance of surface flow visualization in measuring velocities and pressures <u>within</u> the flow field of a turbine cascade.

As an illustration of this, consider the flow field around a saddle point of separation 0, as shown in Fig. 9. (This would correspond to S_{S1} in Fig. 6 or to the cylinder saddle point in Fig. 7 and 8.). The sketch in Fig. 9 shows an idealized picture of time-averaged streamlines in a plane of symmetry that contains the attachment lines of saddle point 0, for a very small region about 0. The upstream flow in the plane of symmetry is divided from the downstream separated flow by separating streamline (undistinguishable by measurement) 00'. The dashed line shown in Fig. 9 is the loci of the points at which the mean velocity in the x-direction, u, is equal to <u>zero</u> and changes sign. Thus, when measuring velocity with say a 5-hole pressure probe, for a given x-location to the right of 0, as the probe is traversed in the y-direction, the probe must be rotated a full 180^{o} at the locus of the dashed line! Again, the dashed line separates the <u>reverse</u> flow contained in ΔY_R from the "return" reverse flow contained in ΔY_F Without the reverse-flow-direction knowledge gained from surface flow visualization (Fig. 6), the pressure probe traverse measurement described would be very difficult to make (and near-to-impossible with a single hot wire!).

<u>Final Remarks</u>

The need to measure and sort out the three-dimensional flow in planar turbine cascades has compelled experimenters to use large scale cascades, so that cascade flow features are large relative to the instrumentation used. The larger scale has meant fewer airfoils in a cascade (typically 4-6), which brings into question the periodicity of such finite cascades. One method of achieving periodicity in at least one passage of a 4-airfoil cascade was discussed here. Having sufficient pressure measurements near the

airfoil leading edges, the ability to adjust boundary layer bleeds and tailboards, and an analytical solution for an infinite cascade flow to compare against, were all key to achieving the periodicity. The reader can use these results to judge the degree of periodicity achieved (or claimed) in other finite cascade experiments.

Three techniques of surface flow visualization that have been used in cascade studies were discussed and evaluated. The most used technique (the oil-film method) was shown to have some limitations when compared to the other two (the oil-dot and the oil-dot-film methods).

Some cascade studies (see the review by Sieverding[5]) have made use of the oil film technique and flow field smoke visualization to propose more complex multi-horseshoe vortex systems than that shown in Fig. 2. Baker[27] has shown that laminar flow can give rise to two, four and six vortex systems (steady and unsteady) in front of an endwall mounted cylinder, contrasted with the single vortex of a turbulent flow (Ref. 23 and 25). It has been argued here that the oil-film technique can result in accumulation lines that can be mistaken for separation lines. Thus, these two facts, a) the possibility of mistaking an accumulation line for a separation line, and b) multiple horseshoe vortex systems seem to occur only in laminar flows, combine to make a case against a turbulent multiple vortex model of endwall flow. Direct measurements in the flow field (Ref. 3, 13, and 22) seem to support the single horseshoe vortex view (i.e. Fig. 2).

References

1. Herzig, H.Z., Hansen, A.G. and Costello, G.R., "A Visualization Study of Secondary Flows in Cascades", NACA Report 1163, 1953.

2. Armstrong, W.D., "The Secondary Flow in a Cascade of Turbine Blades", A.R.C. Report and Memorandum No. 2979, Mar. 1955.

3. Langston, L.S., Nice, M.L., and Hooper, R.M., "Three-Dimensional Flow within a Turbine Cascade Passage", ASME J. of Engr. for Power, 99, Jan. 1977, pp. 21-28.

4. Marchal, P. and Sieverding, C.H., Secondary Flow within Turbine Bladings", AGARD-CPP-214 (Netherlands) Secondary Flow in Turbomachinery, Mar. 1977.

5. Sieverding, C.H., "Recent Progress in the Understanding of Basic Aspects of Secondary Flows in Turbine Blade Passages", ASME J. of Engr. for Gas Tur. and Power, 107, 1985, pp. 248-257.

6. Moore, J. and Tilton, J.S., "Tip Leakage in a Linear Turbine Cascade", ASME J. of Turbo., 110, Jan. 1988, pp. 18-26.

7. Bindon, J.P., The Measurement and Formation of Tip Clearance Loss", ASME J. of Turbo., 111, July 1989, pp. 257-263.

8. Yamamoto, A., "Interactions Mechanisms Between Tip Leakage Flow and the Passage Vortex in a Linear Turbine Rotor Cascade", ASME J. of Turbo., 110, July 1988, pp. 329-338.

9. Yaras, M., and Sjolander, S.A., "Development of the Tip-Leakage Flow Downstream of a Planar Cascade of Turbine Blades: Vorticity Field", ASME paper 89-GT-55, IGTI, Toronto, June, 1989.

10. Salvage, J.W., "A Review of the Current Concept of Cascade Secondary Flow Effects", von Karman Inst. for Fluid Dyn., Technical Note 95, March 1974.

11. Gostelow, J.P., Cascade Aerodynamics, Pergamon, 1984, pp. 48-53.

12. Hah, C., "A Navier-Stokes Analysis of Three-Dimensional Turbulent Flows Inside Turbine Blade Rows at Design and Off-Design Conditions", ASME J. of Engr. for Gas Turbines and Power, 106, 1984 pp. 421-429.

13. Yamamoto, A., Production and Development of Secondary Flows and Losses in Two Types of Straight Turbine Cascades: Part 1- A Stator Case, Part 2- A Rotor Case", ASME J. of Turbo., April, 1987, pp. 186-200.

14. Howarth, L. "Laminar Boundary Layers", Handbuch der Physik, VIII/1, S. Flugge, ed., Springer-Verlag, 1959, pp. 318-321.

15. Merzkirch, W., Flow Visualization, 2nd ed., Academic Press, 1987, pp. 82-87.

16. Langston, L.S., and Boyle, M.T., "A New Surface-Streamline Flow-Visualization Technique", J. Fluid Mech., 125, 1982, pp. 53-57.

17. Gaugler, R.E., and Russell, L.M., "Comparison of Visualized Turbine Endwall Secondary Flows and Measured Heat Transfer Patterns", ASME J. of Engr., for Gas Turbines and Power, 106, 1984. pp. 168-172.

18. Boyle, M.T., Simonds, M., and Poon, K., "Comparison of Secondary Flow in a Vane Cascade and a Curved Duct", ASME J. of Turbo., 111, Oct. 1989, to appear.

19. Shin, H.W., Greitzer, E.M., Cheng, W.K., Tan, C.S., and Shippee, C.L., "Circulation Measurements and Vortical Structure in an Inlet-Vortex Flow Field", J. Fluid Mech., 162, 1986, pp. 463-487.

20. Gregory-Smith, D.G., Graves, C.P., and Walsh, J.A., "Growth of Secondary Losses and Vorticity in an Axial Turbine Cascade", ASME J. of Turbo., 110, Jan. 1988, pp. 1-8.

21. Jilek, J., "An Experimental Investigation of the Three-Dimensional Flow within Large Scale Turbine Cascades", ASME paper 86-GT-170, IGTI, Dusseldorf, June, 1986.

22. Harrison, S., "Secondary Loss Generation in a Linear Cascade of High-Turning Turbine Blades", ASME paper 89-GT-47, IGTI, Toronto, 1989.

23. East, L.F. and Hoxey, R.P., "Low Speed Three-Dimensional Turbulent Boundary Layer Data", Royal Aircraft Estab., Tech. Rep. No. 69041, Parts I and II, 1969.

24. Dickinson, S.C., "Time Dependent Flow Visualization in the Separated Region of an Appendage-Flat Plate Junction", Exper. in Fluids, 6, 1988, pp. 140-143.

25. Echerle, W.A., and Langston, L.S., "Horseshoe Vortex Formation around a Cylinder", ASME J. of Turbo., 109, April 1987, pp. 278-285.

26. Echerle, W.A. and Langston, L.S., "Measurements of a Turbulent Horseshoe Vortex formed around a Cylinder, NASA Contractor Report 3986, 1986, pp. 96-97.

27. Baker, C.J., "The Laminar Horseshoe Vortex", J. of Fluid Mech., 95, 1979, pp. 347-367.

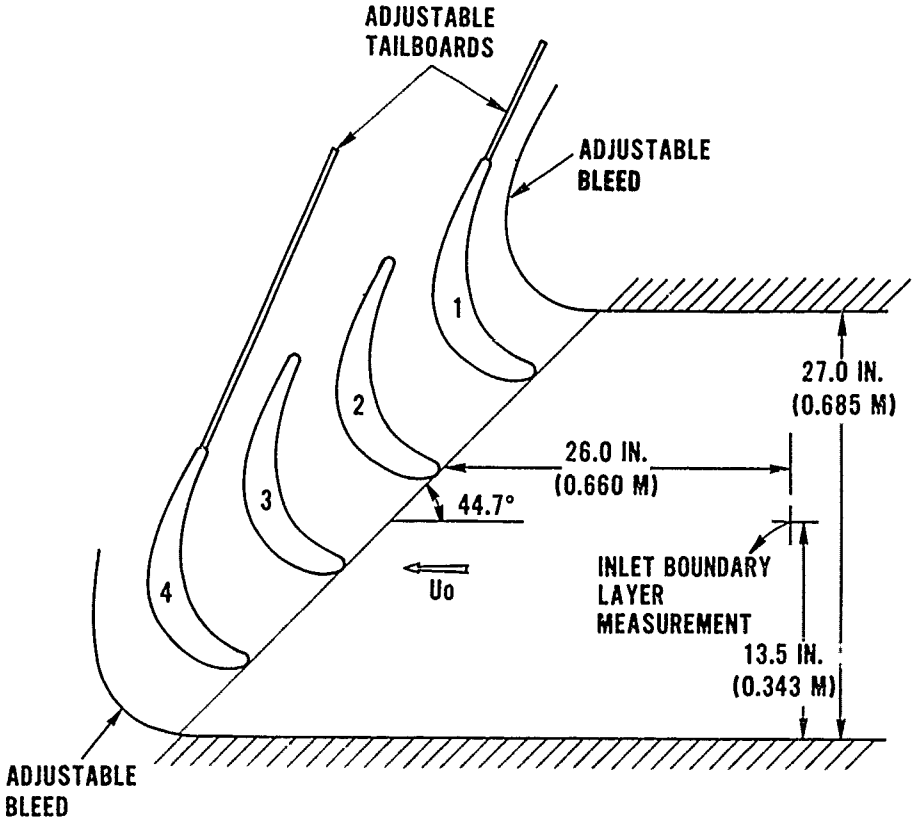


Figure 1 Cross sectional view of cascade test section from Ref. 3.

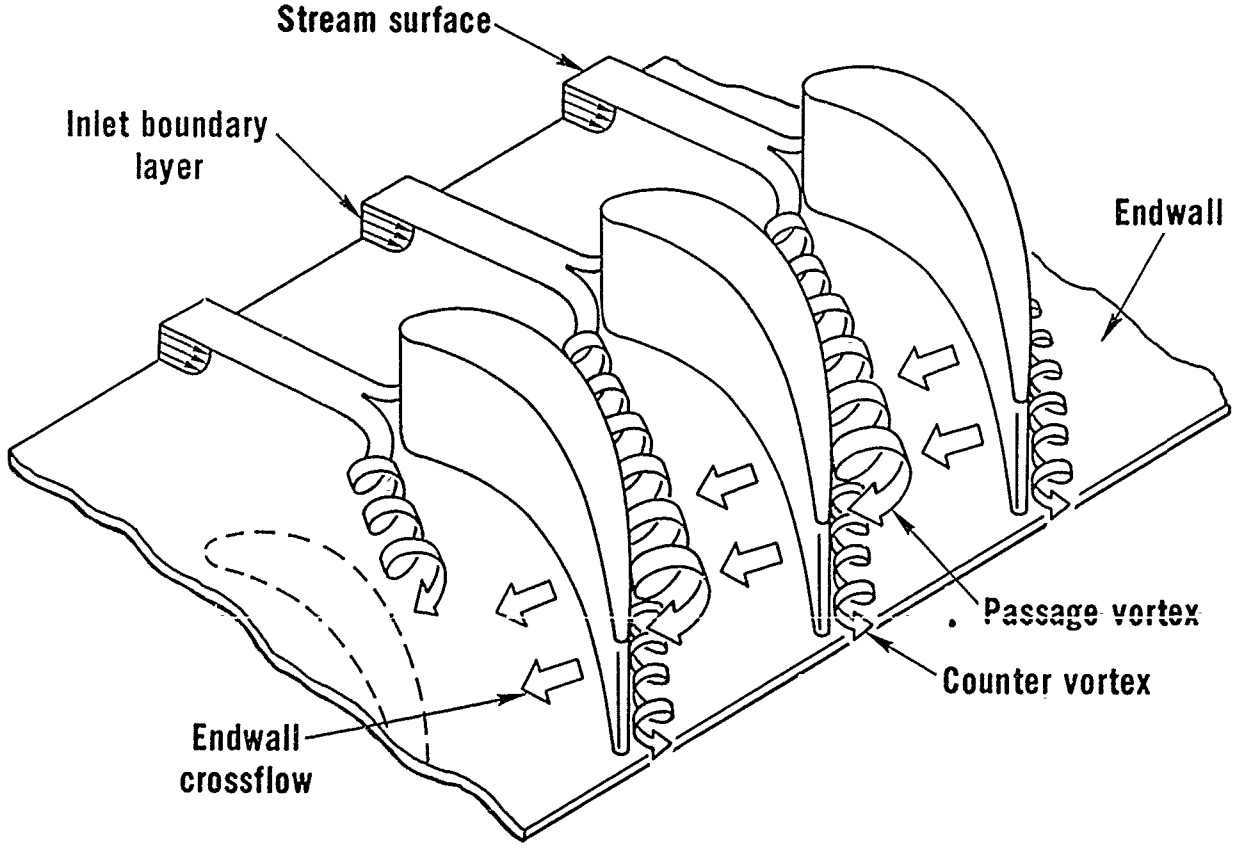


Figure 2 The separation of a boundary layer entering a planar turbine cascade. The saddle point occurs where the horseshoe vortex formed.

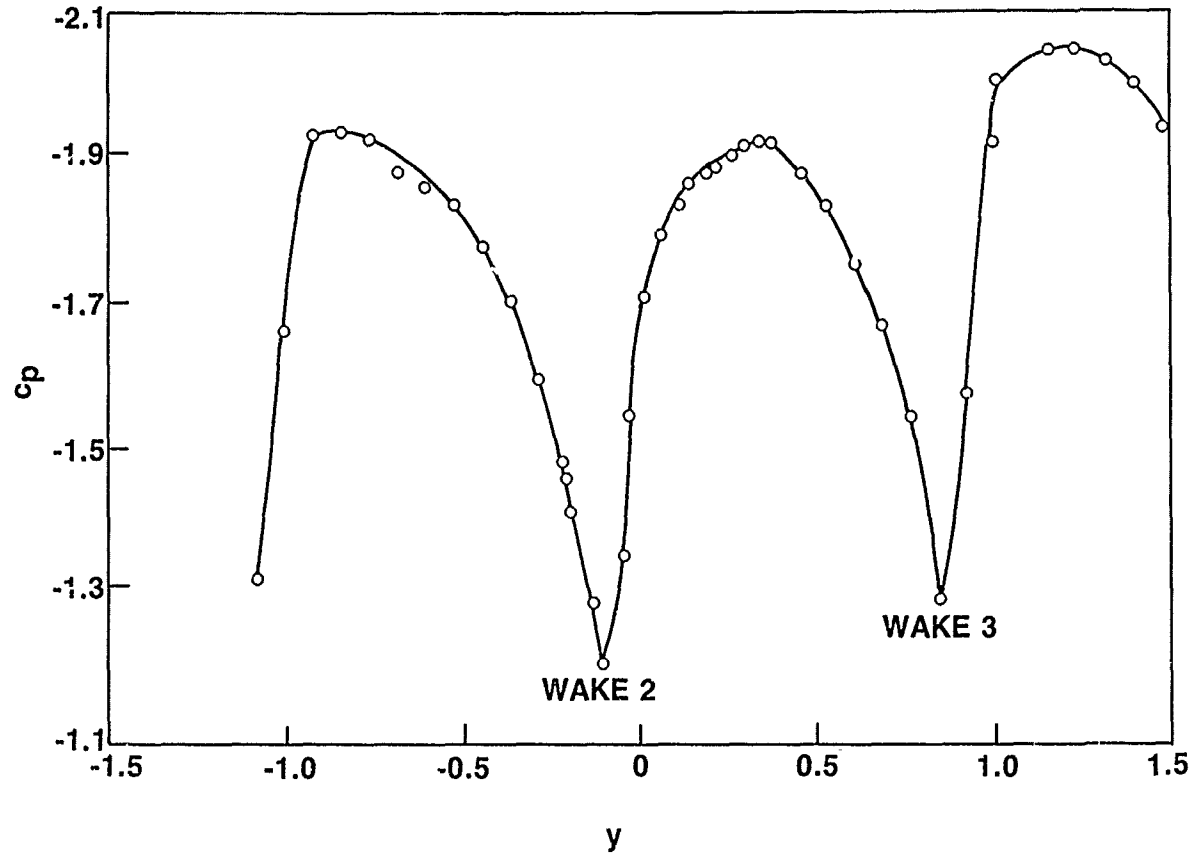


Figure 3 The pressure distribution as a function of gapwise distance as measured on the endwall, about 0.1 b_x (axial) downstream of the cascade trailing edge. (The curve is a fit of the data).

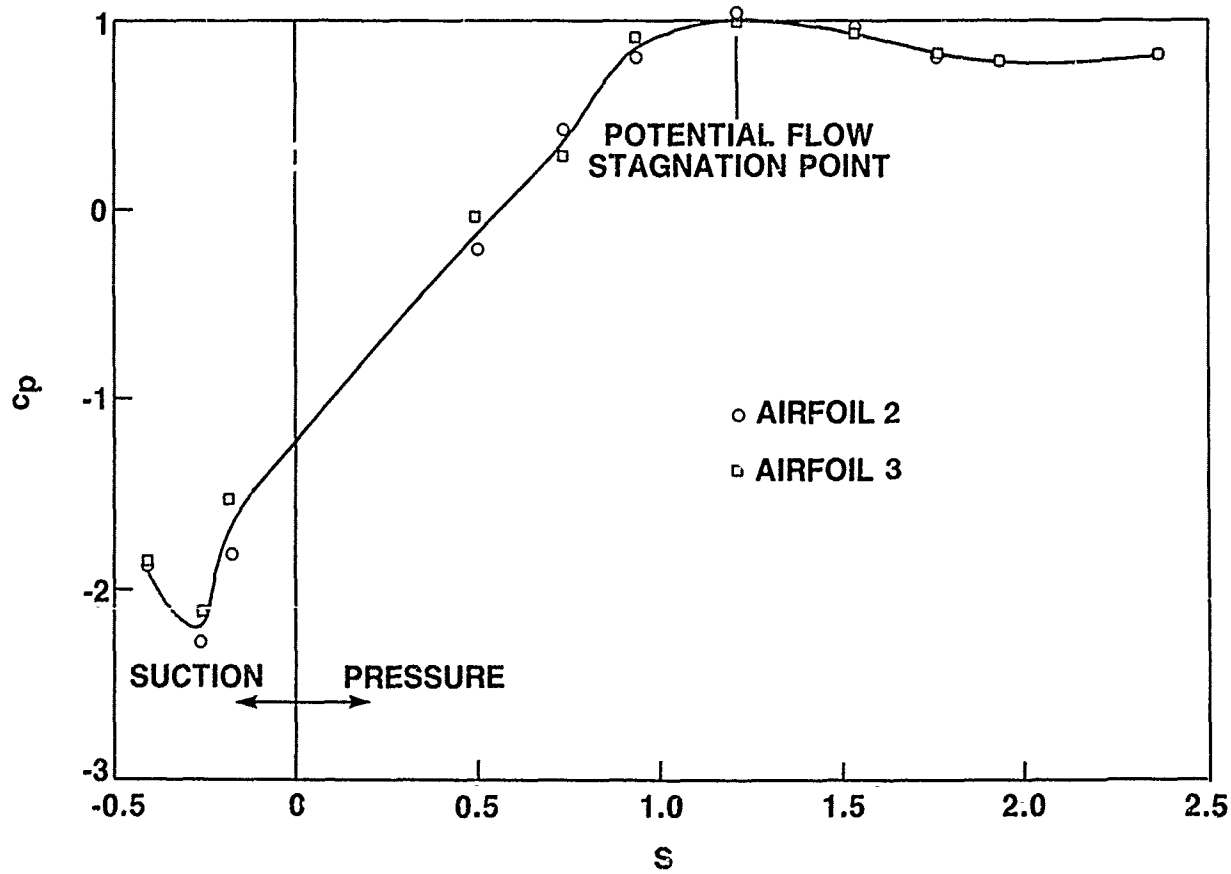


Figure 4 The pressure distribution on airfoils 2 and 3 near the leading edge as a function of nondimensional airfoil distance from the camber line. The curve is the result of a potential flow calculation.

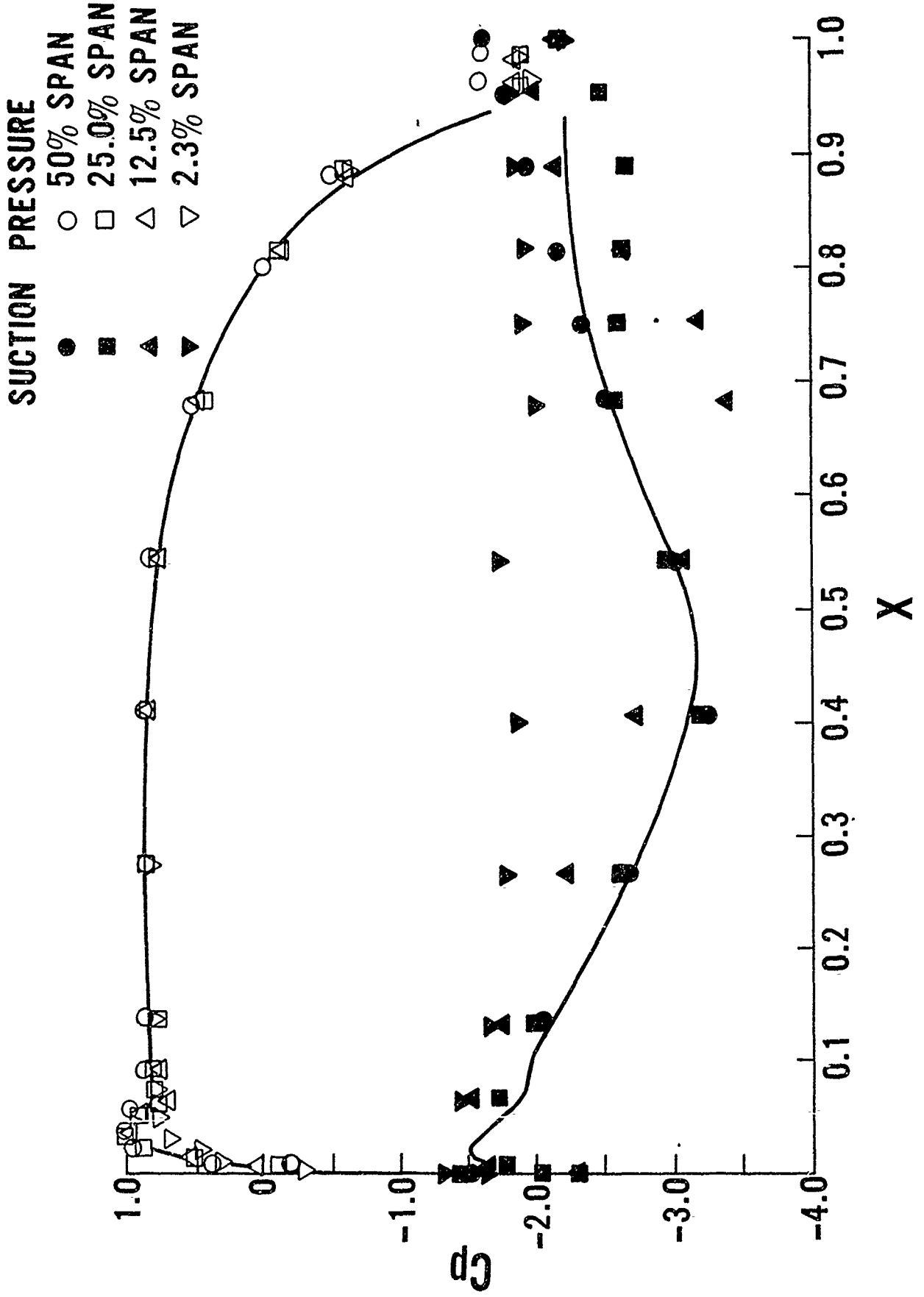


Figure 5 The pressure distribution on airfoils 2 and 3 as a function of axial distance from the leading edge. The curve is a result of a potential flow calculation.

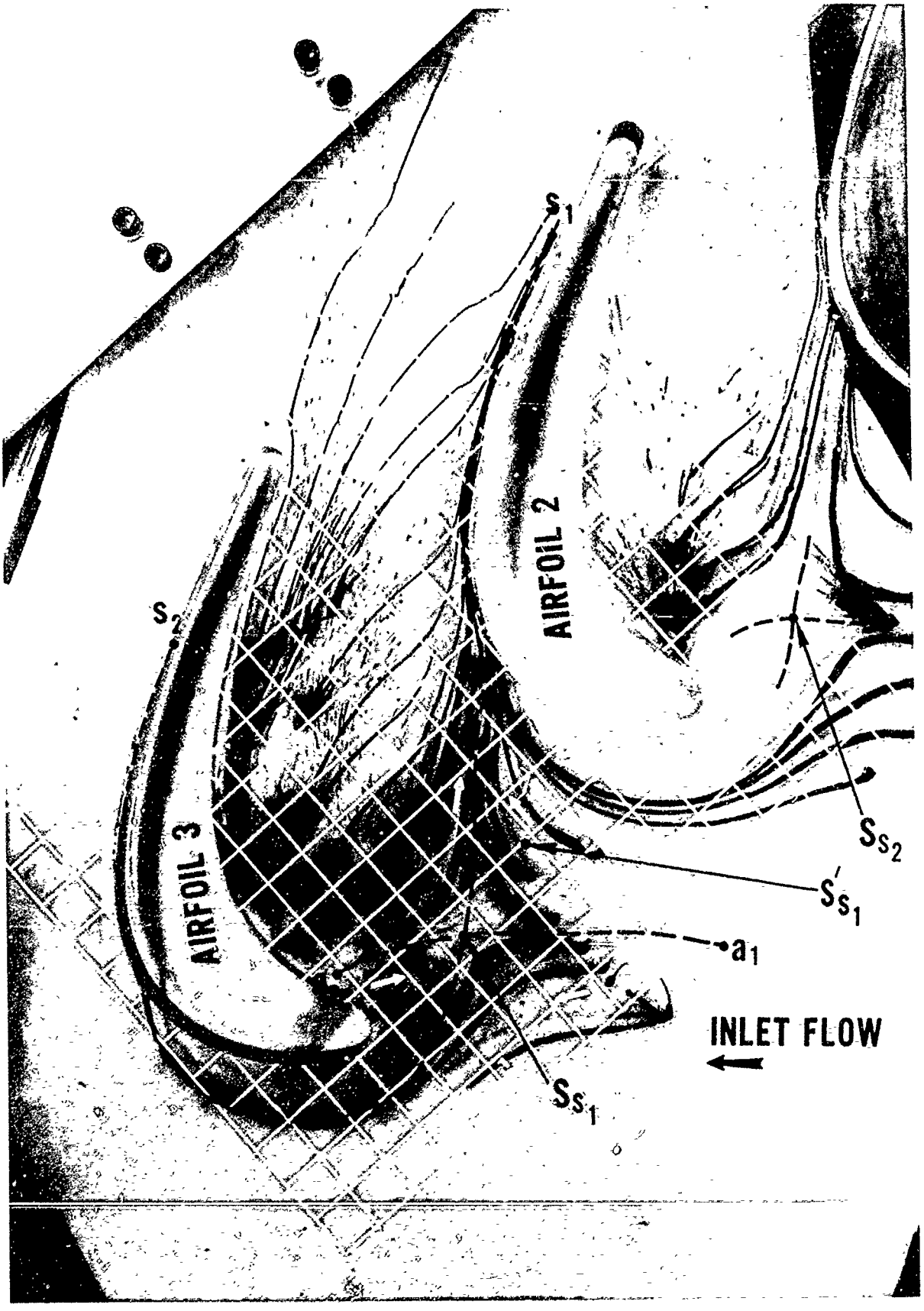


Figure 6 Oil-dot limiting streamlines on the plexiglas endwall of the cascade (Fig. 1) as viewed from outside of the wind tunnel. (As shown, airfoils 2 and 3 have been removed).

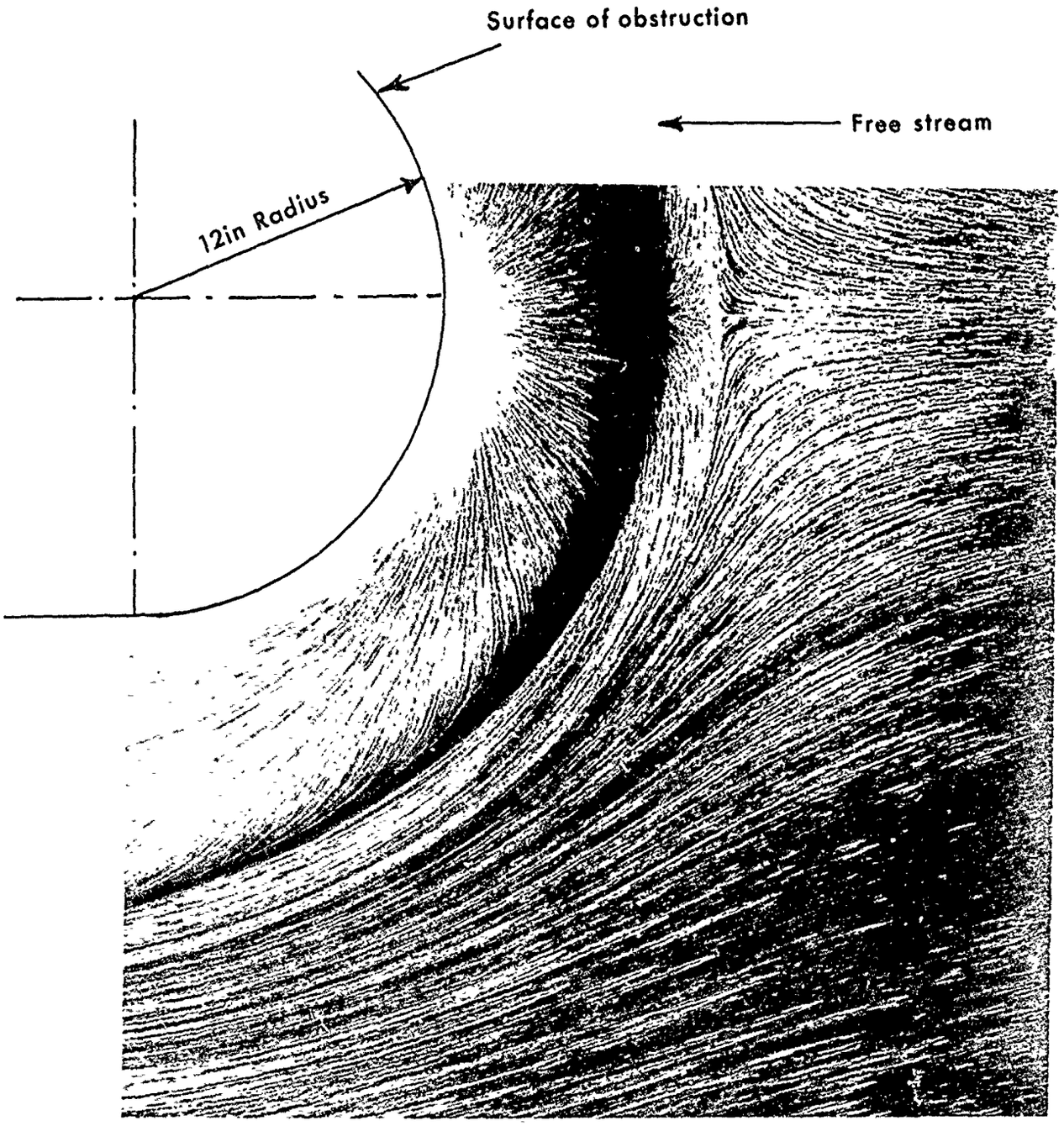


Figure 7 Oil-film limiting streamlines obtained by East and Hoxey[23] on the endwall in front of a cylindrical obstruction. The saddle point is on the symmetry line, approximately one radius from the leading edge.

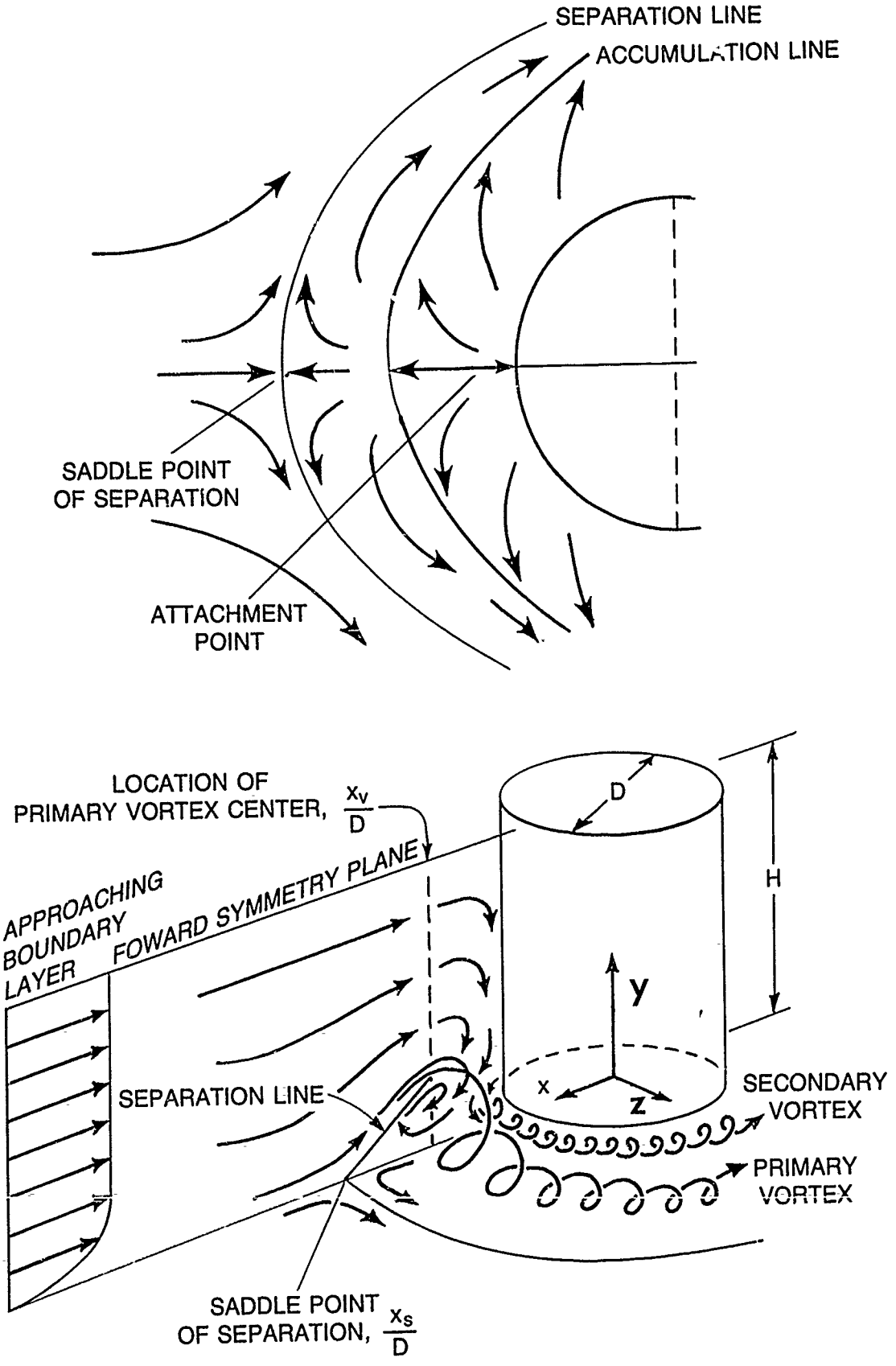


Figure 8 Cylinder experiment of Eckerle and Langston[25,26]. Upper picture is a sketch of oil-dot-film flow visualization results on the endwall. Lower picture shows the measured formation of the horseshoe (primary) vortex.

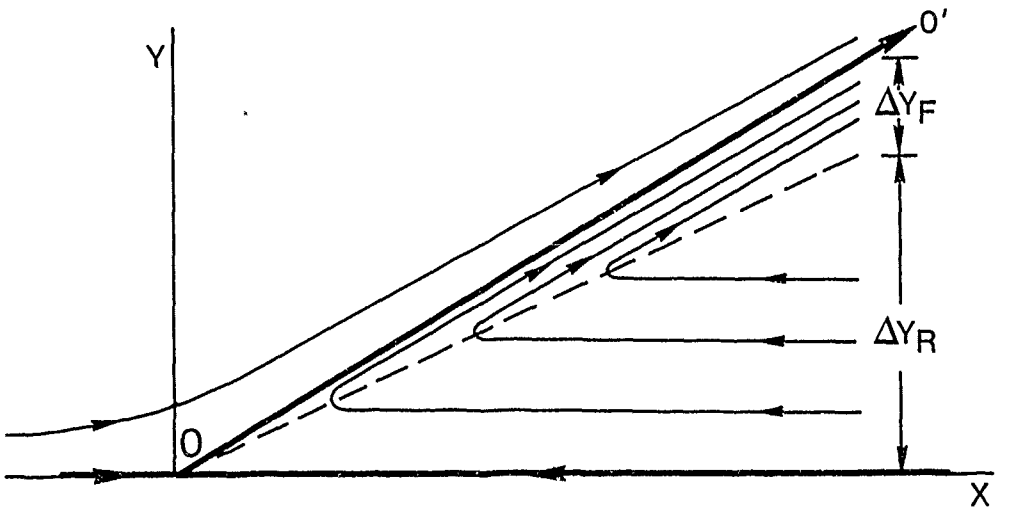


Figure 9 Mean streamlines around a saddle point 0 in the plane of symmetry containing the attachment line. The mainstream flow is in the plus x direction, from left to right.

DISCUSSION

Bullock, USA

A rather exhaustive study was conducted by NACA at Langley Field, VA. Jack Erwin did most of the work as I recall. I believe Drs A. Kantrowitz and S. Bogdonoff were also involved. Some work may have been reported in "Princeton Series". NASA Technical Publications (Notes and Reports) contain the important material.

Author's Reply:

Thank you for your comment. I am aware of early work at NACA Lewis but I was not aware of the Langley work. I will certainly look into the Langley reports.

Chen, Switzerland

May I have a fundamental question about the flow visualization on the wall surface? The streamlines are only a mathematical formulation for the flow. Usually, we cannot see it. But in the flow visualization of your Fig 7, we see clearly streaklines. We have noticed in our experience that a normal boundary layer will only show a wiped-out surface without any flow structure. Only a three-dimensional boundary layer with very thin tangentical component and very thick axial one has such separated streakline. Then the distances of the streaklines corresponds to the wavelength of a kind of Ekman layer instability (Stewartson layer). My question on Prof Langston is: Would you see another mechanism for this separation into individual streaklines of the boundary layer?

Author's Reply:

I don't quite know how to answer your question. Fig 7 concerns the East and Hoxey cylinder data (Ref 23). You might try to analyze their data (tabulated in Ref 23) or equivalently, the data of Eckerle & Langston (Ref 25 and tabulated in Ref 26) to see if there could be another mechanism for separation.

LOSSES IN THE TIP-LEAKAGE FLOW OF A PLANAR CASCADE OF TURBINE BLADES

M.I. Yaras, Graduate Research Assistant
S.A. Sjolander, Associate Professor

Department of Mechanical and Aerospace Engineering
Carleton University
Ottawa, Ontario
Canada K1S 5B6

SUMMARY

The paper examines the total pressure losses in the tip-leakage flow of a planar cascade of turbine blades. The objective is to clarify the loss mechanisms which affect the tip gap flow as well as to provide additional data on tip-leakage losses for use in correlations. Clearances of from 1.5 to 5.5 percent of the blade chord are considered. The flow has been measured also for zero clearance to identify the conventional secondary flow component of the loss. The data presented in the paper clarify the role played in the evolution of the tip-leakage losses by the viscous stresses and separation bubbles inside the tip gap, the "sudden expansion" as the flow emerges from the gap, and the mixing out process as the tip-leakage vortex develops downstream of the trailing edge. The direct loss within the clearance gap is found to be relatively unimportant for the full range of clearances. The measurements are compared with commonly-used correlations for the tip-leakage losses.

NOMENCLATURE

c = blade chord length

c_x = blade axial chord length

C_{Po} = $(P_O - P_{OIN})/(1/2\rho V_{IN}^2)$ = total pressure loss coefficient

C_{Po}' = local mass-averaged total pressure loss coefficient (see Eqn. (2))

C_{Po}'' = total pressure loss coefficient averaged over reference mass flow (see Eqn. (1))

C_{q_s}'' = mass-averaged coefficient of secondary kinetic energy for downstream flow

C_{q_n}'' = mass-averaged coefficient of gap kinetic energy normal to chord line

h = blade span

H = δ^*/θ = boundary layer shape factor

m_{GAP} = mass flow rate through tip gap

m_{REF} = mass flow rate for semi-passage at inlet

P_O = total pressure

P_{OIN} = reference total pressure, on centreline at inlet

q = $1/2\rho V^2$ = dynamic pressure

S = blade spacing

t_{MAX} = blade maximum thickness

u,v,w = components of velocity in the x, y and z directions

u' = root mean square velocity fluctuation in the x direction

V = resultant velocity

V_{IN} = reference velocity, on centreline at inlet

V_n = component of velocity normal to area of interest

x,y,z = co-ordinates in axial, tangential, and spanwise directions respectively

x' = co-ordinate in chordwise direction

Y = total pressure loss coefficient based on outlet dynamic pressure

y' = local pitchwise co-ordinate (see Fig. 2)

β = blade metal angle (see Fig. 2)

γ = blade stagger angle (Fig. 2)

δ = boundary layer thickness

δ^* = boundary layer displacement thickness

δ^{**} = boundary layer energy thickness

θ = boundary layer momentum thickness

μ = viscosity

ρ = density

σ = blade row solidity (c/S)

τ = tip gap

1.0 INTRODUCTION

Tip leakage is a significant source of losses in all unshrouded turbomachines. For example, in axial-flow turbines the tip-leakage losses can account for as much as one third of the losses through a stage (eg. Waterman, [1]). A detailed understanding of the physical origins of these losses is important in several ways. It ensures that appropriate parameters are

used to correlate the losses. It can form the basis for simple analyses for predicting the losses. And finally, an understanding of the physics is necessary for developing design modifications which can reduce the losses. The present paper examines in detail the tip-leakage losses in a planar cascade of turbine blades. The same apparatus has been used previously to investigate other aspects of the tip leakage flow, namely: the effects of the leakage on the blade loading near the tip (Sjolander & Amrud, [2]); the behaviour of the flow inside the gap (Yaras et al., [3]); and the development of the tip leakage vortex downstream of the trailing edge (Yaras & Sjolander, [4]).

Tip-leakage losses are generated in three general regions:

(a) within the gap itself;
(b) as the flow emerges from the gap and mixes with the passage flow;
(c) and downstream of the trailing edge as the tip leakage vortex diffuses outward.

Somewhat different loss mechanisms are dominant in each of the regions, as discussed later. Estimates of the losses in each region can therefore be used to identify the relative importance of different loss mechanisms in determining the overall tip-leakage losses. Most previous experimental studies have not been detailed enough to allow such a sub-division of the losses

In most earlier studies, the tip leakage losses have been estimated from measurements made downstream of the trailing edge only. For example, the flow downstream of compressor rotors has been studied extensively by Inoue and his co-workers (eg. [5-6]) and by Lakshminarayana and his co-workers (eg. [7]). Schmidt et al. [8-9] investigated the effect of leakage on the spanwise loss distribution in an isolated compressor rotor and similar measurements were made by Patel [10] for an axial-turbine rotor. Patel also examined the effects of blade tip treatment. More recently, Yamamoto [11-12] has investigated the tip leakage flow downstream of a linear turbine cascade. While such studies provide useful data and insights into some of the effects which influence the tip-leakage losses, they give a somewhat incomplete picture.

Two recent studies by Bindon [13] and Dishart & Moore [14] come closest to the present one in aims and levels of experimental detail. Bindon examined three clearances in a linear cascade of turbine blades, although detailed data were obtained only for a clearance of 2.5 percent of the blade chord. Measurements were made in the tip gap and at the trailing edge plane. The author notes that there is considerable uncertainty in the losses obtained inside the gap. Bindon concludes that of the tip leakage losses generated up to the trailing edge, about 40 percent occurred within the gap, due mainly to the separation bubbles formed on the blade tip. In addition, he indicates that the fluid of low total pressure which is discharged into the passage from the separation bubbles contributes significantly to the mixing losses after the flow leaves the gap He thus attaches great importance to the separation bubbles on the blade tip. This led him to suggest rounding of the corner at the pressure surface to reduce the losses, even though the gap mass flow rate might be increased. This idea was examined further by Morphis & Bindon [15]. Bindon's results leave unanswered the question of how much additional loss occurs due to mixing downstream of the trailing edge. Dishart & Moore investigated the tip-leakage losses in a linear turbine cascade with a clearance of 2.1 percent of axial chord. They measured the flow at the gap outlet and at 40 percent axial chord downstream of the trailing edge. The authors also calculated the fully mixed-out losses. They found that the losses measured at the gap exit represented only about 17 percent of the total mixed-out losses. They also found that nearly 90 percent of the final losses had occurred by the downstream measurement plane. Thus Dishart & Moore's results imply that the losses inside the gap play a smaller role in the overall losses than was concluded by Bindon. However, their data do not make clear the relative roles played by the immediate mixing of the gap and passage flows and by the subsequent diffusion of the tip-leakage vortex. On the other hand, the losses due to both the latter effects are likely to vary directly with the tip-leakage mass flow rate. Therefore, one might conclude that the total losses can be reduced by decreasing the gap mass flow rate, even though that might increase in the gap losses. This conclusion is of course the opposite of that arrived at by Bindon. The apparently contradictory results may simply be the result of differences in the flow conditions in the two experiments. More data are clearly needed to clarify these issues.

The present study significantly extends the range of data available for clarifying the tip-leakage loss mechanisms.

2.0 EXPERIMENTAL APPARATUS AND PROCEDURES

2.1 Test Section and Test Cascade

The test section used for the measurements is shown schematically in Figure 1; it has been described in detail in the earlier papers. As shown, a linear cascade of five blades is used. The blades have a chord length of 250 mm. The clearance was adjusted by inserting shims between the side walls and the tip-wall window, beginning about two chord lengths upstream of the leading edge. Clearances of 3.8 to 13.7 mm were used and they were set with an estimated accuracy of $\pm$ 0.2 mm.

The test cascade represents the tip section of a low-pressure turbine of fairly recent design. The geometry of the cascade is summarized in Figure 2. As tested, the blade row has slightly different stagger and solidity than it does in the engine. As a result, the cascade blade is somewhat more forward-loaded than the actual rotor blade. In the test section, the blade has a Zweifel loading coefficient of about 0.75. Dishart & Moore's [14] cascade had slightly higher loading, with a Zweifel coefficient of about 1.1.

2.2 Instrumentation and Data Acquisition

The middle blade in the cascade is instrumented over half its span with 14 rows of static pressure taps, each row having 73 taps. These provide a very detailed picture of the blade loading. As shown in Figure 2, the endwall is also instrumented with an array of static taps.

The flow inside the tip gap was measured using a three-hole pressure probe and a seven-hole pressure probe was used for the downstream measurements. The use of these probes and the uncertainty of the measurements have been discussed in detail by Yaras et al. [3] for the three-hole probe and by Yaras & Sjolander [4] for the seven-hole probe.

The three-hole probe is 0.7 mm thick and 2.0 mm wide. Its thickness corresponds to 9 to 14 percent of the clearance heights for which gap measurements were made. For flow in the plane of the probe, the flow angles inferred from the probe measurements are estimated to be accurate to within ±2.5 degrees while the dynamic and total pressures are estimated to be accurate to within ±5 percent of the local dynamic pressure. Inside the gap, the flow can be misaligned in pitch relative to the probe. Calibration has shown that under these conditions the inferred flow angles are still satisfactory but the total pressures are underestimated. The implications of this are discussed further in section 3.4.

The seven-hole probe has an outer diameter of 2.4 mm and the total cone angle of the face is 60 degrees. Like the three-hole probe, the seven-hole probe is used in the non-nulling mode. It was therefore calibrated in steps of 5 degrees through all combinations of pitch and yaw out to 50 degrees of misalignment for both angles. Inferred flow angles are estimated to be accurate to within ±2 degrees and the total and dynamic pressures to within ±5 percent of the local dynamic pressure.

All pressures were measured with capacitive-type pressure transducers. The analog output of the transducers was converted to digital form, with 12-bit resolution, using a data acquisition system controlled by a microcomputer.

3.0 EXPERIMENTAL RESULTS

3.1 Operating Conditions

All measurements were made at a blade Reynolds number of $4.3 \times 10^5 \pm 2$ percent based on the undisturbed inlet velocity and blade chord. The inlet velocity was about 30 m/s so that conditions were essentially incompressible. The turbulence intensity, u'/U, at the cascade inlet was about 1.5 percent.

Four clearances from 1.5 to 5.5 percent of the blade chord were examined. For reference, measurements were also made for zero clearance. Table 1 summarizes the locations at which the flow field was traversed for each clearance. As seen, the gap flow was measured only for the three largest clearances. The measurements for 2.8 percent clearance were made at an early stage and the downstream traverses were not detailed enough to provide reliable mass-averaged loss coefficients. For all clearances the boundary layer on the tip wall was traversed with a small pitot tube at 1.32 chord lengths upstream of the leading edge. The resulting boundary layer parameters are also included in Table 1. Some variation in the boundary layer with clearance is evident. As noted earlier, the clearance is varied by moving the tip wall outward using spacers. A ramp is provided to give a reasonably step-free transition between the fixed and moveable parts of the tip wall. Nevertheless, the boundary layer is disturbed. This probably accounts for the variation in the boundary layer with clearance. In any case, the boundary layer is seen to be quite thin compared with the gap heights.

3.2 Averaging Procedures and Experimental Uncertainty

Total pressure losses and other flow quantities need to be expressed in mass-averaged form. To be comparable, the values of quantities obtained at different planes must be averaged over the same mass flow rate, ideally over the same streamtube. The spanwise extent of the streamtube is not important so long as it includes all of the fluid which experiences loss. Bindon [13] integrated his downstream losses over an area one blade spacing in the pitchwise direction and 1/4 chord in the spanwise direction. This area was observed to include the entire extent of the tip-leakage fluid. On the other hand, Dishart & Moore [14] integrated over the full span of their cascade. While this assures that equal mass flows are considered at upstream and downstream planes, it is then necessary to subtract the secondary losses measured at the "hub" wall, to isolate the tip-leakage losses.

In the present study, the flow quantities were averaged over the mass flow rate measured over one pitch and half the span at the inlet to the cascade, this is referred to as the "reference mass flow rate", m_{REF}. The mass-averaged total pressure loss coefficient then takes the form:

$$C''_{Po} = \frac{\int_{\Delta z}\int_{\Delta y} C_{Po}(y,z)\rho V_n \, dydz}{m_{REF}} \quad . \tag{1}$$

For downstream planes, $\Delta y = S$ and $\Delta z = h/2$ as for the inlet flow. Similar integrals are evaluated to obtained average values of other flow quantities.

For the gap flow, the limits of integration are the dimensions of the gap. For this region, a local mass-averaged loss coefficient is also defined:

$$C'_{Po} = \frac{\int_0^{\tau} C_{Po}\rho V_n \, dz}{\int_0^{\tau} \rho V_n \, dz} \quad . \tag{2}$$

C_{Po}' was evaluated as a function of the chordwise position along the gap.

The mass flow rates measured over the downstream planes were found to be about 90 to 95 percent of the reference mass flow rate. Therefore, the full extent of the inlet streamtube was not included in the downstream measurements. The lower flow rate is mainly due to displacement of freestream fluid away from the tip wall, as a result of endwall boundary layer growth and the development of the tip leakage vortex. The missing fluid can therefore reasonably be assumed to be freestream fluid which experienced essentially no loss.

Since different reference mass flow rates are used in Bindon's, Dishart & Moore's and the present experiment, the absolute values of the loss coefficients are not comparable. However, the relative magnitudes in different regions of the flow can be compared, as was done in Section 1.0.

The uncertainty in individual probe measurements was discussed in Section 2.2. The uncertainty in the mass averaged quantities is more difficult to quantify. The total pressure distribution in the freestream at the cascade inlet has been found to vary with time due to fouling of the screens in the settling chamber. The screens are cleaned regularly but some variation in the inlet loss coefficient is inevitable during a particular series of measurements. The inlet flow was measured at two widely separated times for 2 and 5.5 percent clearance. The losses quoted in Table 2 are the average values and the individual values differed from them by less than ±0.01. Thus, the uncertainty in the inlet mass-averaged quantities is estimated to be about ± 0.01. The varying inlet total pressure also affects the measurements at the downstream planes and the seven-hole probe introduces additional uncertainty there. We estimate the uncertainty in the downstream mass-averaged quantities to be at least ±0.03.

3.3 Inlet, Profile and Secondary Losses

Table 2 lists the mass-averaged loss coefficients measured at the inlet for each clearance. All losses are measured relative to the total pressure on the centre line at the inlet. However, there are some regions in the freestream at the inlet where the total pressure is slightly higher than on the centreline. As a result, the inlet "loss" coefficient turned out to be positive for zero clearance for which the endwall boundary layer was quite thin. The inlet loss values are subtracted from the downstream measurements to obtain the net losses across the blade row.

It is conventional to separate the tip-leakage losses from the secondary and profile losses which will also be present in the flow downstream of the trailing edge. This is normally done by subtracting the losses measured for zero clearance. Such a subdivision is undoubtedly open to criticism. There is clearly an interaction between the endwall boundary layer and the tip leakage flow. Likewise, the effect of tip-leakage on the blade loading near the tip (eg. see Sjolander & Amrud, [2]) will alter the losses in the blade boundary layers on that part of the blade. To allow the present data to be analyzed in alternative ways, the results are presented in Table 2 both as measured as well as decomposed into the conventional components. The approach taken here has been to assume that both secondary and profile losses are constant with clearance. Thus, the tip-clearance loss coefficient at a given plane was obtained by subtracting the net loss coefficient obtained at the same plane with zero clearance. This approach leads to some error since the secondary losses can be expected to vary with the observed changes in the endwall boundary layer thickness. The magnitude of the effect can be estimated from correlations for the effect of inlet boundary layer thickness on the secondary losses. For example, for the range boundary layer thicknesses obtained here, Dunham [16] suggested that the secondary loss would vary by a factor $f(\delta^*/c) = 0.0055 + 0.078\sqrt{(\delta^*/c)}$. This indicates that the secondary loss would vary by at most ± 15 percent over our range of inlet conditions. In view of the uncertainties in both the losses and the boundary layer measurements, it seems reasonable assume a constant secondary loss.

3.4 Clearance Gap Losses

Earlier in the present research program, flow visualization was conducted and flow field measurements were made inside the tip gap for several clearances [2-?]. The objectives were to clarify the physics of the gap flow and to obtain values of the gap mass flow rates. The total pressure losses were also calculated, for example, Figure 3 shows a contour plot of the loss coefficients obtained inside the gap for 2.8 percent clearance. The gap flow measurements were concentrated on the blade mean line. Therefore, they do not include the losses which occur between the mean line and the gap outlet at the pressure surface. However, a few measurements were also made at the gap discharge. These allow the magnitudes of the losses which were omitted to be estimated.

Figure 4 shows the local mass-averaged loss coefficients obtained at the mean line and gap outlet for 2.8 percent clearance. The results are typical of those obtained for the other clearances. Although the gap outlet results are rather sparse, they clearly indicate that very little additional loss occurs between the mean line and the outlet. This is in fact consistent with our physical understanding of the gap flow. As would be expected, separation bubbles were observed on the blade tip at the pressure surface corner. The size and strength of the bubbles varied with chordwise position, as indicated in the contour plot, Figure 3. This probably accounts for the peaks in the loss coefficients obtained on the mean line, as shown in Figure 4. Both flow visualization and the probe measurements indicated that the bubbles reattached on the blade tip well before the outlet of the gap. It seems likely that the gap losses occur mainly through the very high shear stresses in the flow at the gap inlet and through the mixing between the main gap flow and the relatively stagnant flow in the separation bubbles. Once the bubbles reattach relatively little additional loss might be expected. This may largely account for the agreement between the mean-line and outlet losses shown on Figure 4. An additional factor is the effect of pitch misalignment on the probe measurements. Since the separation bubbles were apparently beginning to reattach near the blade mean line, the probe is likely to have been somewhat misaligned in pitch for some of the measurements made there. As noted in Section 2.2, the probe will indicate low total pressures and therefore higher losses under such conditions. The net effect appears to be that measurements made on the mean line give a good estimate of the full losses inside the gap.

Table 2 shows the gap losses averaged over both the local gap mass flow rate and over the semi-passage (reference) mass flow rate. On a local basis, the losses are seen to decrease with increasing clearance. This seems consistent with the behaviour of the tip separation bubbles noted by Yaras et al. [3]. For very small clearances the size of the bubble seems to be limited by the constraining effect of the adjacent endwall. As the clearance increases, the bubble becomes larger both in absolute terms and relative to the gap height. As the clearance increases further, the bubble seems to remain at its natural size and therefore occupies a decreasing fraction of the gap height. The local losses would be expected to be a maximum for the clearance at which the separation bubble occupies the largest fraction of the gap height. That point appears to occur at about 2 percent clearance for the present flow.

The flow in the tip gap includes some fluid from the inlet endwall boundary layer. This fluid has already experienced some loss which should not be charged to the clearance gap. Based on smoke and surface oil flow visualization, Sjolander & Amrud [2] estimated that about 1/4 of the original endwall boundary fluid was driven through the tip gap; the rest was driven across the passage to form the passage vortex in the usual way. Data presented in the next section suggests that the fraction may be larger. However, in the absence of better quantitative information and to allow for this effect in a very crude way, one quarter of the inlet boundary loss was subtracted from the measured gap loss. The result is taken as the "true" net loss within the gap.

3.5 Downstream and Fully Mixed-Out Losses

Figures 5 to 7 show the contours of total pressure loss obtained at the trailing edge plane for 0, 2 and 5.5 percent clearance. It is seen from Figure 5 that although the secondary vortex is large it is fairly weak. This is probably due to the relatively low turning of about 45 degrees for the present cascade.

It is clear that over the range of clearances examined here, the passage outlet flow is dominated by the tip-leakage vortex. A small passage vortex is just discernible at the endwall near mid passage. The remaining fluid from the inlet endwall boundary therefore must be largely mixed with and inseparable from the tip-leakage fluid. Thus, subdividing the flow into leakage and secondary components for purposes of correlating losses, as is usually done, does not follow from any natural subdivision within the present flow. It is probable that for very small clearances the endwall boundary layer will separate ahead of the leading edge to form the usual horseshoe vortex. Amrud [17] saw evidence of such a separation from surface flow visualization in the present cascade at less than 1 percent clearance. However, for the present range of clearances the tip leakage and secondary aspects of the flow are inseparable. It would be of considerable interest to know whether the picture is different for a substantially thicker inlet boundary layer.

The development of the mass-averaged loss coefficients with downstream distance is shown in Figure 8. The inlet losses have been subtracted to give the net losses across the blade row. The mixed-out values were calculated from the measurements at Plane C2, the last traverse plane. The losses clearly grow substantially as the vortices mix with the freestream flow over the first couple of axial chord lengths downstream of the trailing edge. It will also be noted that for 1.5 and 2 percent clearance, the losses are greater than the secondary losses (zero clearance) by roughly a constant amount over the first axial chord length. Thus, if the losses are subdivided into secondary and tip-leakage components, the conclusion would be that the observed growth in losses with downstream distance occurs almost entirely in the secondary component. Even allowing for the considerable uncertainty in the measurements, the loss increase seems to be concentrated disproportionately in the secondary component. This is rather difficult to accept physically.

The apparent physical inconsistencies which arise from subdividing the losses into secondary and tip-leakage components prompted us to examine the flow in terms of the blade "end losses". The end losses are obtained by subtracting the blade profile losses from the observed downstream losses. The physical picture which emerges is discussed with reference Figures 9 and 10. The bar charts show the loss development for the two cases for which complete data sets are available, namely 2 and 5.5 percent clearance. The lower section of the stacked bars shows the end losses measured at each station. Like other workers (eg. Moore & Adhye, [18], Dishart & Moore, [14]), we have found it helpful to identify the secondary kinetic energy present in the flow at each position. For the tip gap flow, the upper part of the bar shows the mass-averaged kinetic energy corresponding to the velocity component normal to the blade chord line. For the downstream planes, the secondary kinetic energy is contained in the components of velocity in the plane normal to the free stream velocity.

Consider first the flow development between the gap and the trailing edge. Figures 9 and 10 show that the gap flow discharges into the blade passage with a very large amount of kinetic energy. A considerable total pressure loss subsequently occurs between the gap and the trailing-edge plane, particularly for the large clearance. However, the increase in loss is much less than the secondary kinetic energy available at the gap outlet. Some of the gap kinetic energy apparently appears as the secondary kinetic energy in the tip-leakage vortex, but the remainder seems to have been largely recovered, presumably as static pressure. The discharge from the gap clearly does not behave simply as a sudden expansion. The orderly shear interaction between the gap and the passage flow, leading to the roll-up of the tip vortex, evidently allows much of the gap kinetic energy to be recovered.

For both cases, the total pressure loss roughly doubles from the trailing edge to Planes C1 and C2, one axial chord length downstream. The loss clearly can not be explained by the loss of secondary kinetic energy between the two planes. Some of the loss is likely due to mixing out of non-uniformities in the streamwise flow. However, the most important reason for the additional loss seems to be provided by the mixing calculations.

As seen from the final two bars, the calculated fully mixed-out losses increased considerably between planes B and C. This was true for all cases examined, as shown in Table 2. We interpret the differences as evidence of an additional loss mechanism which acts between the two planes but which is not taken into account by the mixing calculation. The calculation assumes that the flow mixes out at constant area to uniform static pressure and streamwise velocity and with no remaining secondary velocity components. Thus, the mixing losses connected will all components of velocity are included. At the upstream planes, the measured static pressure distributions are used. Therefore, all pressure forces acting on the

control volume in the streamwise direction are likewise taken into account. However, although the control volume extends to the endwall, the force due to the wall shear stress is not included in the momentum balance. The increase in mixed-out losses suggests that the losses due to the endwall shear stresses are in fact considerable.

The difference between the calculated mixing losses at planes B and C is thus interpreted as the total pressure loss due to the endwall shear stress between those two planes. It is seen from Figures 9 and 10 that when this loss is added to the measured loss at plane B, it accounts for the missing loss between the two planes. Furthermore, it is noticeable that the magnitude of the wall loss is roughly proportional to the gap kinetic energy in each case. This seems physically reasonable The tip-leakage vortex is expected to increase the local wall shear stresses and therefore increase the entropy production on the endwall. As the clearance is increased, the gap kinetic energy increases and the vortex becomes larger and stronger Therefore, one would expect the wall loss to vary with the gap kinetic energy, or mass flow, as observed.

It is seen that growth of the end losses is largely complete one axial chord length downstream of the trailing edge More interestingly, the losses observed at this plane agree well with the sum of the losses and the secondary kinetic energy at the gap outlet. Thus, a good estimate of the final loss can evidently be obtained by assuming that all of the gap kinetic energy is ultimately lost. This assumption has sometimes been used in the past but was applied to just the tip-leakage component of the loss. The quantitative agreement could to some degree be fortuitous since, as noted, some of the gap kinetic energy is in fact recovered and part of the final loss is apparently due to wall shear stress. On the other hand, the greater the recovery of the gap energy, the stronger is the tip leakage vortex and the greater the loss production on the endwall. The recovery could therefore be regarded as inherently temporary, leading to loss processes which assure that the energy is ultimately dissipated. More data would be highly desirable to confirm this potentially useful result.

To demonstrate briefly that the "end loss" rather than "tip-leakage loss" approach appears to produce the more physically plausible and internally consistent results, the bar chart for the tip-leakage components at 2 percent clearance is shown in Figure 11. Both the total pressure losses and secondary kinetic energies for zero clearance have been subtracted to obtain the tip-leakage components at each plane. As seen, the final tip-leakage loss does not match the gap outlet kinetic energy very well. There is also the unexplained constancy of the loss between planes B and C. Somewhat different trends occurred in the corresponding data for 5.5 percent clearance. The results for tip leakage are of course more sensitive to the uncertainties in the measurements. However, it may simply be, as we believe, that this is not a very appropriate way to look at the present data.

3.6 Significance of Gap Losses

As discussed in Section 1.0, earlier studies had been inconclusive about the relative importance of the loss within the gap itself. For discussion purposes the gap losses will be compared with the losses measured one axial chord length downstream. This is done on the basis that a designer will be most interested in the losses up the inlet of the following blade row, which will be some distance downstream.

It is evident from Figures 9 to 11 and Table 2 that the gap loss decreases in importance as the clearance increases. In terms of end losses, the gap loss varies from about 25 to 10 percent of the "final" (Plane C2) loss as the gap increases from 2 to 5.5 percent. The corresponding figures are about 60 to 25 percent for the tip-leakage losses.

Figure 12 shows an alternative way of looking at the data. The discussion of Section 3.5 suggested that the losses downstream of the gap vary with the dynamic pressure at the gap outlet and thus with the square of the gap mass flow rate Figure 12 shows the variation of the non-gap end loss (that is, the end loss at Plane C2 minus the gap loss) with the gap flow rate. The non-gap end loss is assumed to approach the normal secondary loss monotonically as the gap flow rate tends to zero. The lower curve shows the gap loss itself. As discussed in Section 3.4, the losses inside the gap rise with decreasing clearance. However, since the gap mass flow is also decreasing, the loss coefficient based on the reference mass flow is not expected to rise significantly and must eventually tend to zero as the gap flow does. Figure 12 indicates that at small clearances the total end loss can be reduced primarily by reducing the loss within the gap. However, it is also clear that the reduction in the total loss will be fairly modest. At larger clearances, the gap mass flow rate becomes dominant Any modifications to reduce the gap losses which also result in an increase in gap flow rate could easily produce a net increase in losses. In summary, for the present cascade the direct losses within the gap appear to be relatively unimportant for the complete range of clearances.

4.0 COMPARISON WITH CORRELATIONS

A number of correlations and simple prediction models for the tip-leakage losses have been proposed Some of the more commonly-used ones are plotted on Figure 13 along with the values measured for the present cascade. The correlations and models are seen to predict a remarkably wide range of losses for a given clearance. Ainley & Mathieson's [22] correlation agrees reasonably well with the present measurements. Dishart & Moore [14] also found that Ainley & Mathieson's correlation agreed well with their measured value. However, in view of the apparently close connection between the tip-leakage and secondary losses, a more relevant comparison is with the combined (end) losses predicted by the model or correlation.

Not all models provide a complete loss prediction system. Among those that do, Ainley & Mathieson's, with modifications made by later authors, is probably the most widely used. Figure 14 shows the end losses (the sum of the secondary and tip-leakage losses) predicted by Ainley & Mathieson's and Dunham & Came's [19] methods together with the measured values. As seen, the agreement is no longer good for Ainley & Mathieson's method. Also, as noted previously by Kacker & Okapuu [23], Dunham & Came's correlation seems to over-estimate considerably the effects of tip leakage

Although the present comparisons are far from exhaustive, they indicate that there is considerable room for improvement in the correlations and models.

5.0 CONCLUSIONS

As with any specific case, the present flow may have features which can not be generalized. It also lacks effects which are present in the actual machine, including compressibility, high levels of freestream turbulence and relative motion at the endwall. With these qualifications, the picture of tip leakage in axial turbines which emerges is briefly summarized.

For all clearances, the tip-leakage and secondary aspects of the flow were found to be essentially inseparable. It was concluded that the losses in the tip region should be viewed as end losses, with secondary losses simply being the limiting value as the clearance tends to zero. This point of view also led to a physically reasonable explanation for the development of the losses.

The clearance flow was found to discharge from the gap with a large amount of kinetic energy normal to the gap exit. However, the gap outlet did not act as a simple sudden expansion. Much of the gap kinetic energy was found to have been recovered by the time the flow reached the trailing edge. The relatively orderly roll-up of the fluid into the tip leakage vortex evidently allowed the recovery to take place. On the other hand, the recovery appeared to be temporary. The losses increased substantially over the first axial chord length downstream of the trailing edge. At that point the loss generation seemed to be largely complete. It was found that the end loss measured one axial chord length downstream agreed well with the sum of the losses within the gap together with a loss equal to the kinetic energy in the flow at the gap outlet. The gap energy seemed to be ultimately lost through two main mechanisms. The energy partly recovered as secondary kinetic energy of the tip-leakage vortex was eventually lost as the vortex mixed with the surrounding freestream fluid. Secondly, the presence of the tip leakage vortex seemed to lead to higher shear stresses and therefore higher entropy production at the endwall. Based on indirect evidence, it was concluded that the loss production at the endwall was in fact substantial. The loss within the tip gap itself was found to be reasonably small compared with the final loss.

Finally, we note that mixing calculations for endwall-bounded flows must apparently be used and interpreted with considerable caution. For all of our cases, substantially higher "fully mixed-out" losses were obtained at one axial chord length downstream compared with the trailing edge plane. As noted above, the difference was attributed loss production at the endwall. We are not aware of previous observations of this effect or comments on its implications for the use of mixing calculations.

ACKNOWLEDGMENTS

Financial support for this study provided by the Natural Sciences and Engineering Research Council of Canada under Grant A1671 and by Pratt & Whitney Canada Inc. is gratefully acknowledged.

REFERENCES

1. Waterman, W.F., "Turbine Loss Correlations and Analysis," von Karman Institute/Pennsylvania State University Lecture Course on Tip Clearance Effects in Axial Turbomachines, April 1986.

2. Sjolander, S.A., and Amrud, K.K., "Effects of Tip Clearance on Blade Loading in a Planar Cascade of Turbine Blades," ASME Journal of Turbomachinery, April 1987, pp. 237-244.

3. Yaras, M., Zhu, Y. and Sjolander, S.A., "Flow Field in the Tip Gap of a Planar Cascade of Turbine Blades," ASME Journal of Turbomachinery, Vol. 111, No. 3, July 1989, pp. 276-283.

4. Yaras, M. and Sjolander, S.A., "Development of the Tip-Leakage Flow Downstream of a Planar Cascade of Turbine Blades: Vorticity Field," ASME Paper No. 89-GT-55, June 1989.

5. Inoue, M., Kuroumaru, M. and Fukuhara, M., "Behaviour of Tip Leakage Flow Behind an Axial Compressor Rotor," ASME Journal of Engineering for Gas Turbines and Power, Vol. 108, No. 1, January 1986, pp. 7-14.

6. Inoue, M. and Kuroumaru, M. "Structure of Tip Clearance Flow in an Isolated Axial Compressor Rotor," ASME Journal of Turbomachinery, Vol. 111, No. 3, July 1989, pp. 250-256.

7. Lakshminarayana, B., Zhang, J., and Murthy, K.N.S., "An Experimental Study on the Effects of Tip Clearance on Flow Field and Losses in an Axial Flow Compressor Rotor," ISABE Paper No. 87-7045, June 1987.

8. Schmidt, M.J.P., Agnew, B., and Elder, R.L., "Tip Clearance Flows - Part 1 Experimental Investigation of an Isolated Rotor," ISABE Paper No. 87-7034, 1987.

9. Schmidt, M.J.P., Agnew, B., and Elder, R.L., "Tip Clearance Flows - Part 2 Study of Various Models and Comparison with Test Results," ISABE Paper No. 87-7035, 1987(b).

10. Patel, K.V., "Research on a High Work Axial Gas Generator Turbine," SAE Paper No. 800618, 1980.

11. Yamamoto, A., "Interaction Mechanisms Between Tip Leakage Flow and the Passage Vortex in a Linear Turbine Rotor Cascade," ASME Journal of Turbomachinery, Vol. 110, No. 3, July 1988, pp. 329-338.

12. Yamamoto, A., "Endwall Flow/Loss Mechanisms in a Linear Turbine Cascade with Blade Tip Clearance," ASME Journal of Turbomachinery, Vol. 111, No. 3, July 1989, pp. 264-275.

13. Bindon, J.P., "The Measurement and Formation of Tip Clearance Loss," ASME Journal of Turbomachinery, Vol. 111, No. 3, July 1989, pp. 257-263.

14. Dishart, P.T., and Moore, J., "Tip Leakage Losses in a Linear Turbine Cascade," ASME Paper No. 89-GT-56, June 1989.

15. Morphis, G., and Bindon, J.P., "The Effects of Relative Motion, Blade Edge Radius and Gap Size on the Blade Tip Pressure Distribution in an Annular Turbine Cascade with Clearance," ASME Paper No. 88-GT-256, June 1988.

16. Dunham, J., "A Review of Cascade Data on Secondary Losses in Turbines," Journal of Mechanical Engineering Science, Vol. 12, No. 1, 1970, pp. 48-59.

17. Amrud, K.K., "Tip Le ge in a Planar Cascade of Turbine Blades," M.Eng. Thesis, Carleton University, Ottawa, Canada, 1985.

18. Moore, J., and Adhye, R.Y., "Secondary Flows and Losses Downstream of a Turbine Cascade," ASME Journal of Engineering for Gas Turbines and Power, Vol. 107, No. 4, October 1985, pp. 961-968.

19. Dunham, J. and Came, P. M. "Improvements to the Ainley & Mathieson Method of Turbine Performance Prediction," ASME Journal of Engineering for Power,Vol. 92, No. 3, July 1970, pp. 252-256.

20. Lakshminarayana, B. and Horlock, J. H., "Leakage and Secondary Flows in Compressor Cascades," ARC R&M 3483, March 1965.

21. Vavra, M.H., Aero-Thermodynamics and Flow in Turbomachines, Wiley, New York, 1960.

22. Ainley, D.G., and Mathieson, G.C.R., "A Method of Performance Estimation for Axial-Flow Turbines," ARC R&M 2974, 1951.

23. Kacker, S.C., and Okapuu, U., "A Mean Line Prediction Method for Axial Flow Turbine Efficiency," ASME Journal of Engineering for Power, Vol 104, No. 1, January 1982, pp. 111-119.

TABLE 1. TEST MATRIX AND INLET BOUNDARY LAYER CONDITIONS

			CLEARANCE, τ/c				
			0.0	0.015	0.020	0.028	0.055
LOCATION x/c_x							
	GAP				X	X	X
P							
L	B	1.03	X	X	X		X
A	C1	1.96	X	X	X		X
N	C2	2.01	X	X	X		X
E							
BOUNDARY LAYER PARAMETERS							
τ (mm)			0.0	3.8	5.1	7.1	13.7
δ^* (mm)			3.6	6.5	4.8	6.8	2.8
θ (mm)			2.8	5.0	3.4	4.2	2.0
δ^{**} (mm)			5.1	9.0	6.1	7.0	3.5
H			1.3	1.3	1.4	1.6	1.4

TABLE 2. MASS-AVERAGED FLOW QUANTITIES

	CLEARANCE (τ/c)				
	0.0	0.015	0.020	0.028	0.055
INLET FLOW					
$C_{Po}''_{(IN)}$	0.0067	-0.0787	-0.0355	-0.0455	-0.0196
GAP FLOW					
m_{GAP}/m_{REF}	-	-	0.073	0.083	0.161
C_{Po}''(for m_{GAP})	-	-	-0.805	-0.461	-0.230
C_{Po}''(for m_{REF})	-	-	-0.0584	-0.0382	-0.0370
$C_{Po}''_{(GAP-1/4IN)}$	-	-	-0.0496	-0.0268	-0.0321
C_{qn}	-	-	0.164	0.176	0.331

TABLE 2. MASS-AVERAGED FLOW QUANTITIES (CONT.)

	CLEARANCE (τ/c)				
	0.0	0.015	0.020	0.028	0.055
DOWNSTREAM FLOW					
q_{OUT}/q_{IN}	2.13	1.95	2.04	-	1.82
C_{Po}''(PROFILE)	-0.063	-0.050	-0.055	-	-0.042
C_{Po}''(PLANE B)	-0.0365	-0.174	-0.158	-	-0.202
C_{Po}''(PLANE C1)	-0.137	-0.251	-0.261	-	-0.392
C_{Po}''(PLANE C2)	-0.137	-0.256	-0.262	-	-0.410
C_{qs}''(PLANE B)	0.0145	0.0301	0.0389	-	0.0889
C_{qs}''(PLANE C1)	0.0053	0.0116	0.0127	-	0.0485
C_{qs}''(PLANE C2)	0.0055	0.0110	0.0118	-	0.0471
FULLY MIXED-OUT VALUES					
C_{Po}''(PLANE B)	-0.073	-0.241	-0.241	-	-0.364
C_{Po}''(PLANE C1)	-0.152	-0.290	-0.307	-	-0.490
C_{Po}''(PLANE C2)	-0.150	-0.294	-0.307	-	-0.507

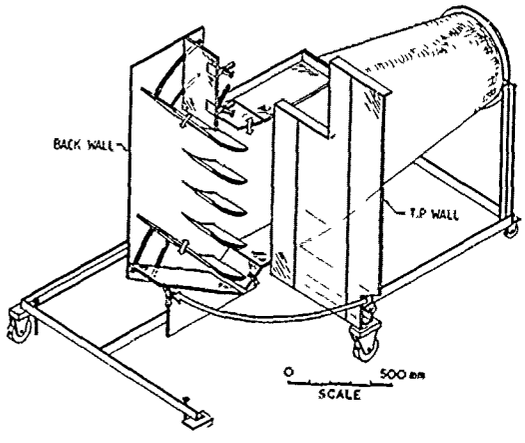
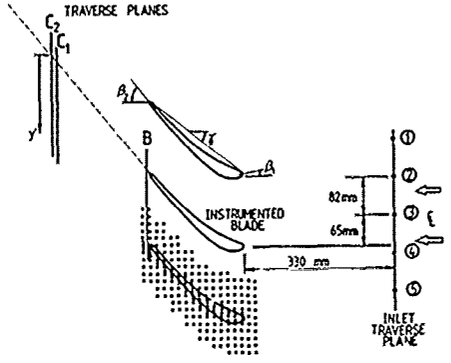


FIGURE 1. CASCADE TEST SECTION



CHORD LENGTH, c	: 250 mm
BLADE THICKNESS, t_{MAX}	: 24.6 mm
BLADE SPAN, h	: 203 mm
BLADE SPACING, S	: 150 mm
STAGGER ANGLE, γ	: 37.2 ± 0.2 deg.
BLADE INLET ANGLE, β_1	: 11.1 ± 0.2 deg.
BLADE OUTLET ANGLE, β_2	: 49.6 ± 0.2 deg.

FIGURE 2. SUMMARY OF CASCADE GEOMETRY.

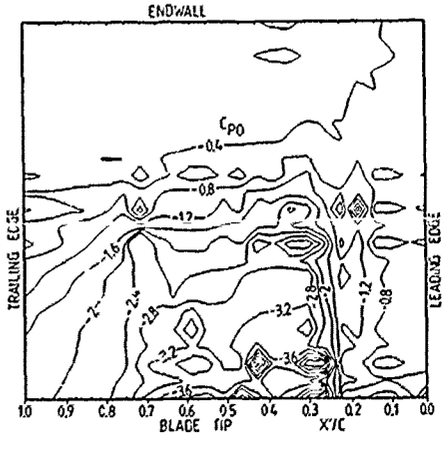


FIGURE 3. LOSS COEFFICIENT DISTRIBUTION WITHIN THE TIP GAP (τ/c = 0.028).

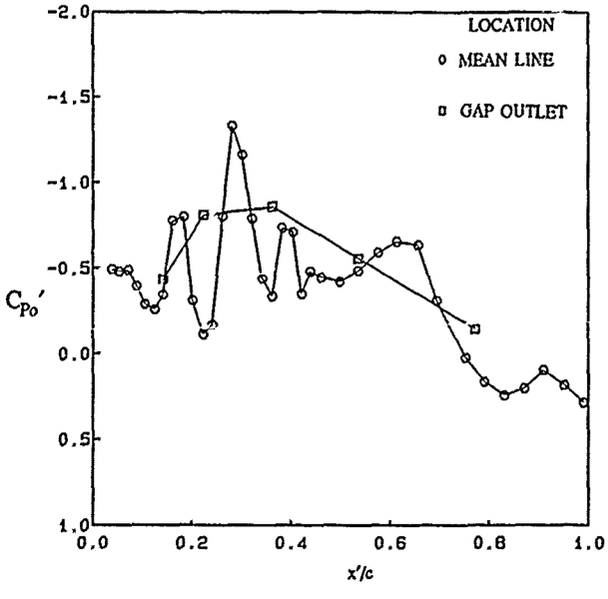


FIGURE 4. LOCAL MASS-AVERAGED LOSS COEFFICIENT IN GAP (τ/c = 0.028).

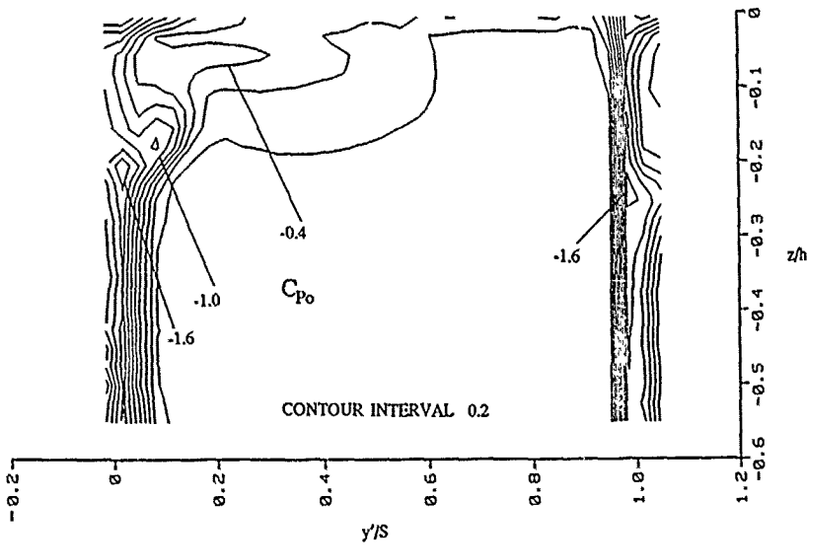


FIGURE 5. TOTAL PRESSURE LOSS COEFFICIENTS AT TRAILING EDGE (PLANE B) FOR $\tau/c = 0$.

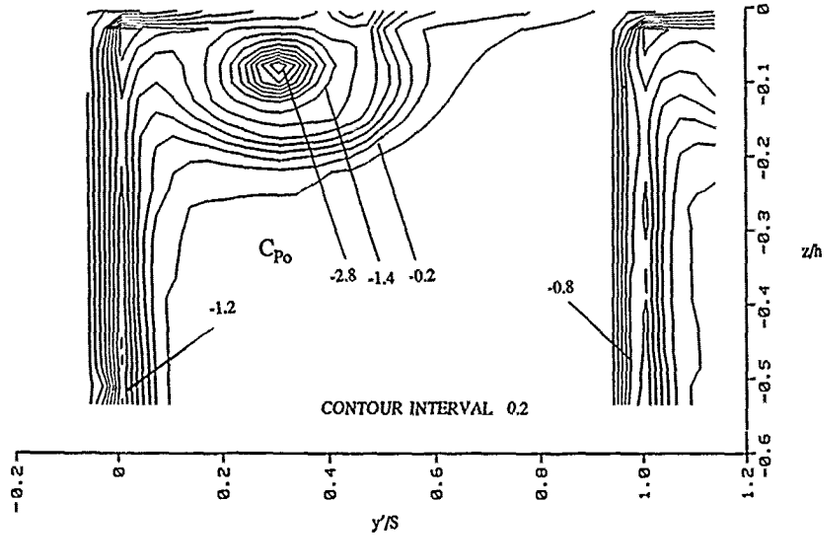


FIGURE 6. TOTAL PRESSURE LOSS COEFFICIENTS AT TRAILING EDGE (PLANE B) FOR $\tau/c = 0.02$.

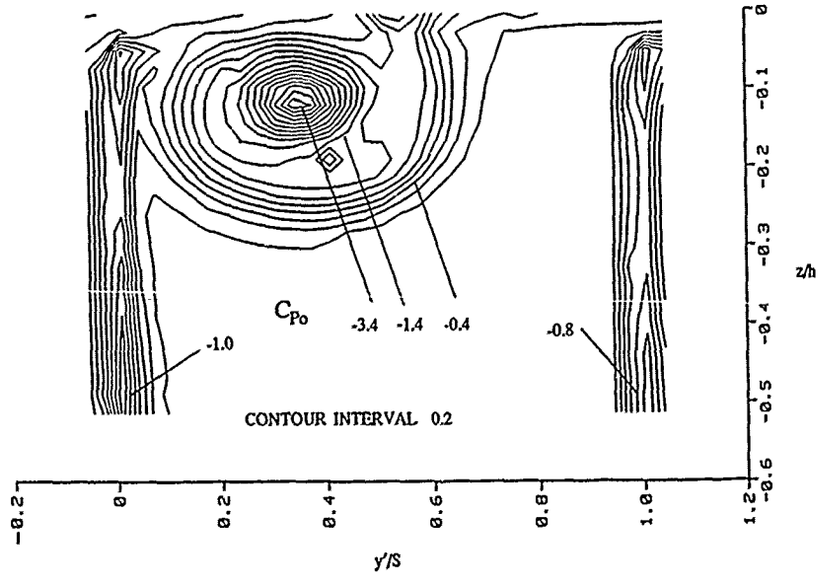


FIGURE 7. TOTAL PRESSURE LOSS COEFFICIENTS AT TRAILING EDGE (PLANE B) FOR $\tau/c = 0.055$.

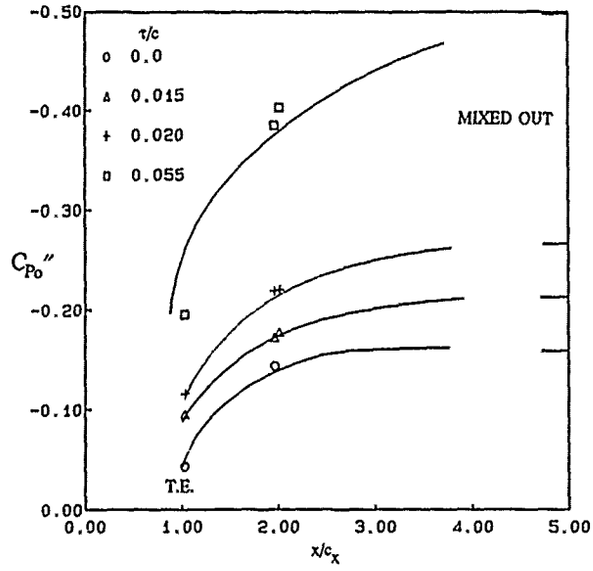


FIGURE 8. VARIATION OF NET TOTAL PRESSURE LOSS COEFFICIENTS WITH DOWNSTREAM DISTANCE.

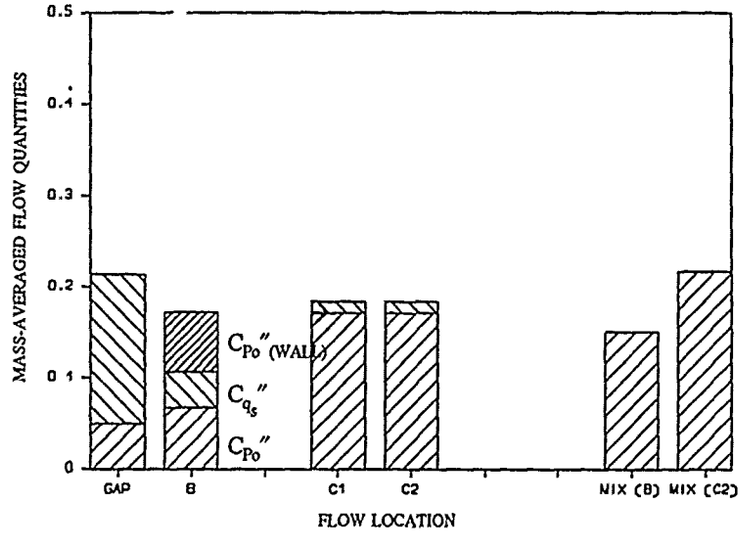


FIGURE 9. DOWNSTREAM DEVELOPMENT OF END LOSSES AND SECONDARY KINETIC ENERGIES (τ/c = 0.02).

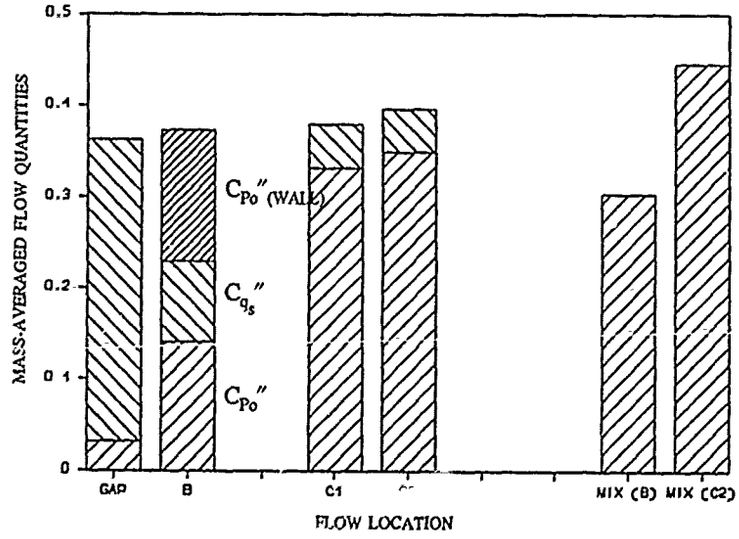


FIGURE 10. DOWNSTREAM DEVELOPMENT OF END LOSSES AND SECONDARY KINETIC ENERGIES (τ/c = 0.055).

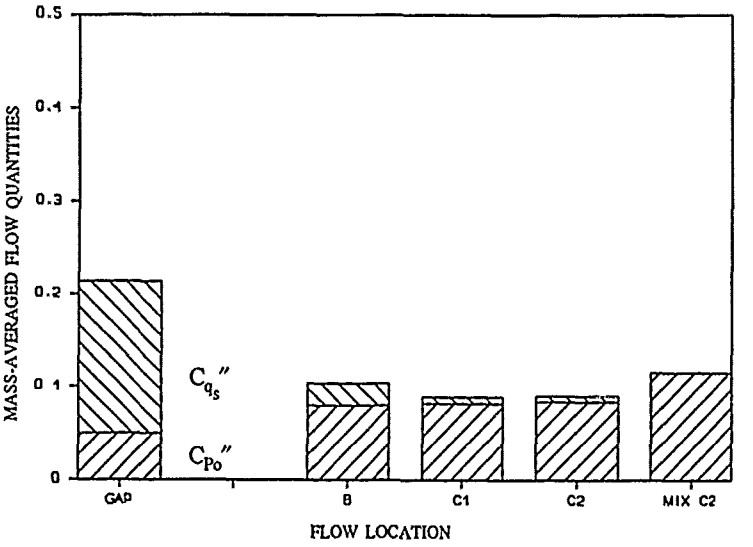


FIGURE 11. DOWNSTREAM DEVELOPMENT OF TIP-LEAKAGE LOSSES AND SECONDARY KINETIC ENERGIES (τ/c = 0.02).

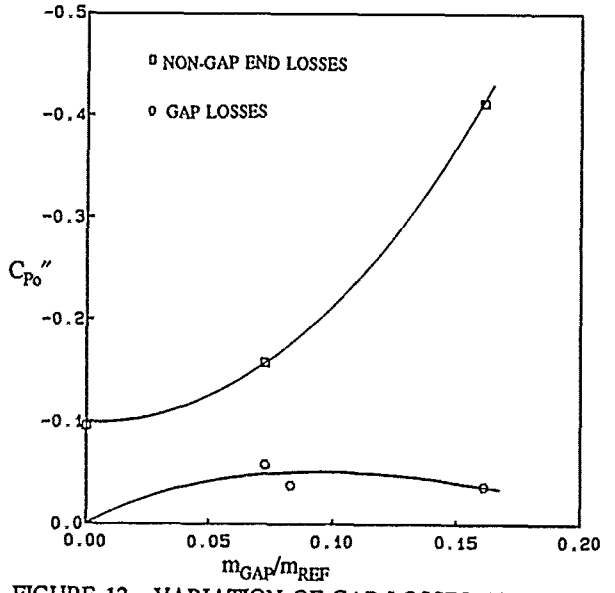


FIGURE 12. VARIATION OF GAP LOSSES AND NON-GAP END LOSSES WITH GAP FLOW RATE.

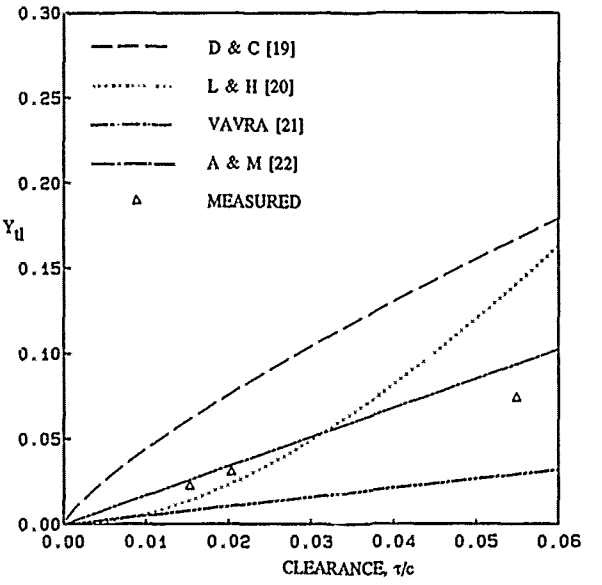


FIGURE 13. COMPARISON WITH TIP-LEAKAGE LOSS CORRELATIONS AND MODELS.

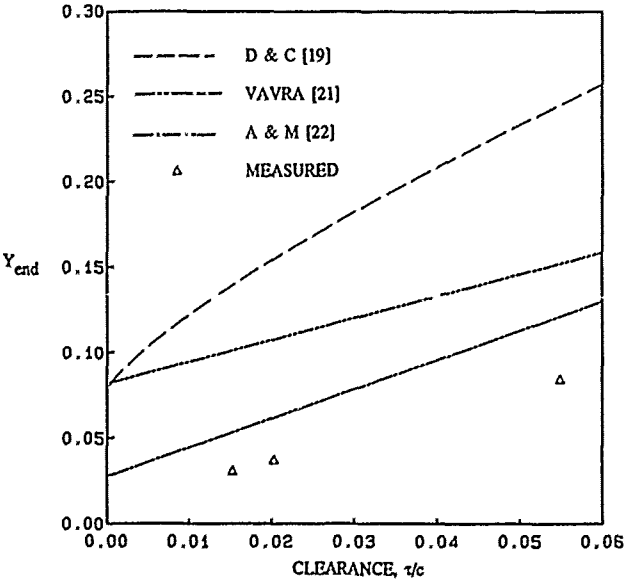


FIGURE 14. COMPARISON WITH CORRELATIONS FOR END (SECONDARY PLUS TIP-LEAKAGE) LOSS COEFFICIENT.

DISCUSSION

Mr. M.A. HOWARD, Rolls Royce, UK

Have you looked at including endwall friction forces in the mixing calculation and if so could you quote average wall skin friction coefficients.

Author's reply :

We have not tried to include the effects of endwall friction in the mixing calculations. In principle, the control volume used for the mixing calculations extends to infinity in the downstream direction. It is thus difficult to see precisely how the endwall effects could be incorporated.

A simple momentum balance between planes B and C indicates that a rather high value of endwall skin friction coefficient is needed to explain the observed increase in loss. It is for this reason that the increase was attributed somewhat tentatively to endwall effects. There may be contributions from other, as yet unidentified, mechanisms. It seems clear from the results that the increase in loss is directly related to the strength of the streamwise vortex, whether secondary or tip clearance.

COMPUTATIONAL PREDICTION AND MEASUREMENTS OF THE FLOW IN AXIAL TURBINE CASCADES AND STAGES

Prof. Dr.-Ing. H.E. Gallus

K. Weskamp J. Zeschky

Institut für Strahlantriebe
und Turboarbeitsmaschinen
RWTH Aachen
Templergraben 55, 5100 Aachen
W.-Germany

Summary

A partially-parabolic program was developed to calculate the three-dimensional, viscous flow through subsonic axial turbine guide vanes and rotor blades. To provide test cases for the calculations, a detailed experimental study of the flow in an axial turbine stage as well as in an axial-flow turbine cascade has been performed. The obtained results and the comparison of the theoretical and experimental data are discussed in this paper.

Nomenclature

b_p	axial blade chord	w	relative velocity in the rotating system
c	velocity	x	axial distance from blade leading edge
h/H	relative blade height	α	angle between the flow direction and the axial direction
k	turbulent kinetic energy	ε	rate of turbulent dissipation
P	static pressure	Ω	loss coefficient $\Omega = (P_{To}-P_T)/(P_{To}-P)$
P_T	total pressure		
P_{To}	total pressure at cascade/stage inlet		
s^i	non-orthogonal coordinates		

Introduction

The Navier-Stokes Equations describing subsonic flows form an elliptic system, where the simultaneous solution for the entire flow field is essential. This is a very extensive and computer-time consuming method and requires a big mainframe computer memory. To reduce the processing time nonviscous solutions with boundary layer adaptions are often used, especially when during the design procedure of a turbomachine several calculations are necessary. However, these methods cannot account for the three-dimensional flow and loss mechanisms, whereas a profound knowledge of these phenomena is required to achieve additional improvements of the efficiency of modern turbomachines. This lead to the development of the partial-parabolic method. It is capable of reproducing the three-dimensional, viscous effects, but requires considerable less computer time and storage than fully elliptic methods /1,2,3/.

The partially-parabolic program passes through the flow field by use of a progressing integration in the main stream direction, which covers the entire cross section of the flow field and contains a pressure correction deducted from the continuity equation. This limits the calculation to flow cases, where no separation is encountered. The code includes terms for the centrifugal- and Coriolis-forces and is therefore applicable for stator and rotor flows. The numerical mesh is refined in the vicinity of the flow channel surfaces to resolve end-wall and profile boundary layers.

Parallel to the theoretical investigations an experimental program has been worked out, which included detailed measurements in a subsonic axial-flow turbine cascade and stage. The objective was to improve the understanding of the three-dimensional flow mechanisms and to provide a benchmark data base for the code verification.

This paper presents the progress in the development of the numerical program and the comparison between computed and experimental data.

The partially-parabolic algorithm

Starting with a given distribution of the profile nodes and geometry of the end-walls, the computational mesh is generated using a numerical transformation suggested by Thames, Thompson and Mastin /4/.

The partially-parabolic algorithm involves iteration between a marching integration of the conservation equations through the flow field and the solution of an elliptic pressure correction equation. The outline of this procedure is illustrated in Fig. 1.

The program requires a start approximation for the pressure field, which is derived from an inviscid quasi-three-dimensional stream surface calculation. The flow properties at the inlet plane, including boundary layers, are obtained from measured data. The equations of motion and energy are solved implicitly to determine the downstream distributions of velocity and temperature. They do not necessarily satisfy the equation of continuity. This is corrected in a first step, when the given pressure field is improved by a global pressure correction. Subsequently, continuity defects are eliminated by local pressure corrections at all volume elements by adding additional forces to the equation of motion. This iterational procedure is continued until the velocity differences converge to a prescribed accuracy. The calculation of the turbulent viscosity distribution downstream follows, either with the mixing length hypothesis or the k-ε-model. The solutional approach is continued from plane to plane to the grid exit. After the cycle through the computational mesh an elliptical pressure correction follows. A simplified equation of motion is solved simultaneously for all volume elements, taking into account the additional forces from the local pressure corrections. The improved pressure field is the input for a renewed partially-parabolic calculation. This cycle of solution is repeated until the pressure differences finally converge to the prescribed accuracy.

Test Rig Description

The first part of the measurements was carried out in a rectangular cascade with divergent end-walls /5/, the second part in a single stage axial turbine /6/. In the cascade and in the turbine stator a two-dimensional profile described in /7/ was used, in the turbine rotor a modified VKI-profile. The geometry data of cascade and turbine are given in Fig. 2.

In the inlet and exit planes of cascade, stator and rotor the flow could be surveyed with pneumatic five-hole probes, head diameter 2.6 mm. Close to the end-walls hot-wire and pneumatic boundary layer probes were used. The probes were traversed radially from hub to tip, within the limits of the specific probe geometry, and circumferentially over two blade pitches. The uncertainty of the probe measurements was about $\pm$ 1 percent in velocity and $\pm$ 0.5 degree in flow angle.

In both the cascade and the turbine stator one of the vanes was furnished with 25 static pressure orifices. These vanes could be traversed radially to measure the pressure distribution with a fine radial resolution. The measurement of the static pressure on the rotor blades presented some difficulties at the beginning, when a commercial scanner was used. The main problems were leakage at the seal where the pressure signal is transduced to the stationary system and uncertainties with the position decoding. Therefore a special approach was made to construct a scanner, which transformed the pressure signal to an electrical signal in the rotating system. Up to 60 pressure taps could be scanned and connected to a rotating transducer. Electrical communication with the transducer was possible through a high-quality slip-ring assembly, reliable position decoding was achieved with a light detector. Using exchangeable rotor blades with 6 pressure taps at the pressure side and 10 taps at the suction side, it was thus possible to measure the pressure distribution in five radial locations. The measurements could be reproduced with an accuracy of $\pm$ 2 percent.

The flow in the cascade was investigated at four different geometries, varying the aspect ratio from 2.5 to 3.5 and the inclination angle of the conical end-wall from 20 to 30 degrees. The data presented here refer to an aspect ratio of 2.5 and an end-wall angle of 30 degrees. Here, the flow has the highest three-dimensional character.

The measurements in the turbine stage were performed with varying mass flow and shaft speed. Only a selection of results at the design point of the stage is shown here.

Rectangular Cascade

The partially-parabolic method is developed for a rotationally symmetric flow, so that the linear cascade is simulated by setting the hub radius to a very high value, in this case 77 m. The computational mesh for this case is depicted in Fig. 3, with 11 nodes in pitchwise and 30 nodes in spanwise direction. At the end-walls a slip condition is used, whereas the profile boundary layers were not resolved. It is necessary to increase the distance between the axial planes at the leading edge. Otherwise the horse-shoe vortex is resolved, and the reversed flow components at the end walls cause numerical instabilities. At the trailing edge a fine mesh is used to achieve a good approximation of the strong pressure gradients.

Fig. 4 shows the calculated and measured secondary flow vectors at cascade exit. The passage vortices dominate the flow pattern at the end-walls, with a radial extension of about 20 percent span. The vortices are produced by the action of the transverse pressure gradient on the end-wall boundary layers. The flow field between them is scarcely influenced. Computation and experiment show the same vortex systems, with good agreement concerning the size and orientation of the vortices.

The diagrams of pitch averaged velocities and flow angles, Fig. 5, elucidate the lower acceleration and the slightly higher overturning at the conical end-wall. These effects are calculated as well as measured. Comparing the computed and measured results, it has to be taken into account, that the profile boundary layers were not resolved in the

calculation. Because of the missing displacement thickness the computed mass-averaged velocities are therefore smaller. The numerical program calculates slightly higher flow angles than the experimental data. One reason for this is, that the flow at the outlet of the rectangular cascade is ducted with an angle of 70 degrees. In the computation the flow at the outlet is not ducted in circumferential direction, since the geometry of the rectangular cascade is simulated as an annular cascade with a large radius.

Stator Flow

The second step in the development of the numerical program was the calculation of the flow through an annular turbine stator vane. Fig. 6 shows the computational mesh, which was refined in the end-wall regions and close to the profile surfaces to resolve the shear layers (30 nodes pitchwise and spanwise). At the solid surfaces a slip condition is used for the modelling of the boundary layers. However, the simultaneous computation of profile and end-wall boundary layers was not successful at the present time, because a strong interaction between the boundary layers on the suction side tip corner close to the trailing edge lead to numerical instabilities. The results presented in this chapter were obtained resolving the shear layers at the end-walls but not at the profile surfaces.

As described above, the partially-parabolic program needs a pressure distribution for the whole flow field as a start approximation. The pressure field is obtained using a non-viscous stream surface calculation, which is not capable of modelling three-dimensional viscous effects as the generation of secondary flows. This is illustrated in Fig. 7, where the measured pressure distributions at the radial locations are compared with the results from a viscous and a non-viscous calculation. There is a good agreement between all results at midspan, but close to the end-walls, where a strong cross-flow component is directed to the suction side, the non-viscous calculation predicts lower pressures at the suction side than measurement and viscous calculation. The partially-parabolic program, which includes end-wall boundary layers and the generation of the passage vortices, shows a good agreement with the measurement even close to the end-walls. The differences at the suction side close to the trailing edge result from the numerical resolution of the profile geometry. The program needs a sharp trailing edge, since no additional lines can be implemented in the H-grid. Therefore, the suction side contour of the profile is moved to the pressure side at the last 20 percent axial chord length. This leads to the calculation of slightly lower pressures in this area. The radial gradient of the static pressure with lower pressure at the hub due to the high circumferential component of the flow and the higher loading at the tip of the stator vanes are reproduced by both numerical methods.

In Fig. 8 a selection of measured results of the stator exit flow is presented as Iso-Mach number and Iso-total pressure losses contours. This data were measured at an axial location 20 percent of the axial chord behind the stator. The estimated 99 percent thickness of the inlet boundary layer was 11.8 and 5.5 percent at tip respectively hub. The distribution of the Mach number shows the higher velocities at the hub and at the suction side margin of the wake area. Apart from this, the Iso-Mach number contours resemble the total pressure losses contours very closely. Significant losses, respectively small velocities, are detected only in the wake of the profile and in the corner between suction side and tip. Two loss cores can be seen at 13 percent and 83 percent span. Fig. 9 shows pictures of surface flow visualization using a white TiO_2-oil mixture on the black stator vanes. The comparison with the pressure losses contours shows, that the loss cores mark the extension of the areas at the trailing edge, where, driven by the passage vortices, low momentum material from the end-wall shear layers is washed onto the suction side of the profile. Thus the loss cores represent accumulations of low energy fluid on the suction side /8,9,10/. The higher acceleration at the hub amplifies this mechanism. This and the smaller inlet boundary layer lead to a thinner outlet boundary layer at the hub than at the tip.

The pitchwise mass-averaged velocities and flow angles at stator exit are shown in Fig. 10. At the end-walls overturning is observed, with the corresponding underturning at the inner side of the passage vortices. This effect is stronger at the tip, because of the thicker inlet boundary layer at the casing. The velocity profiles show the higher velocity at the hub, only very small gradients at the end-walls, especially at the hub, and slight perturbations at the radial locations of the two loss cores. These effects are reproduced by the calculation in a good quality. Some of the differences to the experimental data may be explained with the numerical difficulties near the corners to resolve the profile boundary layers.

Rotor Flow

The terms describing the influence of the centrifugal and Coriolis-forces were implemented in the numerical method to calculate the rotor flow. For preliminary calculations a grid with 30 nodes in pitchwise and 11 nodes in spanwise direction was used (Fig. 11). At present time only test cases were solved to demonstrate the numerical stability of the method.

The following data were computed for a test case, where the inlet velocity distribution corresponds to the measured mass-averaged values of the stator exit flow. The pitch angle was constant, corresponding to the measured midspan value.

Fig. 12 presents the measured pressure distribution at three radial locations at the rotor blade. The non-uniform stator exit flow and the different circumferential speed across the spanwise direction cause a displacement of the stagnation point. Close to the hub the low circumferential speed and the high stator outlet velocity move the stagnation point to the pressure side. This causes a high acceleration at the leading edge to the suction side, with no further acceleration downstream. Near the tip, the stagnation point is moved to the suction side. Here the flow on the suction side is accelerated up to a position of 60 percent axial chord. Because of the inlet conditions, the calculated pressure distributions are only comparable at midspan. There are differences at the leading edge, which is resolved as a triangle in the numerical mesh. Otherwise the agreement is fairly good.

The calculation of the flow within the rotor passage and at the rotor exit is shown in Fig. 13 and Fig. 14. A comparison with experimental data has not yet been made since the uniform inlet pitch angle assumed for the first calculations does not describe the real flow at the rotor inlet. Therefore, the discussion of the results can only extend to whether the basic physical phenomena are reproduced. The plots of the secondary flow vectors (Fig. 13) show the development of the two passage vortices, with increasing intensity to the rotor exit plane. The suction side leg of the horse-shoe vortex is visible at plane 10, but is covered by the passage vortex downstream. The pitchwise averaged velocity profiles are presented in Fig. 14. The basic effect is the reversing of the velocity gradient from high inlet velocities at the hub to high outlet velocities at the tip due to the different circumferential speed across the spanwise direction.

In the present work emphasis is given to the final implementation of the simultaneous calculation of end-wall and profile boundary layers for stator and rotor flows. Subsequent to this, a detailed theoretical investigation of the rotor flow follows, which is supported by the measurement of the instantaneous rotor flow. This includes the application of three-dimensional hot-wire probes in the exit plane and the Laser-Doppler-Anemometry within the rotor passage.

Conclusion

A partially-parabolic method for industrial use was developed for the calculation of the flow in high turning subsonic turbine stators and rotors. Parallel to this, detailed measurements at various points of operation have been carried out in a rectangular cascade and a single-stage turbine to provide test cases for the calculation.

The comparison between calculation und measurement shows, that essential three-dimensional effects can be described with the aid of the partially-parabolic program. This includes the representation of end-wall boundary layers and the coupled generation of secondary flows. Both, calculation and measurement, show the same vortex systems, and the agreement of the pitch averaged flow at stator exit is fairly good. Further improvement is to be expected, when the difficulties concerning the simultaneous computation of profile- and end-wall boundary layers are removed.

The final goal of the work is the calculation of the rotor flow including tip clearance, with the experimental verification of the program.

References

/1/ Patankar, S.V., Spalding, D.B.: "A Calculation Procedure for Heat, Mass and Momentum Transfer in Three-Dimensional Parabolic Flows", Int. J. Heat Mass Transfer, Vol. 15, 1972

/2/ Moore, J., Moore, J.G.: "A Calculation Procedure for Three-Dimensional, Viscous, Compressible Duct Flow - Part I and II", Trans. ASME, JFE, 1979

/3/ Moore, J., Moore, J.G.: "Three-Dimensional, Viscous Flow Calculations for Assessing the Thermodynamic Performance of Centrifugal Compressors - Study of the Eckardt Compressor", Centrifugal Compressors, Flow Phenomena and Performance, AGARD-CP-282, 1980

/4/ Thames, F.C., Thompson, J.F., Mastin, C.W.: "Numerical Solution of the Navier-Stokes Equations for Arbitrary Two-Dimensional Airfoils", Proc. of the NASA Conference on Aerodynamic Analyses Requiring Advanced Computers, 1975

/5/ Gallus, H.E., Lawerenz, M., Zebner, H.: "Kanalkontureinfluß", Internal report

/6/ David, O., Gallus, H.E., et al.: "Seitenwandgrenzschichten und Sekundärströmungseffekte in stark umlenkenden Turbinengittern", Internal report

/7/ Utz, C.: "Experimentelle Untersuchung der Strömungsverluste in einer mehrstufigen Axialturbine", Thesis E.T.H. Zürich, Diss.-Nr. 4894, 1972

/8/ Sieverding, C.H.: "Recent Progress in the Understanding of Basic Aspects of Secondary Flows in Turbine Blade Passages", ASME Paper 84-GT-78, 1984

/9/ Zunino, P., Ubaldi, M., Satta, A.: "Measurements of Secondary Flows and Turbulence in a Turbine Cascade Passage", ASME Paper 87-GT-132, 1987

/10/ Gregory-Smith, D.G., Graves, C.P., Walsh, J.A.: "Turbulence Measurements and Secondary Flows in a Turbine Rotor Cascade", ASME Paper 88-GT-244, 1988

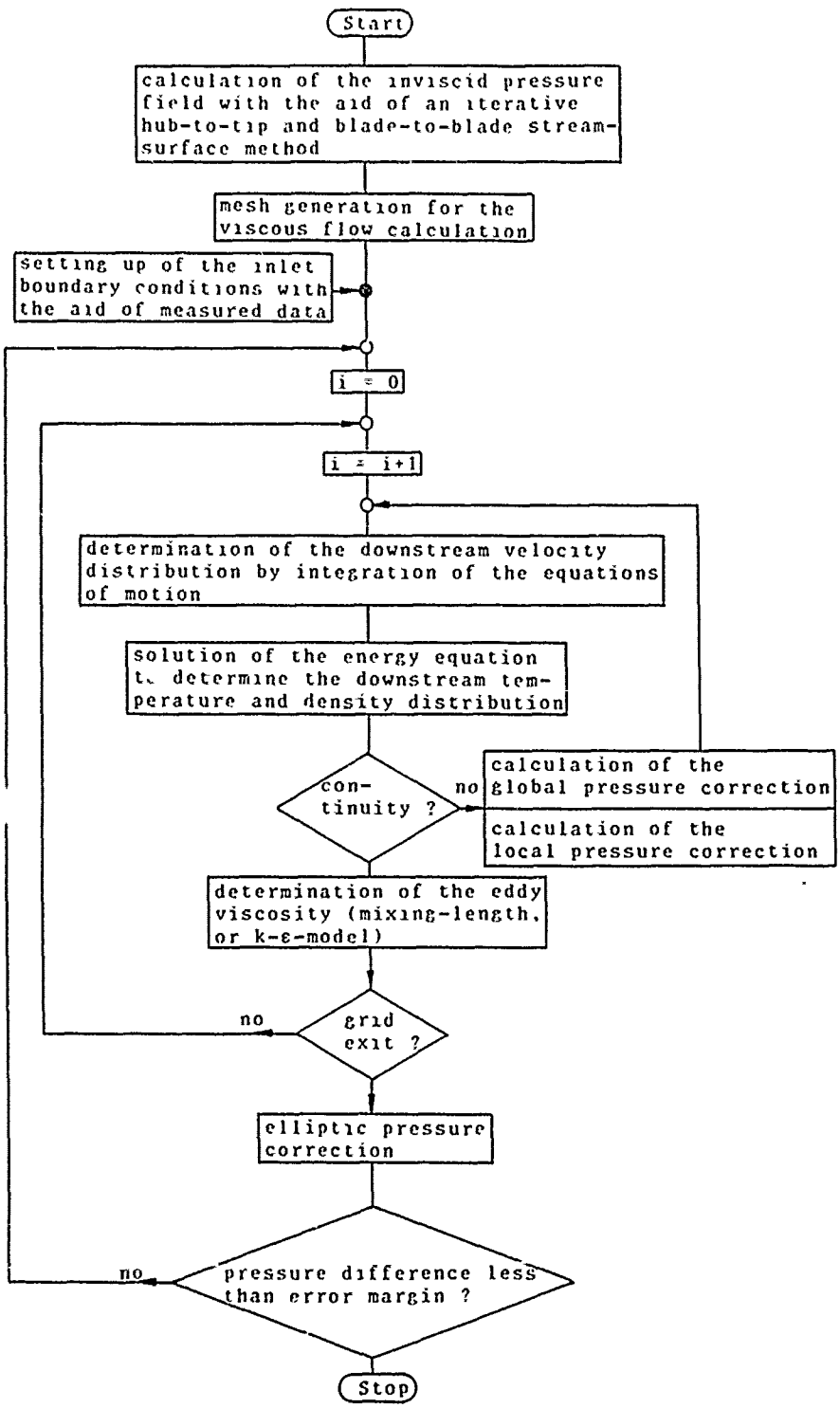
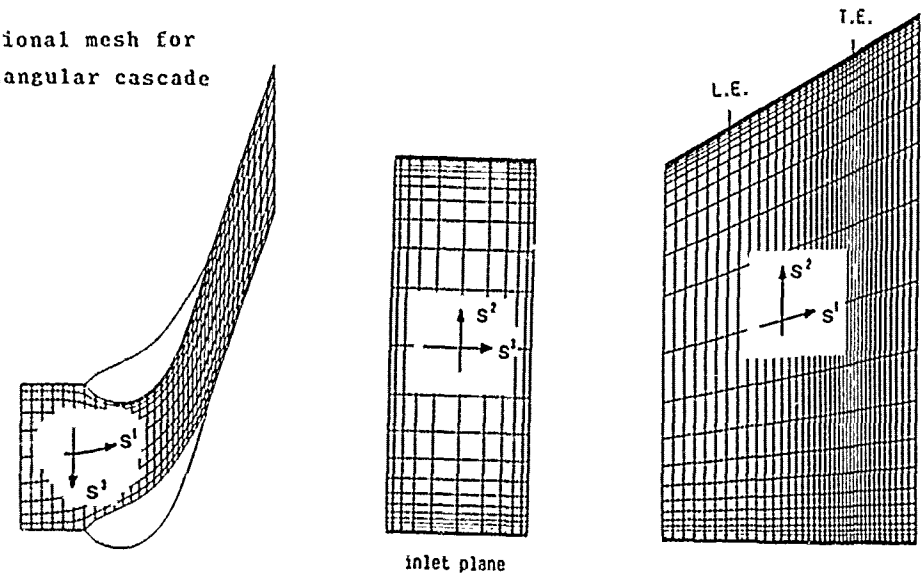


Fig. 1: Condensed form of the partially-parabolic solution procedure

Fig. 2: Cascade and turbine design data (angles are measured relative to the axial direction)

	cascade	stator	rotor
Inlet blade angle	0°	0°	40.7°
Exit blade angle	70°	70°	-61.2°
Blade chord	62 mm	62 mm	60 mm
Span	variable	55 mm	55 mm
Pitch (midspan)	50 mm	47.6 mm	41.8 mm
Aspect ratio	variable	0.887	0.917
Reynolds number (based on chord and exit velocity)	6.8×10^5	6.8×10^5	4.9×10^5
Rotational speed	-	-	3500 rpm
Blade number	7	36	41
Mean radius	-	272.5 mm	272.5 mm
Rotor stator axial gap	-	-	15 mm

Fig. 3: Computational mesh for the rectangular cascade



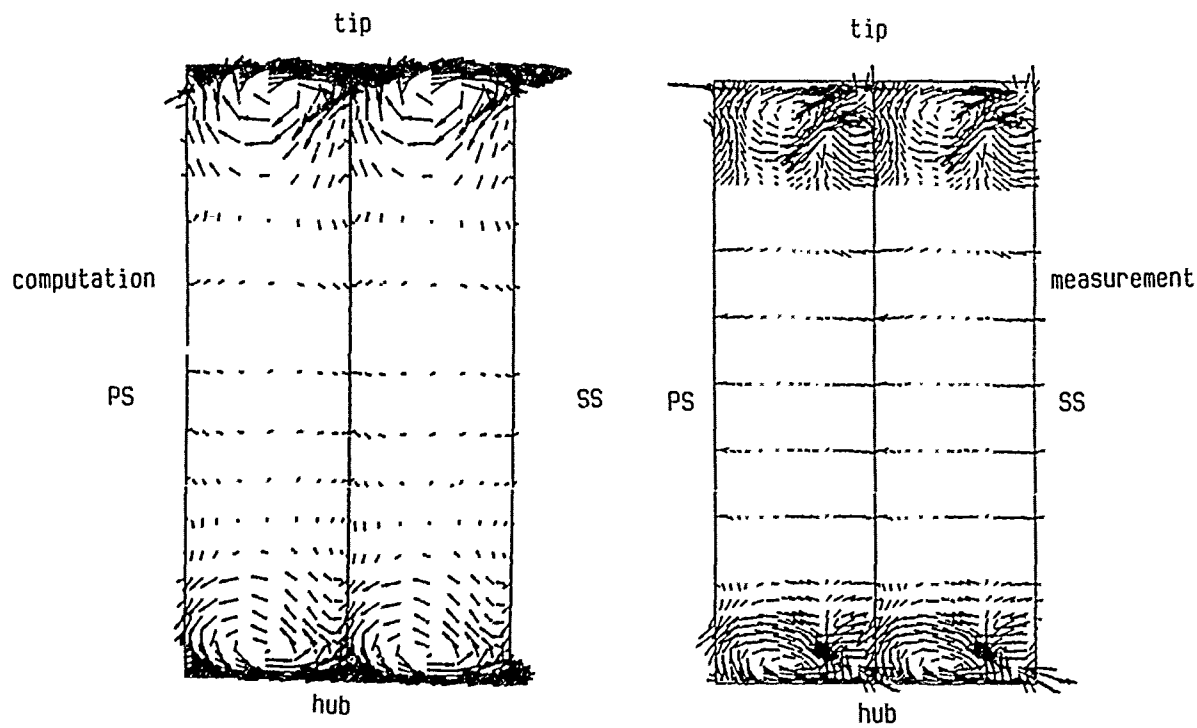


Fig. 4: Comparison of measured and calculated vortex systems downstream of the cascade

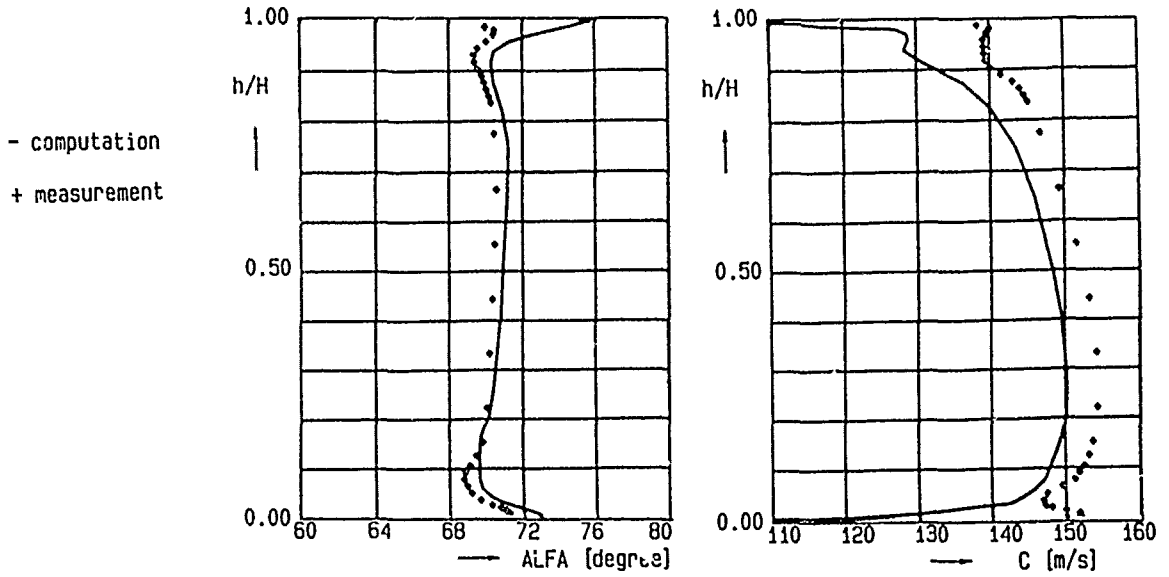


Fig. 5: Comparison of measured and calculated distribution of flow velocity and yaw angle downstream of the cascade, pitchwise mass averaged

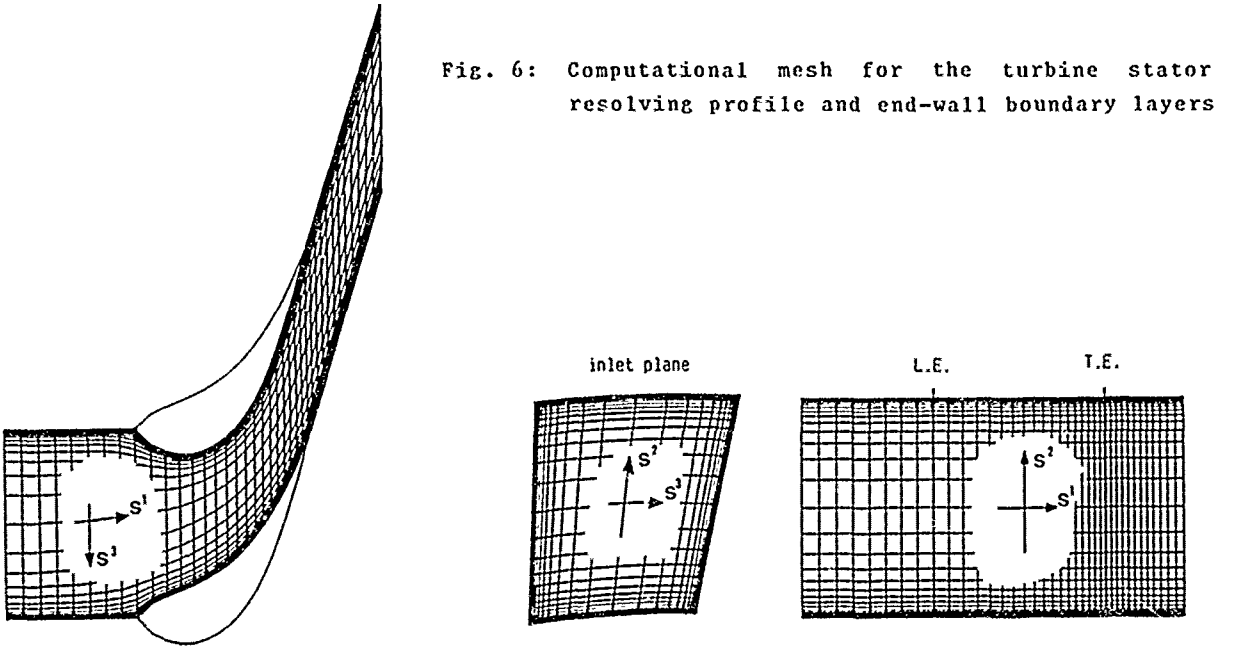


Fig. 6: Computational mesh for the turbine stator resolving profile and end-wall boundary layers

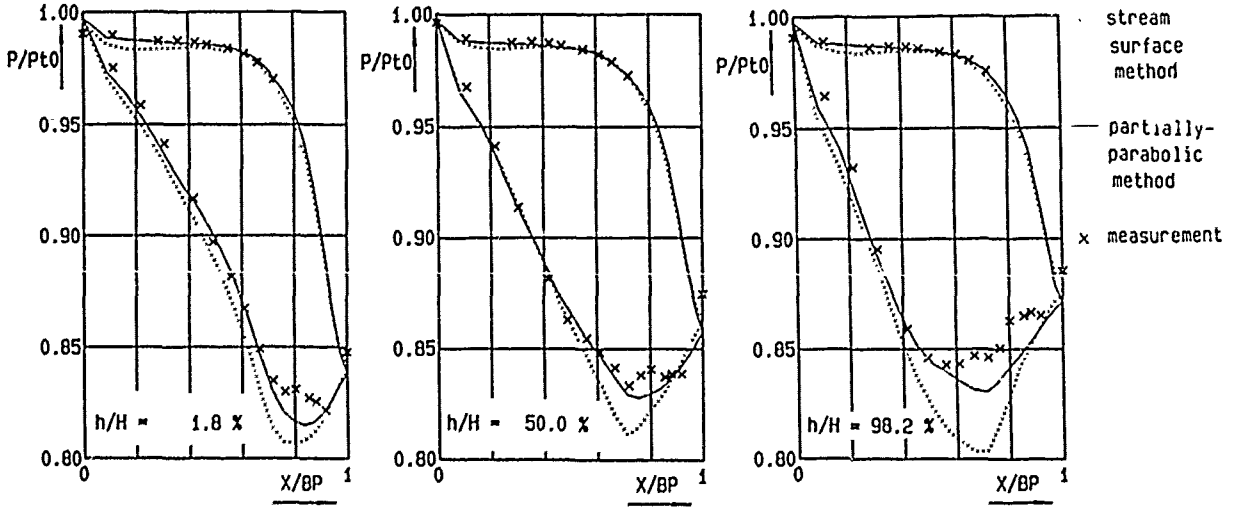


Fig. 7: Measured and computed pressure distribution on the turbine guide vanes

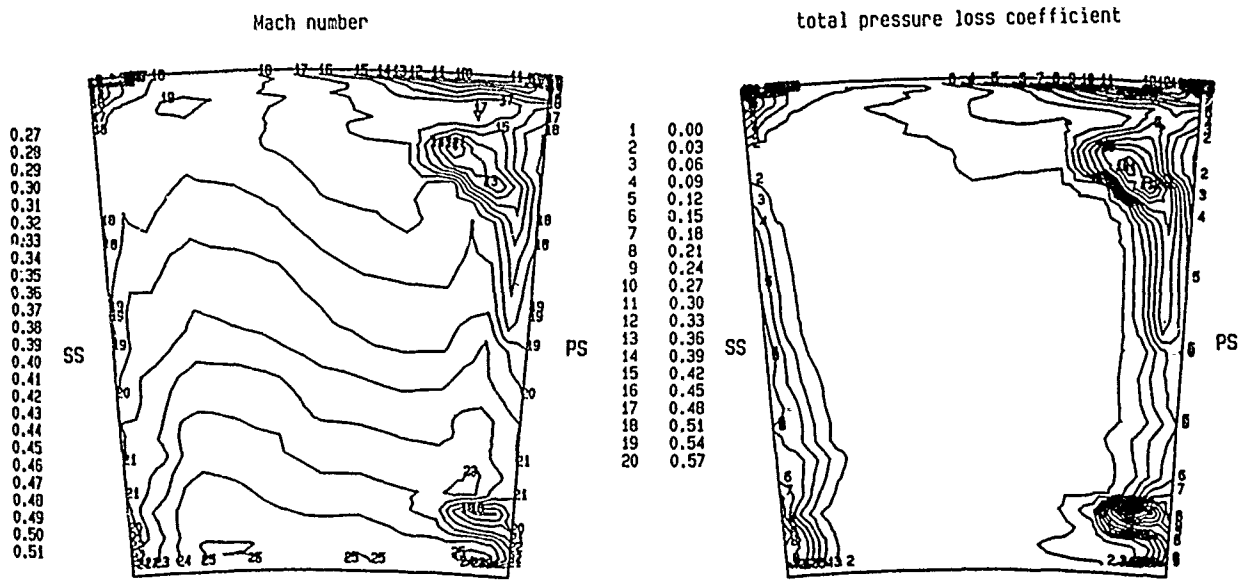


Fig. 8: Area plots of the turbine stator exit flow, Mach number and total pressure losses

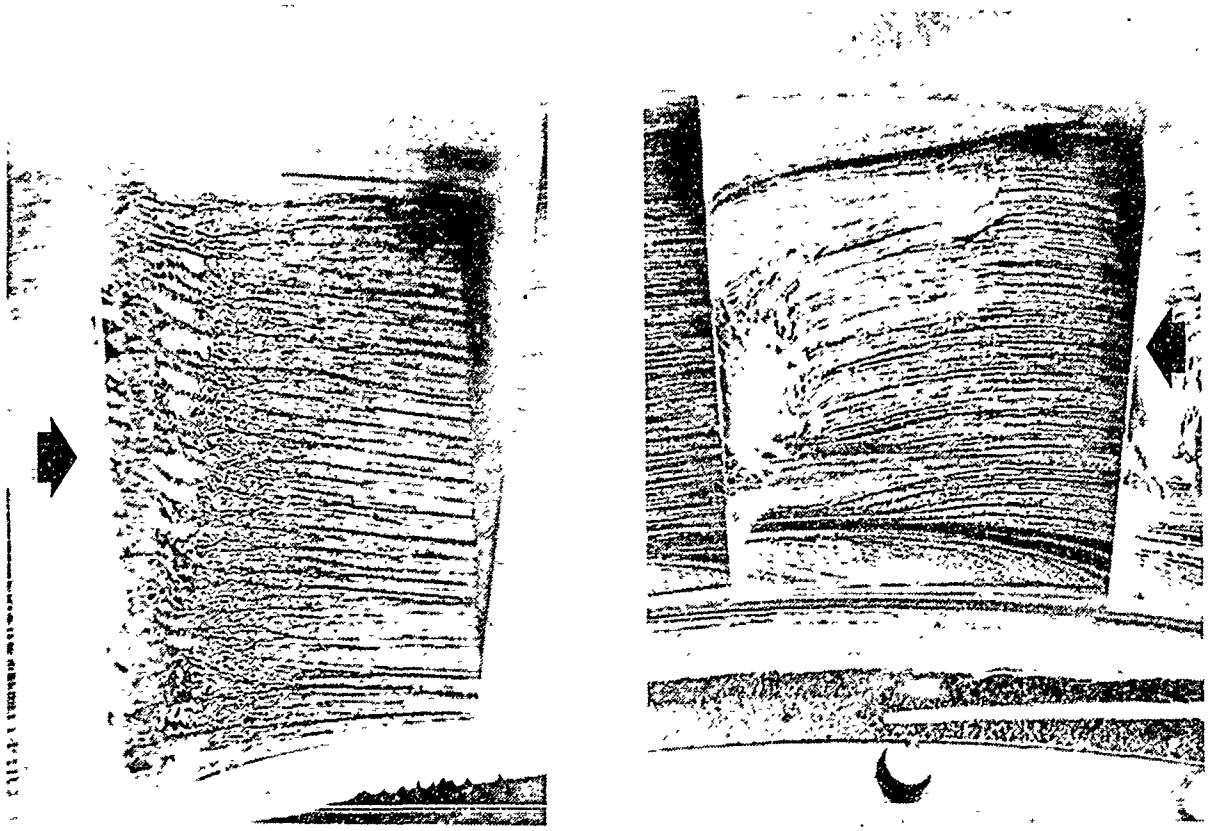


Fig. 9: Surface flow visualization in the turbine stator with a white TiO_2-oil mixture

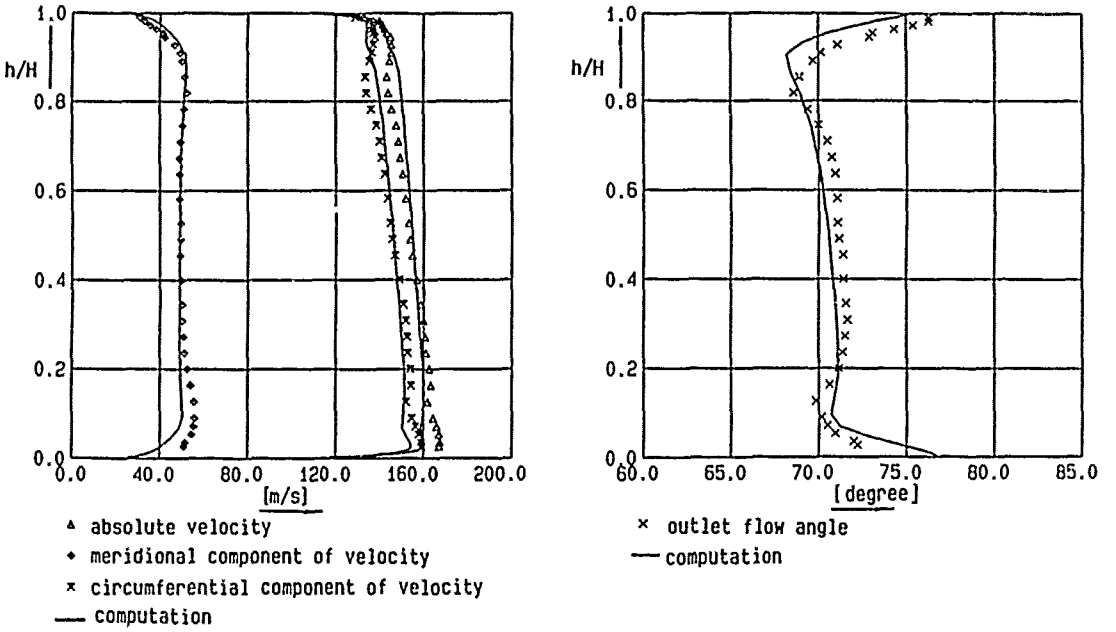


Fig. 10: Comparison of measured and calculated distribution of flow velocity and yaw angle at stator exit, pitchwise mass averaged

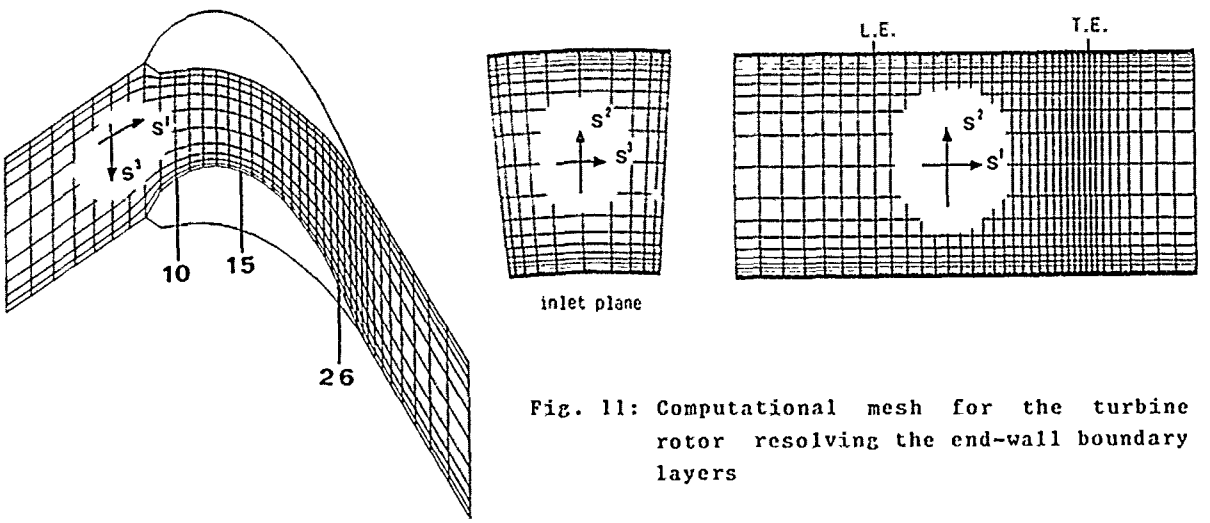


Fig. 11: Computational mesh for the turbine rotor resolving the end-wall boundary layers

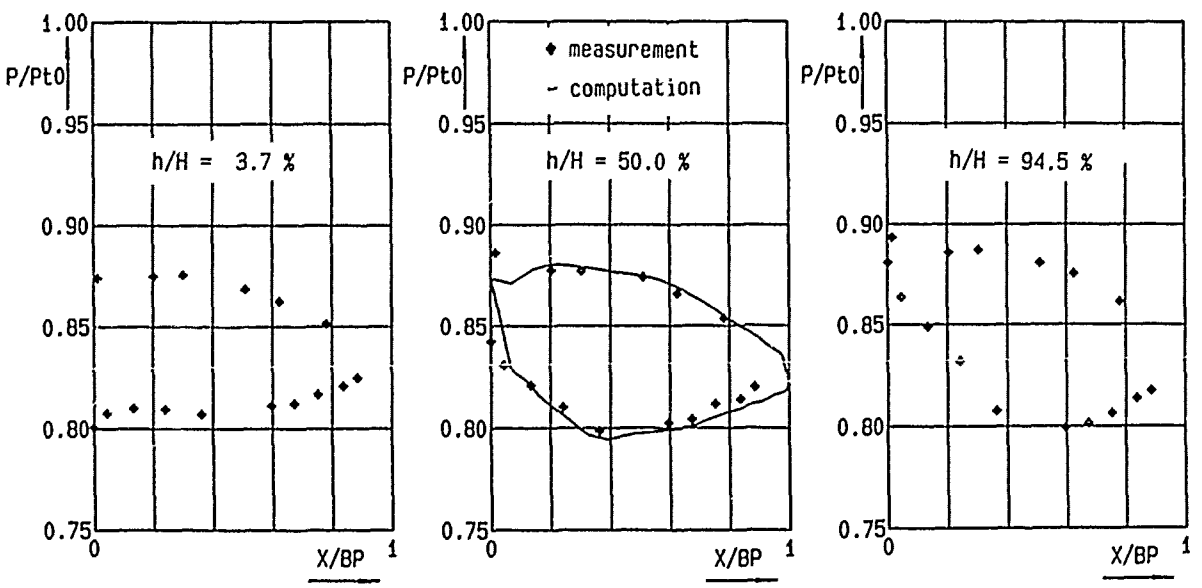


Fig. 12: Measured and computed pressure distribution on the turbine rotor blades

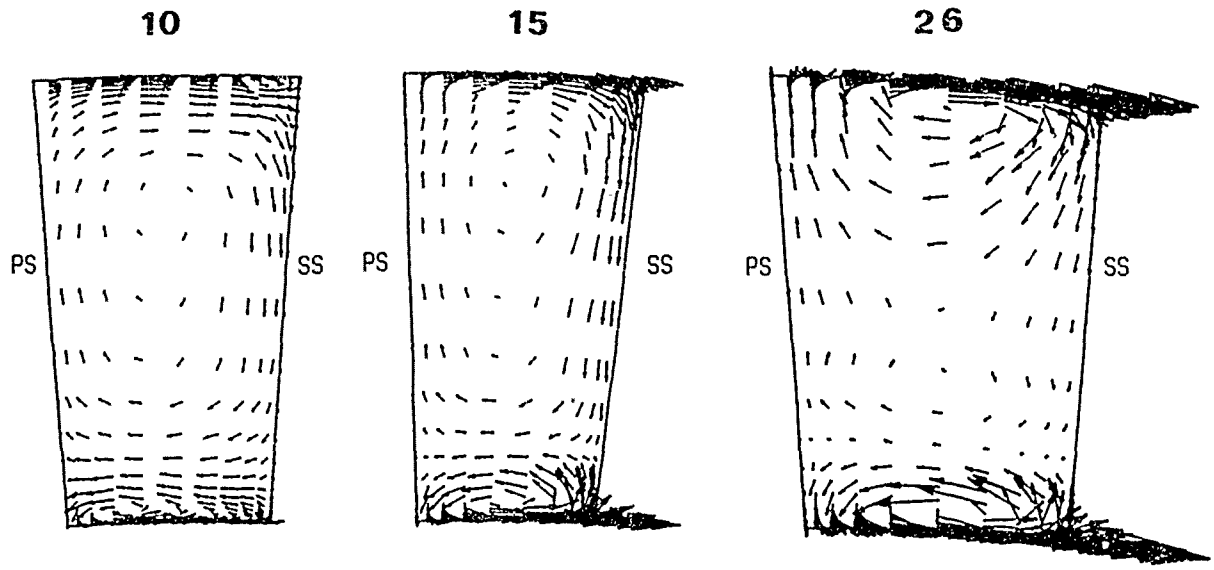


Fig. 13: Calculated secondary flow fields in different axial planes inside the rotor blade passage (see Fig. 11)

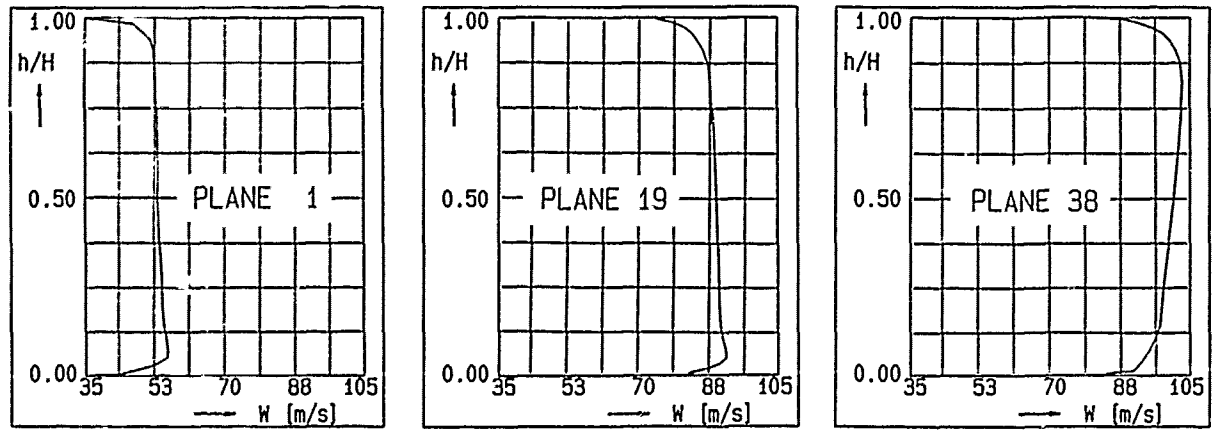


Fig. 14: Calculated distribution of flow velocity in different axial planes in the rotor flow (pitchwise averaged)

ANALYSIS OF THE ROTOR TIP LEAKAGE FLOW WITH TIP COOLING AIR EJECTION

by

W.Koschel, H.Schmidt and A.Vornberger
Institute for Jet Propulsion and Turbomachinery
Technical University of Aachen
Templergraben 55, D-5100 Aachen
Federal Republic of Germany

SUMMARY

A numerical simulation of turbine rotor tip leakage flow has been carried out taking into account tip coolant flow injection. The numerical scheme is based on a Finite Element method for the integration of the Navier-Stokes equations in the conservative form using an explicit two-step Taylor-Galerkin algorithm. The application of unstructured grids together with local refinement strategies allows a detailed resolution of viscous flow phenomena in the clearance gap. The analysis is performed for an HP turbine blade with a tip groove without and with tip coolant flow injection. The effect of varying clearance height and of wall motion is also considered. Results on 2D-flow computations are presented and discussed as regard to viscous flow effects and to the relative mass flow discharge in the tip clearance for the different investigated configurations.

NOMENCLATURE

C	mass matrix
	lumped mass matrix
F	flux vector
h	blade height
N	shape function
P	pressure
R	residual
t	time
T	temperature
u,v	components of velocity
U	flow vector
y	clearance height
ρ	density
τ	stress tensor
ν	viscosity
β	injection angle
Ω	computational domain

Subscripts

c	coolant flow
i	number of nodal point
j	number of direction (x,y,z)
t	total

Superscripts

n	time level

1. INTRODUCTION

Analysis of overall performance of aerodynamically high-loaded axial turbine stages for aeroengine applications shows that tip clearance losses represent between 25 and 35 percent of the total stage loss and may even be higher in the case of small size engines [1]. Though a lot of turbine testing and basic experimental work has been carried out in order to identify the most significant parameters that characterise the tip clearance losses and to analyse the complex flow phenomena associated with tip leakage, the full physical understanding of the complex flow has not yet been achieved [2].

Therefore most of the experimental work in the past was limited to the development of empirical correlations which relate the tip clearance losses to geometry or additionally to geometry and flow parameters like profile drag coefficient and profile tip loading [3], [4]. Empirical correlations of this type are widely used by engine manufacturers in the turbine design process. Booth, who evaluated some of these proposed loss correlations for different shroudless axial turbine stages came up with the conclusion that none of these more or less simple models will predict the correct loss trends [5].

The most known theoretical model available up to now is an efficiency loss model based on the induced drag of a potential vortex and radial kinetic energy of the fluid in the blade boundary layer developed by Lahshmirayana [6]. Since it is based on data of incompressible compressor flow it turned out not to be adequate to predict turbine leakage. First attempts to describe the tip leakage flow by numerical simulation were made by Wadia and Booth [7] and by Hah [8].

In recent years more powerful Euler- and Navier-Stokes codes became available which allow a more detailed flow analysis. Therefore it seems reasonable to apply more advanced methods to simulate the tip clearance flows and to include the derived models into the design codes.

The present paper reports on a numerical simulation of turbine rotor tip leakage flow with special emphasis on the effect of tip coolant air injection. A FEM based Navier-Stokes code using unstructured grids with local refinement has been applied to analyse the tip leakage flow. This numerical work is part of a comprehensive experimental and theoretical research program which is carried out in order to get a more detailed physical understanding on the effects of cooling air ejection onto the turbine stage flow and loss production.

2. TIP LEAKAGE FLOW MODEL

2.1 BASIC LEAKAGE FLOW PHENOMENA

The tip leakage flow of a turbine rotor blade is mainly a pressure-driven phenomenon caused by the pressure difference between the profile pressure and suction side in the tip region. The shear forces due to viscous effects caused by the relative motion between turbine rotor and outer casing wall and the shear forces at the blade tip directly balance the pressure forces. In the case of tip coolant flow injection the corresponding momentum must be taken into account. Injection flow velocity and angle and furtheron the coolant mass flow will be the governing parameters for this additional momentum. The different directions in which the above mentioned forces act are responsible for the pronounced threedimensional character of the leakage flow. From previous investigations it is known that the tip leakage discharge flow behaves like a free jet that penetrates into the main turbine flow. The subsequent mixing and turning by the main flow interfered by secondary flow effects will cause the observed turning of the rotor exit flow in the upper blade region. Based on this physical model a stepwise theoretical approach can be made starting from the tip leakage flow simulation and coupling it to the turbine main flow computation.

2.2 CONCEPT OF THE NUMERICAL APPROACH

The following analysis will be limited to the simulation of the tip clearance flow taking into account tip coolant flow injection. The geometry and the aerothermodynamic conditions are taken from a high-loaded turbine rotor blade of a midsize aeroengine HP-turbine. The turbine blade is shroudless with a groove for coolant air ejection at the tip. The coolant flow is fed by 9 radial bores. A view of the blade with the arrangement of the coolant bores is shown in Fig. 1.

The threedimensional problem of this tip-leakage flow is reduced in this approach to a viscous 2D-flow analysis by applying in a first step the well-known quasi-threedimensional model of Lakshminarayana [6]. By this model the velocities and the directions of the leakage flow in the gap along the tip profile can be determined as schematically shown in Fig. 2. The distribution of circulation along the profile which is needed as an input for Lakshminarayana's model can be calculated by using the FEM-code of which a more detailed description will be given later on. In this case the code is applied in the non-viscous formulation.

In the following second step a 2D-Navier-Stokes approximation is carried out in order to simulate the viscous tip leakage flow. The computational domain is hereby defined by the sectional plane in the main flow direction, which is determined in the first step as indicated in Fig. 2.

The numerical scheme is based on a Finite Element method for the integration of the Euler- and Navier-Stokes equations in the conservative form using an explicit two-step Taylor-Galerkin algorithm. The great flexibility of the FEM regarding the spatial discretisation by applying unstructured grids with local mesh refinement makes this method very suitable for a detailed analysis of viscous effects in tip leakage flows.

3. FINITE ELEMENT APPROXIMATION

3.1 GOVERNING EQUATIONS

The Navier-Stokes equations governing compressible flow can be written in conservative form:

$$\frac{\partial U}{\partial t} + \frac{\partial F_j}{\partial x_j} = 0 \qquad (1)$$

where

$$F_j = F_j^E - F_j^V$$

with

$$U = \begin{pmatrix} \rho \\ \rho u_j \\ \rho e \end{pmatrix} \qquad F_j^E = \begin{pmatrix} \rho u_j \\ \rho u_i u_j + \delta_{ij} p \\ u_j(\rho e + p) \end{pmatrix} \qquad F_j^V = \begin{pmatrix} 0 \\ \tau_{ij} \\ u_i \tau_{ij} + k \frac{\partial T}{\partial x_j} \end{pmatrix}$$

The summation convention is employed and the range of j depends upon the number of space dimensions. Fj represents the inviscid Euler part of the flux-vector whereas the viscous contributions are gathered in Fj . By input parameters the code can be forced to work with the inviscid or viscous equation set. In case of the viscous option a full approximation of the Reynolds' stress tensor is calculated.

Assuming a Newtonian fluid the stress tensor is proportional to the rate of strain and can be written using Stokes postulate as:

$$\tau_{ij} = \mu\left(\frac{\partial u_i}{\partial x_j} + \frac{\partial u_j}{\partial x_i}\right) - \frac{2}{3}\mu\delta_{ij}\frac{\partial u_j}{\partial x_j} \qquad (2)$$

Sutherland's viscosity equation, the equation of state and the Prandtl number are specified to close the system of equations.

3.2 DISCRETISATION

To obtain geometrical flexibility triangular Finite Elements with linear shape functions N_i are used to subdivide the computational domain. The differential equation system (1) can be expressed in a weighted residual formulation.

$$\int_\Omega \left(\frac{\partial U}{\partial t} + \frac{\partial F_j}{\partial x_j} \right) N_i d\Omega = 0 \tag{3}$$

Applying Gauss' divergence theorem inserting standard Finite Element approximations

$$U = \sum N_i U_i \qquad F = \sum N_i F_i \tag{4}$$

with $F_i = F(U_i)$

and replacing the time derivative by a type of Lax-Wendroff scheme yields

$$C \Delta U^{n+1} = \Delta t \int_\Omega F_j^{n+1/2} \frac{\partial N_i}{\partial x_j} d\Omega - \int_\Gamma F_j^{n+1/2} N_i n_j d\Gamma \tag{5}$$

with $\Delta U^{n+1} = U^{n+1} - U^n$

where n_i corresponds to the outward normal unit vector on the boundary of the domain and C represents the standard Finite Element mass matrix defined as:

$$C_{ij} = \int_\Omega N_i N_j d\Omega \tag{6}$$

For computational efficiency the integration of the fluxes in Eq. (6) is carried out in a two-step scheme [9].

First step:
$$\int_\Omega U_e^{n+1/2} P_e d\Omega = \int_\Omega U_i^n N_i d\Omega + \frac{\Delta t}{2} \int_\Omega F_j \frac{\partial N}{\partial x} d\Omega \tag{7}$$

where P_e denotes a piecewise constant shape function.

With this equations $U_e^{n+1/2}$ can be computed for each element explicitly. Using these values constant within each element the flux-vectors on the RHS of Eq. (5) are defined.

Using

$$F_j^{n+1/2} = F_j(U_e^{n+1/2}) \tag{8}$$

constant with each element the flow vectors of equation (7) (second step) are defined.

To obtain finally the following global equation system all integrations are exactly performed and the element matrices are assembled in an usual finite element way.

Due to the explicit formulation of the time step, stability of the scheme is bonded by a local Courant number criterion which requires:

$$\Delta t \leq \frac{CFL\, \Delta h}{|u_i \mu_i|^{1/2} + a} \tag{9}$$

where a denotes the local speed of sound, and h is a representative element length, taken as the minimum height in each tetrahedron. The CFL-number is limited by the numerical scheme chosen. The transient scheme employing the iterative solution procedure, requires a CFL-number of 0,5 whereas for the diagonalized system values ranging from 0.8 to 0.9 and in combination with the residual averaging approach from 1.2 to 1.3 are appropriated.

Convergence acceleration is realised by using local time stepping. Linearised characteristic relations are used for specifying inflow and outflow boundary conditions [10], whereas in case of solid walls non-slip condition is implied [11]. Further details regarding the numerical method are given in [12] and [13].

3.3 MESH GENERATION

The mesh generator which has been developed very recently has the ability to generate unstructured triangular meshes automatically starting from a given domain boundary [14]. In Fig. 3 the procedure of the mesh generation is schematically shown. Starting at the smallest side of the domain boundary, triangles are generated by defining a new point inside the domain so that the new element is nearly equilateral and does not cross any given face. Before storing the new element it has to be decided whether there exists a point in the already generated grid that should be used in lieu of the new point. The new elements reduce the remaining domain which still has to be subdivided by the described procedure until the computational domain is totally filled with triangles.

The element side length can be taken from a background mesh, so that the local grid density can be varied. Information about local mesh stretching and its direction can also be taken from the background mesh. Examples of two different types of local mesh refinements with stretching and with a continiously increasing grid density prescribed by a correspondent background mesh are shown in Fig. 4.

4. LEAKAGE FLOW SIMULATION

4.1 PARAMETER

From the analysis made by Booth et al. [15] it is known that the momentum balance in the clearance gap and consequently the character of the boundary layer development of the leakage flow is strongly influenced by the clearance height. Therefore the numerical simulation was carried out for different relative tip clearance heights varying from y/h = 1% to 3%. In order to analyse the effect of the tip groove on the leakage flow a blade configuration with a filled-up groove was taken as a baseline. Thus 3 different configurations: flat blade, blade with tip groove and blade with tip groove and coolant flow injection were included into the study. Another important paramcter is the wall motion. Therefore the two extreme cases with no wall motion and with an outer circumferential speed of the rotor of u = 442 m/s were considered. The investigated configurations and parameters are presented in Fig. 5.

4.2 COMPUTATIONAL GRID

The whole spectrum of the possibilities by applying the generation strategy for unstructured grids with local refinement has been applied to the present problem. Fig. 6 shows the generated mesh for the blade tip of the groove configuration without coolant flow ejection. In the inlet flow region at the pressure side the grid density was continiously increased whereas in the gap the grid was stretched in the flow direction as can be seen from the enlargement in Fig. 6. The stretching is reasonable since the flow gradients in the radial direction due to the shear stresses are greater than in the flow direction. At the suction side the grid density becomes progressively coarse in the main flow direction. In the region of the discharge jet and in the vicinity of the casing wall the fine stretched grid was kept to allow for a sufficient resolution of local viscous flow effects like separation and reattachement. Thus a limitation of computing time and storage capacity could be achieved without loosing accuracy in flow regimes with strong local flow gradients.

4.3 BOUNDARY CONDITIONS

The computation of the tip leakage flow is carried out in the relative system of the moving blade. The no-slip boundary conditions are used as well at the blade tip as at the casing wall. In the inlet plane the total temperature T_t, the total pressure p_t and the flow angle β are specified. At that location it is assumed that the flow is uniform in the main flow direction. The conditions at the outlet are given by the static pressure at the blade tip suction side, which is obtained by the Euler-solution of the main flow field of the turbine rotor. For the simulation of the clearance flow in the presence of coolant flow injection the values of the total pressure, the total temperature and the injection angle of the coolant flow have to be prescribed at the injection bore. The computational domain with the boundary conditions is shown in Fig. 7.

5. ANALYSIS OF RESULTS

5.1 DEVELOPMENT OF BOUNDARY LAYERS

For the smallest relative clearance height of y/h = 0.01 the velocity profiles have a parabolic shape in the case without rotor motion. The typical velocity vectors of the tip clearance flow for the baseline (flat) blade configuration are shown in Fig. 8. The Reynolds number which is based on the clearance height amounts to 2300 and therefore the flow can be regarded as being fully laminar. With increasing relative clearance height and growing Reynolds number a separate development of the boundary layers at the casing wall and at the rotor tip can be observed. In the presence of a rotor motion the velocity profiles in the gap are composed of a parabolic shape and of a triangular shape due to the motion related shear stresses.

These general statements are also valid for the development of the boundary layers at the tip clearance inlet of the blade configuration with a tip groove as can be seen from the velocity vector plot in Fig. 9. But when the tip clearance flow enters the groove, a separation takes place which leads to the development of an isolated vortex within the groove. With increasing clearance height this vortex is growing and enhances the disturbance of the boundary layers in the clearance gap as can clearly be seen in Fig. 9, where the velocity fields of the tip groove configuration are compared for two different relative clearance heights. These two cases were considered without coolant flow injection, but with wall motion.

If coolant air is injected into the blade tip groove, two vortices are obtained within the groove as shown in Fig. 10 where the velocity field, the Mach number distribution and corresponding pressure field are plotted. In this case the relative clearance height is y/h = 0.03.

Interesting flow phenomena can be detected by a detailed analysis of different tip clearance flow regions. In Fig. 11 the enlarged views of the velocity field and of the Mach

number distribution at the clearance inlet reveal that local separation takes place at the blade wall. Another important result as regard to the physical understanding is obtained by the analysis of the tip leakage discharge flow. The discharge flow shows the typical behaviour of a free jet. In the discontinuity region which is limited by the outer free jet boundary and by the wall boundary layer of the casing some stretched vortices can be seen. The expansion of this vortices is obviously hindered whereas at the inner jet boundary in the direction of the main flow region a fully developed vortex flow is observed. Since in the present case the flow computation was limited to a 2D-domain and did not include the interaction of the jet flow with the rotor main flow, the rolling up of the jet to form the tip vortex could not obtained.

5.2 DISCHARGE MASS FLOW

All configurations under investigation were evaluated as regard to the tip clearance discharge mass flow which can be regarded as a measure of the losses of the flow within the tip clearance. First the influence of the tip geometry on the discharge mass flow without coolant air injection was analysed. In Fig. 13 the relative tip leakage mass flow is plotted versus the relative tip clearance height. The discharge mass flow of the flat tip configuration without motion was taken as a reference value. The influence of wall motion is included too. From these results it can be concluded that

- the relative discharge mass flow grows nearly linearly as the clearance height increases,
- the different blade geometries - flat tip and tip with groove - have only a slight influence on the amount of the leakage discharge mass flow at the same conditions,
- the wall motion reduces the discharge mass flow of about 10 % for the selected rotational case.

In Fig. 14 the relative tip leakage mass flow is plotted versus the relative clearance height for the cases with tip coolant injection. There the effect of wall motion causing a reduction of the discharge mass flow is more pronounced. In consequence care should be taken, if cascade measurements on tip discharge mass flow are applied to the design of rotor blades with tip coolant injection. Finally it can be stated by comparison of the 3 configurations that in the presence of the wall motion the influence of the considered geometries with and without coolant air injection is only a minor one.

6. CONCLUSIONS

The results obtained in the first step of a comprehensive numerical study dedicated to turbine rotor tip leakage flow phenomena indicates that the FEM Navier-Stokes code with unstructured grids and local refinement turned out to be a powerful tool for resolving local viscous effects. By detailed flow analysis of the boundary layer development in the clearance gap a better physical understanding was achieved which will help in the later evaluation of loss mechanisms associated with tip clearance flow. Furtheron the results of the flow simulation show that the coolant flow injection turned out to have a minor effect on the discharge mass flow. A pronounced influence of wall motion is observed for the blade with coolant flow injection.

ACKNOWLEDGEMENT

Financial support for this study by the Deutsche Forschungsgemeinschaft (DFG) is gratefully acknowledged.

REFERENCES

[1] Boyle, R.J., Haas, J.E. and Katsanis, T.: Comparison between Measured Turbine Stage Performance and the Predicted Performance Using Quasi-3D Flow and Boundary Analyses. NASA TM-83640, Presented at the 20th Joint Propulsion AIAA, SAE, ASME Conference, Cincinnati, Ohio, June 11-13, 1984

[2] Booth, T.C., Dodge, P.C. and Hepworth, H.K.: Rotor Tip Leakage: Part I - Basic Methodology. J. of Eng. for Power, Vol. 104, 1982, pp. 154-161

[3] Yamamoto, A., Takahara, K., Nouse, H., Mimura, F., Inoue, S. and H. Usui: An Experimental and Analytical Study of Blade Tip-Clearance Effects on an Axial-Flow Turbine Performance. National Aerospace Lab. NAL-TM-466T, 1981

[4] Farokhi, S.: Analysis of Rotor Tip Clearance Loss in Axial-Flow Turbines. J. Propulsion 4 (1988), pp. 452-457

[5] Booth, T.C.: Turbine Loss Correlations and Analysis. Importance of Tip Clearance Flows in Turbine Design. VKI Lecture Series 1985-05 on Tip Clearance Effects in Axial Turbomachines, April 15-19, 1985

[6] Lakshminarayana, B.: Methods of Predicting the Tip Clearance Effects in Axial Flow Turbomachinery. Transactions of the ASME, Journal of Basic Engineering, Vol. 92, Sept. 1970, pp. 467-482

[7] Wadia, A.R. and T.C. Booth: Rotor Tip Leakage: Part II - Design Optimization through Viscous Analysis and Experiment. Transactions of the ASME, Journal of Engineering for Power, Vol. 104, January 1982, pp. 162-169

[8] Hah, C.: A Numerical Modeling of End Wall and Tip Clearance Flow of an Isolated Compressor Rotor. Transactions of the ASME, Journal of Engineering for Gas Turbines and Power, Vol. 108, Jan. 1986, pp. 15-21

[9] Zienkiewicz, O.C., Morgan, K., Peraire, J., Vahdati, M. and R. Löhner: Finite Elements for Compressible Gas Flow and Similar Systems, 7th International Conference on Computing Methods in Applied Sciences and Engineering, December 1985

[10] Usab, W.J. and E.M. Murman: Embedded mesh solution of the Euler equations using a multiple-grid method. Advances in Computational Transonics. Pineridge Press., 1985, pp. 447-472

[11] Oden, J.T., Stroublis, R.T. and P. Devloo: Adaptive Finite Element Methods for the Analysis of Inviscid Compressible Flow: Part 1. Fast Refinement/Unrefinement and Moving Mesh Methods for Unstructured Meshes, Comp. Meth. Appl. Eng. 59, 327-362, 1986

[12] Koschel, W., Lötzerich, M. and A. Vornberger: Solution on Unstructured Grids for the Euler- and Navier-Stokes-Equations. AGARD Symposium on Validation of Computational Fluid Dynamics, Lisbon, May 1988, AGARD CP No. 437, pp. 26-1/26-16

[13] Koschel, W. and A. Vornberger: Turbomachinery Flow Calculation on Unstructured Grids using Finite Element Method, Finite Approximations in Fluid Mechanics II, Notes on Numerical Fluid Mechanics, Vol. 25, Vieweg, Braunschweig 1989, pp. 236-248

[14] Peraire, J., Vahdati, M., Morgan, K. and O.C. Zienkiewicz: Adaptive Remeshing for Compressible Flow Computations. J. Comp. Physics, 1987

[15] Booth, J.C., Dodge, P.R. and H.K. Hepworth: Rotor Tip Leakage: Part I - Basic Methodology. Transactions of the ASME, Journal of Engineering for Power, Vol. 104, January 1982, pp. 154-161

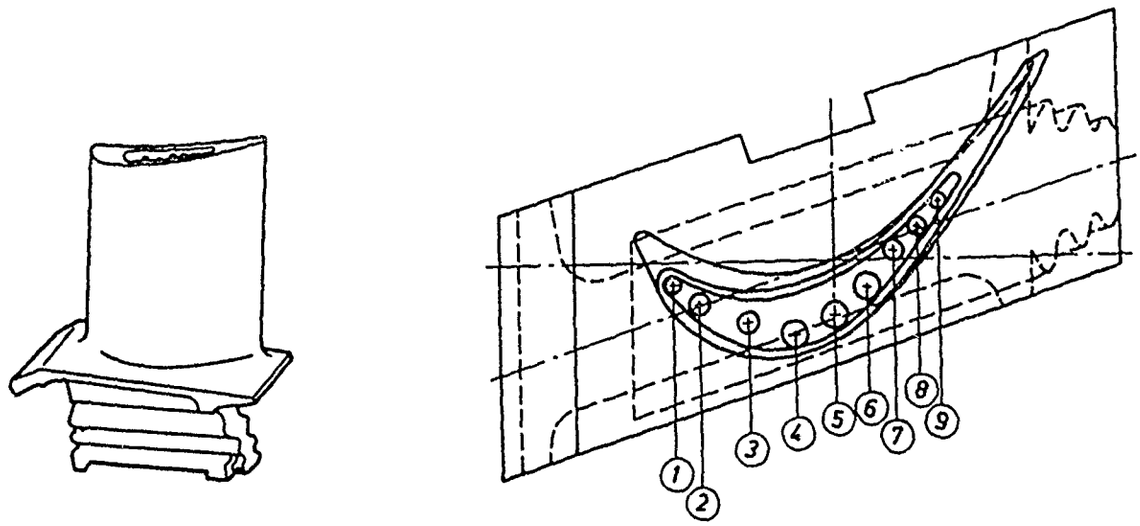


Fig. 1: HP turbine blade with tip groove

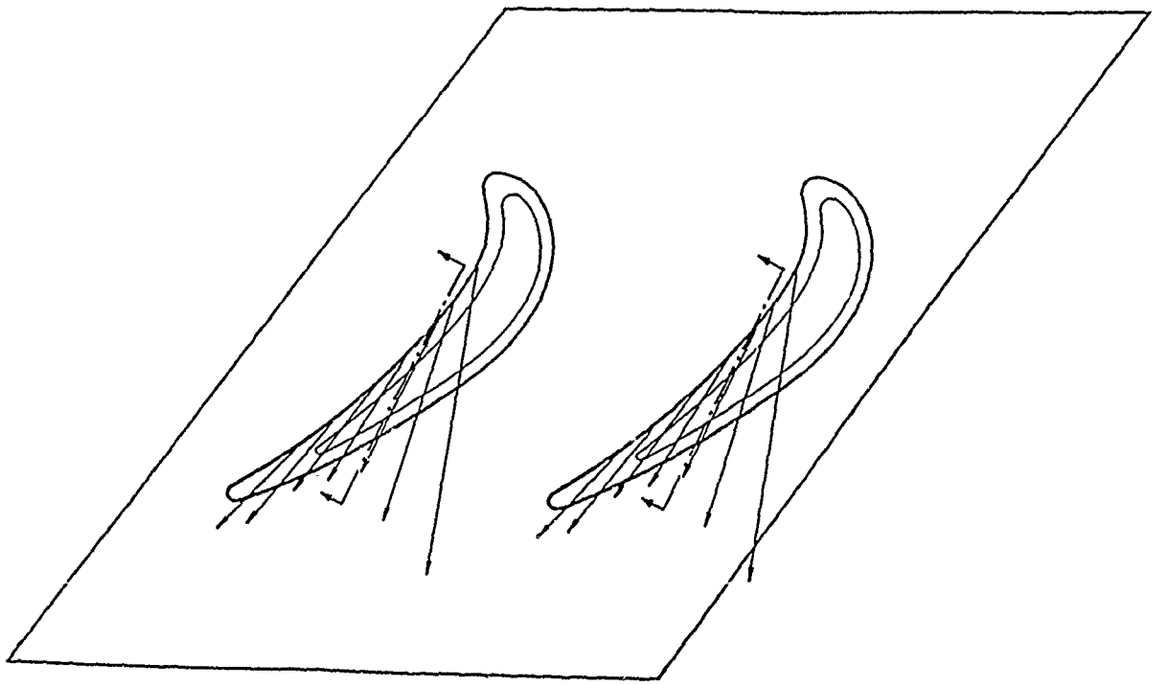
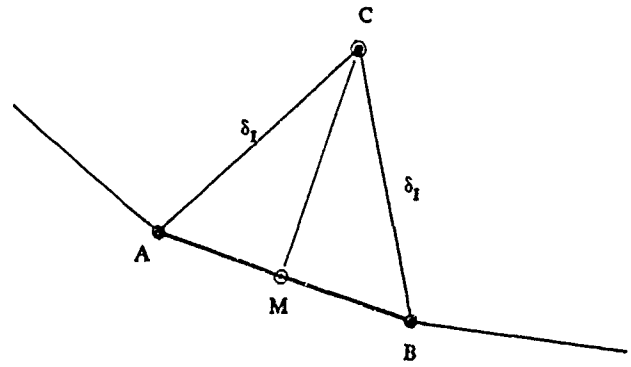
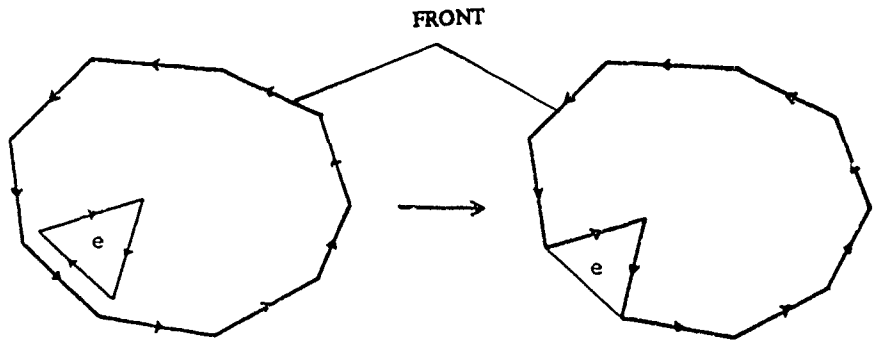


Fig. 2: Tip clearance flow direction determined by Lakshminarayana's model



GENERATING A TRIANGLE USING A CHOSEN SIDE AB IN THE FRONT



UPDATING THE FRONT WHEN A NEW ELEMENT IS GENERATED

Fig. 3: Mesh generation procedure

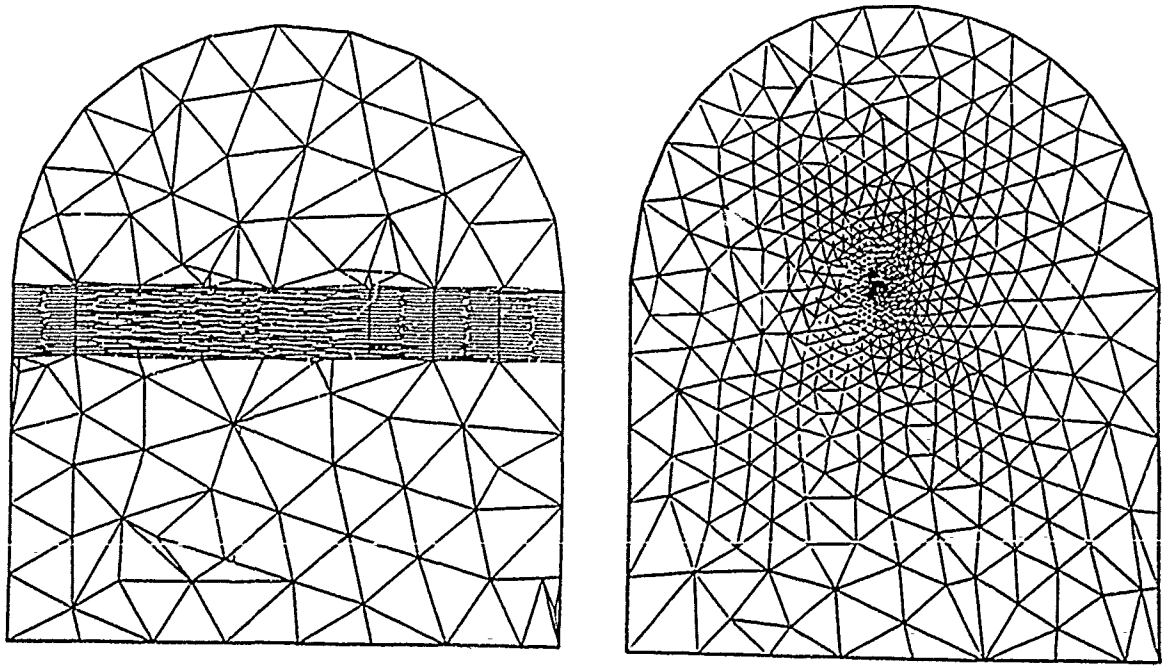
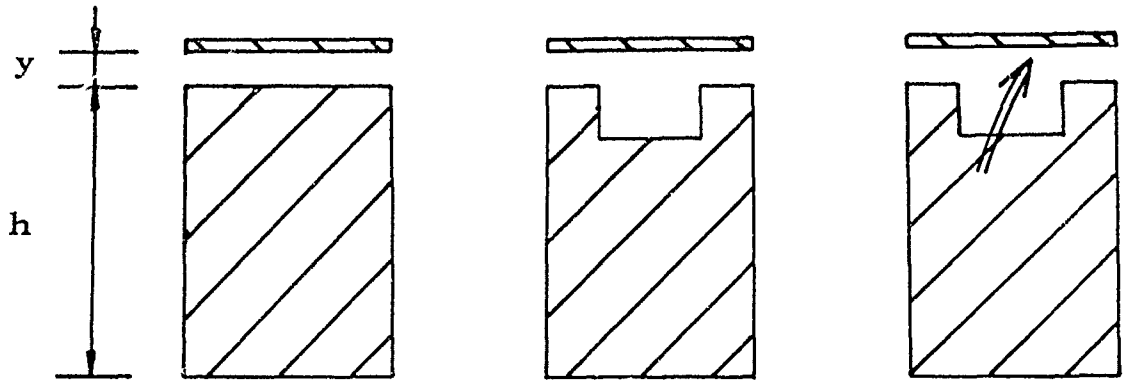


Fig. 4: Local mesh refinement



Parameter: Relative Tip Clearance Heights
y/h = 0.01 ; 0.02 ; 0.03

Influence of Wall Motion
u = 0 m/s and u = 442 m/s

Fig. 5: Tip geometries and parameter variations

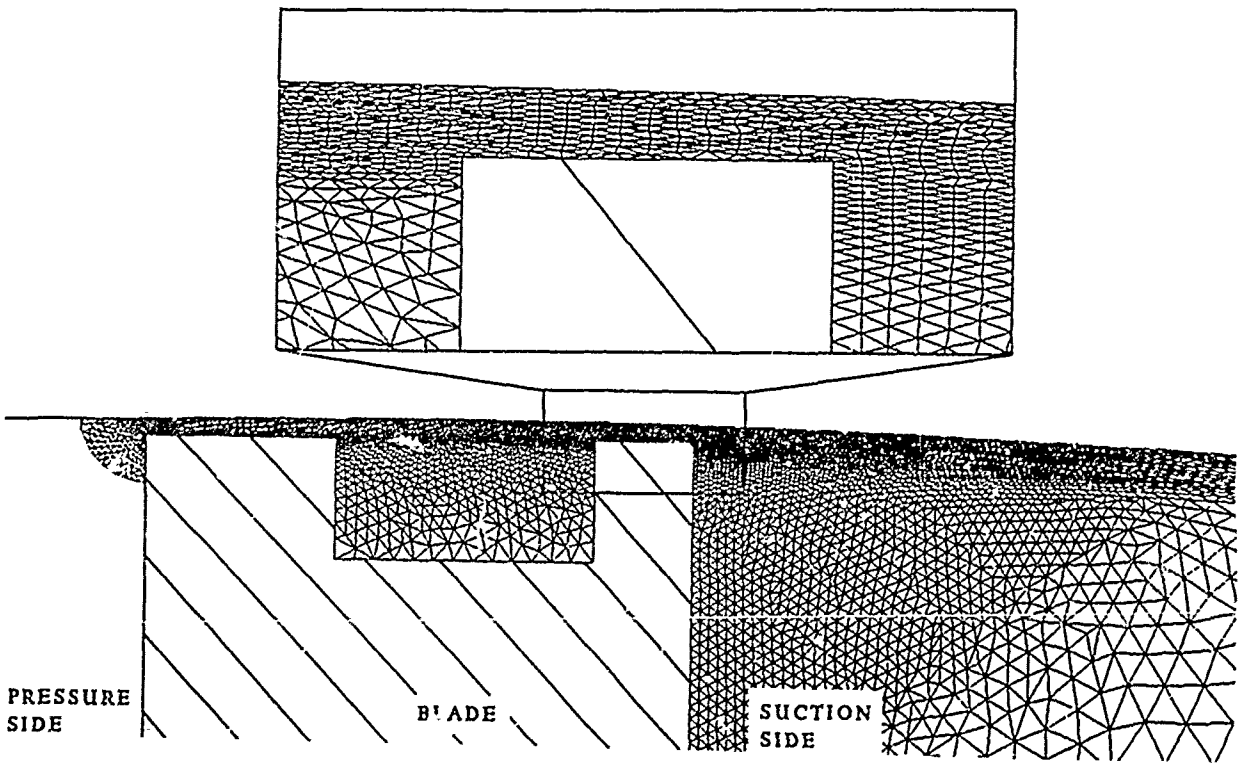


Fig. 6: Computational grid of the blade tip region

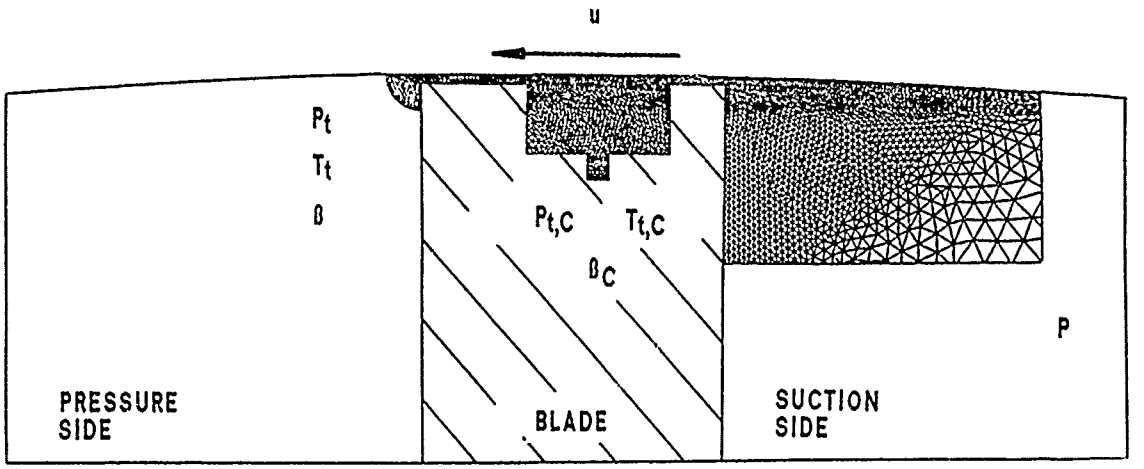


Fig. 7: Computational domain and boundary conditions

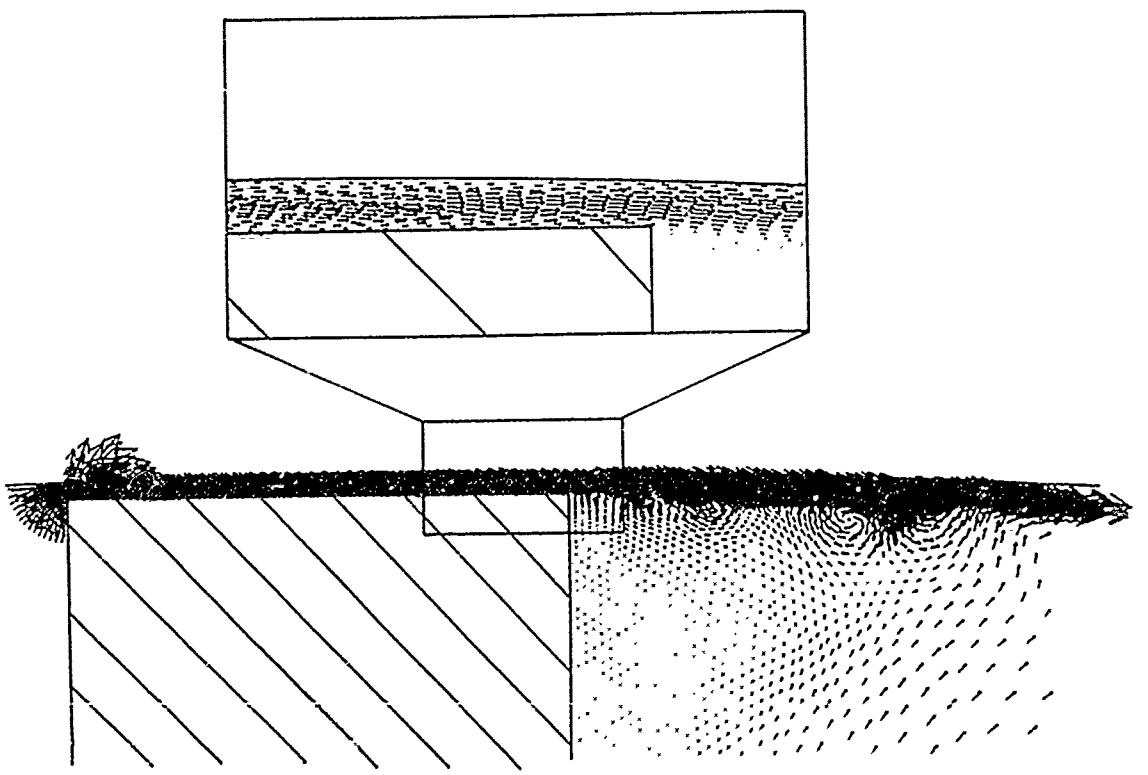
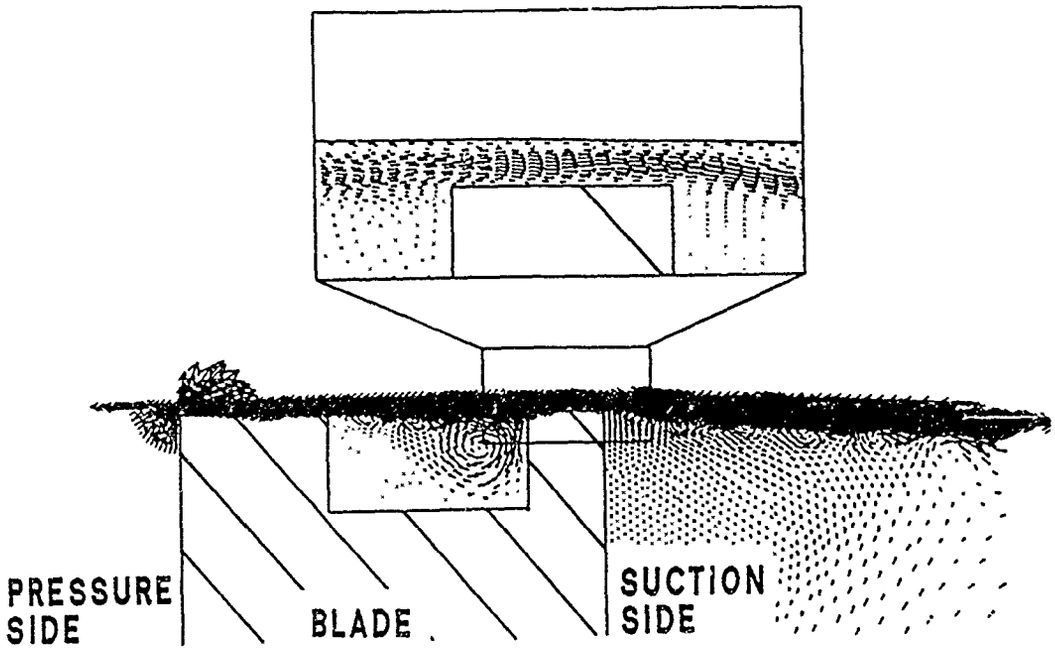
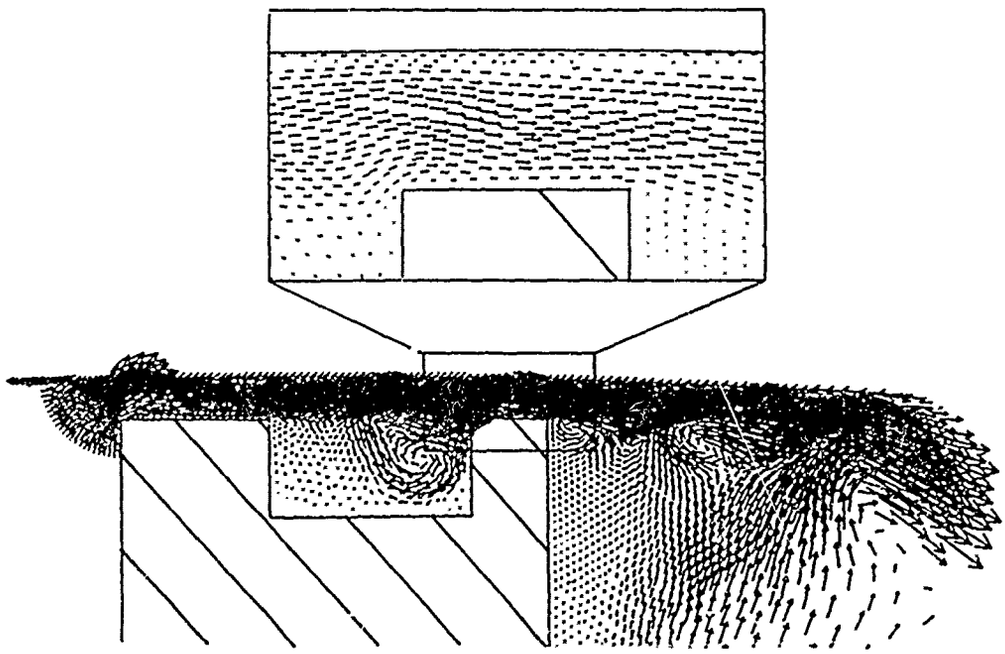


Fig. 8: Tip leakage flow for the baseline flat blade configuration without wall motion; y/h = 0.01

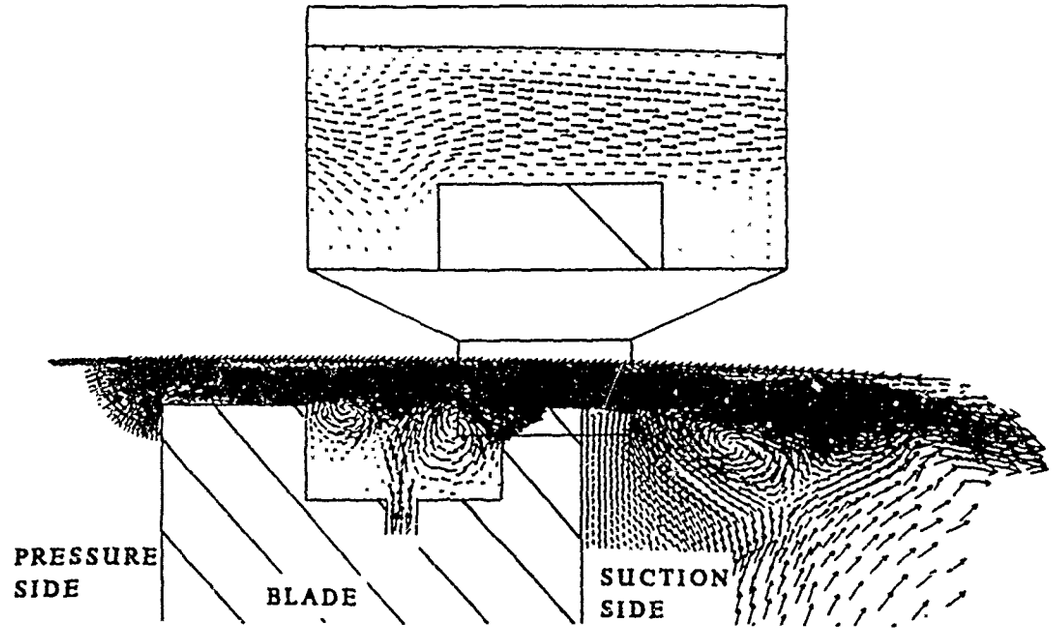


VELOCITY FIELD
RELATIVE TIP CLEARANCE HEIGHT y/h = 0.01

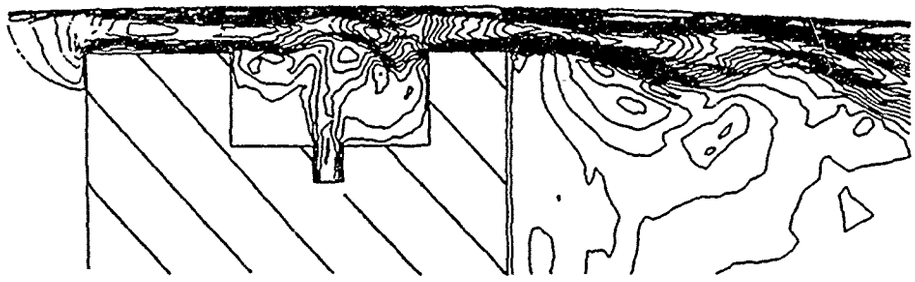


VELOCITY FIELD
RELATIVE TIP CLEARANCE HEIGHT y/h = 0.03

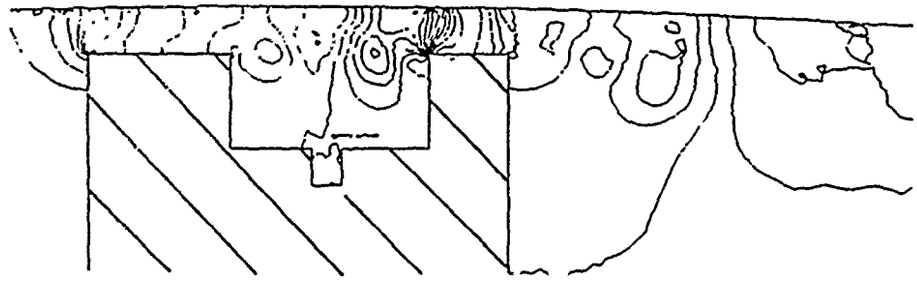
Fig. 9: Tip leakage flow without coolant injection and with wall motion u = 442 m/s; influence of the relative clearance height



Velocity Field



Distribution of Mach Numbers



Pressure Field

Fig. 10: Tip leakage flow with coolant injection and with wall motion; y/h = 0.03

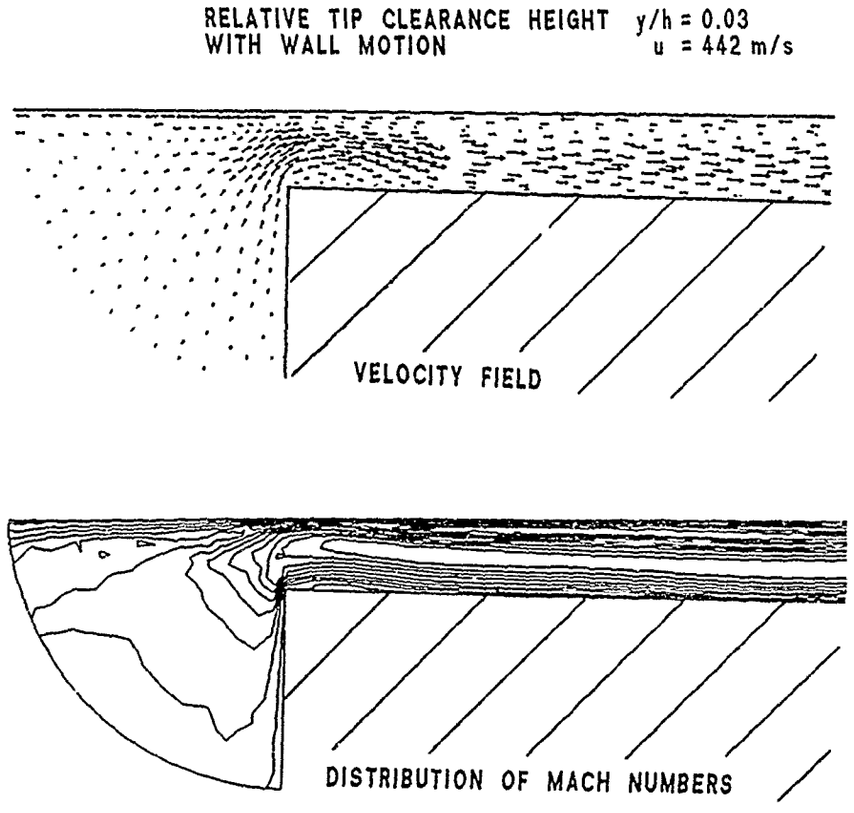


Fig. 11: Detail of the tip clearance inlet flow; flat configuration with wall motion

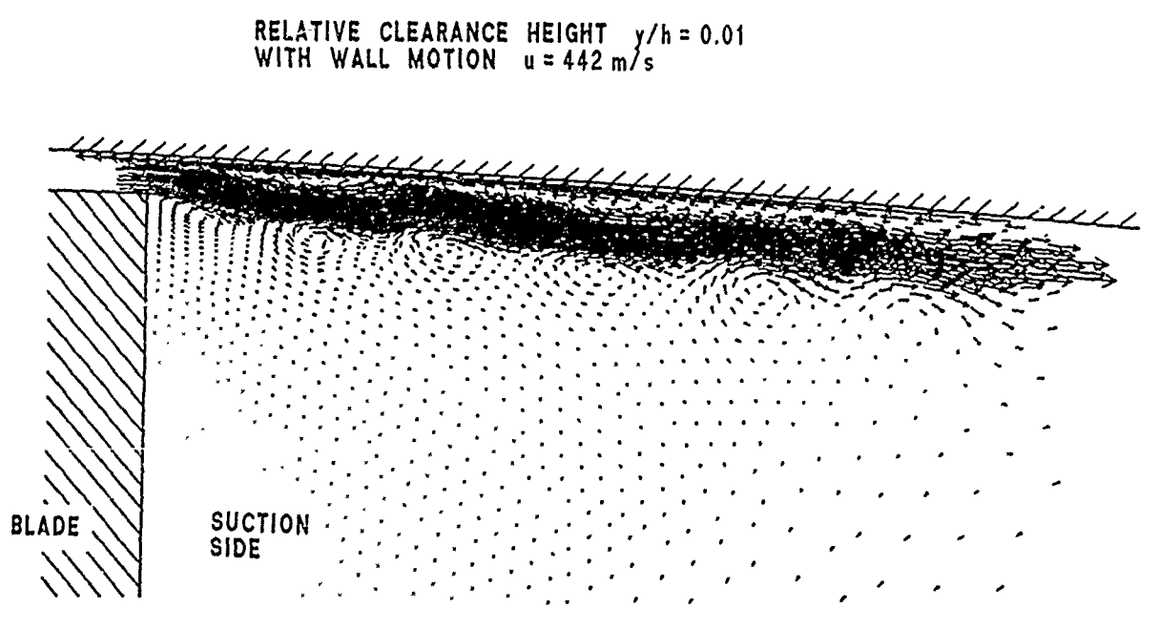


Fig. 12: Detail of tip leakage discharge flow; with wall motion

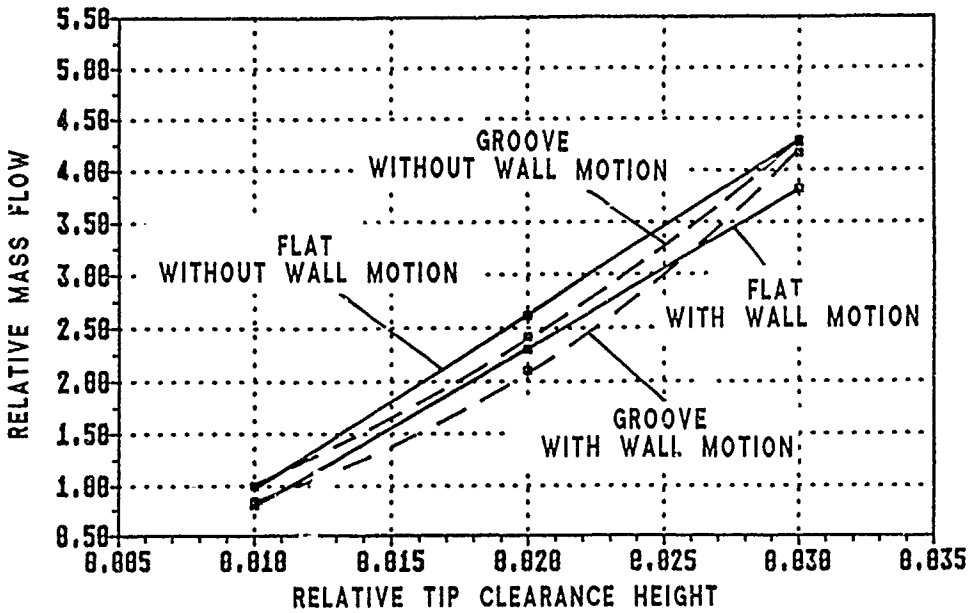


Fig. 13: Relative tip leakage mass flow versus relative tip clearance height; without coolant injection

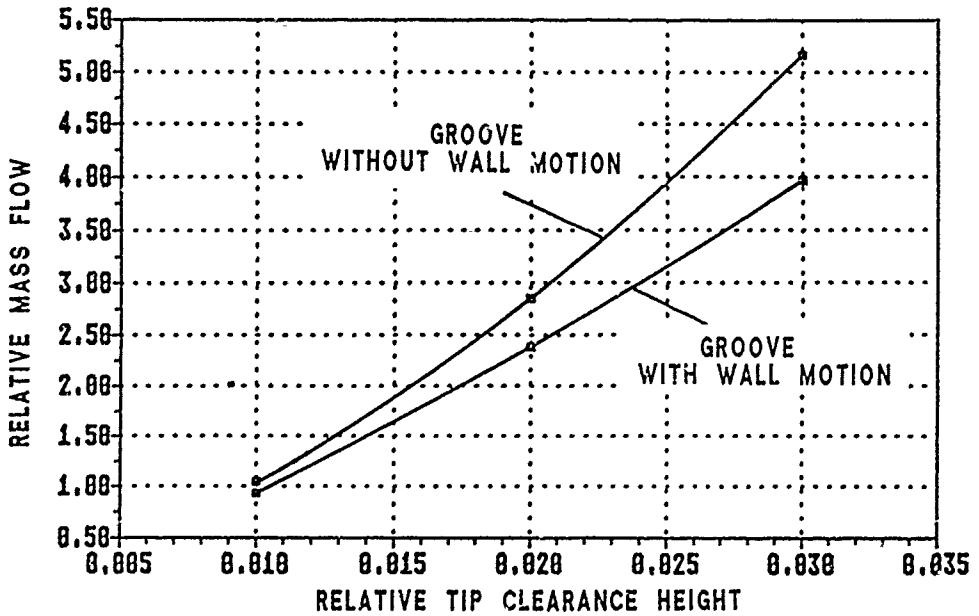


Fig. 14: Relative tip leakage mass flow versus relative tip clearance height; with coolant injection

Detailed Heat Transfer Measurements in Nozzle Guide Vane Passages in Linear and Annular Cascades in the Presence of Secondary Flows

N. W. Harvey
Rolls-Royce plc.
P.O. Box 31
Derby DE2 8BJ
United Kingdom

Z. Wang, P. T. Ireland and T. V. Jones
University of Oxford
Department of Engineering Science
Parks Road
Oxford OX1 3PJ
United Kingdom

Abstract

Two transient techniques are used to measure the heat transfer coefficient distributions in nozzle guide vanes passages. The first employs liquid crystal methods in a Cold Heat Transfer Tunnel and examines the flow in a two-dimensional cascade The second uses localised thin film heat transfer gauges within an annular cascade at engine representative Mach numbers and Reynolds numbers. The techniques are described and the resulting heat transfer coefficient distributions are discussed and interpreted in terms of the secondary flows and vortex structures. Typical heat transfer distributions are presented over the endwalls and blade surfaces. An analysis of the endwall heat transfer results is presented for the annular cascade.

c	specific heat capacity of model material	t_2	time for second calibrated colour display
h	heat transfer coefficient	x	distance measured from geometric stagnation line along blade surface
k	thermal conductivity of model material	$T(n,t)$	temperature
n	distance into the model material measured normal to the surface	$T_{crystal}$	calibrated liquid crystal colour display temperature
p	pressure surface length	T_{gas}	gas temperature
p_0	stagnation pressure	$T_{initial}$	temperature before flow initiation
Re_{inlet}	inlet Reynolds number based on true chord	α	thermal diffusivity of model material
s	suction surface length	ρ	density of model material
t	time		
t_1	time for first calibrated colour display		

Table A-1: Nomenclature for Part-A

Introduction

Heat transfer measurements have been made in two wind-tunnels using different transient techniques. A comparatively new method which uses thermochromic liquid crystals has been applied to a three blade linear cascade to demonstrate the advantage of a full surface coverage measurement. The experimental technique is fully described in Part A and the heat transfer results briefly discussed. A very comprehensive study of the endwall heat transfer distribution in an annular cascade is then presented in Part B. These measurements are supported by surface shear flow-visualisation. A novel method of predicting the heat transfer levels from an inviscid computation coupled with an integral boundary layer analysis has been developed and applied to the endwall.

Part-A Full surface heat transfer measurements using liquid crystals

A-1 Introduction

The experimental technique applied to the linear cascade was originally developed [11,7] as a means of measuring heat transfer coefficients within models of complex cooling passages. The advantage of the method is that accurate maps of heat transfer coefficient (h) are readily generated over the entire surface of the region of interest. In flow domains where there are high spatial gradients in h the problems of providing sufficient gauging to adequately define the flow can be severe. A three blade cascade was manufactured to demonstrate the suitability of the technique to the measurement of blade external heat loads. The preliminary low speed results have been presented in [21].The subsequent work has improved the operation of the wind-tunnel to expand the range of flow speeds over which measurements can be made. Heat transfer measurements have been made over the entire passage at engine representative Mach numbers.

Colour	*Crystal 1*	*Crystal 2*
red	$40.3°C$	$35.4°C$
yellow	$40.5°C$	$35.7°C$
blue	$40.7°C$	$35.9°C$

$T_{initial}$	$70.7°C$
T_{gas}	$27.6°C$
$\sqrt{\rho ck}$	$569.0 Wm^{-2}k^{-1}sec^{0.5}$

Table A-2: Experimental temperatures and thermal product

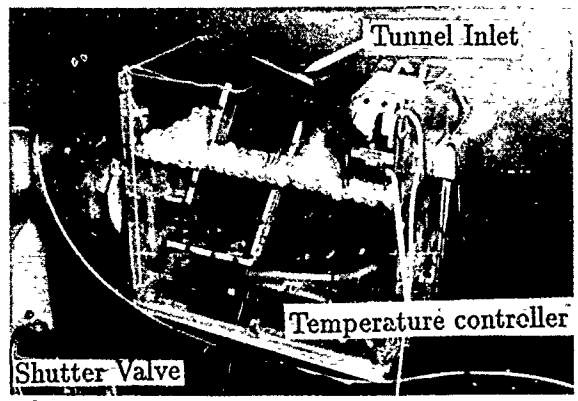


Figure A-1: Experimental facility

A-2 Experimental technique

The transient liquid crystal method is based on measuring the change in temperature of a model when subjected to a flow at a different temperature. The surface temperature is obtained from monitoring the colour of a coating of liquid crystals applied to the surface. The test section is initially at a uniform temperature and the surface temperature response is monitored using thermochromic liquid crystals. It can be shown [11,16,19] that under the test conditions, the conduction of heat in a direction parallel to the surface has a negligible effect on the surface temperature rise. The surface temperature history is then governed by the one-dimensional transient conduction equation.

$$\frac{\partial^2 T}{\partial n^2} = \frac{1}{\alpha}\frac{\partial T}{\partial t} \tag{1}$$

with the following boundary and initial conditions

$$-k\frac{\partial T}{\partial n}_{n=0} = h(T_{gas} - T_{n=0}) \tag{2}$$

$$-k\frac{\partial T}{\partial n}_{n=\infty} = 0 \tag{3}$$

$$T(n,0) = T_{initial} \tag{4}$$

The solution to these equations for a constant heat transfer coefficient and gas temperature can be written

$$\frac{T_{crystal} - T_{initial}}{T_{gas} - T_{initial}} = 1 - e^{\frac{h^2 t}{\rho ck}} erfc\left(\frac{h\sqrt{t}}{\sqrt{\rho ck}}\right) \tag{5}$$

From which it can be seen that, provided T_{gas},$T_{initial}$ and $\sqrt{\rho ck}$ are known, a knowledge of the surface temperature at a particular time after gas flow initiation is sufficient to yield the heat transfer coefficient. Alternatively, the time taken for any point on the surface to reach a particular temperature can be used. This approach permits a simple sort of surface thermometer to be employed. Originally , [7,11,24,40,26] , researchers applied a coating which melted at an accurately known temperature. More recent work has utilised thermochromic liquid crystals to indicate either a series of a single isotherm. These substances scatter light over a range about a preferred wavelength which varies as a function of temperature. As a consequence, they appear to change colour over a certain temperature range. A typical example of a chiral nematic, [28], sort of liquid crystal supplied by BDH[1] appears red at 40.3°C and, as the temperature is increased, passes through the full visible spectrum over a range of 0.5°C. (see Table A-2)

The accuracy of the measurement is dependent on a sufficiently rapid crystal response, and earlier tests [18,2] on the chiral nematic type of liquid crystal employed showed that the time response was of the order of milliseconds. The tests reported here are all long enough for the response of the crystal to be considered instantaneous.

Although it is possible to establish the temperature at any point within the colour display band by monitoring the colour of the coating, [9], it is more accurate in practice, to select a crystal which is optically active over a narrow range of temperature and acquire one reading from a single colour. In situations where more than one temperature is required, combinations of different liquid crystal devices have been employed [5,6,17,18,19]. This mixing is possible since the crystals are supplied as micro-capsules. The active liquid crystal is in the form of tiny spheres ($10\mu m$ in diameter) encased in a protective shell of gelatin and gum arabic [32]. When applied to the surface, the coating consists of a single layer of capsules containing the required liquid crystal material. The capsules are fixed to the surface with a glue which results in a surface roughness which is smaller than the capsule size. For these tests the surface of the coated model can be considered to be hydraulically smooth.

A coating which consisted of two different liquid crystals was applied to the turbine passage. In this way two values of heat transfer coefficient could be calculated at many points on model. With a model initial temperature of $70.7°C$ the heat transfer coefficient at certain locations was too low for the surface to cool to the colour display temperature of 'Crystal 2' (Table A-2) during the test time.

Under the test conditions the transient method can be shown to be equivalent to measuring heat transfer coefficients under isothermal wall conditions. The thermal boundary conditions of the transient technique have been considered in

[1]BDH Ltd,Poole,Dorset BH12 4NN,UK.

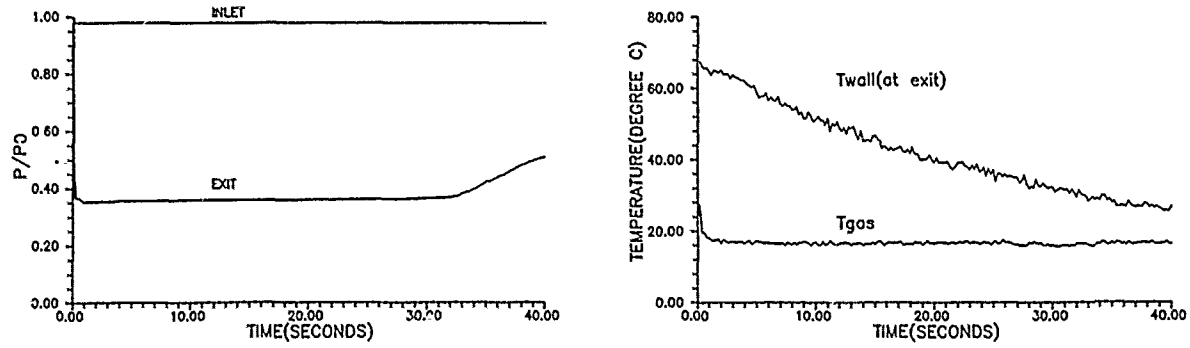


Figure A-2: Pressure and temperature throughout a typical test

[1,17,19,29]and the data presented over the turbine cascade in the present report was confirmed as being measured for a time invariant heat transfer coefficient from the agreement between the values calculated for the two crystal temperatures.

The experimental uncertainty is a function of the temperatures used in the test. For this work, the greatest experimental uncertainty in the heat transfer data was 6.0%. The analysis used was that given in Appendix 4-B of [19].

A-3 Experimental facility and test procedure

The experimental facility is shown in Figure A 1. During the experiment dry air at atmospheric pressure is drawn through the tunnel to an evacuated tank. Initially the cascade is isolated from the $28m^3$ tank by a shutter valve. The heat transfer analysis assumes that the test flow results in a step change in h and hence it is essential that the valve opens rapidly. The pneumatically actuated valve incorporates a tapered shutter which is supported on tracks by roller bearings. Tests revealed that the valve opened in less than 60milliseconds.

The aerofoil profile has previously been studied by Watt et al. [41] and many of the cascade details (Table A-3) in this reference are the same for the current tests. The perspex working section was immersed in a water tank and heated to about $70^{\circ}C$. Complete temperature uniformity prior to the test was ensured by continuously circulating the water. Temperature controlled air was introduced into the tunnel just downstream of the turbine blades and passed out through the tunnel inlet. A digital controller was used to set the power to an electrical heater in order that the air passing through the cascade could be set at the same temperature as the water. A temperature controlled guard heater was also installed in the section downstream of the blades. The hot air flow was maintained through the model up until the time that the shutter valve opens. In this way an initial model temperature uniformity of better than $0.2^{\circ}C$ was provided.

During the test the air temperature was measured by a thermocouple at the tunnel inlet and the static pressure recorded both at inlet and downstream of the blading. A second throat at the valve uncoupled the flow through the cascade from the steadily rising pressure in the tank. No heat transfer data was analised once the flow at the second throat became unchoked. This occurs at 32 secs for the particular test which is detailed in Figure A-2. The heat transfer coefficient was calculated from flat plate correlations [34] for the tunnel entry length of $270mm$. This value was found to to be within 10%

Blade dimensions	
Profile scale	1 : 1
True chord length	$69.0mm$
Axial chord length	$37.4mm$
Pitch spacing	$57.4mm$
Span	$50.0mm$
Suction surface length	$83.6mm$
Pressure surface length	$67.0mm$
Entry length	$270.mm$

Test parameters	*Low speed*	*High speed*
Inlet Mach number	0.06	0.18
Re_{inlet}	93000	250424
Calculated boundary layer thickness	$8.0mm$	$6.33mm$

Table A-3: Cascade Details

of the measured heat transfer coefficient.

A-4 Discussion of results

The aim of this work was to demonstrate that a new transient technique could be applied to the measurement of heat transfer coefficients in a turbine cascade. A comprehensive study of the flow field was not undertaken but it should be noted that the technique, as a matter of course, generates complete contours. In other words, the data presented in Figures A 3 to A-6 have not been numerically smoothed. This ensures that quite subtle features in the contours are preserved.

A particularly interesting feature is evident on the endwall at both flow speeds adjacent to the blade leading edge. The endwall contours in Figures A-3 and Figure A-4 reveal the expected peak in h near to the blade leading edge. As the incident boundary layer approaches the blade it is subject to an adverse pressure gradient and the flow 'rolls up' to form a vortex. Within this part of the separation system, heat transfer to the endwall is found to be highest at the flow attachment

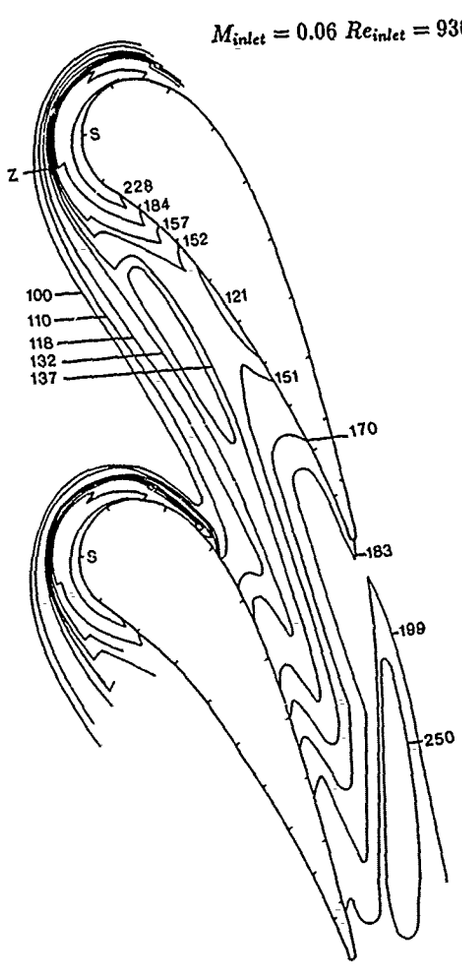


Figure A-3:

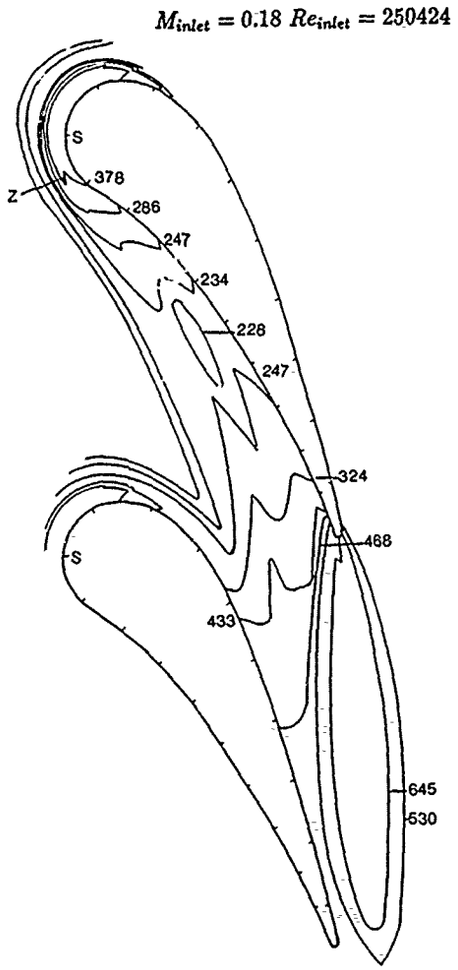


Figure A-4:

Heat transfer coefficient ($Wm^{-2}K^{-1}$) distributions on the endwall. The geometric stagnation point is indicated (S) and the feature marked Z is referred to in the text. The marks around the blades are at intervals of ten percent of the blade lengths on each side. The flow direction is from left to right.

point. For a symmetrical obstacle such as a cylinder, this point will be on the line of symmetry, and for the turbine blade will be close to the geometrical stagnation point. Levels of heat transfer coefficient on the endwall then decrease as one moves away from the obstacle and hence the attachment point. However, at a certain distance from the cylinder, this monotonic decrease is arrested, and a second peak in h is observed [17,19].The endwall contours as they pass through this region are then folded back and are 'Z' shaped as marked in Figures A–3 and A–4. This effect was first observed using the same transient technique under the vortex structure at the front of pedestals used in cooling passages [17,19]. The separation which forms at the junction between the pedestal and the cooling passage wall is strongly related to that ahead of the turbine blade. Much flow visualisation work for the pedestal established this peak as being at the attachment line of a second vortex ahead of the horseshoe vortex.

Flow field studies by other workers [38,22] have also succeeded in classifying the vortex system as being comprised of two main vortices (the 'horseshoe' vortex adjacent to the obstacle, and the 'separation' vortex upstream). In fact a small counter vortex must exist between the two though its influence on heat transfer appears to be insignificant. The first association of the heat transfer distribution to the double main vortex structure is given in [19]. The same phenomenon around turbine blades has also been observed using a steady state heated coating method [14] and the mass transfer analogy method [13].

Clearly flow visualisation would be required for a full discussion of the features observed though it is thought likely that the pressure side leg of the horseshoe vortex remains close to the blade, and that the attachment line under this vortex is responsible for the bend in the contours on the endwall adjacent to this surface. Over the pressure surface of the blade, the levels of h are lower towards the endwall. This tendency of the horseshoe vortex to reduce heat transfer to the obstacle, in this case the blade, near to the junction with the endwall has been observed previously over a pedestal placed in fully developed channel flow [1,17]. It was found that this phenomenon was dependent on the thermal boundary layer in the incident flow. The former study showed that, when the heat transfer was only to the obstacle itself, the vortex system acted to increase heat transfer in the vicinity of the junction. These thermal boundary conditions were achieved by wrapping an insulated perspex cylinder with an electrical heater but supplying no heat at the windtunnel endwall. Comparison was made to the results of tests using the transient method applied to an identically dimensioned cylinder in the same flow

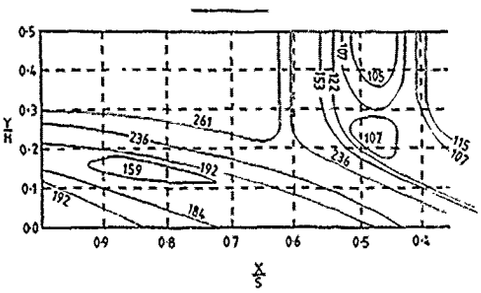


Figure A-5: Suction surface

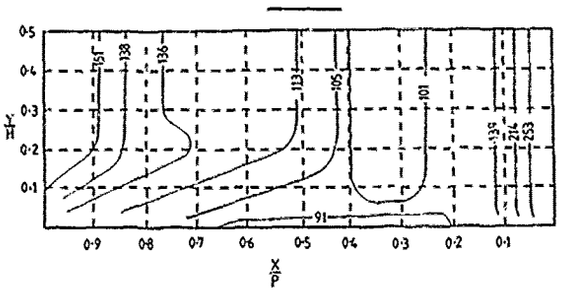


Figure A-6: Pressure surface

Contours of heat transfer coefficient($Wm^{-2}K^{-1}$) on the blade surface. The flow direction is from right to left.

field. In this case, both thermal and hydrodynamic boundary layers were present in the flow just upstream of the pedestal. Around the front of the pedestal, it was found that the major influence of the vortex system was to reduce heat transfer levels from the mid span values close to the cylinder extremities.

The endwall heat transfer distribution at both inlet Mach numbers also indicate that, under the influence of the cross passage pressure gradient, the outer separation vortex traverses the passage and comes close to the suction surface of the blade at between 35% and 40% of the suction surface length. Inspection of the suction surface contours for the low Mach number data, Figure A-5, then reveals evidence of three dimensional effects from about this position. Interestingly, the levels of heat transfer coefficient are, up until about the 60% line, *increased* from the mid-span values. This is thought to be due to an attachment line between the counter rotating vortices (specifically, the suction surface side leg of the horseshoe vortex, and the pressure side separation vortex which has crossed the passage). As discussed above, if only one vortex is close to the blade, as is the case on the pressure surface , then no such attachment occurs, and heat transfer levels are not necessarily increased—depending on the presence or not of the thermal boundary layer. Beyond 60%, for the low Mach number results, a rise in heat transfer for flow remote from the vortex system and away from the endwalls , identified as transition, masks the influence of this line.

Amongst the highest levels of heat transfer to the endwall are those recorded behind the aerofoil in the wake region. This was the case even for the low speed data which was entirely subsonic and hence this enhancement is *not* associated with any compressible flow phenomena. One method of confirming the validity of the steady heat transfer coefficient is to calculate the ratio of the colour change times $\frac{t_1}{t_2}$ on the surface of the model. It can be shown[21] that this ratio shold be uniform over the surface provided that the driving gas temperature and intial temperature are uniform. The two event times and their ratio are plotted in Figure A-7 for the suction surface in a region of supersonic flow.

A-5 Conclusions

This work has demonstrated that a novel method of measuring heat transfer coefficient can be applied successfully to turbine cascades. The advantages of a full surface measurement has been demonstrated by the detail of the contours of heat transfer coefficient presented.

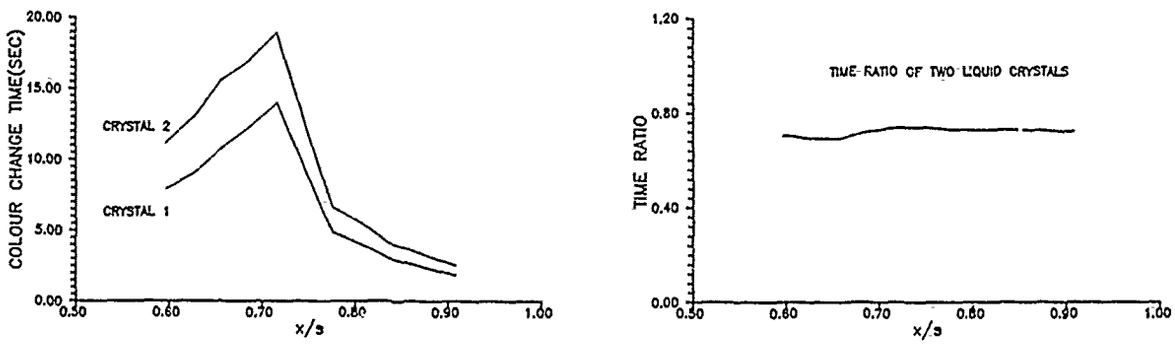


Figure A-7: t_1 and t_2 on the suction surface for an inlet Mach number of 1.8

Part-B Measurements in an annular cascade

B-1 Introduction

Local heat transfer measurements have been made on an HP NGV in annular cascade at engine representative Reynolds numbers and Mach numbers using the thin film gauge technique described by Schultz et al. [35,37]. The technique is briefly reviewed and the measured hub end wall heat transfer is presented. A new analysis method is introduced, together with flow visualization results for the vane. The heat transfer patterns are discussed in the light of these results.

B-2 Experimental technique

Thin film gauges are painted onto machineable glass ceramic (Corning macor) blades. The working section is initially at ambient temperature and is subject to a step in convective heating when the tunnel is operated, and the gauges measure

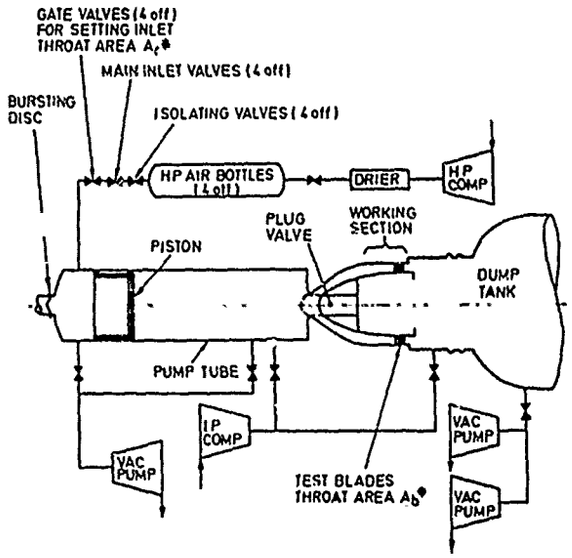


Figure B-1: Schematic diagram of ILPC facility

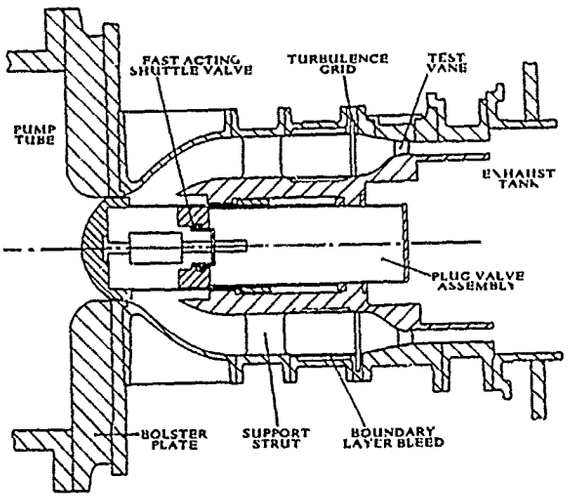


Figure B-2: General assembly of working section

c	true chord
c_{ax}	axial chord
c_p	specific heat capacity of air
h	heat transfer coefficient
k	thermal conductivity of air
Ma	Mach number
Nu	Nusselt number $= \frac{hc}{k}$
n	distance normal to surface
s	stream-wise co-ordinate
(s,β,n)	co-ordinate system aligned with stream lines
Re	Reynolds number
r	radial distance from the z axis
r_b	true local body radius
r_m	equivalent body radius
RC	time constant
T	temperature
t	time
T_{gas}	gas temperature
Tu	turbulence intensity
T_{wall}	wall temperature
(u,v,w)	velocity components in the streamwise co-ordinate system
(u_z,u_r,u_θ)	velocity components in cylindrical polar co-ordinates
V	voltage
z	axial distance
(z,r,θ)	cylindrical polar co-ordinates
α	thermal diffusivity of substrate
β	distance normal to s and n
δ_{99}	boundary layer thickness
ϕ	angle from the vertical
μ	dynamic viscosity of air
ρ	air density

Table B-1: Nomenclature for Part–B.

the surface temperature response. Making the same assumptions as for the liquid crystals the surface temperature history is again governed by the one dimensional transient conduction equation.

$$\frac{\partial^2 T}{\partial n^2} = \frac{1}{\alpha}\frac{\partial T}{\partial t} \tag{6}$$

The surface temperature is converted to heat transfer rate by an electrical analogue of the conduction process. The variation of voltage with time and distance along an R–C transmission line is given by

$$\frac{\partial^2 V}{\partial n^2} = RC\frac{\partial V}{\partial t} \tag{7}$$

which is analogous to the transient conduction equation. Provided the transmission line is long enough, compared with the flow duration, for it to appear semi-infinite then there is a direct analogue between the input voltage and surface temperature on one hand and input current and surface heat transfer rate on the other. The theory is given more fully in [36,30,31].

B-3 Experimental facility and test procedure

The NGV cascade was tested in the Isentropic Light Piston Facility (ILPC) at the Royal Aerospace Establishment(Pyestock). The ILPC is described fully by Brooks et al. in [3]. A schematic diagram is included as Figure B-1. The theory of this facility is described by Jones et al. in [23]. Briefly, the ILPC is a transient facility which provides a means of generating a short-duration steady flow through the working section for up to one second at engine representative Mach numbers, Reynolds numbers and gas-to-wall temperature ratios. A new working section was made for these tests, shown in Figure B-2. As can be seen the NGV was tested with an inlet contraction representative of the engine combustor exit nozzle. A pneumatically actuated plug valve separated the working section from the piston tube. This opened in under $50ms$ to allow the air in the piston tube (compressed by the high pressure air driving the piston) through the working section,

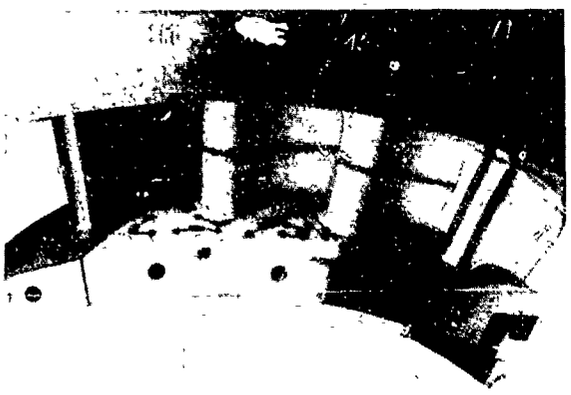


Figure B-3: Detail of thin film gauges on hub end wall

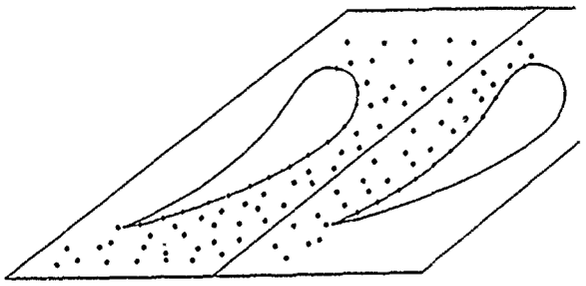


Figure B-4: Location of hub end wall thin film gauge centres



Figure B-5: Front view of hub end wall flow visualization

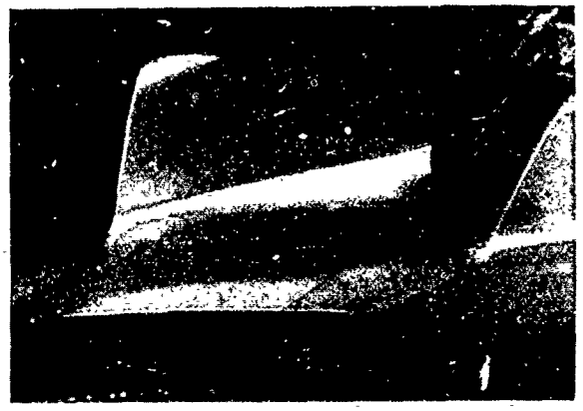


Figure B-6: Rear view of hub end wall flow visualization

Blade dimensions (mid-height)	
Scale	1 : 1
True chord length	70.1 *mm*
Axial chord length	37.5 *mm*
Span (at trailing edge)	37.4 *mm*
Span (at contraction inlet)	120.0 *mm*

Test Conditions (mid-height)	
Exit Ma	0.884
Exit Re (true chord)	2.57×10^6
Initial T_g/T_w	1.29
Hub inlet δ_{99}	2.7% span
Casing inlet δ_{99}	2.3% span
Inlet T_u (leading edge)	6.3%

Table B-2: Test Details

once it had reached the required temperature and pressure. Pressure oscillations in the flow due to finite piston mass and sudden expansion into the working section volume were within 6% of the mean total pressure. The test conditions for the results reported here are given in Table B-2. At three positions around the annulus sets of four vanes were held in cassettes which allowed instrumented vanes to be removed and fitted without the need for de-rigging. Details of the instrumented machineable glass vanes with hub end wall thin films are shown in Figures B-3 and B-4.

Upstream of the inlet contraction the boundary layer was bled off through perforated walls in the parallel duct. The turbulence was generated using radial bars positioned at the start of the contraction, where the boundary layer into the vanes was assumed to begin. Boundary layer thicknesses were measured using pitot traverses one axial chord upstream of the vanes. The inlet temperature was measured using fast response thermocouples and the inlet turbulence intensity using a constant temperature hot wire anemometer.

B-4 Experimental results

B-4.a Flow visualization

To aid the interpretation of the results a number of flow visualization techniques were used. The results of a two colour fluorescent dye technique are presented in Figures B-5 and B-6. The vane aerofoils and platforms downstream of the leading edge were painted with one fluorescent dye in a silicon oil and paraffin suspension (which shows darker in the figures). Upstream of the vane leading edge the platforms are painted in another dye (which shows lighter in the figures). The penetration of the second dye into the passage during the run clearly highlights the passage secondary flows. Drawing on the excellent review of secondary flows by Sieverding [39] (and the work of the researchers contained in his review) the interpretation of these results is as follows. As the inlet boundary layer approaches the vane leading edge it experiences an adverse pressure gradient and is 'rolled up' into the leading edge horseshoe vortex resulting in a small region of reverse

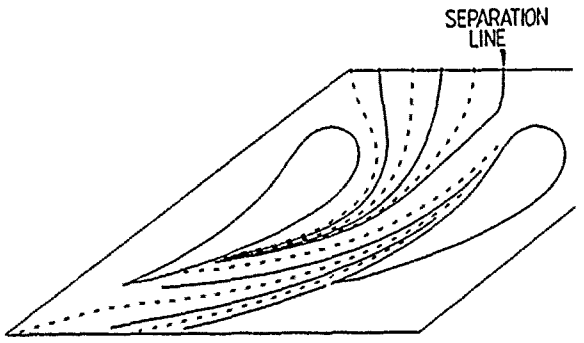


Figure B-7: Hub end wall streamline pattern from 3-D calculation

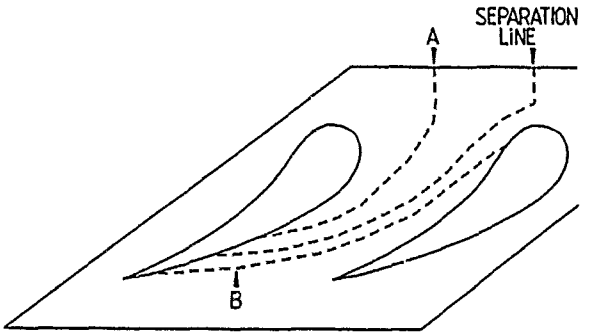


Figure B-8: Hub end wall streamline pattern from flow visualization

flow Away from the leading edge, as the boundary layer enters the passage the low momentum fluid is overturned by the cross-passage pressure gradient and is swept toward the adjacent suction surface. A clear separation line is visible marking the limit of the penetration of the bottom of the inlet boundary into the passage. It is assumed that the pressure surface leg of the horseshoe vortex is also swept across the passage, remaining just downstream of the separation line. The suction surface side leg of the horseshoe vortex remains close to the aerofoil and is quickly swept up onto the vane surface. In Figure B-6 a line can be seen on the rear of the aerofoil. The fluid in the overturned boundary layer is swept off the end wall and up the blade until it can no longer overcome the radial pressure gradient whereupon it separates off the surface from this line, feeding the passage vortex. Dye is entrained along this line, perhaps helped by the presence of the suction surface leg of the horseshoe vortex which remains close to the aerofoil surface – but the evidence is not conclusive. The dye travels to the trailing edge where the downwash in the wake carries it back onto the hub platform, clearly showing how the wake impinges on the end wall. Downstream of the separation line a new boundary layer forms in the pressure surface end wall corner region. As this boundary layer grows and loses momentum it too is swept across the platform by the cross-passage pressure gradient.

B-4.b Hub platform heat transfer

Figure B-9 shows contours of Nu derived from the measured local heat transfer rates. The contours are interpolated from the data using a quadratic surface fitting routine. This necessarily involves some smoothing of the data and provides less resolution than the full coverage obtained from liquid crystals. The results presented are a composite picture averaged from a number of runs with an overall uncertainty of 5%. The heat transfer patterns are similar to those observed by Georgiou et al. [12] in a linear cascade. High heat transfer can be seen around the leading edge, as with the liquid crystals, but the thin films have not resolved any other features in this region, in particular low heat transfer at the separation line in front of the horseshoe vortex. There is a characteristic V shape in the contours at the inlet with a region of low heat transfer intruding into the passage. After this the heat transfer increases in the passage up to the throat, as would be expected in accelerating flow. A plateau of high heat transfer around the pressure surface trailing edge falls away markedly toward the suction surface endwall corner. To help interpret these results, which are not readily explicable in terms of the observed secondary flows, a new analysis method was developed to calculate the measured Nu.

B-5 Analysis method and results

Dejarnette et al. [10] in a review of approximate heat transfer analyses described the application of the 'axisymmetric analogue' developed by Cooke [8]. Making the assumption that along an endwall streamline the cross flow in the boundary layer is negligible (that is, skew through the boundary layer is ignored) the general 3-D boundary layer equations can be reduced to a form identical to those for axisymmetric flow. Provided that the streamlines can be predicted the method allows the heat transfer to be calculated along them and a picture of the surface heat transfer to be built up. Using a streamwise oriented co-ordinate system (s, b, n) and making the usual boundary layer assumptions the momentum, energy and continuity equations reduce to

$$\rho\left(u\frac{\partial u}{\partial s}+w\frac{\partial u}{\partial n}\right) = \rho_1 u_1\frac{\partial u_1}{\partial s}+\frac{\partial}{\partial n}\left(\mu\frac{\partial u}{\partial n}\right) \tag{8}$$

$$\rho c_p\left(u\frac{\partial T}{\partial s}+w\frac{\partial T}{\partial n}\right)+\rho_1 u u_1\frac{\partial u_1}{\partial s} = \frac{\partial}{\partial n}\left(k\frac{\partial T}{\partial n}\right)+\mu\left(\frac{\partial u}{\partial n}\right)^2 \tag{9}$$

$$\frac{1}{r_m}\frac{\partial}{\partial s}(\rho r_m u)+\frac{\partial}{\partial n}(\rho w) = 0 \tag{10}$$

Here the subscript 1 refers to free stream conditions. The variable r_m is an equivalent body radius derived from the true local body radius r_b modified to allow for lateral convergence (or divergence) of the streamlines. In a cylindrical polar co-ordinate system (z, r, ϕ), best suited for an axisymmetric end wall, r_m is given by

$$r_m = r_b\frac{\partial\phi}{\partial\beta}\frac{u_z}{V}\left[1+\left(\frac{\partial r}{\partial z}\right)\right] \tag{11}$$

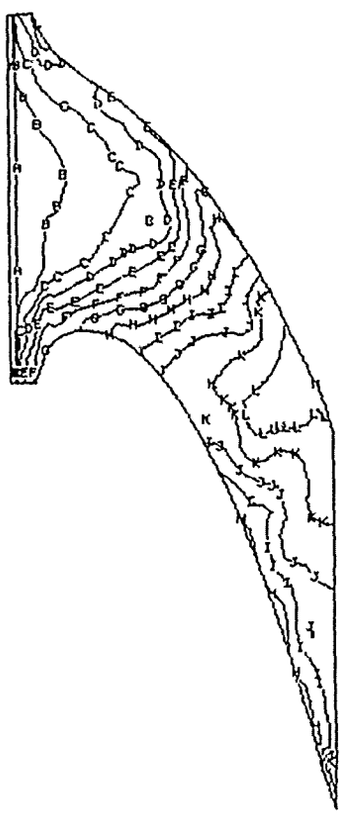


Figure B-9: Contours of measured hub end wall Nu

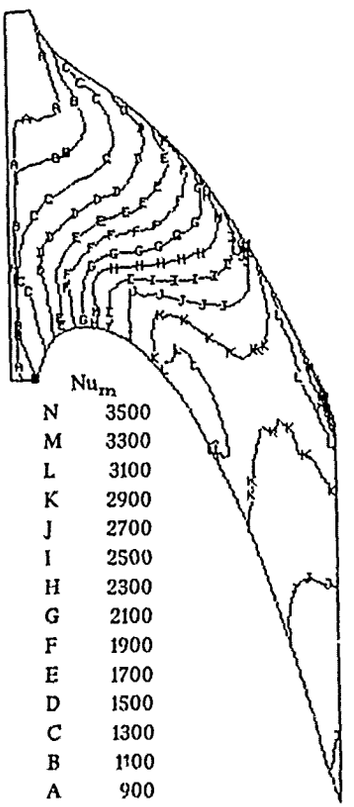


Figure B-10: Contours of hub end wall Nu calculated without axisymmetric analogue

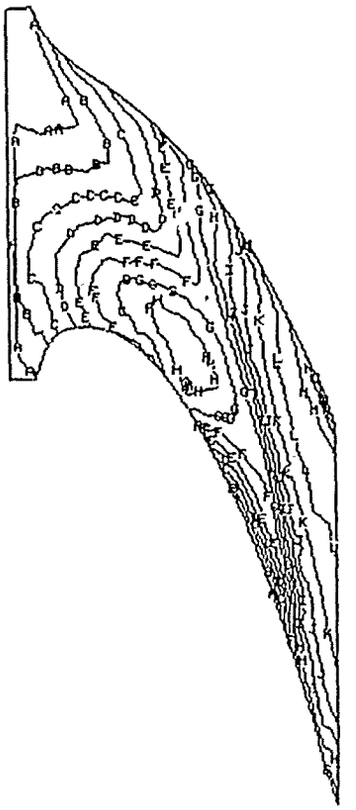


Figure B-11: Contours of hub end wall Nu calculated using axisymmetric analogue

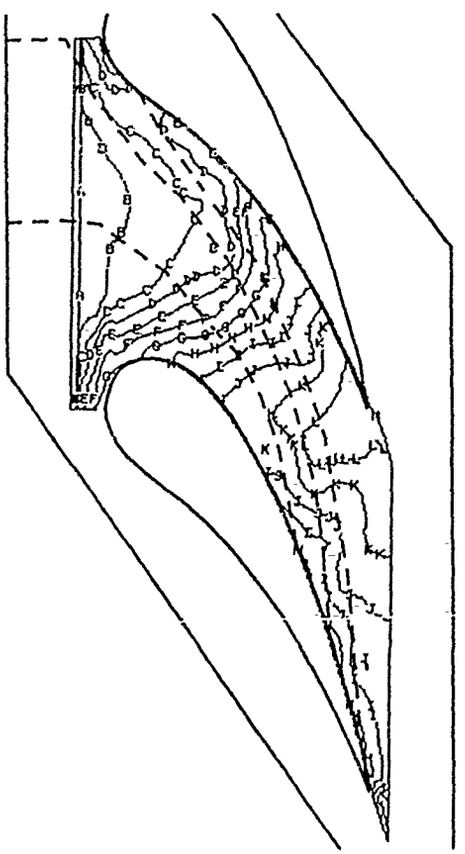


Figure B-12: Hub end wall Nu overlaid with visualized streamlines

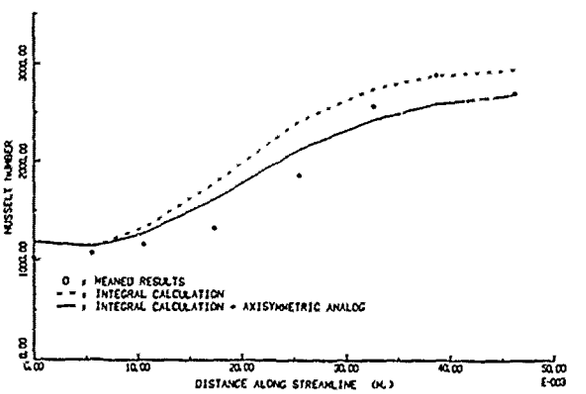


Figure B-13: Comparison of measured and calculated Nu along streamline A

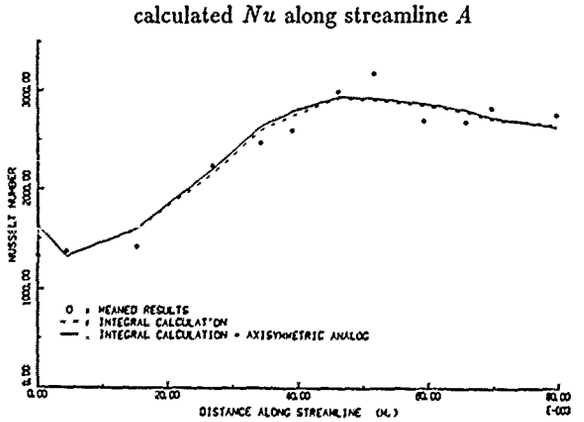


Figure B-14: Comparison of measured and calculated Nu along streamline B

where $\partial\phi/\partial\beta$ is given by numerically integrating the equation

$$\frac{\partial}{\partial s}\left[\ln\left(\frac{\partial\phi}{\partial\beta}\right)\right]_{\beta,n} = \frac{1}{r_b V}\left(\frac{\partial u_\phi}{\partial\phi} - \frac{u_\phi}{u_z}\frac{\partial u_z}{\partial\phi}\right) \tag{12}$$

along a streamline using the local flow conditions. For heat transfer on an end wall the dominant secondary flow arises from the vorticity in the inlet boundary layer. Since the convection of this inlet vorticity through the passage is an inviscid process, it was proposed to model the rolling up of the inlet boundary layer using the DENTON 3-D inviscid Euler solver with the measured inlet boundary layer as input to the calculations. The calculated streamline pattern is shown in Figure B-7, together with streamlines derived from the flow visualization in Figure B 8. The separation lines and the streamlines downstream of them match well. Upstream of the separation line the calculation suggests, unrealistically, that the streamlines will converge at the point of minimum pressure on the platform. The flow conditions calculated by the 3-D code were used together with Ambrok's simple integral method [27] and the axisymmetric analogue to derive the heat transfer values, assuming fully turbulent boundary layers everywhere. Figure B-10 shows the Nu patterns calculated without the axisymmetric analogue and Figure B-11 the Nu patterns with the effect of the streamline convergence included. The failure of the 3-D code to correctly calculate the streamlines for the inlet boundary layer results in an obvious region of low heat transfer when the streamline convergence is taken into account. Behind the separation line a new boundary layer is assumed to start in the pressure surface end wall corner. In this region, where the streamlines are largely parallel, the calculation gives good agreement with the measured results. Using the observed end wall flow pattern the heat transfer was recalculated along the two streamlines A and B, shown in Figure B-8. The results of this are shown in Figures B-13 and Figure B-14. As can be seen, if the streamlines are known, the heat transfer can be calculated to within 15% of the measured values.

B-6 Discussion of results

Figure B-12 shows the observed end wall streamlines overlaid on the measured heat transfer contours. Using this and the analysis already described we can now interpret the measured results.

1. The separation line clearly correlates with the top edge of the V–shaped region at the inlet and the edge of the plateau of high heat transfer near the pressure surface trailing edge.

2. The high heat transfer at the leading edge is at the attachment point of the horseshoe vortex.

3. Upstream of the separation line the inlet boundary layer is swept across the passage. As it does so the streamlines converge and the boundary layer thickens, offsetting to some extent the effect of the flow acceleration in the passage. This gives rise the V–shaped region of relatively low heat transfer.

4. As the overturned boundary layer approaches the aerofoil suction surface, the effect of the streamline convergence outweighs that of the flow acceleration and the heat transfer begins to drop.

5. Behind the separation line the pressure surface side leg of the horseshoe vortex enhances the heat transfer while near still near the leading edge. As the vortex moves downstream it is stretched so that its effect quickly becomes too small to be resolved by the thin films. A new boundary layer forms in the pressure surface end wall corner and is swept across the passage. As boundary layer initiation occurs along the blade at the higher flow velocities the heat transfer increases. The highest velocities near the pressure surface are at the trailing edge causing the region of high heat transfer here. Generally the heat transfer downstream of the separation line can simply be explained in terms of boundary layer growth in a favourable pressure gradient.

6. The region of high heat transfer near the pressure surface trailing edge drops off markedly toward the adjacent suction surface. In the suction surface end wall corner the inlet boundary layer is now being rolled up into the passage vortex. This vortex is held tightly into the wall by the inwardly acting radial pressure gradient. This core of cold fluid above the end wall boundary layer reduces the heat transfer in the corner.

7. Downstream of the passage the new end wall boundary layer continues growing, enhanced by a slight diffusion of the flow, with a corresponding drop in the heat transfer.

B-7 Conclusions

1. Detailed heat transfer measurements have been made using thin film gauges on the platform of an annular NGV with engine representative geometry and flow conditions. The coverage of films obtained probably represents the practical limit on what can be achieved using the thin film technique.

2. A novel method for the calculation of end wall heat transfer has been demonstrated, provided that the streamline pattern can be calculated.

3. The measured heat transfer patterns can be interpreted in terms of the secondary flow features in the passage.

Acknowledgements

The authors gratefully acknowledge the support of the Ministry of Defence (Procurement Executive) and Rolls-Royce plc for the work reported here. The technical assistance of Mr. P. J. Timms and Mr. K. J. Walton was also much appreciated.

References

[1] Baughn, J. W., Ireland, P. T.,Jones, T. V. and Sanei, N. A comparison of the transient and heated-coating methods for the measurement of local heat transfer coefficients on a pin fin,1988, *ASME paper 88-GT-180*

[2] Bonnett, P. Applications of liquid crystals,1989, *D. Phil thesis, University of Oxford*

[3] Brooks,A. J., Colbourne,D. E., Wedlake,E. T., Jones,T. V., Oldfield,M. L. G., Schultz,D. L., and Loftus.,P. J. The isentropic light piston annular cascade facility at RAE pyestock,1985, *AGARD CP 390*, Paper 31

[4] Byerley, A. R. B., Ireland, P. T. and Jones, T. V. Detailed heat transfer measurements near and within the entrance of a film cooling hole,1988, *ASME paper 88-GT-155*

[5] Byerley, A. R. B., Ireland, P. T. and Jones, T. V. Detailed heat transfer measurements near the entrance to an inclined film cooling hole inside a gas turbine blade, *UK National Heat Transfer Conference, Glasgow, UK, September,1988* , paper C164/88

[6] Byerley, A. R. B. Heat Transfer near the entrance to a film cooling hole in a gas turbine blade,1989 *D.Phil. thesis, University of Oxford*

[7] Clifford, R. J., Jones, T. V. and Dunne, S. T. Techniques for obtaining detailed heat transfer coefficient measurements within gas turbine blade and vane cooling passages,1983, *ASME paper 83-GT-58*

[8] Cooke, J. C. An axially symmetric analogue for general three-dimensional boundary layers,1959, ARC, R & M 3200

[9] Cooper, T. E., Field, R. J. and Meyer, J. F. Liquid crystal thermography and its application to the study of convective heat transfer *ASME Journal of Heat Transfer* vol. 97,1975, pp 442-450

[10] DeJarnette, H. H. F. R., Hamilton, H. H. , Weilmunster, K. J. and Cheatwood, F. M. A review of some approximate methods used in aerodynamic heating analyses,1987, *J. Thermophysics*, 1(1)

[11] Dunne, S. T. A study of flow and heat transfer in gas turbine blade cooling passages,1983, *D.Phil. thesis, University of Oxford*

[12] Geogiou, D. P., Godard, M. and Richards, B. E. Experimental study of the iso-heat-transfer-rate lines on the end wall of a turbine cascade,1979, *ASME Paper*, 79-GT-20

[13] Goldstein, R. J. and Spores, R. A. Turbulent transport on the endwall in the region between adjacent turbine blades,1988, ASME *Journal of Heat Transfer*, Vol. 110, pp862-869.

[14] eele, S. A., Russell, L. M. and Torres, F. J. Use of a liquid-crystal, heater-element composite for quantitative, ution heat transfer coefficients on a turbine airfoil, including turbulence and surface roughness effects,1987, *A 87355*

[15] H , ussell, L. M. and Torres, F. J. Evaluation of a method for heat transfer measurements and therma ng a composite of a heater element and liquid crystals ,1987,*NASA TM 81639*

[16] Ireland, P. T. and Jones, T. V. The measurement of local heat transfer coefficients in blade cooling geometries,1985, *AGARD Conf. 390 , Heat Transfer and Cooling in Gas Turbines*

[17] Ireland, P. T. and Jones, T. V. Detailed measurements of heat transfer on and around a pedestal in fully developed flow,1986, *Proc. 8th Int. Heat Transfer Conf.,San. Francisco,*(Hemisphere),vol.3, pp 975-980

[18] Ireland, P. T. and Jones, T. V. The response time of a surface thermometer employing encapsulated thermochromic liquid crystals,1987, *J.Phys. E:Sci.Instrum.* vol.20 pp 1195-1199

[19] Ireland, P. T. Internal cooling of turbine blades ,1987, *D.Phil. thesis, University of Oxford*

[20] Ireland, P. T. and Jones, T. V. Note on the double crystal method of measuring heat transfer coefficient,1987, *Oxford University, Department of Engineering Science Report No. 1710/87*

[21] Ireland, P. T., Wang, Z., Jones, T. V. and Byerley, A. R. A cold heat transfer tunnel employing liquid crystals for measuring full surface heat transfer coefficients over turbine blade passages, 1988, Imperial College of Science Technology and Medicine Publication, Report No. TPS/88.008, , pp 19-1 to 19-12.

[22] Ishii, J. and Honami, S. A three-dimensional turbulent detached flow with a horseshoe vortex,1985, *ASME paper 85-GT-70*

[23] Jones. T. V., Schultz, D. L. and Hendley, A. On the flow in and isentropic light piston tunnel, 1973, ARC, R & M 3731

[24] Jones, T. V. and Russell, C. M. B. Heat transfer coefficients on finned tubes,1981, *ASME HTD vol. 21, pp17-25*

[25] Jones, T. V. and Hippensteele, S. A. High resolution heat-transfer-coefficient maps applicable to compound-curve surfaces using liquid crystals in a transient wind tunnel,1987, *ASME HTD vol. 71, pp 1-9*

[26] Jones, R. A. and Hunt, J. L. Use of fusible temperature indicators for obtaining quantitative aerodynamic heat-transfer data, 1966, *NASA TR R-230*

[27] Kays, W. M. Convective Heat and Mass Transfer,1979, *McGraw-Hill*

[28] McDonnell, D. G. and Sage, I. New thermochromic liquid crystals *Recent Advances in Medical Thermology, ed. by Ring, E F J and Phillips, B* (New York:Plenum), 1982, pp. 305

[29] Metzger, D. E. and Larson, D. E. Use of melting point surface coatings for local convection heat transfer measurements in rectangular channel flows with 90-deg turns, 1986, *ASME Journal of Heat Transfer* vol. 108

[30] Oldfield,M. L. G. Jones,T. V. and Schultz,D. L. On-line computer for transient turbine cascade instrumentation,1978, *IEEE Trans. AES*, 14:738

[31] Oldfield,M. L. G., Burd,H. J. and Doe,N. G. Design of wide-bandwidth analogue circuits for heat transfer instrumentation in transient tunnels,1982, In *16th Symp. of* ICHMT, Hemisphere publ., Dubrovnik

[32] Parsley, M. Thermocromic liquid crystals ,1986, *BDH publication*

[33] Saabas, H. J., Arora, S. C. and Abdel Messeh, W. Application of the transient test technique to measure local heat transfer coefficients associated with augmented airfoil cooling passages,1987, *ASME paper 87-GT-212*

[34] Schlichting, H. S. Boundary layer theory, Mc Graw-Hill Book Company,1979

[35] Schultz,D. L., Jones,T. V., Oldfield,M. L. G., and Daniels,L. C. A new transient cascade facility for the measurement of heat transfer rate,1977, *AGARD CP 229*, Paper 31

[36] Schultz,D. L. and Jones,T. V. Heat transfer measurements in short-duration hypersonic facilities,1973, NATO Advisory Group for Aeronautical Research and Development, AGARDOGRAPH 165

[37] Schultz,D. L., Oldfield,M. L. G. and Jones,T. V. Heat transfer rate and film cooling effectiveness measurements in a transient cascade,1980, *AGARD CP 281*, Paper 8

[38] Sieverding, C. H. Recent progress in the understanding of basic aspects of secondary flows in turbine passages,1985, *Journal of Engineering for Gas Turbines and Power* vol. 107, pp 248-257

[39] Sieverding, C. H. Secondary flows in straight and annular turbine cascades. Stow and Hirsch,*Thermodynamics & Fluids of Turbomachinery*,Nato,1985,Vol. II,pages 621-624,

[40] Throckmorton, D. A. and Stone, D. R. Model wall and recovery temperature effects on experimental heat-transfer data,1974, *AIAA Journal* vol.12, pp 169-170

[41] Watt, R. W., Allen, J. L., Baines, N. C., Simons, J. P. and George, M. A study of the effects of thermal barrier coating surface roughness on the boundary layer characteristics of gas-turbine aerofoils,1987, *ASME paper 87-GT-223*

DISCUSSION

Langston, USA

The double horseshoe vortex model you propose is an interesting one. However, to my knowledge, we haven't seen such a structure in direct flow field measurements, made in inlet guide vane passages such as yours. (For example, see Marchal & Sieverding [1977], AGARD or Yamamoto [1987], ASME.) Did you make any direct flow field measurements to support your double vortex model?

Author's Reply:

In neither facility (Linear or Annular Cascade) were flow field measurements made in the passage with (for instance) a live wire probe. Therefore, there are no such measurements to support the double vortex structure which is derived here from the endwall heat transfer contours of the linear cascade.

Hennecke, Germany

How did you measure the heat transfer coefficient distribution on the blade surface (Fig A-5 and A-6)?

Author's Reply:

The heat transfer coefficient distribution on the blade surface was measured using the liquid crystal technique, in exactly the same manner as it was used on the endwalls. The perspex working section enables the progress of the liquid crystal colour changes line to be viewed on all surfaces of the working section.

Effects of Secondary Flow on Heat Transfer in Rotating Passages

Joan G. Moore and John Moore

Mechanical Engineering Department
Virginia Polytechnic Institute and State University
Blacksburg, Virginia 24061-0238

ABSTRACT

Secondary flow in rotating cooling passages of jet engine turbine rotors is considered. A Navier-Stokes calculation procedure for turbulent flow is used to compute flow development in a radially outward flow channel, round a sharp 180 degree bend, and in the radially inward flow channel downstream. Areas of high and low heat transfer are explained by secondary flow development and quantitative results show regions of design interest.

NOMENCLATURE

A	area, Eqs. 27 and 28
A	dimensionless distance through the channel, Fig. 9
c_f	skin friction coefficient
c_p	specific heat capacity
d	width of square channel
h	heat transfer coefficient, Eq. 1
H	rothalpy, Eq. 12
k	thermal conductivity of air
L	mixing length
M	Mach number
$\dot{m}$	turbine mass flow rate
$\dot{m}_c$	coolant mass flow rate
n	coordinate normal to the wall
N	rotational speed
Nu	Nusselt number, Eqs. 1, 27 and 31
p	static pressure
P_t	total pressure
Pr	Prandtl number, Eq. 6
r	radius
$\underline{r}$	position vector
R	gas constant
Ra	Rayleigh number, Eq. 4
Re	Reynolds number, Eq. 2
Ro	Rossby number, Eq. 3
T	temperature
T*	rotary stagnation temperature, Eq. 32
T_{tr}	relative total temperature, Eq. 34
u,v,w	cartesian velocity components
$\bar{u}$	mean velocity
$\underline{u}$	relative velocity vector
W	magnitude of the relative velocity
x,y,z	cartesian coordinates
"y"	distance to the nearest wall
γ	ratio of specific heat capacities, c_p/c_v
δ_3	$P_{t3}/(P_{t,ref} = 101325\ Pa)$
θ_3	$T_{t3}/(T_{t,ref} = 288.15\ K)$
λ	friction coefficient, Eq. 28
μ	effective viscosity
ρ	density
τ	dimensionless temperature, Eq. 13
$\underline{\omega}$	rotation rate vector

Overbar

-	average
≈	mass average

Subscript

b	turbine blade surface
g	mean, cooling air
i	cooling channel inlet, Section A-A
N	turbine nozzle exit
o	no rotation
w	cooling channel wall
ℓ,t	laminar, turbulent
1	compressor inlet
2	compressor exit
3	turbine inlet

INTRODUCTION

The design of multi-pass cooling systems for high temperature gas turbine rotor blades requires a detailed understanding of the distributions of heat transfer around the surfaces of the cooling passages. These distributions are determined by the development of a compressible flow with heat transfer in a rotating passage of rapidly changing geometry. There are significant effects of Coriolis forces and curvature causing secondary flows and modifications of the turbulence structure. There are effects of buoyancy opposing and enhancing a flow with non-uniform density in a strong centrifugal pressure field. And in addition to heat transfer there are significant energy changes due to work input and extraction in the rotor. All these effects are interactive in a way which challenges flow modellers and experimenters in their attempts to aid designers.

Typical Multi-Pass Cooling Geometry

Figure 1 shows a typical jet-engine multi-pass cooling geometry, modelled after the design studied by Clifford [1]. The blade has two coolant flow paths, one cooling the leading edge and feeding film cooling holes, and the second, with the multi-pass flow path, providing internal cooling for the rest of the blade. In this paper, we are principally concerned with the first two legs of the multi-pass flow path - the radially-outward leg, the sharp 180 degree bend, and the radially-inward leg. We consider steady 3-D compressible turbulent flow in the rotating reference frame and investigate the resultant heat transfer distributions.

DIMENSIONAL ANALYSIS

Following Guidez [2] and Morris and Ayhan [3], a dimensional analysis of the problem gives

$$Nu = f(Re, Ro, Ra, M, Pr, \text{geometry}).$$

Here, we take

$$\text{Nusselt number, } Nu = \frac{hd}{k_w} \tag{1}$$

$$\text{Reynolds number, } Re = \frac{\rho_g \bar{u} d}{\mu_w} = \frac{\dot{m}_c}{d\mu_w} \tag{2}$$

$$\text{Rossby number, } Ro = \frac{\omega d}{\bar{u}_i} \tag{3}$$

$$\text{Rayleigh number, } Ra = \frac{\rho_{gi}^2 \omega^2 r_i d^3 (T_w - T_{gi}) Pr}{\mu_w^2 T_{gi}} \tag{4}$$

$$\text{Mach number, } M = \frac{\bar{u}_i}{\sqrt{\gamma R T_{gi}}} \tag{5}$$

$$\text{Prandtl number, } Pr = \frac{c_p \mu_\ell}{k_\ell} \tag{6}$$

The geometry considered is a channel of square cross section of side d, with the orientation shown in Fig. 2. The fluid is air with a Prandtl number of 0.7 and the Mach numbers are small (except in the trailing edge holes).

The flow is governed by inertia, viscous, Coriolis and buoyancy forces. The relative significance of these is given by

$$\frac{\text{Inertia}}{\text{Viscous}} = Re\ , \quad \frac{\text{Coriolis}}{\text{Inertia}} = Ro\ , \quad \frac{\text{Buoyancy}}{\text{Inertia}} = \frac{Ra}{Re^2 Pr} = \frac{\omega^2 r_i d}{\bar{u}_i^2} \left(\frac{T_w - T_{gi}}{T_{gi}}\right) . \tag{7}$$

Trends and Ranges of Parameters

To determine the trends in these parameters and to gain insight into the fluid mechanics of multi-pass cooling flows, the authors developed a paper engine in which to mount the blade of Fig. 1. This engine has the following design conditions

$$\frac{P_{t2}}{P_{t1}} = 25\ , \quad \frac{\dot{m}\sqrt{\theta_3}}{\delta_3} = 10.4 \text{ kg/s}\ , \quad \frac{N}{\sqrt{\theta_3}} = 4738. \text{ RPM}$$

The first stage turbine rotor has $r_{mean} = 0.37$ m, $r_{hub}/r_{tip} = 0.86$, and a square cooling passage of side, $d = 5$ mm. It operates with $M_{Nexit} = 1.0$, $T_b = 1200$ K, and $T_w = 1100$ K, where T_b is the blade surface temperature and T_w is the wall temperature of the cooling channel.

The trends and the ranges of the flow parameters are shown in Fig. 3. Clifford [1] indicates that this cooling geometry allowed turbine inlet temperatures to rise from 1500 to 1700 K in the years 1970 to 1980. Extrapolating that performance by simply increasing the coolant mass flow rate, one can estimate flow parameters up to turbine inlet temperatures of 2000 K. For example, since the Reynolds number is proportional to the coolant mass flow rate, it rises linearly with turbine inlet temperature. Figure 3 shows the Reynolds number rising from 40,000 to 200,000 as the turbine inlet temperature is raised from 1500 K to 2000 K; the cooling flow is turbulent.

From 1500 K to 2000 K turbine inlet temperature, we have increased the turbine speed by only 15 percent. Thus, to a first approximation, the Rossby number varies inversely as the coolant mass flow rate. Figure 3 shows it falling from 0.14 to 0.03. In this range, the transverse pressure gradients due to Coriolis acceleration, shown in Fig. 2, cause important secondary flows in the cross-sectional plane in the straight radial legs. Indeed, because the radial flow reverses sign, the secondary flows will tend to have the opposite sense in the two legs. The sense of the secondary flows is indicated by the lower case symbols p^+ and p^-, representing the pressure and suction sides of the channel, respectively. In the channel endwall boundary layers, hot gas will tend to be convected towards the suction sides, p^-, where there will be less cooling than otherwise. Conversely, on the pressure sides, p^+, the heat transfer will be enhanced. The upper case symbols P^+ and P^- indicate the pressure and suction sides of the turbine blade, respectively.

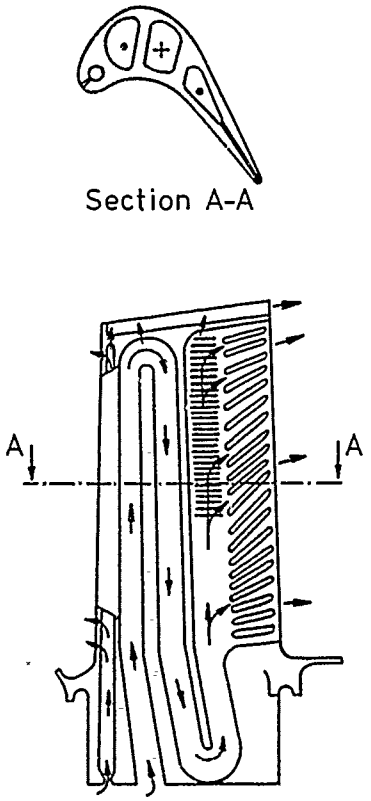


Fig. 1. Typical jet-engine multi-pass cooling geometry based on the turbine rotor blade of Clifford [1].

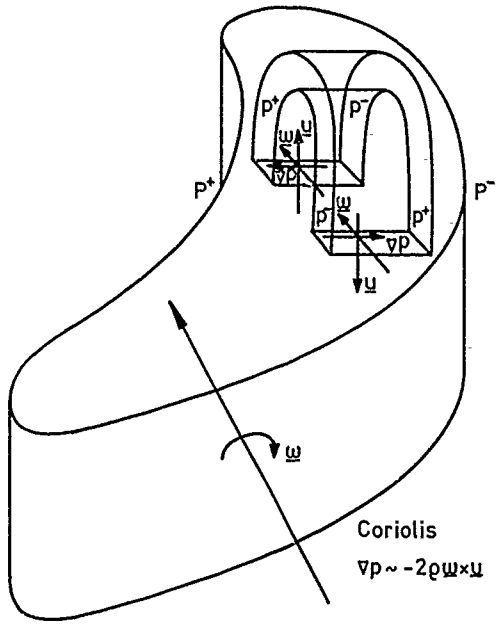


Fig. 2. Schematic of 180 degree bend in a multi-pass cooling system of a turbine rotor blade, showing transverse pressure gradients due to Coriolis acceleration.

p^+, p^- - pressure and suction sides of cooling channel.

P^+, P^- - pressure and suction sides of turbine blade.

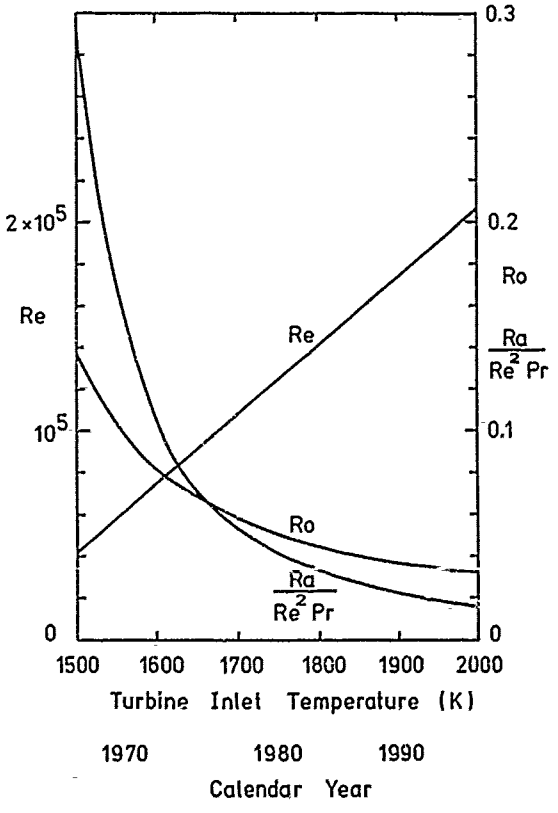


Fig. 3. Trends in dimensionless parameters governing the fluid mechanics of multi-pass cooling flows.

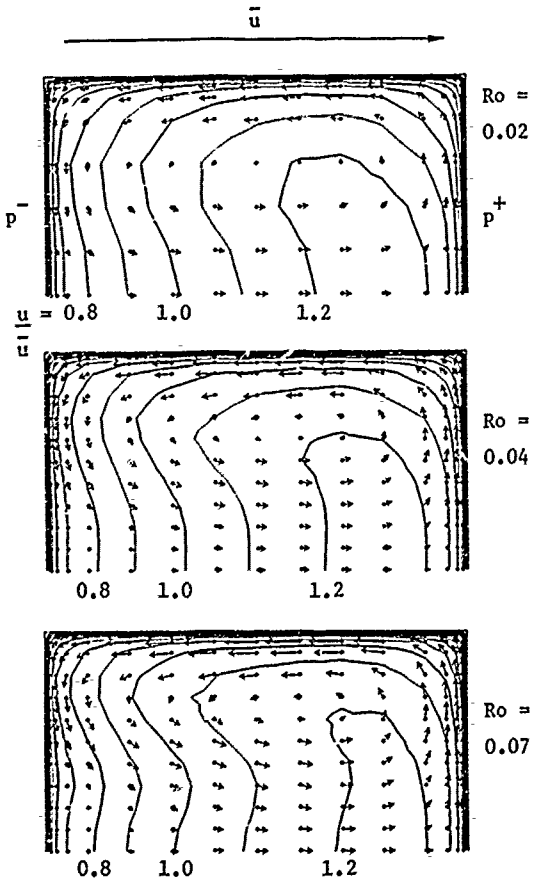


Fig. 4. Calculated secondary flow vectors and primary flow velocity contours for fully developed flow in Moore's rotating channel of square cross-section. Re = 20,000.

While the Coriolis forces mostly cause secondary flow in the cross-sectional plane, the buoyancy of hot gas in the strong centrifugal pressure field causes mostly longitudinal secondary flows in the radial legs. In fact, the buoyancy of the hot wall layers tends to oppose radially outward flow and support radially inward flow. For example, the accumulation of hot gas near the suction surface in the outward leg combined with the effect of buoyancy accentuates the reduction in the heat transfer from that surface.

From 1500 K to 2000 K, the Rayleigh numbers slowly rise from about 3×10^8 to 5×10^8, and this suggests that buoyancy effects are becoming more important. But actually the ratio Ra/Re^2Pr is falling and buoyancy is becoming less important in the flow development relative to inertia forces. Figure 3 shows Ra/Re^2Pr falls from about 0.3 at 1500 K to 0.1 at 1600 K and 0.02 at 2000 K.

In summary, the trend suggested by this simple engine study appears to be towards more coolant flow and higher Reynolds numbers. There seem to be decreasing but still appreciable effects of Coriolis driven transverse secondary flows and buoyancy driven longitudinal secondary flows. For example, at a turbine inlet temperature of 1800 K, we may expect

$$Re = 140{,}000,\ Ro = 0.045,\ Ra = 4.5 \times 10^8,\ \text{and}\ \frac{Ra}{Re^2 Pr} = 0.033$$

Results of three-dimensional flow calculations under these conditions are presented in the last section of this paper.

FLOW MODELS FOR PRESENT CALCULATIONS

Equations for 3-D Flow Calculations

The compressible flow in a multi-pass cooling channel is governed by the same equations as flow in the impeller of a centrifugal compressor. The major difference is the non-adiabatic wall boundary condition. We therefore used the Moore Elliptic Flow Program, the basis of which is described in reference 4, and which was employed, for example, for the centrifugal compressor calculations of reference 5.

The equations are written in the form:

Continuity:

$$\nabla \cdot \rho \underline{u} = 0 \tag{8}$$

Momentum:

$$\rho \underline{u} \cdot \nabla \underline{u} - \nabla \cdot \mu \nabla \underline{u} = \nabla \cdot \mu \overline{\nabla \underline{u}}^T - \nabla p - 2\rho \underline{\omega} x \underline{u} - \rho \underline{\omega} x (\underline{\omega} x \underline{r}) \tag{9}$$

Energy:

$$\rho \underline{u} \cdot \nabla H - \nabla \cdot (\mu/Pr) \nabla H = 0 \tag{10}$$

Perfect gas:

$$p = \rho R T \tag{11}$$

$$H = c_p T + 0.5(\underline{u} \cdot \underline{u}) - 0.5\omega^2 r^2 \tag{12}$$

and we take c_p to be a constant.

Fully Developed Flow

One of the important factors in any 3-D flow calculation is the flow distribution at the inlet. This is especially true in a rotor where distributions of both total pressure and total temperature influence the subsequent secondary flow development [6]. Figure 1 shows the flow entering the cooling channel with a sharp turn at the blade root. It will then take many channel diameters before the flow recovers from this abrupt entrance condition and becomes fully developed. One approach could then be to start the channel flow calculation upstream of the blade root and calculate the flow development including local flow separations and reattachment. This approach is similar to that used by the authors in their study of the flow and heat transfer in turbine tip gaps [7].

Here, we adopted a different approach. We performed calculations of fully developed flow in a radially-outward flow channel. A Prandtl mixing-length turbulence model was developed which reproduces the major effects of rotation on the flow in Moore's rotating square channel [8]. This turbulence model was then used to calculate fully developed flow with heat transfer at the blade mean radius, section A-A, in the radially outward leg in Fig. 1. The coolant flow conditions used were those from Fig. 3 at a turbine inlet temperature of 1800 K. This fully developed flow provided the initial conditions for the 3-D flow calculation in the cooling channel, starting at section A-A.

Equations for Fully Developed Flow Calculations

The channel direction was taken as radially outwards ($x = r$). The continuity and momentum equations were simplified with the approximations

$$\frac{\partial \rho u}{\partial x} = \frac{\partial u}{\partial x} = \frac{\partial v}{\partial x} = \frac{\partial w}{\partial x} = 0$$

and

$$\frac{\partial p}{\partial x} = \text{constant}.$$

In the solution procedure, $\frac{\partial p}{\partial x}$ was adjusted to give the specified mass flow rate.

To simplify the energy equation, the shape of the temperature profile was taken as independent of x;

$$\tau \equiv \frac{T_w - T}{T_w - \bar{T}} \qquad \text{and} \qquad \frac{\partial \tau}{\partial x} = 0. \tag{13}$$

The kinetic energy of the flow was neglected to form the following equation for τ

$$\rho v \frac{\partial \tau}{\partial y} + \rho w \frac{\partial \tau}{\partial z} - \frac{\partial}{\partial y}\frac{\mu}{Pr}\frac{\partial \tau}{\partial y} - \frac{\partial}{\partial z}\frac{\mu}{Pr}\frac{\partial \tau}{\partial z} = \frac{\rho u}{T_w - \bar{\bar{T}}}\left[\tau \frac{d\bar{\bar{T}}}{dx} - \frac{\omega^2 r}{c_p}\right] . \tag{14}$$

T_w was taken as constant and $T_w - \bar{\bar{T}}$ was specified for the plane. $\frac{d\bar{\bar{T}}}{dx}$ was adjusted so that $\bar{\bar{\tau}} = 1$.

The Viscosity Model

The effective viscosity and the effective thermal conductivity are taken as the sum of the laminar and turbulent contributions. The near-wall values are found by a logarithmic averaging procedure used by the authors for many years [9]. Thus

$$\mu = \mu_\ell + \mu_t \text{ , away from wall;} \tag{15}$$

$$\mu = [\mu_\ell (\mu_\ell + \mu_t)]^{1/2} \text{ , near wall.} \tag{16}$$

$$\mu/Pr = \mu_\ell/Pr_\ell + \mu_t/Pr_t \text{ , away from wall;} \tag{17}$$

$$\mu/Pr = [\mu_\ell/Pr_\ell(\mu_\ell/Pr_\ell + \mu_t/Pr_t)]^{1/2} \text{ , near wall.} \tag{18}$$

$Pr_\ell = 0.7$;

$Pr_t = 0.9$.

In the Prandtl mixing length viscosity model

$$\mu_t = \rho L^2 \left|\frac{du}{dy}\right| . \tag{19}$$

The effective velocity gradient is given by

$$\left|\frac{du}{dy}\right| = \left[\left(\frac{\partial u_i}{\partial x_j} + \frac{\partial u_j}{\partial x_i}\right)\frac{\partial u_i}{\partial x_j}\right]^{1/2} \tag{20}$$

but it is limited, to prevent the turbulent viscosity from going to zero in the middle of the duct where $du/dy = 0$, by

$$\left|\frac{du}{dy}\right| > 1.55 \frac{\bar{u}}{d} Re^{-1/8} . \tag{21}$$

The mixing length L is calculated in two parts:

(a) The inner layer region includes a van Driest modification.

$$L = 0.41 \left|y\right| \left[1 - \exp\left(\frac{-\left|y\right|(\rho\tau)^{1/2}}{26\mu_\ell}\right)\right] , \tag{22}$$

where τ is the local shear stress.

(b) The outer layer model modifies a no-rotation mixing length of $0.08 \frac{d}{2}$ by a curvature and rotation modification factor F which is a function of a generalized form of the gradient Richardson number [10].

$$L = 0.08 F \frac{d}{2} \tag{23}$$

$$F = 1 - \beta Ri \text{ for } Ri < 0 \text{ (Pressure side/concave wall)}$$

$$F = \frac{1}{1 + \beta Ri} \text{ for } Ri > 0 \text{ (Suction side/convex wall)}$$

$$Ri = S(1 + S) \tag{25}$$

$$S = \frac{2\frac{|\underline{u}|}{R_n}\underline{n}\cdot\underline{N} - 2\frac{(\underline{\omega}\times\underline{u})\cdot\underline{N}}{|\underline{u}|}}{\frac{\alpha|\underline{u}|}{\frac{d}{2}} - \frac{|\underline{u}|}{R_n}\underline{n}\cdot\underline{N}} \tag{26}$$

Here, R_n is the local radius of curvature of the flow, $\underline{n}$ is the unit vector in the direction of the principal normal to the local streamline, and $\underline{N}$ is the unit vector normal to the shear layer or normal to the wall for a two-dimensional boundary layer. The constants α and β were taken as 0.67 and 4, respectively.

The inner layer equation is used when $0.41 \left|y\right| < 0.08 F \frac{d}{2}$.

This model of turbulence modification due to curvature and rotation incorporates features from the models developed by Johnston and Eide [11] and Adams and Johnston [12]. It represents an attempt to generalize their approaches for application in three-dimensional duct flows.

MOORE'S ROTATING CHANNEL

Imagine a straight rotating channel with the orientation of the radial outflow leg in Figs. 1 and 2. One of the authors (JM) measured fully developed flow in such channels for his master's thesis in 1967 [8]. One of the channels had a square cross section and was tested with a Reynolds number of 20,000 at Rossby numbers up to 0.024. Figures 4-8 show calculation results with the present flow model for that channel.

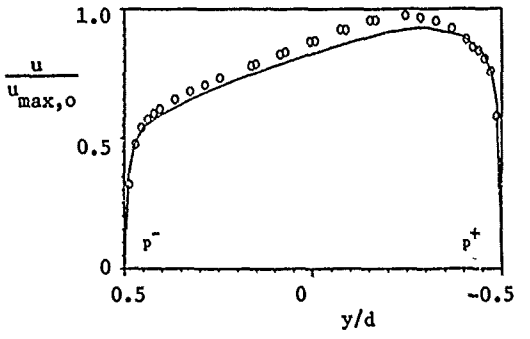


Fig. 5. Centerline velocity profiles in Moore's rotating square channel for Re = 20,000 and Ro = 0.02. o - measured; ——— calculated.

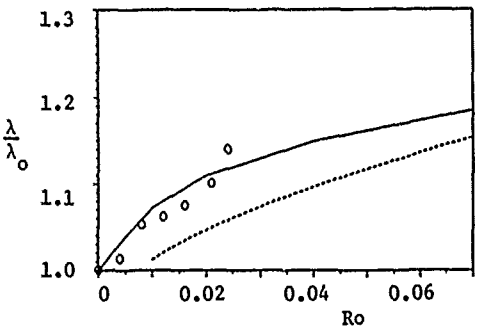


Fig. 7. Variation of friction factor with Rossby number for Moore's rotating square channel, Re = 20,000. o - measured; ——— calculated; - - - correlation of Ito and Nanbu for circular pipes [13].

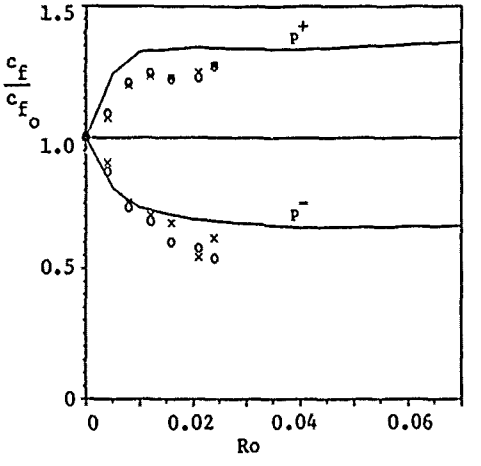


Fig. 6. Variations of centerline wall shear stresses with Rossby number for Moore's rotating square channel, Re = 20,000, o, × - measured; ——— calculated.

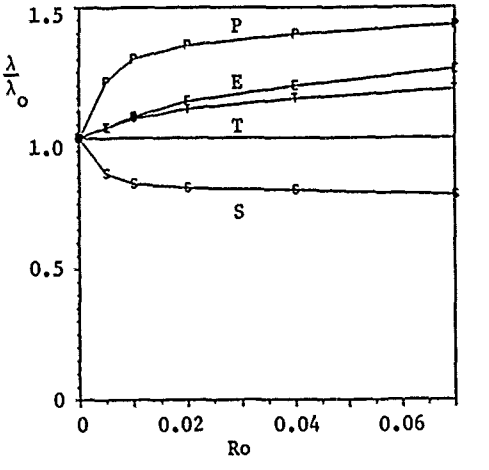


Fig. 8. Calculated contributions to the friction factor from the individual surfaces of Moore's rotating square channel. Re = 20,000. P - pressure side; S - suction side; E - endwall; T - total.

Calculated secondary flow vectors and primary flow velocity contours are presented in Fig. 4 for Rossby numbers of 0.02, 0.04, and 0.07. As the Rossby number increases, the secondary flow in the endwall boundary layers strengthens causing increased convection of low momentum fluid towards the suction side (p^-). The net result is a thickening of the suction surface boundary layer and a thinning of the pressure surface layer. This is seen more clearly in Fig. 5 which shows a comparison of the measured and calculated centerline velocity profiles at a Rossby number of 0.02.

The variations of the centerline shear stresses with Rossby number are plotted in Fig. 6. On the pressure side, the wall shear stress is enhanced by rotation compared with the no-rotation value, while on the suction side the wall shear stress is reduced. The present flow model gives a reasonable representation of these variations. It suggests that most of the changes occur in the Rossby number range 0.-0.02 and that subsequently the skin friction coefficients change by smaller amounts. At Ro = 0.02, the changes are significant, about +30 percent on the pressure side and about -40 percent on the suction side, on the centerline.

The overall friction factor for the channel increases with rotation, as seen in Fig. 7. A Rossby number of 0.02 gives about a +10 percent increase, with the flow model and the data in good agreement. For comparison, the correlation of Ito and Nanbu [13] for turbulent flow in a rotating straight pipe of circular cross section is shown. This gives the same general trend with Rossby number but misses the initial more rapid increase; perhaps this is associated with the flow near the corners of the square channel.

The contributions to the friction factor from the individual surfaces are compared with the overall variation in Fig. 8. The endwall, E, follows closely the trend of the total, T, while the net increase on the pressure side, P, outweighs the net decrease on the suction side, S.

The quantitative agreement between the calculation results in Figs. 5, 6 and 7 and Moore's measurements and the qualitative trends seen in Figs. 4 and 8 suggested that the present turbulent flow model could be used to gain insight into developing flow in multi-pass cooling geometries.

MULTI-PASS COOLANT FLOW AND HEAT TRANSFER

Model Multi-Pass Cooling Geometry

The coolant flow path in Fig. 1 was modelled as a square-cross-section channel, as shown in Fig. 9. The channel started at section A-A in Fig. 1, it proceeded radially outwards for 3.7d to a 180 degree bend with a dividing web of thickness d/3. After the bend, it extended radially inwards a distance 10d. The channel had a width d of 5 mm, and the pressure and suction faces were parallel to the axis of rotation, as shown in Fig. 2.

The location along the duct is indicated by a parameter, A, which in the straight legs is simply measured in duct widths, d. A = 0 at the inlet to the bend and A = 2 at the exit of the bend. The flow inlet is at A = -3.7 and the flow exit is at A = 12, as shown in Fig. 9.

The finite-difference grid used for the 3-D flow calculation is also shown in Fig. 9. This was a 45 x 19 x 19 grid. The grid was symmetrical in the cross-sectional plane with grid points at 0., 0.004, 0.012, 0.025, 0.05, 0.1, 0.2, 0.3, 0.4, 0.5, etc. For fully developed flow with no rotation, this near-wall spacing corresponded to a y^+ of 24 based on the mean wall shear stress.

Initial Conditions—Fully Developed Flow

As discussed above, the initial conditions for the 3-D flow calculation were established by calculating fully developed flow with heat transfer at A = -3.7, section A-A. The calculation was performed for Re = 140,000, Ro = 0.045, Ra = 4.5×10^8, $\bar{T}$ = 901.5 K, T_w = 1100 K, p = 2.46 MPa, and $\bar{u}$ = 138 m/s. A reference calculation with no rotation, Ro = Ra = 0, was also performed for comparison.

Figure 10 shows the velocity and temperature distributions with rotation. Qualitatively the velocity distribution is similar to that in Fig. 4 at Ro = 0.04. But the endwall and pressure surface boundary layers are thinner at the engine conditions; and the secondary flow vortex is centered closer to the pressure-side/endwall corner. The maximum secondary velocity is about 9 percent of the mean velocity compared with a value of 7 percent found by interpolation in Fig. 4 at Ro = 0.045. Both maxima are in the endwall boundary layers for flow from the pressure side to the suction side. The static temperature distribution is similar in shape to the throughflow velocity distribution with cold air located towards the pressure side where the throughflow velocities are highest. The low momentum boundary layer fluid on the suction side, especially near the centerline, is also hot, and thus we can expect both low shear stresses and low heat transfer from that wall.

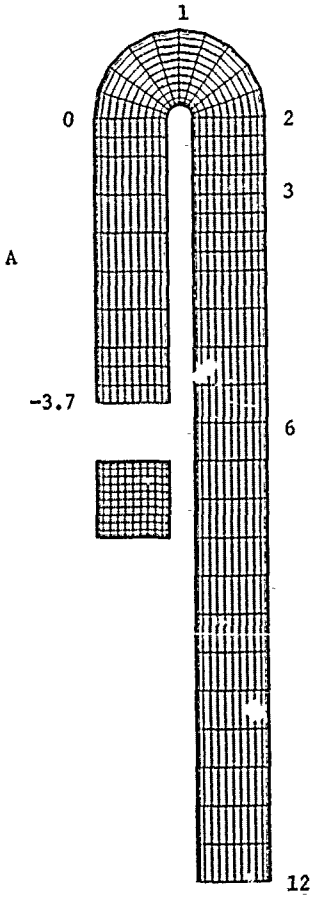


Fig. 9. Model multi-pass coolant flow path, starting at section A-A in the radially outward leg of Fig. 1. Grid for 3-d flow calculation.

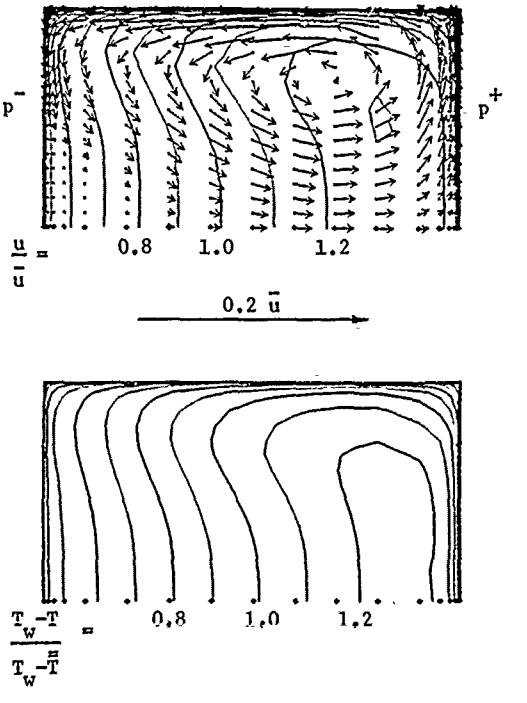


Fig. 10. Velocity and temperature distributions at section A-A, the inlet for the 3-D flow calculation, see Fig. 9.

Heat Transfer Coefficients

The mean Nusselt number at any section along the channel is found by integrating the heat flux from the wall around the periphery of the channel. This is normalized with the difference between the wall temperature, T_w, and the local mass-averaged static temperature, $\bar{T}$, together with the channel width, d. Thus

$$\overline{Nu} \equiv \frac{1}{A} \iint \frac{\left(k \frac{\partial T}{\partial n}\right)_w d}{k_w(T_w - \bar{T})} dA \qquad (27)$$

For the fully developed flow with rotation, $\overline{Nu} = 255$. Compared with the no-rotation value

$$\frac{\overline{Nu}}{\overline{Nu}_o} = \frac{255.}{197.} = 1.29 .$$

Friction Coefficients

The friction coefficient is similarly defined,

$$\lambda \equiv \frac{1}{A} \iint \frac{8\left(\mu \frac{\partial u}{\partial n}\right)_w}{\bar{\rho}\, \bar{u}^2} dA . \qquad (28)$$

where $\bar{\rho} = \frac{\bar{p}}{RT}$ and $\bar{p}$ is the area-averaged static pressure over the channel cross-section.

With rotation, $\lambda = 0.0172$, and compared with no rotation

$$\frac{\lambda}{\lambda_o} = \frac{0.0172}{0.0145} = 1.19 .$$

Comparison with Other Correlations

These increases of 19 percent in the mean friction coefficient and 29 percent in the mean Nusselt number may be compared with the results of Fig. 7. The calculations for incompressible flow at a Reynolds number of 20,000 gave an increase in the friction factor of 16 percent at Ro = 0.045. The Ito and Nanbu friction correlation for circular pipes [13],

$$\frac{\lambda}{\lambda_o} = 0.942 + 0.058\ (Ro^2 Re)^{0.282} , \qquad (29)$$

gives an increase of 23 percent. Of course, the Ito and Nanbu correlation does not account for buoyancy effects; but still all these results are suggesting increases in momentum and heat transfer due to rotation in the engine. It is interesting then to evaluate the change in mean Nusselt number predicted by Morris and Ayhan's correlation [3],

$$\frac{\overline{Nu}}{\overline{Nu}_o} = \left[\frac{Ra}{Re^2}\right]^{-0.186} Ro^{0.33} = 0.73 . \qquad (30)$$

This predicts a decrease in mean heat transfer in the engine of 27 percent, of the same order as the decreases they estimated for other engine conditions. There appears to be a basic discrepancy here.

Heat Transfer and Friction Contributions

Compared with the mean no-rotation values, the mean heat transfer coefficients for the pressure, endwall and suction surfaces were

$$\frac{\overline{Nu}_p}{\overline{Nu}_o} = 1.87 , \quad \frac{\overline{Nu}_e}{\overline{Nu}_o} = 1.38 , \text{ and } \frac{\overline{Nu}_s}{\overline{Nu}_o} = 0.54 ;$$

and the mean friction coefficients for the three surfaces were

$$\frac{\lambda_p}{\lambda_o} = 1.67 , \quad \frac{\lambda_e}{\lambda_o} = 1.28 , \text{ and } \frac{\lambda_s}{\lambda_o} = 0.52 .$$

Note especially the factor of 3-4 difference between the heat and momentum transfer on the pressure surface and those on the suction surface.

3-D Flow and Temperature Distributions

The results presented in the rest of the paper are for fully 3-D flow. Starting with the initial conditions of Fig. 10, the results in Figs. 11-16 were obtained. The 3-D flow calculation took 4 hours of CPU time on an IBM 3084.

Figure 11 shows the throughflow velocity vectors on three planes, parallel to the axis of rotation. One plane is near the pressure side, p^+, in the outward leg; this becomes the suction side, p^-, of the inward leg; and the relative location of the plane across the duct is 0.004. The middle plane, m, is midway between the pressure and suction surfaces. The third plane is near the suction side, p^-, in the outward leg and its relative location is 0.996.

In the outward leg, the near wall velocities are much higher on the pressure side as prescribed by the flow in Fig. 10. Little change in the flow distribution occurs until about one duct width upstream of the bend. Then there is a rapid development, which is particularly evident on the suction side as the endwall boundary layer fluid convects to the inside of the bend. The strong secondary flow persists near

this surface all around the bend; entering the bend, there is flow separation on the outer wall, but leaving the bend, there is apparently little backflow near the corner with the dividing web. In contrast, there is a large region of flow separation occurring on the web downstream of the bend at mid-height and extending to the new suction surface. This large separation zone extends 2-3 duct widths downstream of the bend. Thereafter the throughflow near the new suction surface gradually recovers, but once again the suction surface has lower velocities than the pressure surface.

The secondary flow velocities and contours of static temperature are shown in Fig. 12, for six cross-sectional planes at A = -3.7, 1, 2, 3, 6 and 12. The locations of these planes are marked on Fig. 9. For reference, T_w = 1100 K, and at the inlet, A = -3.7, $\bar{u}$ = 138 m/s and $\bar{T}$ = 901.5 K. To help the reader follow the flow development, we have also prepared Fig. 13, which shows the cooling channel in a view similar to Fig. 2. The static temperature contours are shown there also. The thick contours represent cold air with a temperature of 900 K. Following those, one can gain a good overall impression of the 3-D flow development from Fig. 13, and then a more detailed understanding of the secondary flows can be obtained from Fig. 12. One notes, for example, that the views in Fig. 12 are seen by an observer following the channel looking downstream with the inner wall (or web) maintained at the bottom.

The secondary velocity vectors in the six views in Fig. 12 are all to the same scale. Thus the maximum secondary velocity of 9 percent of u seen in Fig. 10, at A = -3.7, is now found to be very small compared with secondary velocities of the order of $\bar{u}$ found in the 180 degree bend.

As the flow enters the bend, the hot air near the suction surface is convected to the inside of the bend, while the cold air moves from the pressure side around the outer wall. A dominant vortex of anti-clockwise sense is established by A = 1. Then by A = 2, a strong convection develops across the middle of the channel from the inside to the outside of the bend; this effectively splits the cold air, leaving some in the corner region between the outer wall and the new suction surface. Most of the cold air, however, follows the anti-clockwise secondary flow path across the new pressure surface, by A = 6, and then across the inner wall, by A = 12. The hot air from the suction surface upstream of the bend is more difficult to trace since it is convected away from the inner wall and mixes as it encounters the flow separation on the web.

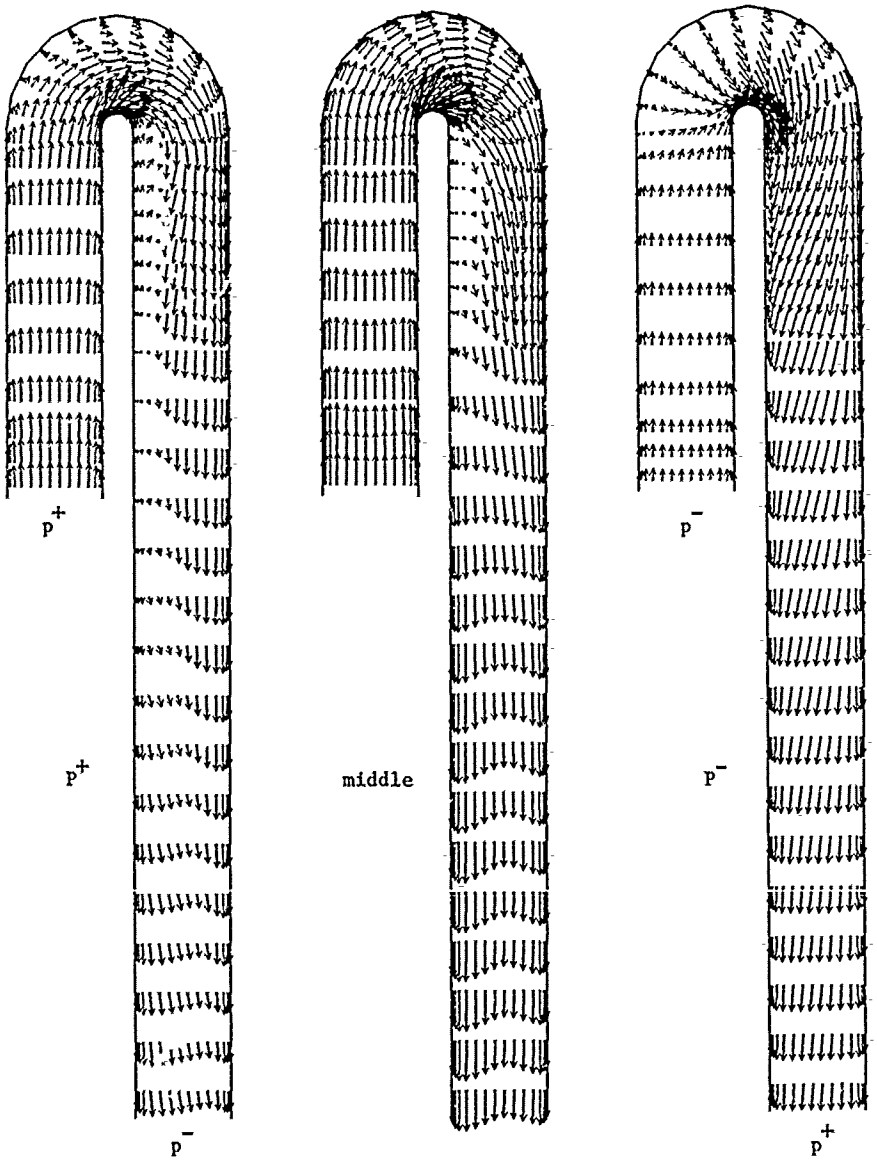


Fig. 11. Throughflow velocity vectors on three planes of the multi-pass cooling channel.

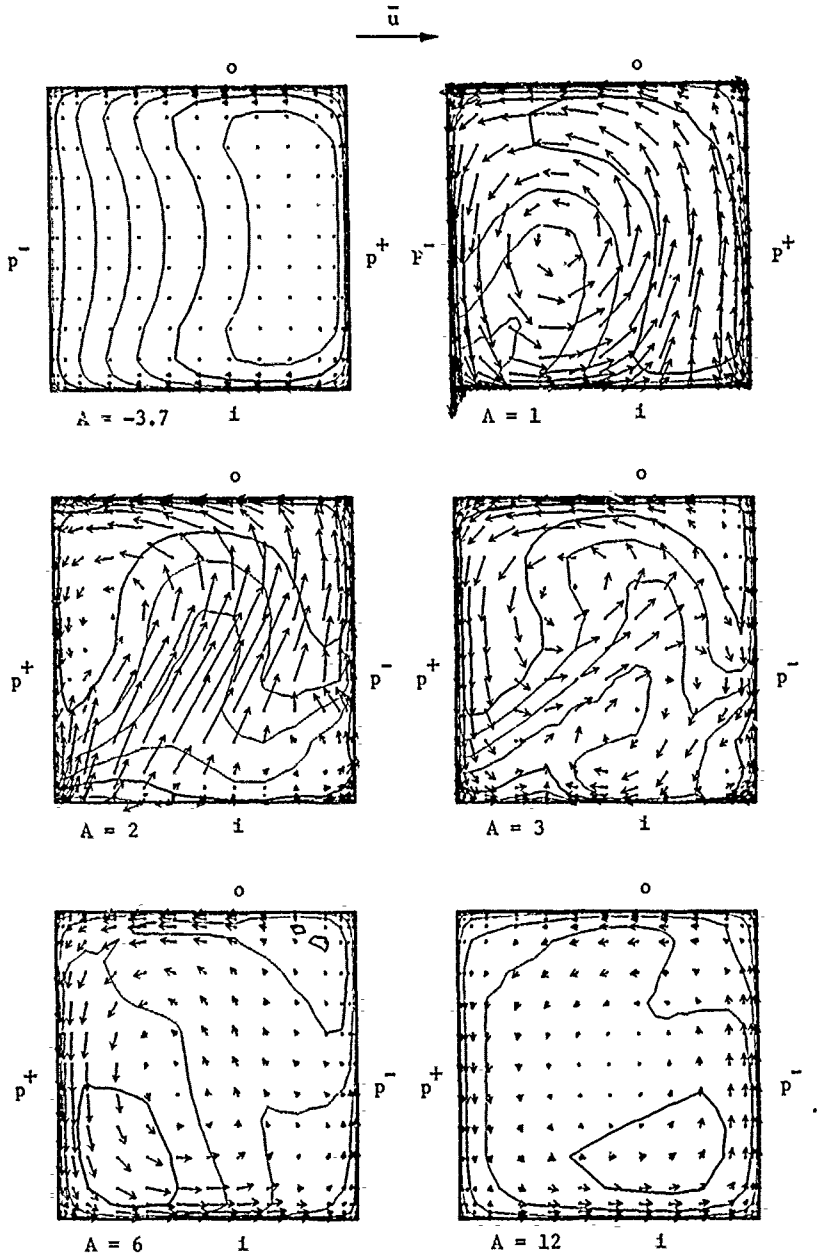


Fig. 12. Secondary flow velocity vectors and contours of static temperature on six cross-sectional planes of the multi-pass cooling channel. i - inner wall, web; o - outer wall. Dark closed contours, T = 900K; T_w = 1100K; contour interval, 25K.

Surface Heat Transfer Distributions

The local Nusselt number is defined as

$$Nu = \frac{\left(k \frac{\partial T}{\partial n}\right)_w d}{k_w (T_w - \bar{T})}, \tag{31}$$

where $\bar{T}$ is the local mass-averaged static temperature; and Nusselt number contours are plotted for the two endwall faces in Fig. 14. Figure 15 then shows the development of the mean Nusselt number $\bar{Nu}$, around the periphery of the channel, as a function of location along the channel.

Initially, from A = -3.7 to A = -1.5, in the 3-D calculation, the mean Nusselt number is about 245. Figure 14 then shows variations from less than 100 on the suction side to more than 400 on the pressure side. Note that the minor contour interval is 25, with dark lines at intervals of 100.

As the flow proceeds around the bend, the hot air near the suction surface is replaced by colder air, as seen in the first four pictures of Fig. 12, at A = -3.7, 1, 2 and 3. The local Nusselt numbers increase correspondingly from less than 100 to over 600. Indeed, the influence of the cold air is felt on this surface, all along the inward leg, as the Nusselt numbers slowly fall to their mean inlet level.

The heat transfer distribution on the other endwall face is more complex. Around the bend, there is a variation from high Nusselt numbers, locally in excess of 800, near the inside to much lower values,

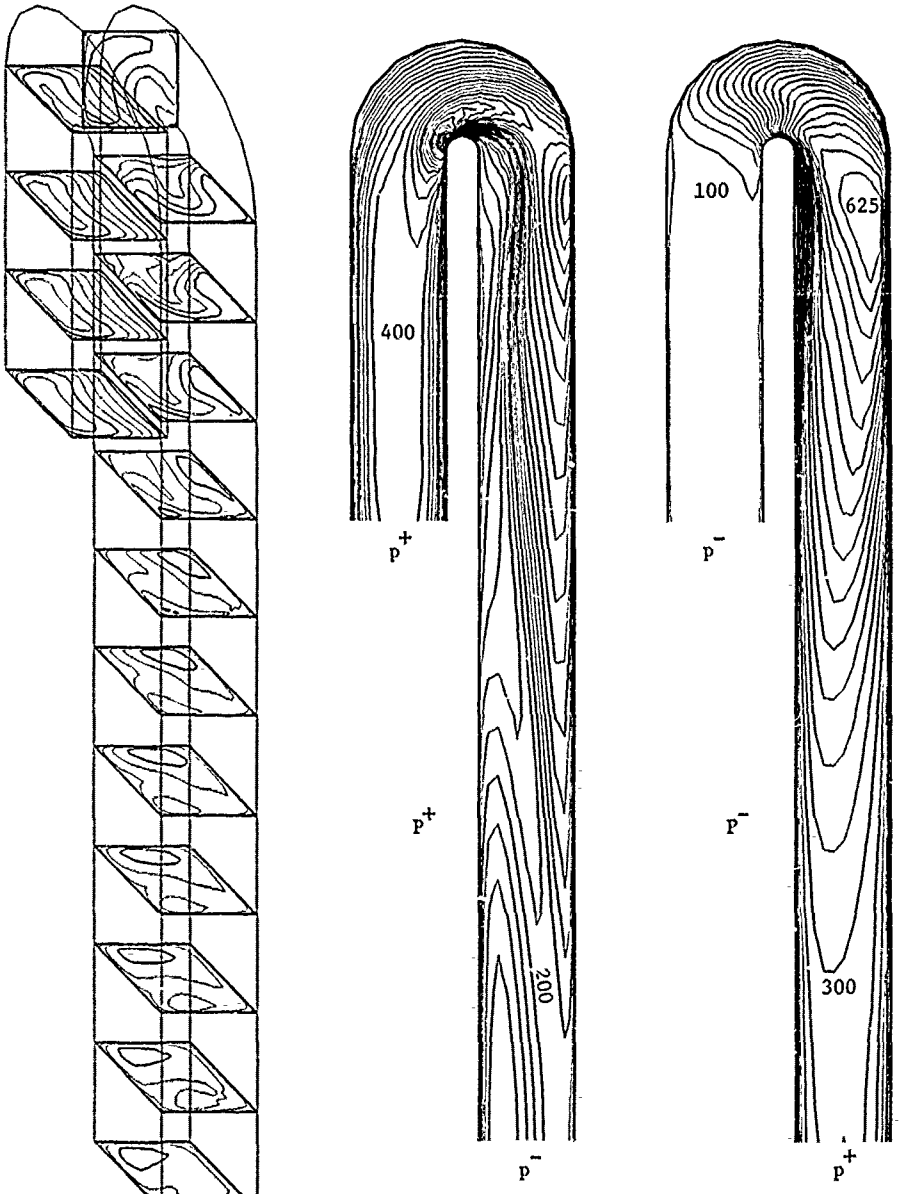


Fig. 14. Contours of local Nusselt number for the two endwall surfaces. Contour interval, 25.

Fig. 13. Three-dimensional view of the development of the static temperature distribution. Dark closed contours, T = 900K; T_w = 1100K; contour interval, 25K.

less than 200, near the outside. The flow then separates from the web, giving Nusselt numbers less than 100, while the cold air splits, as seen in Fig. 12, giving Nusselt numbers in excess of 500. The two influences of the flow separation and the split-off cold air linger along the inward leg until finally the main body of the cold air convects around to restore the Nusselt numbers to their mean inlet level of about 250.

The rapid rise in the mean Nusselt number around the bend and its slower decay to the initial level are seen in Fig. 15. Near the exit of the bend, at A = 2, peak levels of about 400 are predicted, i.e. about 1.6 times the inlet value, or twice the no-rotation value.

Energy Transfer

The overall energy transfer from the blade to the air is of prime interest here because of the cooling it provides, but it is also interesting thermodynamically because of the combination of the heat and work transfers. In the rotor blade, the heat input results in a change of rotary stagnation temperature T*, where

$$T^* = T + \frac{W^2}{2c_p} - \frac{\omega^2 r^2}{2c_p} = \frac{H}{c_p} . \tag{32}$$

or

$$T^* = T_{tr} - \frac{\omega^2 r^2}{2c_p} \tag{33}$$

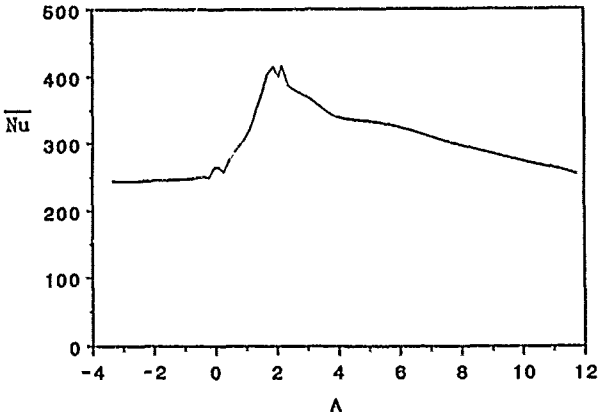


Fig. 15. Variation of mean Nusselt number around the outer 180 degree bend in the multi-pass cooling geometry of Fig. 1.

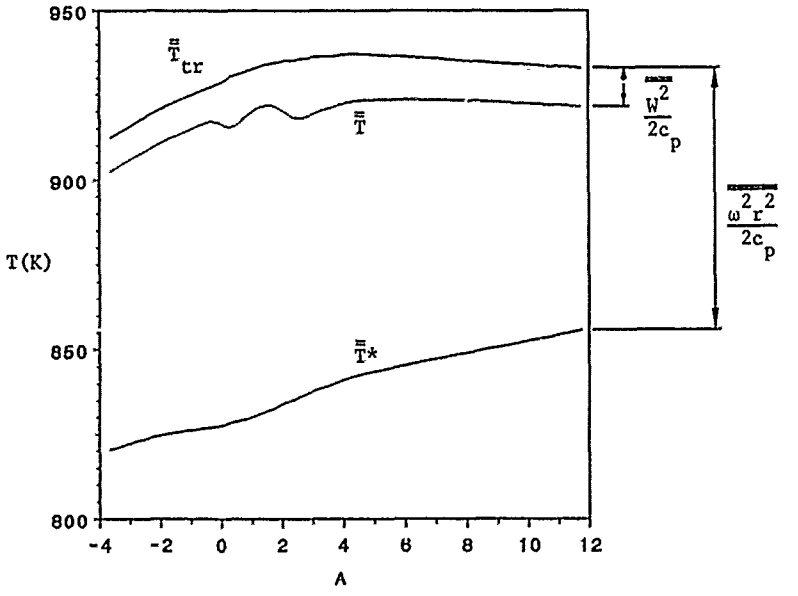


Fig. 16. Energy transfer to the cooling air revealed by mass-averaged temperatures.

with $$T_{tr} = T + \frac{W^2}{2c_p} . \qquad (34)$$

Here H is the rothalpy, $W^2/2c_p = (\underline{u} \cdot \underline{u})/2c_p$ is the relative kinetic energy, and T_{tr} is the relative total temperature.

Figure 16 shows the energy transfer for the air in the multi-pass cooling channel in terms of the mass-averaged temperatures $\bar{T}^*$, $\bar{T}$, and $\bar{T}_{tr}$. Notice how $\bar{T}^*$ rises monotonically, while $\bar{T}$ fluctuates around the bend due principally to changes in relative kinetic energy. Notice also how $\bar{T}$ rises more rapidly than $\bar{T}^*$ in the outward leg due to work input from the rotor; and how $\bar{T}$ actually <u>falls</u> in the inward leg, in spite of the heat transfer, because of work extraction.

The overall change in $\bar{T}^*$ represents the net heat input,

$$\bar{T}^*_{out} - \bar{T}^*_{in} = 36.4 \text{ K} .$$

The overall Nusselt number based on the inlet temperature difference $T_w - \bar{T}_{in}$ is therefore

$$Nu_{overall} = 284. ,$$

and

$$\frac{Nu_{overall}}{\overline{Nu}_o} = \frac{284.}{197.} = \underline{1.44}$$

The combined effects of the 180 degree bend, rotation and buoyancy have increased the overall Nusselt number by 44 percent over the value for fully developed flow with no rotation.

SUMMARY AND CONCLUSIONS

3-D flow and heat transfer in a typical multi-pass cooling system for a high temperature gas turbine rotor blade have been calculated. A preliminary engine study was performed to determine the trends in the dimensionless variables characterizing the fluid mechanics of multi-pass cooling flows. This suggested that above a turbine inlet temperature of 1700 K, Reynolds numbers would be rising above 100,000 and Rossby numbers would be falling below 0.05. The ratio of buoyancy to inertia forces is given by $Ra/(Re^2Pr)$, and this too was predicted to fall below 0.05, for the particular engine conditions studied. Thus, with increasing turbine inlet temperatures, there seem to be decreasing but still appreciable effects of Coriolis driven transverse secondary flows and buoyancy driven longitudinal secondary flows. Based on this study, conditions were chosen for a 3-D flow calculation corresponding to a turbine inlet temperature of 1800 K.

The Moore Elliptic Flow Program was used for the calculations because compressible flow in a multi-pass cooling channel is governed by the same equations as flow in the impeller of a centrifugal compressor. The major difference is the non-adiabatic wall boundary condition. But the energy transfer can be handled with the same rothalpy equation.

The 3-D flow calculation was started with fully developed flow in the radially outward leg of the cooling channel. This was calculated using MEFP by introducing approximations into the full 3-D flow equations. A Prandtl mixing length turbulence model was developed including the effects of rotation and curvature on turbulence modification. This represents an attempt to generalize the approaches of Johnston et al. for application in three-dimensional duct flows. It was tested by comparing with the data of J. Moore for fully developed flow in a rotating square channel. The turbulence model was then used to calculate fully developed flow with heat transfer at the predicted engine conditions.

At the engine conditions, both the mean friction coefficient and the mean Nusselt number for fully developed flow were predicted to increase with rotation. This was in general agreement with the friction data of Moore and the friction correlation of Ito and Nanbu. Altogether, these results suggest an increase of about 20 percent over the values with no rotation. In contrast, the correlation of Morris and Ayhan predicts a decrease in the mean heat transfer of 27 percent, for the same engine conditions.

The full 3-D flow with heat transfer was calculated starting at the mean radius of the rotor blade. The square channel then had 3.7 channel widths radially outward before a sharp 180 degree bend which was followed by a radially inward leg of 10 channel widths in length. The mean heat transfer for this whole geometry was calculated to be 44 percent higher than the corresponding value for fully developed flow with no rotation. The calculation showed a rapid rise of about 60 percent in mean Nusselt number around the bend followed by a slower decay. The areas of high heat transfer were generally explained by the secondary flow of cold air which was followed in the calculation results. An area of low heat transfer was observed in the results downstream of the bend and this was associated with flow separation on the dividing web.

ACKNOWLEDGEMENTS

The authors wish to thank Rolls-Royce plc, Aero Division, for supporting this work under a cooperative agreement with Virginia Polytechnic Institute and State University.

REFERENCES

1. Clifford, R. J., "Rotating Heat Transfer Investigations on a Multi-Pass Cooling Geometry," AGARD Conference Proceedings No. 390 on Heat Transfer and Cooling in Gas Turbines, Bergen, Norway, May 1985.
2. Guidez, J., "Study of the Convective Heat Transfer in Rotating Coolant Channel," Trans. ASME, J. of Turbomachinery, Vol. 111, pp. 43-50, January 1989.
3. Morris, W. D., and Ayhan, T., "Observations on the Influence of Rotation on Heat Transfer in the Coolant Channels of Gas Turbine Rotor Blades," Proc. Instn. Mech. Engrs., Vol. 193, pp. 303-311, 1979.
4. Moore, J. G., "An Elliptic Calculation Procedure for 3-D Viscous Flow," AGARD Lecture Series No. 140 on "3-D Computation Techniques Applied to Internal Flows in Propulsion Systems," June 1985.
5. Moore, J., and Moore, J. G., "3-D Viscous Flow Calculations at Design and Off-Design Conditions for the NACA 48-Inch Radial Inlet Centrifugal Impeller," Proceedings of the Eighth International Symposium on Air Breathing Engines, pp. 139-148, Cincinnati, Ohio, AIAA Paper ISABE 87-7008.
6. Hawthorne, W. R., "Secondary Vorticity in Stratified Compressible Fluids in Rotating Systems," Univ. of Cambridge, Dept. of Engineering Report No. CUED/A-Turbo/TR 63, 1974.
7. Moore, J., Moore, J. G., Henry, G. S., and Chaudhry, U., "Flow and Heat Transfer in Turbine Tip Gaps," ASME Paper No. 88-GT-188.
8. Moore, J., "Effects of Coriolis on Turbulent Flow in Rotating Rectangular Channels," MIT Gas Turbine Laboratory Report No. 89, January 1967.
9. Moore, J., and Moore, J. G., "Calculation of Five Turbulent Flows Using the Moore Cascade Flow Program," The 1980-81 AFOSR-HTTM-Stanford Conference on Complex Flows: Comparison of Computation and Experiment, Vol. III, Stanford University, California, 1981, pp. 1453-1458.
10. So, R. M. C., "A Turbulence Velocity Scale for Curved Shear Flows," J. of Fluid Mechanics, Vol. 70, Part 1, pp. 37-57, 1975.
11. Johnston, J. P., and Eide, S. A., "Turbulent Boundary Layers on Centrifugal Compressor Blades: Prediction of the Effects of Surface Curvature and Rotation," Trans. ASME, J. of Fluids Engineering, Vol. 98, pp. 374-381, 1976.
12. Adams, E. W., and Johnston, J. P., "A Mixing-Length Model for the Prediction of Convex Curvature Effects on Turbulent Boundary Layers," Trans. ASME, J. of Engineering for Gas Turbines and Power, Vol. 106, No. 1, pp. 142-148, January 1984.
13. Ito, H., and Nanbu, K., "Flow in Rotating Straight Pipes of Circular Cross Section," Trans. ASME, J. of Basic Engineering, Vol. 93, pp. 383-394, September 1971.

ÉTUDE THÉORIQUE DE L'ÉCOULEMENT DANS UN CANAL EN ROTATION. APPROCHE EXPÉRIMENTALE PAR LA VISUALISATION DE L'ÉCOULEMENT DANS UN CANAL COURBE

par Joël GUIDEZ, Pierre-Jacques MICHARD, Denis DUTOYA et Jean PERUCCHINI

Office National d'Études et de Recherches Aérospatiales
29, avenue de la Division Leclerc
92320 CHATILLON

RÉSUMÉ

Une étude, à la fois expérimentale et théorique, des transferts chaleur et de l'écoulement dans un canal en rotation est en développement à l'ONERA. Canal qui simule de manière simplifiée une cavité interne d'aube de rotor de turbine.

Sur le plan expérimental, il est montré que la vitesse de rotation a pour effet d'accroître les échanges thermiques par convection à l'intérieur du canal. Ce phénomène est expliqué par les écoulements secondaires induits par la force de Coriolis.

Sur le plan théorique, les équations de Navier-Stokes sont résolues numériquement en 3D (méthode instationnaire, implicite avec directions alternées). Les résultats obtenus pour les régimes laminaire et turbulent mettent en évidence les structures secondaires (deux et quatre tourbillons).

Parallèlement, en analogie rotation-courbure, la visualisation des lignes de courant par des bulles d'air ou d'hydrogène, dans un canal hydraulique, fait apparaître ces mêmes structures d'écoulement.

THEORETICAL STUDY OF THE FLOW IN A ROTATING CHANNEL. EXPERIMENTAL STUDY THROUGH FLOW VISUALIZATION IN A CURVED CHANNEL

ABSTRACT

An experimental and theoretical study of the heat transfer and flow in rotating channels is in development at ONERA. These channels simulate some simple internal cavities of turbine blades.

It has been experimentally demonstrated that the rotation speed induces a global enlancement of the heat transfer coefficient. This phenomenon can be explained by the secondary flows connected to the Coriolis force.

Theoretically, the Navier-Stokes equations that govern this problem are numerically solved in 3D (time marching, A.D.I. method). For laminar and turbulent flows, the results obtained point out the secondary structures (two and four vortices).

In addition, by means of rotation-curvature analogy, the visualization of the streamlines in a water-channel flow with air or hydrogen bubbles shows the same flow structures.

NOTATIONS

C, Cp	chaleur spécifique
D_H	diamètre hydraulique
e	épaisseur de paroi
E	énergie = $C_vT+V^2/2$
Σ_K	nombre d'Ekman
F_{ce}	force centrifuge
F_{co}	force de Coriolis
h	coefficient d'échange thermique
H	excentricité = $(r_e + L/2)$
k	conductivité thermique
L_λ	luminance monochromatique
L^o_λ	luminance du corps noir
$\dot{m}$	débit d'air
Nu	nombre de Nusselt
P	pression
Pr	nombre de Prandtl
Pr_t	nombre de Prandtl turbulent
q_{cond}	flux de conduction
q_{inc}	flux de rayonnement incident en provenance du four
r, R	rayon
Ra	nombre de Rayleigh
Re	nombre de Reynolds
Ro	nombre de Rossby
$\bar{T}$	température moyenne
Ta	température de l'air
T_{four}	température du four
T_p	température de paroi
t	temps
u, v, w	composantes de vitesse de l'écoulement
V	vitesse = $\sqrt{u^2 + v^2 + w^2}$
x, y, z	coordonnées

Symboles grecs

β	coefficient d'expansion
ε	émissivité
λ	longueur d'onde
μ	viscosité dynamique
ν	viscosité cinématique
ρ	masse volumique
σ	constante de Stefan
ω	vitesse de rotation

Indices

o	canal statique
e	entrée du canal rectiligne
i	conditions génératrices

1. INTRODUCTION

Dans le but d'étudier l'influence des effets de la rotation sur les transferts de chaleur convectifs dans les cavités internes des aubes de rotor de turbine, une étude expérimentale a été développée à l'ONERA [1]. Cette étude, comme celles conduites avec d'autres installations [2], [3] et [4], où l'axe du canal étudié est perpendiculaire à l'axe de rotation, met en évidence la modification des échanges convectifs par rapport à ceux obtenus dans un canal statique.

Ces modifications sont liées à la force de Coriolis qui induit des écoulements secondaires et aux poussées d'Archimède, près des parois, qui sont en grande partie à mettre au compte de la force centrifuge.

Parallèlement à cet aspect expérimental, une approche théorique par la modélisation numérique de l'écoulement dans un canal en rotation est en développement. Cette approche consiste à résoudre les équations de Navier-Stokes en 3D. Différents codes de calcul ont été réalisés. Les premiers ne permettent que la prise en compte de géométries simples et correspondent à une étape heuristique. Dans une seconde étape, l'effort a porté sur la mise en oeuvre d'un code plus général qui est en cours de validation. L'intérêt de ce code, au-delà de la prévision des effets de la rotation dans un canal de géométrie simplifiée, sera de permettre la restitution des écoulements et transferts de chaleur dans les cavités internes réelles d'aubes de rotor (fig. 1 [5]). C'est-à-dire de simuler les effets associés aux fortes courbures (fig. 2), ou aux perturbations liées aux "promoteurs de turbulence" (nervures, picots, pontets, fig. 3) avec ou sans rotation.

2. GÉNÉRALITÉS

Comme cela vient d'être précisé dans l'introduction, les cavités internes des aubes de turbines modernes sont de géométries complexes. Cette complexité est liée à la recherche d'une augmentation artificielle de la turbulence de l'écoulement par la géométrie (courbures successives, promoteurs de turbulence), ce qui conduit à intensifier les échanges convectifs.

A cette géométrie s'ajoute la rotation pour les aubes de rotor.

Si l'étude conjuguée géométrie complexe et rotation est intéressante sur un plan pratique, elle ne permettrait pas de séparer aisément chacun des effets les uns par rapport aux autres. Aussi, la démarche classique consiste à étudier indépendamment chacun des phénomènes avant de les rassembler.

De plus, la prévision de ces écoulements turbulents ($10000 \leq Re_{D_H} \leq 60000$), qui ne peut se faire autrement que par la résolution des équations de Navier-Stokes en 3D, nécessite une validation des codes avec le modèle de turbulence utilisé. Cette dernière remarque induit également une démarche allant graduellement vers la complexité.

Donc, dans une première étape, la géométrie retenue correspond à des canaux rectilignes à sections rectangulaires.

Sur la figure 4, une cavité interne simplifiée d'aube de turbine est représentée avec les forces de Coriolis et centrifuge induites par la rotation. Deux canaux rectilignes dits "centrifuge" et "centripète" sont raccordés par une partie courbe. Les résultats expérimentaux laissent apparaître une modification importante du transfert de chaleur convectif avec la vitesse de rotation [1], [2], [3] et [4]. Une augmentation globale de l'échange de chaleur par convection est constatée, augmentation qui est la résultante d'effets locaux : augmentation le long des faces de pression (dans le canal interne) et diminution le long des faces de dépression.

Ces modifications des transferts de chaleur avec la vitesse de rotation sont expliquées par l'effet des écoulements secondaires associés à la force de Coriolis, et par celui des poussées d'Archimède qui est d'autant plus significatif que l'écart de température entre la paroi et l'écoulement est important.

Les écoulements secondaires, en particulier, induisent une distorsion des profils de vitesse débitante, par rapport à ceux obtenus dans un canal statique, et donc des différences dans les coefficients de frottement. Les variations locales de coefficients d'échange qui en résultent, associées au brassage de l'écoulement, conduisent à une augmentation globale des transferts de chaleur.

Les équations qui régissent l'écoulement d'un fluide compressible à l'intérieur d'un canal rectiligne en rotation sont présentées ci-dessous pour un système d'axe lié à ce canal (fig. 5). Celles-ci laissent notamment apparaître les termes relatifs à la force centrifuge ($\rho\omega^2 x$, $\rho\omega^2 y$) et à la force de Coriolis ($2\rho\omega v$ et $-2\rho\omega u$) [6].

Il vient :

. l'équation de continuité

$$\frac{\partial \rho}{\partial t} + \underline{\nabla} \cdot \left(\rho \underline{V} \right) = 0$$

. de quantité de mouvement

$$\frac{\partial}{\partial t}\left(\rho \underline{V} \right) + \underline{\nabla} \cdot \left(\rho \underline{V}\,\underline{V} + p\,\underline{\underline{I}} - \underline{\underline{\tau}} \right) = \rho \Omega^2 \underline{r} + 2\rho \underline{V} \wedge \underline{\Omega}$$

. d'énergie

$$\frac{\partial}{\partial t}\left(\rho E\right) + \underline{\nabla} \cdot \left(\rho \underline{V} E + \underline{V} p - \underline{V} \cdot \underline{\underline{\tau}} + \underline{q}\right) = \rho \Omega^2 \underline{r} \cdot \underline{V}$$

$\underline{\Omega}$ = vecteur rotation (0, 0, ω)

$\underline{r}$ = rayon (x, y, 0)

$\underline{V}$ = vecteur vitesse (relatif) (u, v, w)

$\underline{\underline{I}}$ = tenseur identité

$\underline{\underline{\tau}}$ = tenseur des contraintes de frottement

$\underline{q}$ = vecteur flux de chaleur

L'analyse dimensionnelle met en évidence les nombres adimensionnels suivants :

Nusselt	$Nu = h D_H / \lambda$	qui caractérise le transfert de chaleur
Reynolds	$Re = \rho \bar{u} D_H / \mu$	" " la turbulence de l'écoulement
Rossby	$Ro = \omega D_H / \bar{u}$	" " l'aspect Coriolis
Ekman	$Ek = Re.Ro = \rho \omega D_H^2 / \mu$	" " " "
Rayleigh	$Ra = \nu^2 \omega^2 H D_H^3 \beta (T_P - T_{a_i}).Pr$	" " l'aspect centrifuge

Ces nombres sont utilisés pour regrouper les résultats relatifs à l'influence des effets de la rotation sur les transferts de chaleur.

3. MESURES THERMIQUES

Une vue générale du banc d'essais est présentée sur la figure 6. Les dimensions et les caractéristiques de cette installation, ainsi que les conditions expérimentales ont été choisies de manière à faciliter la prise des mesures. De plus, afin d'utiliser une technologie aussi simple que possible, la vitesse de rotation et le niveau de température des maquettes d'essais ont été réduits par comparaison à ceux rencontrés par une aube réelle (ω_{max} = 5000 rpm et Tp_{max} = 400°C au lieu de 13000 rpm et 1000°C pour une aube de rotor).

Deux maquettes d'essais (fig. 7 et 8) semblables tournent à l'intérieur d'un four électrique ($T_{four,max}$ = 1200°C et P = 45 kW). Cet ensemble est placé dans une enceinte à vide (pression $\leq$ 20 Pa). Ainsi, les maquettes sont chauffées extérieurement par le flux de rayonnement qui provient du four électrique (la convection externe est négligeable en raison du faible niveau de pression qui règne dans l'enceinte). Elles sont refroidies par circulation d'air (alimentation par le bas de l'arbre tournant et sortie vers le haut) dont le débit (5 à 50 g/s) est mesuré par un "col sonique".

Quatre groupes de joints tournants assurent l'étanchéité de part et d'autre de l'alimentation en air et de l'enceinte à vide.

Un moteur électrique entraîne l'arbre supportant les maquettes par une courroie dentée.

Les mesures sont réalisées à partir de thermocouples embarqués implantés selon différentes sections (fig. 7). Un pyromètre infrarouge à court temps de réponse ($\Delta t \simeq 10$ µs) et de résolution spatiale de l'ordre de 1,2 mm permet l'obtention de profils de température de luminance dans une section de la maquette d'essai [7]. Sur la figure 8, un exemple de profil obtenu par voie pyrométrique est présenté avec une maquette comparable à la cavité de la figure 4. A partir de deux angles de visée (θ = + et -45°) le profil de température est reconstitué et cela pour deux vitesses de rotation. La distorsion du profil avec une élévation de la vitesse de rotation apparaît clairement. Les points c, d, e et f délimitent une section $(x - r_B)/D_B$ = 9,5 du canal centrifuge et il est à noter que le transfert de chaleur par convection augmente fortement pour la face de pression (intrados pour l'aube de rotor) puisque la température de paroi diminue par rapport au cas à basse vitesse de rotation (ω = 50 rd/s). Au contraire pour la face de dépression (ou extrados pour l'aube) l'échange diminue. L'intérêt des mesures réalisées par pyrométrie infrarouge est l'observation directe de l'influence, sur le plan thermique, des effets associés à la rotation et en particulier de l'effet Coriolis qui induit un comportement de l'écoulement différent pour les deux faces opposées "intrados" et "extrados". Les écarts constatés avec les valeurs délivrées par les thermocouples s'expliquent par les réflexions du flux provenant du four sur l'élément de surface observé. Le signal pyrométrique prenant la forme :

$$u = \int_{\Delta\lambda} F_\lambda \cdot \left(\varepsilon_\lambda L^\circ_{\lambda, T_P} + (1 - \varepsilon_\lambda) L_{\lambda, env.} \right) d\lambda$$

fonction interne du pyromètre — émission propre de l'élément de surface — réflexion de l'environnement

L'obtention des coefficients d'échange se fait par un bilan thermique au niveau de chaque thermocouple aussi bien en régime transitoire que permanent par :

$$\rho c e \frac{dT_P}{dt} = \varepsilon \left(q_{inc} - \sigma T_P^4 \right) - h \left(T_P - \overline{T}_a \right) + q_{cond}$$

Pour la maquette présentée figure 7 et pour le canal centrifuge le rapport du nombre de Nusselt avec rotation (Nu_ω) au nombre de Nusselt obtenu en état statique (Nu_o) est présenté en fonction du nombre de Rossby qui caractérise l'aspect Coriolis. Les valeurs sont assez bien correlées avec le nombre de Rossby et comme cela vient d'être dit plus haut, l'échange convectif augmente de manière importante pour la face intrados et diminue, dans ce cas, dans une moindre proportion pour la face extrados. Ce type de résultat est conforme à ce qui a été obtenu par Morris [2] et Johnson [3].

4. RÉSOLUTION NUMÉRIQUE DES ÉQUATIONS DE N.S. DANS UN CANAL EN ROTATION

La prévision des écoulements et transferts de chaleur dans une cavité interne d'aube de rotor nécessite de résoudre les équations de N.S. en 3D. Cette modélisation doit être validée dans un certain nombre de configurations élémentaires avant d'être utilisée pour des géométries quelconques. La comparaison du calcul avec les résultats expérimentaux présenté au chapitre 3 en est un exemple.

Différents codes ont été développés pour résoudre le système 1 du chapitre 2. Les premiers permettent de traiter l'écoulement pour des géométries simples, en l'occurence un canal rectiligne ou une boucle en rotation. Le principe du calcul est classique. Il s'agit d'une méthode de différence finie centrée, construite sur un réseau 3D curviligne orthogonal, et dont le caractère conservatif est assuré par l'intégration des équations de bilan sur des volumes élémentaires associés à chaque noeud du réseau. Ces volumes d'intégration sont formés à l'intérieur du domaine de calcul à partir de trois points consécutifs dans chaque direction. Sur les limites, des "vitesses de glissement" fictives sont stockées, et les équations de bilan sont intégrées sur le demi-volume associé au point considéré, en tenant compte des conditions aux limites par l'intermédiaire de fonctions de paroi. La discrétisation spatiale fournit un système de $5.N_x.N_y.N_z$ équations d'évolution (N_x, $_y$ et $_z$ = nombre de points du réseau dans les différentes directions), qui est intégré au cours du temps grâce à une méthode semi-implicite. Les opérateurs à inverser sont linéarisés, puis factorisés dans chaque direction (méthode A.D.I.) et le calcul consiste en une série d'inversion de matrices tridiagonales par blocs (5 x 5) [8].

Actuellement, l'effort porte sur un code plus général, tant en ce qui concerne la géométrie (réseau curvuligne quelconque) que les conditions aux limites. La technique d'intégration dans le temps est analogue à ce qui vient d'être décrit. La discrétisation spatiale utilise une méthode de volumes finis avec décomposition des flux (de type Steger et Warming [9]) et schéma décentré à 5 points.

La particularité principale de ce code, qui a été conçu pour la prévision des écoulements dans un moteur diesel, est de permettre la modification de la géométrie à chaque pas en temps. Pour ce qui est du maillage, une transformation qui change le domaine physique de calcul en un assemblage de parallélépipèdes facilite la mise en oeuvre de la méthode. Les conditions aux limites sont très diverses : température ou flux imposé sur des portions de parois, injection ou aspiration locale d'écoulement. Pour les précisions concernant ce code le lecteur pourra se reporter aux références [10] et [11].

Sur la figure 9 un exemple de résultats de calculs 3D asymptotique en écoulement laminaire est présenté. Les conditions d'écoulement sont : $Re_{D_H} = 1000$; $Ro = 0{,}125$ et $E_K = 125$, ce calcul correspond à une situation ou x>> devant a et b. Les gradients de vitesses longitudinaux $\partial u / \partial x$ sont supposés négligeables. La quantité $(1/\rho)(\partial P/\partial x) - \omega^2 x$ est fixée, elle est homogène sur toute la section et elle conditionne le débit. La figure 9a, sur laquelle apparaît un système à deux vortex correspond à un maillage 40 x 40 et a été obtenu après 1000 itérations (D_H = 10 mm, $t = 5.10^{-5}$s, CFL de 80). Pour un autre cas, $Re_{D_H} = 500$, $Ro = 0{,}25$ et $E_K = 125$, figure 9b, la structure secondaire de l'écoulement est modifiée avec un système à quatre vortex. La recirculation intense des deux tourbillons supplémentaires est à noter. Ce type de résultat est conforme à ce qui a été obtenu par Khesgi et Scriven [12] ou Speziale et al [13].

Un exemple de résultats obtenus en 3D dans une boucle en rotation est présenté figure 10. Le maillage (16 x 32) x 96 reproduit un canal à section rectangulaire (a/b = 2) comparable à celui expérimenté et présenté figure 7. Les recirculations ainsi que des profils de vitesse axiales sont dessinés sur la figure 10. Ils mettent en évidence la complexité de l'écoulement qui dans ce cas est turbulent : Re = 40000, Ro = 0,06 et E_K = 2400. Les conditions génératrices sont : pression d'arrêt et enthalpie d'arrêt imposées. A l'aval, seule la pression statique est imposée. Le flux est nul aux parois (écoulement adiabatique).

Ces résultats obtenus avec le programme de calcul simplifié (1ère étape, voir plus haut) met en évidence la faisabilité du calcul en régime turbulent. Ils sont encourageants et l'étude numérique va être poursuivie avec le code en cours de développement (2ème étape) qui permettra alors une analyse quantitative des échanges thermiques avec les différentes parois.

5. VISUALISATION DES LIGNES DE COURANT DANS UN CANAL COURBE

Une approche expérimentale de visualisation des écoulements secondaires dans un canal courbe a été entreprise. En effet, l'analyse des équations de quantité de mouvement met en évidence le comportement similaire, aux effets centrifuges près, de l'écoulement dans un canal rectiligne en rotation avec celui rencontré dans un canal courbe. Dans les deux cas, les trajectoires des particules dans un repère Galiléen sont courbes et les phénomènes sont conditionnés par l'interaction entre les forces d'inertie dues à la courbure et l'inhomogénéité de la vitesse de l'écoulement causée par les frottements près des parois [14].

L'intérêt d'une telle visualisation est de mettre en évidence les structures secondaires créées par ce phénomène. D'apporter des éclaircissements sur la dualité deux et quatre tourbillons, d'obtenir des renseignements sur l'épaisseur des zones de recirculation et par là même des centres tourbillonnaires.

Sur le plan pratique, l'analogie rotation-courbure se fait en écrivant l'égalité des accélérations de Coriolis et centrifuge associée à la courbure :

$$2\omega\bar{u} = \bar{u}^2 / R \quad \Longrightarrow \quad R = \bar{u} / 2\omega$$

et en terme de nombre de Rossby équivalent pour la courbure :

$$Ro_{courbure} = D_H/2R$$

L'analogie air-eau est réalisée par la conservation du nombre de Dean :

$$D_n = Re_{D_H} \cdot \Psi^{-1/2} \qquad \text{avec} \quad \Psi = 2R/D_H = 1/Ro_{courbure}$$

Les valeurs retenues pour l'expérience relatée ici sont (fig. 11) :

$$R = 0{,}12 \text{ m} \; ; \; D_H = 40 \text{ mm} \; ; \; Re_{DH} = 18000 \; ; \; Ro_{courbure} = 0{,}166,$$

avec un canal en Altuglass (parois transparentes) à section rectangulaire de hauteur a = 60 mm et de largeur b = 30 mm (a/b = 2, fig. 7). Ces dimensions ont été choisies de manière à permettre une visualisation pratique des lignes de courant par des bulles d'air ou d'hydogène. Les bulles d'hydrogène sont obtenues par électrolyse à partir de deux grilles (fils de 0,5 mm, mailles 2 x 2 mm) espacées de 2 mm et soumises à une tension électrique de 40 V. En position verticale elles occupent la presque totalité de la section interne du canal. L'injection est réalisée à 12,5 x D_H (500 mm) de la partie courbe.

Un éclairage par tranche de 2 mm d'épaisseur permet de visualiser les lignes de courant aussi bien verticalement (l'éclairement est courbe de manière à épouser la courbure du canal) qu'horizontalement (éclairage plan) et ainsi de reconstituer l'écoulement secondaire (fig. 12).

Sur la figure 12.1, l'écoulement au voisinage de la paroi supérieure est visualisée et la circulation est centripète, puis la recirculation longe la paroi interne (fig. 12.2). Sur la figure 12.3 (éclairage horizontal au milieu du canal) une légère centrifugation apparaît. Le long de la paroi externe (fig. 12.4.1) les deux noyaux se dessinent nettement avec une remontée de l'écoulement sur la demi-hauteur supérieure et une descente pour l'autre partie (voir également les recirculations fig. 10). Une instabilité au niveau de la paroi externe, dans la zone centrale apparaît à l'examen des figures 12.4.1 et 4.2. Dans cette zone de séparation des deux tourbillons, les lignes de courant montent ou descendent en intermittence qui pourrait s'expliquer par la naissance, puis la disparition, de deux petits tourbillons supplémentaires. Pour les figures 12.1 à 4.2, la visualisation a été réalisée par des bulles d'air et l'écoulement peut être considéré comme établi à l'entrée du canal courbe puisque la partie rectiligne à section rectangulaire est de 1 m, soit 25 x D_H.

Le système d'injection de bulles d'hydrogène a été utilisé pour obtenir des bulles de plus petit diamètre (d $\simeq$ 5/100 mm) que celui des bulles d'air (d $\simeq$ 0,5 mm) qui ainsi suivraient mieux l'écoulement. En fait, il n'a pas été remarqué de différence notable de comportement entre les deux types de bulles pour des vitesses de l'écoulement > 0,4 m/s.

Cependant, en inclinant de quelques degrés le système de génération de bulles d'hydrogène, une structure à quatre tourbillons stationnaires a été mise en évidence (fig. 12.4.3, visualisation des lignes de courant au voisinage de la paroi externe). Lorsque l'inclinaison devient importante (45° pour la figure 12.4.4) la structure devient disymétrique.

Donc, la structure naturelle semble être un système à deux vortex, mais une faible perturbation peut induire un système à quatre tourbillons. Une plus forte perturbation conduit à des circulations asymétriques. Ces résultats sont qualitativement inchangés lorsque le nombre de Reynolds varie dans une plage de 10000 à 60000.

Sur la figure 12.1, il est à noter que la trajectoire des bulles fait un angle de l'ordre de 45° par rapport à la tangente à l'axe du canal. Pour les faces interne et externe (fig. 12.2 et 12.4.1), l'angle entre l'horizontal et la trajectoire des bulles est moindre ; respectivement 25° et 15°.

Ces angles sont plus faibles lorsque le nombre de Reynolds augmente.

L'épaisseur des zones de recirculation est mince et de l'ordre de 5 à 10 % du diamètre hydraulique.

Il en résulte qu'une modélisation correcte en régime turbulent de ce type d'écoulement ne pourra se faire qu'en raffinant le maillage près des parois.

En guise de conclusion à ce chapitre, sur un plan purement pragmatique, il vient une question :

- quel peut être l'indicence, sur le plan des échanges convectifs, de ces différentes structures, deux, quatre tourbillons ou asymétrique ?

En effet, les effets d'entrée jouant un rôle important sur le développement des structures secondaires, dans les situations réelles (cavité interne d'aube), les phénomènes décrits plus haut peuvent apparaître ce qui rend les prévisions délicates.

6. CONCLUSION

La connaissance des écoulements et transferts de chaleur dans les canaux internes des aubes de rotor de turbines est nécessaire pour l'optimisation de la géométrie de ces cavités dans le but d'obtenir la meilleure efficacité thermique.

A l'ONERA un montage d'essais a été réalisé pour évaluer l'influence des effets de la rotation sur les échanges convectifs dans un canal qui simule, de manière simplifiée, une cavité interne d'aube de rotor de turbine. Les expériences ont été conduites avec deux maquettes constituées de tubes à sections rectangulaires de rapport 2 et 0,5 entre les côtés. Avec ces géométries les coefficients d'échanges convectifs sont notablement modifiés par rapport à ceux rencontrés dans un canal statique. Lorsque la vitesse de rotation s'élève, l'échange convectif global s'accroît ; l'augmentation est importante sur la face de pression du canal alors qu'il diminue le long de la face de dépression.

Ces effets s'expliquent principalement par les écoulements secondaires induits par la force de Coriolis.

Parallèlement à cette approche expérimentale, une modélisation numérique par la résolution des équations de Navier-Stokes en 3D est en cours de développement. Les résultats obtenus en écoulement laminaire sont conformes à ceux publiés par d'autres auteurs [12] et [13] et il apparaît pour certaines valeurs des nombres de Rossby et d'Ekmann des recirculations à deux ou quatre tourbillons.

Pour l'écoulement turbulent, une modélisation tridimensionnelle complète d'une boucle avec les canaux : centrifuge, courbe et centripète a été réalisée. La complexité des écoulements secondaires, en particulier dans la partie courbe est très nette, la distorsion des profils de vitesse axiale apparaît avec, comme prévisible, une intensité bien moindre qu'en régime laminaire. Ce type de calcul va être poursuivi avec un code NS 3D qui est en cours de validation et qui permettra une analyse quantitative des échanges thermiques avec les parois.

Les écoulements secondaires qui prennent naissance dans un canal rectiligne en rotation peuvent être étudiés expérimentalement et plus simplement dans un canal courbe en effectuant une analogie rotation-courbure. Les conditions expérimentales étant définies à partir d'une situation analysée sur le plan thermique (maquette a/b = 2, Re_{DH} = 18000 et Ro = 0,16).

La visualisation des trajectoires de bulles d'air ou d'hydrogène dans le canal courbe, à partir de l'éclairement de différents plans horizontaux et verticaux, met en évidence un système à deux tourbillons. Cependant, une perturbation modérée de l'écoulement réalisée à 12,5 x D_H à l'amont du canal courbe conduit à une modification de cette structure vers un système à quatre tourbillons. Une perturbation plus importante induit une organisation asymétrique.

Ces résultats qualitatifs rejoignent ce qui à été prédit par Soh [16] en écoulement laminaire sur l'influence des conditions amonts sur les structures secondaires.

RÉFÉRENCES

[1] - GUIDEZ, J. (1989)
Study of the convective heat transfer in rotating coolant channel.
J. of Turbomachinery, vol. 111, pp. 43-50.

[2] - MORRIS, W.D., HARASGAMA, S.P. and SALEMI, B. (1988)
Measurements of turbulent heat transfer on the leading and trailing surfaces of a square duct rotating about an orthogonal axis.
ASME Paper 88-GT-114.

[3] - JOHNSON, B.V., KIM, J.C. and WAGNER, J.H. (1986)
Rotating heat transfer experiments with turbine air foil internal flow passages.
ASME Paper 86-GT-133.

[4] - ISKAKOV, K.M. and TRUSHIN, V.A. (1985)
The effect of rotation on the heat transfer in a radial cooling channels of turbine blades.
Thermal Engineering, n° 32 (2).

[5] - DAMBRINE, B. et MASCARELL, J.P. (1988)
Dimensionnement en fatigue et fluage des aubes de turbine.
La Recherche Aérospatiale, vol. 1, pp. 35-45.

[6] - SPALDING, D.B. and SKIADARESSIS, D. (1978)
Heat transfer in ducts rotating around a perpendicular axis.
6th Int. Heat Transfer Conference, Toronto, vol. 2, pp. 91-95.

[7] - CHARPENEL, M. et WILHELM, J. (1985)
Pyrométrie I.R. pour la mesure de températures d'aubes de turbine.
AGARD-CP-390, pp. 29.1-29.10, Norway.

[8] - DUTOYA, D. (1979)
A program for calculating boundary layers and heat transfer along compressor and turbine blades.
T.P. ONERA n° 1979-88 and Proceedings of the first int. Conf. of the Numerical Methods in Thermal Problems, Pineridge Press, Swansea.

[9] - STEGER, J.L. and WARMING, R.F. (1981)
Flux vector splitting of the inviscid gasdynamic equation with application to finite difference methods.
J. Comput. Phys., vol. 40, n° 2.

[10] - ERRERA, M.P. (1987)
Numerical prediction of fluid motion in the induction system and the cylinder in reciprocating engines.
S.A.E. paper 870594, Detroit.

[11] - ERRERA, M.P., LABBÉ, J. et JÉROT, A. (1988)
Three-dimensional numerical and experimental analysis of in-cylinder flow in an internal combustion engine.
S.A.E. paper 880106, Detroit.

[12] - KHESGI, H.S. and SCRIVEN, L.E. (1985)
Heat transfer and fluid flow in rotating coolant channels.
Physics of Fluids, october 1985.

[13] - SPEZIALE, C.G. (1982)
Numerical study of viscous flow in rotating rectangular ducts.
J. Fluid Mechanics, vol. 122.

[14] - BRADSHAW, P. (1969)
The analogy between streamline curvature and buoyancy in turbulent shear flow.
J. Fluid Mechanics, vol. 36, pp. 177-191.

[15] - GHIA, K.N., GHIA, U. and SHIN, C.T. (1987)
Study of fully developed incompressible flow in curved ducts, using a multi-grid technique.
J. of Fluids Engineering, vol. 109, pp. 226-236.

[16] - SOH, W.Y. (1988)
Developing fluid flow in a curved duct of square cross-section and its fully developed dual solutions.
J. of Fluid Mechanics, vol. 88, pp. 337-261.

[17] - CHENG, K.C. and YUEN, F.P. (1987)
Flow visualisation experiments on secondary flow patterns in an isothermally heated curved pipe.
J. of Heat Transfer, vol. 109, pp. 55-61.

[18] - HILE, P., VEHRENKAMP, R. and SCHULZ-DUBOIS, E.O. (1985)
The development and structure of primary and secondary flow in a curved square duct.
J. Fluid Mechanics, vol. 151, pp. 219-241.

REMERCIEMENTS

Les auteurs remercient la DRET (Direction des Recherches et Études Techniques) ainsi que la SNECMA qui ont supporté financièrement les recherches décrites dans cette publication.

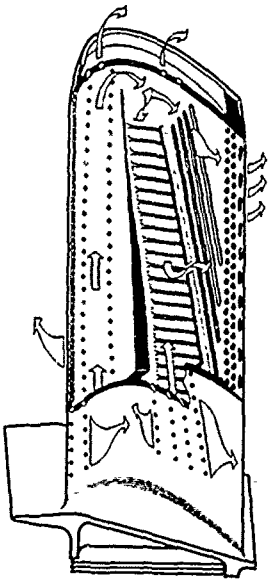


Fig. 1: Exemple de cavité interne complexe d'aube de rotor de turbine.



Fig. 2: Exemple de retournement simple-visualisation avec une solution d'eau et de Teepol -$Re_{DH} \simeq 15000$

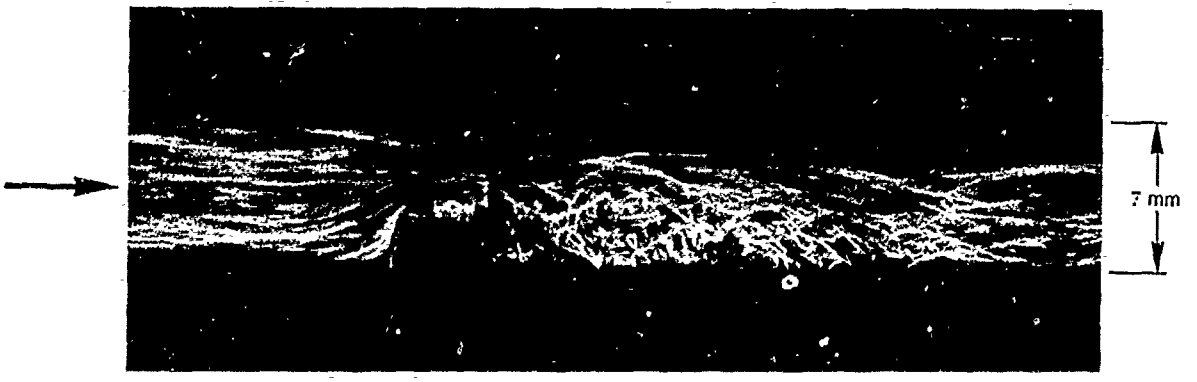


Fig. 3: Exemple de perturbateur-Nervure à section carrée-visualisation par bulles d'air- $Re_{DH} \simeq 15000$

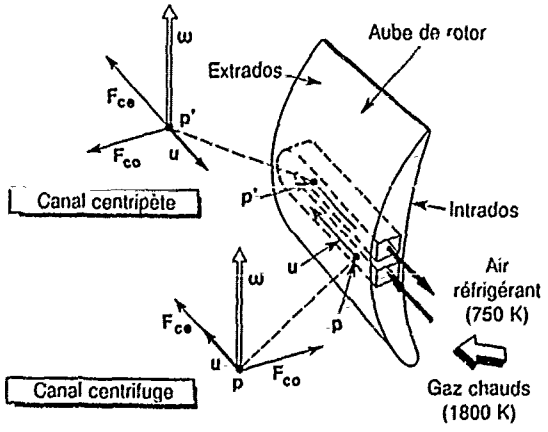


Fig. 4: Exemple de cavité interne

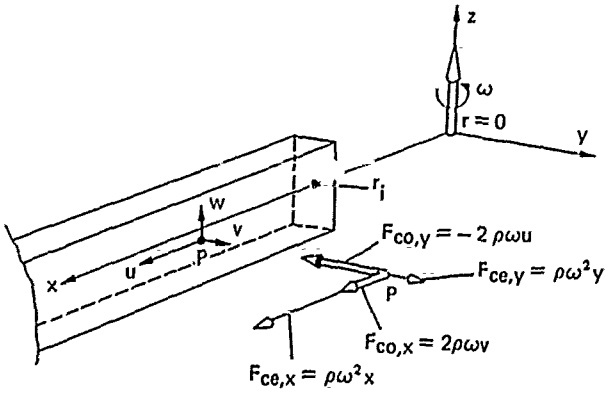


Fig. 5: Représentation d'un canal rectiligne dans le système d'axe tournant.

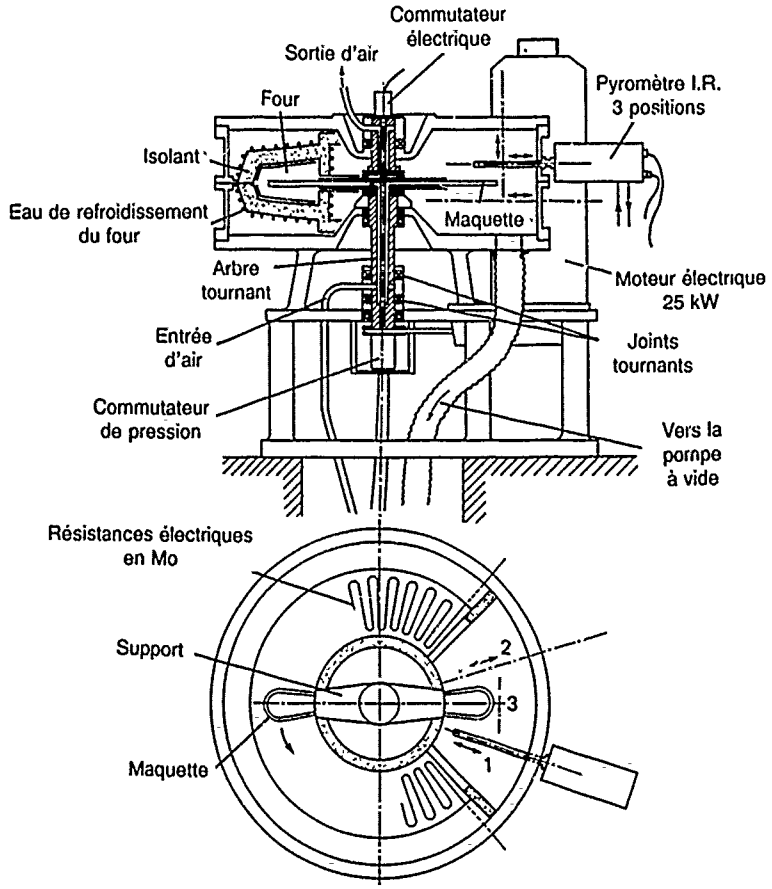


Fig. 6: Banc d'essais.

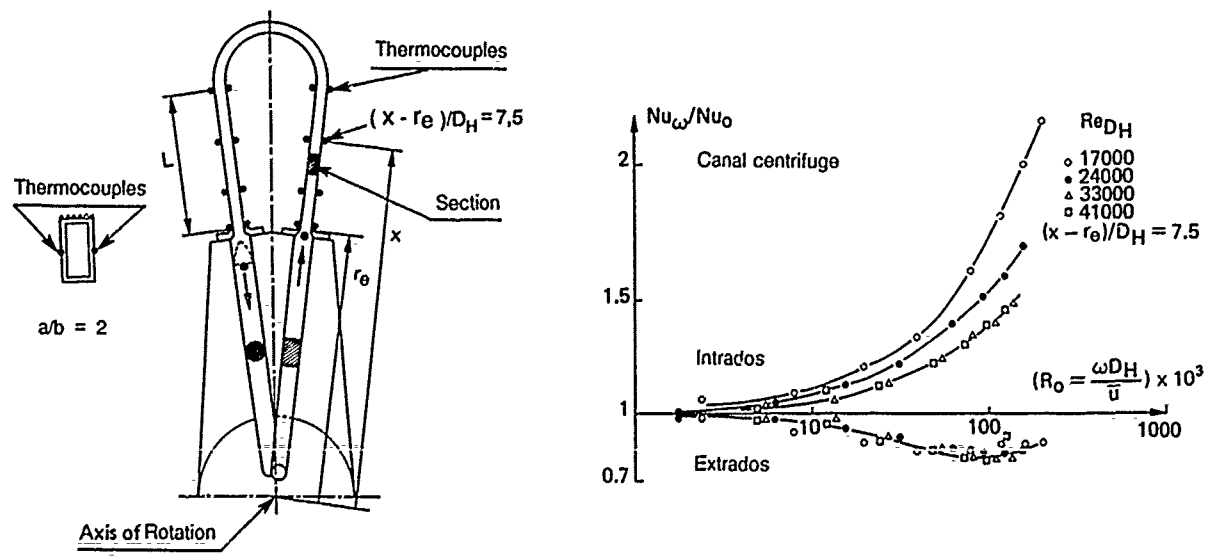


Fig. 7: Maquette d'essais a/b = 2 et rapport Nu_ω/Nu_o en fonction du nb. de Rossby

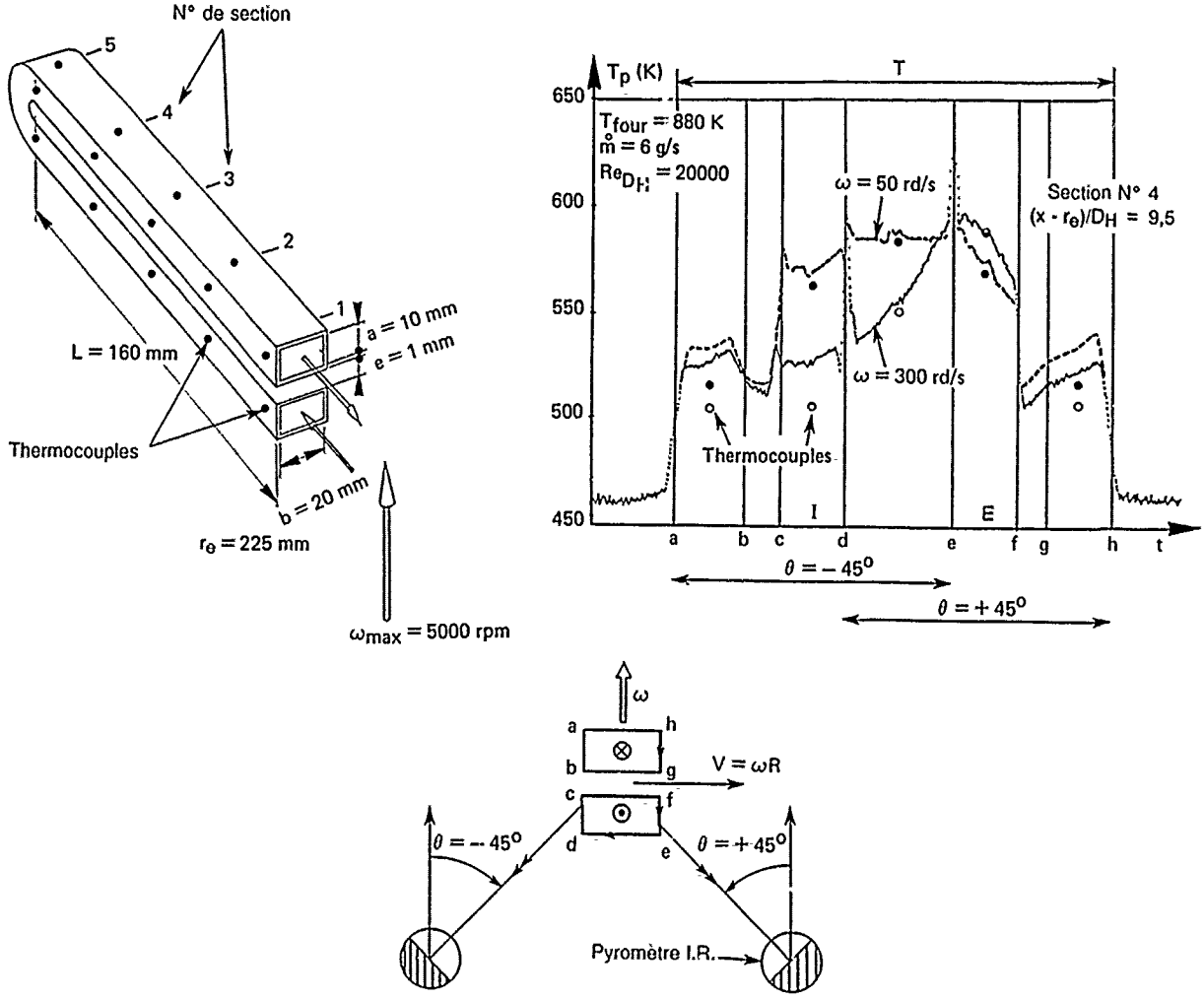


Fig. 8: Exemple de températures de luminance obtenues avec le pyromètre I.R. pour deux vitesses de rotation. $\omega = 50$ et 300rd/s , maquette a/b = 0,5 , $(x-r_e)/D_H = 9,5$

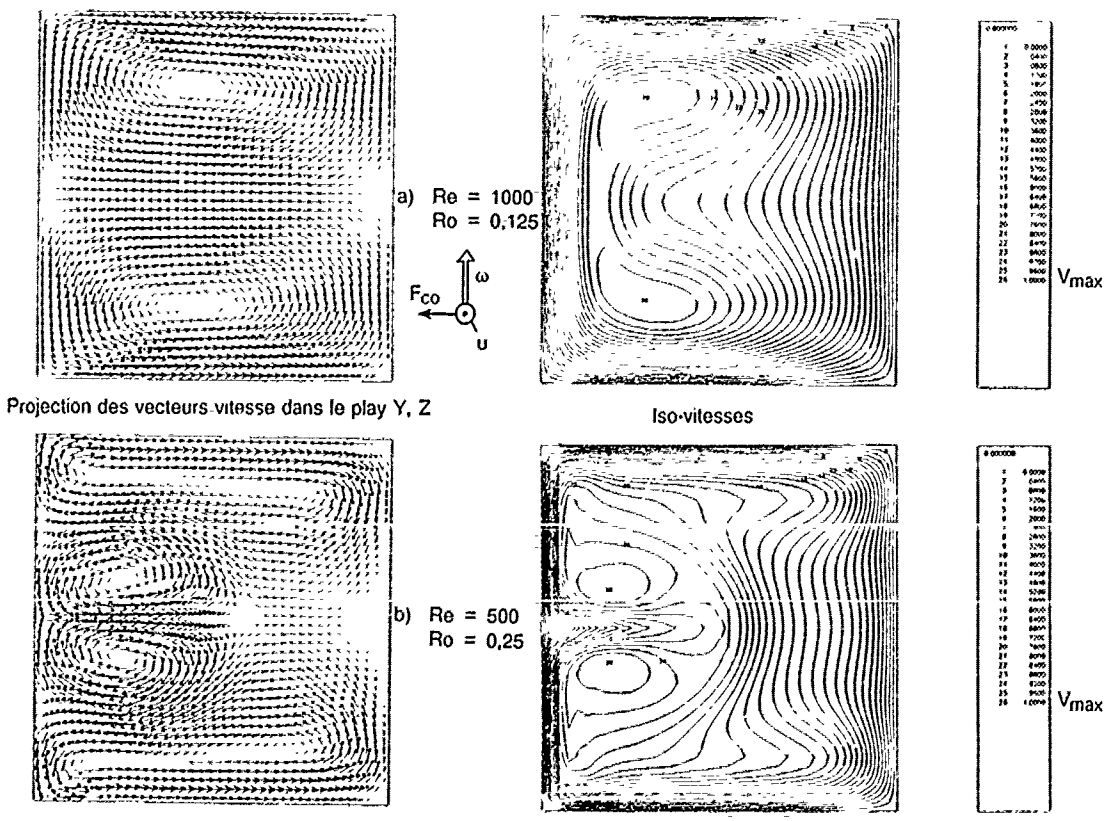
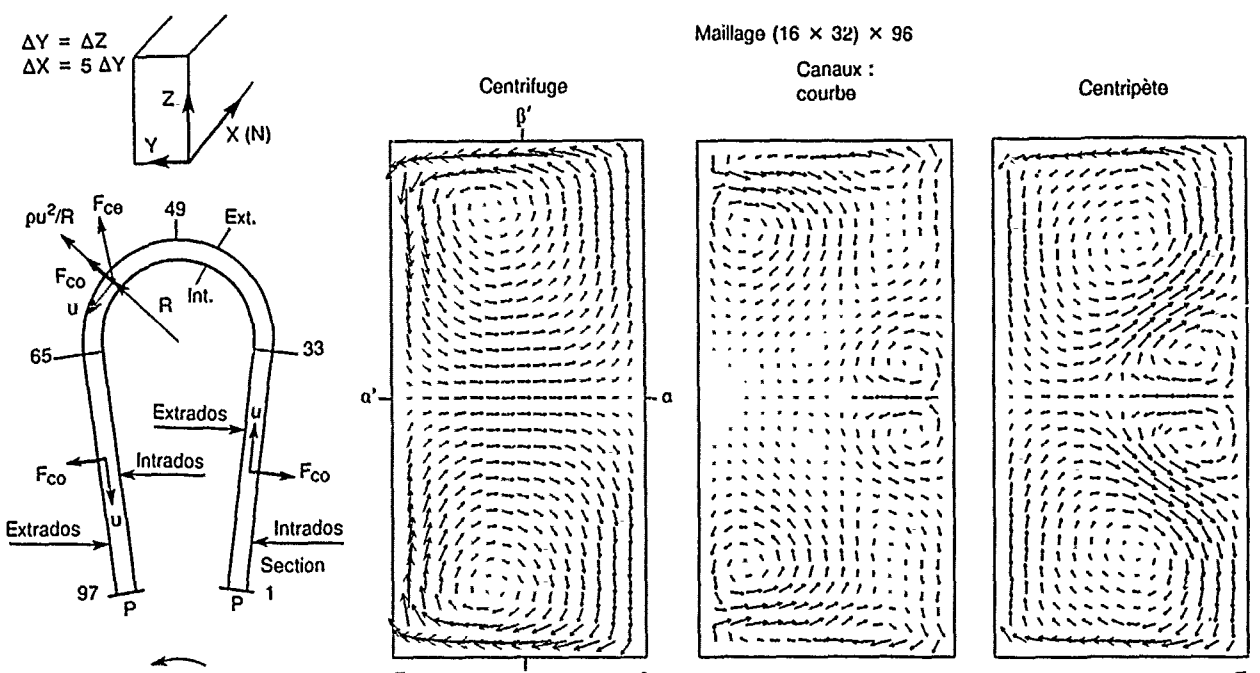
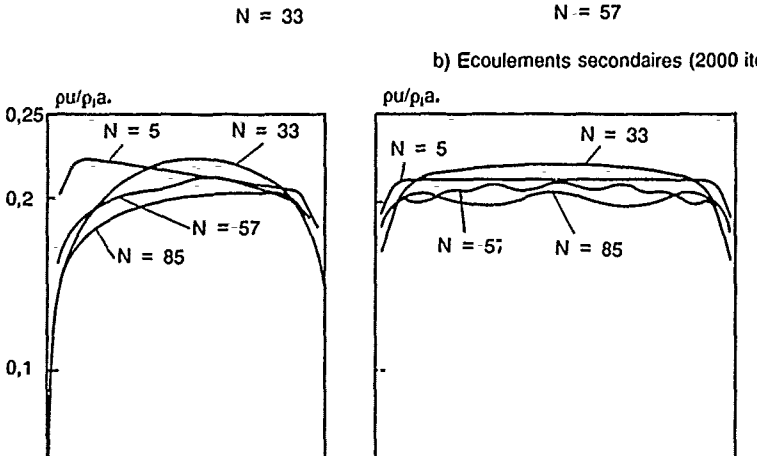


Fig. 9: Calculs d'écoulements 3D asymptotiques (maillage 40x40 $\Delta t = 5.10^{-5}$ s)





c) Profils de vitesse axiaux $a_i = \sqrt{C_p}\ T_i$

Fig. 10: Calculs 3D dans une boucle - Ecoulement turbulent : Re = 40000 ; Ro = 0,06

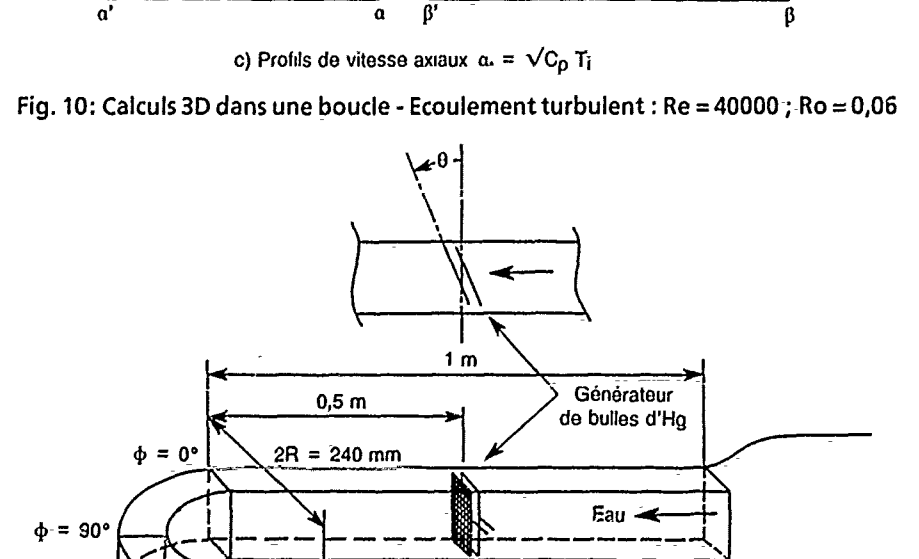


Fig. 11: Canal courbe - D_H = 40mm - R = 120mm.

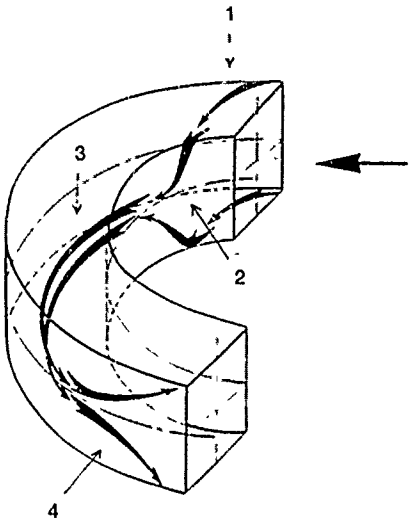
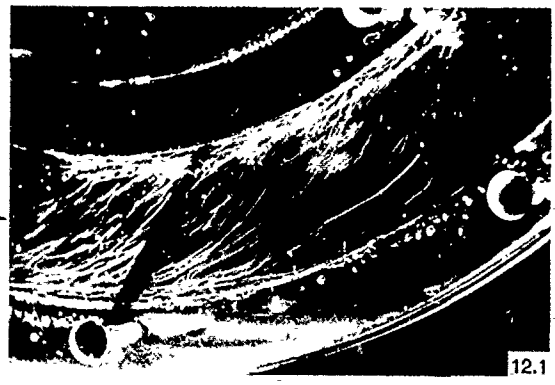
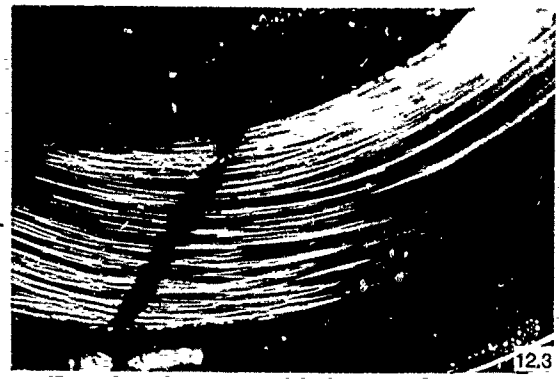


Fig. 12: Visualisation des lignes de courant
dans un canal courbe.
Analogies : rotation ⇒ courbure
Air ⇒ eau

Re = 18000 ; Ro = 0,16



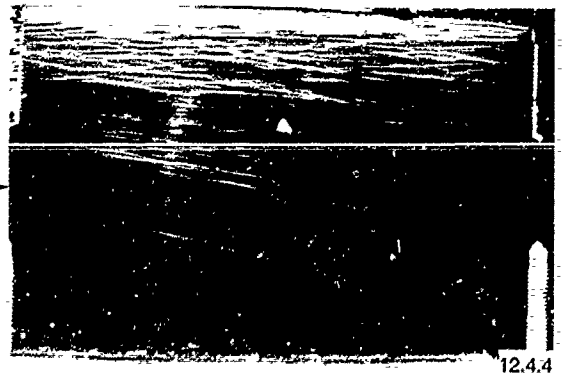












DISCUSSION

D.K. HENNECKE, Technische Hochschule, Darmstadt, Germany

In your measurements, what kind of velocity distribution in the inlet cross section of the test section did you try to achieve and how did you do it ?

Author's reply:

The shape of the inlet part, just before the test section (centrifugal duct) has been chosen with with the industrial partnet (SNECMA) in order to have a similar shape of the channel before the blade.
Therefore, in order to compute accurately the flow in 3D (and consequently the friction and the heat transfer coefficients within the test section) it is necessary to start the computation near the axis of rotation owing to the Coriolis force which induces secondary flow from the hub.

J.MOORE, Virginia Polytechnic Institute, US

The orientation of your bend is at 90 degrees to that used in our paper. Are you also planning to test different bend orientations ?

Author' s reply

With the first test section ($a/b \simeq 2$), the objective was specifically the study of the two channels :

- the centrifugal channel one
- the centripetal channel one

Therefore, the radius of the curved part which connects the two ducts has been chosen in order to minimize the perturbation of the flow induces by the bend.

But, with the second test section ($a/b \simeq .5$), the geometry is close to a real cavity of blade and the orientation of the bend is at 90^{o} by comparison to the first test section and like the one computed in the paper of Mr and Mrs. Moore.

THE EFFECT OF SECONDARY FLOW ON THE REDISTRIBUTION OF THE TOTAL TEMPERATURE FIELD DOWNSTREAM OF A STATIONARY TURBINE CASCADE

W.E. CARSCALLEN
Associate Research Officer
Gas Dynamics Laboratory
National Research Council, Canada
Ottawa, Ontario, Canada K1A 0R6

P.H. OOSTHUIZEN
Professor
Department of Mechanical Engineering
Queen's University
Kingston, Ontario, Canada K7L 3N6

SUMMARY

Early testing at the National Research Council of Canada's (NRCC) Highly Loaded Turbine Test Rig revealed that the total temperature downstream of a turbine nozzle was redistributed relative to the nozzle inlet total temperature distribution and furthermore there was an apparent change in area averaged total temperature across the stator row. In order to examine these observations a transonic planar cascade of the exhauster type was constructed at NRCC. Tests were carried out at pressure ratios giving nozzle isentropic exit Mach numbers ranging from low subsonic to low supersonic. Wedge probes were used to measure total pressure, total temperature and flow angles downstream of the nozzle blades.

Test results indicated that exit total temperature distributions are highly redistributed and possible reasons for this phenomenon are discussed. Results of area averaged aerodynamic losses are also given and their relation to the change in total temperature across the nozzle blades are discussed.

NOMENCLATURE

Cpo = local total pressure loss coefficient, $(Po_1-Po_2)/(Po_1-Psm_2)$

$\overline{Cpo}$ = area weighted mean of Cpo
DTo = local total temperature differential between exit and inlet, To_2-To_1

$\overline{DTo}$ = spanwise or pitchwise mean of DTo

$\overline{\overline{DTo}}$ = area weighted mean of DTo
k = ratio of specific heats
m = mass flow
Ma = Mach number
Po = local total pressure
PR = nozzle total-to-static pressure ratio, Po_1/Psm_2
Ps = local static pressure
Psm = mean static pressure
Rf = recovery factor, (Taw-Ts)/(To -Ts)
Taw = adiabatic wall temperature
To = total temperature
Ts = static temperature
y = distance from wall

δ = boundary layer thickness

Subscripts

1 = nozzle inlet plane
2 = nozzle exit plane
∞ = freestream conditions

INTRODUCTION

A joint research program between the National Research Council of Canada (NRC) and Pratt and Whitney Canada (P&WC) was initiated in the early 1970's. This program studied an aggressive design of a highly loaded, low wheel speed gas generator turbine stage of a typical P&WC aviation gas turbine engine of about 600 shaft horsepower. The objectives of this experimental and theoretical research program were to explore design rules for highly loaded turbines and evaluate and improve current design and analysis tools. In support of this work a highly loaded turbine test rig (HLTTR) was constructed in which a three times engine size stage (stator and rotor or stator alone) could be operated at representative Reynolds and Mach numbers. A description of the facility and some results

of the research program have been published by Moustapha [1,2], Williamson [3,4,5] and Schaub [6].

Unpublished results of total temperature traverses taken downstream of the stator blade row (no rotor installed) indicated a nonuniform distribution of total temperature. This result was unexpected, as the total temperature probes had been calibrated over the Mach number range, the total temperature profile upstream of the stator blade row was uniform, there was no work done by the stator blades on the flow and the flow of air through the stator blade row was assumed a priori, to be adiabatic. Figure 1 is a total temperature contour plot at the stator exit; as can be readily seen there are distinct 'wakes' from the stator blades. Also apparent is the close spacing of the contour lines at the hub indicating a gradient in the total temperature. An area weighted average of the total temperature was made at the rotor exit, and when compared to the upstream total temperature, an apparent nominal increase in total temperature of 4.4 degrees Celsius was observed.

This research program indicated that there was a redistribution of the gas stream total temperature profile as it passed through the stator blade row, and an increase in the area weighted average of total temperature. The redistribution of the total temperature profile and the apparent change in total temperature were detected in both cold and hot gas tests when either a wedge or cobra probe was used for flow measurements. No published literature could be found which addressed these observations. Private communications with engineers at both Pratt & Whitney Canada Inc. and Westinghouse Canada Inc. indicated that this phenomenon had never been observed and the design of engines was carried out assuming there was no change in the total temperature distribution through non-cooled stator blade rows.

The initial hypothesis put forth to explain these phenomena was that heat transfer was occurring between the test rig and the gas stream flowing through the nozzles, the driving temperature gradient being the difference between the ambient test rig temperature and the depressed static temperatures in the nozzles. It was further hypothesized that the local boundary layer recovery factors were sufficiently depressed by the action of the secondary flows in the nozzle, that heat transfer could occur to the extent the total temperature was redistributed and the average raised. [7]

In order to investigate these phenomena an experimental program was initiated on a separate planar cascade rig. The goals of this program were to reproduce the redistribution of total temperature in a highly loaded, high turning angle planar cascade, and to study the effect of secondary flows on local heat transfer coefficients at representative engine Mach and Reynold's numbers.

The purpose of this paper is to describe the experimental facilities and the preliminary results of this short term research program.

TEST FACILITIES AND TEST METHODS

Transonic Planar Cascade. The planar cascade constructed for this experimental investigation was an exhauster type with six blades and five nozzle passages. The highly loaded, transonic turbine stator blades were scaled to 4.3 times engine size and employed the mid-span profiles of the blades used in the NRC HLTTR. The distinguishing feature of this transonic planar cascade, versus the traditional two-dimensional cascade, was the requirement for three-dimensional flow within the nozzle passages. Though spanwise pressure gradients could not be simulated, the use of an extended inlet bellmouth of 6.67:1 aspect ratio allowed endwall boundary layers to be grown to one-tenth blade span in height, resulting in the classic horseshoe vortices and the associated three-dimensional flows [7]. Adjustable boundary layer bleeds were installed on both sidewalls adjacent to and upstream of the first and sixth blades to remove sidewall boundary layers and developing corner vortices. Variation in periodicity, as measured by the comparison of static pressures at midspan and downstream of the blades making up the centre nozzle passage with those of the two bounding nozzle passages, was less than 0.5 % for the range of cascade operating pressure ratios of 1.07 to 3.0. An adjustable, porous, 3/16 inch thick aluminum tail board allowed fine adjustment in periodicity between nozzle passages and the elimination of shock wave reflection by the tailboard. Tailboard porosity was 23 percent with 3/16 inch holes normal to the tailboard surface on 3/8 inch pitch. Hole depth to diameter ratio was one. The cascade was operated by a 2680 horse power exhauster facility, capable of continuously drawing 10 pounds of air per second at 2 psia. A schematic representation of the planar cascade is given in Figure 2.

Major specifications and design conditions of the planar cascade are as follows:

Blading

Blade chord, C	8.032 in
Axial blade chord, Cx	3.33 in
Blade pitch, S	5.817 in
Blade span, H	4.44 in
Blade aspect ratio, H/C	0.871
Solidity, C/S	0.876
Design turning angle	76 deg
Nozzle throat width	1.215 in
Number of blades	6

Design conditions

Inlet total temperature	70 F
Inlet total pressure	14.7 psia
Pressure ratio	2.3
Inlet Mach Number	.112
Exit Mach Number	1.2
Mass flow rate (total)	8.5 lb/s
Reynolds Number (axial)	213000

Data Acquisition System. The data acquisition system was a Hewlett Packard 3054C Data Acquisition and Control System. L.C. Smith traverse gear, controlled by the HP 3054C system was used to traverse the wedge and total head probes in the pitchwise, spanwise and yaw directions. Static pressures were scanned and measured by a ganged miniature Scanivalve system. Wedge and total head probe pressures were measured with stand alone Statham pressure transducers. Control of the Scanivalve, measurement and recording of the pressure transducers was carried out by the HP 3054C system.

Probes and Probe Calibrations. Inlet boundary layer profiles were measured using a 0.0625 inch diameter total head tube. Downstream total pressures and temperatures were measured with 3/16 inch diameter United Sensor model WT187 wedge probes. Calibration of the wedge probes was carried out at the NRC's National Aeronautical Establishment transonic 5 inch by 5 inch pilot tunnel. Wedge probe calibration extended over a Mach number range of 0.4 to 1.2 with a bias to the transonic region (Ma=0.9 to 1.2). Post processing of these data indicated that the probe total temperature recovery factor, Alpha, was Mach number dependent. Fortunately, data from a previous calibration of two of the wedge probes covering a Mach number range of 0.58 to 0.85 with a few data at a nominal Mach number of 1.5 were available. Data from all the probe calibrations were used in the calculation of a probe recovery factor, Alpha. It was appreciated that this probe recovery factor would be an average value for all the wedge probes, but the trend of Alpha versus Mach number would be more correctly represented. Figure 3 is a plot of Alpha versus Mach number.

Calibration of the copper constantan thermocouples used to measure inlet and exit total temperatures was carried out at the NRC's Division of Physics. Accuracy of the thermocouple calibration was +-0.36 F (20:1 odds) with a resolution of 0.045 F. Accuracy of the differential temperature measurements between exit and inlet total temperatures (DTo) was +- 0.063 F (20:1 odds). Error analysis was carried out using the method of Moffat [8].

Instrumentation. Instrumentation was designed to explore flow angles, total and static pressures and total temperatures. Mass flow through the centre nozzle passage was measured by traversing the inlet or exit flow area over one blade pitch and one half span.

Nozzle inlet conditions were globally defined by comparison of spanwise inlet velocity profiles taken at the five mid-pitch locations between nozzle blades. Detailed investigations of the inlet flow in the centre nozzle passage was permitted by spanwise and pitchwise traversing through a slot upstream of the centre nozzle passage. Measurements were carried out at 60 % axial chord length upstream of the blades.

The two blades bounding the centre nozzle passage were equipped with four static pressure tappings at midspan on the suction surface and one tapping on the trailing edge of the pressure surface at the nozzle throat. Eleven tappings were positioned midway between the two blades on the endwall. Five blades of the cascade had static tappings at 30 % of axial chord to allow measurement of periodicity.

Downstream static pressures were measured by 16 tappings spread over three complete blade pitches and located such that no shock waves covered a tapping at design conditions. These static tappings and the downstream traverse slot were at 23 % axial chord length downstream of the blades. The downstream slot allowed spanwise and pitchwise traverses to be carried out using a wedge probe to measure both total temperature and pressure. The wedge probe total temperature thermocouple was connected electrically in series to a thermocouple measuring the inlet total temperature. Thus change in total temperature between inlet and exit was measured and recorded.

Wedge probe total temperature and pressure ports were limited in approach to the endwall by contact between the wedge probe tip and the endwall. This occurred when the total pressure port and total temperature ports were .164 inches and .078 inches from the endwall. Considerable care was taken to ensure adequate sealing of the traverse slot, and final checks were made with smoke to ensure no detectable leaks were present.

The wedge probe was operated under computer control, being automatically nulled via a binary search routine at each preselected measurement station before readings of probe yaw angle, total temperature and total pressure were recorded. The software allowed a total of 20 spanwise and 20 pitchwise positions to be surveyed; for these experiments 7 uniformly dispersed spanwise positions from the endwall to 55 % of blade span and 17 non uniformly dispersed pitchwise positions (biased to high gradient areas) covering 120 % of blade pitch were surveyed.

Experiments were conducted at 7 nominal pressure ratios ranging from low subsonic to supersonic exit flow conditions. Pressure ratios are as follows: 1.07, 1.20, 1.40, 1.60, 1.90, 2.30 and 3.00.

Local wedge probe static pressures were not used to calculate local Mach numbers as wedge probe calibration results indicated that the wedge probe static pressure tappings read high for Mach numbers greater than 0.4 with errors up to 50 % at a Mach number of 1.2. Calculation of local Mach numbers was carried out with pitchwise variation in static pressure being obtained by linear interpolation amongst the 16 downstream static pressure tappings and constant spanwise static pressure being assumed.

Traverse pitchwise and spanwise positional accuracies were limited by gear play in the L.C. Smith traverse equipment and were estimated (20:1 odds) as +-0.008 inches and +-0.009 inches respectively, whilst yaw positional accuracy based on gear play and the ability of the software to 'null' the wedge probe was estimated at +-0.14 degrees.

The ability to determine gas flow direction from probe yaw angle was more difficult to estimate, as the probe may be 'nulled' in a shear flow but not be pointing into the gas flow. In areas of high shear it is estimated that the measured gas flow direction is within +- 10 degrees, whilst in non-shear flow areas it is estimated that the error in gas flow direction is +-0.14 degrees. An example of this problem is displayed in Figure 4 which is a pitchwise plot of spanwise averaged exit flow angles. The ordinate axis is the distance from the stacking axis of blade number 4, the abscissa axis is the exit flow direction. Flow from the suction surface of the blade is to the left side of the plot. It is readily seen that there is an apparent underturning of the flow from the pressure surface and an apparent overturning of the flow from the suction surface as the probe traverses the blade wake. This apparent underturning / overturning is the result of the probe yawing away from the flow direction as the nulling algorithm nulls the probe's two static pressure taps in the high shear flow associated with the blade wake.

Wedge probe calibration indicated that measurement of total temperature was unaffected by yaw angles up to 30 degrees, whilst measurement of total pressure was more strongly dependent on yaw angle with the wedge probe under estimating the total pressure by 1.8 % at 10 degrees, 7.5 % at 20 degrees and 19 % at 30 degrees. Accuracy of total pressure measurements was estimated to be (20:1 odds) +-0.48 % of total pressure. While the accuracy of the static pressure measurements was estimated at (20:1 odds) +-0.20 % of reading, the assumption of no spanwise static pressure gradient overlooks the fact that the shock waves emanating from the trailing edges of the blades are three dimensional surfaces and errors of the order of magnitude of 40 % in the local static pressure could be present. Due to the disposition of the downstream endwall static pressure taps, and shock waves being a local phenomenon, these uncertainties were expected to affect a small proportion of the readings.

An indication of the errors introduced by errors in flow angles and local static pressure may be seen by comparing the ratio of measured exit to inlet mass flow of the centre nozzle passage as a function of pressure ratios as shown in Table 1 below.

Pressure Ratio	m_2/m_1	Ma
1.2	1.06	0.52
1.4	1.12	0.71
1.6	1.16	0.85
1.9	1.25	1.00
2.3	1.18	1.16

TABLE 1

RESULTS AND DISCUSSION

Inlet Conditions. Inlet turbulence level at midspan was assessed using a constant temperature hot-wire anemometer mounted at midspan and midpitch, 60 % of an axial chord length upstream of the blade leading edges. The measured axial turbulence level was 3 % of the inlet velocity at design conditions. This value is low by actual turbine inlet standards. No provisions were made to increase the turbulence levels by screens or grids as it was felt that turbulence decay rates would be large, introducing additional uncertainties into experimental results.

Inlet traverses were conducted at five mid-pitch locations and 60 % axial chord upstream. The velocity profiles were essentially flat, with boundary layers being 10 % blade span in thickness. A detailed spanwise and pitchwise inlet velocity profile traverse upstream of the centre nozzle passage indicated local flow acceleration due to the proximity of the blade leading edges.

Area and Mass Averaged DTo. Figure 5 is a plot of both area and mass averaged values of DTo versus isentropic exit Mach number. Note the PRs at which the discrepancy between the two curves is the greatest. They are the same PRs that indicated the largest errors in exit mass flow, see Table 1. Though this plot shows an apparent dependence on Mach number of $\overline{DTo}$ it does indicate that $\overline{DTo}$ has an average nominal positive value of 1.6 F. This value of $\overline{DTo}$ may be attributed to heat transfer from the vanes and endwalls of the cascade to the airflow at locally low static temperatures. Infrared pictures were taken of the cascade when operating at a PR of 2.30. These pictures indicated that the cascade was operating 7 F below the ambient temperature due to the above heat loss mechanism. A simple, natural convection calculation was carried out to determine the change in total temperature through the planar cascade due to the heat gain by the planar cascade from the surrounding ambient air. This calculation indicated a change in $\overline{DTo}$ of 1.8 F.

Differential Total Temperature Contours. Figure 6 is a graph of differential total temperature contour plots between the inlet total temperature (nominally 530 R) and the local exit total temperature. The plots are for PRs equalling 1.20, 1.40, 1.60, 1,90, 2.30, 3.00 respectively. These data were taken at 23 % of an axial chord length downstream of the blade row and are plotted as projected on a plane orthogonal to the inlet flow direction. As noted earlier, the data were taken over 55 % of blade span and 120 % of blade pitch with the traversed area being centered at mid-pitch between the two blades bounding the centre nozzle passage. The wake is evident between the pitchwise distances of 0.5 and 2.0 inches. The abscissa axis is the spanwise distance from the cascade endwall along the blade. Midspan is at 2.2 inches. The ordinate axis is the pitchwise distance from the stacking axis of blade number 4. Flow from the suction surface is to the left end of the ordinate. Contour spacing is 2 F over a range of -24 to 14 F. The thick line denotes the zero differential total temperature curve. Contour lines in the centre of the blade wake are always negative indicating that the local total temperature is below the inlet total temperature. Contour values elsewhere are as noted.

It is evident from the plots for PRs of 1.20 to 1.90 that the blade wakes are bowed, with the midspan portion listing to the pressure surface and the endwall wall portion listing to the suction surface. Bowing of the blade wake is not noted in the plots for PR=2.30 and PR=3.00 and the flow patterns better define the blade trailing edge as projected on a surface at 76 degrees. This is attributed to the flow field through the nozzle becoming better defined as the trailing edge shock waves fully develop. Also note that the area of maximum DTo depression migrates from the midspan position to near the endwall and from the pressure surface to the suction surface as the PR increases. The value of the DTo depression becomes greater and achieves a maximum between the pressure ratios of 1.60 and 1.90. It then lessens as sonic and finally supersonic flows are achieved. Table 2 lists the maximum DTo depression as a function of PR.

PR	DTo (F)
1.07	-2.3
1.20	-4.5
1.40	-8.1
1.60	-22.0
1.90	-23.8
2.30	-12.7
3.00	-8.1

TABLE 2

Associated with the depression of DTo in the wakes is the elevation in total temperature at the edge of the blade wakes with DTo rising to values between +4 and +10 F.

A physical mechanism which results in DTo being negative in the blade wake and positive at the sides of the wake is viscous heating of a high speed boundary layer on the blade in which the inner layers of the boundary layer experience a static temperature rise. Assuming an adiabatic blade, the static temperature rise is accompanied by heat conduction and convection away from the blade and out of the boundary layer. The heat conducted and convected away from the blade raises the static temperature of the gas stream outside the boundary layer, resulting in an increase in total temperature outside the boundary layer. The temperature of the blade surface when steady state is achieved, will be at the adiabatic wall temperacure. Noteworthy is the fact that at the blade surface the velocity is zero and thus the adiabatic wall temperature is equal to the local total and static temperatures.

$$Taw=Ts(0)=To(0) \qquad \text{at } y=0$$

Thus, within the boundary layer, local total temperature is depressed relative to the freestream total temperature. Extrapolation of this concept leads to the conclusion that the expected minimum total temperature of the wake behind the blade will be Taw.

Figure 7 is an illustration of non-dimensional Ts* and To* approaching an adiabatic wall. The illustration is composed of two graphs. The left graph is a plot of the velocity profile. The right graph is a plot of the non dimensional temperatures Ts* and To*. The To* profile, a function of Ts* profile outside the boundary layer for a constant velocity distribution and a function of the velocity and Ts* profile inside the boundary layer, displays the anticipated behaviour. The To* profile displays an increase in value at $y/\delta=3$, reaching a maximum at $y/\delta=.8$ and then falling in value to Taw at $y/\delta=0$.

In order to compare the simple theory outlined above with experimental results, DTo may be defined for a given Mach number as follows:

$$DTo=Taw-To_{\infty} \qquad (1)$$

The recovery factor Rf, used to describe the relationship between the freestream total (To_{∞}) and static (Ts_{∞}) temperatures and the adiabatic wall temperature (Taw), is redefined as follows:

$$Rf=(Taw-Ts_{\infty})/(To_{\infty}-Ts_{\infty}) \qquad (2)$$

Combining equations 1 and 2 with the following isentropic relationship,

$$To_{\infty}/Ts_{\infty}=1+((k-1)/2)Ma^2 \qquad (3)$$

the following equation relating DTo to Rf and Ma may be derived,

$$DTo=To_{\infty}(Rf-1)(1-(1+((k-1)/2)Ma^2)^{-1}) \qquad (4)$$

Figure 8 displays two plots, firstly a plot of equation 4 with Rf=.88, a nominal Rf value for flat plates, [9] and secondly, the minimum measured values of DTo in the blade wakes for seven values of PR studied. The ordinate is the isentropic exit Mach number and the abscissa is DTo in degrees F. The experimental and theoretical data display the same trend for $0 < Ma < 0.7$, although the experimental data are more depressed. The experimental data at $0.7 \leqslant Ma < 0.95$ plunge and reach values three times lower than the theory would indicate. At Ma=0.95 the experimental data rise rapidly to values much less negative than theory would indicate. This is to be expected as the present data are taken downstream of the blade trailing edges and as such the wake total temperature will be partially mixed out. The pattern displayed by DTo versus Ma is similar to that displayed by the area averaged values of Cpo versus Ma shown in Figure 9. These extreme excursions in the data are associated with the flow field developing a boundary layer / shock wave system associated with supersonic flow.

Figures 10 and 11 are graphs of DTo versus pitchwise position and DTo versus spanwise position respectively. In the spanwise direction the values of DTo are predominantly positive and increasing in value from the endwall to midspan. There is some dependence on PR, with the midspan values of DTo for PRs of 1.60 and 1.90 becoming negative whilst the midspan values for the other PRs are all positive.

Comparison of the two Figures reveals that considerable variation of DTo occurs in the pitchwise direction, with the depth of the negative depression in the blade wake and the elevation of DTo in the positive direction on either side of the blade wake strongly PR dependent. This variation in the pitchwise direction is up to an order of magnitude larger than variation in the spanwise direction. It is noteworthy that the shape of the curves has the same form as that shown in Figure 7; that is, the DTo distribution becoming positive as the wake is approached and then going negative as the wake is entered, reaching a maximum negative value at mid-wake. This distribution of total temperature through the wake is similar to the distribution of total temperature found within the Ranque-Hilsch vortex tube [10,11,12]. It is interesting to note that although the vortex flow is rotational in nature, both wake and vortex flows are characterised by high shear flow phenomenon.

Differential Total Pressure Loss Contours. Figure 12 is a graph of total pressure loss coefficient contour plots, displayed in similar fashion to the previous group of Figures. Total pressure loss coefficient is defined as follows:

$$Cpo=(Po1-Po2)/(Po1-Psm2)$$

The downstream mean static pressure Psm2, is obtained by area averaging the readings from the downstream wall static pressure taps. Contour spacing is 0.05 with a range of 0.05 to 0.6.

Trends in the distribution of Cpo are identical in nature to the DTo trends outlined above, with the areas of maximum Cpo mapping onto the areas of maximum DTo depression. Secondary flow losses associated with the passage vortex on the suction surface are very distinct for PRs up to 1.90 but disappear as the flow becomes sonic.

Migration of the maximum loss area from the midspan to the endwall region can be explained by using Figure 9 which is a plot of area averaged Cpo versus isentropic Mach number. In a planar cascade, there is no radial pressure gradient and the flow could be expected to initially become sonic at mid passage. Figure 9 displays that as the flow approaches and exceeds Mach 1 the losses decrease in magnitude; thus, as the flow becomes sonic from the midspan area outward to the endwalls, the maximum loss area preceds the sonic zone's growth.

CONCLUSION

An exit survey of a transonic cold flow planar cascade with highly loaded, high turning stator blades has shown that there is modification to the uniform inlet total temperature distribution resulting in a radically redistributed total temperature profile at exit. The redistribution of the total temperature profile is strongly Mach number dependent with maximum redistribution taking place just prior to the flow becoming supersonic. The maximum negatively depressed values of DTo differ from those calculated by preliminary analysis and indicate that the depressions are not just a function of adiabatic wall temperature. Pitchwise variation of DTo is up to an order of magnitude larger than the spanwise variation. The area of maximum negative depression in the DTo contour plots is at the same position as the area of maximum Cpo losses, which indicates the depression in DTo is linked to the production of entropy. The exit contour plots of DTo map one to one with the exit contour plots of Cpo. As the data were produced by independent measurements, this confirms that the redistribution of total temperature is a real phenomenon and not a measurements problem. The variation of area average Cpo

versus Ma indicate that the losses increase as the flow attains high subsonic speeds and then decrease abruptly, once supersonic flow is attained.

REFERENCES

1 Moustapha, S.H. and Williamson, R.G., 1986,
"Effect of Two Endwall Contours on the Performance of a Annular Nozzle Cascade",
AIAA Journal, Vol 24, No. 9, pp 1524-1530.

2 Moustapha, S.H., Okapuu, U., and Williamson, R.G., 1987,
"The Influence of Rotor Blade Aerodynamic Loading on the Performance of a Highly Loaded Turbine Stage",
ASME Journal of Turbomachinery, Vol 109, No. 2, pp 155-162.

3 Williamson, R.G., and Moustapha, S.H., 1986,
"Annular Cascade Testing of Turbine Nozzles at High Exit Mach Numbers"
Journal of Fluids Engineering, Vol 108, No. 3, pp 313-320.

4 Williamson, R.G., and Moustapha, S.H. and Huot, J.P., 1986,
"The Effect Of a Downstream Rotor on the Measured Performance of a Transonic Nozzle",
ASME Journal of Turbomachinery, Vol 108, No. 2, pp 269-274.

5 Williamson, R.G., Moustapha, S.H., Hout, J.P. and Okapuu, U., 1987
"A Research Program on the Aerodynamics of a Highly Loaded Turbine Stage"
AGARD PEP CP-421, pp 9-1 to 9-16.

6 Schaub, U.W., Williamson, R.G., Huot, J.P. and Moustapha, S.H. "An Experimental Assessment of the Influence of Downstream Conditions on the Performance of a Transonic Turbine Nozzle",
ASME Gas Turbine and Aeroengine Congress and Exposition, June 4-8, 1989, Toronto, Ontario, Canada. Paper 89-GT-283.

7 Sieverding, C.M., 1985,
"Recent Progress in the Understanding of Basic Aspects of Secondary Flow in Turbine Blade Passages",
ASME Journal of Engineering for Gas Turbine and Power, Vol 109, pp 229-236.

8 Moffat, R.J., 1988,
"Describing the Uncertainties in Experimental Results"
Experimental Thermal and Fluid Science 1988

9 Schapiro, A.H.,1953,1954,
"The Dynamics and Thermodynamics of Compressible Fluid Flow",
The Ronald Press Company, Volumes I and II.

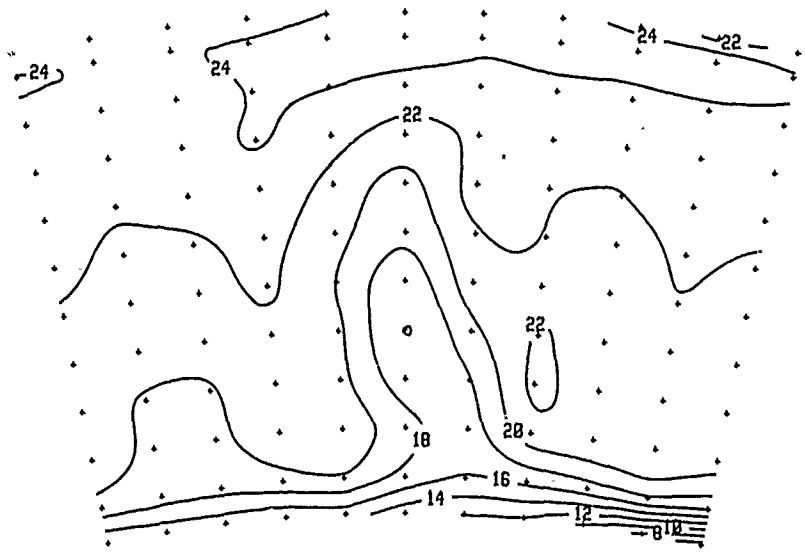
10 Westley, R., 1954,
"A Bibliography and Survey of the Vortex Tube",
The College of Aeronautics,Cranfield
Note No. 9, March, 1954.

11 Collins, R.L., Lovelace, R.B., 1979,
"Experimental Study of Two-Phase Propane Expanded through the Ranque-Hilsch Tube"
ASME Journal of Heat Transfer, Vol 101, pp 300-305.

12 Balmer, R.T., 1988,
"Pressure-Driven Ranque-Hilsh Temperature Seperation in Liquids"
Journal of Fluids Engineering, Vol 110, pp 161-164.

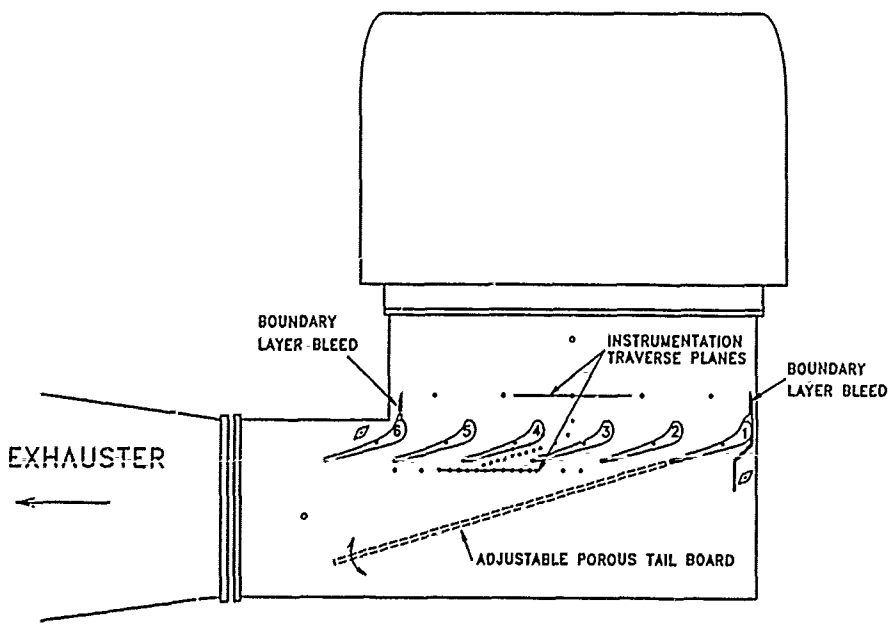
ACKNOWLEDGMENTS

The authors are indebted to Drs. R.G. Williamson and M.K.Y. Lai for their valuable input and encouragement in the evaluation of these results, to Messrs. P.S. Hunt, M. McMullin and B.J. Day for their assistance in the design, assembly and operation of the facility, to Mr. M. Klein for his assistance in securing the experimental data and to Mr. P.Ouellette for his assistance in the preparation of the graphics.



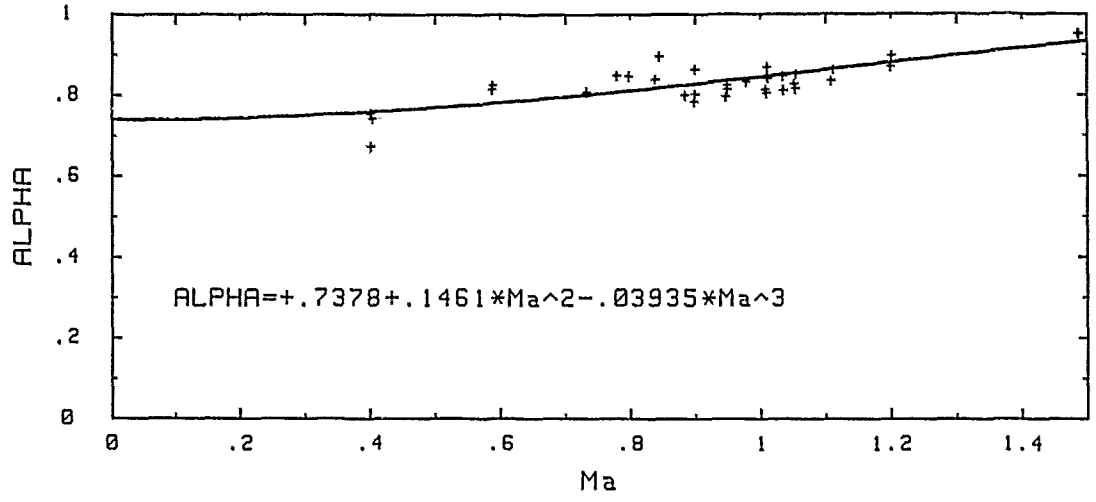
CONTOUR PLOT OF TOTAL TEMPERATURE AT STATOR EXIT

FIG. 1



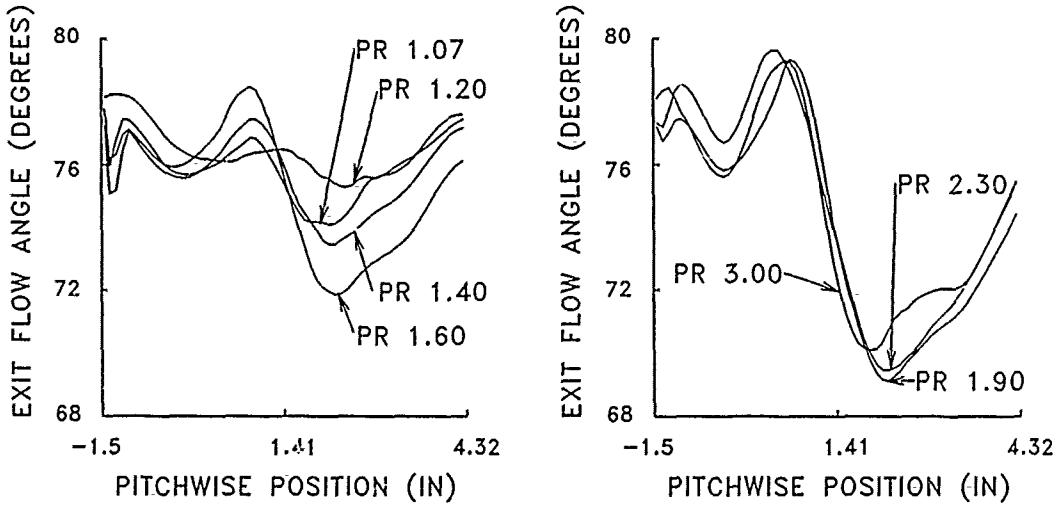
CASCADE

Fig.2



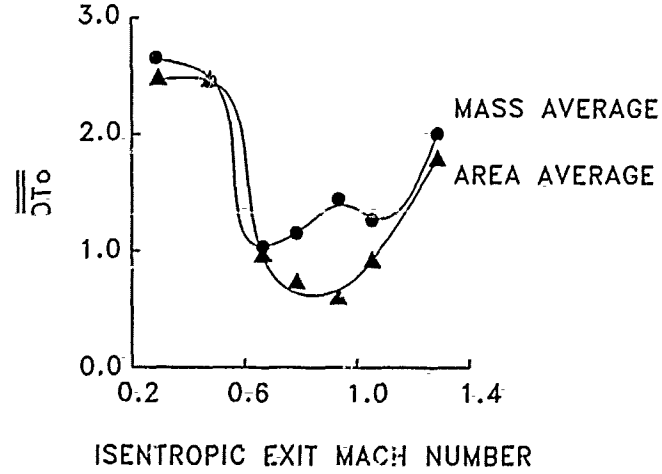
ALPHA vs Ma

FIG. 3



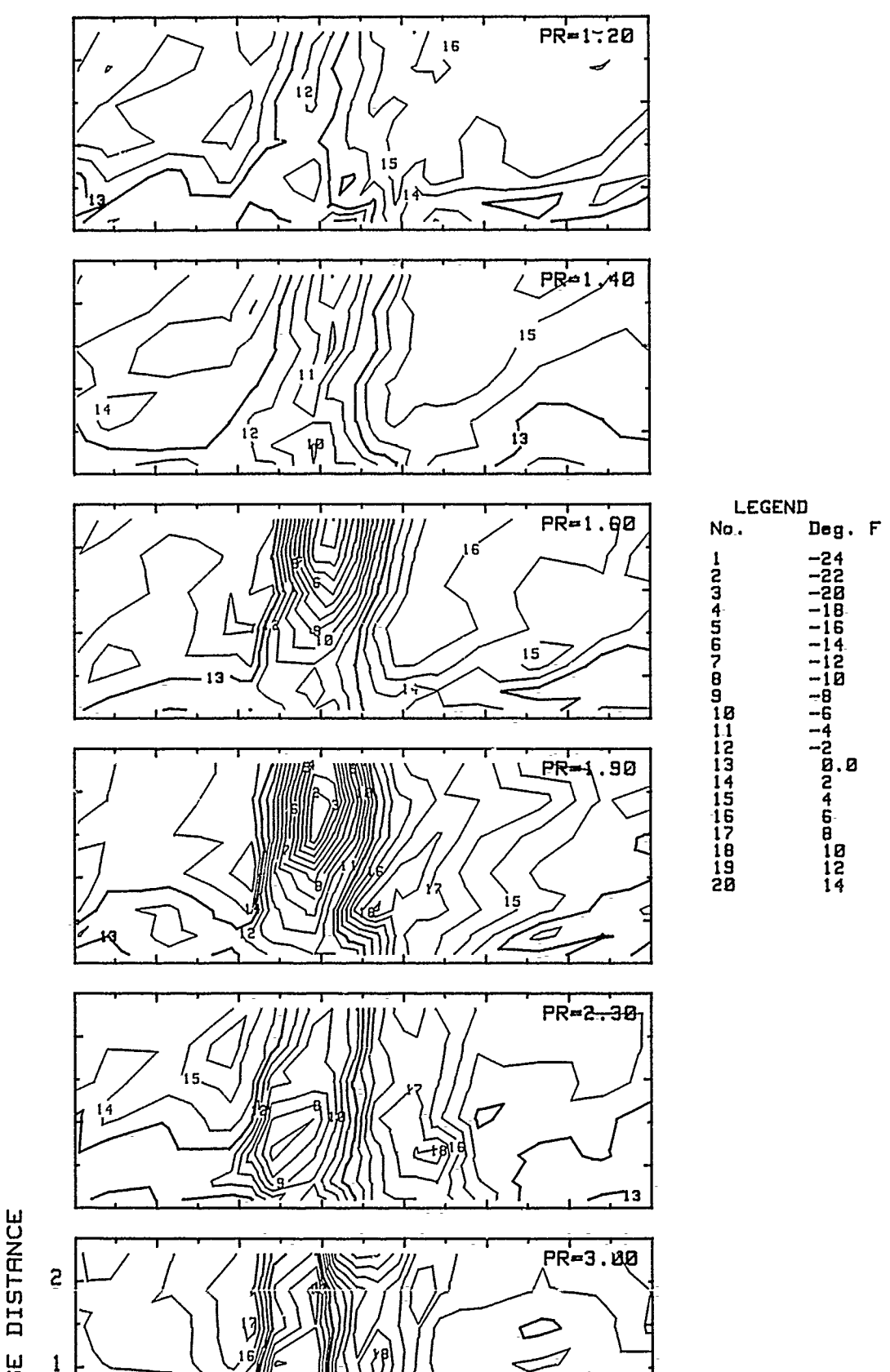
EXIT FLOW ANGLE vs PITCHWISE POSITION

FIG. 4



AVERAGE DTo vs ISENTROPIC EXIT MACH NUMBER

FIG. 5



CONTOUR PLOT OF CHANGE IN TOTAL TEMPERATURE

FIG. 6

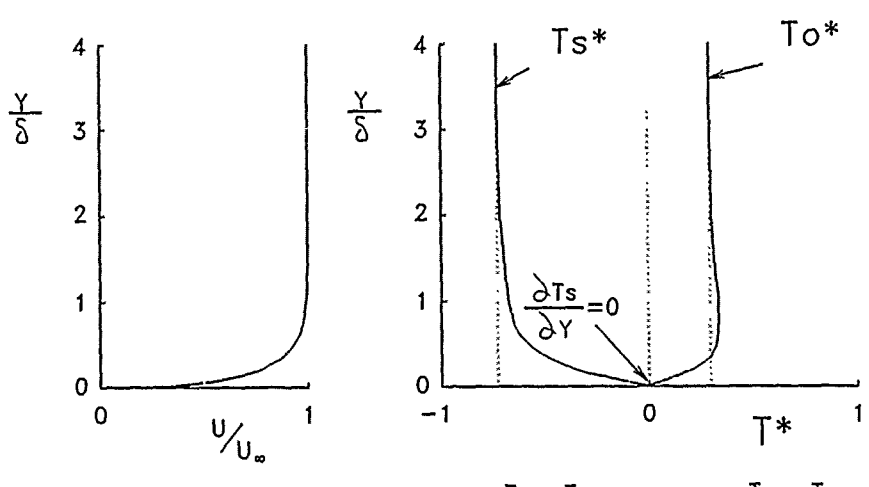
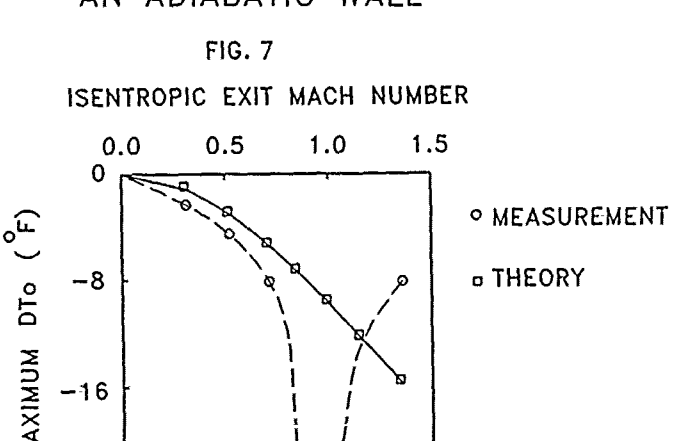


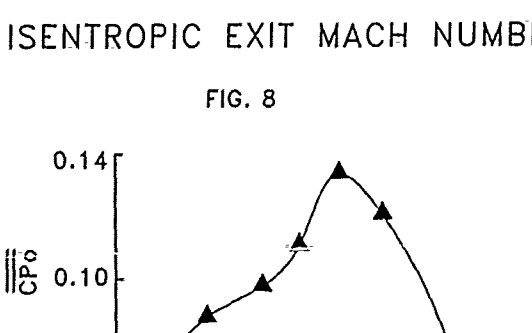
ILLUSTRATION OF Ts* AND To* DISTRIBUTION APPROACHING AN ADIABATIC WALL

FIG. 7



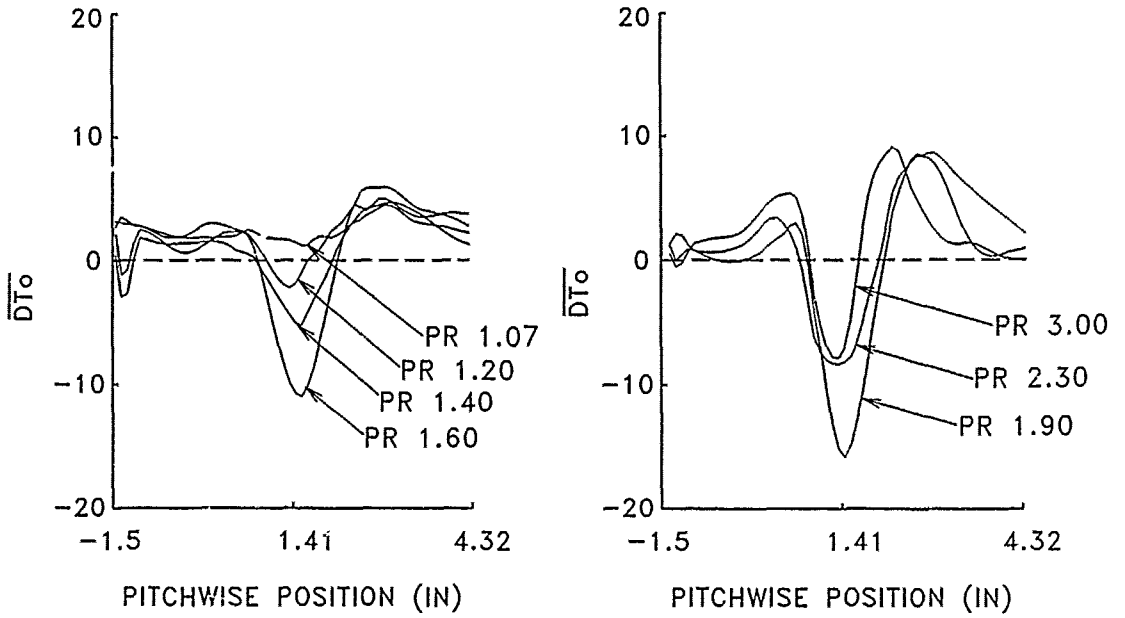
MAXIMUM TOTAL TEMPERATURE DIFFERENTIAL vs ISENTROPIC EXIT MACH NUMBER

FIG. 8



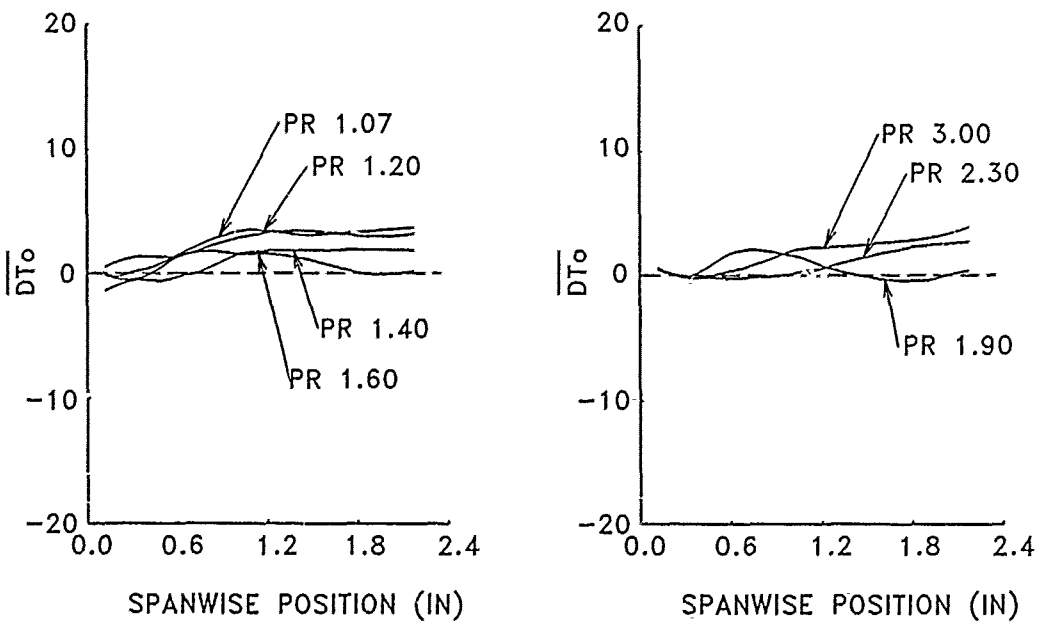
AREA AVERAGE CPo vs ISENTROPIC EXIT MACH NUMBER

FIG. 9



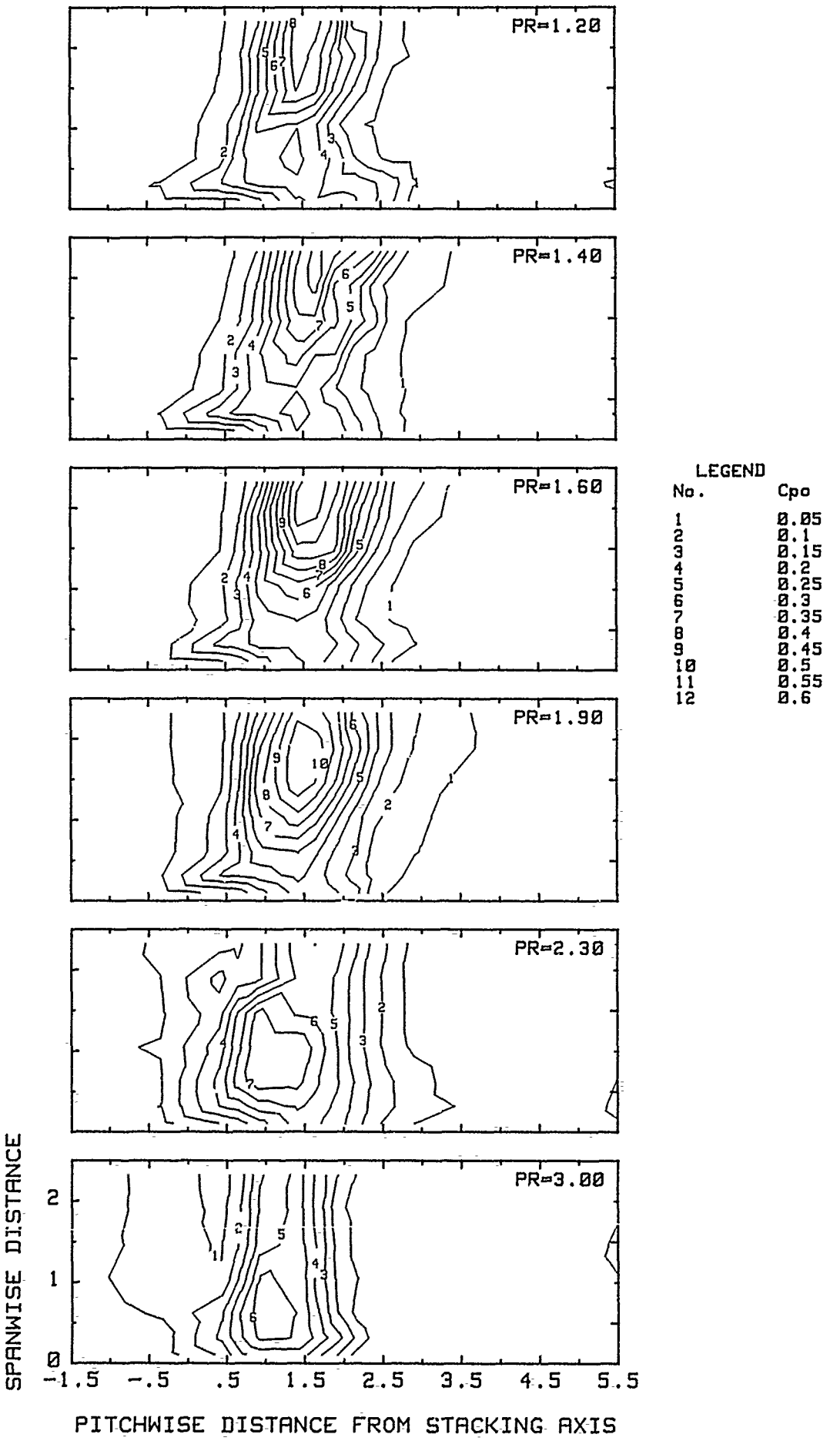
TOTAL TEMPERATURE DIFFERENCE vs PITCHWISE POSITION

FIG. 10



TOTAL TEMPERATURE DIFFERENCE vs SPANWISE POSITION

FIG. 11



CONTOUR PLOT OF TOTAL PRESSURE LOSS DISTRIBUTION

FIG. 12

DISCUSSION

Epstein, USA

Your temperature nonuniformity results can be completely explained by the presence of a spanwise vortex street in the blade wakes. These vortices have been observed in essentially every turbomachine in which they have been looked for, both turbines and compressors. The vortices, whose strength varies with the wake width, and the square of the Mach Number, generate intense cold spots due to unsteady flow (they move at a velocity different both from the mean freestream and the wake) - temperature depressions as low as 80 C for a 300 K mean flow temperature have been observed in vortex cores in the wake of airfoils at a freestream Mach Number of 1.4. The presence of the row of vortices has the effect of depressing the mean temperature of the wake - as is well known from cylinder studies going back to Eckert in the 1930's. The spanwise variation is caused by radial transport in the vortex cores. This topic has been addressed by Kurosaka in JFM, Epstein in JofP(AIAA), and an MIT Thesis of Kotedis, among others. Also, the Ranque - Hilsch tube operates due to unsteady pressure (acoustic) forces as pointed out by Kurosaka. Similar phenomena exist in your experiment in each blade wake.

Author's Reply:

I would like to thank Dr. Epstein for his comments and excellent references. Having reviewed the references I think it is premature to state "your temperature non uniformity results can be completely explained by the presence of a spanwise vortex street in the blade wakes....". My reasons are as follows:

The original work of Eckert and Weise [A1, A2] concerned the circumferential variation of local adiabatic surface temperature on a cylinder immersed in a high subsonic air stream. Eckert and Weise determined that the recovery factor (based on upstream conditions and the adiabatic surface temperature) became negative at the trailing edge of the cylinder. The theory proposed by Kurosaka et al [A3] to explain the "Eckert-Weise Effect"; that is "the time-varying static pressure field due to the vortex movement separates the instantaneous total temperature into hot and cold spots located around vortices; once time-averaged, however, the total temperature distribution conceals the presence of hot spots and takes the guise of a colder wake"; assumes a-priori that the disposition of the total temperature on the cylinder should be mimicked in the flow. I believe that the disposition of total temperature about the cylinder is a local effect caused by the interaction of the cylinder boundary layer and fluctuating wake. This would also be true for the results of Thomann [A4] who extended the work of Eckert and Weise to included contour plots of the recovery factors on the endwall of his test facility.

Another area of concern I have with the theory proposed by Kurosaka et al is the ability to generate a time-averaged flow in which the total temperature is depressed within in the wake without a concomitant area of elevated total temperature. This appears to violate the law of energy conservation.

The data (Figures 6, 10) distinctly display an area of depressed total temperature in the wake and a concomitant area of elevated total temperature at the outside edges of the wake and into the passage flow. It should be pointed out that my data are time-averaged not timeresolved. Figure F1 is a contour plot of the recovery factors displayed in a similar fashion to Figures 6 and 12. The recovery factor is defined as:

$$Rf=(Towp - Ts)/(To-Ts)$$

Where Towp is the corrected wedge probe total temperature. The other variables are defined as in the paper. It is readily apparent that the recovery factor is less than 1.0 in the wakes indicating that the local wake total temperature is less than the upstream total temperature whilst at the edge of the wake and into the flow the recovery factors are greater than 1.0 indicating an area of elevated total temperature as is expected. This topography of total temperature is similar in nature to that found on a flat plate exposed to a high speed flow, to the Ranque-Hilsch tube and other examples as pointed out by Eckert [A2]. This total temperature topography is not supported by the theory of Kurosaka et al.

The final area of concern I have is your comment (attributed to McCune) that the vorticies strength vary with the square of the Mach Number. Specifically you state [A5]: "He shows that the pressure field fluctuations from the vortices change the total temperature distribution in the fluid and that the amplitude of this effect scales with the square of the freestream Mach number". Thus, one can conclude that the total temperature depression in the blade wake should follow a Mach Number trend, and in fact, should vary as the square of the Mach number. If one combines the Mach number data from Table 1 and the local total temperature differential between exit and inlet data (DTo) from Table 2 it is apparent that the data does have a Mach number trend, but, hardly one describing a second order relationship.

In conclusion I do not think that my data may be "completely" explained by the theories proposed to date. There is ample evidence to support that the energy separation is caused by the effects of unsteady pressures and is enhanced by resonance (acoustic or ultrasonic, McDuffie [A6]). There is still no unified theory that explains all the results published to date and thus the explanation for energy separation still eludes us.

REFERENCES

A1 Eckert, E.R.G., 1984, "Experiments on Energy Separation in Fluid Streams," Mechanical Engineering, October 1984, pp. 58-65.

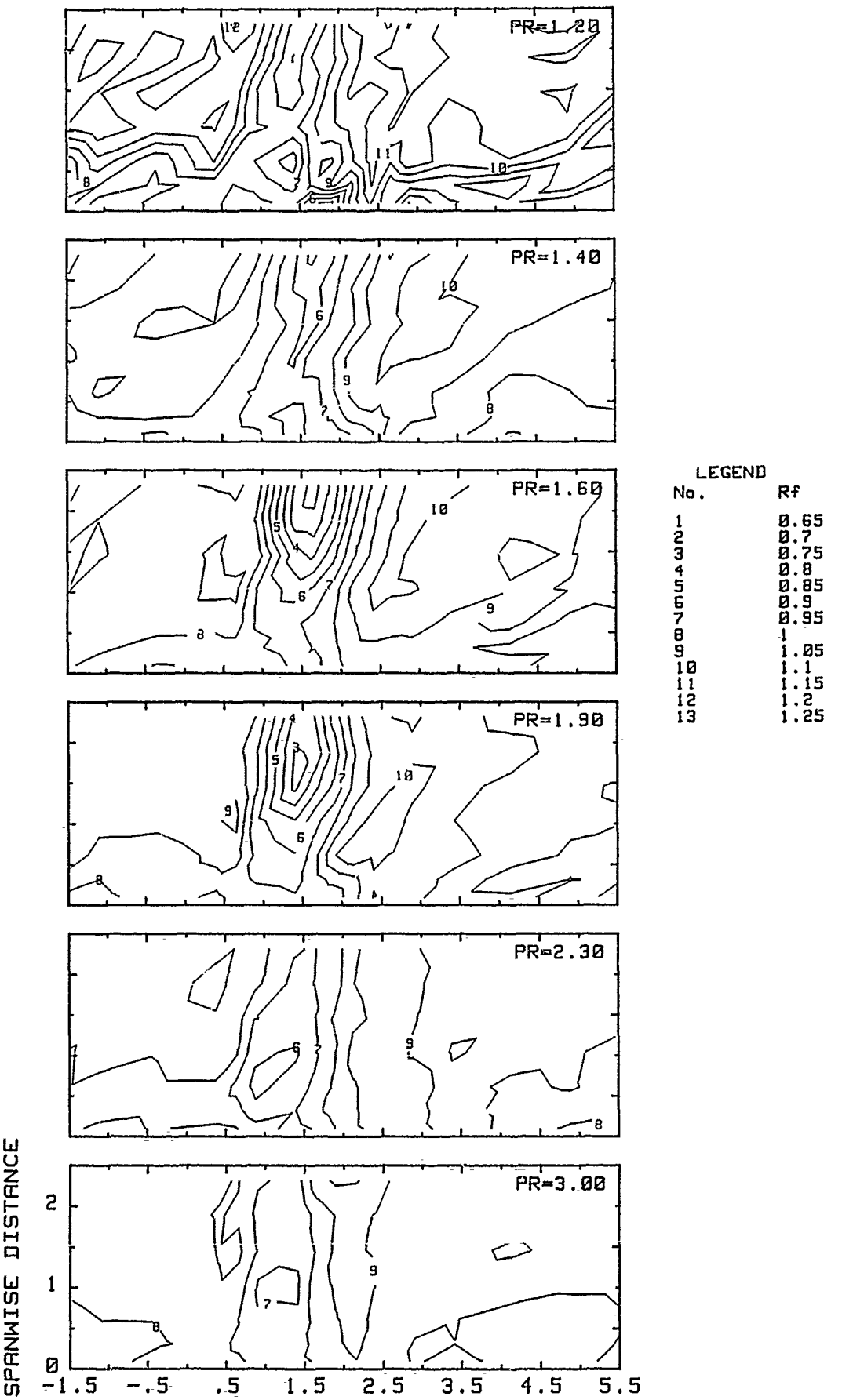
A2 Eckert, E.R.G., 1986, "Energy Separation in Fluid Streams," International Committee on Heat and Mass Transfer, Vol 13," 1986, pp. 127-148.

A3 Kurosaka, M., Gertz, J. B., Graham, J. E., Goodman, J. R., Sundaram, P., Riner, W. C., Kuroda, H., Hankey, W. L., 1987, "Energy Separation in a Vortex Street," Journal of Fluid Mechanics, Vol 178, pp. 1-29.

A4 Thomann, H., 1959, "Measurement of the Recovery Temperature in the Wake of a Cylinder and of a Wedge at Mach Numbers Between 0.5 and 3," FFA Report 84, Stockholm, 1959.

A5 Epstein, A. H., Gertz, J. B., Owen, P. R., Giles, M. B., 1988, "Vortex Shedding in High-Speed Compressor Blade Wakes," Journal of Propulsion, Vol 4, No. 3, 1988, pp. 236-244.

A6 McDuffie, N. G., 1979, "Resonance in a Ranque-Hilsch Vortex Tube," ASME Journal of Heat Transfer, 79-HT-16.



CONTOUR PLOT OF RECOVERY FACTOR DISTRIBUTION

FIG. F1

Hennecke, Germany

I want to support Dr. Epstein's written comment. Cases with total temperature redistribution are, for instance, the flat plate in high speed flow (your fig. 7) or the Hilsch tube. Relevant to this case, however are the results for cylinders in cross flow where the unsteady pressure fluctuations due to Von Karman vortex streets cause regions of increased and decreased total temperature. A relevant paper was recently published by E.R.G. Eckert where the mechanism is explained. I think the results can be applied to your cascade.

Author's Reply:

Thank you for your comments, I will obtain the paper you have referenced and review it.

Moore, USA 27-3

From the discussions of Professors Epstein and Henneke, it is not clear whether this redistribution of total temperature has ever been measured before in a turbine blade row. Can the discussors and the author please clarify this point?

Author's Reply:

AUTHOR - I have been unable to find any reference to the redistribution of total temperature downstream of a turbine blade row. I would like to point out that Dr. R.G. Williamson, who observed this phenomenon, in the early 1980s, at the NRC on data taken on the Highly Loaded Turbine Test Rig, was also unable to find any published references.

L. FOTTNER - As far as I know there is no information on this problem for actual turbine cascades.

D. HENNECKE - I have not seen those results on a turbine cascade either. My comment referred to a cylinder in cross flow.

Sieverding, Belgium

What are the physical reasons for the temperature rise outside of the wake? Could you make some comments on the probe blockage effect? Did the probe span the full blade height for all traverses or was it gradually immersed. In the latter case the blockage effect increases with increasing immersion of the probe into the channel.

Author's Reply:

I attribute the elevated temperatures outside of the wake to turbulent convection from the heated wake boundaries to the main stream.

The effect of probe blockage was assumed to be minimal due to the large scale of the facility (4.3 times engine size). Investigations carried out by Schaub et al (see ref. 6) on the NRC Highly Loaded Turbine Test Rig (HLTTR) showed that the probe affected the static pressure distributions on the downstream suction surface of the blades. This effect is dependent on both the pitchwise and spanwise location of the probe. The design of the planar cascade was based on the HLTTR which was designed to a nominal three times engine scale and there must be some effects due to probe blockage, but I am unable quantify them. The traverses were initiated with the probe fully immersed ie. 100% of the blade span, as the traverse

progressed the probe was retracted until at the end of the traverse the probe had been retracted 55% of blade span.

Jones, UK

I am not aware of the relative humidity in your laboratory but it is possible that as the air passing through the cascade came from the laboratory without drying that condensation may have taken place. These effects can have an influence on the flow prior to the formation to condensation shocks.

Author's Reply:

The potential problem of condensation shocks was addressed in the design of the planar cascade. The method of Smoulderen (1956) was used to determine if condensation shocks would occur within the cascade when drawing air from the laboratory. The result of this study was negative i.e., no condensation shocks would occur. As pointed out in the Introduction of my paper, R.G. Williamson in his investigations on the HLTTR found a redistribution of the total temperature profile for both cold and hot gas tests ie. the inlet air was heated to a temperature such that the static temperature of the air leaving the turbine nozzle cascade was at ambient room temperature, thus alleviating the condensation problem.

Weyer, Germany

We have to fulfill the energy conservation laws! Thus, did you check - by integration - the total energy at inlet and outlet and do they agree to each other?

In a highly turbulent or fluctuating flows that turn in a curved channel, normal pressure gradients initiate an unmixing process of high speed and low-speed (turbulent or fluctuating) flow spots; this might lead to distinct energy or total temperature distributions as shown.

Author's Reply:

Yes, I did attempt, by integration to compare the inlet and outlet total energy. Unfortunately, in high shear flows the wedge probe when used to measure total pressure and temperature may be nulled very accurately, but unfortunately did not point in the gas flow direction. This lead to errors in the computed local mass flow (this is shown in Table 1). Thus I was unable to compare the inlet and exit total energy flow. I did compare the area weighted energy and ascribed the small difference in total temperature to heat transfer from the laboratory to the cascade.

REPORT DOCUMENTATION PAGE

1. Recipient's Reference	2. Originator's Reference	3. Further Reference	4. Security Classification of Document
	AGARD-CP-469	ISBN 92-835-0544-1	UNCLASSIFIED

5. Originator	Advisory Group for Aerospace Research and Development North Atlantic Treaty Organization 7 rue Ancelle, 92200 Neuilly sur Seine, France
6. Title	SECONDARY FLOWS IN TURBOMACHINES
7. Presented at	the Propulsion and Energetics Panel 74th (A) Specialists' Meeting, held in Luxembourg, 30 August—1 September 1989.

8. Author(s)/Editor(s)	9. Date
Various	February 1990
10. Author's/Editor's Address	**11. Pages**
Various	356

12. Distribution Statement	This document is distributed in accordance with AGARD policies and regulations, which are outlined on the Outside Back Covers of all AGARD publications.

13. Keywords/Descriptors

Turbine blades;
Cascades fluid dynamics;
Compressors;
Computation of 3D flow
End wall flow;
Heat transfer
Computational fluid dynamics;
Tip Leakage flow;
Secondary flow;
Tip clearance flow
Turbines guide vanes (EDC)
Turbomachines

14. Abstract

These proceedings contain

The Conference Proceedings contains the 24 papers presented at the Propulsion and Energetics Panel 74th *B* Specialists' Meeting on "Secondary Flows in Turbomachines", which was held 30 August—1 September 1989 in Luxembourg.

The Specialists' Meeting was arranged in the following sessions: Basic Flow Phenomena (6); Experimental Results (5); Three-Dimensional Computation and Comparison with Experiments (5); Tip Clearance Flows (4); and Secondary Flow Effects on Heat Transfer (4). The Technical Evaluation Report is included at the beginning of the Proceedings. Questions and answers of the discussions follow each paper.

The Specialists' Meeting offered a forum for experts to discuss on computational and experimental methods and results for secondary flow in cascades, compressors and turbines. CFD was found to be an adequate tool to represent qualitative phenomena, but on the accuracy of predicting losses and exit angles there was some disagreement. Many papers dealt with experimental investigations which are obviously essential for evaluating secondary flow models.

Keywords: Three dimensional flow computations; Cascade structures; Axial flow compressors; Airfoils; Turbulent flow/Mixing; Nozzle guide vanes; Transonic nozzles. Aspect ratio. Centrifugal impellers; Radial compressors; Blade tips;

AGARD Conference Proceedings No.469 Advisory Group for Aerospace Research and Development, NATO SECONDARY FLOWS IN TURBOMACHINES Published February 1990 356 pages The Conference Proceedings contains the 24 papers presented at the Propulsion and Energetics Panel 74th *B* Specialists' Meeting on "Secondary Flows in Turbomachines" which was held 30 August—1 September 1989 in Luxembourg. The Specialists' Meeting was arranged in the following sessions: Basic Flow Phenomena (6); Experimental Results (5); Three-Dimensional Computation and P.T.O.	AGARD-CP-469 Cascades Compressors Computation of 3D flow End wall flow Heat transfer Leakage Secondary flow Tip clearance flow Turbines Turbomachines	AGARD Conference Proceedings No.469 Advisory Group for Aerospace Research and Development, NATO SECONDARY FLOWS IN TURBOMACHINES Published February 1990 356 pages The Conference Proceedings contains the 24 papers presented at the Propulsion and Energetics Panel 74th *B* Specialists' Meeting on "Secondary Flows in Turbomachines" which was held 30 August—1 September 1989 in Luxembourg. The Specialists' Meeting was arranged in the following sessions: Basic Flow Phenomena (6); Experimental Results (5); Three-Dimensional Computation and P.T.O.	AGARD-CP-469 Cascades Compressors Computation of 3D flow End wall flow Heat transfer Leakage Secondary flow Tip clearance flow Turbines Turbomachines
AGARD Conference Proceedings No.469 Advisory Group for Aerospace Research and Development, NATO SECONDARY FLOWS IN TURBOMACHINES Published February 1990 356 pages The Conference Proceedings contains the 24 papers presented at the Propulsion and Energetics Panel 74th *B* Specialists' Meeting on "Secondary Flows in Turbomachines" which was held 30 August—1 September 1989 in Luxembourg. The Specialists' Meeting was arranged in the following sessions: Basic Flow Phenomena (6); Experimental Results (5); Three-Dimensional Computation and P.T.O.	AGARD-CP-469 Cascades Compressors Computation of 3D flow End wall flow Heat transfer Leakage Secondary flow Tip clearance flow Turbines Turbomachines	AGARD Conference Proceedings No.469 Advisory Group for Aerospace Research and Development, NATO SECONDARY FLOWS IN TURBOMACHINES Published February 1990 356 pages The Conference Proceedings contains the 24 papers presented at the Propulsion and Energetics Panel 74th *B* Specialists' Meeting on "Secondary Flows in Turbomachines" which was held 30 August—1 September 1989 in Luxembourg. The Specialists' Meeting was arranged in the following sessions: Basic Flow Phenomena (6); Experimental Results (5); Three-Dimensional Computation and P.T.O.	AGARD-CP-469 Cascades Compressors Computation of 3D flow End wall flow Heat transfer Leakage Secondary flow Tip clearance flow Turbines Turbomachines

Comparison with Experiments (5); Tip Clearance Flows (4); and Secondary Flow Effects on Heat Transfer (4). The Technical Evaluation Report is included at the beginning of the Proceedings. Questions and answers of the discussions follow each paper.

The Specialists' Meeting offered a forum for experts to discuss on computational and experimental methods and results for secondary flow in cascades, compressors and turbines. CFD was found to be an adequate tool to represent qualitative phenomena, but on the accuracy of predicting losses and exit angles there was some disagreement. Many papers dealt with experimental investigations which are obviously essential for evaluating secondary flow models.

ISBN 92-835-0544-1

Comparison with Experiments (5); Tip Clearance Flows (4); and Secondary Flow Effects on Heat Transfer (4). The Technical Evaluation Report is included at the beginning of the Proceedings. Questions and answers of the discussions follow each paper.

The Specialists' Meeting offered a forum for experts to discuss on computational and experimental methods and results for secondary flow in cascades, compressors and turbines. CFD was found to be an adequate tool to represent qualitative phenomena, but on the accuracy of predicting losses and exit angles there was some disagreement. Many papers dealt with experimental investigations which are obviously essential for evaluating secondary flow models.

ISBN 92-835-0544-1

Comparison with Experiments (5); Tip Clearance Flows (4); and Secondary Flow Effects on Heat Transfer (4). The Technical Evaluation Report is included at the beginning of the Proceedings. Questions and answers of the discussions follow each paper.

The Specialists' Meeting offered a forum for experts to discuss on computational and experimental methods and results for secondary flow in cascades, compressors and turbines. CFD was found to be an adequate tool to represent qualitative phenomena, but on the accuracy of predicting losses and exit angles there was some disagreement. Many papers dealt with experimental investigations which are obviously essential for evaluating secondary flow models.

ISBN 92-835-0544-1